The frozen tropics: an investigation into palaeoglaciations within northern Perú

Ethan Lee

BSc, MSc

Thesis submitted for the degree of

Doctor of Philosophy

School of Geography, Politics and Sociology

Newcastle University

April 2024

The candidate confirms that the work submitted is his own, except where work which has formed part of jointly authored publications has been included. The contribution of the candidate and the other authors to this work has been explicitly indicated below. The candidate confirms that appropriate credit has been given within the thesis where reference has been made to the work of others.

The work presented in Chapter 3 of this thesis has appeared in the following publication:

Lee, E., Ross, N., Henderson, A.C.G., Russell, A.J., Jamieson, S.S.R. and Fabel, D. (2022) 'Palaeoglaciation in the Low Latitude, Low Elevation Tropical Andes, Northern Perú', *Frontiers in Earth Science*, 11. DOI: 10.3389/feart.2022.838826

> EL designed the study and led the work; NR, AH, AR, SJ and DF provided guidance on the conceptualisation, research analysis and content, manuscript structure and suggested figures. AH, AR and NR conducted field reconnaissance of the study area prior to this research. EL conducted the data collection and analysis, led the writing of the manuscript and creation of the figures. NR, AH, AR, SJ and DF contributed to the interpretation and discussion of the results and aided in reviewing and editing the manuscript.

Covid-19 Impact Statement

The Covid-19 pandemic has severely disrupted this PhD project. The most affected aspect of this PhD was the fieldwork, crucial for the acquisition of geochronological data. Field work was initially planned to be conducted at the end of 2020, beginning of 2021. Due to the UK national lockdown, and international health warnings, along with other lockdowns within Perú, this was delayed until January 2023. The late timing of the fieldwork, within the final year of my PhD, resulted in significant delay in the collection of samples for lab analysis for the generation of a geochronology of my study site. Furthermore, shortly after the collection and analysis of samples, the Accelerator Mass Spectrometer (AMS) at the Scottish Universities Environmental Research Centre (SUERC) developed mechanical issues. This has delayed the ability for me to receive dates in a timely fashion and has only exacerbate the effects Covid-19 had on my PhD project.

The inability to collect samples in a timely manner has had a cascading effect on the content and focus of my thesis. Firstly, Chapter 3, of the geomorphological mapping, was conducted and published before fieldwork could be conducted. This limited the scope, and the depth in which Chapter 3 could be written, meaning there may potentially be a) minor differences between the published work and that shown in the Chapter 3, and b) interpretation differences between Chapter 3, and those in subsequent chapters. Effort was made to ensure continuation of the same narrative, without compromising on the scientific integrity, and generating conflicting information from the already published work. A more significant hinderance has been on my capacity to produce chronological dates from collected samples within the timeframe of this thesis. Consequently, the sections of my thesis concern with the study regions Local Last Glacial Maximum (LLGM), and other potential advanced periods, lack chronological controls that would be expected in similar palaeoglacial studies. This has led to the PISM numerical model being used to provide estimated dates, along with comparing the timing of advance in the model, forced using the EPICA temperature time series, to other studies of palaeoglacial advances within the tropical Andes that have dated moraines.

In addressing these challenges, I had to significantly adapted my research approach using the PISM model outputs and findings from conducted palaeoglacial studies. Despite the constraints imposed by the pandemic, I have endeavoured to ensure the integrity of my work by leveraging alternative methodologies and sources of data. However, the limitations imposed by the delayed fieldwork remain a significant obstacle, shaping the PhD and depth of my research outcomes.

Abstract

Tropical glaciers are sensitive indicators of global climate changes, and how these changes influenced the tropics. Recent research has primarily focused on locations where glaciers are still present, or in high elevation locations with recently vacated glacial cirques. Locations that are fully deglaciated, at low elevations (i.e., < 4,000 m asl) are rarely investigated. These are below the traditional latitudinal Last Glacial Maximum snowline elevation, primarily located within a latitudinal data gap between Perú and Ecuador. This thesis reconstructs the ice masses of the Lagunas de Las Huaringas, northern Perú, an area below 4,000 m asl, to assess their extent and nature, and determine the palaeoclimate they may have existed under. This was achieved by: i) remotely sensed geomorphological mapping of palaeoglacial evidence, to enable a first-order reconstruction of glacier extent and temperature cooling, ii) fieldwork to validate remote mapping, and to acquire samples for cosmogenic nuclide dating, and iii) the first use of PISM, a three-dimensional model, over tropical glaciers, to determine their likely climate envelope and response to climate change during advance to, during, and deglaciation from their past extents (38 ka – 16 ka). Research here demonstrates that glaciers were present, and extensive, within the Laguna de Las Huaringas region, with palaeoglacial landforms extending from source area elevations (~3,900 m asl) to their most extensive ice marginal positions downvalley (~2,800 m asl). Temperature cooling estimates from geomorphological evidence and numerical modelling suggest that extensive cooling (-10°C from present) and a wetter climate (+30% modern) was necessary for extensive glaciation to occur. This is one of the coldest estimates acquired within the tropical Andes. Modelled maximum ice extents, that are assumed to be the region's Local Last Glacial Maximum (25.4 ka), or its regional maximum advance during the LGM, falls within the range of previously dated tropical Andean LLGM advances, indicating an early-LLGM for the region. This resulted in an ice plateau configuration, with outlet glaciers extending down valley; different from that determined solely by geomorphological mapping of a cirque-to-valley glaciation. The Las Huaringas ice masses were extremely sensitive to temperature changes, with deglaciation being associated with small increases in temperature (e.g., -10°C to -8.5°C from present), deglaciating immediately after the termination of the LLGM period (~17 ka). This thesis highlights that relatively low elevation tropical locations, formerly thought not to have supported extensive glaciers due to being below the South American LGM snowline, were likely glaciated during the last glacial cycle. This has important implications for our understanding of the last glacial climate conditions within the tropics, along with the timing of the LGM across the Andes. Future work should focus on cosmogenic dating to determine the timing of glacial advances at the Lagunas de Las Huaringas, along with further low elevational regions within the latitudinal data gap.

Acknowledgments

I would like to give a massive thank you my supervisory team: Neil Ross, Andrew Henderson, Andy Russell, Stewart Jamieson, and Derek Fable. It has been a journey with the unforeseen circumstances we all found ourselves in just after the start of the first year of this PhD. An extra special thanks to Neil for being there during the lockdown periods to discuss 'world occurrences' and PhD work during the pandemic, for reading all of my chapters (no matter how long they were), and providing insightful and important ideas, improvements, and refinements, that have got the thesis to this state. Also, a massive thank you to Andrew Henderson conducting fieldwork with me in Perú – bringing a wealth of experience which I could tap into. It was touch and go when we were blocked on route to the field site, it was also very touch and go when I was laying on a hospital bed for 4 hours, however, we made it through to the other side with the rocks and cores. Thank you to Stewart for his knowledge and insights with the PISM modelling of my study site. For making it as painless as it could be for a student who has had no interaction or knowledge on how to model before doing this PhD. Lastly, to Andy Russell and Derek Fabel providing corrections and comments on my PhD and enabling me to get across the finish line.

A special thank you goes out to Oliver who aided me and Andy H while conducting fieldwork in Perú. From negotiating our passage through roadblocks, providing locals with information on what we were doing, to ensuring we knew what was on the menu. We could never have done the fieldwork without you. I wish you all the best and hope to meet you again soon. I would also like to thank Rodolfo from the Universidad de Piura (UDEP) for providing information on where to find weather station information, ground control stations for correcting dGPS, and for storing equipment we used for fieldwork at your radar station. It was a pleasure to have met you, both in the UK, and in Perú.

Thank you to the IAPETUS2 Natural Environment Research Council (NERC) Doctoral Training Partnership (DTP) for the funding of this PhD Studentship. Without their support, this PhD would not have been possible.

I would like to thank all current and former staff at the School of Geography at Newcastle University that I have known through the duration of my PhD. Andy L, Bethan, Chris, Christine, Louise, Maarten, Mark, Matt, Nick, Owen, Rachel, Seb, and Stuart, who always hear new stories of what has been going on in the PGR office from us all – 'meatgate' will never happen again. I would also like to thank Ana, Safaa, and Rupert for providing me with all the help I needed for conducting any lab work, equipment needed for fieldwork, and for approving all my risk assessments – I might have forgot to put Perúvian roadblocks and political unrest… oops.

I would like to give a huge thank you to all the PGR colleagues in the office to kept me sane over the years while completing this thesis: Becky, Jake, Holly, Emma, Alex, Sonam, Hannah, Sophie, Bridget, Martin, Harley, Gunjan, and Nishi. Thank you for putting up with me, no matter how 'problematic' I could be. Thank you for the lunch time discussions, the pub visits, and the incredible friendships you all gave me over the years. Also, to all the other countless other PhD students who has passed through the offices, at both Northumberland House and the Henry Daysh Building. To everyone who has talked to me, been interested in my research, or just been there through the years, good luck with your own research and your future. Maybe I shall see you all again.

Finally, personalised thanks to those who have been a massive part of my PhD. Firstly, I must have a special thanks to (now Dr) Holly, thank you so much for letting me stay in your home for the final two years of my PhD while you were away in Canada having your own adventures – we finally made it! Secondly, (soon to be Dr) Becky, thank you for grounding and centring me when I was complaining too much about my PhD. Thank you for also keeping me sane when you *finally* came in, after I was pestering you to come into the office. You are almost at the finish line yourself, just one final push! Thirdly, Emma, we both liked to complain together and voice our problems. I always enjoyed our lunch time antics and hearing what problems you were having with netball that week. Lastly, (soon to be Dr) Martin, you were gone too soon, we all missed you in the office, but we knew you was in a big boy job. My fondest memories were watching the Formula 1 2021 final, and you trying to teach me golf. I hope your final few months of your PhD all come together!

Most importantly, a thank you to my family, my Mum and Dad, my brother Jack, Sister-in-Law Rachel, and my niece and nephew Phoebe and Dean. Thank you for putting up with my sporadic visits home, with long periods of being away, but always supporting me in everything I do. Also, a massive thank you to my Mum for reading the thesis, maybe not understanding everything, but ensuring it sounded right, and that spellings and grammar were correct. You will now have me home almost continuously now, so I hope you do not get bored of me now that I am back from education.

Lastly, and by no means least, to my partner, Tom. For putting up with me switching from being stressed about work, to spells of me not messaging back for hours while concentrating on my PhD writing. Now that my PhD is over, we can finally go on that holiday we have been talking about. Maybe somewhere hot?

Education – completed.

Table of Contents

List of Figures

List of Tables

List of Abbreviations

^{14}C	Carbon-14
AABR	Area-Altitude Balance Ratio
ACR	Antarctic Cold Reversal
ALOS	Advanced Land Observing Satellite
asl	Above Sea Level
ATLR	Atmospheric Temperature Lapse Rate
BR	Balance Ratio
°C	Celsius
CLIMAP	Climate: Long range Investigation, Mapping, and Prediction
$DDF_{ice/snow}$	Degree Day Factor of Ice/Snow
DEM	Digital Elevation Model
dGPS	Differential Global Positioning System
E	Enhancement Factor
ELA	Equilibrium Lime Altitude
ENSO	El Niño-Southern Oscillation
EPICA	European Project for Ice Coring in Antarctica
ITCZ	Intertropical Convergence Zone
K	Kalvin
ka	Thousand
km	Kilometres
LGM	Last Glacial Maximum
LLGM	Local Last Glacial Maximum
MARGO	Multiproxy Approach for the Reconstruction of the Glacial Ocean surface
m	Metres
MIS	Marine Isotope Stage
mm w.e. d^{-1} °C)	mm water equivalent per day per degrees Celsius
n	Glens n
PISM	Parallel Ice Sheet Model
PLJI	Perúvian Low Level Jet
q	Pseudo-plastic exponent q (sliding law)
QIC	Quelccaya Ice Cap
$\theta_{refreeze}$	Refreezing factor

SALLJ	South American Low Level Jet
SASM	South American Summer Monsoon
SIA	Shallow Ice Approximation
SPOT	Satellite Pour l'Observation de la Terre
SRTM	Shuttle Radar Topography Mission
SSA	Shallow Shelf Approximation
SST	Sea Surface Temperatures
TCN	Terrestrial Cosmogenic Nuclides
xP	Precipitation Fraction
YD	Younger Dryas
yrs	Years
ΔT	Temperature Change

Chapter 1. Introduction

1.1. Background and rationale

To understand the modern and future glacier changes, we need to place current changes in the context of longer-term variations (Tierney *et al.*, 2020a). Tropical glaciers, located in the low latitude mountains, are extremely sensitive to local temperature variations, reacting earlier than mid- and high-latitude glaciers, making them excellent physical indicators of current and past climate change (Kaser, 1999; Zemp *et al.*, 2019; Taylor *et al.*, 2022). These glaciers leave evidence that can be used to aid in inferences of past climate they were generated under (Otto and Smith, 2013; Pearce *et al.*, 2017; Chandler *et al.*, 2018) that can provide high resolution chronologies of advance and retreat patterns (Kirkbride and Winkler, 2012).

Studies across the Tropical Andes that focus on dating evidence of palaeoglacial advances, have used radiocarbon (^{14}C) (Clapperton, 1987b; Clapperton, 1990; Clapperton, 1993; Helmens *et al.*, 1997b), and more recently, terrestrial cosmogenic nuclide (TCN) exposure dating (Mahaney *et al.*, 2010; Smith *et al.*, 2011; Shakun *et al.*, 2015b; Bromley *et al.*, 2016). These have provided well constrained timings of glacial advances in high elevation locations across the Tropical Andes. They show advances during their local last glacial maximum (LLGM) were generally earlier than the northern hemisphere at ~25 ka (Shakun and Carlson, 2010) but there is much variability (± 7 ka) in their timings spatially (Palacios *et al.*, 2020). The term 'LLGM' refers to the more regional LGM advances (e.g., within a valley, study region, or the Andes), while 'LGM' pertains to the global timing generally linked to the maximum extent of global ice sheets. Other periods of advance, or standstills, are also dated. In Perú, the Antarctic Cold Reversal (ACR; 14.7-13.0 ka) is documented (Martin *et al.*, 2020), but advances during the Younger Dryas (YD; 12.9-11.7 ka) are limited, being identified within Ecuador, Venezuela and Colombia (Angel *et al.*, 2017). This complex pattern of readvances and standstills can make determinations of the influence of post-LLGM glaciation in the tropical Andes difficult.

Most studies are concerned with dating palaeoglacial advances primarily present evidence from locations where glaciers are still present at high elevations (> 4,000 m asl) (e.g., Farber *et al.*, 2005; Smith and Rodbell, 2010; Bromley *et al.*, 2016), or recently vacated their glacial cirques (e.g., Smith and Rodbell, 2010; Blard *et al.*, 2014; Shakun *et al.*, 2015b). From previous reviews (Shakun and Carlson, 2010; Angel *et al.*, 2017; Mark *et al.*, 2017), and the Informal Cosmogenic-nuclide exposure-age database (ICD-D) of TCN ages (https://version2.ice-d.org/alpine/), there is a clear latitudinal knowledge gap of 5° for TCN and ^{14}C dates (Figure

1.1) between studies in northern Perú (7°S) and Ecuador (2°S). This latitudinal 5° gap region has an average elevation < 4,000 m asl, below the modern threshold of where glaciers persist. Regions at such low elevation can provide further confidence of LLGM advances due to limited, or no complications of Holocene advances generated under a highly variable climate. The primary motivation of this thesis is to detail evidence, and potential timing, of palaeoglacial advances within this spatial knowledge gap, while providing an understanding of the climatic conditions that some of the lowest glacial evidence in the tropical Andes could have been produced under. The study region in this thesis is the Lagunas de Las Huaringas in northern Perú (Figure 1.1). This is where Clapperton (1993) estimated glaciers to have been present during the LGM period, but has received no further attention or mention within the literature, but is where clear evidence of former glaciers existed.

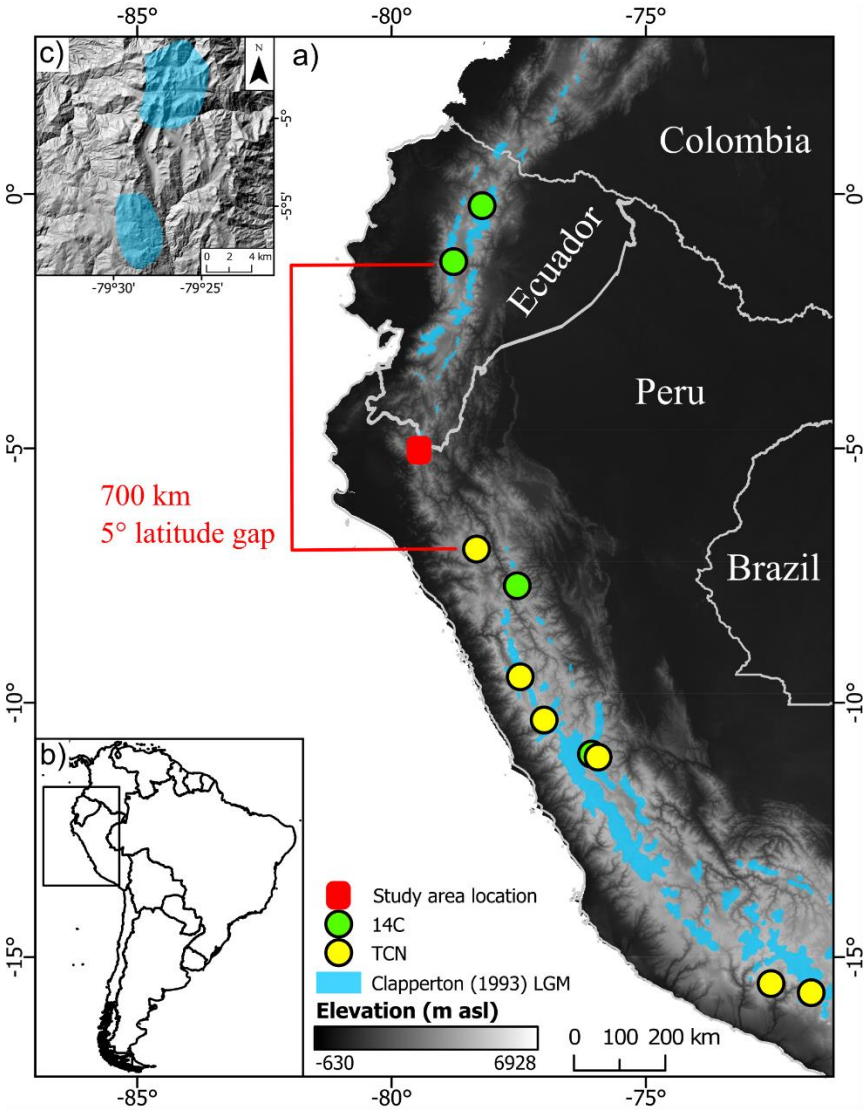

Figure 1.1: a) Spatial location the latitudinal gap and surrounding studies indicating if they have used TCN dating or ^{14}C dating of LLGM evidence. Blue polygon represents the estimated LGM extent from Clapperton (1993). Red box indicates this thesis study area of the Las Huaringas. b) the location of Peru is South America and c) shows the location that is shown in Figure 1.2. Base map is a 90 m SRTM DEM (NASA JPL, 2013).

Evidence for past glaciation can also be used to indirectly provide estimates on the potential palaeoclimate glaciers existed under. There are a limited number of studies across the tropical Andes that determine palaeoclimate, however they have been limited to temperature cooling estimates by reconstructing equilibrium line altitudes (ELAs), primarily during their regional LLGM (Rodbell, 1992; Klein *et al.*, 1999; Porter, 2001; Mark *et al.*, 2005; Ramage *et al.*, 2005; Smith *et al.*, 2005b; Stansell *et al.*, 2007; Úbeda *et al.*, 2018). These provide a record of temperature cooling estimates across differing climatic circulatory systems (e.g., inner, and outer tropics). Most glacial-based climate interpretations indicate a cooling > 4°C across the tropical Andes, much cooler than estimated sea surface temperatures (SST) (Lea *et al.*, 2000; Tierney *et al.*, 2020b). Palaeoclimate reconstructions in the northern tropical Andes (Columbia and Venezuela) required more temperature cooling than regions at higher elevations to allow glaciers to reach their regional LLGM extents (Mark *et al.*, 2005; Mark and Helmens, 2005; Stansell *et al.*, 2007). These estimates however, do not account for precipitation differences that could offset some warming if precipitation increases (Martin *et al.*, 2020). While debated in the literature (e.g., Baker *et al.*, 2001a; Baker *et al.*, 2001b; Nunnery *et al.*, 2019), palaeoprecipitation studies agree precipitation patterns were different during the LGM. If precipitation rates, and patterns, had indeed changed, it will have important implications on temperature reconstructions for tropical Andean glaciers.

While this thesis shall use geomorphological mapping to identify moraines and potential sample locations for TCN dating, the Parallel Ice Sheet Model (PISM) will also be used (Winkelmann *et al.*, 2011; The PISM authors, 2018) for the first time in the tropical Andes. This is to assess the potential climatic envelope glaciers existed under, taking into account precipitation as well as temperature changes. It shall also provide an understanding of the glaciers dynamics that may not be clear from the geomorphological record such as glacial readvances over older advances, and periods of standstills or retreat. The use of numerical modelling in this thesis is the first time a three-dimensional numerical model is used regionally within the tropical Andes. PISM has been used extensively in similar topographical regions outside of the tropical Andes (Candaş *et al.*, 2020; Köse *et al.*, 2022). This proves credence that it is possible to reconcile complex glacial-topographic interactions, but has yet to be tested on tropical glaciers that incur different mass balance regimes making them extremely sensitivities to their surrounding climate (Kaser and Osmaston, 2002). The use of PISM within a unique and unmodelled setting, a tropical setting, also provides useful insights to their strengths and shortfalls, directing future modelling efforts in the region.

1.2. Study region rationale

The study region of the Lagunas de Las Huaringas (here after referred to as Las Huaringas) (5°00'S, 79°27'W) (Figure 1.2) is located within the Cordillera Huamaní, in northern Perú (Lila *et al.*, 2016). This region, at a latitude of ~5°00'S, is within the data gap between 2-7°S, at a low elevation for the tropical Andes (maximum elevation ~3,900 m asl). The underlying geology comprises Paleogene to Neogene age volcanic-sedimentary rocks (Gómez *et al.*, 2019), and is not currently glaciated. The main valley, the Shimbe valley (Figure 1.2), stretches north to south for ~22 km and is characterised by two major depressions; a smaller up valley section occupied by Laguna Shimbe 2 and a larger section occupied by Laguna Shimbe, the latter having an estimated maximum water depth of ~30 m from prior fieldwork conducted by the thesis supervisors attempting to collect lake core samples. Within the Shimbe valley and throughout the study area, there are a number of smaller valleys with lakes dammed by ridges or bedrock, indicative of past glacial erosion, the most striking of which are situated on the western side of the Las Huaringas Massif with lakes such as L. Millionaria, L. El Toro etc.

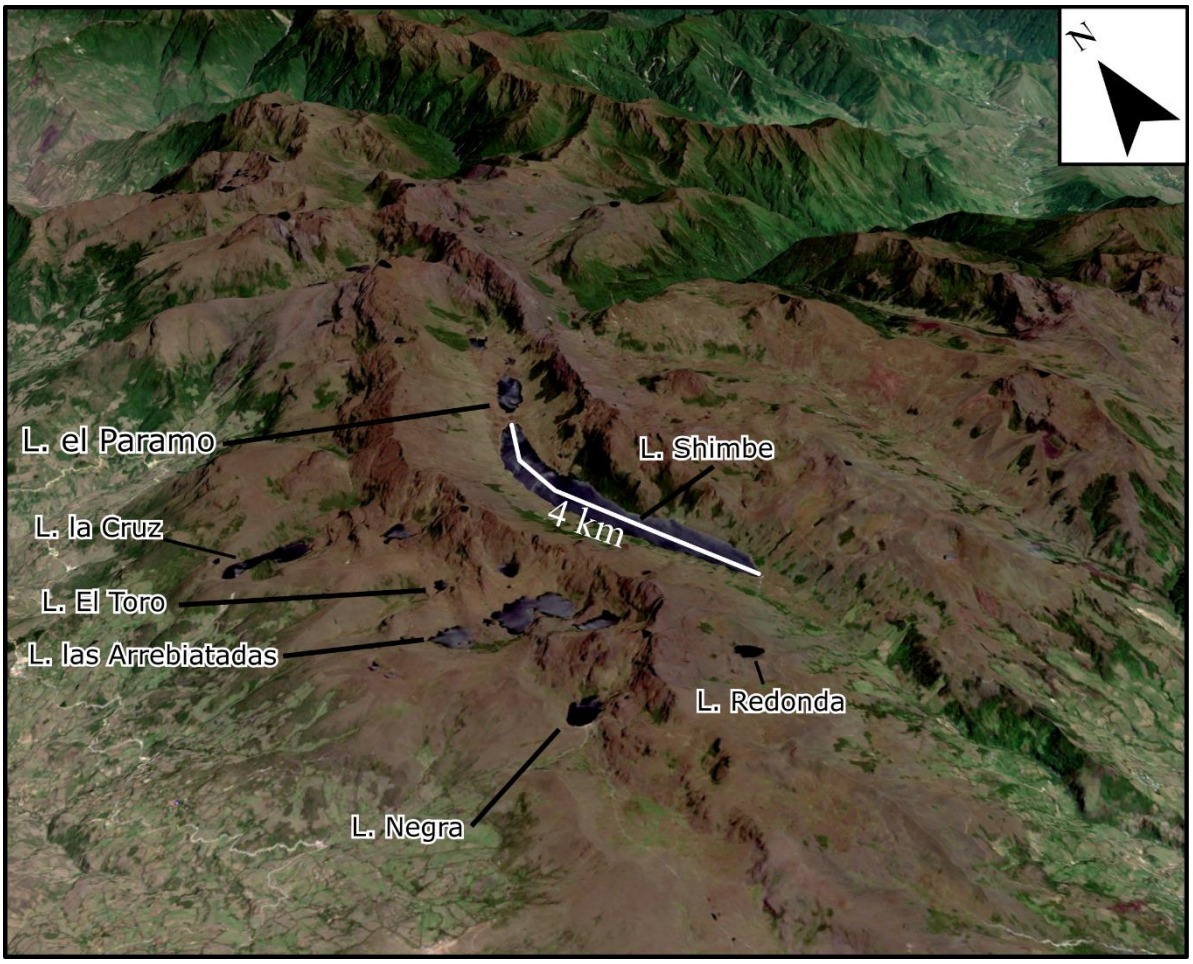

Figure 1.2: A Sentinel-2 optical imagery of the Las Huaringas (red box in Figure 1.1), draped over the 30 m ALOS DEM (Tadono *et al.*, 2014). The main central valley (Shimbe Valley) with the largest lake, Laguna Shimbe. Arcuate moraines and lake-filled depressions are seen on its western edge (left side of the image) with their lake names detailed.

The climate of the Las Huaringas is tropical, modulated by tropical Pacific sea surface temperatures (SST) and ocean temperatures at depths. These drive variations in the El Niño-Southern Oscillation (ENSO) that itself influences interannual precipitation and air temperature variability (Garreaud, 2009; Kiefer and Karamperidou, 2019). Other influences include the transfer of moisture via the easterlies, which originate from the Atlantic Ocean, and track over the Amazon Basin incurring evapotranspiration. The easterlies flow over the eastern Andes brings enhanced precipitation, predominantly during the summer months, in response to the migration of the ITZC southwards (Garreaud, 2009; Álvarez-Villa *et al.*, 2011; Staal *et al.*, 2018). On average, the Las Huaringas region receives ~400 mm of precipitation per year, with the majority of precipitation falling between October and April (tropical summer season) with very little between June and August (tropical winter season). The intra-annual temperature variation of ~0.5°C is exceeded by the diurnal temperature variation of ~4°C.

This region, along with other potentially formerly glaciated regions that surround here, has received little to no attention in the literature pertaining to palaeoglacial geomorphology, the timing of any advances using geochronological techniques, or any form of detailed investigation (Lee *et al.*, 2022). Clapperton (1993) suggested an area, within the Las Huaringas region, was likely to have been glaciated during the global LGM (Figure 1.1 a). This LGM extent was generated for the entire South American Andes, using his extensive field experience, and early-Landsat and topographical maps, mapping any region above 3,400 m asl as having the potential to be covered by glacial ice. Preliminary investigations of the field area by Prof Andrew Henderson (a supervisor of this PhD thesis), exhibited extensive palaeoglacial evidence within the region confirming Clapperton's assumptions, at least for this region, warranting further investigation. While the elevation of this region is below the modern-day snowline (Hammond *et al.*, 2018), it is also below the assumed South American LLGM snowline (Broecker and Denton, 1990a), leading to the potential of this region to either not be glaciated during the overall South American LLGM, or if it was glaciated, be completely deglaciated after any regional LLGM advances due to their potentially being not enough temperature cooling to allow extensive glaciation. This has the potential to provide a region that is free from complications of Holocene climate fluctuations, that may have provided glacial extents near to, or overlapping with LLGM extents (Smith and Rodbell, 2010). This enables an increased confidence of the regions LLGM timing and climate influence on regional glaciation due to no or little post-deposition modification of the regions LLGM advance chronology by later readvances. Its location, and subsequent investigation within this thesis shall bridge the latitudinal knowledge gap, detailing a location that incurred potential extensive glaciation during its regional LLGM. The filling of this spatial gap allows us, to fully compare the timing

and extent of glaciers within this low latitudinal area to the surrounding regions. It shall also enable a comparison of studies latitudinally to discern any variations in maximal extents, and their timings, due to local climatic processes during the LLGM.

1.3. Research aims and objectives

The overarching aim of the thesis it to understand the glacial history within the Las Huaringas using geomorphological mapping and TCN dating of the evidence. Numerical modelling shall also be used to provide an evaluation of the dynamics that may have occurred within this region. This thesis also aims to estimate the potential palaeoclimate under which the maximum glaciation could have existed under using shall be determined using glacial reconstruction from the geomorphological record through ELA reconstructions, and glacial numerical modelling. Through a comprehensive investigation of the study region, this thesis can add to the growing body of research investigating glacial advances across the tropical Andes. While understanding how glaciers have has responded to climate perturbations in the past, we can better understand, and anticipate, changes due to future climate warming. To achieve this aim, a series of research questions (RQs), and associated objectives, have been outlined below:

RQ1: Has the Lagunas de Las Huaringas been glaciated in the past, and what was the maximum extent of glaciation? (Chapter 3, Chapter 4, and Chapter 6)

RQ2: When did the glaciations within the study region occur, and when was the most extensive glaciation? (Chapter 4 and Chapter 6)

RQ3: What were the climate conditions at the time of when glaciers were present? (Chapter 3 and Chapter 5)

RQ4: What was the glacial dynamics of the ice masses during advance to, during, and retreat from, the maximum glacial extent? (Chapter 6)

To address the above RQ's, along with the overall thesis aim, the following objectives are outlined below:

- Conduct remote-sensed geomorphological mapping of the Las Huaringas region to evaluate the presence of evidence that details palaeoglacial advances or standstills, to understand past glacial dynamics within the region, and provide a potential first-order estimate of temperature cooling during it most extensive glaciation.

- Undertake fieldwork to evaluate and amend remotely conducted geomorphological mapping, in order to create a comprehensive geomorphological map of the region and collect samples from identified moraines for dating.
- Using the maximum reconstructed glaciation extent, set up and constrain the PISM parameter choices. This shall also assess the effect of model parameters on model output.
- To numerically model the former ice masses of Las Huaringas with a time varying climate to assess the temperatures and precipitation required for maximum glaciation.

1.4. Thesis structure

This thesis comprises eight chapters, each detailing the reconstruction of palaeoglaciations and potential climate of the research region.

Chapter 2 – Provides a detailed literature review on understanding of the overall state of palaeoglaciological studies within the tropical Andes. This will also outline the gap in knowledge which this thesis shall fill.

Chapter 3 – Comprises the remote geomorphological mapping of the study region to inform the reconstructions of palaeoglacial extents during their most extensive positions – assumed to be their regional LLGM extent – while providing a first order estimates of palaeoclimate using ELA reconstructions and atmospheric temperature lapse rates – **RQ1** + **RQ3**.

Chapter 4 – Details the sampling strategy for the TCN dating of identified moraines, taken during field work conducted in January 2023. This also evaluates the remotely sensed geomorphological mapping against in-field geomorphological mapping of the in visited field locations – **RQ1** + **RQ2**.

Chapter 5 – Details the sensitivity analysis of the PISM model against under studied, and unconstrained, parameters within the model. This is in order to parameterise and facilitate later time-transient modelling of the study region. This chapter aids in understanding the climatic envelope upon which glaciers extent to their assumed regional LLGM extents – **RQ3**.

Chapter 6 – Conducts time-transient modelling of the study region to observe how the glacial systems behaves against time-varying temperature before, during, and after the LLGM – **RQ1** + **RQ2 + RQ4**.

Chapter 7 – Synthesises the key findings from the results, critically evaluating the findings of this thesis, and how the research shown within this thesis has addressed the RQs, along with where future work could focus towards.

Chapter 8 – Presents the conclusions from this research.

Chapter 2. Literature Review: tropical Andean palaeoglacial reconstructions

2.1. Introduction

Tropical glaciers are extremely sensitive to climate (Kaser, 1999) making them clear indicators of both past, present, and future, climate change (Vuille *et al.*, 2008). Within the palaeorecord, there is a large body of research that has attempted to understand the timing of past glacial advances, having generated an extensive database of dated moraines that detail multiple periods of glacial advances and standstill, throughout the tropical Andes (e.g., Clapperton *et al.*, 1997b; Mahaney *et al.*, 2010; Carcaillet *et al.*, 2013; Blard *et al.*, 2014; Emmer *et al.*, 2021). These advance chronologies allow an appreciation of the potential palaeoclimate, inferred by geomorphological evidence of palaeoglacial advances (e.g., Porter, 2001; Smith *et al.*, 2005b; Bromley *et al.*, 2011a), that can be matched against other palaeorecords (e.g., Lea *et al.*, 2000; Lea *et al.*, 2003; Vizy and Cook, 2007; Tierney *et al.*, 2020b). These can provide an interregional comparison of the climate across the tropical Andes, and how the glacial advance, and estimated climate, fits in with the global climate system (e.g., Thompson *et al.*, 2011). While the timing of glacial advances is generally well constrained, there are still a limited number of studies that attempt to reconstruct glacial extents using the geomorphological record, equilibrium line altitudes (ELAs), and regional ice configuration patterns. Further, there are still extensive areas, that are below the traditional reconstructed South American LGM snowline (Broecker and Denton, 1990a), that housed glacial ice potentially during the LGM that are still yet to be investigated. This review examines the current understanding presented in the research of palaeoglaciations across the Ecuadorian and Perúvian Andes and details the gaps in the literature that this thesis shall attempt to fill.

2.2. The tropical Andes and their glaciers

2.2.1. The tropical Andes

The Andes, or Andean Mountains, are the longest continental mountain range in the world at 9,000 km long (Smith *et al.*, 2008), and cover a latitudinal range of ~66°. Located along the western edge of South America, the mountain chain extends from the northernmost regions of Venezuela (12°N) to the southernmost regions in Chile (56°S), and have an average elevation of ~4,000 m. The Andes can be split into three distinct climate-driven classifications, the Dry Andes (southern Bolivia and Chile), the Wet Andes (south Chile), and the Tropical Andes (Bolivia, Peru, Ecuador, Venezuela, and Colombia). Peru being the focus of this thesis. The

Andes are instrumental for the formation of moisture transport from the Amazon to the rest of the South American continent (Garreaud *et al.*, 2010).

2.2.2. Tropical glaciers

Tropical glaciers are defined by Kaser (1999, p. 93) as being situated within '1) the astronomical tropics between 23.5° north and south; 2) the area where the daily temperature variation exceeds the annual temperature variation, and 3) the oscillation area of the Inter Tropical Convergence Zone (ITCZ).' This unique location makes them extremely sensitive to temperature changes, being distinctive indicators of climate (Veettil and Kamp, 2019). The tropical Andes (Figure 2.1a) hosts 99% of the worlds tropical glaciers, and 4% (~2,500 km^2) of the global mountain glacier area (Bennett and Glasser, 2009). The remaining 1% of tropical glaciers are outside of South America, found in Mexico (Figure 2.1b), east Africa (Figure 2.1c), and Indonesia (Figure 2.1d), on local topographical highs, or along the top of volcanoes.

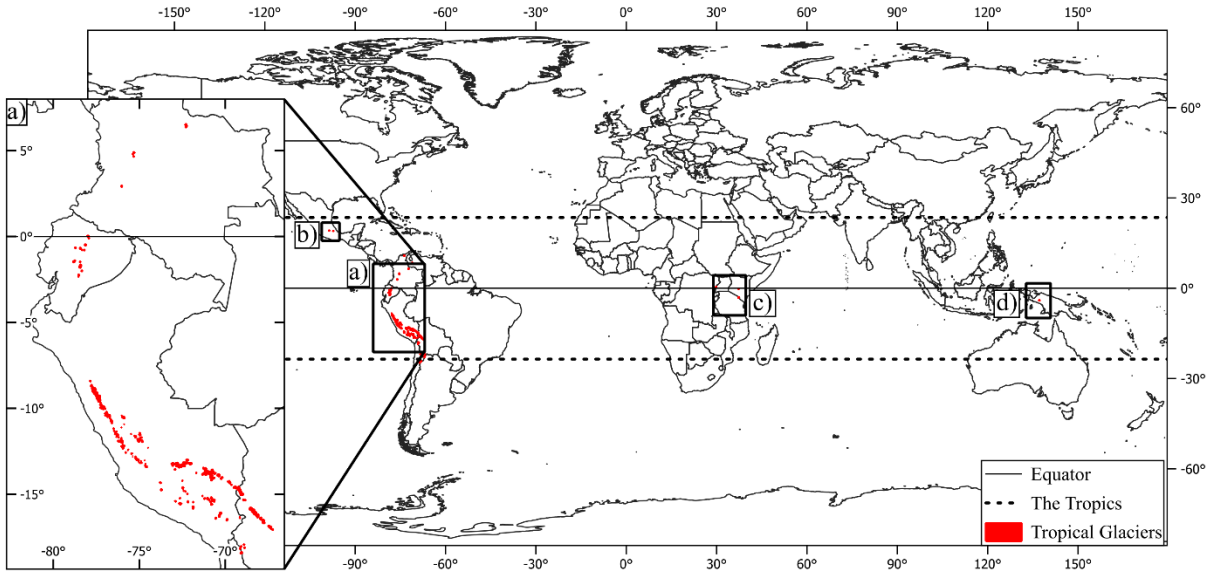

Figure 2.1: The tropical glaciers are located within a) the tropical Andes, b) Mexico, c) Kenya, Uganda, and Tanzania, and d) Indonesia.

Tropical glaciers within the Andes cover high mountain regions within; Colombia (Rabatel *et al.*, 2018), Venezuela (Ramírez *et al.*, 2020), Ecuador (Vuille *et al.*, 2008), Perú (Taylor *et al.*, 2022), and Bolivia (Seehaus *et al.*, 2020). The majority of global tropical glaciers are located within the Perúvian Andes covering 1,603 km^2, being ~68% of the total glaciated area in the tropical Andes (Veettil and Kamp, 2019).

Tropical Andean glaciers are found in preferred orientations and aspects (Kaser and Osmaston, 2002). Poleward facing glaciers (south) have greater insulation from solar radiation, while equatorial facing glaciers (north) have increased exposure. This favours the formation and

preservation of poleward facing glaciers (Evans and Cox, 2005; Evans and Cox, 2010; Veettil *et al.*, 2017). Another factor that influences the orientation and aspect of tropical glaciers are gradients in snow precipitation. An east-west gradient is seen, with the lowest snowlines along the eastern side of the Andes, and the highest on the western side (Porter, 2001). This is driven by precipitation attenuated by the ITCZ associated with the easterly trade winds, which can also allow the development of glaciers at lower elevations in the eastern regions of the Andes (Hastenrath, 2009).

2.2.3. What makes tropical glaciers 'unique'?

Tropical glaciers are unique when compared to extra-tropical glaciers, which can make them difficult to study. In contrast to higher latitude glaciers, tropical glaciers primarily lose mass all year round, while their mass balance is extremely sensitive to their surrounding climate (Kaser and Osmaston, 2002). While accumulation sources are similar to non-tropical glaciers, they incur accumulation within the same seasons as their ablation, that can cause important changes in their dynamics (Favier *et al.*, 2004). Tropical glaciers are unique in that a large percentage of their ablation can occur by the process of sublimation, the evaporation of ice directly to a gas, that can account for up to 81% of ablation in extreme circumstances (Winkler *et al.*, 2009; Fyffe *et al.*, 2021). This can make their response to climatic warming more abrupt than those in extra-tropical locations. Further, the effects of insolation forcing (Lee *et al.*, 2021b) and localised effects of sea surface temperatures (SST) (Pierrehumbert, 1995), can make tropical glaciers an ideal study region for understand climate changes during the Late Quaternary (Bromley *et al.*, 2016).

Tropical glaciers can be classified by the tropical zone they are situated in, that can dictate their accumulation and ablation patterns. These are generally controlled by regional precipitation (Troll, 1941; Kaser and Osmaston, 2002). These categories are:

i) The outer tropical zone (Figure 2.2a), distinctive seasons and a unimodal precipitation pattern, ablation occurs all year round, whilst accumulation only occurs during the austral summer (wet season), when enhanced ablation takes place (Francou *et al.*, 2004).
ii) The inner tropical zone (Figure 2.2b), where stable humidity and air temperatures bring bimodal precipitation seasons, allows accumulation and ablation to occur simultaneously and are thus more sensitive to temperature changes (Favier *et al.*, 2004).

These pronounced wet-dry seasons, are in stark contrast to temperate or extra-tropical glaciers (Figure 2.2c), characterised by distinct seasons for ablation (summer) and accumulation (winter) (Benn *et al.*, 2005; Smith *et al.*, 2008).

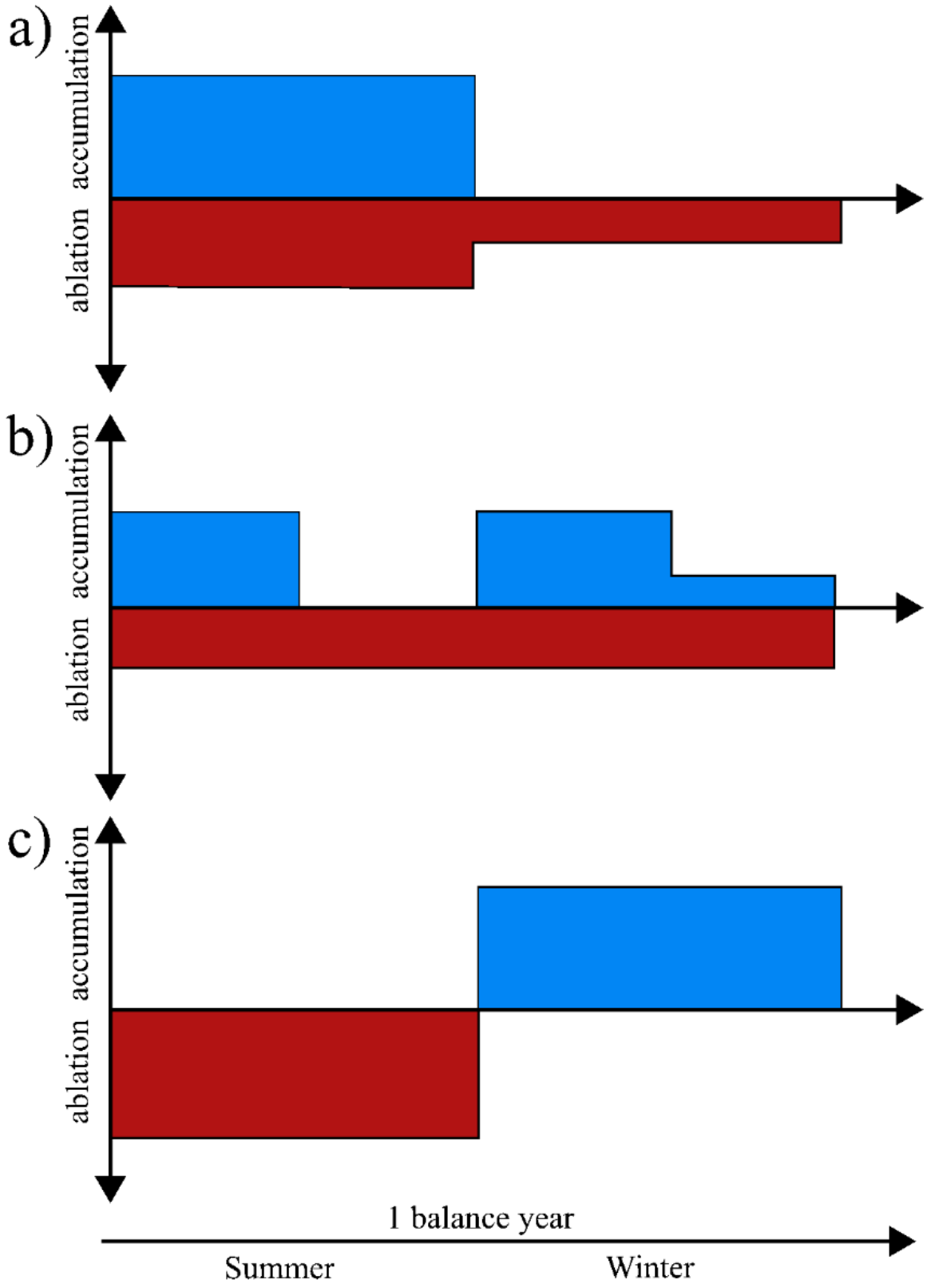

Figure 2.2: Idealised mass balances of, a) outer tropics, b) inner tropics, and c) temperate or extra-tropical glaciers (modified from Rodbell *et al.*, 2009).

2.3. Modern and palaeoclimate within the tropical Andes

2.3.1. Contemporary tropical Andean climate

Regional precipitation patterns (Figure 2.3) in the tropical Andes are primarily controlled by the flow of moisture by the ITCZ (Hastenrath, 2002; Álvarez-Villa *et al.*, 2011), and broadly align with tropical zones (Figure 2.3; blue and red boxes) and the tropical easterlies. The seasonality, with the movement of moisture, is affected by the trajectory of these easterlies. During the austral winter (June to August), the mid-level westerlies are situated ~10°S due to the migration of the ITCZ southward, while the upper-level jet stream is situated over the subtropical Andes (~30°S). During the austral late-spring and summer months (December to February) the flow is disrupted by the Bolivian High, and becomes situated over the Bolivian Altiplano (Espinoza *et al.*, 2020) bringing increased precipitation to the outer tropics region (see Cusco climate graph in Figure 2.3).

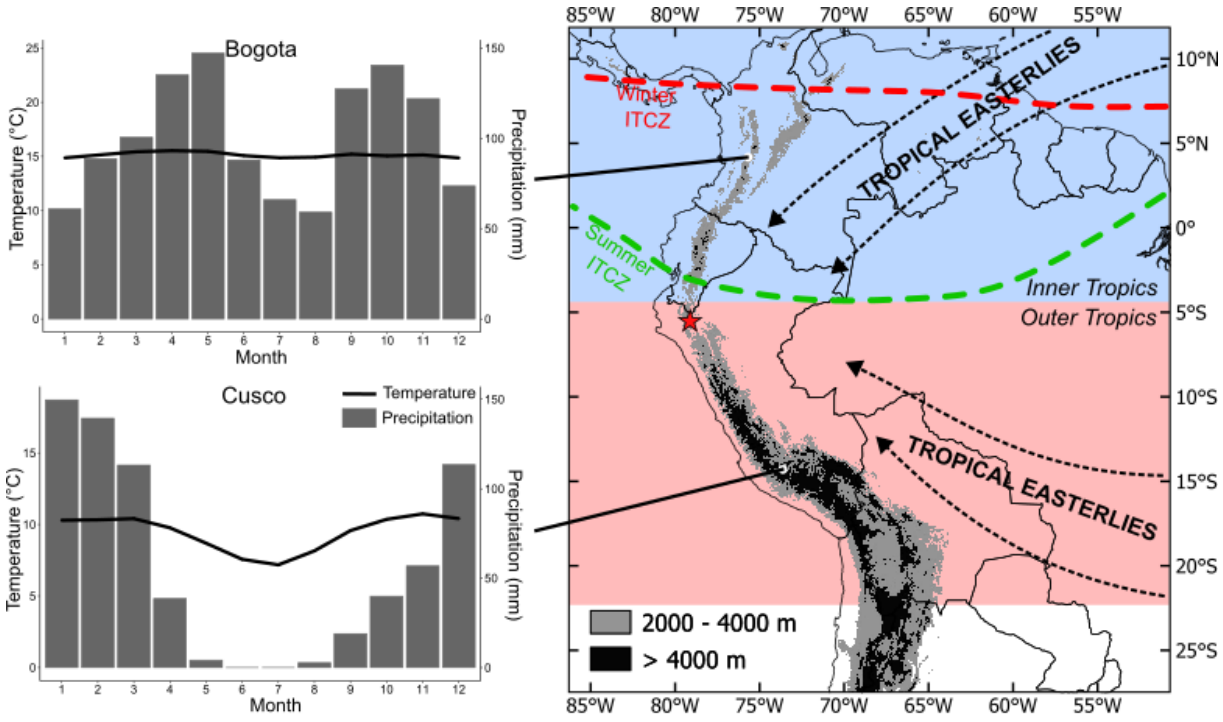

Figure 2.3: The tropical zones of the inner (blue) and outer (red) tropics (based on Rabatel *et al.* (2013a)), characterised by differing seasonal patterns, primarily seen in change in precipitation (mm), while temperatures (°C) vary very minorly (± 1-3°C). The two main tropical easterly trade wind directions are denoted by the dashed arrows (modified from Rodbell *et al.*, 2009). The location of the ITCZ during the summer (green dashed) and winter (red dashed). Climate data are averages from the CRU-TS v4 dataset (Harris *et al.*, 2020). Red star the location of this thesis study location seen in Figure 1.2.

The movement of moisture is also affected by how it is transported by the tropical easterly trade winds (Figure 2.3), that route across the Amazon Basin to the Andes (Figure 2.4). Moisture acquired by the easterly trade winds via evapotranspiration over the Amazon Rainforest results in ~25-50% of recorded total annual rainfall over the tropical Andes (Staal *et al.*, 2018). These

air masses are then transported upwards through orographic convection, over the eastern tropical Andes where this process is most predominant during the austral summer months (Garreaud *et al.*, 2003; Bendix *et al.*, 2006; Vizy and Cook, 2007; Garreaud, 2009; Trachte, 2018; Espinoza *et al.*, 2020). This leads to an asymmetry in precipitation rates, with the eastern tropical Andes incurring higher precipitation rates (Kumar *et al.*, 2019), that can exceed 6,000-7,000 mm mean annual precipitation.

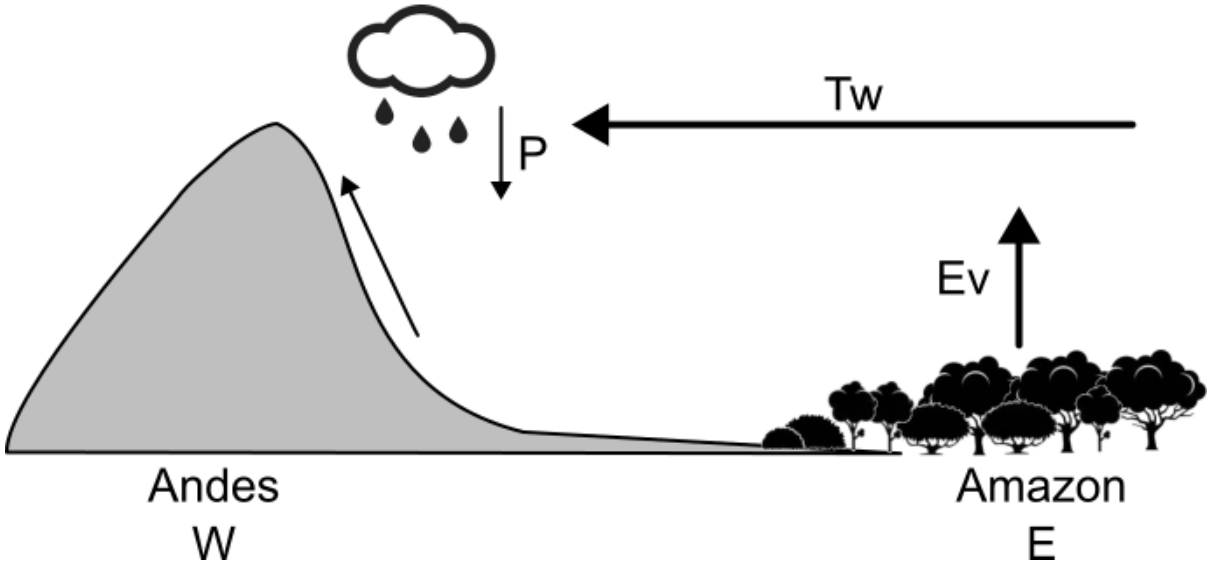

Figure 2.4: A schematic of the transport of moisture by the easterly trade winds (Tw) collecting evapotranspiration (Ev) from the Amazon basin (in the east) and precipitating (P) over the central Andes (to the west) modified from Builes-Jaramillo and Poveda (2018).

Studies have shown that this seasonal moisture flow is variable in magnitude, and is affected on interannual and multidecadal timescales by the ENSO and Pacific SSTs (Francou and Pizarro, 1985; Garreaud and Aceituno, 2001; Kiefer and Karamperidou, 2019). The ENSO phenomenon is an episodic variation in trade winds and SSTs causing regional climate variations which can exacerbate glacial conditions of melt or advance (Veettil, 2012). El Niño years bring warm and dry conditions enhancing ablation, while La Niña years bring cold and wet conditions enhancing accumulation. The effect of El Niño and La Niña years are not uniform across the tropical Andes and do not exhibit uniformity even at and intra-country level (Rabatel *et al.*, 2013a). For example, the El Niño Costero, in 2017, brought El Niño conditions after the El Niño season of 2014-2016, to the coastal regions of Perú and Ecuador, as opposed to the basin wide conditions which affect the north-western coast of South America (Ramírez and Briones, 2017), enhancing the El Niño's effect within this localised region.

Due to the latitudinal range, solar radiance is constantly high, leading to homogenous temperatures across the inner and outer tropical Andes throughout the year. Temperatures only increase by 1-2°C throughout the year in the austral summer when compared to the austral

winter – this range far exceeded by the diurnal temperature range (5-10°C) (Martin *et al.*, 2020). This homogeneity of annual temperatures is controlled by the occurrence of incident solar radiation (Rabatel *et al.*, 2013a). Within the inner tropics, incident solar radiation is approximately constant throughout the year (Figure 2.3; Bogota), while within the outer tropics it is seasonal with temperatures being attenuated by the cloud seasonality (Figure 2.3; Cusco) (Sicart *et al.*, 2010) with maximum cloud cover in the austral summer leading to decreased incident solar radiation.

2.3.2. Reconstructed tropical Andean palaeoclimate at the LGM

Tropical temperatures during the LGM have been a topic of great debate due to differing magnitudes of cooling indicated from different sources (e.g., MARGO Project Members, 2009; Loomis *et al.*, 2017; Tierney *et al.*, 2020b). Some of the first estimates of SST temperatures during the LGM came from the CLIMAP project (1976) that suggested that tropical SST were only cooled by 0.8°C on average between 26 ka and 19 ka. More recently, SST reconstructions indicate temperature cooling during the LGM between ~-1.7 ± 1.0°C to -3.5 ± 0.3°C (Lea *et al.*, 2000; Ballantyne *et al.*, 2005; MARGO Project Members, 2009; Tierney *et al.*, 2020b), from 35 ka to around 20 ka before warming occurred (Figure 2.5).

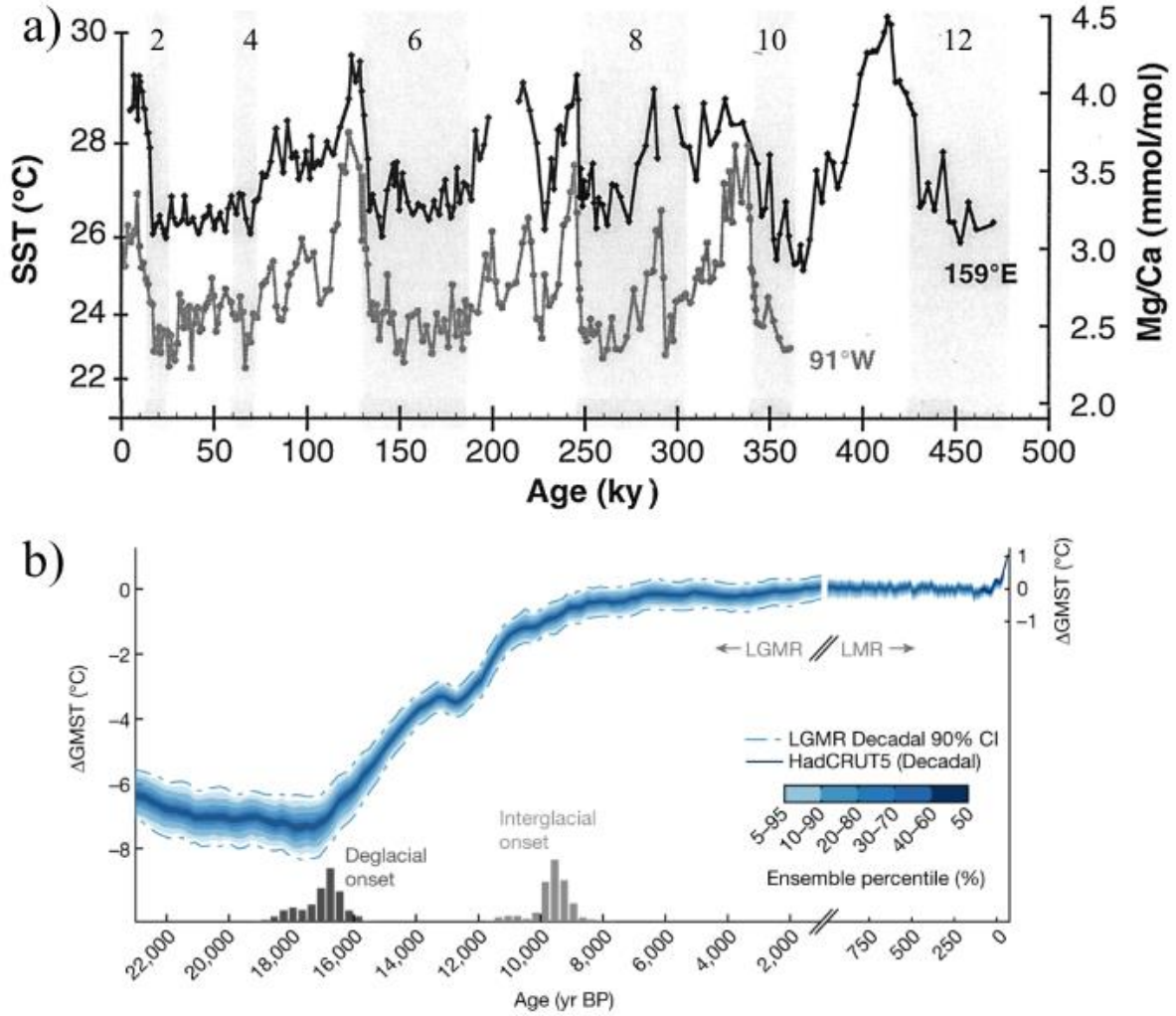

365 **Figure 2.5**: Examples of a SST time series from a) the equatorial Pacific at the Cocos Ridge (90°57′W, 2°16′N) and Java Plateau (159°22′E, 0°19′N) detailing long term SST (500 ka to present) based on the relationship with Mg/Cs (SST (°C) = 0.089−1*ln[Mg/Ca (m) /0.3]) Shaded correspond to marine isotope stages (modified from Lea *et al.*, 2000). b) Global mean surface temperature (GMST) from 22 ka to present, relative to the preindustrial last millennium
370 average (1000-1850 CE), with the Last Glacial Maximum Reanalysis (LGMR) and the Last Millennium Reanalysis (LMR) v2.1 (Tardif *et al.*, 2019). All show, that after 20 ka there is a rise in SST and the onset of deglacial conditions (modified from Osman *et al.*, 2021).

ELA reconstructions provide estimations of temperature cooling over the land. Palaeo-ELA temperature reconstructions have been used across the tropical Andes, in locations were no
375 glaciers exist today (e.g. Stansell *et al.*, 2007), to where glaciers still persist (e.g. Rodbell, 1992). A collection of studies that conduct ELA reconstructions and subsequent palaeotemperature estimations are summarised in Table 2.1. Most studies also reconstruct their glacier areas and extent as the reconstruction is required for ELA reconstruction, however, most only reconstruct singular glaciers and may not be entirely representative of their regional temperature cooling.
380 The majority of the studies within the tropical Andes that indicate cooling, detail cooling more than the global average during the LGM (~-6°C) (Seltzer *et al.*, 2021). The highest amount of cooling seen in the Merida Andes within Venezuela with a depression of between -6.1 ± 1.0°C

and -8.8 ± 2.0°C, (Stansell *et al.*, 2007). Studies in Perú yield a range of estimated cooling, from -2°C to -6.4°C. The location with the lowest amount of cooling are seen in locations where glaciers were more likely constricted by their surrounding topography (e.g., valleys), and were westward facing (Ramage *et al.*, 2005; Smith *et al.*, 2005b). In Perú, there was less cooling in locations that primarily faced eastward (Rodbell, 1992) or relatively unconstrained by topography (Bromley *et al.*, 2011a; Úbeda *et al.*, 2018). The most amount of cooling are seen in locations where ice is currently not present, and found at lower temperatures, while those with the least cooling are where glaciers currently exist or are at higher elevations, thus require less temperature cooling to incur glaciation. Ice cores taken from the Huascaran ice cap in Perú, and Sajama ice cap in Bolivia, also provide indications of temperature cooling, with estimates between 8-12℃ (e.g. Thompson *et al.*, 1995; Thompson *et al.*, 1998). However, isotopic evidence, such as ice cores, primarily reflects precipitation changes within the Tropical Andes due to the importance of moisture in the tropics, but can be used to infer temperature changes.

Table 2.1: A selection of studies with their determined ELA change (ΔELA) from their LLGM ELA to present, and their corresponding temperature change (ΔT) within the tropical Andes ordered from the most northern latitude to the most southern. Uncertainty given if provided within the relevant study.

Location	Method	ΔELA (m)	ΔT (°C)	Reference
Merida Andes, Venezuela	AAR (0.66-0.87); AABR (5, 10, 15) + EMBE/ATLR	-850-1420	-8.8 ± 2 -6.4 ± 1	Stansell *et al.* (2007)
Bogotá, Colombia	*	-1217	-7.9	Mark *et al.* (2005)
Bogotá, Columbia	AABR (1.0, 5.0, 7.0) + ATLR	-1300	-6 - -8	Mark and Helmens (2005)
Cordillera Blanca and Oriental, Perú	THAR + ATLR	~-1000	-5 - -6	Rodbell (1992)
Cordillera Blanca, Perú	*	-1058	-6.1	Mark *et al.* (2005)
Southern Andes (8-22°S)	AAR (0.6) + ATLR	-900 ± 135	-5 - -6.4	Porter (2001)
Junin Valleys, Perú Milluni Valley, Bolivia	THAR (0.4) + ATRL	-300-600	-2 - -4	Smith *et al.* (2005b)
Junin Plain, Perú	THAR (0.45); AAR (0.65); AABR (0.65, 0.7) + ATLR	-220-550	-2.5 ± 1	Ramage *et al.* (2005)
Nevado Coropuna, Perú	MELM + ATLR	-550-770	-4.5 - -5.2	Bromley *et al.* (2011a)
Nevado Coropuna, Perú	AABR (1, 1.5, 2, 2.6, 3) + ATLR	-991	-6.4	Úbeda *et al.* (2018)
Central Andes	*	-804	-7.2	Mark *et al.* (2005)
Perúvian-Bolivian Andes	THAR (0.45), EMBE	500-1200	-5 - -9	Klein *et al.* (1999)
Cordillera Real, Bolivia	THAR (0.37, 0.5), EMBE	-300 ± 100	-3.5 ± 1.6	Seltzer (1992)

AAR = Accumulation-Area Ratio, Ratio, AABR = Area-Altitude Balance Ratio, MELM = Maximum Elevation of Lateral Moraines, THAR = Toe-to-Headwall Altitude Ratio, CF = Cirque-floor Altitude, ATLR = Air Temperature Lapse Rate, EMBE = Energy Mass-Balance Equation
*Mark et al. (2005) combines a number of studies in their results thus no method is reported

Precipitation during the LGM, globally, is of great debate, the same is seen within South America with there being latitudinal differences. Palaeolake studies present regional variability in precipitation patterns (Figure 2.6). Studies within Bolivia (Rodbell, 1993b; Clapperton *et al.*,

1997a; Baker *et al.*, 2001b; Fritz *et al.*, 2004; Chepstow-Lusty *et al.*, 2005), detail a wetter and colder region LLGM than today but leading to drier conditions after 15 ka (Figure 2.6a). Baker *et al.* (2001b) hypothesises that this increased precipitation was due to an intensified South American Summer Monsoon (SASM) (Figure 2.7) enhanced by increased land-sea temperature gradients in combination with peak wet-season insulation due to orbital variations (Baker *et al.*, 2001a). However, other palaeolake studies within the Bolivian Altiplano (Sylvestre, 2002; Placzek *et al.*, 2013; Nunnery *et al.*, 2019) present little to no precipitation change when compared to present, but had enough moisture to maintain lakes within the southern Altiplano with some variation in lake levels (Figure 2.6b). Baker *et al.* (2001a) found from palaeolake Salar de Uyuni (southern Altiplano) that the regional LLGM was wetter by a minimum of 30% higher-than-modern precipitation, due to the above mentioned SASM intensification.

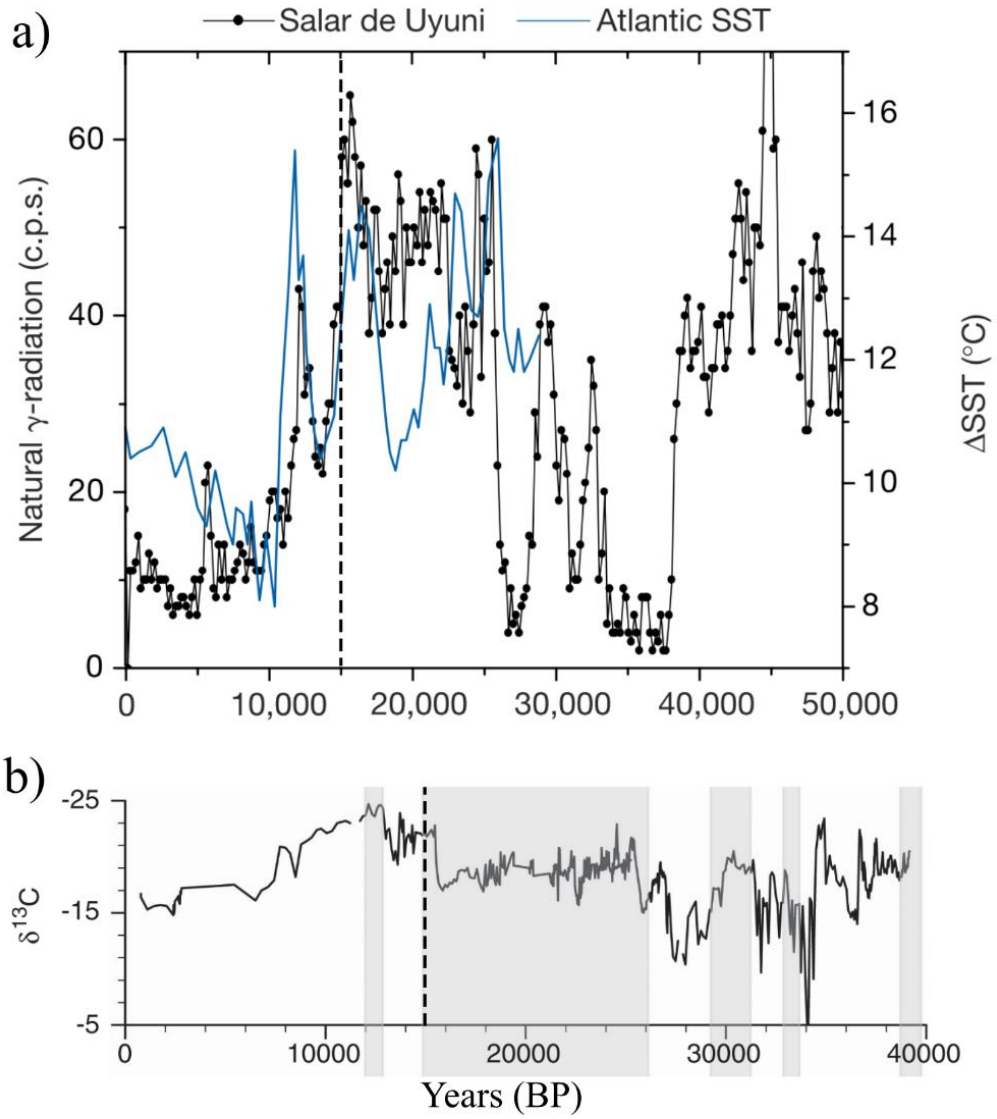

Figure 2.6: Lake level records within the tropical Andes, a) details the natural γ-radiation, a proxy of effective moisture in Salar de Uyuni, Bolivia, against reconstructed SST offset in the western and eastern Tropical Atlantic (Müller *et al.*, 1998) (figure from Baker *et al.*, 2001a), b) details $\delta^{13}C$, another proxy of lake level, in Salar de Coipasa, Bolivia (figure from Nunnery *et al.*, 2019). On all figures' dashed line is centred on 15 ka.

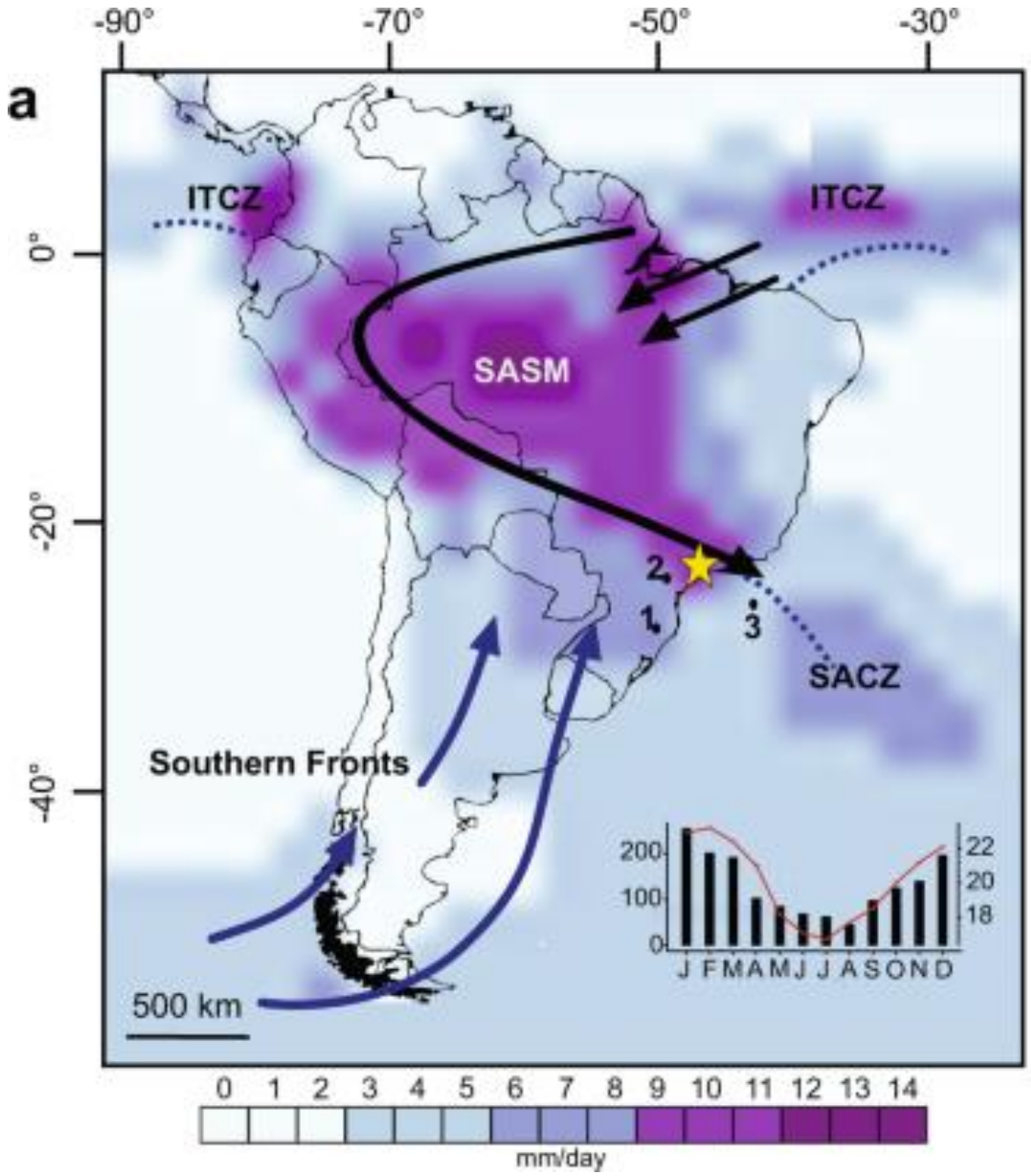

Figure 2.7: The moisture patters of the SASM (black arrows) stemming from the Atlantic and paralleling the Andes towards southeast, and the location on the ITCZ and the South American Convergence Zone (SACZ). Figure from Rodríguez-Zorro *et al.* (2020).

Not all records agree that precipitation increased, or was similar to present, during the Andeas LLGM, with evidence in locations that have teleconnections to the tropical Andes indicating a dryer climate, primarily within the northern Andes (Heusser and Shackleton, 1994; Behling and Hooghiemstra, 1999; Vélez *et al.*, 2003) and Amazon basin (Mourguiart and Ledru, 2003; Novello *et al.*, 2019). The northern tropics (e.g., Venezuela and Colombia) detail little to no precipitation changes, attributed primarily to the displacement of the ITCZ southward in response to northern hemispheric cooling and the southerly displacement of the Bolivian High (Peterson and Haug, 2006; Deplazes *et al.*, 2013; Stríkis *et al.*, 2015; Novello *et al.*, 2017). Palaeoecological studies within the Amazon Basin detail a drier climate (Sifeddine *et al.*, 2003; Häggi *et al.*, 2017; Wang *et al.*, 2017; Smith *et al.*, 2020) negating the effect of

evapotranspiration from the Amazon basin (see Figure 2.4) to the precipitation over the tropical Andes (Vizy and Cook, 2007). If the Amazon basin was indeed drier, Vizy and Cook (2007) hypothesise that increased precipitation in the Perúvian and northern Bolivian Andes would be possible due to the South American Low Level Jet (LLJ) (Figure 2.8) being able to impinge more closely on to the eastern Andean mountains enhancing convection over the tropical Andes. The ITCZ would have been displaced more southerly due to the cooler temperatures in the northern hemisphere (Figure 2.8), this would have been able to displace circulatory patterns that would have provided enhanced moisture (Ramirez *et al.*, 2023). This would bring increased precipitation, and would strengthen east-west gradient in ELA depressions during the LGM, even if the Amazon basin was drier than today (Garreaud *et al.*, 2003).

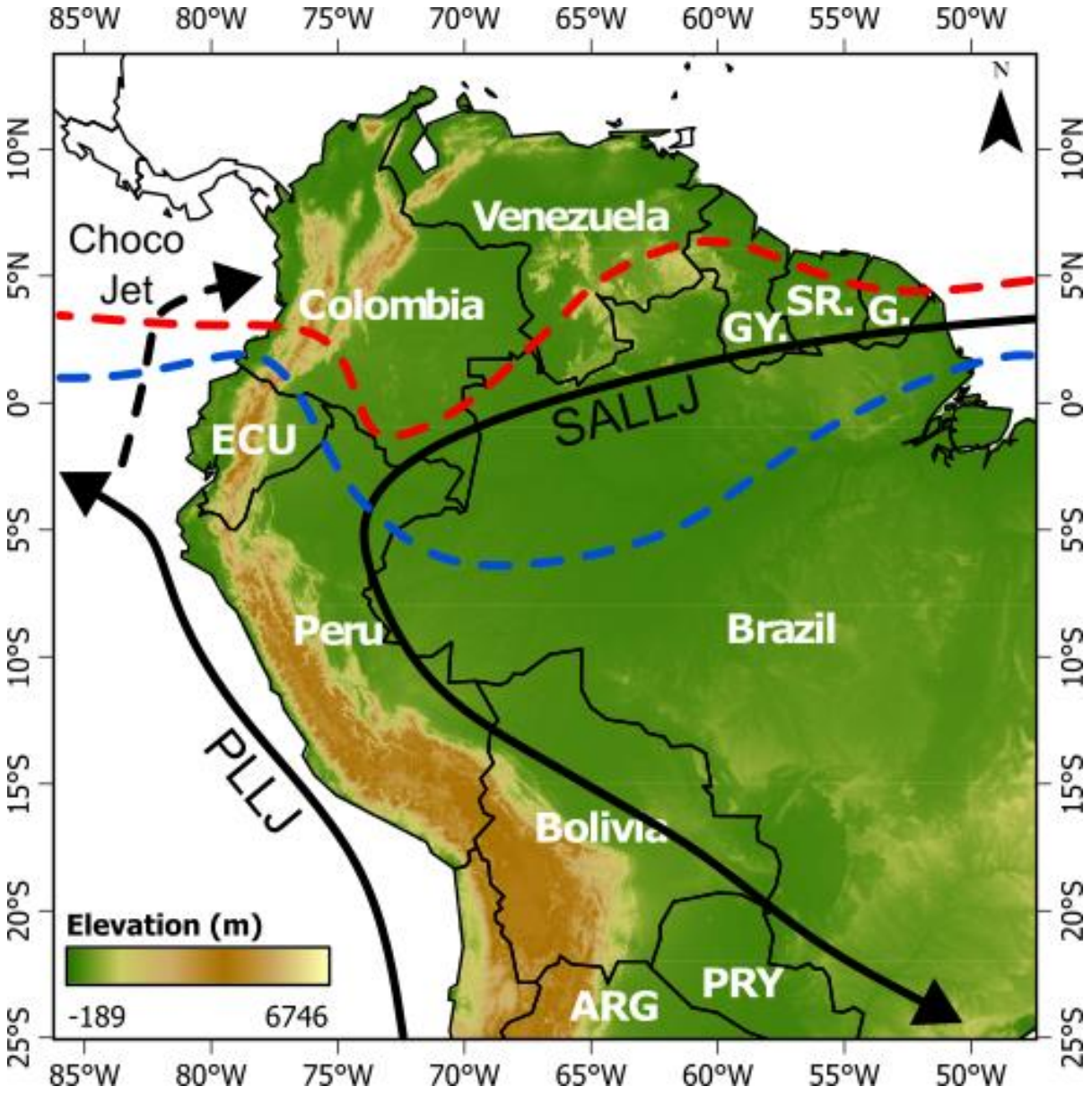

Figure 2.8: The South American Low Level Jet (SALLJ), that follows the SACZ, along with the Perúvian Low Level Jet (PLLJ) important for moisture transport over the Andes (Espinoza *et al.*, 2020). The mean modern ITCZ position (red dashed line), and the mean late-glacial ITCZ position (blue dashed line) (Ramirez *et al.*, 2023).

2.3.3. Key themes of tropical Andean climate

Overall, SST and glaciological estimates all indicate a cooler LLGM within the tropics, however, the discrepancy in the temperature cooling from high elevation glaciers suggest that SST underestimate the significance of LLGM cooling (Loomis *et al.*, 2017; Tierney *et al.*, 2020b). This is potentially due to lapse rates being steeper during the LGM, enhancing cooling needed over land (Loomis *et al.*, 2017), or that SST reconstruction incur errors due to difficulty in the parameterisation of tropical convective processes (Crowley, 2000; Tripati *et al.*, 2014). Palaeo-precipitation studies show more variability across the tropical Andes, with the Bolivian Altiplano and regions of the northern Andes indicating a wetter LLGM (Baker *et al.*, 2001a; Baker *et al.*, 2001b; Nunnery *et al.*, 2019), while locations within the northern Amazon, an important source of moisture, indicate a drier LLGM (Mourguiart and Ledru, 2003; Novello *et al.*, 2019). The variability in observations are primarily linked to changes in the ENSO, intensification of the SASM, and the displacement of the ITCZ that can shift the movement of moisture north or south dependant on its position (Segura *et al.*, 2019; Rodbell *et al.*, 2022).

Latitudinally there is a clear increase in temperature cooling seen in palaeoglacial ELA reconstructions within the northern Andes (Venezuela and Colombia), when compared to more southern tropical Andes locations (Perú and Bolivia). However, they do not take into account precipitation differences that would affect estimated temperature cooling (Klein *et al.*, 1999), while there is a clear gap spatially that makes conducting latitudinal comparisons difficult. The large latitudinal gap in northern Perú and southern Ecuador, where the study is, can provide a bridge between the two primary areas of climate estimates. This thesis, while conducting similar ELA reconstructions to determine temperature cooling, shall use numerical modelling to allow the influence of increase precipitation to be considered. This shall determine the climatic envelope glacier that occupied the Las Huaringas could have existed under.

2.4. Morphology and scale of reconstructed ice masses

2.4.1. Evidenced for glacial reconstructions

There is a plethora of glacial geomorphological evidence (Figure 2.9) that allows the characterisation of glaciations (Cook and Swift, 2012). Such glacial geomorphological evidence that can be used are, a) moraines, b) overdeepenings, c) glacial eroded bedrock, d) glacial cirques, and d) the valley geometry. The mapping of such evidence can provide studies with a preliminary understanding of the glacial history, climate, extent, thickness, and ice dynamics. Evidence can also be used and targeted for TCN sample collection that can aid in the development of advance-retreat chronologies (Sutherland *et al.*, 2019). Mapped evidence can

also be used to constrain numerical models (Ely *et al.*, 2019) in order to parameterise them to best represent the glacial dynamics that can be inferred from the palaeoglacial geomorphological evidence.

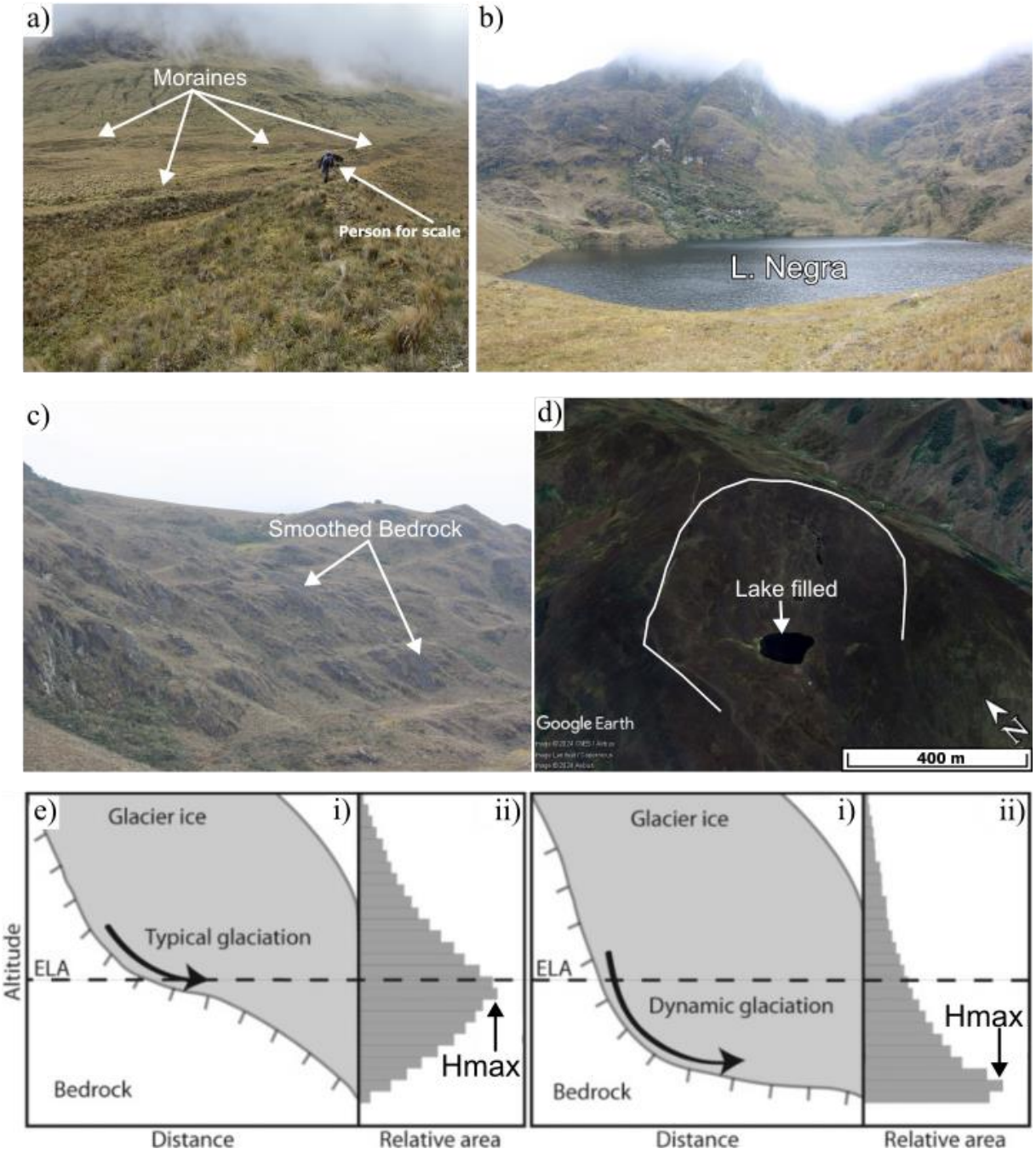

Figure 2.9: Geomorphological evidence that have been used to aid in reconstructing palaeoglacial advances; a) moraines from the Shimbe valley (arrows indicate some moraines) Prof Andy Henderson for size, b) glacial overdeepenings of Laguna Negra (now lake filled), c) glacial eroded bedrock surfaces at the headwall of Laguna Negra (image from Andy Henderson), d) glacial cirque of the Huancabamba 4 with a lake filled overdeepening in the centre (oblique image from Google Earth™, and e) i) an example of simple 2d valley geometry, and how this ii) generates the hypsometric frequency distribution with the Hmax, the elevation where most of the valley area is at being a proxy for the valleys ELA (Barr and Spagnolo, 2014).

Moraines (Figure 2.9a) are the clearest palaeoglacial evidence that denote where the glaciers' frontal position was at the time of deposition (Blard *et al.*, 2014; Stansell *et al.*, 2015) and are the most used evidence in glacial reconstructions (e.g. Esper Angillieri, 2013; Vilímek *et al.*, 2016). Terminal moraines detail the maximal extent of the glacier, while lateral moraines can provide inferences of glacial thicknesses (Benn and Evans, 2014; Pearce *et al.*, 2017). Large moraines are generated at times of enhanced glacial erosion, or the amount of time the glacier occupied that extent (Antoniazza and Lane, 2021). These large moraines are generally generated at periods of more extensive glacial ice, for example at the region LLGM. Smaller moraines that are found generally within the confines of these large moraines, denote advances younger the moraine in front of it (i.e., YD moraines behind the LLGM moraines) or standstill events during retreat phases. Moraines can be used for TCN dating methods to determine when these moraines were deposited.

Glacial overdeepenings (Figure 2.9b) are large erosional features generated as glaciers advance downvalley and erode their bed (Cook and Swift, 2012). These overdeepenings become filled with water, forming into lakes post-glaciation and form basal lacustrine sediment layers (Cook and Swift, 2012). These is used extensively throughout the tropical Andes to understand glacial retreat through a studied valley, if either one, or multiple, lakes are present (e.g. Abbott *et al.*, 2003; Rodbell *et al.*, 2008; Stansell *et al.*, 2010; Stansell *et al.*, 2014). If multiple lakes are present within the same valley system, they can be used to provide minimum and maximum limiting ^{14}C ages of deglaciation, e.g., the lowest lake should have the oldest ages, while the highest lake should have the youngest.

Glacial eroded bedrock surfaces (Figure 2.9c) are where the bedrock that has been eroded down to, and itself eroded by, glacial action. Similar to moraines, these can be dated providing the timing on when the surface was uncovered by a retreating glacier, thus providing a general date for the onset of deglaciation (e.g. Hall *et al.*, 2009; Alcalá *et al.*, 2011). Briner and Swanson (1998) suggests that the use of glacially plucked bedrock for dating, can minimise the potential for inherited age due to the level of erosion they incur. They can only be used to determine the date at which they were uncovered, which could be in the middle or end of a deglacial phase. These should be used in combination with moraines, or other glacial geomorphology in front or behind them, to enable an understand on the rate of deglaciation (e.g. Hall *et al.*, 2009; Smith *et al.*, 2009; Carcaillet *et al.*, 2013; Blard *et al.*, 2014)

Glacial cirques (Figure 2.9d) are erosional features from the source locations of glaciers (Barr and Spagnolo, 2015). These cirques are generally arcuate features, that show a transition from a steep headwall to a more shallow overdeepened floor, generally infilled with a lake or a bog

(Evans and Cox, 1974). Cirque distribution can help determine the presence, or absence, of glaciers within a region, with more developed cirques indicating more extensive glacial presence within a region (Principato and Lee, 2014). Cirque aspect is generally dictated by variations in solar radiation (Chueca and Julián, 2004), and the prevailing wind direction of the region (Evans, 1977). While the cirque floor altitude can also indicate climate that was able to support glaciation (Principato and Lee, 2014; Barr and Spagnolo, 2015), that can also be used as a proxy of the average ELA during glaciations (e.g. Mitchell and Humphries, 2015).

Lastly, valley geometry (Figure 2.9e) and morphology can an indicator of former glacial presence in a valley (Brocklehurst and Whipple, 2004). It would be expected that the most extensive glacial advance (and/or longest lived), would have exhibited the largest influence on valley form and morphology, due to the extended opportunity for erosion. Morphometric analysis of these valleys, such as a valleys hypsometry, can indicate the ELA. Many studies attribute this to the LLGM glacial advances (Egholm *et al.*, 2009; Barr and Spagnolo, 2014) or older (Steer *et al.*, 2012). Once they valley has become completely or partly deglaciated fluvial processes take over and may begin to remove or lessen the signature of glaciation.

2.4.2. Perúvian vs. Ecuadorian palaeoglacial reconstruction

Perú has received the most attention in recent years (Seehaus *et al.*, 2019; Emmer *et al.*, 2021), while Ecuador has had more limited attention. Across Perú and Ecuador (Rodbell *et al.*, 2002; Francou, 2004), there are a limited number of studies that conduct detailed geomorphological mapping in conjunction with fully reconstructing past glacial extents from the geomorphological record (Ramage *et al.*, 2005). Many studies (e.g. Smith *et al.*, 2005b; Shakun *et al.*, 2015b; Emmer *et al.*, 2021) only attempt to map moraines to facilitate TCN sample collection. This lack of reconstruction of palaeoglaciers limits our understanding of the glaciation style, while also preventing a full appreciation of how sampled moraines were generated. Further, as discussed previously, reconstructed glaciers can provide a preliminary understanding of the palaeoclimate they were generated under, which can further provide credence to dated evidence of past advances, placing them in the wider context of the global climate and important global events (e.g., Heinrich events) (Temovski *et al.*, 2018).

Within Peru, only a few attempt to reconstruct either just their palaeoglacial extents (Ramage *et al.*, 2005), or reconstruct palaeoglacial surfaces (Raasveldt, 1957; Mark *et al.*, 2002). Most of these reconstructions focus on reconstructing cirque to valley glaciation styles (Figure 2.10), this may be because many glaciers that are reconstructed sit within glacial valleys. Ice caps are

present within Perú, such as the Nevado Coropuna (e.g. Bromley *et al.*, 2016; Úbeda *et al.*, 2018), that have had their former extents expanded in line with ice cap glaciations. However, when studies do reconstruct glacial ice extents, they have primarily been limited to reconstructing a few glaciers (Ramage *et al.*, 2005), a singular glacial valley (Bromley *et al.*, 2016), or individual glaciers (Stansell *et al.*, 2017). This may be due to targeting a limited number of valleys for geochronology generation, but prevents further comparisons of adjacent glacial valleys, and interregional comparison of similar topography or adjacent regions.

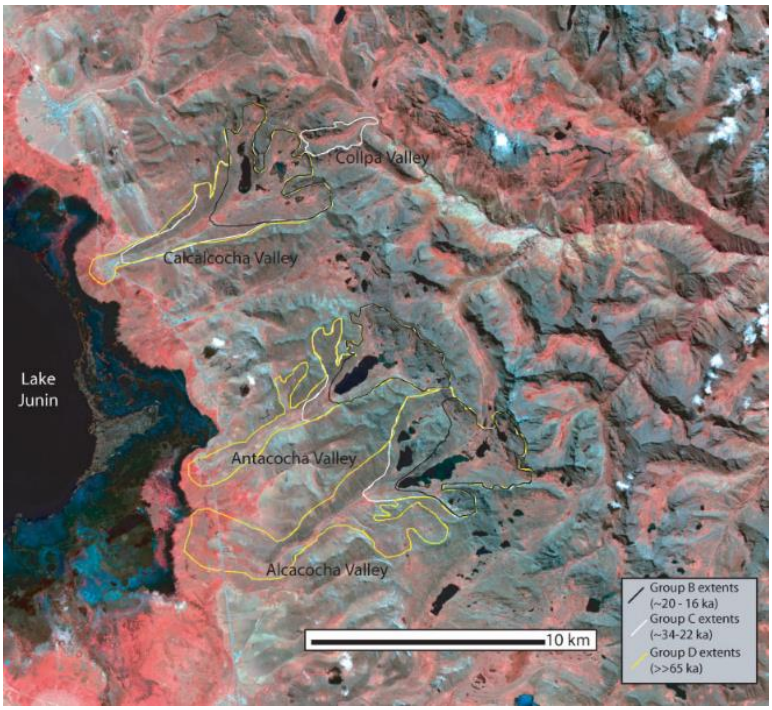

Figure 2.10: Four reconstructions of glacial extents at multiple time periods (LLGM group C moraines) within the Junín Plain region in central Perú by (Figure from Ramage *et al.*, 2005). This shows that they have been reconstructed as a cirque to valley glaciation.

Within Ecuador, located within a differing climatic regime of the inner tropics, many glaciers sit within different topographical regions when compared to Perúvian glaciers, and this is reflected in reconstructed glacial extents. Most glaciers within Ecuador now only exist as ice caps on top of volcanoes (e.g., Volcán Gayambe, Volcán Antisana and Volcán Cotopaxi), these act as local topographic highs that enable glaciation to occur. Many reconstructions have thus occurred in locations where glaciers are deglaciating on volcanoes (Clapperton, 1990) (Figure 2.11), or where ice cap glaciation is inferred from the geomorphological record (Clapperton *et al.*, 1997b). There are very limited studies within Ecuador that attempt to reconstruct glacial extents from the mapped palaeoglacial geomorphology. While moraines are mapped, these have not been explicitly linked into reconstructed ice extents – only Clapperton and McEwan (1985) attempt to detail glacial extents inferred from the geomorphology. This lack of overall reconstruction of glacial extents from the already mapped geomorphological record limits our overall ability to understand glacial changes in area extent across Ecuador, or Andes as a whole.

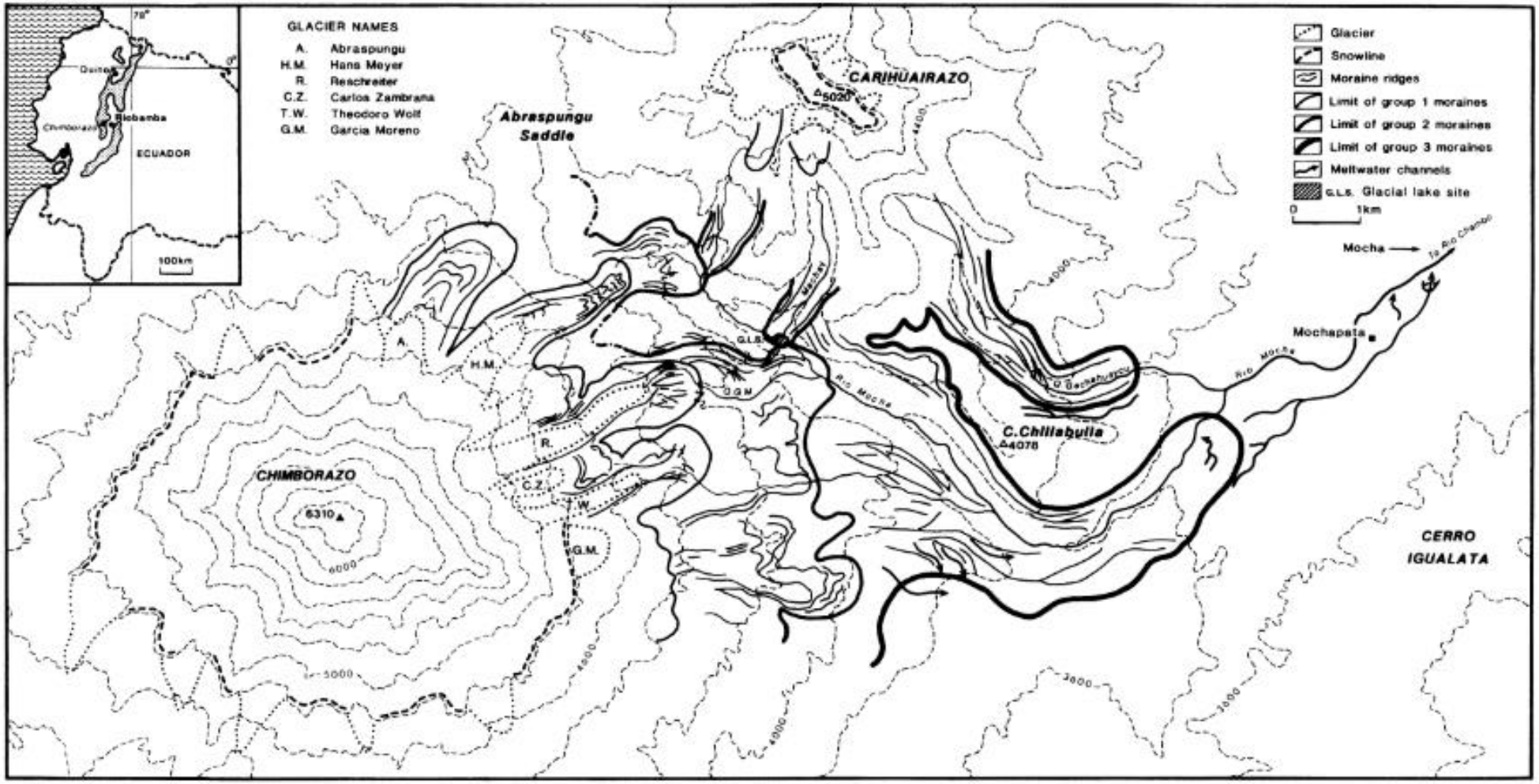

Figure 2.11: Geomorphology map from Chimborazo and Carihuairazo ice caps, in Ecuador from (Clapperton and McEwan, 1985) detailing glaciation at multiple periods, group 3 moraines (thickest line) detail the regions LLGM extent, from the Chimborazo volcano connecting with glaciers coming off the Carihuairazo volcano.

2.4.3. Valley vs. ice plateau reconstructions

From the above styles of glaciation that are seen within different topographical settings, we can use the contemporary record to inform how glaciers could be reconstructed. Both valley-based glaciers, and plateau ice fields or ice caps, are seen across contemporary ice masses within the tropical Andes, in particularly in Perú. The use of modern glacial proxies, in periods of glacial retreat, could led to potential misinterpretations of the geomorphological evidence. This can then have implications on the style of glaciation that is reconstructed, and on the palaeoclimate interpretations for past glaciations (Úbeda *et al.*, 2009), such as ELA lowering that could detail erroneous temperature and snowline reconstructions (Rea *et al.*, 1998).

Evidence of potential misinterpretations have been noted within the UK, within the Lake District (Figure 2.12), one of the most studied locations for glaciation. A number of interpretations of the same geomorphological evidence have been noted throughout the years (Manley, 1961; Sissons, 1980; Wilson and Clark, 1998; McDougall, 2013), primarily detailing a cirque-to-valley configuration, primarily due to the lack of up valley evidence. These have potential underestimated the glacial ice extent within the region (Figure 2.12a). McDougall (2013) reinterpreted the geomorphology within the eastern Lake Distract as an icefield or ice cap (Figure 6.12b), with ice that reached over the top of local topography and connected with ice that was traditionally thought to be confined to their own individual valley.

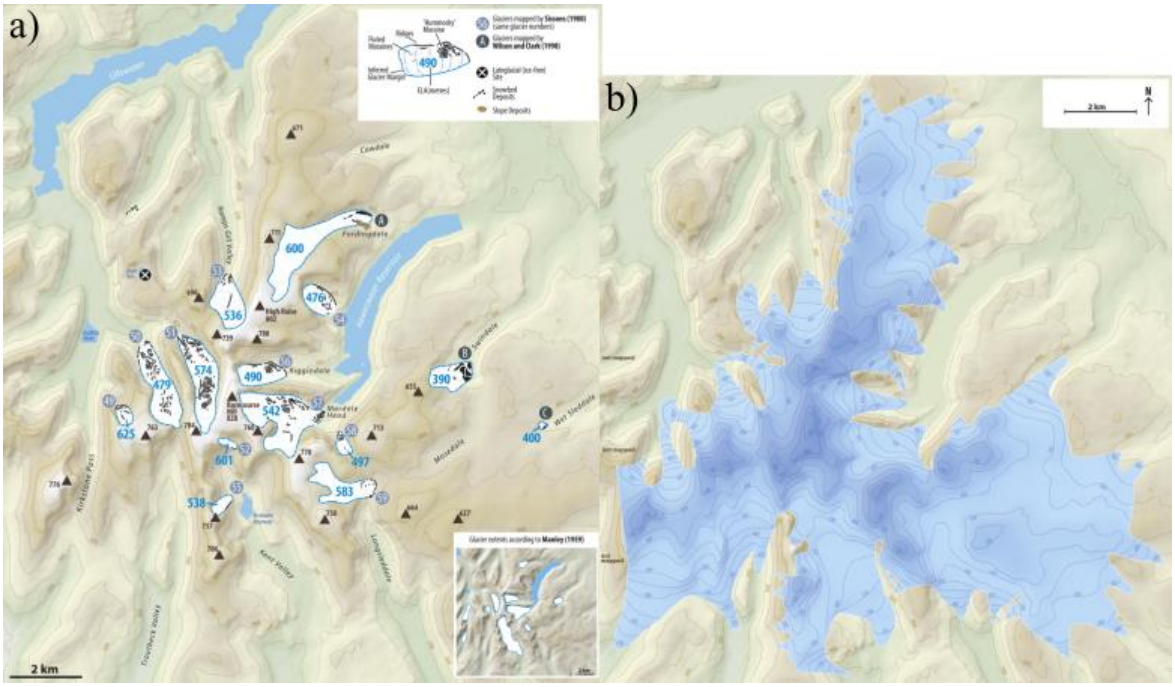

Figure 2.12: Reinterpretation of evidence in the eastern Lake District, UK, with an initial a) valley-based glaciers reconstructed by Sissons (1980), Wilson and Clark (1998), and Manley (1961) (inset bottom right), to b) a more expansive ice plateau, or ice-field, configuration building ice over valley tops. Figures from McDougall (2013) Figures 2 (a) & 7 (b).

This reinterpretation has identified the necessity for researchers to critically analyse the evidence within their study site and attempt to reconcile how features link to the morphology of former ice extents and thicknesses. Reinterpretations have already been identified in regions of extensive glacial research where initial valley reconstructions were made, but have since favoured an ice plateau, ice-field, or ice cap, configuration reconstruction (Ballantyne, 1989; McDougall, 2001; Lukas and Bradwell, 2010; Ballantyne and Stone, 2012; Brown *et al.*, 2013). Such evidence used is the presence of lateral moraines that extend up valley, or can be tied to the high ground above the valley wall (McDougall, 2013). These can be difficult to map if evidence is fragmented or reworked by postglacial processes. Other difficulties can come from the absence of any evidence on high ground where ice could have been present. Polythermal glaciation with cold based glacial ice in the accumulation zone (Gilbert *et al.*, 2014) would limit the generation of evidence within highland regions, or provide no evidence, while cold based ice within downvalley positions provide limited geomorphological evidence (i.e., bouldary moraines) for interpretations of glacial ice extents (Reinardy *et al.*, 2019).

2.4.4. Warm based vs. cold based glaciation

The geomorphological record can aid in reconstructing the dynamics and morphology of former glaciers; however, the type of thermal regime can make such evidence either hard to discern or be totally absent from the record. While an entirely cold based glacier within the tropical Andes is not identified within the current literature, polythermal glaciers are common within mountain regions (Lai and Anders, 2021). These are glaciers that have a mixture of warm, and cold based ice throughout their glacial extent. These can either be at the terminating end due to thinner ice being effected by the surrounding climate (Carrivick *et al.*, 2023), or at the accumulation zone (Gilbert *et al.*, 2014). Within these cold based zones, there is the potential for limited erosion that can cause inheritance, and older dates from TCN techniques.

While it was traditionally inferred that cold based ice generates no evidence, ice with cold based portions still exhibit subtle evidence of erosive and depositional features (Cuffey *et al.*, 2000; Waller, 2001). Such depositional evidence is boulder moraines, moraines on top of undisturbed landscapes, and the absence of glaciofluvial features (Staiger *et al.*, 2005). These can be hard to identify within remotely sensed imagery, while also being difficult to see in the field (Smith *et al.*, 2009). However, depositional evidence within the accumulation region may still be absent due to accumulations regions being primarily erosive, and the source area of downvalley depositional features. If such evidence is identified however, cold base glaciation may have existed within the region.

Such evidence has been identified within the tropical Andes by Smith *et al.* (2009) at Nevado Sajama in Bolivia, with bouldery moraines and bouldery drift (Figure 2.13). Such evidence is important, not just for understanding the dynamics of glaciers, but also for understanding potential areas that may be impossible to be dated accurately using TCN dating techniques – due to the problems of nuclide inheritance from the lack of glacial erosion required to 'reset' the exposure and already incurred nuclides (Ivy-Ochs and Schaller, 2009). This is the only reporting of cold based glacial ice explicitly within the tropical Andes. Other studies have estimated that glaciers within the tropical Andes, at least in Perú, were polythermal (Rodbell *et al.*, 2008; Stansell *et al.*, 2013; Stansell *et al.*, 2015; Angel, 2016). It is likely that ice reported in Smith *et al.* (2009) was also polythermal due to there being other evidence of moraines within their study area, but little evidence identified up valley near their headwalls. This is important for future mapping across the tropical Andes. Cold based glaciation can influence ice reconstructions from the geomorphological record (example in section 2.4.3.), and for TCN sample taking for geochronology generation, as cold based glaciation may not allow adequate erosion of the rock surface leading to older dates that what should be expected (Çiner *et al.*, 2017).

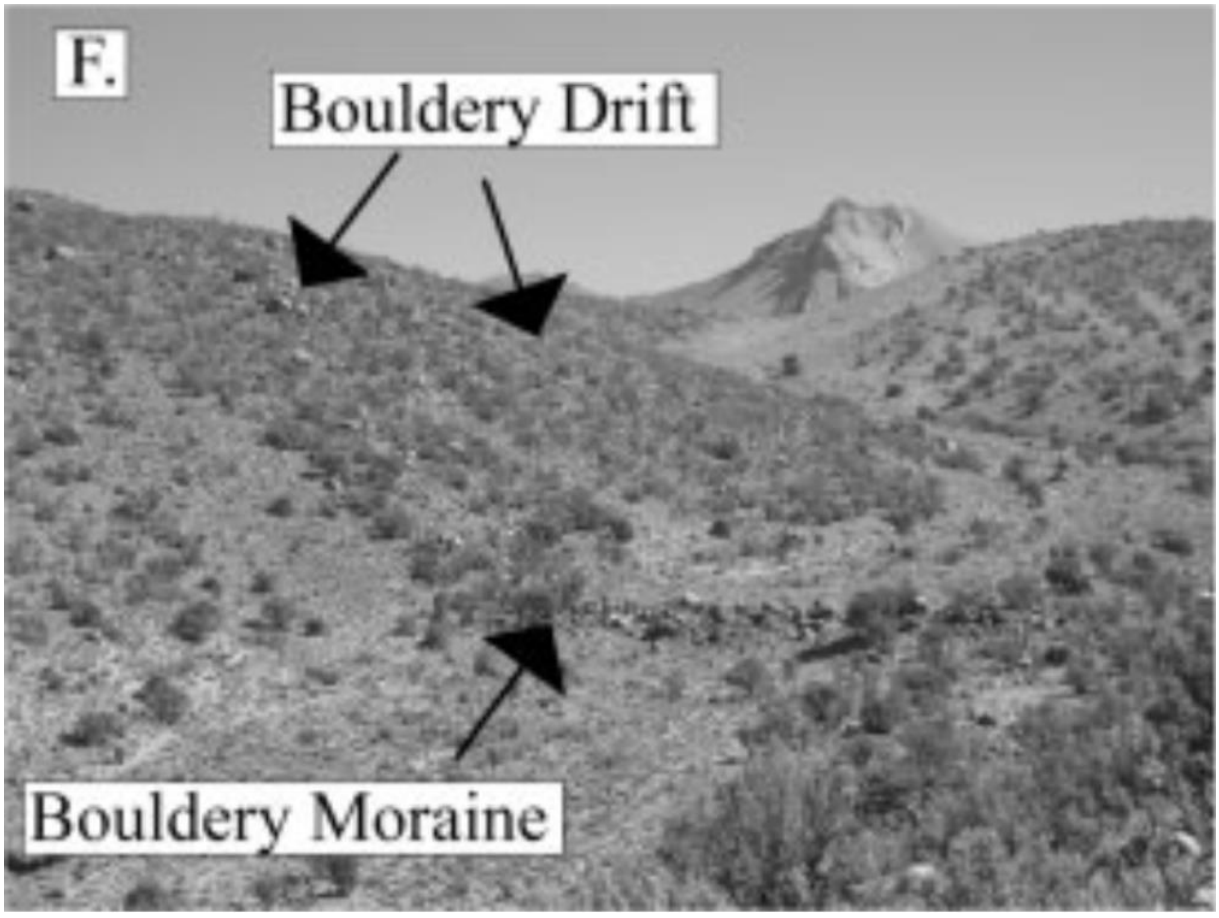

Figure 2.13: Bouldery moraines within the Nevado Sajama in Bolivia, evidencing potential cold based glaciation within the tropical Andes. The bouldery moraine and bouldery drift are difficult to identify within the field and could easily be missed. Image from Smith *et al.* (2009).

2.4.5. Key themes of glacial reconstructions

The number of studies that have generated reconstructions of glacial ice extents from the geomorphological records are limited. They primarily map moraines to date advances (Shakun *et al.*, 2015b). This limits our understanding of how glacial extents may differ latitudinally across the tropical Andes. Studies that are available that detail glacial reconstructions at their respective LLGM advances, generally Perúvian glaciers within a cirque-to-valley glaciation setting (Ramage *et al.*, 2005), while Ecuadorian glaciers are in an ice cap configuration (Clapperton and McEwan, 1985). These reconstructions are potentially influenced by the surrounding modern-day glacial setting, at least in Perú, that does suggest a cirque-to-valley configuration, but the geomorphological evidence may be interpreted incorrectly, as mentioned previously by the absence of up valley geomorphology, and by the censoring of evidence by post-glacial processes. Polythermal glaciation (Smith *et al.*, 2009) within the accumulation zone may prevent the generation of geomorphological evidence up valley, that may lead to the reconstruction of ice being confined to the glacial valley. Subsequent revaluations of glacial evidence in locations of extensive study have shown reinterpreted are needed to accurately represent the ice extents at their LLGM extents (McDougall, 2013). This leads to the need to evaluate the mapped geomorphology and understand just how the evidence was produced.

2.5. The Last Glacial Maximum in the tropical glacial Andes

2.5.1. The use of dating techniques in reconstructing glaciations

'Terrestrial *in situ*-produced Cosmogenic Nuclides' (TCN; Gosse and Phillips, 2001) are one of the most used methods in modern studies to determine the timing of exposure of a rocks surface, using the amount of cosmogenic nuclides that have accumulated within the rock (Figure 2.14). These are generated by the process of 'spallation', removing protons and neutrons from isotopes within the rock to leave behind a lighter nucleus, and a different isotopes (Dunai, 2010). These nuclides are dated by measuring their concentrations, compared to their original isotopic state. Certain nuclides can be used for this purpose, as they are a rare geological material only produced by cosmic rays, and they are stable and/or long-lived elements. It is assumed that the rocks sampled have been eroded to a sufficient depth to remove all previously accumulated, or 'inherited', nuclides (Figure 2.14 iv). It is also assumed that they have not been recovered (e.g., by sediment or ice) post-exposure, and that the production rate of the nuclides under study are known (Gosse and Phillips, 2001; Ivy-Ochs and Schaller, 2009). A production rate can then be used to determine their exposure age. However, these production rates need to be generate locally, which is uncommon due to the study site locations, and are then normalised

to the production at Sea Level and High Latitude (SLHL) by using the detection of nuclear disintegrations in photographic film for different latitudes and altitudes (e.g. Lal, 1991) or from neutron flux measurements at different latitudes and altitudes (Desilets and Zreda, 2003). The use oif differing production rates, even those near to or at the locality, can cause age differences of around 20% (Gosse and Phillips, 2001).

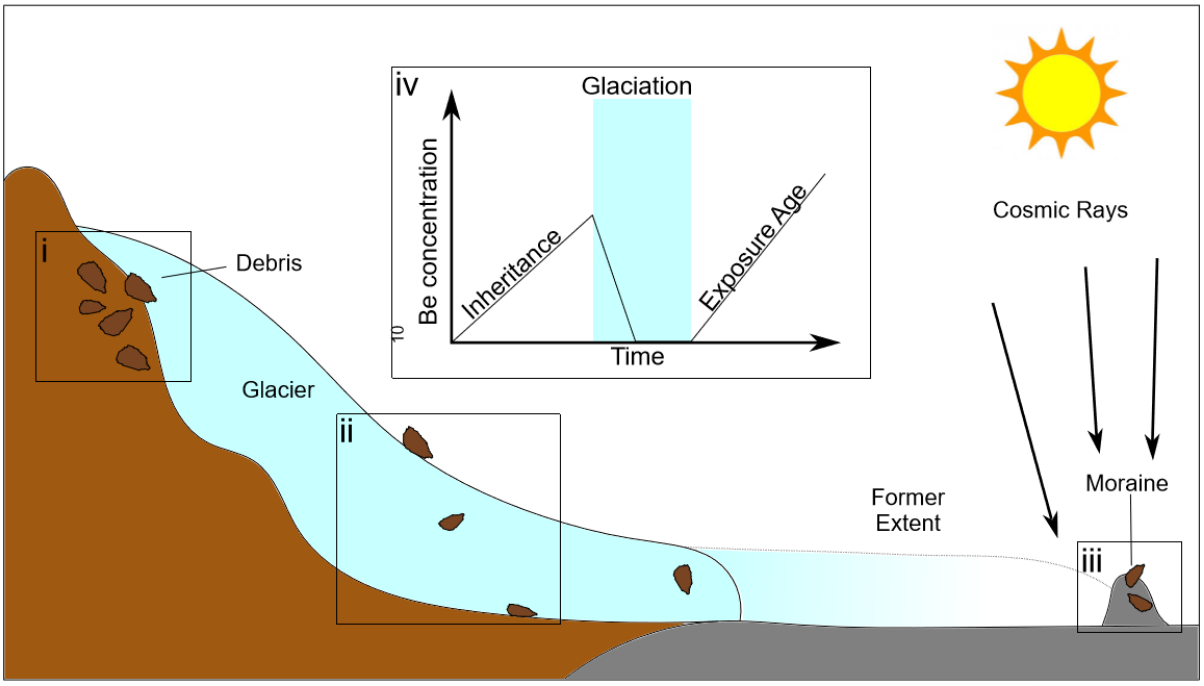

Figure 2.14: The assumption behind TCN dating; i) debris is eroded and entrained by the glacier and is; ii) transported supra-, en- or sub-glacially, being eroded and removing inherited nuclides before; iii) being deposited as moraine or boulder, exposed to cosmic rays with which to sample from; iv) a graph (modified from Ivy-Ochs and Briner, 2014) showing an ideal exposure with inheritance being eroded during glaciation and an exposure age after glaciation. A modified of the figure from Davies (2020).

Radiocarbon (^{14}C), was widely used in older studies across the tropical Andes e.g. Herd and Naeser, 1974; Rull and Schubert, 1989; Heine and Heine, 1996; Farber et al., 2005). The method indirectly dates moraines by dating organic materials (Jull, 2013) that are found in front of, behind, underneath, or within the boundary of a moraine (Figure 2.15). This technique assumes that the organic material was in equilibrium with carbon-14 (^{14}C) production within the Earth's atmosphere. Once the organic material dies, it is removed from this equilibrium and begins to decay at the speed of its half-life (~5,700 yrs) (Jull, 2018). The amount of ^{14}C within the organic material can then be matched with time periods of increased and decreased carbon in the atmosphere to determine date of deposition. This age can then primarily give limiting ages for glaciations (Rodbell *et al.*, 2009). Due to recalculation of the historical carbon content of the Earth's atmosphere, older ages need to be recalibrated to newer calibration curves, primarily to IntCal20, which provides mean probability on the age of the organic matter along the carbon curve.

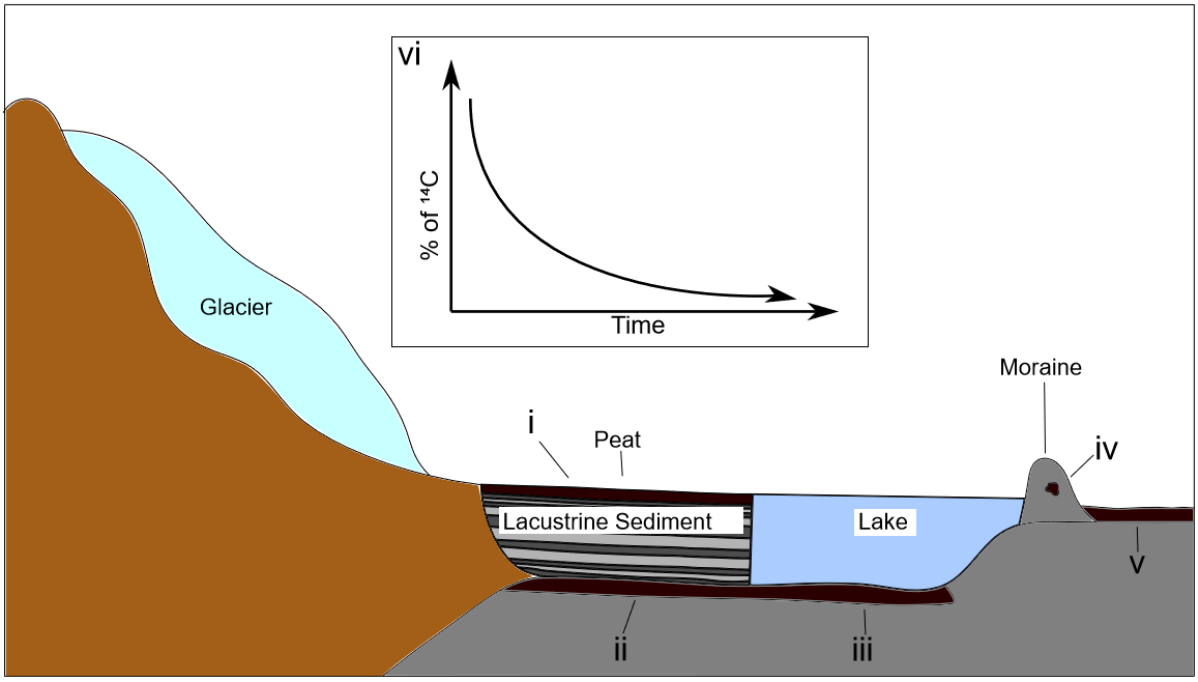

Figure 2.15: Radiocarbon dating using peat from; i) behind the moraine on top of (*) and ii) below lacustrine sediment (**); iii) below a present lake (**), iv) within the moraine (**) and; v) in front of the moraine (**); vi) showing the percentage of ^{14}C and its time since the biological material died. * = minimum-limiting ages; ** = maximum-limiting ages. Figure modified from Davies (2020).

2.5.2. Current understanding of the Last Glacial Maximum timing

The above understanding on how climate was different in the LGM within the tropical Andes, along with the evidence that studies look for in-order to reconcile and detail glacial advances, have been used extensively. This section shall present an overview of advances identified during their individual regional LLGM advances (Figure 2.16) from both ^{14}C (Table 2.1) and TCN (Table 2.2) studies. These primarily focus in Perú and Ecuador, due to their proximity to the study area (Chapter 1). Only published ages are used and recalculated where possible.

Most TCN dates are recalculated by Shakun *et al.* (2015a), but studies published after, or not recalculated, were recalculated in the CRONUS-Earth online calculator. All TCN ages were recalculated using the Kelly *et al.* (2015) production rate, and the Lal (1991)/Stone (2000) scaling method using the reported sample descriptions (erosion, shielding etc.) of each study. ^{14}C ages were recalculated in the Calib 8.20 calculator, using IntCal20 curve, and use 2σ analytical error to provide the error range for the recalibrated ages. Where ages are unable to be recalculated, they are clearly denoted. Outliers (in red) are determined both in this thesis and by Shakun *et al.* (2015a) determined by comparison to other sample ages within the same study, or by the relevant study itself if they determine an age as an outlier.

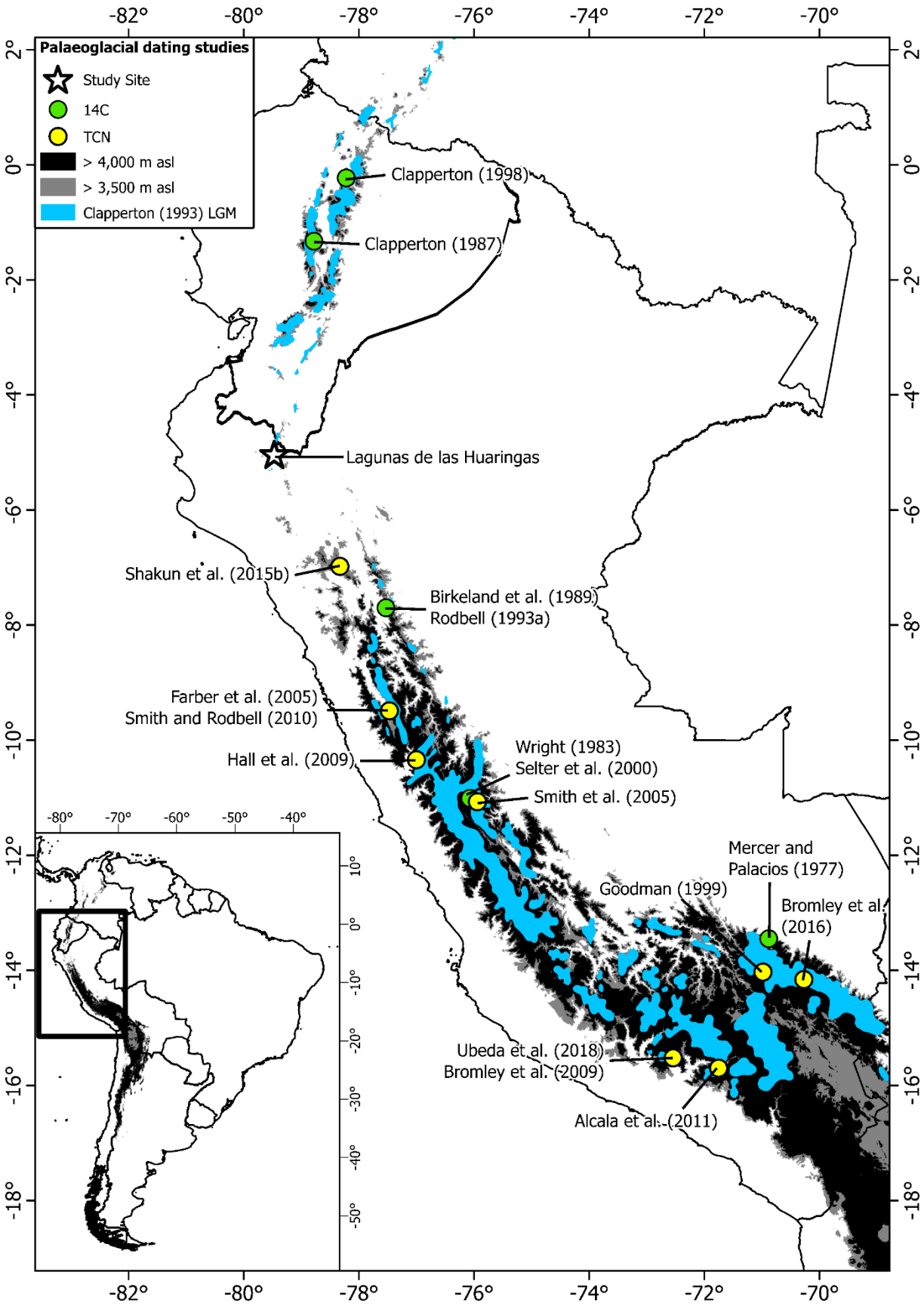

Figure 2.16: A collection of palaeoglacial studies that utilise ^{14}C or TCN dating techniques and their geographic position, along with the references of the studies. The dates and studies can be found in Table 2.2 for ^{14}C dating, and Table 2.3 for TCN dating studies. Blue polygons are the estimated South American LLGM extent of ice masses within the tropical Andes from Clapperton (1993). Star details the study region (Figure 1.2).

Table 2.2: Palaeoglaciation studies identifying LLGM glaciation advances, using radiocarbon dating (green dots in Figure 2.16)

Region	Locality	Lat (DD)	Lon (DD)	Summit Elev	Sample Elev	14C Age	Cal BP Date	Feature Dated	Sample	Lab ID	Interpretation	Reference
Potrerillos plateau, Ecuador		-0.23	-78.22	4462 m	3500 m	30,000	*	Laval flow	Organic matter underlying two interbedded tills	-	Indicates that glaciers advanced to this point twice after that date	Clapperton (1998)
Chimborazo and Carihuairazo, Ecuador		-1.33	-78.78	5202 m	3770 m	33,290 ± 300	37,162-35,156[1]	Unit 5 peat below upper till	Peat underlying till	SRR-3028		Clapperton (1987)
Chimborazo and Carihuairazo, Ecuador		-1.34	-78.78	5202 m	3870 m	38,520 ± 580	41,021-40,034[1]	Unit 5 peat below upper till	Peat underlying	SRR-3029	Minimum-limiting date for full glacial provides the potential for a two-phase early LLMG advance after 39.7 ka	Clapperton (1987)
Chimborazo and Carihuairazo, Ecuador		-1.36	-78.82	5202 m	3750 m	35,400± 680	39,786-37,306[1]	Unit 5 peat below upper till	Compacted peat under till	SRR-2583		Clapperton (1987)
Cordillera Vilcanota, Perú	Upismayo Valley	-13.45	-70.88	5645 m	4450 m	28,560 ± 770	32,400-29,271[1]	Outer most lateral moraine	Peat underlaying glacial sediment	DIC-681	Advance early-LLGM	Mercer and Palacios (1977)
Cordillera Vilcanota, Perú	Upismayo Valley	-13.45	-70.88	5645 m	4020 m	14,010 ± 185	15,529-14,441[1]	Moraine	Lenses of peat under moraine	I-9623	Glacier advances near late last glacial	Mercer and Palacios (1977)
Cordillera Blanca, Perú	Manachaue Valley	-7.70	-77.53	6000 m	3590 m	12,100 ± 190	12,693-11,638[1]	Laguna Baja basal layer	Organic sediment in lake core	GX-12854	Deglaciation age of Manachaque valley	Birkeland et al. (1989)
Cordillera Blanca, Perú	Rurec	-9.50	-77.32	6000 m	4000 m	19,700 ± 340	22,583-21,012[1]	Lateral moraine	Basal organic matter bog within moraine confines	GX-14599	Rurec G2 moraines older than dated bog could be much older estimated older than 27 ka cal BP.	Rodbell (1993a)
Cordillera Blanca, Perú	Rurec	-9.50	-77.32	6000 m	4100 m	18,000 ± 290	20,481-19,054[1]	Lateral moraine	Basal organic matter bog within moraine confines	GX-14600		Rodbell (1993a)
Cordillera Blanca, Perú	Manachaue Valley	-7.70	-77.53	6000 m	4000 m	13,280 ± 190	14,572-13,430[1]	Oldest moraine	Peat exposure in lake-sediment section inside the oldest Manachaque moraines	GX-15850	GX-15850 provides minimum-limiting age for retreat from LLGM. GX-14356 confirms Birkeland et al. (1989) date of the lake	Rodbell (1993a)
Cordillera Blanca, Perú	Manachaue Valley	-7.70	-77.53	6000 m	3590 m	12,300 ± 220	13,207-11,828[1]	Laguna Baja basal layer	Basal organic matter bog within moraine confines	GX-14356		Rodbell (1993a)
Junín Plain, Perú	Lake Junín	-11.01	-76.07	5000 m	4085 m	23,980 ± 320	26,939-25,628[1]	Base of clay layer	Organic material	Beta-3217		Wright (1983)
Junín Plain, Perú	Lake Junín	-11.01	-76.07	5000 m	4085 m	12,010 ± 110	12,156-11,653[1]	Top of clay layer	Organic material	Beta-3216	These mark the end of LLGM glaciation.	Wright (1983)
Junín Plain, Perú	Lake Junín	-11.01	-76.07	5000 m	4085 m	17,795 ± 145	20,080 - 19,139[1]	10.79 m	Organic macrofossils	AA-24003		Seltzer et al. (2000)
Junín Plain, Perú	Lake Junín	-11.01	-76.07	5000 m	4085 m	25,700 ± 330	28,550 - 27,263[1]	14.74 m	Organic macrofossils	OS-18137	Base of core denotes start of LLGM glacial ice, and OS-18137 denotes potential deglaciation of lake.	Seltzer et al. (2000)
Junín Plain, Perú	Lake Junín	-11.01	-76.07	5000 m	4085 m	39,020 ± 1,045	42,409-40,173[1]	Base of core; 18.4 m	Mollusks	AA-24004		Seltzer et al. (2000)

* could not be recalculated; [1] recalculated in this study using INTCAL20, red = outlier

Table 2.3: Palaeoglaciation studies identifying LGM glaciation advances, using TCN exposure dating (yellow dots in Figure 2.16), studies collated as a mixture of from within this thesis, and from Shakun *et al.* (2015a).

Region	Locality	Lat (DD)	Lon (DD)	Summit Elev	Sample Elev	Method	Calendar Age	Feature Dated	Sample	Lab ID	Interpretation	Reference
Quelccaya Ice Cap, Perú		-14.03	-70.98	5645 m	4670 m	26Al + 10Be	25,460 ±1,600*	Medial moraine	Boulder	C10	Moraine stabilisation ~25.5 ± 1.3 ka and deglaciation at ~17.5 ± 0.3 ka	Goodman (1999)
Quelccaya Ice Cap, Perú		-14.03	-70.98	5645 m	4655 m	26Al + 10Be	17,554 ± 300*	Medial moraine	Boulder	C11		Goodman (1999)
Cordillera Carabaya, Perú	Minas Tira	-14.16	-70.27	5800 m	4626 m	10Be	25,751 ± 899[1]	Terminal moraine: outer terminal moraine	Boulder	NT-11-08		Bromley et al. (2016)
Cordillera Carabaya, Perú	Minas Tira	-14.16	-70.27	5800 m	4582 m	10Be	24,466 ± 855[1]	Terminal moraine: outer terminal moraine	Boulder	NT-11-05		Bromley et al. (2016)
Cordillera Carabaya, Perú	Minas Tira	-14.16	-70.27	5800 m	4563 m	10Be	23,870 ± 830[1]	Terminal moraine: intermediate landform	Boulder	NT-11-13		Bromley et al. (2016)
Cordillera Carabaya, Perú	Minas Tira	-14.16	-70.27	5800 m	4560 m	10Be	21,119 ± 733[1]	Terminal moraine: proximal ridge	Boulder	NT-11-18	Glacial maximum ~25.8 ± 0.9 ka early-LLGM extent	Bromley et al. (2016)
Cordillera Carabaya, Perú	Lagunas Aricoma	-14.32	-69.83	5800 m	4769 m	10Be	18,822 ± 658[1]	Lateral moraine	Boulder	ARC-09-25		Bromley et al. (2016)
Cordillera Carabaya, Perú	Lagunas Aricoma	-14.34	-69.83	5800 m	4769 m	10Be	18,787 ± 762[1]	Lateral moraine	Boulder	ARC-09-26		Bromley et al. (2016)
Cordillera Carabaya, Perú	Lagunas Aricoma	-14.32	-69.83	5801 m	4716 m	10Be	25,709 ± 939[1]	Lateral moraine	Boulder	ARC-09-44	Deglaciation occurred after 18.8 ± 0.7 ka	Bromley et al. (2016)
Cordillera Blanca, Perú	Rurec	-9.48	-77.47	6000 m	3816 m	10Be	20,516 ± 2,198[2]	Terminal moraine	Boulder	K-2		Farber et al. (2005)
Cordillera Blanca, Perú	Rurec	-9.48	-77.47	6000 m	4007 m	10Be	20,637 ± 1,128[2]	Terminal moraine	Boulder	K-7		Farber et al. (2005)
Cordillera Blanca, Perú	Rurec	-9.49	-77.46	6000 m	3748 m	10Be	20,823 ± 915[2]	Terminal moraine	Boulder	Perú-18		Farber et al. (2005)
Cordillera Blanca, Perú	Rurec	-9.49	-77.45	6000 m	4001 m	10Be	21,812 ± 842[2]	Terminal moraine	Boulder	HU-2		Farber et al. (2005)
Cordillera Blanca, Perú	Rurec	-9.48	-77.48	6000 m	3847 m	10Be	22,280 ± 1,261[2]	Terminal moraine	Boulder	K-4		Farber et al. (2005)
Cordillera Blanca, Perú	Rurec	-9.49	-77.45	6000 m	3983 m	10Be	22,608 ± 882[2]	Terminal moraine	Boulder	HU-4		Farber et al. (2005)
Cordillera Blanca, Perú	Rurec	-9.49	-77.45	6000 m	4015 m	10Be	22,802 ± 966[2]	Terminal moraine	Boulder	HU-1		Farber et al. (2005)

* could not be recalculated; [1] recalculated in this study; [2] recalculated by Shakun et al. (2015a); [3] recalculated by Mark et al. (2017); [4] recalculated by Bromley et al. (2009), red = outlier

Table 2.3: *Continued*

Region	Locality	Lat (DD)	Lon (DD)	Summit Elev	Sample Elev	Method	Calendar Age	Feature Dated	Sample	Lab ID	Interpretation	Reference
Cordillera Blanca, Perú	Rurec	-9.49	-77.45	6000 m	3839 m	10Be	23,347 ± 1,139[2]	Terminal moraine	Boulder	Perú-21		Farber et al. (2005)
Cordillera Blanca, Perú	Rurec	-9.49	-77.48	6000 m	3728 m	10Be	24,200 ± 1,310[2]	Terminal moraine	Boulder	K-3		Farber et al. (2005)
Cordillera Blanca, Perú	Rurec	-9.48	-77.47	6000 m	3884 m	10Be	27,523 ± 1,188[2]	Terminal moraine	Boulder	K-5b		Farber et al. (2005)
Cordillera Blanca, Perú	Rurec	-9.48	-77.47	6000 m	3884 m	10Be	27,836 ± 1,575[2]	Terminal moraine	Boulder	K-5a		Farber et al. (2005)
Cordillera Blanca, Perú	Rurec	-9.49	-77.46	6000 m	3829 m	10Be	32,760 ± 2,476[2]	Terminal moraine	Boulder	K-1	Age of Rurec moraines mean 24.7 ± 4.5 ka LGM date	Farber et al. (2005)
Cordillera Blanca, Perú	Rurec	-9.49	-77.46	6000 m	3815 m	10Be	33,775 ± 1,731[2]	Terminal moraine	Boulder	K-10		Farber et al. (2005)
Cordillera Blanca, Perú	Jeullesh Valley	-10.00	-77.28	6000 m	4316 m	10Be	84,255 ± 4,869[1]	M1; Left Lateral moraine	Boulder	PE05-JEU-17		Smith and Rodbell (2010)
Cordillera Blanca, Perú	Jeullesh Valley	-10.00	-77.28	6000 m	4314 m	10Be	49,279± 2,426[1]	M1; Left Lateral moraine	Boulder	PE05-JEU-18		Smith and Rodbell (2010)
Cordillera Blanca, Perú	Jeullesh Valley	-10.00	-77.28	6000 m	4327 m	10Be	49,844 ± 2,518[1]	M1; Left Lateral moraine	Boulder	PE05-JEU-19		Smith and Rodbell (2010)
Cordillera Blanca, Perú	Jeullesh Valley	-10.00	-77.28	6000 m	4304 m	10Be	74,750 ± 2,939[1]	M1; Left Lateral moraine	Boulder	PE05-JEU-21		Smith and Rodbell (2010)
Cordillera Blanca, Perú	Jeullesh Valley	-10.00	-77.28	6000 m	4332 m	10Be	72,134 ± 3,067[1]	M1; Right lateral moraine	Boulder	PE05-JEU-23		Smith and Rodbell (2010)
Cordillera Blanca, Perú	Jeullesh Valley	-10.00	-77.28	6000 m	4332 m	10Be	75,512 ± 5,312[1]	M1; Right lateral moraine	Boulder	PE05-JEU-24		Smith and Rodbell (2010)
Cordillera Blanca, Perú	Jeullesh Valley	-10.00	-77.28	6000 m	4333 m	10Be	44,769 ± 1,764[1]	M1; Right lateral moraine	Boulder	PE05-JEU-26	M1: pre-LLGM 44.8 ± 1.8 ka	Smith and Rodbell (2010)
Cordillera Blanca, Perú	Jeullesh Valley	-10.00	-77.27	6000 m	4354 m	10Be	38,731 ± 1,717[1]	M2; Right lateral moraine	Boulder	PE05-JEU-05		Smith and Rodbell (2010)
Cordillera Blanca, Perú	*Jeullesh Valley*	*-10.00*	*-77.27*	*6000 m*	*4352 m*	*10Be*	*57,327 ± 3,095[1]*	*M2; Right lateral moraine*	*Boulder*	*PE05-JEU-06*		Smith and Rodbell (2010)
Cordillera Blanca, Perú	Jeullesh Valley	-10.00	-77.27	6000 m	4362 m	10Be	32,234 ± 1,747[1]	M2; Right lateral moraine	Boulder	PE05-JEU-07		Smith and Rodbell (2010)
Cordillera Blanca, Perú	Jeullesh Valley	-10.00	-77.27	6000 m	4407 m	10Be	35,088 ± 1,294[1]	M2; Right lateral moraine	Boulder	PE05-JEU-08		Smith and Rodbell (2010)
Cordillera Blanca, Perú	Jeullesh Valley	-10.00	-77.27	6000 m	4403 m	10Be	34,113 ± 1,263[1]	M2; Right lateral moraine	Boulder	PE05-JEU-09		Smith and Rodbell (2010)
Cordillera Blanca, Perú	Jeullesh Valley	-10.00	-77.27	6000 m	4424 m	10Be	63,569 ± 2,595[1]	M2; Right lateral moraine	Boulder	PE05-JEU-10	M2; early-LLGM minimum 32.2 ± 1.7 ka	Smith and Rodbell (2010)
Cordillera Huayhuash, Perú	Milo Valley	-10.34	-77.00	5000 m	4297 m	10Be	25,720 ± 1,061[1]	Left lateral end moraine	Boulder	MIL-01	One date shows LLGM ~25.7 ka	Hall et al. (2009)

* could not be recalculated; [1] recalculated in this study; [2] recalculated by Shakun et al. (2015a); [3] recalculated by Mark et al. (2017); [4] recalculated by Bromley et al. (2009), red = outlier

760

Table 2.3: *Continued*

Region	Locality	Lat (DD)	Lon (DD)	Summit Elev	Sample Elev	Method	Calendar Age	Feature Dated	Sample	Lab ID	Interpretation	Reference
Junín Plain, Perú	Alcacocha (W)	-11.07	-75.94	5000 m	4382 m	10Be	20,678 ± 956[2]	Group C; terminal moraine	Boulder	PE02-ALC-03		Smith et al. (2005)
Junín Plain, Perú	Alcacocha (W)	-11.07	-75.94	5000 m	4378 m	10Be	23,095 ± 1,254[2]	Group C; terminal moraine	Boulder	PE01-ALC-26		Smith et al. (2005)
Junín Plain, Perú	Alcacocha (W)	-11.07	-75.94	5000 m	4377 m	10Be	27,886 ± 1,181[2]	Group C; terminal moraine	Boulder	PE02-ALC-02		Smith et al. (2005)
Junín Plain, Perú	Alcacocha (W)	-11.07	-75.94	5000 m	4388 m	10Be	34,745 ± 1,911[2]	Group C; terminal moraine	Boulder	PE01-ALC-28		Smith et al. (2005)
Junín Plain, Perú	Alcacocha (W)	-11.07	-75.94	5000 m	4385 m	10Be	34,912 ± 1,996[2]	Group C; terminal moraine	Boulder	PE01-ALC-29		Smith et al. (2005)
Junín Plain, Perú	Alcacocha (W)	-11.07	-75.94	5000 m	4383 m	10Be	35,193 ± 1,896[2]	Group C; terminal moraine	Boulder	PE01-ALC-27	LLGM date to 29.4 ± 1.5 ka	Smith et al. (2005)
Junín Plain, Perú	Antacocha (W)	-11.04	-75.97	5000 m	4264 m	10Be	28,277 ± 1,146[2]	Group C; terminal moraine	Boulder	PE01-ANT-14		Smith et al. (2005)
Junín Plain, Perú	Antacocha (W)	-11.04	-75.96	5000 m	4275 m	10Be	29,880 ± 1,210[2]	Group C; terminal moraine	Boulder	PE01-ANT-08		Smith et al. (2005)
Junín Plain, Perú	Antacocha (W)	-11.04	-75.96	5000 m	4274 m	10Be	30,006 ± 1,213[2]	Group C; terminal moraine	Boulder	PE01-ANT-09		Smith et al. (2005)
Junín Plain, Perú	Antacocha (W)	-11.04	-75.96	5000 m	4267 m	10Be	31,242 ± 1,257[2]	Group C; terminal moraine	Boulder	PE01-ANT-10		Smith et al. (2005)
Junín Plain, Perú	Antacocha (W)	-11.04	-75.96	5000 m	4265 m	10Be	32,025 ± 1,274[2]	Group C; terminal moraine	Boulder	PE01-ANT-13		Smith et al. (2005)
Junín Plain, Perú	Antacocha (W)	-11.04	-75.96	5000 m	4269 m	10Be	33,111 ± 1,364[2]	Group C; terminal moraine	Boulder	PE01-ANT-12		Smith et al. (2005)
Junín Plain, Perú	Antacocha (W)	-11.04	-75.96	5000 m	4266 m	10Be	33,744 ± 1,412[2]	Group C; terminal moraine	Boulder	PE01-ANT-11		Smith et al. (2005)
Junín Plain, Perú	Antacocha (W)	-11.04	-75.97	5000 m	4262 m	10Be	33,960 ± 1,364[2]	Group C; terminal moraine	Boulder	PE01-ANT-15	LLGM dated to 31.5 ± 1.3 ka	Smith et al. (2005)
Junín Plain, Perú	Calcalcocha (W)	-10.97	-76.02	5000 m	4315 m	10Be	35,535 ± 1,513[2]	Group C; terminal moraine	Boulder	PE01-CAL-17		Smith et al. (2005)
Junín Plain, Perú	Calcalcocha (W)	-10.97	-76.02	5000 m	4317 m	10Be	24,430 ± 1,138[2]	Group C; terminal moraine	Boulder	PE01-CAL-18	LLGM dated to 30.4 ± 1.3 ka	Smith et al. (2005)
Junín Plain, Perú	Collpa (E)	-10.93	-75.94	5000 m	4162 m	10Be	26,679 ± 1,154[2]	Group C; terminal moraine	Boulder	PE02-COL-01		Smith et al. (2005)
Junín Plain, Perú	Collpa (E)	-10.93	-75.94	5000 m	4168 m	10Be	26,815 ± 1,244[2]	Group C; terminal moraine	Boulder	PE02-COL-03		Smith et al. (2005)
Junín Plain, Perú	Collpa (E)	-10.93	-75.94	5000 m	4208 m	10Be	27,244 ± 1,176[2]	Group C; terminal moraine	Boulder	PE02-COL-07		Smith et al. (2005)
Junín Plain, Perú	Collpa (E)	-10.93	-75.94	5000 m	4159 m	10Be	27,557 ± 1,381[2]	Group C; terminal moraine	Boulder	PE02-COL-02		Smith et al. (2005)
Junín Plain, Perú	*Collpa (E)*	*-10.93*	*-75.94*	*5000 m*	*4164 m*	*10Be*	*24,923 ± 1,167[2]*	*Group C; terminal moraine*	*Boulder*	*PE02-COL-04*	LLGM dated 27.1 ± 1.2 ka	Smith et al. (2005)

* could not be recalculated; [1] recalculated in this study; [2] recalculated by Shakun et al. (2015a); [3] recalculated by Mark et al. (2017); [4] recalculated by Bromley et al. (2009), red = outlier

Table 2.3: *Continued*

Region	Locality	Lat (DD)	Lon (DD)	Summit Elev	Sample Elev	Method	Calendar Age	Feature Dated	Sample	Lab ID	Interpretation	Reference
Junín Plain, Perú	Calcalcocha (W)	-10.97	-76.02	5000 m	4315 m	10Be	35,535 ± 1,513[2]	Group C; terminal moraine	Boulder	PE01-CAL-17		Smith et al. (2005)
Junín Plain, Perú	Calcalcocha (W)	-10.97	-76.02	5000 m	4317 m	10Be	25,430 ± 1,138[2]	Group C; terminal moraine	Boulder	PE01-CAL-18	LLGM dated to 30.4 ± 1.3 ka	Smith et al. (2005)
Junín Plain, Perú	Collpa (E)	-10.93	-75.94	5000 m	4162 m	10Be	26,679 ± 1,154[2]	Group C; terminal moraine	Boulder	PE02-COL-01		Smith et al. (2005)
Junín Plain, Perú	Collpa (E)	-10.93	-75.94	5000 m	4168 m	10Be	26,815 ± 1,244[2]	Group C; terminal moraine	Boulder	PE02-COL-03		Smith et al. (2005)
Junín Plain, Perú	Collpa (E)	-10.93	-75.94	5000 m	4208 m	10Be	27,244 ± 1,176[2]	Group C; terminal moraine	Boulder	PE02-COL-07		Smith et al. (2005)
Junín Plain, Perú	Collpa (E)	-10.93	-75.94	5000 m	4159 m	10Be	27,557 ± 1,381[2]	Group C; terminal moraine	Boulder	PE02-COL-02		Smith et al. (2005)
Junín Plain, Perú	*Collpa (E)*	*-10.93*	*-75.94*	*5000 m*	*4164 m*	*10Be*	*24,923 ± 1,167[2]*	*Group C; terminal moraine*	*Boulder*	*PE02-COL-04*	LLGM dated 27.1 ± 1.2 ka	Smith et al. (2005)
Cajamarca Valley, Perú	North Camp	-6.99	-78.33	4080 m	3886 m	10Be	22,103 ± 1,180[2]	Lateral moraine (S)	Boulder	MC-NC-9		Shakun et al. (2015b)
Cajamarca Valley, Perú	North Camp	-6.98	-78.34	4080 m	3912 m	10Be	22,347 ± 1,317[2]	Lateral moraine (N)	Boulder	MC-NC-6		Shakun et al. (2015b)
Cajamarca Valley, Perú	North Camp	-6.99	-78.33	4080 m	3866 m	10Be	23,347 ± 1,299[2]	Lateral moraine (S)	Boulder	MC-NC-10		Shakun et al. (2015b)
Cajamarca Valley, Perú	North Camp	-6.99	-78.33	4080 m	3897 m	10Be	24,417 ± 1,288[2]	Lateral moraine (S)	Boulder	MC-NC-7		Shakun et al. (2015b)
Cajamarca Valley, Perú	North Camp	-6.99	-78.33	4080 m	3897 m	10Be	24,764 ± 1,296[2]	Lateral moraine (S)	Boulder	MC-NC-8		Shakun et al. (2015b)
Cajamarca Valley, Perú	North Camp	-6.98	-78.34	4080 m	3913 m	10Be	24,835 ± 1,513[2]	Lateral moraine (N)	Boulder	MC-NC-5		Shakun et al. (2015b)
Cajamarca Valley, Perú	*North Camp*	*-6.98*	*-78.34*	*4080 m*	*3926 m*	*10Be*	*43,393 ± 2,049[2]*	*Lateral moraine (N)*	*Boulder*	*MC-NC-2*		Shakun et al. (2015b)
Cajamarca Valley, Perú	*North Camp*	*-6.98*	*-78.34*	*4080 m*	*3927 m*	*10Be*	*59,721 ± 3,262[2]*	*Lateral moraine (N)*	*Boulder*	*MC-NC-3*		Shakun et al. (2015b)
Cajamarca Valley, Perú	*North Camp*	*-6.98*	*-78.34*	*4080 m*	*3927 m*	*10Be*	*143,387 ± 5,818[2]*	*Lateral moraine (N)*	*Boulder*	*MC-NC-4*	LLGM dated to 23.7 ± 1.3 ka	Shakun et al. (2015b)

* could not be recalculated; [1] recalculated in this study; [2] recalculated by Shakun et al. (2015a); [3] recalculated by Mark et al. (2017); [4] recalculated by Bromley et al. (2009), red = outlier

765

Table 2.3: *Continued*

Region	Locality	Lat (DD)	Lon (DD)	Summit Elev	Sample Elev	Method	Calendar Age	Feature Dated	Sample	Lab ID	Interpretation	Reference
Cajamarca Valley, Perú	San Cirilo	-6.90	-78.61	4140 m	3960 m	10Be	17,746 ± 1,083[2]	Moraine ridge	Boulder	SC-7		Shakun et al. (2015b)
Cajamarca Valley, Perú	San Cirilo	-6.92	-78.59	4140 m	3970 m	10Be	19,604 ± 950[2]	Terminal moraine	Boulder	SC-12		Shakun et al. (2015b)
Cajamarca Valley, Perú	San Cirilo	-6.90	-78.61	4140 m	3964 m	10Be	20,030 ± 906[2]	Bedrock	Bedrock	SC-8		Shakun et al. (2015b)
Cajamarca Valley, Perú	San Cirilo	-6.90	-78.61	4140 m	3955 m	10Be	20,825 ± 827[2]	Moraine ridge	Boulder	SC-6		Shakun et al. (2015b)
Cajamarca Valley, Perú	San Cirilo	-6.93	-78.61	4140 m	3859 m	10Be	21,095 ± 849[2]	Moraine ridge	Boulder	SC-3		Shakun et al. (2015b)
Cajamarca Valley, Perú	San Cirilo	-6.91	-78.61	4140 m	3954 m	10Be	21,498 ± 895[2]	Moraine ridge	Boulder	SC-5		Shakun et al. (2015b)
Cajamarca Valley, Perú	San Cirilo	-6.93	-78.60	4140 m	3923 m	10Be	22,206 ± 851[2]	Moraine ridge	Boulder	SC-2		Shakun et al. (2015b)
Cajamarca Valley, Perú	San Cirilo	-6.91	-78.62	4140 m	3939 m	10Be	23,907 ± 1,004[2]	Moraine ridge	Boulder	SC-9		Shakun et al. (2015b)
Cajamarca Valley, Perú	San Cirilo	-6.94	-78.59	4140 m	3969 m	10Be	25,390 ± 1,224[2]	Terminal moraine	Boulder	SC-13		Shakun et al. (2015b)
Cajamarca Valley, Perú	*San Cirilo*	*-6.93*	*-78.61*	*4140 m*	*3902 m*	*10Be*	*29,592 ± 1,182[2]*	*Terminal moraine*	*Boulder*	*SC-4*		Shakun et al. (2015b)
Cajamarca Valley, Perú	*San Cirilo*	*-6.92*	*-78.59*	*4140 m*	*3933 m*	*10Be*	*40,828 ± 1,939[2]*	*Terminal moraine*	*Boulder*	*SC-11*		Shakun et al. (2015b)
Cajamarca Valley, Perú	*San Cirilo*	*-6.91*	*-78.62*	*4140 m*	*3931 m*	*10Be*	*42,906 ± 2,091[2]*	*Terminal moraine*	*Boulder*	*SC-10*	LLGM dated to 21.4 ± 2.3 ka	Shakun et al. (2015b)
Cajamarca Valley, Perú	Galeno	-6.98	-78.31	4080 m	3845 m	10Be	18,685 ± 670[2]	Terminal moraine	Boulder	MC-G-4		Shakun et al. (2015b)
Cajamarca Valley, Perú	Galeno	-6.89	-78.31	4080 m	3854 m	10Be	19,207 ± 682[2]	Terminal moraine	Boulder	MC-G-2		Shakun et al. (2015b)
Cajamarca Valley, Perú	Galeno	-6.98	-78.31	4080 m	3891 m	10Be	19,805 ± 706[2]	Terminal moraine	Boulder	MC-G-3		Shakun et al. (2015b)
Cajamarca Valley, Perú	Galeno	-6.98	-78.31	4080 m	3830 m	10Be	19,953 ± 712[2]	Terminal moraine	Boulder	MC-G-9		Shakun et al. (2015b)
Cajamarca Valley, Perú	Galeno	-6.98	-78.31	4080 m	3827 m	10Be	20,032 ± 724[2]	Terminal moraine	Boulder	MC-G-8		Shakun et al. (2015b)
Cajamarca Valley, Perú	Galeno	-6.98	-78.31	4080 m	3939 m	10Be	20,699 ± 840[2]	Terminal moraine	Boulder	MC-G-7		Shakun et al. (2015b)
Cajamarca Valley, Perú	Galeno	-6.98	-78.31	4080 m	3932 m	10Be	21,159 ± 811[2]	Terminal moraine	Boulder	MC-G-6		Shakun et al. (2015b)
Cajamarca Valley, Perú	*Galeno*	*-6.98*	*-78.31*	*4080 m*	*3889 m*	*10Be*	*22,867 ± 1,405[2]*	*Terminal moraine*	*Boulder*	*MC-G-1*	LLGM could not be entirely determined; average of dates are to 19.9 ± 1.0 ka	Shakun et al. (2015b)
Cajamarca Valley, Perú	*Galeno*	*-6.98*	*-78.31*	*4080 m*	*3930 m*	*10Be*	*40,251 ± 1,435[2]*	*Terminal moraine*	*Boulder*	*MC-G-5*		Shakun et al. (2015b)

* could not be recalculated; [1] recalculated in this study; [2] recalculated by Shakun et al. (2015a); [3] recalculated by Mark et al. (2017); [4] recalculated by Bromley et al. (2009), red = outlier

Table 2.3: *Continued*

Region	Locality	Lat (DD)	Lon (DD)	Summit Elev	Sample Elev	Method	Calendar Age	Feature Dated	Sample	Lab ID	Interpretation	Reference
Ampato Volcanic Complex, Perú	*Huayuray valley*	*-15.75*	*-71.75*	*6288 m*	*4444 m*	*36Cl*	*13,300 ± 400**	*Right lateral moraine*	*Boulder*	*Hualca 1*		Alcalá et al. (2011)
Ampato Volcanic Complex, Perú	Huayuray valley	-15.70	-71.80	6288 m	4408 m	36Cl	17,900 ± 100*	Right lateral moraine	Boulder	Hualca 2		Alcalá et al. (2011)
Ampato Volcanic Complex, Perú	*Huayuray valley*	*-15.70*	*-71.80*	*6288 m*	*4512 m*	*36Cl*	*11,700 ± 200**	*Right lateral moraine*	*Boulder*	*Hualca 3*		Alcalá et al. (2011)
Ampato Volcanic Complex, Perú	Huayuray valley	-15.70	-71.80	6288 m	4144 m	36Cl	16,800 ± 400*	Right lateral moraine	Boulder	Hualca 4		Alcalá et al. (2011)
Ampato Volcanic Complex, Perú	*Huayuray valley*	*-15.75*	*-71.75*	*6288 m*	*4886 m*	*36Cl*	*12,600 ± 400**	*Bedrock*	*Bedrock*	*Patapampa 4*	LLGM deglaciation dated between 17.9 ka and 16.8 ka	Alcalá et al. (2011)
Nevado Coropuna, Perú	Pomullca Valley	-15.52	-72.55	6377 m	4915 m	36Cl	20,900 ± 400*	Terminal-lateral moraine	Boulder	NCNE04		Úbeda et al. (2018)
Nevado Coropuna, Perú	Pomullca Valley	-15.51	-72.54	6377 m	5052 m	36Cl	18,600 ± 2,300*	Terminal moraine	Boulder	NCNE05	LLGM dated ~20.9 ± 0.4 ka, readvance ~18.6 ± 2.3 ka	Úbeda et al. (2018)
Nevado Coropuna, Perú	Queñua Ranra Valley	-15.51	-72.56	6377 m	5013 m	36Cl	17,900 ± 1,800*	Lateral moraine	Boulder	NCNE02		Úbeda et al. (2018)
Nevado Coropuna, Perú	Quebradas Ullullo	-15.52	-72.60	6377 m	4971 m	3He	21,140 ± 900[4]	Lateral moraine	Boulder	NC1		Bromley et al. (2009)
Nevado Coropuna, Perú	Quebradas Santiago	-15.49	-72.57	6377 m	4641 m	3He	20,680 ± 400[4]	Lateral moraine	Boulder	NC9		Bromley et al. (2009)
Nevado Coropuna, Perú	Quebradas Santiago	-15.49	-72.57	6377 m	4899 m	3He	21,030 ± 900[4]	East lateral moraine	Boulder	NC10	LLGM dated 20.95 ± 0.2 ka	Bromley et al. (2009)

* could not be recalculated; [1] recalculated in this study; [2] recalculated by Shakun et al. (2015a); [3] recalculated by Mark et al. (2017); [4] recalculated by Bromley et al. (2009), red = outlier

From the collection of studies that date their regional LLGM glacial advances across the Peruvian and Ecuadorian Andes, there are a plethora of studies within Perú, while Ecuador is lacking in more recent studies that use modern dating techniques (e.g., TCN dating). Table 2.2 and Table 2.3 delineate their LLGM within their respective studies regions that shows a distinct variability in the range of ages that are inferred to be from their individual regional LLGM advance. There are overall dates ranging between 16.8 ± 0.4 ka to 40.1 ± 1.0 ka (5 and 95 percentiles: 35.9 ka and 17.9 ka). Older ages, and thus evidence of older glaciations, have been identified within the tropical Andes that represent the Pliocene-Pleistocene Boundary within the Colombian Cordillera (van der Hammen *et al.*, 1973; Helmens *et al.*, 1997a; Helmens, 2011), however, LGM ages are more abundant in the literature, potentially due to their better preservation when compared to earlier glaciations (Angel, 2016).

There are clearly regions or areas that have incur older assigned LLGM advances, such as the Cordillera Blanca (e.g., Smith and Rodbell, 2010; 32.2 ± 1.7 ka), while others are assigned younger LLGM advances such as the Ampato volcanic complex (e.g., Alcalá *et al.*, 2011; between 17.9 ka to 16.8 ka) that could denote potentially a different cooling event (e.g. Older Dryas) that might have overridden their LLGM advance evidence, or are close to their former most extensive positions. Across the dataset, the average age of the South American LGM advance is around 25.3 ± 5.8 ka, and a median age of 23.9 ka, both indicating an early LLGM in the tropical Andes. An 'average' age may not be entirely representative indication of the LLGM timing due to the latitudinal range of study regions within Table 2.2 and Table 2.3 but can give an indication for regions that have no dates. With the presence of older ages (> 40 ka) may indicate the influence of inheritance of nuclides due to not enough erosion occurring to reset the cosmogenic signal, thus providing older ages (Cockburn and Summerfield, 2004; Ivy-Ochs and Briner, 2014), while post depositional processes could produce younger ages, this may explain the wide spread of ages assigned to the LLGM (Applegate *et al.*, 2010).

In the spatial distribution of the collated dated moraines, there is a latitudinal gap between studies (Figure 2.14) – this is situated in southern Ecuador (2°S) and northern Perú (7°S). This region is below 4,000 m asl, that has traditionally not been extensively investigated for palaeoglaciation. This may limit latitudinal comparisons of glacial advance timings, along with climate cooling estimates, limiting a full understanding of palaeoclimate across the tropical Andes, during the LLGM. There has previously been evidence identified at such elevations below 4,000 m asl in the tropical Andes, from within the Cajamarca Valley region by Shakun *et al.* (2015b). This evidence extended down to 3,827 m asl that represents LLGM extents. While the maximum elevation of the Las Huaringas (~3,900 m asl), that of terminal moraines,

is around the elevation evidence was identified within the Cajamarca Valley (23.7 ± 1.3 ka). This provides a clear justification for the investigation of any palaeoglaciation that might have occurred below an elevation of 4,000 m, as well as the need to understand if extensive glacial systems could persist at such elevations within the spatial latitudinal gap.

2.5.3. Andean snowline depression during the LGM

At the timing of the South American LLGM, the configuration of the snowline was very similar to the present-day snowline with an east to west gradient – higher in the west, lower in the east (Klein *et al.*, 1999; Porter, 2001) (Figure 2.17). The LLGM snowline was depressed by between 800 - 1,200 m across the tropical Andes (Broecker and Denton, 1990a), that corresponded to a temperature cooling of 5 – 7.5°C (Klein *et al.*, 1999). The snowline within the tropical Andes is higher than mid- and low-latitude locations within South America. These are reconstructed by a number of ELA reconstructions (Benn *et al.*, 2005) from the geomorphological record of locations currently, and formerly, glaciated. There is however, a high level of variation in snowline depressions across the tropical Andes (Bromley *et al.*, 2011a) that may potentially be due to modification of the LLGM evidence within the geomorphological record from later Holocene readvances due to moraine reworking that can either degrade glacial evidence or entirely remove evidence from the record (Rodbell *et al.*, 2009). This can then lead to misinterpretations of moraines generated during their LLGM with younger advance evidence.

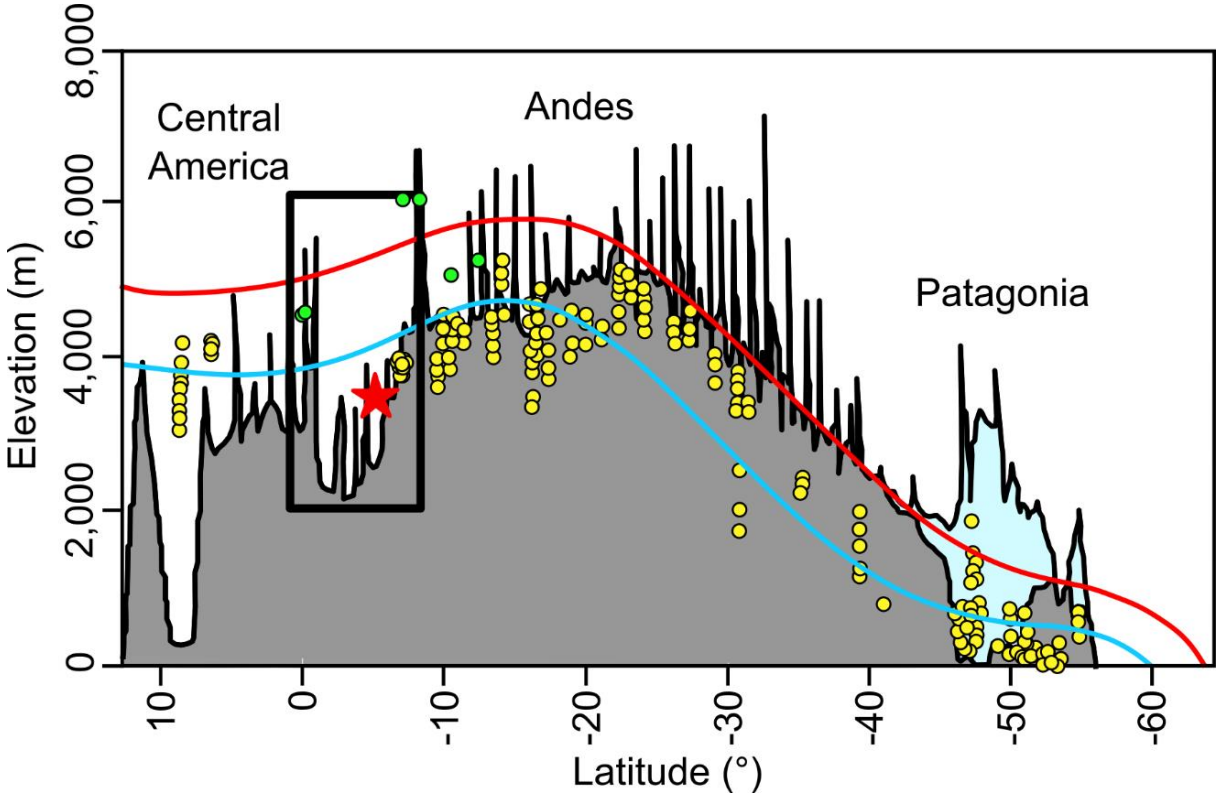

Figure 2.17: The estimated modern (red line) and South American LLGM snowline (blue line) across South America, with TCN dates from the ICD-D database (shown in Balco, 2019) (yellow dots) (Table 2.3) with added ^{14}C studies (green dots) (Mercer and Palacios, 1977; Clapperton, 1987a; Rodbell, 1993b; Clapperton, 1998) (Table 2.2). Red star indicates the study site location and elevation. Figure was remade and modified from Broecker and Denton (1990b) (orginally in Broecker and Denton, 1990a) with data from Porter (1977); Porter (1988) and Skinner and Porter (1987), while the best controls on snowlines come from the Columbian (Herd, 1975), Ecuadorian (Clapperton, 1987a), and the Chilian Andes (Porter, 1981).

Many locations that attempt to determine the timing of their regional LLGM have their highest elevations above the South American LGM snowline, with many having also incurred younger glacial advances during the late-glacial or Holocene. The study location in this thesis has its maximum elevation (~3,900 m asl) (red star in Figure 2.15) ~500 m below the South American LGM snowline. This provides an indication that the current estimation of the South American LLGM snowline across the tropical Andes is incorrect and requires further investigation in regions below it. However, there are no other studies between the latitude of -2° and -7° that attempt to do so (Figure 2.17 black box), with the region between these latitudes where their maximum elevations are below the LGM snowline. Glaciation below this snowline may yield evidence of LLGM glacial advances that is unmodified by later Holocene readvances, allowing us to confidently establish pre-Holocene glacial extents, ELA depressions, along with estimated palaeoclimate.

This low elevation glaciation, below the South American LLGM snowline, and that tropical glaciers sensitivity to temperature changes (Kaser and Osmaston, 2002), may have led to an environment that is very marginal for glacial ice to exist. This potentially propagated the traditional thought that, below the LLGM snowline, there was no or at least no major, glacial presence. If this marginal glaciation existed, it would have important implication of palaeoclimate within the tropical Andes and would necessitate further investigation into regions below 4,000 m asl.

2.5.4. Key themes of dating studies

While there are a plethora of dating studies, the most recent studies are centred within Perú (Emmer *et al.,* 2021). Ecuador has the fewest dating studies, which only use ^{14}C. This differential in the number of studies is further exacerbated by the spatial latitudinal gap between studies in Perú and Ecuador. These limits, not only the latitudinal comparisons in the timing of the LLGM, while presenting difficulties in fully understanding the timing of the LLGM within the tropical Andes, but also differences in dating techniques, making any comparisons on the timing of advances difficult to reconcile.

The elevations of the studies presented in Tables 2.2 and 2.3 are situated between maximum valley top elevations of 4,080 m asl and 6,377 m asl, either above the present-day snowline, or at least above the LLGM snowline. There is no other study, within Perú or Ecuador, that attempts to understand glacial advances in locations that are entirely below the South American LLGM snowline. Glaciation below the LLGM snowline would have important ramifications for the potential palaeoclimate within the tropical Andes during the LLGM and would require a revaluation of the South American LLGM snowline with the tropical Andes. The study region (Figure 1.2) within this thesis shall detail a region of potential LLGM glaciation, below the LGM snowline, providing justification for future studies in such locations.

2.6. Numerical modelling of tropical glaciers

Three-dimensional numerical glacial models allow the implementation of ice physics that can produce glaciologically realistic ice extents within the chosen model domain. These can be as complex as full Stokes numerical models (e.g., Elma/Ice Gagliardini *et al.*, 2013) to more simple flowline models (e.g., Maussion *et al.*, 2019). Numerical glacial models, however, need to be tied into the empirical geomorphological record to ensure accurate modelling of glacial behaviour and also allowing model parameterisation (Ely *et al.*, 2019). As computational power increases, numerical models can model glacial systems are increasingly finer resolutions – down to hundreds of metres. Within this thesis the Parallel Ice Sheet Model (PISM) (The PISM authors, 2018) is used, it is a hybrid shallow-ice shallow-shelf approximation model. PISM scales well in a parallel work environment and can utilise High Performance Computing (HPC) to speed up numerical computation.

There are advantages of using PISM, such as it being used extensively within numerous extra-tropical locations, such as the Alps (Seguinot *et al.*, 2018; Jouvet *et al.*, 2023), the High Mountain Asia (Gantayat and Ramsankaran, 2023; Yan *et al.*, 2023), the Anatolian Mountains (Candaş *et al.*, 2020; Köse *et al.*, 2022), the Rocky Mountains (Silwal *et al.*, 2023), Cordilleran Ice Sheet (Seguinot *et al.*, 2016), New Zealand (Golledge *et al.*, 2012), and Patagonia (Leger *et al.*, 2022; Martin *et al.*, 2022; Yan *et al.*, 2022; Wolff *et al.*, 2023), that provide justification for its use in high mountainous environments. The model is computationally efficient and able to be scaled in a high-performance computing environment, using multiple CPU cores to allow parallelised workloads, that can decrease computation time with increased complexity, such as high resolutions to overcome important ice topographical interactions. Disadvantages are that the model itself was first made to model ice sheets, and not smaller scale valley glaciers, this may mean that the model is unable to capture the intricacies of valley glaciers. This is followed

by that it is only an ice approximation model, using hybrid Shallow Ice Approximation and Shallow Shelf Approximation, that not a complex or precise are a higher order, or full-Stokes model that can take into account more complex interactions. Due to other studies (referenced above) having used it to some success in similar environments.

2.6.1. Numerical models as predictors of climatic envelopes

Using PISM, or almost any numerical model, climate can be entered to force glacial growth or retreat within a chosen model domain. This can be entered as a steady state climate (e.g., +1/-1 to modern climate), or temporally varying using the palaeorecord (i.e., ice cores). Steady state climate allows the user to model ice to important time periods (e.g., the LGM), letting ice reach equilibrium with surrounding climate. PISM allows temperature and precipitation to be varied to give a regional estimate on paleoclimate, that can help test the inferred climate from glacial ELA reconstructions or other paleotemperature indicators, along with precipitation change estimates from the palaeorecord (e.g., paleolakes). However, ice can be modelled to similar terminal positions, at different climate combinations, when model parameters, that are not well defined within the glaciological literature, are varied (example in Figure 2.18). This is an advantage of numerical models, as they allow us to understand the potential climatic envelope which glaciers could exist under.

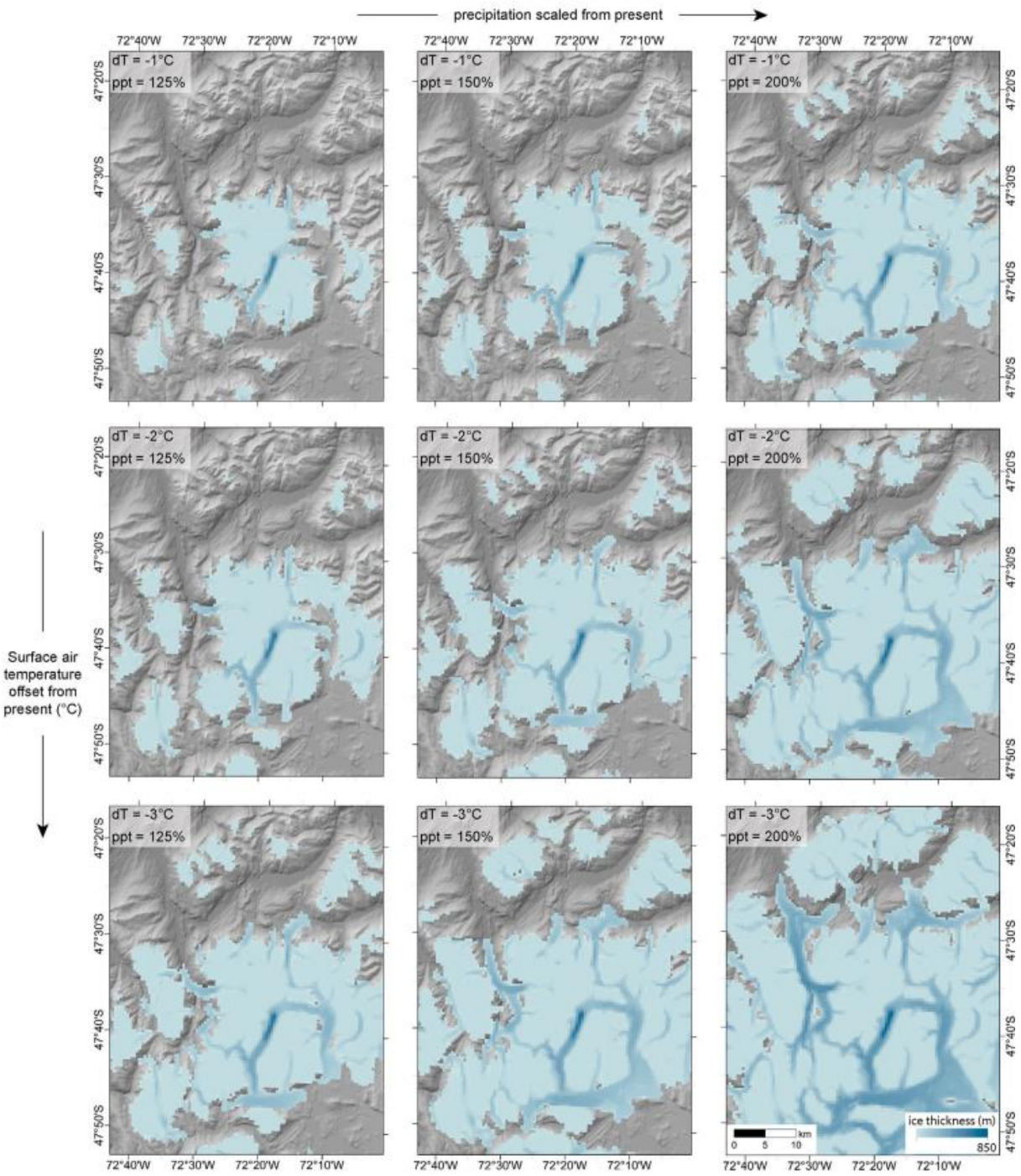

Figure 2.18: An example of a PISM model output from Martin *et al.* (2022) (Figure 6), with ice thickness output, detailing the effect of varied combinations of precipitation scaling (between 125% and 200%), and surface air temperature offset from present (between -1°C and -3°C).

2.6.2. Issues of modelling studies in the tropics

Although globally there has been a number of numerical modelling studies of glaciers and ice sheets, there is seemingly a large gap in the use of such studies across the tropical Andes, bar a singular study from Richardson *et al.* (2024a). While numerical modelling over glacial areas has been conducted in the tropics, they have been limited to mass balance modelling, and simple flow line models over present day glaciers (Seehaus *et al.*, 2020; Lozano Gacha and Koch,

2021; Stansell *et al.*, 2022). These have provided some key understandings, such as how tropical glacier mass balances being influenced by net radiation (Lozano Gacha and Koch, 2021), while simple flow models show that numerical modelling of palaeoglaciers within singular valleys in the tropical Andes can accurately reconstruct their past extents (Stansell *et al.*, 2022). The first three-dimensional modelling of tropical glaciers was conducted using Úa, finite element ice flow model, over the Shallap and Zongo glaciers (Richardson *et al.*, 2024b). While this modelling was not conducted over palaeoglaciers, nor using PISM, it showed that tropical glaciers are extremely sensitive to changes in modern climate, and that modelling can be done.

This lack of glacial numerical modelling efforts within the tropical Andes may be due to the darth of studies that attempt to parameterise key glaciological physics and climate variables that are needed to parameterise glacier models. Much of the parameterisation input within numerical glacial models have been determined over non-tropical glacial environments (e.g., Greenland), or in locations with long term glacier monitoring has existed (e.g., the Alps). Due to tropical glaciers being under different climatic conditions and having differing mass balance dynamics, numerical models may be parameterised incorrectly, that may limit their usefulness for accurate glacial modelling. Therefore, the use of PISM within this thesis will require an extensive sensitivity test to understand how the parameters effect glacial area and volume within the model domain, while also attempting to parameterise the model for time varying numerical modelling. This use of PISM in this thesis will make one of the first studies to use numerical modelling techniques for palaeoglaciation within the tropical Andes.

2.7. Chapter summary

Tropical glaciers within the tropical Andes have received an extensive amount of attention in the literature, pertaining to the timing of their furthest extents during their region LLGM. These studies, however, are focused on regions that incur maximum elevations that were above the South American LLGM snowline, this has led no study of glaciations occurring below this. This has led to a large latitudinal data gap between studies of northern Perú, and those in southern Ecuador. Further, glacial reconstructions, informed by the geomorphological record are limited, with very few studies attempting to place mapped and dated LLGM moraines with reconstructed ice extents. While these studies have generated a well constrained timing of their individual regional LLGM extents, at least across Perú, there is little understanding of the thermal regime and glacial configurations (valley or ice field/cap) that would have important implications on palaeo-ELA reconstructions that may change the South American LLGM snowline estimate and depression (Broecker and Denton, 1990a). These overall limit our ability

to understand any regional and latitudinal differences in both, the timing of the LLGM within the tropical Andes, along with the climate required to generate such glaciations.

This thesis aims to map any palaeoglacial evidence, and use this evidence to enable the reconstruction of the study regions LLGM glacial extent within Las Huaringas. This shall facilitate the addition of data that is situated within this latitudinal data gap identified in this Chapter, and in a location that is below the assumed South American LLGM snowline. Due to its elevation and position, this study region shall allow a more confident determination on the timing of the regions LLGM advance, without later Holocene readvances complicating the overall advance/retreat chronology. This thesis shall also attempt to determine the climatic envelope under which glaciers could have existed within this region using PISM, for the first time in a tropical setting, a three-dimensional numerical glacial model.

Chapter 3. Geomorphological evidence of past glaciation within the Lagunas de Las Huaringas

3.1. Introduction

While there are numerous palaeoglaciological studies from the South American tropical region (Figure 2.14), these typically focus on locations where ice masses still exist (e.g. Cordillera Blanca, Perú) (Farber *et al.*, 2005; Glasser *et al.*, 2009), or high elevation locations that glaciers have recently vacated their cirques (Smith and Rodbell, 2010; Blard *et al.*, 2014; Shakun *et al.*, 2015b). Further, there has been relatively little modern mapping concerned with the identification of the glacial geomorphology and reconstruction of potential glacial dynamics (section 2.4.2). The exceptions are investigations of individual glacial valleys (e.g. Małecki *et al.*, 2018) and the mapping of glacial lakes (e.g. Vilímek *et al.*, 2016).

Palaeoglacial evidence in lower elevation tropical Andean regions (i.e., with summit peaks < 4,000 m asl) has rarely been identified and investigated. As a result, there is relatively limited understanding of the general presence of such evidence at such elevations, and if there is, their glacial dynamics and whether they were able to persist in these regions after their regional LLGM extents compared to higher elevation or higher latitude locations. This has led to a dearth of studies that identify and analysis palaeoglacial geomorphological evidence at such elevations, while reconstructions of the maximum period of glacial ice is lacking, and limits comparison between regions.

If glaciers were able to persist at such low elevations during the regions LLGM, this can have important ramifications for the potential climatic dynamics within the tropical Andes. Providing further justification for a wetter palaeoclimate, with a substantial temperature cooling, potentially more so than those previously estimated (Bromley *et al.*, 2011a; Quesada-Román *et al.*, 2020) (seen in Section 2.3.2.). Further, the identification of ice in a region with its entire elevation range below the South American LLGM snowline (Broecker and Denton, 1990b), could also mean a reconfiguration of the assumed snowline across the latitudinal span of the tropical Andes is required. This would also mean regions at similar altitudes could have incurred glacial ice during the LLGM have gone unstudied, leaving a gap in our overall knowledge of the LLGM within the tropical Andes.

The aim of this chapter is present the mapping of palaeoglacial geomorphological evidence, along with reconstructed glacial ice at the identified maximum extent, and temperature cooling estimates. This chapter provides: i) a detailed remote-sensing derived glacial geomorphological map of the region; ii) a reconstruction of the likely maximum glacial extent, along with a reconstructed equilibrium line altitude (ELA) for the reconstructed ice masses; and iii) ELA-

derived palaeotemperature estimates for the LLGM) used to discuss the palaeoclimate implications of these findings. This mapping and preliminary outcome, provide the fundamental basis for (a) fieldwork and sampling for geochronology (Chapter 4), and (b) the numerical modelling (Chapter 5 and 6).

3.2. Methods and data

3.2.1. Datasets

The generated geomorphological map and glacial reconstructions were based on analysis of multiple remotely sensed high-resolution images and digital elevation models (DEMs) (Appendix A Table A.1). Newly acquired high resolution tri-stereo from the Satellite Pour l'Observation de la Terre (SPOT) 7 (1.5 m) and archived Pléiades (0.5 m) imagery was obtained through the European Space Agency (ESA) from Airbus Defence and Space. Large portions of Las Huaringas were cloud covered in the Pléiades imagery, leading to the eastern side of Las Huaringas and the Laguna Shimbe valley not being mapped at the highest resolution. As a result, these areas were mapped using the most recent cloud free image which could be obtained from Landsat 8 (30 m, pansharpened to 15 m), Sentinel-2A (10 m), RapidEye (~5 m) or PlanetScope (~4 m). Openly available imagery from Google Earth™ and Bing Maps, with a mixture of resolutions, were used to complement the other optical datasets.

DEMs used included: (i) the 30-m resolution Advanced Land Observing Satellite (ALOS) DEM from the Japan Aerospace Exploration Agency (JAXA; https://global.jaxa.jp). This DEM was generated from images acquired between 2006 to 2011 from the Panchromatic Remote-sensing Instrument for Stereo Mapping (PRISM) sensor onboard the ALOS (Tadono *et al.*, 2014). Elevations for the ALOS DEM are relative to the EGM96 geoid. From this point onwards within this thesis, all elevations derived from the ALOS DEM shall be described as relative to above sea level (asl); (ii) a new high-resolution DEM of the study area generated from the tri-stereo SPOT 6/7 imagery. The process for generation of this DEM, along with an evaluation of its uncertainty, is outlined below in section 3.2.2. The 30 m ALOS DEM was initially used for macro scale geomorphological mapping, with the higher resolution DEM needed to permit identification of smaller scale landforms (e.g., recessional moraines) (Pearce *et al.*, 2014; Chandler *et al.*, 2018) and to confirm the interpretation of any landforms identified and mapped using the lower-resolution datasets.

3.2.2. Digital elevation model generation

SPOT 7 tri-stereo imagery acquired on 11th May 2020 was used to generate the high-resolution DEM (Figure 3.1), with images processed using a similar method to Lovell *et al.* (2019). The SPOT 7 images were processed to the primary product level by Airbus Defence and Space. The three SPOT 7 images were used to generate point clouds within ERDAS Imagine 2018's Photogrammetry Suite. Using the LAS Dataset to Raster tool in ArcMap 10.6.1 the point cloud was processed into a DEM. To generate the DEM, the rational polynomial coefficients (RPCs) provided with each image were used for georeferencing and corrections due to satellite characteristics. The tri-stereo imagery was tied together using ~100 tie-points, although those with the highest RMSE were removed to minimise the RMSE for the triangulation. This generated a RMSE of 0.07 pixels for the tied-together images. A point cloud with over 28.4 million points was generated, producing a DEM with a spatial resolution of ~2.5 m.

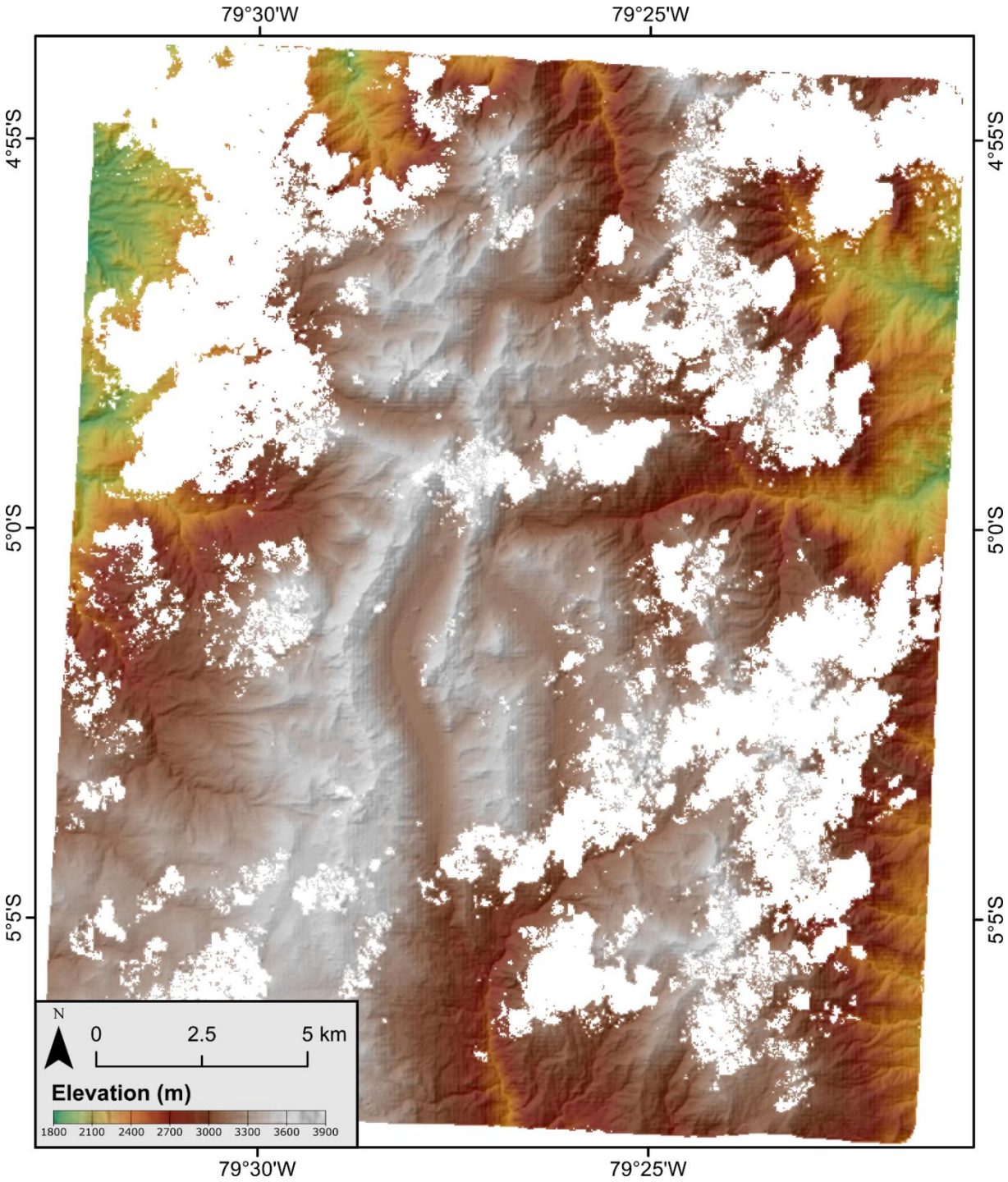

Figure 3.1: The 2.5 m horizontal resolution SPOT 7 derived DEM of the Las Huaringas area as a hillshaded image (azimuth: 315°, z-factor: 1) overlain by elevation. White 'fuzzy' areas are no data generation errors removed due to cloud cover precluding data capture.

To interpolate across the point cloud and generate a DEM, Guo *et al.* (2010) suggests that the use of simple interpolation techniques (such as Natural Neighbour, Inverse Distance Weighting and Triangulated Irregular Network methods) are more efficient for high density data, such as that used within this study. To determine the best technique to interpolate between no data points within the DEM the 'linear', and 'natural neighbour' approaches within the LAD Dataset

to Raster tool were compared against each other. The 'simple' interpolation was discounted as is can only interpolate over no data areas which are the size of a few pixels. Using previously collected and processed dGPS points, acquired from the study area in 2017 as a control on absolute elevation, we determined the most accurate interpolation technique to be 'Natural Neighbour'. Acquired dGPS points have a conservative estimate of uncertainty of ~5 m due to the long baseline between rover and the local base station. The 'Natural neighbour' method produced an elevation RMSE of 2.10 m compared to 2.14 m for the 'linear' interpolation method, and there was no difference in the computational time between the two methods. Although there is very little difference in the RMSE of the two methods, the 'Natural neighbour' method was used to generate the DEM.

Large-scale landforms identified throughout the 30 m ALOS DEM and satellite imagery, demonstrated that the 2.5 m SPOT DEM was well aligned and thus the generated DEM required no further georeferencing. Many locations covered by the SPOT DEM were affected by cloud cover in the original imagery, while its resolution is not fine enough to allow adequate mapping of more subdued moraines (< 2 m relief).

3.2.3. Geomorphological mapping

Geomorphological mapping was conducted following well-established remotely sensed techniques (Chandler *et al.*, 2018). Glacial geomorphological features were mapped, along with general non-glacial geomorphological features (i.e., landslide features) to add further understanding of the region. This was conducted using the criteria shown in Table 3.1, following a similar criteria to Glasser *et al.* (2008, p. 369). Small adjustments were also made to the identification criteria for some features due to Glasser *et al.* (2008, p. 369) mapping features in currently glaciated locations where landforms had a 'fresher' appearance than those in our study area. Images were used in the 'true colour' band combinations for their respective sensors, which allow a good assessment of landforms. To further enhance landform detection, where landforms were ambiguous by two-dimensional mapping, Google Earth™ was used for three-dimensional projection of remotely sensed imagery over topographic data, albeit sometimes at a lower resolution or lower quality imagery (Chandler *et al.*, 2018). The mapping of glacial geomorphology includes moraines, trimlines, glacial lineations, cirques headwalls, boulders, glacially smoothed bedrock, and overdeepenings. Non-glacial geomorphic features (e.g., streams and lakes) were also mapped to add context to the mapping. Due to datasets from multiple sensors being used to map features, and the errors and uncertainties associated with each of them, we conservatively estimate that mapped features may be horizontally offset from

their true position by a maximum of ± 30 m (Appendix A Figure A.1). Three members of the supervisory team visited the field area prior to this PhD commencing, providing some limited ground truthing to mapped features within the Laguna Shimbe valley. Systematic and extensive fieldwork (seen in Chapter 4) had not yet been undertaken prior to this chapter being written.

Table 3.1: Criteria for landform identification on remotely sensed imagery loosely modified from the landform identification criteria from Glasser *et al.* (2008, p. 369)

Landform	Identification criteria	Identification limitations	Reconstruction significance
Moraines	Are linear, curved or sometimes sinuous ridges. Prominent features of singular or multiple ridges. Lateral moraines found along the sides of valleys; terminal moraines cut across a valley. Moraines can also be rocky in appearance or subdued.	Shadows can preclude moraine identification. Could be misidentified as trimlines if low in height. Moraines may not be prominent enough to be identified within the remote imagery. Other linear features could be misidentified as moraine features.	Denotes the maximum extent of a glacier at a certain point in time before retreat (after an advance phase) or a standstill during deglaciation. Multiple moraines in proximity denote a fluctuating glacial margin or recessional moraines.
Glacial deposits	Complex moraine systems with multiple moraines nested together, while glacial deposits have a clear colour difference when compared to the surrounding ground, being lighter in colour along with the moraines on top.	Shadowing from the surrounding terrain, while vegetation can cover the glacial deposits making it hard to discern from the surrounding terrain.	Maximum extents of glaciers, and a location of glacial activity. Deposition of former supraglacial material providing indication of potential sedimentation transportation pathways.
Smoothed bedrock/steep sloped bedrock	Rock which is bare or lightly vegetated. Visible joints seen. Generally near cirque headwalls. Can be stepped features with small bodies of water in between rock outcrops or within larger joints. Steep sloped bedrock are steeply inclined bedrock, usually location on the top of valley walls.	Vegetation cover and any shadowing can preclude identification.	Areas of glacial activity. Evidence of basal ice at pressure melting point allowing erosion to occur. Could be used to see areas of erosion compared to area of deposition.
Cirque headwalls	'Bowl' or amphitheatre-shaped depressions in the side of valleys or high relief ground. Either shallow and vegetated, or steep and bare bedrock with or without an overdeepening infilled with a lake. The edges of the cirque can be sharp or rounded.	Could be confused with large landslip features.	Indicates the origin location of glacial ice. Also indicates restricted glaciation. Cirques on valley walls, could have coalesced with the main valley glacier if one was present.

Glacial lineations	Linear landforms running parallel with the direction the glacier was flowing. Identified in between moraines.	Vegetation may cover over glacial linear features.	Indicates area of glacial activity. Shows the direction of ice flow.
Boulders	Large generally circular features which can be found on or near moraines, or along the valley side or floor. Can also occur in boulder moraines, where boulders are deposited in a linear line along the side of valleys.	Could be covered in vegetation. Size of boulder could be smaller than image resolution precluding their mapping.	Indicates the erosion of a glacier and where it has been deposited either during advance, or glacial retreat. Can be used to determine where to take sample for dating techniques.
(Palaeo) Hill slope failures	On the side of valley walls, or large pronounced moraines, where there is a change in colour compared to the surrounding ground. If fresh they are light in colour, while if they are palaeo, they are either darker in colour or be lightly vegetated over with clear scarp/source area scar.	If vegetated could be obscured from mapping. Unlikely, but could cover or bulldoze other geomorphological features.	Unstable ground potentially due to glacial material.
Waterbodies	Freshwater bodies found within overdeepenings and depressions. Usually found within a glacier cirque. Some small lakes are found independent of a glacial overdeepening but can form in a depression in the ground, for example within joints in bedrock.	Reflectance of remotely sensed image can make the colours of lakes change from the expected colour. If smaller lakes are covered by shadow, they will not be easily indefinable. Smaller water bodies may be smaller than the image resolution and may preclude their mapping.	They indicate presence of glacial overdeepenings if occupied by one water body. Multiple smaller water bodies may indicate glacial erosion of the bed rock.
Rivers/streams	Linear when flowing down steep slopes, but sinuous features when on the valley floor. Occupy the lowest elevation in a valley, that conjoin with other streams down valley.	Hard to determine where they start near the headwaters due to being small streams. When reaching further down valley, may become obscured by vegetation which prevent accurate delineation.	Indicate the lowest elevation within a valley. Provide inferences on the influence of fluvial processes.

3.2.4. Palaeoglaciological reconstruction

We reconstructed the extent of all glaciers hypothesized to have occupied the Las Huaringas region to their most prominent and most extensive mapped moraine. In the absence of any dating control on these moraines and any large moraines between the cirque and these lower moraines, for this chapter we assumed that they represent the regions LLGM extents due to the lack of another evidence downvalley from these moraines. This is consistent with the approach of other studies where dating controls are unavailable (e.g. Emmer *et al.*, 2021). However, there is potential for some of the most downvalley glacial evidence in our study area to pre-date, or even post-date, the regional LLGM. A number of studies have identified pre-LLGM moraines downvalley of glacial cirques within the northern tropical Andes (e.g. Goodman *et al.*, 2001; Dirszowsky *et al.*, 2005), although these would likely have much less relief and be less distinct compared to LLGM moraines. Without dating of moraines to create a chronology of glacial advances, it is currently not possible to definitively constrain the age of the moraines within the Las Huaringas region.

We extracted basic metrics from these reconstructed glaciers, such as their mean, minimum and maximum elevations, glacier aspect, and length. Where glaciers split into multiple outlets, we took the longest length. The cirque floor elevation was also extracted from the cirques from which glaciers were hypothesised to have originated from. Glacier ice surface contours were generated with contour intervals of 100 m to create ice surface profiles during their maximum extents. Contours were generated within ArcPro drawn by hand, in accordance with well established procedures detailed by earlier studies of glacier reconstructions (e.g. Sissons, 1974; Bendle and Glasser, 2012), across the glacier profiles. These contours were adjusted to be in-line with observed modern day glacial dynamics (Ng *et al.*, 2010), with ice thickness reduced below the ELA (generation discussed below) closest to the terminus (convex contours), and with greater ice thickness above the ELA in areas closest to the headwall (concave contours).

The subjective nature of palaeo ice extent reconstruction is the main source of uncertainty for reconstructing palaeoglacier extents and thicknesses. Whilst lateral-terminal moraines provide elevation constraint and delimit glacier margins, they are not always present or easily identifiable. In such cases, a best estimate of the ice margin was determined using the elevation from the DEM using the terminus elevation of surrounding glaciers as a reference. This ‘best estimate’ approach was primarily used at the terminus of the palaeoglaciers where no well-defined (or mapped) terminal moraine could be delineated. This was also used in locations where lateral moraines are mapped on one side of the valley but were not apparent on the other. Uncertainty can also be seen in the glacier ice surface contours. Where ice split into two or

more outlets from one accumulation source (e.g., Huancabamba 1), there may be some uncertainty as to how well they may represent their LLGM ice surfaces. However, these were produced to provide a visual representation and were not used for any analysis going forward in this thesis.

Lastly, the reconstructed glaciers have also been assumed to have advanced synchronously across the region. Whilst this would not impact maximum extent calculations (i.e., area and ELAs), without any dating of these features there are implications for LLGM timing and glacial-climate interactions. However, this can give a best estimate on how these glaciers would have looked at their most extensive setting which would be classed as their LLGM advance if dated within the timing the global LGM (i.e., between 40-20 ka).

3.2.5. Palaeo-equilibrium line altitude reconstruction

The ELA is the theoretical line where accumulation and ablation are equal (Benn *et al.*, 2005) and has been frequently used as a proxy of the surrounding climate conditions of temperature and precipitation for the reconstruction of tropical Andean glaciers and climate (Porter, 2001; Mark and Helmens, 2005; Bromley *et al.*, 2011a; Martin *et al.*, 2020). Although the ELA would not have been static for long periods of time due to the varying climate conditions, the reconstructed palaeo-ELA inferred in this chapter is assumed to be at its lowest potential elevation and thus represents the time the glaciers were at their most extensive (i.e., the LLGM).

To reconstruct palaeo-ELAs we used the ArcGIS Toolbox created by Pellitero *et al.* (2015) which reconstructs palaeo-ELAs using a generated glacier DEM and using a number of different methods (Median Glacier Elevation (MGE), Accumulation Area Ratio (AAR) and Area Altitude Balance Ratio (AABR)). We generated the glacier DEM using vertices of the glacier extent polygon to act as elevation and used the natural neighbour interpolation method to reconstruct a flat glacier surface, as used in other studies for ELA reconstructions (e.g. Lee *et al.*, 2021a). This was then inputted into the Pellitero *et al.* (2015) tool using the AABR method to generate the ELAs, as it has been shown to be the most accurate in reconstructing ELAs due to the ability to use differing balance ratios (BR) that can be inferred from modern day glaciers (Santos-González *et al.*, 2013; Pearce *et al.*, 2017; Quesada-Román *et al.*, 2020). One of the main sources of uncertainty for the reconstruction of palaeo-ELAs using the AABR method is the choice of the BR that defines the ratio between accumulation and ablation (Rea, 2009). There is however a lack of data on balance ratios across the tropical Andes, thus making the choice of BR difficult to determine. Tropical glaciers generally have high ablation rates

throughout the year, and also have small ablation areas (Rea, 2009; Oien *et al.*, 2022b). As such, some studies have assigned high balance ratios. For example, Quesada-Román *et al.* (2020) used a value of 2. To account for the uncertainty in constraining the BR for tropical glaciers, several balance ratios were tested; 1.00, 1.25, 1.50, 1.75, 2.00, 2.25 and 2.50, with 1.75 being the global average (Rea, 2009). The use of multiple BR results in variations in reconstructed ELAs by only a few tens of meters, or a ~0.87% difference (if any difference is seen). The BR of 1.75 was therefore used within this study as a median between the two extremes. It is acknowledged that the balance ratio could be higher, however, without any studies determining BR of tropical glaciers, the global average is used.

3.2.6. Palaeotemperature reconstruction

The reconstructed palaeo-ELAs and subsequent ELA change (ΔELA) were used to reconstruct palaeotemperature. Given the uncertainty about past climate within the tropics as a whole (Loomis *et al.*, 2017), three potential air temperature lapse rates (ATLR) were used to calculate temperature change (ΔT): -5.5°C/km, -6.5°C/km and -7.5°C/km (Quesada-Román *et al.*, 2020). Although the ELA is controlled by a range of climate conditions, including precipitation (e.g. Stansell *et al.*, 2007), temperature has an overarching influence (Kaser and Osmaston, 2002). The palaeo-ELA was compared to the modern snowline in order to calculate ΔELA. In this region the snowline lies above the highest local summit and therefore the nearest identifiable snowline that intercepted topography was used to infer the modern ELA. The elevation of 4,600 m asl from a location ~8°S was used from Figure 2 of Hammond *et al.* (2018), where snow precipitations occurs. While this may not be the exact snow line elevation for this region, it provides an estimated snowline level that can aid in performing the first order estimates of palaeotemperature. A higher or lower modern snowline elevation would influence the reconstructed palaeotemperature estimates by generating more, or less temperature, cooling respectively.

Due to the inability of this thesis to attribute the advances, and climate cooling, to any specific time or event due to the lack of dating controls on the mapped moraines here, it is impossible to infer any regional or hemispheric scale palaeoclimatic significance from the analysis within this chapter. Therefore, for this palaeotemperature reconstruction it is assigned to the regions LLGM, due to the most downvalley mapped moraine being used. Fieldwork in Chapter 4 shall attempt to collect samples for cosmogenic dating to enable an age control on these most extensive moraines, that can then be used to link timing to climate conditions.

3.3. Results and discussion; geomorphological interpretated and reconstructions

Initially, this section describes the results of the geomorphological mapping (Figure 3.2) and reconstructed glacial ice extents (Figure 3.3) and metrics (Table 3.2). We provide a localised description and interpretation of our results for five geographical areas (shown in Figure 3.3). These areas are: i) Laguna Shimbe valley (LS); ii) eastern glacier valley (EG); iii) western glacier cirques (WG); iv) northern glacier valleys (NG); and v) south-eastern glacier cirques (SEG). Reconstructed glacial ELAs and the estimated palaeotemperatures are discussed.

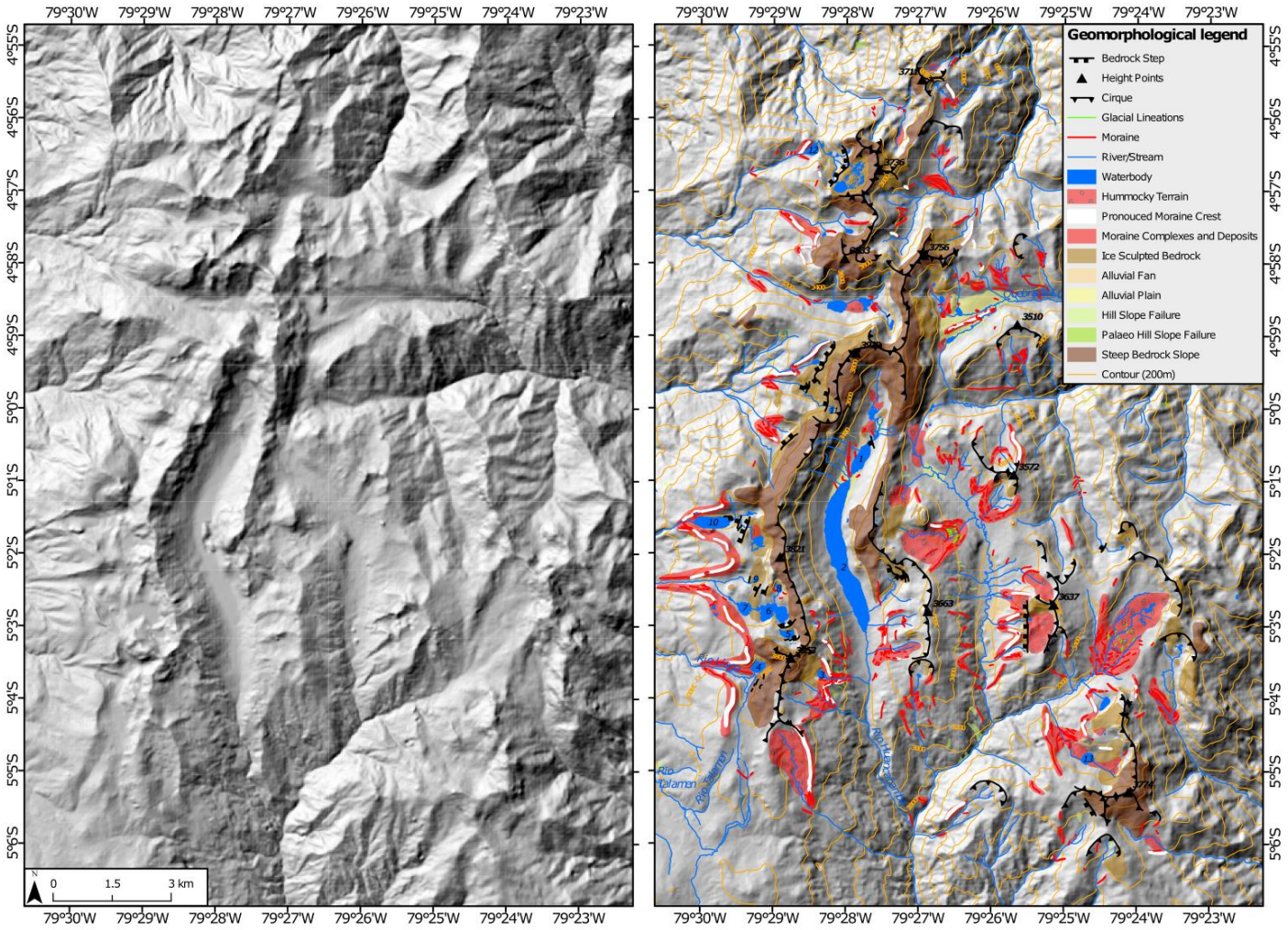

Figure 3.2: a) ArcPro basemap imagery without interpretation of geomorphic features within the Las Huaringas, b) the geomorphological map. Basemap is a hillshade of the 30 m ALOS DEM (Azimuth: 315°, Z-factor: 1). Lake names are: 1 – L. Shimbe 2; 2 – L. Shimbe; 33 – L. Redonda; 4 – L. Negra; 5 – L. las Arrebiatadas 1; 6 – L. las Arrebiatadas 2; 7 – L. las Arrebiatadas 3; 8 – L. las Arrebiatadas 4; 9 – L. el Toro; 10 – L. Millionaria; 11 – L. el Rey Inca; 12 – L. Negra de San Pablo; and 13 – L. Redondo de Zapalche.

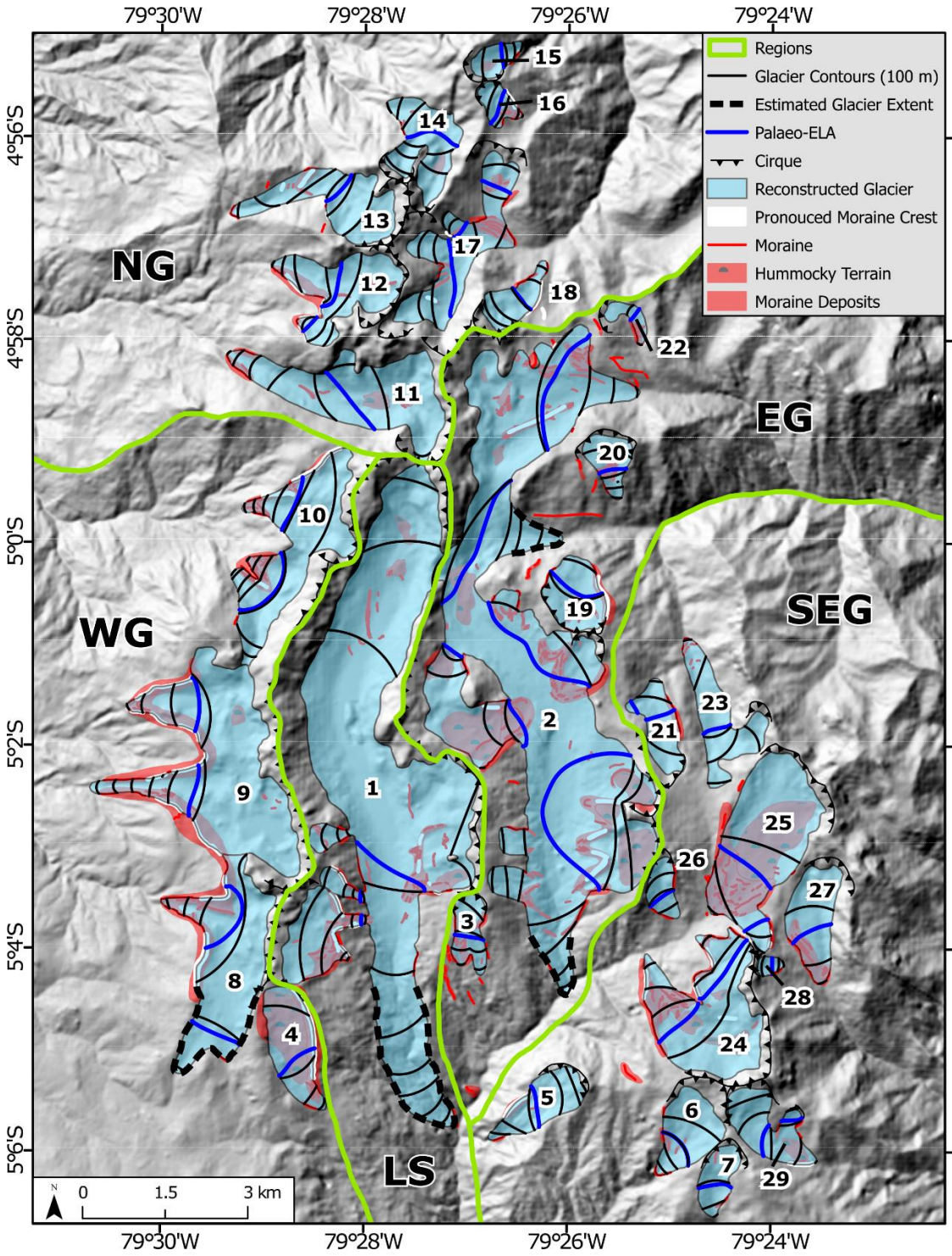

Figure 3.3: Reconstructed glacial extents within the Las Huaringas along with reconstructed ELAs, glacier surface contours (100 m interval) and geomorphic evidence (i.e., moraines) used to delineate glaciers. Glaciers 1, 2 and 8 have estimated glacier extents shown by the dashed lines. Extents are overlying a 30 m ALOS DEM hillshade (azimuth: 315°, z-factor 1). The five areas defined for interpretations are delineated by thick green lines. Names and reconstructed ELA elevations of glaciers relate to those shown in Table 3.2 within the ELA reconstruction section. Acronyms are LS – Laguna Shimbe valley (Figure 3.4); EG – Eastern Glacier valley (Figure 3.6); SEG – South-Eastern Glacial cirques (Figure 3.11); WG – Western Glacier cirques (Figure 3.14); and NG – Northern Glacier valleys (Figure 3.18). Subset 1 shown by the dashed lines corresponds to the topographical dip shown in detail within Figure 3.5.

Table 3.2: Metrics of area, length, glacier elevation, aspect, cirque floor elevation for reconstructed glaciers. Glacier # corresponds to the numbers in Figure 3.3. Glacier names are derived from either a named lake that occupies a depression within the valley, the cirque the glacier occupied (e.g., Shimbe), or the nearest named river the valley flows into (e.g., Huancabamba). Aspects are visualised in Appendix B Figure B.1.

				Elevation (m asl)				
Glacier Name	**#**	**Area (km^2)**	**Length (km)**	**Min**	**Max**	**Mean**	**Cirque Floor**	**Aspect (°)**
*Shimbe Glacier	1	18.46	12.67	2652	3761	3346	3415	177
*Huancabamba 1	2	21.00	8.64	2953	3624	3322	3364	126
Huancabamba 2	3	0.69	1.56	3259	3668	3471	3532	178
Huancabamba 3	4	1.51	2.46	3356	3750	3581	3465	160
Huancabamba 4	5	1.11	2.03	2930	3521	3223	2191	232
Huancabamba 5	6	1.27	1.84	3112	3525	3376	3217	197
Huancabamba 6	7	0.64	1.42	3193	3527	3365	3277	197
*Negra Glacier	8	3.88	3.89	3345	3775	3626	3547	239
Arrebiatadas Glacier	9	6.39	4.42	3045	3694	3512	3506	287
el Rey Inca Glacier	10	3.65	2.27	3066	3710	3443	3492	290
Palo Blanco 1	11	3.68	4.79	2988	3726	3328	3293	300
Palo Blanco 2	12	2.08	2.43	3177	3764	3481	3442	296
Palo Blanco 3	13	2.00	3.35	3124	3620	3414	3567	275
Aranza 1	14	1.54	2.68	3071	3632	3348	3361	240
Aranza 2	15	0.40	1.02	3258	3631	3482	3396	56
Aranza 3	16	0.38	0.94	3350	3649	3518	3532	132
Aranza 4	17	2.52	3.01	3116	3577	3326	3309	58
Aranza 5	18	0.68	1.57	3148	3618	3408	3354	47
Quebrada Los Rosarios 1	19	1.15	1.52	3254	3522	3370	3227	351
Quebrada Los Rosarios 2	20	0.66	1.25	3062	3432	3321	3178	163
Quebrada Los Rosarios 3	21	0.93	1.77	3168	3442	3305	3246	354
Quebrada Los Rosarios 4	22	0.26	1.21	3194	3382	3299	3331	127
Quebrada Los Rosarios 5	23	1.56	2.98	2980	3460	3192	3301	315
Redondo de Zapalache 1	24	3.64	2.81	3109	3563	3382	3319	324
Redondo de Zapalache 2	25	4.15	3.26	3182	3516	3326	3264	205
Redondo de Zapalache 3	26	0.47	1.20	3217	3569	3401	3268	169
Samaniego 1	27	1.42	2.16	3086	3343	3237	3291	190
Samaniego 2	28	0.13	0.50	3341	3543	3448	3341	77
Samaniego 3	29	1.26	2.07	3203	3686	3418	3339	131

*Maximum glacial extent was estimated by surrounding glacier terminus elevations

After, using the information from the geomorphological mapping and reconstructed glacial extents, palaeo ELAs are reconstructed. These are then used to inform the palaeotemperature interpretation using the regions mean ELA depression, along with determining if any gradient exists in the region for ELAs.

Before moving into the discussion, it should be noted that the geomorphic mapping shown within this section is not constrained by any substantive field ground truthing which is typically

standard in geomorphological studies (Chandler *et al.*, 2018). Due to this, this chapter cannot extract finer details in the geomorphic record, nor make any major inferences in the connectivity of the features to one another. Instead, an approach of reporting the 'discovery' of the palaeoglaciation of Las Huaringas, to define the macro-scale geomorphology, reconstruct the maximum extent and glacial dynamics of the study area and to showcase the substantial potential of the study area for further investigation. Further, in this chapter a new 2.5 m resolution DEM was generated, being the highest resolution DEM of the area available, clouds precluded mapping of certain areas of the region, whilst also reducing the general image quality limiting its use for mapping small-scale (< 1 m) geomorphic landforms (e.g., recessional moraines). Therefore, all attempts were made to use the 2.5 m DEM for mapping, but most mapping was conducted on other, coarser freely available imagery.

3.3.1. Laguna Shimbe valley

The mapped geomorphology (Figure 3.4a) suggests a large valley glacier formed in the central Laguna Shimbe valley (LS) during the LLGM (Figure 3.4b). This glacier ('Shimbe Glacier') likely extended to a minimum elevation of 2,652 m asl, 12.7 km down valley, with a reconstructed area of 18.46 km^2. Lateral moraines are located along the western wall of the Shimbe valley, at ~3,420 m asl and ~3,340 m asl respectively and constrain the lateral and vertical extent of the glacier. However, the maximum extent of the Shimbe Glacier cannot be established confidently due to downvalley evidence being difficult to discern. This may be due to postglacial erosion and fluvial reworking. As a result, we provide a hypothesised maximum LLGM limit for the Shimbe Glacier.

Between the hypothesised maximum glacial extent, and moraines further up valley (~9 km), little geomorphic evidence is apparent (Figure 3.4). This may be due to rapid retreat from its maximum extent during deglaciation, burial of evidence (e.g., by peat accumulation) or fluvial reworking of evidence. Some moraines are observed, though they are likely due to ice flow from glacial cirques on either side of the main valley. Closely spaced (~20 m) moraines between Laguna Shimbe 2 (lake #1) and the larger Laguna Shimbe (lake #2) (Figure 3.4) could indicate glacial advances that postdate the LLGM, either during the late-glacial or early-Holocene. Glacial advances of these ages have been documented in a number of studies in Perú (e.g. Bromley *et al.*, 2011b) and northern Bolivia (e.g. Zech *et al.*, 2007).

Glacial cirques are located along the LS valley walls with cirque floor elevations between ~3,370 to 3,550 m asl (Figure 3.4). These cirques contain geomorphic evidence with moraines

both within and just outside their cirque confines, indicating that during their maximum extent these would have coalesced with the main trunk of the Shimbe glacier. Closely spaced moraines just beyond, or within, the glacial cirques suggests that glaciers that occupied these cirques became decoupled from the Shimbe glacier during post-LLGM deglaciation and did not reconnect during any subsequent glacial advances. The geomorphic evidence suggests that the Shimbe glacier did not advance back to, or close to, its former extent after deglaciation from its LLGM maximum.

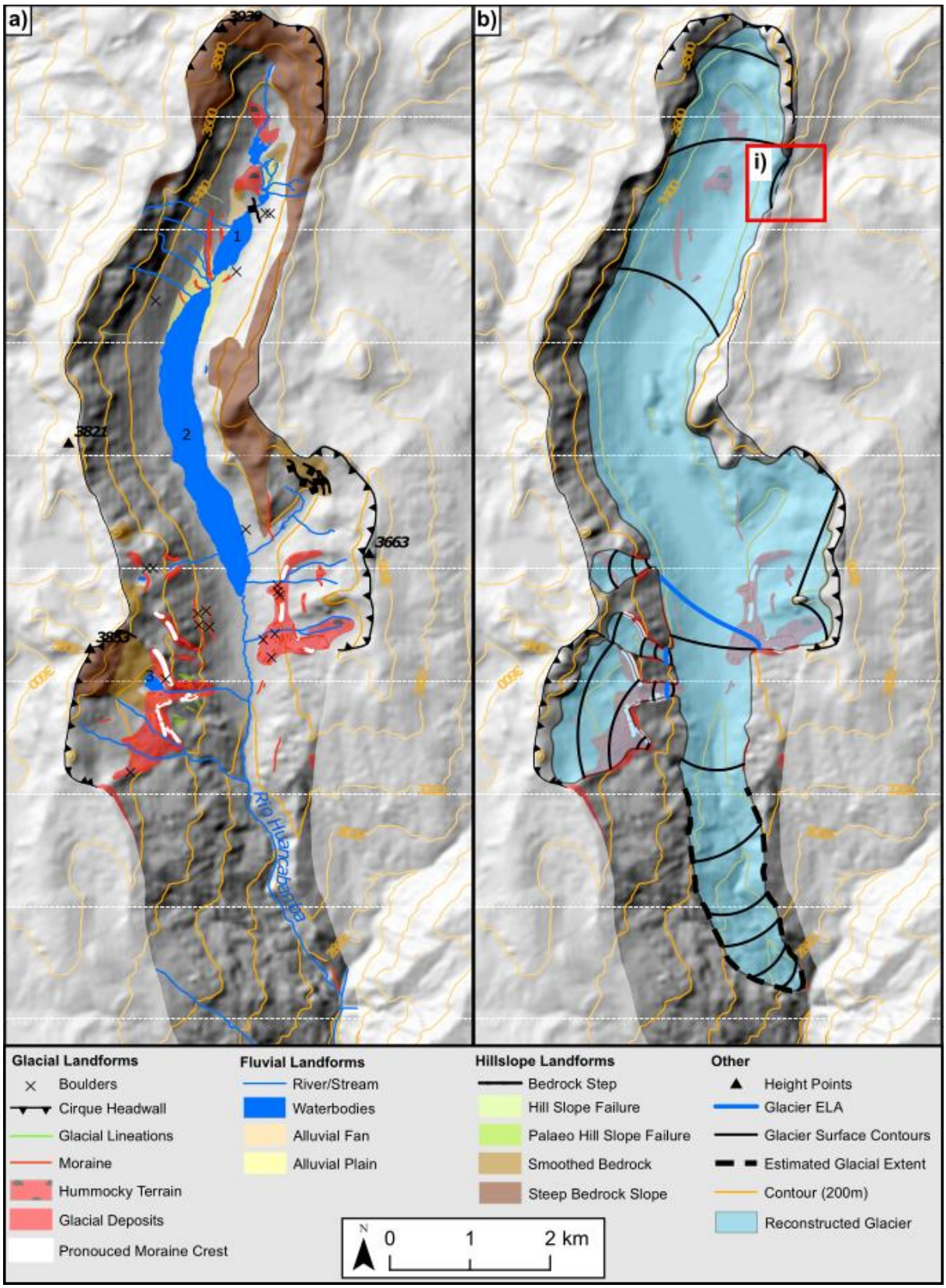

Figure 3.4: The Laguna Shimbe valley (LS) with a) mapped glacial geomorphology, and b) reconstructed glacier to its estimated LLGM extent. Base map is a hillshade of the 30 m ALOS DEM (azimuth: 315°, z-factor 1). i) denotes the extent of Figure 3.5. Lake names: 1 – L. el Paramo, 2 – L. Shimbe. Coordinate location: -5.03°, -79.47°.

Near the head of the Shimbe Valley there is a topographic dip ('col') at ~3,460 m asl on the eastern valley wall (Figure 3.5). This dip features smoothed bedrock, compared to the rougher surrounding valley walls, indicating it has been smoothed by glacial ice. Either a localised glacier was present at this location adjacent to the Shimbe glacier, or the Shimbe glacier was thick enough to overcome the valley topography and flow into the adjacent valley. To allow ice to overcome the topographical dip, it would have required a minimum ice thickness of ~200 m thicker than any other LLGM reconstructed ice masses across the study area.

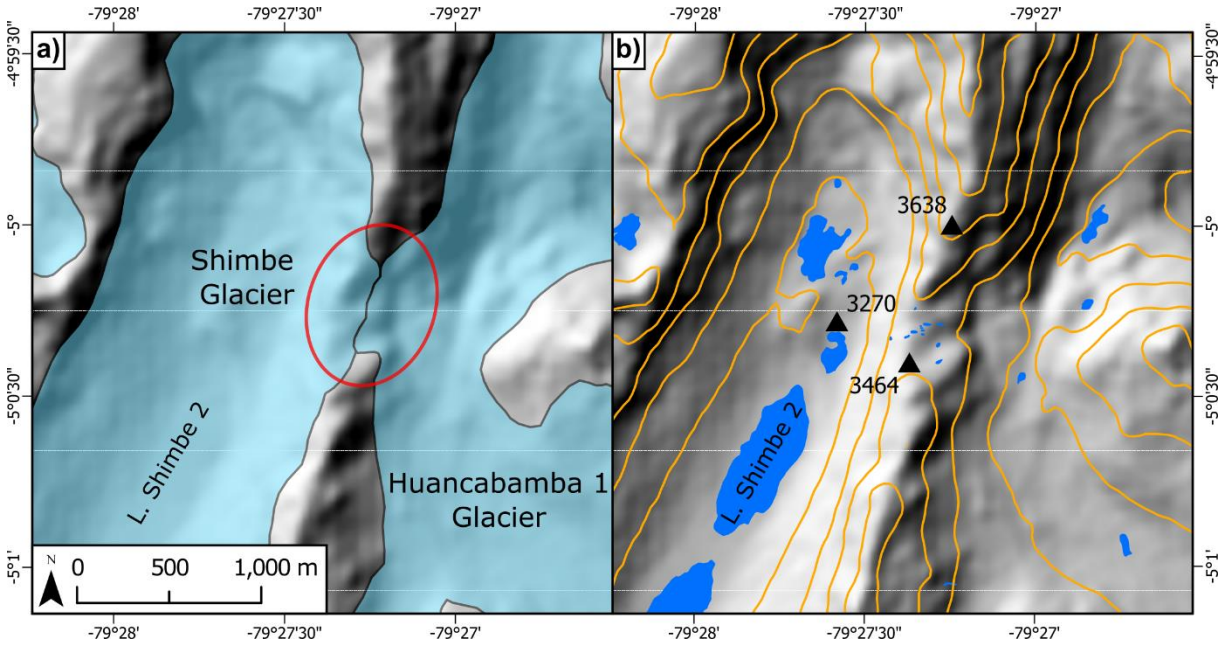

Figure 3.5: Confluence of glacier ice at the topographical dip with the location can be seen in Figure 3.4 i), a) shows the connection (red circle) between the Shimbe glacier and Huancabamba 1 glacier during their LLGM maximum extent, while b) in a topographical dip with 100 m contour intervals, detailing a maximum elevation within the dip of 3,464 m asl that is lower than the surrounding valley wall ridges (3,638 m asl).

3.3.2. Eastern glacial valley

The valley to the east of LS exhibits extensive evidence of glaciation with a number of mapped moraines along the valley walls and floor, 8 distinct glacial cirques, and 19 mapped glacial lineations (Figure 3.6a). The evidence suggests one of the largest glaciers within the Las Huaringas region, with a reconstructed estimate of the Huancabamba 1 glacier area of 21 km^2 (Figure 3.6b). The extents and area metrics of the reconstructed glacier are an estimate, due to the absence of any discernible cross valley terminal moraines downvalley. The geomorphic evidence within the EG suggests an interconnected glacial valley system with three terminus locations, that can be split into two distinct 'zones'; i) the valley running south paralleling the Shimbe valley with a single terminus, and ii) the two valleys, with a terminus each, to the north

which run eastward – all hypothesised to have terminated at ~3,000 m asl due to the absence of obvious terminal moraines. All valleys within the EG area contain valley wall cirques with cirque floor elevations ranging from 3,178 – 3,420 m asl. At their largest extent, glaciers flowing from these cirques would have connected with the main valley glacier during the LLGM. Similar to the cirque glaciers reconstructed in the LS area, mapped moraines beyond and within their cirque extents suggests that after deglaciation from the LLGM any subsequent readvances would not have resulted in reconnection with any main valley glacier, otherwise such evidence beyond their cirque confines would likely have been removed by glacial erosion.

These two zones are split by the topographical dip (Figure 3.5 and Figure 3.6), through which the Shimbe and Huancabamba 1 glaciers could have potentially been connected at the height of their LLGM glacial extents. Evidence for this is smoothed bedrock exposed in the topographical dip between LS and EG suggesting that at some point the Shimbe glacier was thick enough (> 200 m thickness) to overcome the topography and make a direct connection between these two glacial masses. Without further infield investigations to collect TCN dates of smoothed bedrock at the valley top to determine timing of deglaciation, we cannot determine whether this occurred at the LLGM or during an earlier glaciation.

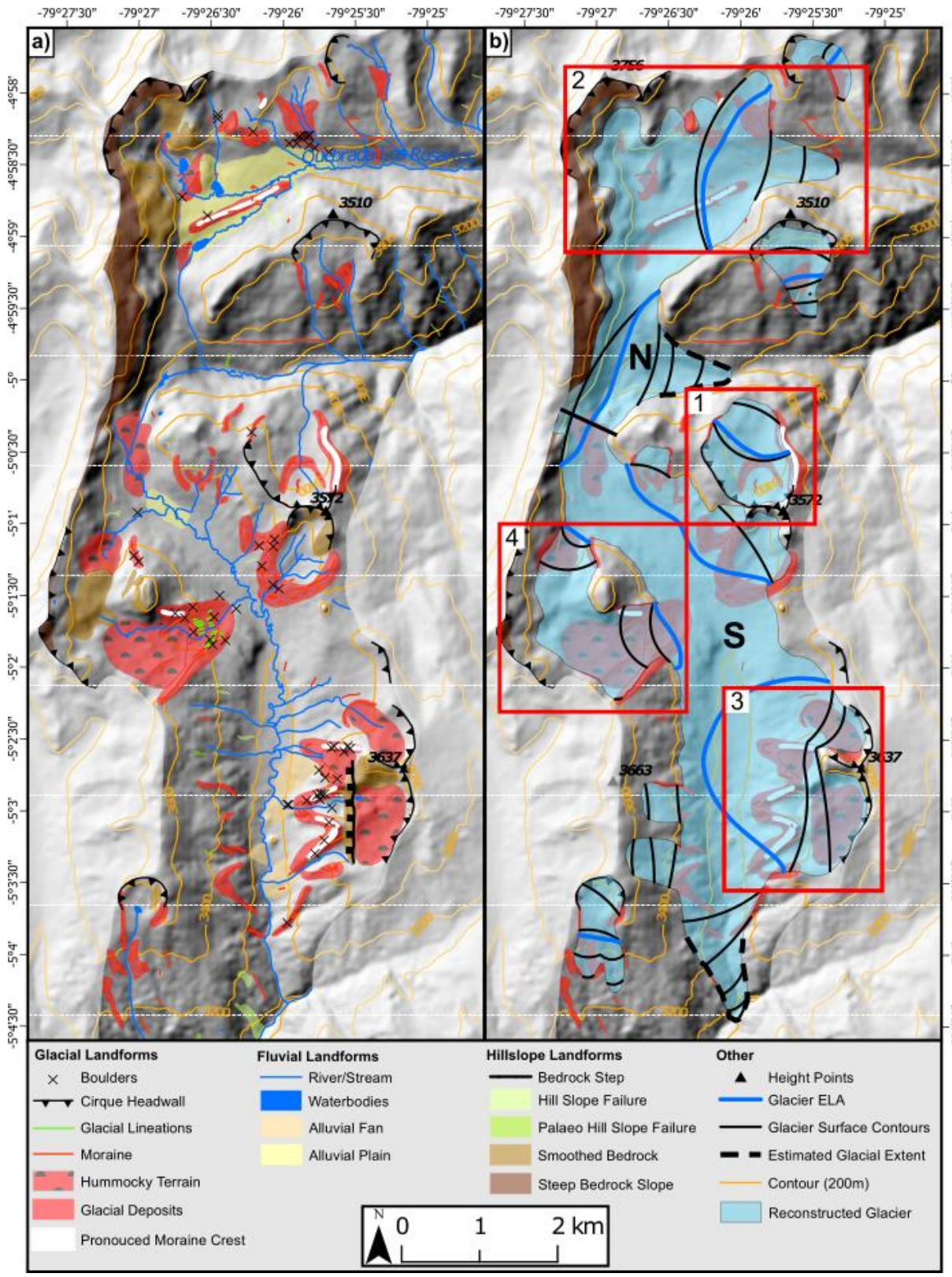

Figure 3.6: The Eastern Glacial valley (EG) with a) mapped glacial geomorphology, and b) the reconstructed glaciers to their estimated LLGM extent. The Huancabamba 1 glacier is split into two zones: the northern (N) and southern (S) zones. The separation is the split at the topographical dip that connected the two valleys, shown in Figure 3.7. Subsets b) 1, 2, 3 and 4 correspond Figures 7, 8, 9 and 10 respectively. Base map is a hillshade of the 30 m ALOS DEM (azimuth: 315°, z-factor 1).

Evidence for the potential ‘spill over’ of ice from the LS to the EG area can be seen within the northern zone of EG (Figure 3.6 section labelled N). This zone has two eastward flowing valleys, with the most southerly valley exhibiting little evidence for glaciation apart from a singular glacial cirque on either side of the valley. The southernmost cirque (Figure 3.7) has a well-developed set of moraines perhaps indicating multiple glacial events. The northernmost valley hosts the most striking evidence with a prominent medial moraine (Figure 3.8) running down the centre of the valley going eastward. This demonstrates that glacial ice flowed both from the glacial cirques in the northern valley and from the south, potentially from ice flowing over from SG area. This southern input is hypothesised due to the absence of a clear glacial cirque above the valley. The medial moraine is located to the southern side of the east-west trending valley, suggesting that ice flow was dominated by flow originating from the northern cirques.

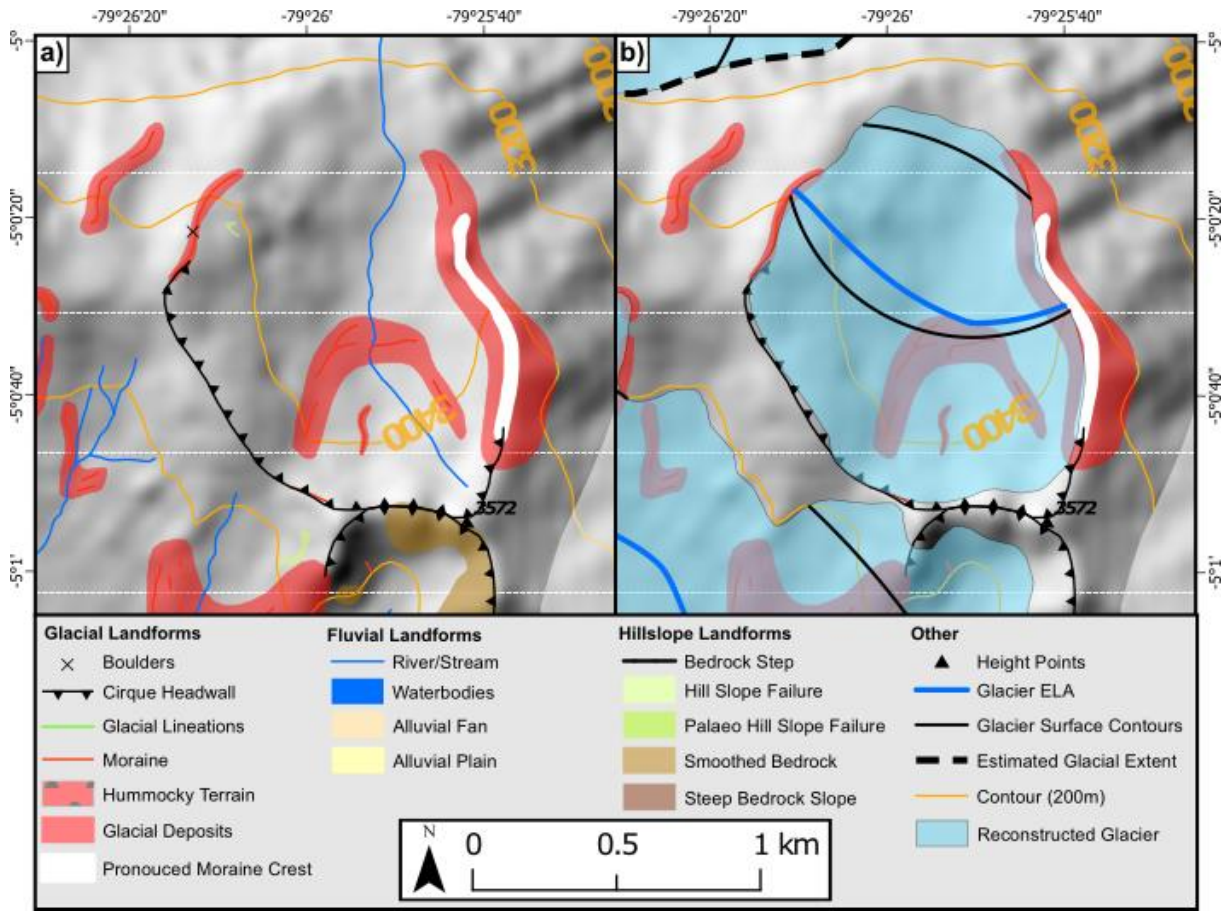

Figure 3.7: The Quebrada Los Rosarios 1 glacier corresponding to Figure 3.6b subset 1 with a) mapped geomorphology and b) the subsequent reconstructed LLGM glacier extent. Base map is a hillshade from the ALOS 30 m DEM.

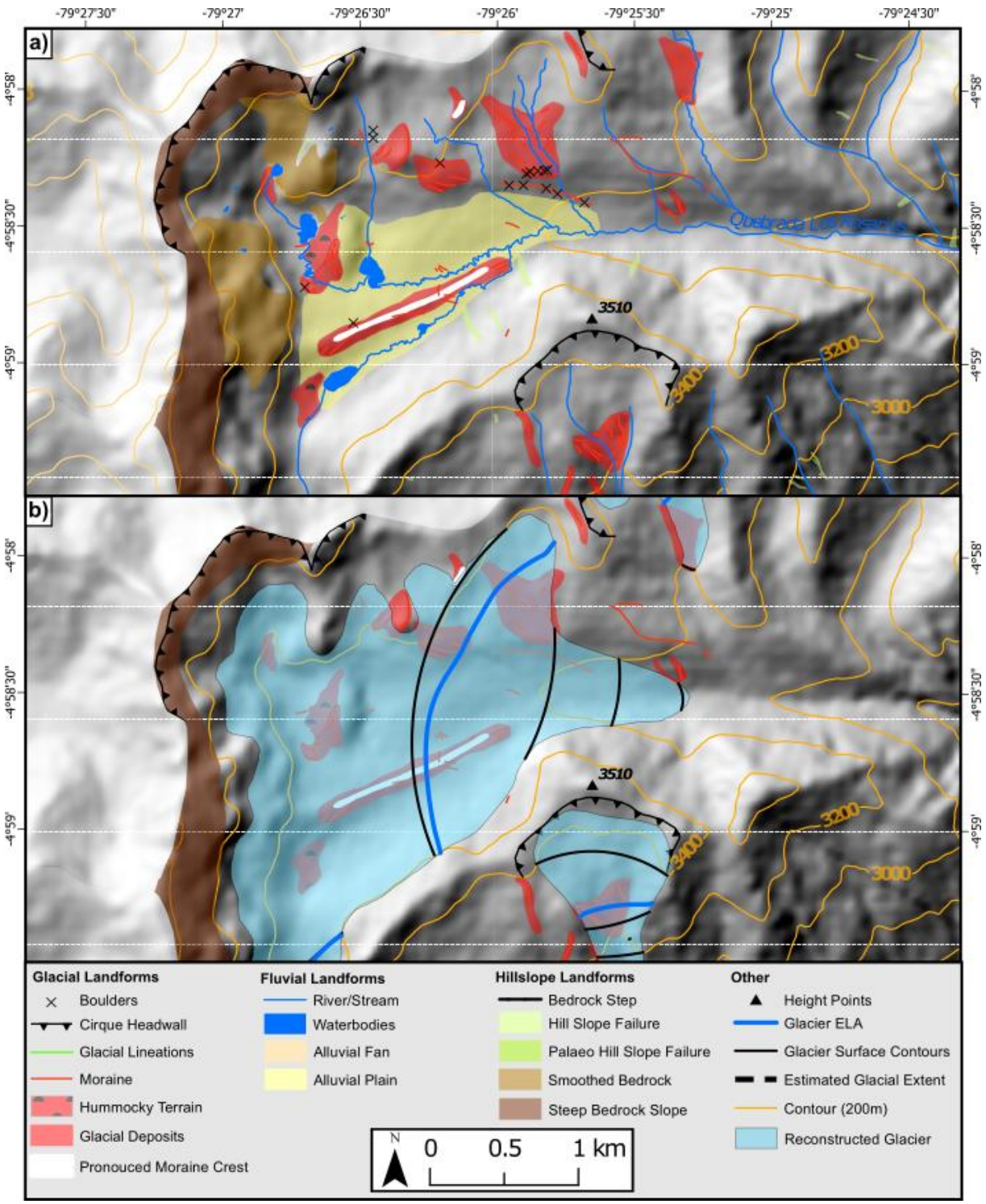

Figure 3.8: The northern section of the Huancabamba 1 glacier corresponding with Figure 3.6b subset 2 with a) mapped geomorphology and b) the subsequent reconstructed LLGM glacier extent. Base map is a hillshade from the ALOS 30 m DEM.

Within the southern zone of the EG area (Figure 3.6 section labelled 'S'), are a number of predominantly westward facing glacial cirques, the majority of which exhibit classic evidence of cirque glaciation. These would have likely contained ice, feeding into the main Huancabamba glacier flowing southward, during their most extensive LLGM extent. Two cirques are of particular interest within the southern zone of the EG: i) one near the southern

end on the east side of the valley (Figure 3.9), and ii) the other on to western flanks (Figure 3.10). The first location contains three reconstructed glacier outlets connecting to an individual cirque. Prominent moraines connect through all three outlets and appear to have once contained lakes within each outlet depression. Moraines may delineate individual advances after the LLGM when they became disconnected from the main valley glacier during deglaciation. These lakes were moraine dammed and drained at some point after deglaciation. This was probably the result of moraine dam failures, evidenced by the lack of an enclosing terminal moraine and deposits of alluvial material in front of the glacial moraines. Within the second location, the glacial cirque splits into two outlets, with the southern outlet being one of only two locations that exhibit possible glacial lineations. There is a potential for these features to be glacial flutes, however because of their small-scale further investigation with a finer resolution DEM along with infield techniques is required.

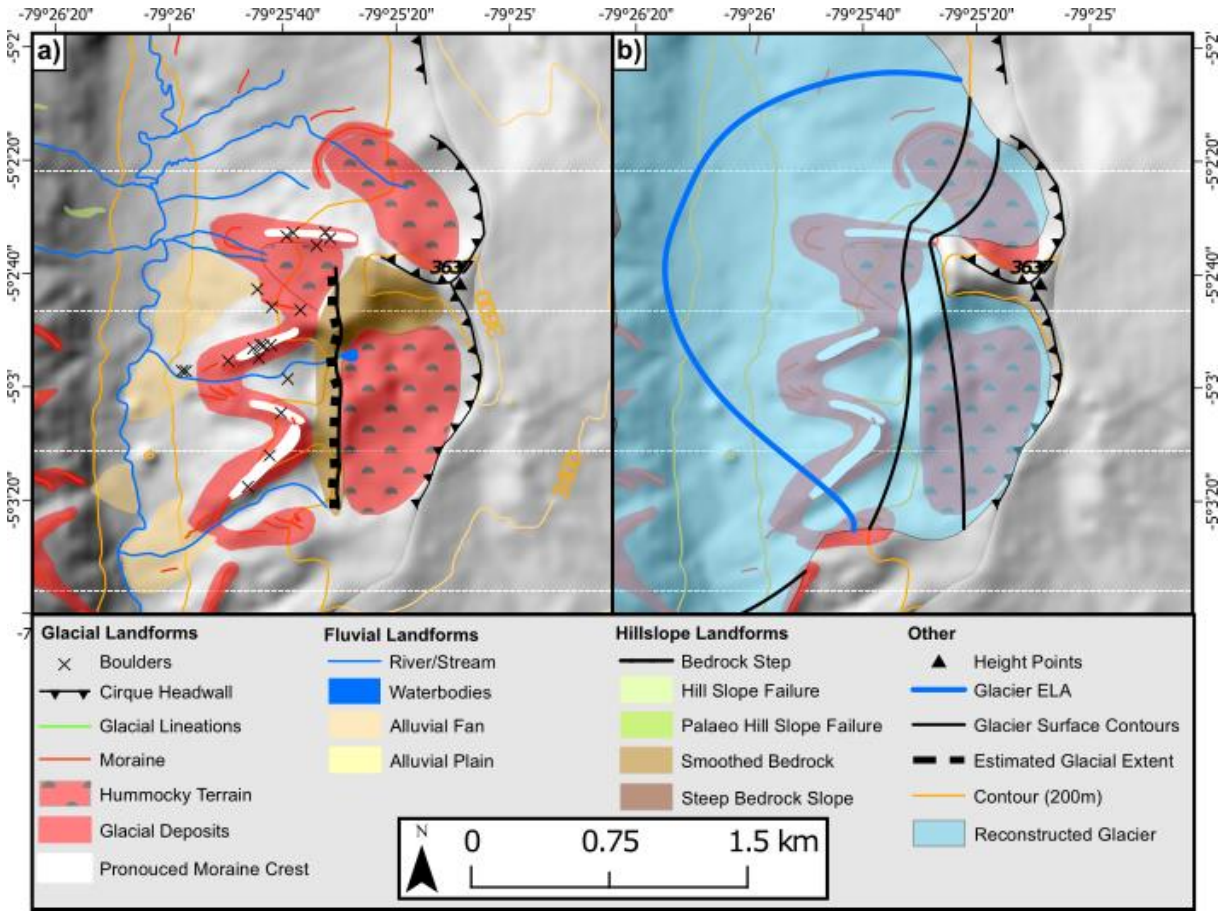

Figure 3.9: Three glacial outlets in the southern section of the Huancabamba glacier, corresponding with Figure 3.6b subset 3 with a) mapped geomorphology and b) the subsequent reconstructed glacier LLGM extent. Base map is a hillshade from the ALOS 30 m DEM.

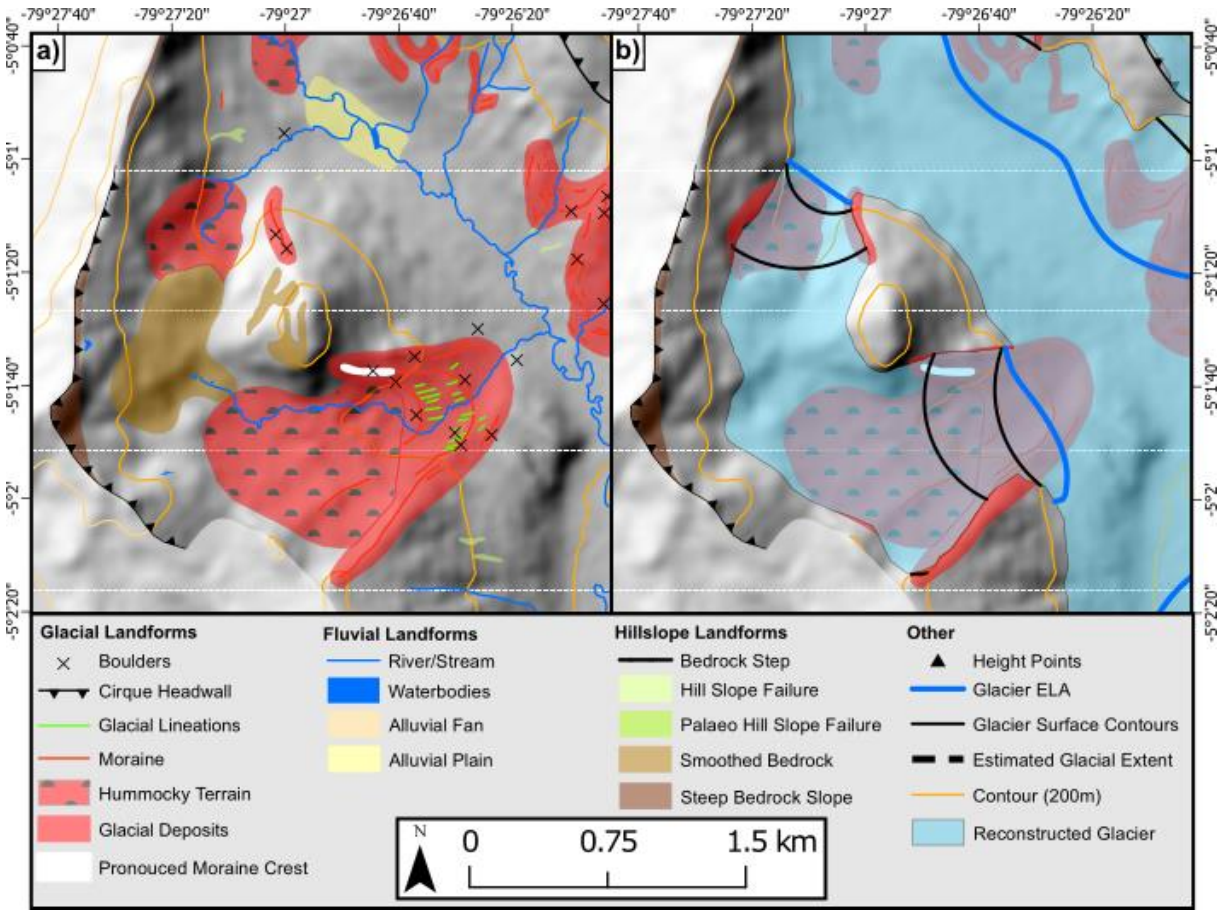

Figure 3.10: The western outlet in the southern section of the Huancabamba glacier with two outlets and the glacier lineations, corresponding with Figure 3.6b subset 4 with a) mapped geomorphology and b) the subsequent reconstructed glacier LLGM extent. Base map is a hillshade from the ALOS 30 m DEM.

3.3.3. South-eastern glacial cirques

Geomorphological evidence within the south-eastern zone (SEG) of the study area (Figure 3.11a), suggests a cirque to valley glacier configuration (Figure 3.11b). There are 12 identified cirques that would likely have contained reconstructed glaciers in this zone. The reconstructed glacial area during the LLGM was 17.7 km^2. Multiple moraines are nested within many of the cirques, but glacial geomorphic evidence is more discontinuous further south. The absence of this evidence is likely due to decreasing topographic elevation, which may not have permitted glacier ice to persist even during the LLGM. Many cirques exhibit extensive erosion with glacially smoothed bedrock indicative of warm-based basal conditions, in line with evidence mapped here, across the study region. Many of the cirques would have contained a separate and confined glacier, with no evidence for ice masses coalescing. The dominant orientation for cirques in this zone is south and south-westward facing, which could be due to the predominant direction of incoming solar radiation in the southern hemisphere.

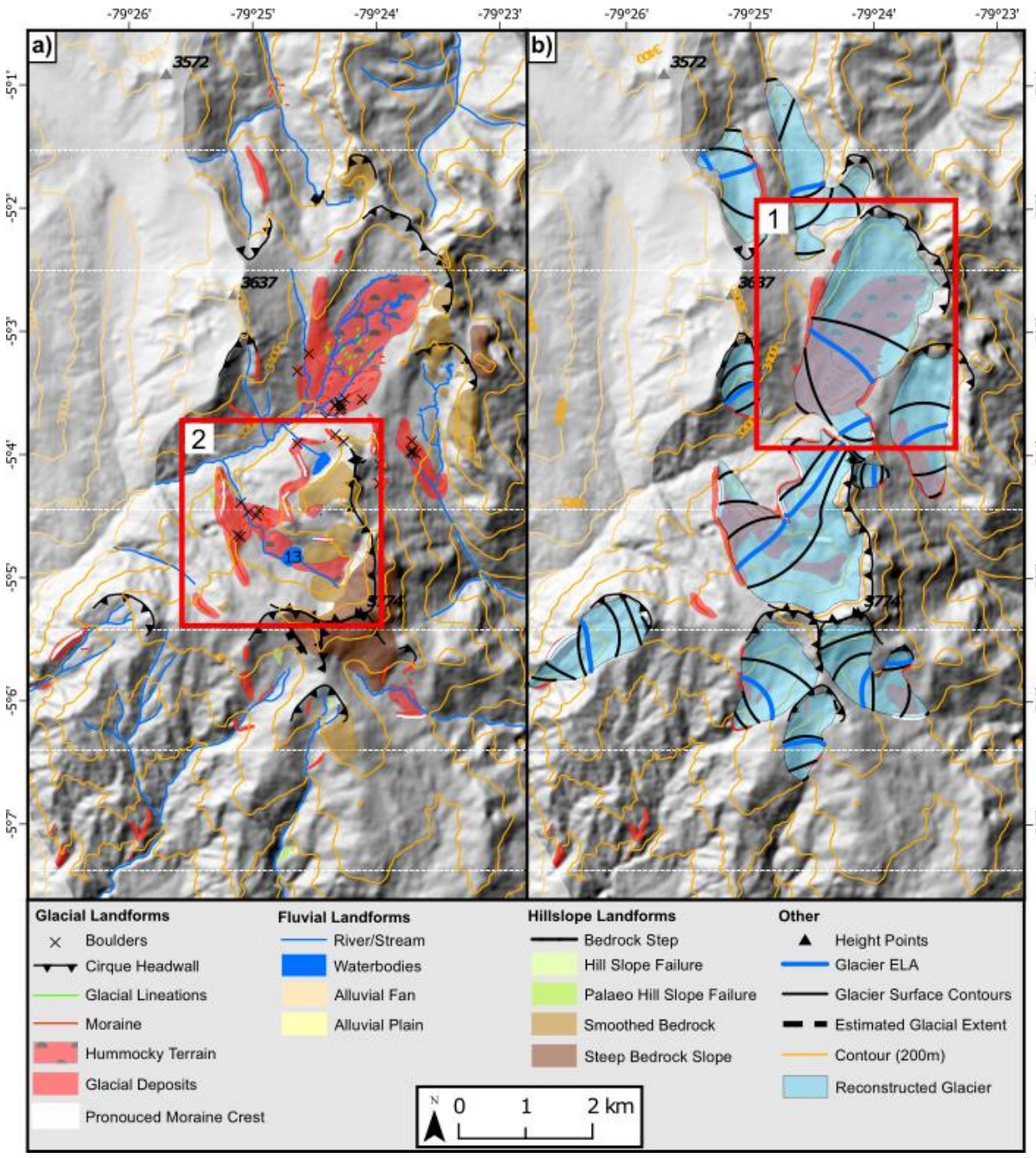

Figure 3.11: The southeastern glacial cirques (SEG) with a) mapped glacial geomorphology, and b) the reconstructed glaciers to their LLGM extents. Subsets b) 1 and a) 2 correspond to Figures 12 and 13 respectively. Base map is a hillshade of the 30 m ALOS DEM (azimuth: 315°, z-factor 1). Lake name: 13 – L. Redondo de Zapalache.

Similar to the EG, the SEG zone is the only other location within the study area to contain mapped linear features (Figure 3.12). 19 features were mapped with lengths between 23 to 100 m. These lineations are located within the extent of the Redondo de Zapalache 2 glacier valley (#25) behind discontinuous closely spaced moraines, with the orientation of the lineations indicating a northeast to southwest direction of glacier flow, similar to that suggested by the lineations in the EG valley. We hypothesise that these lineations are only found in these two locations due to their relatively unusual location on flat terrain. The remainder of the study area

either lacks wide areas of sufficiently flat terrain where such lineations may develop, or lineations may have existed previously but have been eroded by post-depositional geomorphic action.

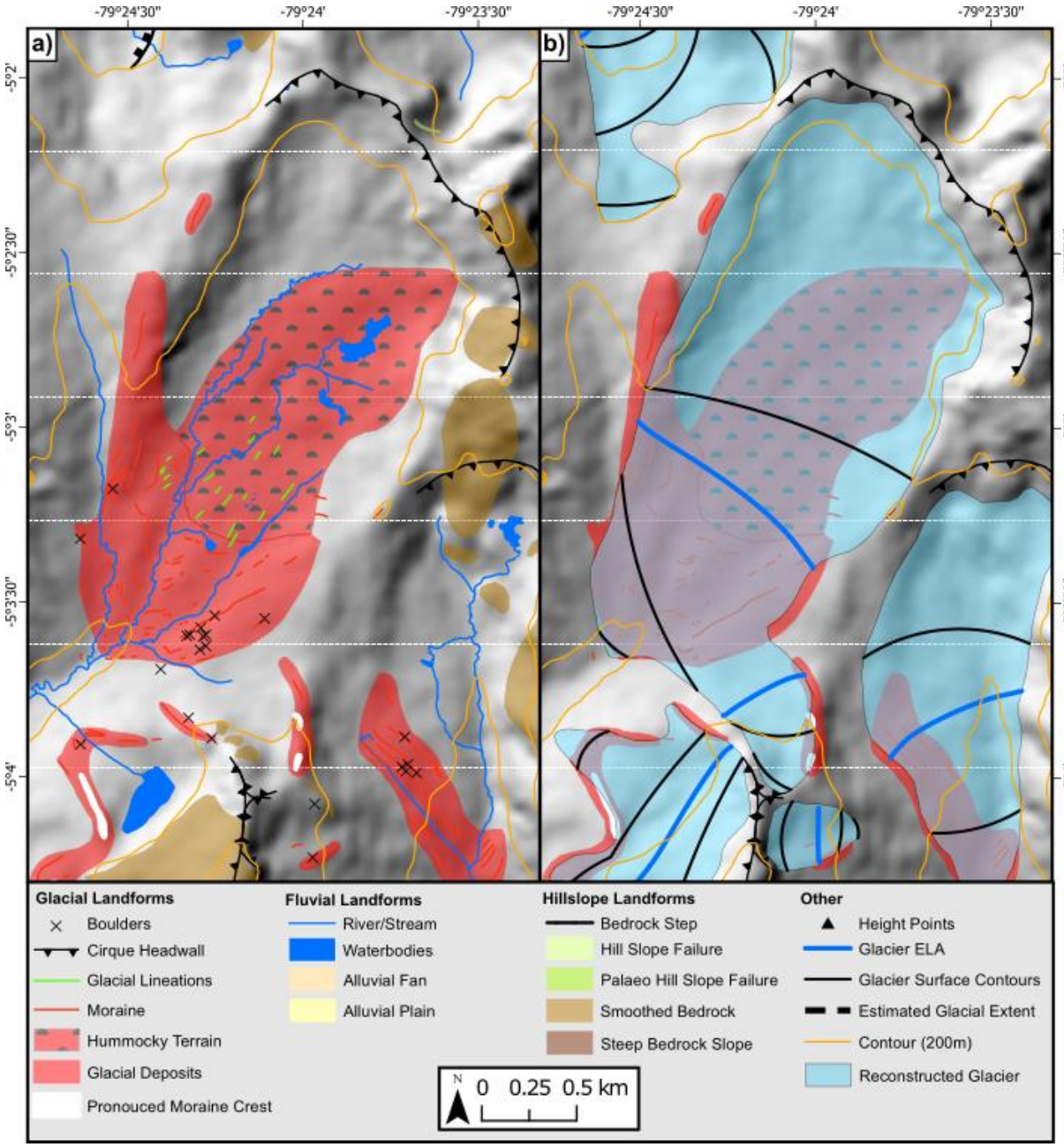

Figure 3.12: The Redondo de Zapalache 2 glacier valley within the southeastern glacier zone, corresponding with Figure 3.11b subset 1 with a) mapped geomorphology and b) the subsequent reconstructed glacier LLGM extent. Base map is a hillshade from the ALOS 30 m DEM.

The Redondo de Zapalache 1 glacier area (#24) (Figure 3.13) is unique compared to the surrounding glacier cirques in the SEG zone, being similar to the two cirque glaciers discussed within the EG. The geomorphological evidence here suggests two glacier outlets that flowed from a shared accumulation zone. The total reconstructed glacier area was 3.6 km^2. Prominent moraines indicate maximum lateral extents of these ice masses. Further lateral moraines up-

valley from these lateral-terminal moraines indicate that the two glacier outlets separated during deglaciation, dividing into two glaciers each occupying their own cirque, and potentially producing moraines suggesting post-LLGM readvance. The westernmost outlet of this glacier contains multiple closely spaced moraines (20-100 m apart) at its terminus potentially indicating a fluctuating ice front.

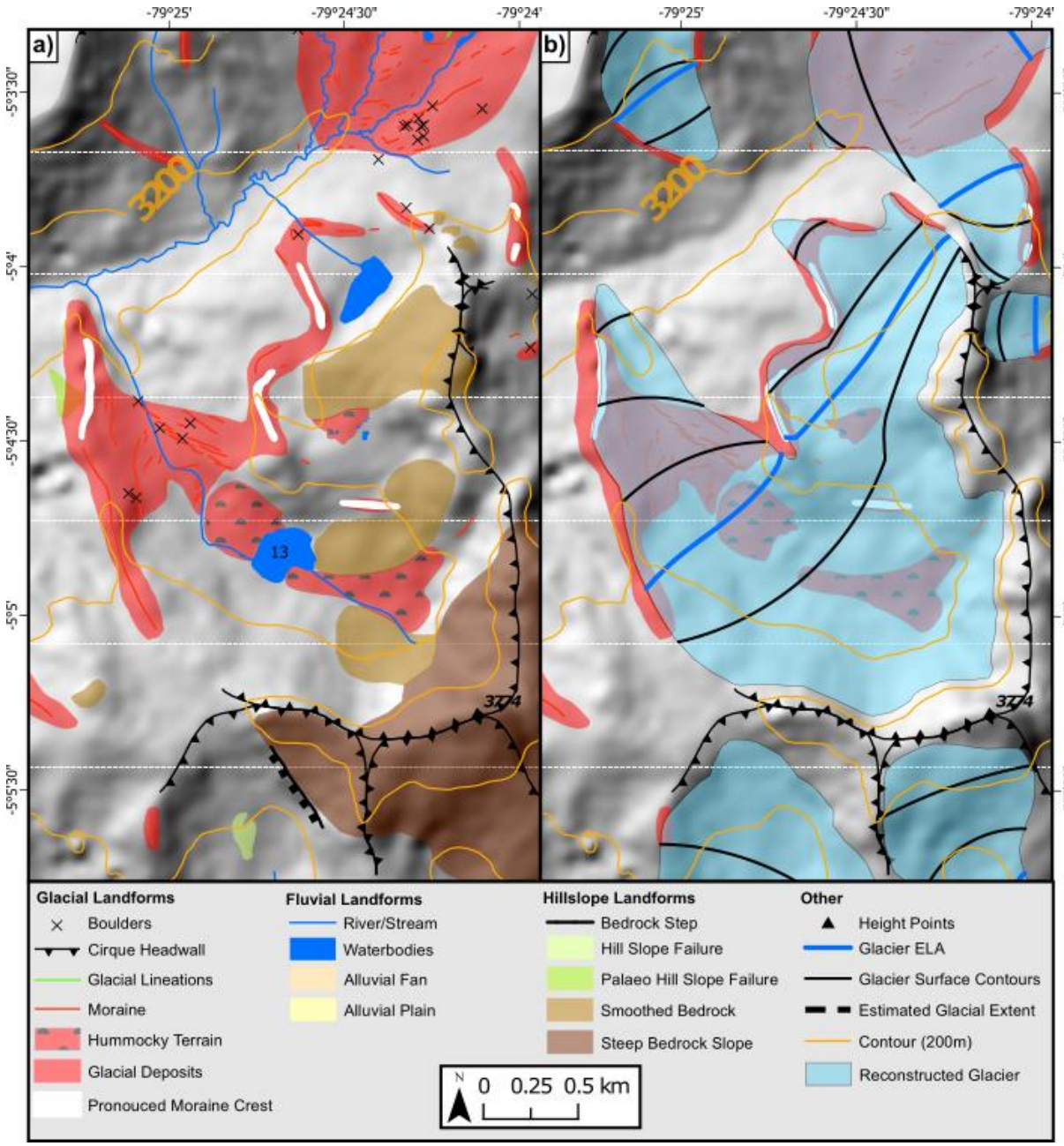

Figure 3.13: The Redondo de Zapalache 1 glacier valley within the southeaster glacier zone, corresponding with Figure 3.11a subset 2 with a) mapped geomorphology and b) the subsequent reconstructed glacier LLGM extent. Base map is a hillshade from the ALOS 30 m DEM.

3.3.4. Western glacial cirques

The western zone of the Las Huaringas region (WG) contains some of the largest and most extensive moraines in the study region (Figure 3.14a). These moraines extend down to a minimum elevation of ~3100 m asl. We reconstructed three glaciers, the Arrebiatadas Glacier, the el Rey Inca glacier and the Negra Glacier (Figure 3.14b), which occupy 5 large west-facing cirques. These cirques have steep headwalls and are well developed, indicating a large amount of backward erosion while also having wide open backwalls that do not follow an amphitheatre-like shape that is seen across the study area; this makes it hard to determine an individual 'source' cirque. Depressions containing water bodies are common across the WG. These 26 bodies of water are either dammed by bedrock (e.g. Lagunas las Arrebiatadas) or a moraine (e.g. Laguna Millionaria), often coinciding with bedrock steps and smoothed bedrock indicating warmed based glaciers that produced glacial erosion with a high discharge of ice and a high mass turnover (MacGregor *et al.*, 2000; Cook and Swift, 2012; Evans, 2021).

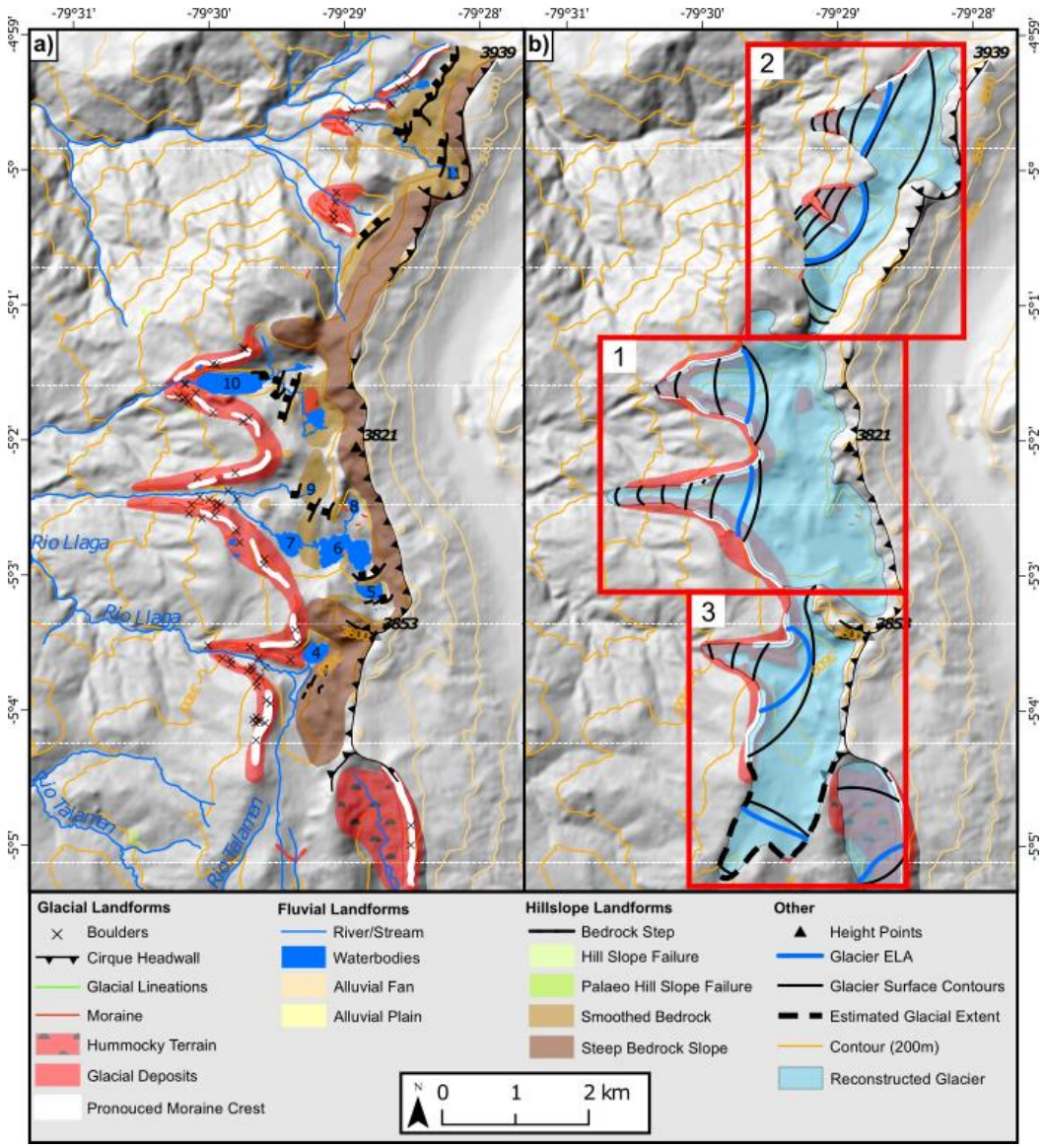

1440 **Figure 3.14**: The western glacial cirques (WG) with a) mapped glacial geomorphology, and b) reconstructed glaciers to their estimated LLGM extents. Subsets b) 1, 2 and 3 correspond to Figures 15, 16 and 17. Base map is a hillshade of the 30 m ALOS DEM (azimuth: 315°, z-factor 1). Lake names: 4 – L. Negra, 5 – L. las Arrebiatadas 1, 6 – L. las Arrebiatadas 2, 7 – L. las Arrebiatadas 3, 8 – L. las Arrebiatadas 4, 9 – L. el Toro, 10 – L. Millionaria, 11 – L. el Ray
1445 Inca.

The form of the Arrebiatadas Glacier (Figure 3.15), and the el Ray Inca Glacier (Figure 3.16) suggest they both potentially had two source areas which coalesced to create an individual ice mass, from which two separate glacial outlets extended from. The Arrebiatadas Glacier area,
1450 covering 6.4 km^2, has well defined and interconnected moraines up-valley. These run down into, and demarcate, the individual outlets providing further evidence that ice came from a single source area. Moraines within the confines of the most extensive terminal moraine of the Arrebiatadas Glacier are closely spaced (20-50 m), which may indicate oscillating climate condition during formation. Similar dynamics are possible for the el Ray Inca Glacier. The el

Ray Inca Glacier covered 3.6 km^2, had prominent lateral moraines on its northern most glacial outlet, and more closely spaced moraines near its terminus. Within the southern outline, it lacks many prominent moraine features but hosts smaller closely spaced moraines.

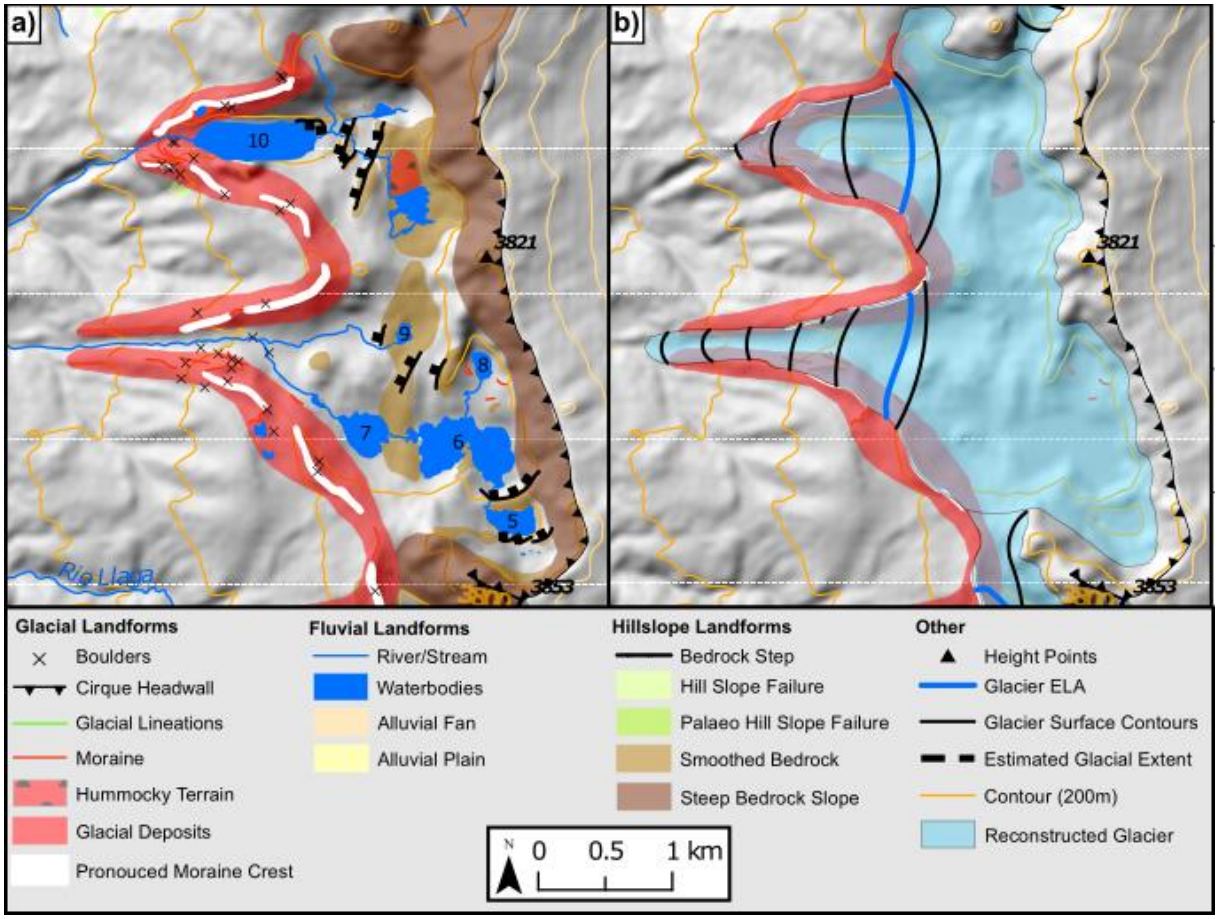

Figure 3.15: The Arrebiatadas Glacier within the western glacier cirques zone, corresponding with Figure 14b subset 1 with a) mapped geomorphology and b) the subsequent reconstructed glacier LLGM extent. Base map is a hillshade from the ALOS 30 m DEM**.**

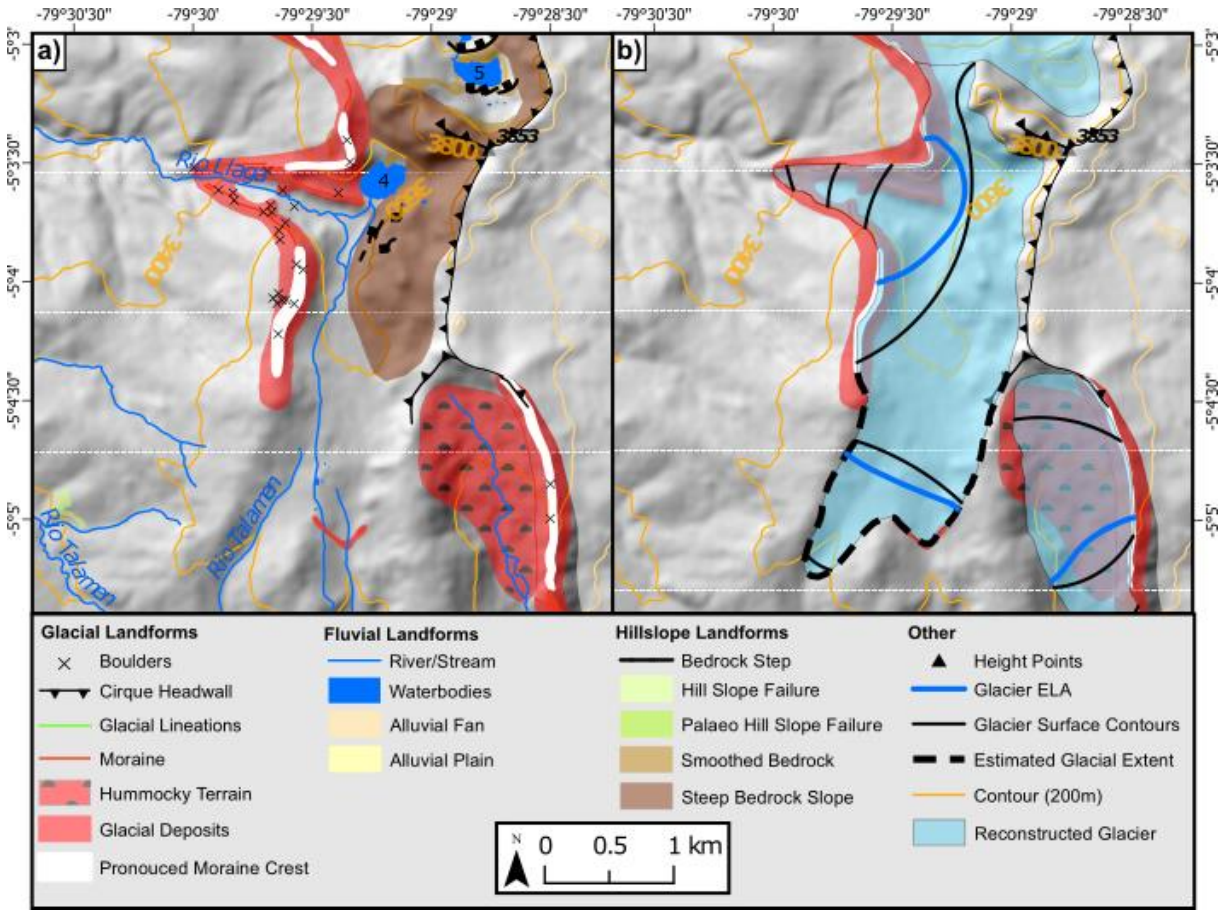

Figure 3.16: The el Ray Inca Glacier within the western glacier cirques zone, corresponding with Figure 14b subset 2 with a) mapped geomorphology and b) the subsequent reconstructed glacier LLGM extent. Base map is a hillshade from the ALOS 30 m DEM.

The Negra Glacier (Figure 3.17), the most southern of the glaciers in the WG area covered an area of 3.9 km^2. This glacier may have connected with the Arrebiatadas system at the LLGM as indicated by lateral moraines which appear to connect. Like other glaciers within WG, geomorphological evidence indicates that glacial ice flowed from a single source zone into two outlets, westward and southward. Although the moraines to the west clearly indicate the former glacier ice extent, little geomorphic evidence for the southern outlet is observed. Although a single moraine is mapped, no further evidence is seen to demark its most southerly advance, potentially indicating reworking from post-glacial fluvial action. Although glacial ice is reconstructed to the only mapped moraine within the outlet, due to the flatter profile of the topography, when compared to the valley that extends out westward, there is the potential for ice to have flowed further south than this position.

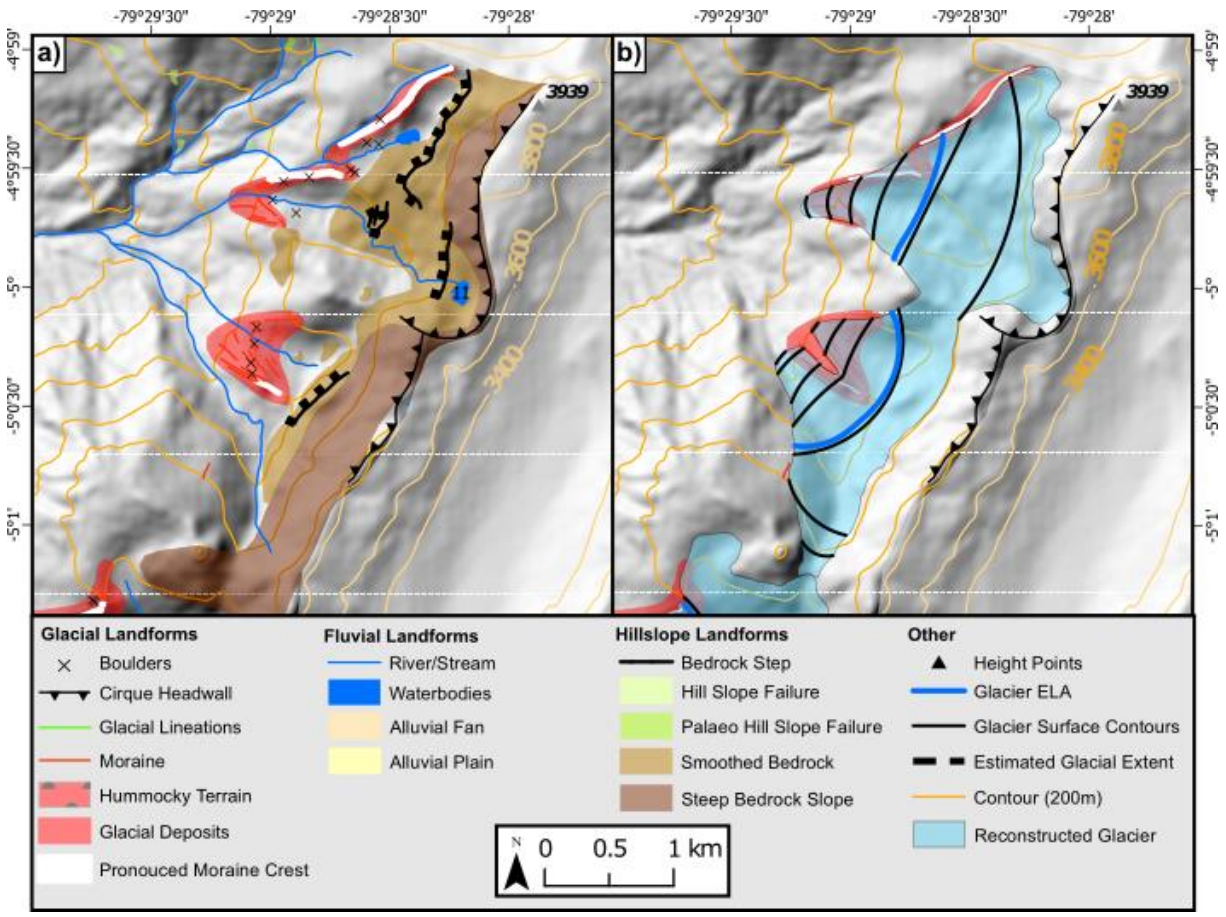

Figure 3.17: The Negra glacier within the western glacier cirques zone, corresponding with Figure 14b subset 3 with a) mapped geomorphology and b) the subsequent reconstructed glacier LLGM extent. Base map is a hillshade from the ALOS 30 m DEM.

3.3.5. Northern glacial valleys

Glaciers reconstructed in the northern glacial valleys (NG) north study region generally exhibit a cirque- to valley-glacier configuration like the glaciers of the SEG area. Geomorphological evidence (Figure 3.18a) suggests the most extensive glaciers developed (Figure 3.18b) on the westward side of the region (mean ice mass area of 2.3 km^2), while smaller glaciers developed to the east (mean ice mass area of 1 km^2). These reconstructed glaciers cover a total area of 9.6 km^2 originating from twelve cirques with cirque floor elevations between 3,257-3,567 m asl One of the most striking features within this zone is the large bowl-like depression eroded down to bedrock with lakes filling the depression and bedrock joints (Figure 3.19). The erosion down to the bedrock, along with headward erosion of the cirque provides further evidence these glaciers had a high mass turnover during the LLGM.

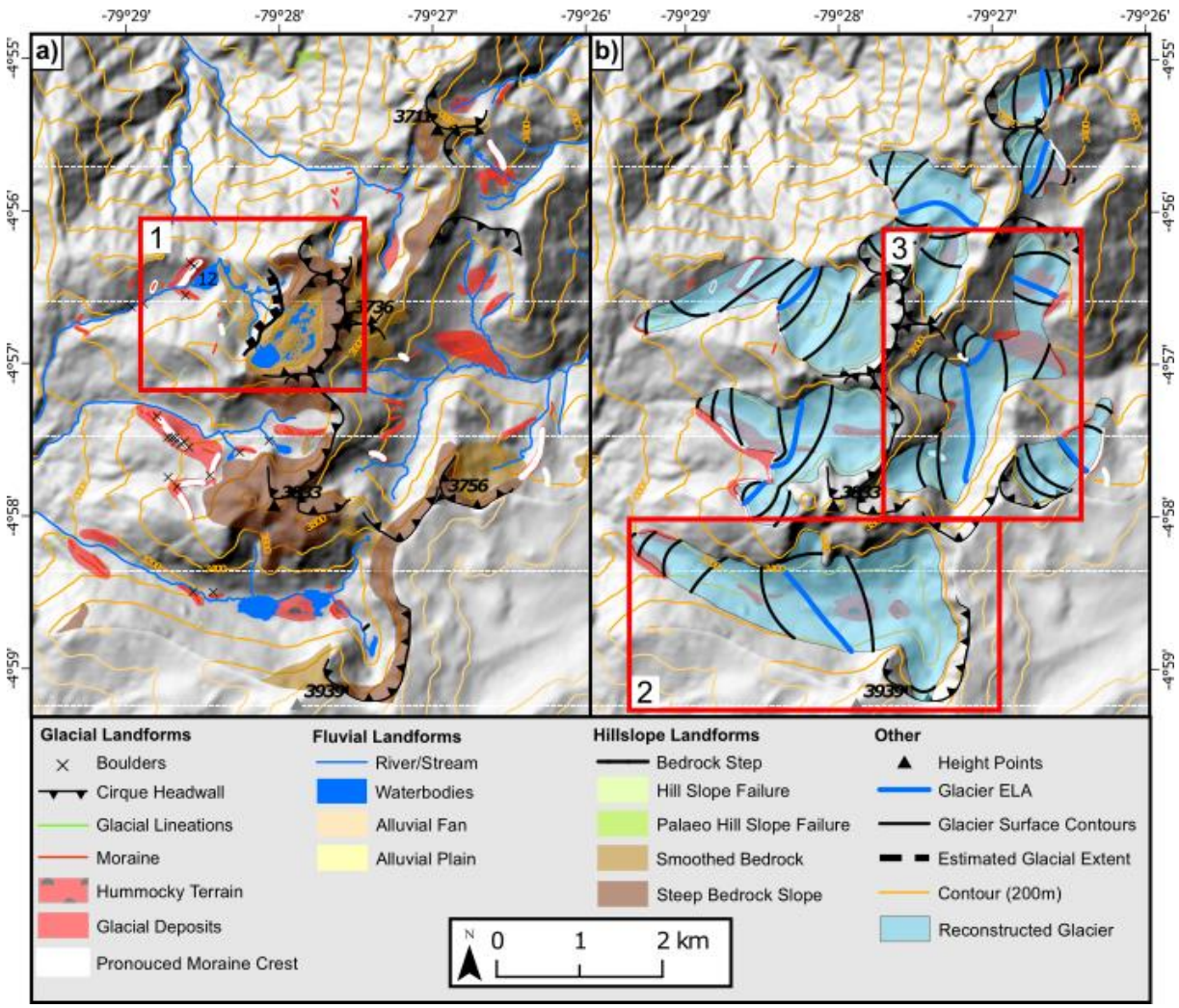

1495 **Figure 3.18:** The northern glacial valleys (NG) with a) mapped glacial geomorphology, and b) the reconstructed glaciers to their estimated LLGM extents. Subsets a) 1 and b) 2 and 3, correspond to Figures 19, 20, and 21 respectively. Base map is a hillshade of the 30 m ALOS DEM (azimuth: 315°, z-factor 1). Lake name: 12 – L. Negra de San Pablo.

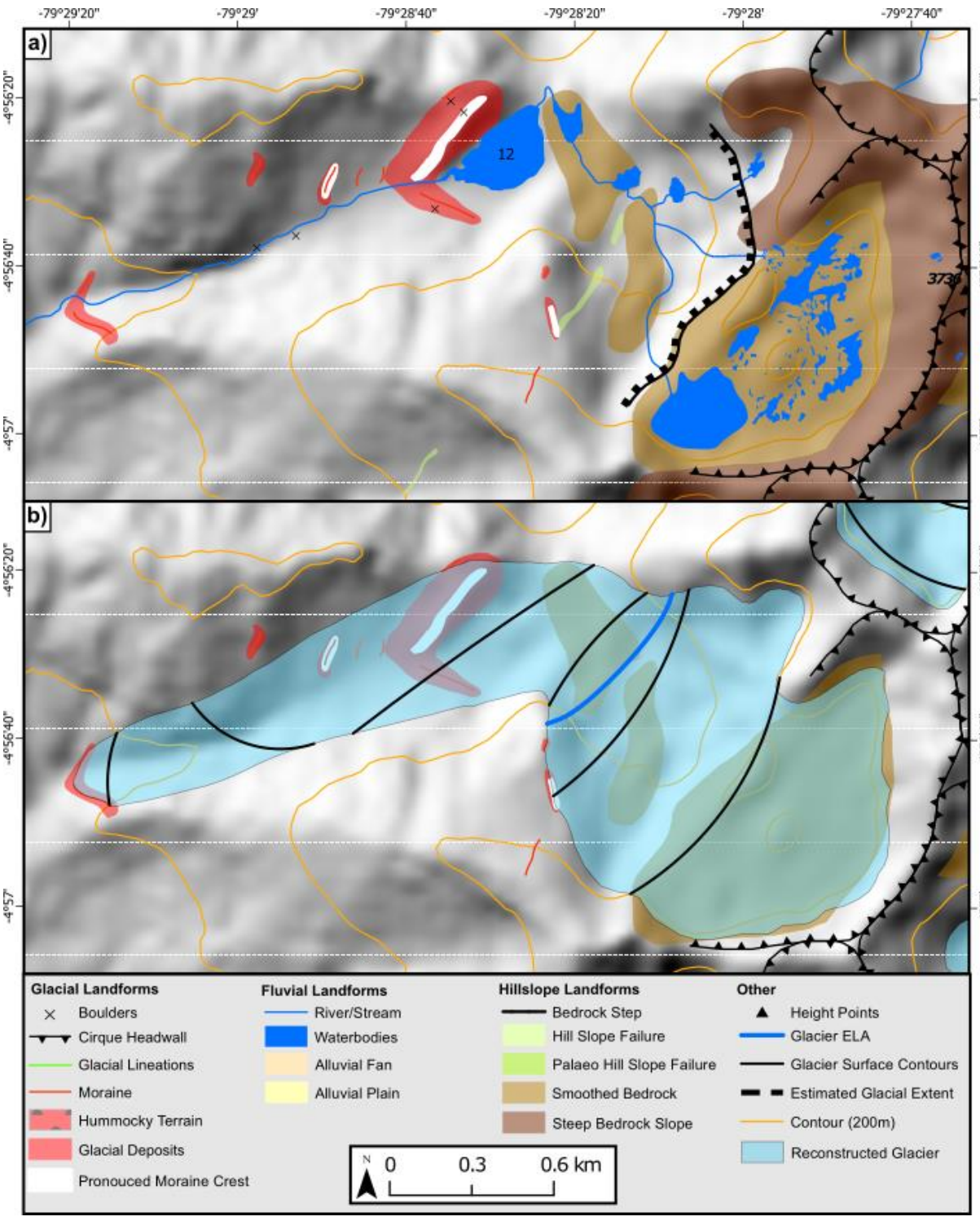

Figure 3.19: The Pablo glacier # within the northern glacier valleys zone, corresponding with Figure 18a subset 1 with a) mapped geomorphology and b) the subsequent reconstructed glacier LLGM extent. Base map is a hillshade from the ALOS 30 m DEM.

Glaciers located on the western side of the NG zone have multiple moraines downvalley. These reach elevations as low as ~3,100-3,200 m asl while each have multiple lakes either occupying a cirque depression or a depression behind a moraine dam further down valley (e.g., Laguna de San Pablo). This is in stark contrast to the eastern glaciers that have either no lake, or relatively small bodies of water. Glaciers in the northwest (Palo Blanco 1, 2 and 3) have reconstructed lengths of 4.79 km, 2.43 km, 2.00 km respectively with the longest seen in Figure 3.20), the longest of any glaciers within the study area, but extend down to similar elevations to that of the Arrebiatadas glaciers. This could be due to the topography having a shallower incline (~-11.4%) compared to those to the immediate west of the Shimbe valley (~-18.5%), thereby allowing ice to flow further down valley while remaining at an elevation high enough to minimise mass loss.

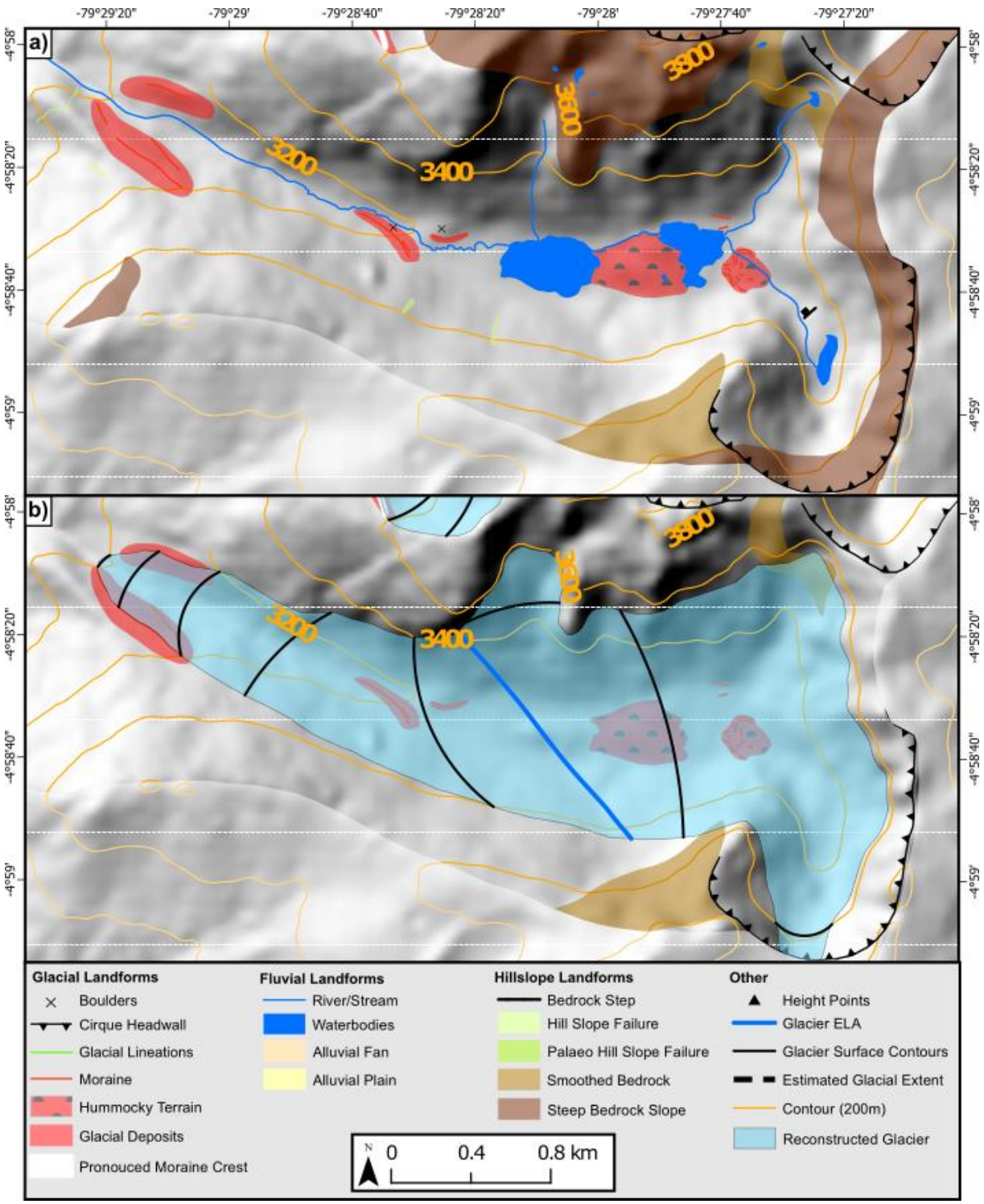

Figure 3.20: The Palo Blanco glacier #11 within the northern glacier valleys zone, corresponding with Figure 18b subset 2 with a) mapped geomorphology and b) the subsequent reconstructed glacier LLGM extent. Base map is a hillshade from the ALOS 30 m DEM.

These moraines are found at a range of elevations between 3,250-3,180 m asl respectively. These could indicate a thinning glacier front during deglaciation from the LLGM. Glacier ice in the valley just above these lateral moraines (to its north) could have flowed down and connected with the main valley glacier during the LLGM (we have mapped this here), but it may have been limited to or just to the edge of the main valley glacier contributing little ice to the general flow of the main glacier.

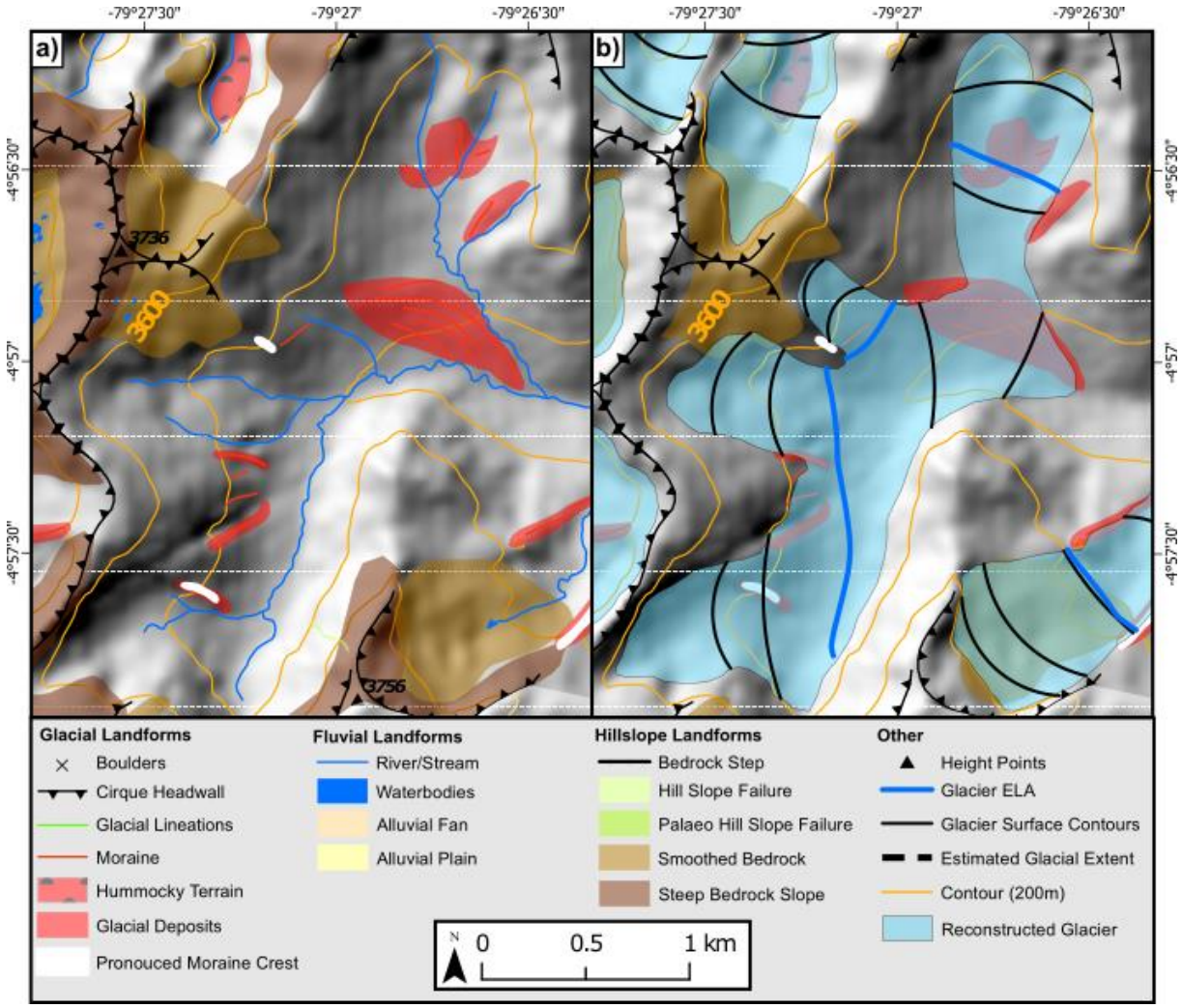

Figure 3.21: The Pablo glacier # within the northern glacier valleys zone, corresponding with Figure 18b subset 3 with a) mapped geomorphology and b) the subsequent reconstructed glacier LLGM extent. Base map is a hillshade from the ALOS 30 m DEM.

3.3.6. Regional overview of the geomorphology

An overarching overview of geomorphology for across the study area clearly shows that this region has been extensively glaciated in the past. We identified a number of moraines; mapping over 830 moraine fragments or singular prominent moraine features, 44 individual glacial cirques with floor elevations ranging from between ~3,150-3,600 m asl, 38 mapped glacial

lineations with lengths between ~23-103 m, 32 bedrock steps, a number of individual boulders within or on moraines, hill slope failures, smoothed bedrock surfaces, and hummocky terrain. All these features are used to evidence glacial activity and their extent within the Las Huaringas region. The furthest downvalley mapped moraines we assume represent the regions LLGM due to there being no discernible evidence further down valley. The presence of such erosive features (e.g., smoothed bedrock, overdeepenings) must represent at least extensive poly-thermal or warm based glaciers were active within the area during its regional LLGM. There are some valleys that did not incur any evidence of a terminal moraine (i.e., the Shimbe valley; section 3.3.1.) that may be due to extensive post-glacial reworking, that provides evidence for glaciers here to been deglaciated for some time after their LLGM.

The reconstructions of the palaeoglaciers here, from the geomorphology, represent primarily a cirque to valley glaciation system. This exemplified by the Shimbe valley (section 3.3.1.) the south-eastern region (section 3.3.3.) and the northern region (section 3.3.5.). There are potential regions that may have seen connected glaciers during their regional LLGM, for example on the eastern valley region (section 3.3.2.) and the western glacial cirques region (section 3.3.4.). Ice plateaus or ice caps are not uncommon in the tropical Andes, and there is the potential for glaciers here to have been a glacial plateau, but using only the geomorphological records here, we estimate a valley glaciation system.

3.3.7. ELA reconstructions and their spatial distribution

The reconstructed ELAs were derived from the reconstructed glacial ice extents using the AABR technique with a balance ratio of 1.75 ± 0.71 (Rea, 2009), ranged from 3,184 ± 27 m asl to 3,776 ± 33 m asl with a mean of 3,422 ± 30 m asl (Table 3.3). Across the tropical Andes these are some of the lowest ELAs to be reconstructed, primarily due to the evidence also being some of the lowest identified. However, the lowest identified ELAs being in the Merida Andes in Venezuela with an overall average reconstructed regional LLGM ELA being 3320 m asl (Stansell *et al.*, 2007). The reconstructed ELAs of glaciers without a confident determination of their terminal extent (e.g., Shimbe and Huancabamba 4 glaciers), may be lower or higher in elevation than that reported here. As expected, using higher and lower balance ratios give lower and higher ELAs respectively. Rea (2009) and Quesada-Román *et al.* (2020) suggest a higher balance ratio may be more accurate for conditions within the tropical Andes. As shown by the comparison of lower and higher balance ratios, in this case, the balance ratios have little effect on the reconstructed ELA elevations with variations of up to only ~20 m. This minimal difference does not affect temperature estimations much (~ ± 0.2°C). We therefore recommend

that similar studies should have confidence in using the global scenario (BR of 1.75) for locations which do not have detailed studies on their AABR determined for modern day ELA. Tropical glaciers have very little information on their BRs making a regional specific recommendation difficult. Although the global balance ratio produces little variance in results, the largest variance stems from accurate delineation of the past glacial extent. If ice limits are not accurate, they could have a large influence on local and regional climate interpretations.

Table 3.3: Results of the palaeo-ELA calculations (m asl) using the AABR method with different ratios.

		AABR ELA elevation (m asl)						
Glacier Name	**#**	**1.0**	**1.25**	**1.5**	**1.75⁺**	**2.0**	**2.25**	**2.5**
*Shimbe Glacier	1	3450	3450	3420	3420	3420	3390	3390
*Huancabamba 1	2	3376	3376	3376	3376	3376	3346	3346
Huancabamba 2	3	3470	3470	3470	3470	3440	3440	3440
Huancabamba 3	4	3630	3600	3600	3600	3600	3600	3600
Huancabamba 4	5	3241	3241	3241	3211	3211	3211	3211
Huancabamba 5	6	3421	3421	3421	3391	3391	3391	3391
Huancabamba 6	7	3404	3374	3374	3374	3374	3374	3374
*Negra Glacier	8	3680	3680	3680	3680	3650	3650	3650
Arrebiatadas Glacier	9	3586	3586	3556	3556	3556	3556	3556
el Rey Inca Glacier	10	3586	3586	3556	3556	3556	3556	3556
Palo Blanco 1	11	3416	3416	3416	3416	3386	3386	3386
Palo Blanco 2	12	3540	3510	3510	3510	3510	3510	3480
Palo Blanco 3	13	3450	3420	3420	3420	3390	3390	3390
Aranza 1	14	3374	3374	3374	3344	3344	3344	3344
Aranza 2	15	3521	3491	3491	3491	3491	3491	3491
Aranza 3	16	3531	3531	3531	3531	3531	3501	3501
Aranza 4	17	3348	3348	3348	3318	3318	3318	3318
Aranza 5	18	3421	3421	3421	3391	3391	3391	3391
Quebrada Los Rosarios 1	19	3396	3396	3396	3396	3396	3396	3366
Quebrada Los Rosarios 2	20	3347	3347	3317	3317	3317	3317	3317
Quebrada Los Rosarios 3	21	3342	3342	3312	3312	3312	3312	3312
Quebrada Los Rosarios 4	22	3309	3279	3279	3279	3279	3279	3279
Quebrada Los Rosarios 5	23	3214	3214	3184	3184	3184	3184	3184
Redondo de Zapalache 1	24	3439	3439	3439	3439	3439	3409	3409
Redondo de Zapalache 2	25	3384	3384	3384	3354	3354	3354	3354
Redondo de Zapalache 3	26	3417	3417	3417	3387	3387	3387	3387
Samaniego 1	27	3259	3259	3259	3259	3259	3259	3259
Samaniego 2	28	3467	3437	3437	3437	3437	3437	3437
Samaniego 3	29	3439	3439	3439	3409	3409	3409	3409
Mean		3430	3422	3420	3422	3418	3400	3398

*Maximum glacial extent was estimated by surrounding glacier terminus elevations
⁺Global average determined by Rea (2009) used for temperature change calculations

Within our ELA reconstruction estimates there is an east-to-west gradient in the spatial distribution within Las Huaringas (Figure 3.22a). On average, the ELAs from glaciers situated on the eastern side of the study region had a lower reconstructed ELA while glaciers to the west had a higher ELA. This may suggest that the glaciers on the east side of Las Huaringas received more precipitation than those on the west side during the LLGM, resulting in a lower ELA. Similar east-to-west gradients have been identified by Porter (2001) and Martini *et al.* (2017) in their ELA reconstruction studies across the tropical Andes and Cordillera Oriental. This gradient is similar to the present day subtropical climate patterns and the movement of moisture via the easterly trade winds and trans-Andean flow, from the Amazon basin to the eastern flanks of the Andean mountains **(**Espinoza *et al.*, 2020**)**. This brings an asymmetric precipitation pattern with increased rates in the east compared to the west **(**Kumar *et al.*, 2019**)**. A similar east-to-west gradient is seen for cirque floor elevations (Figure 3.22b). When compared with ELA elevations (Figure 3.22c), it could suggest that ELAs were lower in the east because the overall elevation is situated lower, but this could simply be because of increased maximum erosion at or below the ELA due to increased accumulation compared to the west, therefore lowering cirque floor elevations.

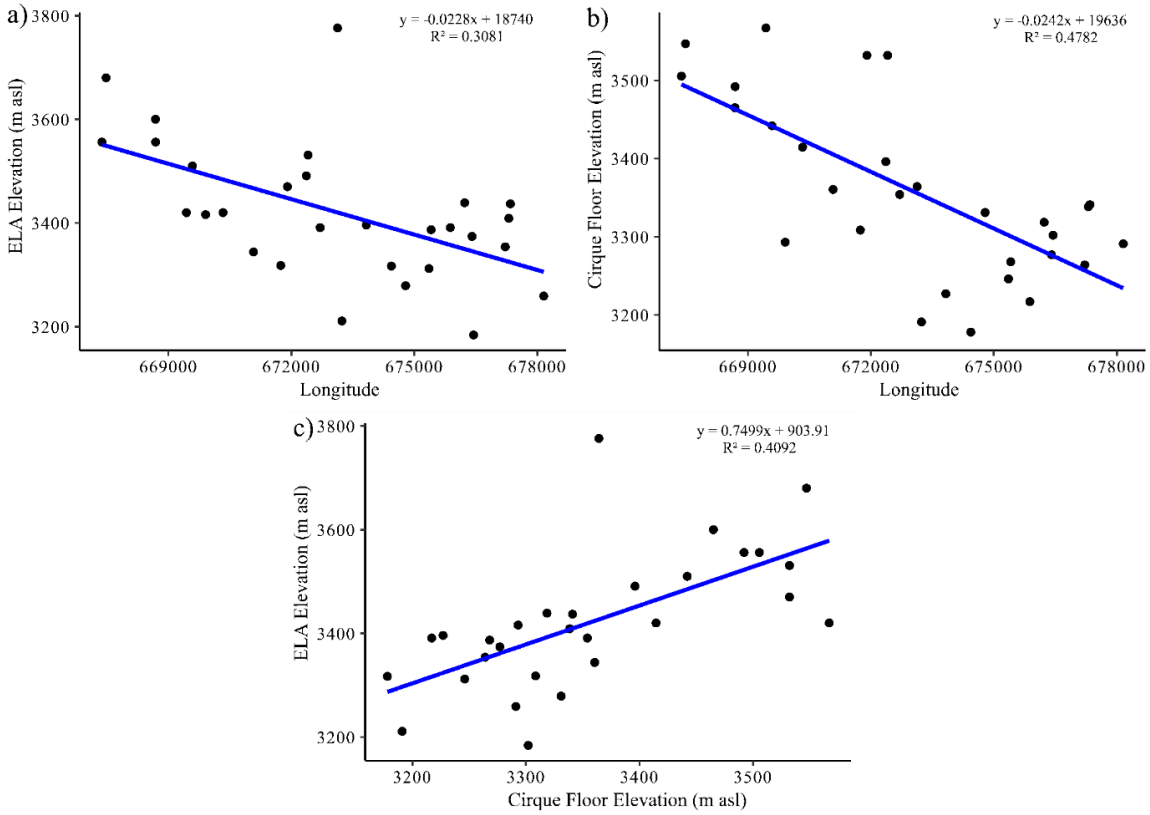

Figure 3.22: Elevations for a) reconstructed glacier ELAs and b) cirque floors against their locations longitudinally, and c) the ELA elevation and cirque floor elevation plotted against each other. All regressions are significant (p = < 0.01).

3.3.8. Palaeotemperature estimate and its comparison to surrounding studies

The reconstructed LLGM ELAs for the Las Huaringas region were used to estimate palaeotemperature. It is simplistic to assume that temperature alone would have changed since the regions LLGM to present, as precipitation would also have changed in response to temperature changes and atmospheric-circulatory system changes. Whilst we acknowledge the likely impact of precipitation changes on palaeo-glacier mass balance, being a key driver of tropical glaciations (Fyffe *et al.*, 2021), a simple palaeotemperature reconstruction can aid in understanding the potential climate the glaciers would have been present under.

The mean ΔELA change across Las Huaringas, from LLGM to present is 1,178 ± 10 m. This represents an average ΔT of -7.6 ± 0.2°C using an ATLR of 6.5°C/km. Lower and higher ATLR predictably result in lower and higher average ΔT, with 6.5°C and 8.9°C using ATLRs of 5.5°C/km and 7.5°C/km respectively. As mentioned previously, this only takes into account that ELA changes are only a function of temperature which is incorrect, as precipitation changes also causes ELA change, but this is a limitation of the method used here and the data available.

Our greatest estimate of temperature cooling (i.e., 8.9°C) is consistent with other palaeo-ELA temperature reconstructions within the tropical Andes (Table 2.1) (Rodbell, 1992; Mark *et al.*, 2005; Mark and Helmens, 2005; Ramage *et al.*, 2005; Smith *et al.*, 2005b; Bromley *et al.*, 2011a; Úbeda *et al.*, 2018). Temperature cooling estimates from valley based glaciers, are considerably lower than those reported by our study, with Ramage *et al.* (2005) estimating a cooling of 2.5°C in Lake Junín, and Smith *et al.* (2005b) estimating a cooling between 2°C and 4°C for the Lake Junín and the Milluni and Zongo valleys. This difference in results may be due to the higher elevation of those study areas, with the maximum elevation in Lake Junín and the Milluni and Zongo valleys being ~4,600 m asl and ~5,600 m asl respectively. This would require less cooling to initiate glaciation compared to lower elevation locations, such as ours. Thus, greater cooling would be needed, if it is assumed only temperature changed, for extensive glaciation within Las Huaringas, due to the massif being below 4,000 m in elevation. However, if precipitation and temperature changed in tandem, then a smaller temperature change may be required (e.g., if the rate of precipitation was higher during the LLGM). Further, the location where the modern-day snow line was taken form (~8°S) which may be incorrect as the snowline could be higher. If the snowline is higher, this would lead to more cooling required to reconstruct the LLGM ELA.

There are very few studies that produce LLGM temperature estimates from low elevation locations, especially in or near our study area. This makes comparisons difficult, as study sites

that are distant from Las Huaringas are likely to be affected by different climate influences. Our higher temperature cooling estimate is closer to estimates from the Merida Andes with a lowest estimated cooling of 6.4°C (Stansell *et al.*, 2007), the High Plain of Bogotá with a cooling of 7.6°C (Mark and Helmens, 2005), and modelled temperature changes across the Bolivian and Perúvian Andes from the Junín Valley, Cordillera Vilcanota and Laguna Kollpa Kkota, where cooling of 5°C to 9°C has been reported (Klein *et al.*, 1999). The two former studies, though higher in latitude (i.e., Venezuela and Colombia), did reconstruct similar temperature cooling from locations with a similar elevation (4,500 m asl) to Las Huaringas. Klein *et al.* (1999) estimates are from across the Bolivian and Perúvian Andes but are from higher elevation locations above 5,000 m asl. Though this is higher in elevation than our area, the temperature cooling estimates are similar. Estimates from other methods are also consistent with our results of a substantial cooling during the LLGM. Analysis of ice-cores from the Huascarán and Samaja ice-caps (Thompson *et al.*, 1995; Thompson *et al.*, 1998; Thompson *et al.*, 2006), suggests potential cooling of between 5°C to 8°C at the LLGM. Our two higher estimates from the ATLR (6.5°C/km and 7.5°C/km) fall within their temperature range.

3.4. Chapter summary

This chapter has demonstrated through detailed mapping of the first evidence for glaciation within the Las Huaringas region of northern Perú. While palaeoglacial reconstructions and subsequent ELA reconstructions have detailed temperature cooling that can be used to test against within the numerical modelling in this thesis (Chapters 5 and 6). This chapter has shown:

- There was the presence of extensive highly erosive warm-, or polythermal-based ice masses, during the regions LLGM capable of generating highly eroded glacial valleys with overdeepenings now lake filled, and glacial smooth bedrock.
- Overall, from the reconstruction, a valley type glaciation is determined from the geomorphological evidence. These include valley glaciers extending from cirques, with some potentially interconnected glacial systems, seen within the WG, and ice potentially connecting over topographical dips in the valley geometry between the LS and EG region.
- Another idea from the presented evidence is that it may also be suggestive of an ice plateau, with an overall interconnected ice system along the high topography. However, here is reconstructed a valley type of glacial system due to the presence of little up valley

evidence that provide evidence of a fully glaciated valley top. The presence of little to no up-valley evidence may be due to their preclusion from post-glacial processes (i.e., fluvial processes), or cold based glaciers being present within the region.

- Palaeotemperatures from ELA reconstructions are between of between 6.5°C and 8.8°C cooler than present were determined. These are within the coolest of other valley palaeoglaciological reconstruction based palaeotemperature estimates.
- Evidence for an ELA asymmetry of east (lowest to east, highest in the west), agrees with the present-day flow of moisture and climate patterns, suggesting that the broader climate circulatory systems in the region may not have been very different at the LLGM.
- The exact timing of this glaciation is unknown. However most extensive moraines are assumed to be of LLGM-age but shall be sampled (Chapter 4) and dated using cosmogenic nuclide dating.
- Moraines set behind the most extensive extents mapped are hypothesized to be younger than the LLGM and are likely late-glacial or early-Holocene in nature. These too shall be sampled (Chapter 4) and dated using cosmogenic nuclide dating while being tested for their potential period of deposition within the numerical modelling (Chapter 6).
- The evidence found within the Las Huaringas region strongly suggests that other relatively low elevation areas of northern Perú, and the surrounding areas of the tropical Andes, were potentially glaciated during the LLGM and warrant further investigation.

Chapter 4. Fieldwork conducted within the Lagunas de Las Huaringas

4.1. Introduction

Remote geomorphological mapping is a useful tool for understanding just what palaeoglacial evidence is present within a particular study region. As shown by Chapter 3, this mapped evidence can then be used in conjunction with other remotely sensed information to provide first-order estimates on potential palaeoclimate. This, however, can only be used with hypothesised timings of when the features were generated. Due to this, the evidence from remotely sensed sources can potentially be misidentified or precluded from the mapping. This can lead to an over-representation of evidence from advances due to their size and ease of identification, while smaller potential standstill or readvances during retreat phases being harder to identify.

To in-fill data gaps mentioned above from the remote mapping, in field study of the region is needed. This allows the collection of in-field geomorphological mapping that can enable to identification of smaller scale features, along with any features that were precluded within the remote data, either by vegetation or the angle which the data was collected (i.e., shadows). In-field investigations can also allow the collection of TCN samples to facilitate the dating of important features. This will allow features to be dated that can place the first-order estimates on palaeoclimate in relation to a time-period (i.e., the regions LLGM or older/younger).

Field work was conducted in the Las Huaringas study area in January 2023. The overarching goals were: (i) recovery of samples for terrestrial cosmogenic nuclide (TCN) dating of boulders and a sediment core for radiocarbon dating; and (ii) collection of GPS data to compare captured ground-based data to the remotely sensed data. This evaluation of, and enhancement to, the geomorphic mapping, and the collection of samples for dating, can aid in constraining numerical modelling (Chapter 6). This will enable the reconstruction of the extent and dynamics of last glacial ice masses in Las Huaringas.

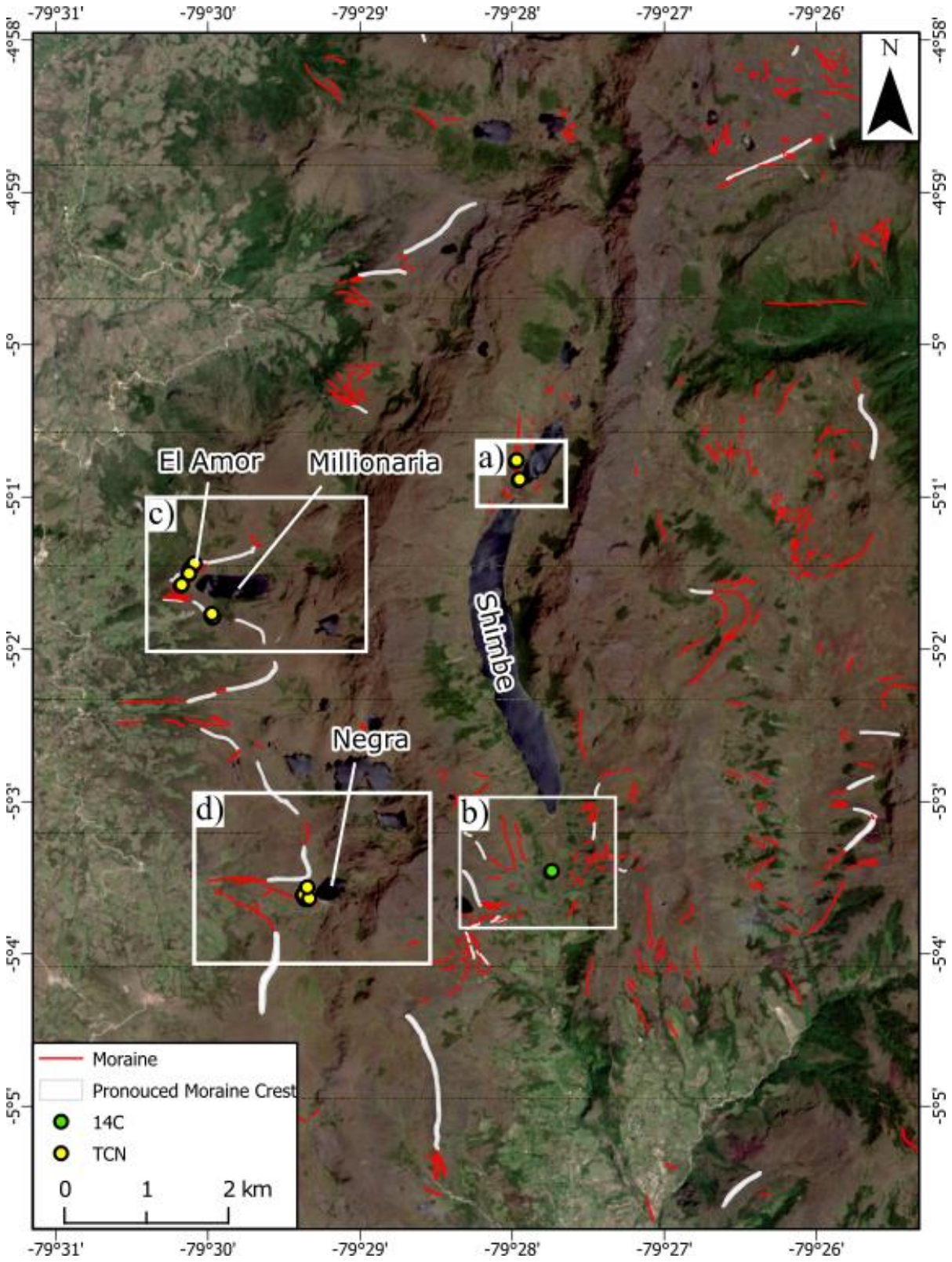

Figure 4.1: Field site (location in Figure 1.1) geomorphological map of Laguna de Las Huaringas; originally from Figure 3.2. Location boxes indicate extents of figures for geomorphological mapping (Lee *et al.*, 2022; Chapter 3), and TCN collection, a) Laguna Shimbe (Figure 4.2), b) southern end of Laguna Shimbe where peat core was taken (Figure 4.6), c) Laguna Millionaria and Laguna El Amor (Figure 4.8), d) Laguna Negra (Figure 4.10). Base image is Sentinel-2B imagery.

Fieldwork within this thesis study was conducted in January 2023. Locations targeted for TCN sample collection within the study site (Figure 4.1) were the Laguna Shimbe valley (Figure 4.1a; Section 4.3.1. and 4.3.2.), the Laguna Millionaria and Laguna El Amor complex (Figure 4.1c; Section 4.3.3. and 4.3.4.), and the Laguna Negra complex (Figure 4.1d; Section 4.3.4. and 4.3.5.). Laguna Shimbe was also targeted for the collection of a peat sediment core for obtaining ^{14}C dates (Figure 4.1b Section 4.3.2.)

The objectives of the fieldwork were to:

- Collect field data to assess the accuracy of the remotely mapped geomorphology and add any palaeoglacial geomorphological features not identified in previous mapping (Chapter 3).
- Obtain samples for future terrestrial cosmogenic nuclide (TCN) dating from boulders/erratics on targeted moraines, and ^{14}C dating from a peat bog identified in front of Laguna Shimbe.
- Characterise the geomorphology of the study area to constrain glacial modelling (Chapter 5 and Chapter 6).

Despite numerous challenges, the fieldwork was completed successfully with 12 boulders sampled for TCN dating, and 2 overlapping peat cores recovered. After the fieldwork, a successful application was made to the Natural Environment Research Council's (NERC) National Environmental Isotope Facility (NEIF) to enable analysis of the collected samples. However, due to timeline constraints, the processing of the samples could not be achieved during the timeframe of the PhD funding. As a result, age estimates derived from dated samples will not be reported within this PhD thesis.

4.2. Methods

4.2.1. Field-based geomorphological evidence

While the remote sensing-derived geomorphology (Lee *et al.*, 2022; Chapter 3) provided an overall understanding of the former glacial extent within the Las Huaringas region, many features were still difficult to definitively identify and map, either due to the resolution (e.g., Landsat 8 30 m/15 m pan), or due to the quality (e.g., PlanetScope 5 m) of the imagery available (Chapter 3). The infield geomorphological mapping focused on three regions (Figure 4.1), chosen for a combination of scientific and practical logistic reasons.

Field observations are only reported from identifiable moraine features within the visited field locations (seen in Figure 4.1); other locations outside of the visited field sites are not included

in this chapter. Any moraine features not identified during the remotely sensed mapping (Chapter 3), were mapped, along their ridge, with GPS points using either a Garmin Etrex 10 or Garmin Etrex 22. Comparing the remote mapping with infield evidence, we were able to compare and assess the accuracy of the mapping (Otto and Smith, 2013; Chandler *et al.*, 2018).

4.2.2. TCN and core collection

The chosen field sites (Lagune Shimbe, Laguna Millionaria/Lagune El Amor, Lagune Negra) were targeted for TCN sample collection, while the southern end of Laguna Shimbe (Figure 4.1b) was targeted for core collection for ^{14}C dating. Moraines selected for TCN sampling were chosen due to both their glaciological significance and infield practicalities. Two samples were collected from the largest and most prominent moraines within Laguna Millionaria and Lagune El Amor, due to their interpretation being the most extensive of glaciation within the western region. These are to provide a timing of when glaciers were at their most maximal extent. Two samples were also taken from moraines within the confines of these prominent moraines, these can then provide further confirmation on the relative age of the prominent moraines but provide a timing of when glaciers here were retreating to their cirques. Four samples were collected from moraines at the immediate downvalley end of Laguna Negra (Figure 4.1a). While these moraines are up-valley from evidence of most extensive glaciation, they are important for understanding the retreat of glaciers within the western cirques from their most extensive advance, these either being standstill events or minor readvances during an overall retreat phase. Two samples for dating were collected from Laguna Shimbe. Because this valley is long and deep valley with two large lakes occupying overdeepenings, it provides evidence of extensive and either sustained, or multiple phases of, glaciation in the region. While there are no Shimbe Valley moraines downvalley that may determine its most extensive glaciation, moraines up-valley were selected to provide detail on the timing of deglaciation in the valley. The small number of samples collected was due to the pragmatism of available time and resources within the field. Locations in the north and east of the Las Huaringas study area that were previously mapped (see Lee *et al.*, 2022; Chapter 3), were not accessed or sampled in the field season. This was due to their relative inaccessibility and time constraints of the fieldwork.

Twelve samples were collected (Table 4.1) using established TCN collection procedures (Dunai, 2010). Samples were taken from large boulders, that were assumed to have been transported by glacial action, and situated on, or very close to, identified moraines of interest. Samples comprised of the upper 5 cm of the boulder surface, collected using an angle grinder, and hammer and chisel. All boulders selected were studied to understand their post depositional

history, i.e., if they had moved since being deposited, which would lead to younger exposure ages. While it would be impossible to conclusively determine that selected boulders have had no, or very little, vegetation cover, it is assumed that the selected boulders had minimal vegetation cover and have not been covered by any vegetation for a large proportion of its time since placement. This is due to in field inspection of the boulder location not incurring extensive vegetation cover, or any evidence of past vegetation cover (i.e., tree stumps etc.) that could have been removed by past human activity. There was no geomorphological evidence to suggest that there has been any post-depositional exhumation of the selected boulders, nor any post-depositional erosion. All surfaces had their shielding factors from surrounding valley sides determined using a compass-clinometer and the CRONUS-Earth online calculator, while the thickness was measured using electronic callipers.

Table 4.1: Summary table of cosmogenic nuclide dating samples collected in the Laguna de Las Huaringas. The shielding factor was calculated with the CRONUS-Earth online calculator (Balco *et al.*, 2008). Sampled boulder images are shown in Figure 4.2.

	Sample name	Location coordinates	Elevation (m)	Sample block size (L x W x H cm)	Orientation / Dip (º)	Sample type	Sample thickness (cm)	Shielding factor
				Laguna Shimbe				
a)	23-LS-1	S 05º 00.891 W 079º 27.958	3235	100 x 110 x 140	324/24	Erratic	1.3	0.941469
b)	23-LS-2	S 05º 00.766 W 079º 27.977	3249	100 x 065 x 115	330/13	Erratic	2.0	0.965008
				Laguna Millionaria				
c)	23-LM-1	S 05º 01.794 W 079º 29.970	3473	150 x 095 x 113	126/26	Erratic	4.4	0.960122
d)	23-LM-2	S 05º 01.774 W 079º 29.981	3465	132 x 112 x 077	137/27	Erratic	1.5	0.983523
e)	23-LM-3	S 05º 01.583 W 079º 30.179	3377	312 x 280 x 202	184/30	Erratic	1.2	0.956312
				Laguna El Amor				
f)	23-LEA-1	S 05º 01.474 W 079º 30.119	3428	183 x 065 x 085	049/13	Erratic	1.1	0.996564
g)	23-LEA-2	S 05º 01.442 W 079º 30.094	3438	570 x 250 x 240	332/12	Erratic	5.0	0.993574
h)	23-LEA-3	S 05º 01.509 W 079º 30.131	3414	165 x 085 x 147	013/28	Erratic	6.0	0.945810
				Laguna Negra				
i)	23-LNG-1	S 05º 03.641 W 079º 29.360	3568	275 x 204 x 046	219/01	Erratic	3.9	0.956562
j)	23-LNG-2	S 05º 03.617 W 079º 29.377	3565	135 x 075 x 110	009/19	Erratic	2.5	0.984484
k)	23-LNG-3	S 05º 03.642 W 079º 29.341	3572	057 x 045 x 040	310/25	Erratic	4.6	0.968829
l)	23-LNG-4	S 05º 03.569 W 079º 29.353	3613	290 x 036 x 115	224/42	Erratic	2.1	0.919645

The sediment (primarily peat) cores were acquired after a peat depth survey. This was carried out to understand where the deepest area within the peat bog, south of Laguna Shimbe was, to acquire the longest core possible. Once the deepest point was determined, the location was cored with a 50 cm peat sampler (Russian corer). A second core was acquired alongside the first but was offset by 25 cm to capture sections of the core that would have become disturbed

due to 5 cm of the corer tip pushing peat to the side. Acquired cores were packaged to maintain moisture and integrity and were transferred to cold storage, under Animal and Plant Health Agency (APHA) storage protocols, within Newcastle University. The first core had a first-order study, using X-ray Fluorescence (XRF) to understand the element composition through the core, with a resolution of 1 cm. This was conducted using a Vanta™ handheld XRF analyser.

Figure 4.2: Field photos of boulders sampled within the visited field sites; a-b) – Laguna Shimbe, c-e) – Laguna Millionaria, f-h) – Laguna El Amor, i-l) – Laguna Negra. Images from Andy Henderson.

4.3. Field areas

4.3.1. Laguna Shimbe – field observations and geomorphological mapping

The Shimbe valley (Figure 4.3) is relatively flat with an average valley floor elevation of 3,230 m asl. It is constrained by steep sided valley walls (~30°) rising to a maximum elevation of

3,939 m asl at the end of the valley. Laguna Shimbe, occupying a glacial overdeepening, is estimated to be the deepest (~30 m depth) and the largest lake (1.5 km^2) within the Shimbe valley and the wider study region. North of Laguna Shimbe are three smaller lakes. The primary lake is Laguna Shimbe 2 (0.2 km^2), the other two are unnamed and are located near the headwall. Geomorphic mapping of the Laguna Shimbe study site (Figure 3.4) (Lee *et al.*, 2022), primarily comprised mapping of lateral moraines parallel to, and further up valley than, Laguna Shimbe. Other mapped glacial moraines were located on the valley walls and are the product of smaller tributary cirque glaciers. These glaciers would likely have fed, and coalesced with, the main Shimbe valley glacier during its maximum glacier extent.

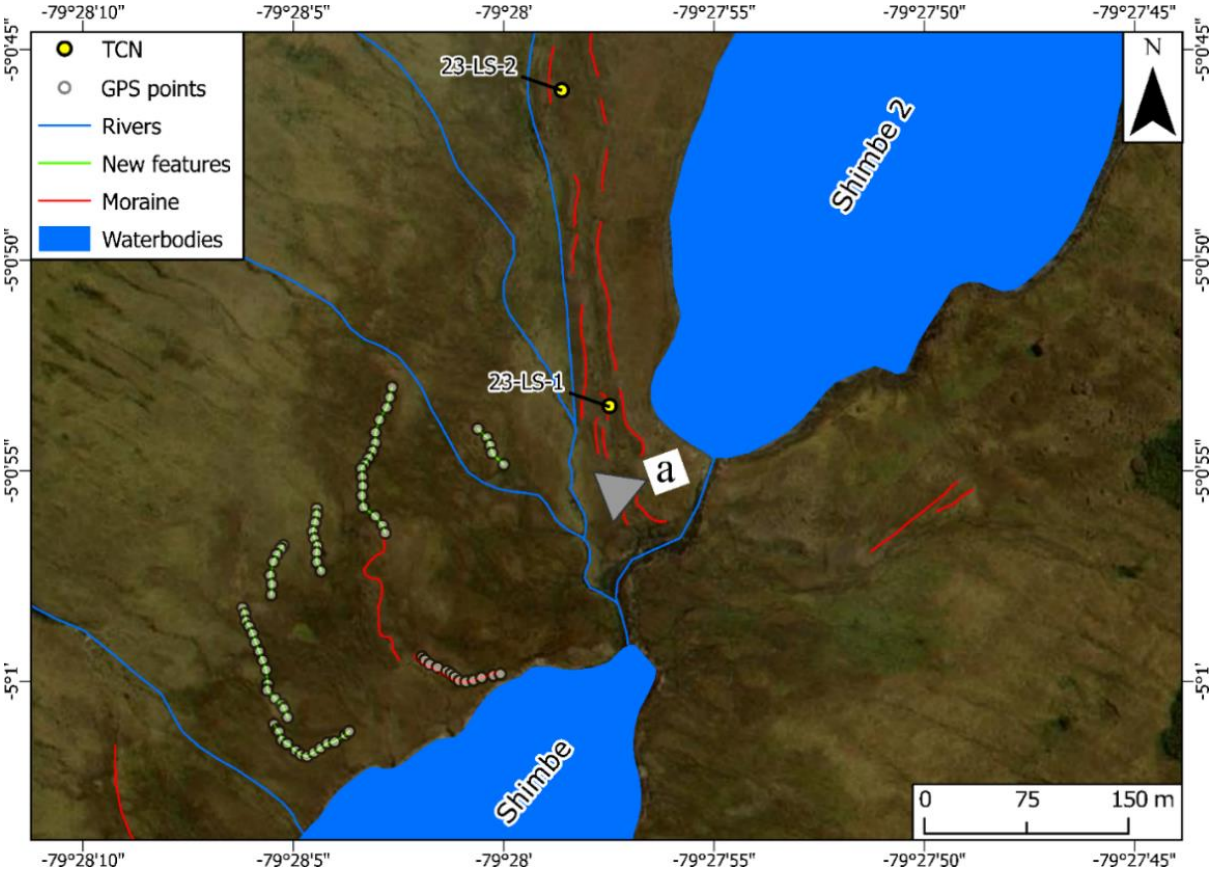

Figure 4.3: A geomorphological map to the northern end of Laguna Shimbe with superimposed GPS points from infield confirmation. Figure location corresponds to Figure 4.1a. 'a' denotes the location Figure 4.7 was taken with approximate direction represented by the triangle with the flat side point away from 'a'. New features are additional moraines in between Shimbe 2 and Shimbe.

Downvalley of Lagune Shimbe, there is a lack of identifiable palaeoglacial geomorphological features that could be mapped remotely (see Figure 3.4 for lack of geomorphology). However, the lack of apparent evidence does not completely rule out glacial advances beyond Laguna Shimbe. An absence of palaeoglacial geomorphological evidence could be due to the imprint of post-glacial processes, such as fluvial and periglacial processes eroding evidence. Due to the

elevation of the valley floor, around 3,230 m, and the presence of extensively eroded overdeepenings that are now lake filled (Shimbe and Shimbe 2), it is highly likely that the valley was extensively glaciated during either the regional LLGM, and/or by pre-LLGM glaciation.

Field observations provide potential support for a maximum extent of glacial ice that would have occupied the Shimbe Valley. A large lateral linear feature was identified along the eastern edge of the valley (Figure 4.4). This is seen by a flatter profile on the valley wall, with a region of increased slope below that slopes downward into the valley floor further downvalley from 3,360 to 3,330 m asl (Figure 4.5) when mapped onto a DEM. This feature is interpreted as a potential ice marginal feature, where the glacier ice was in contact with the valley side. A similar feature, however, was not apparent on the western edge of the valley, but this could have been removed by post-glacial processes such a mass movement activity.

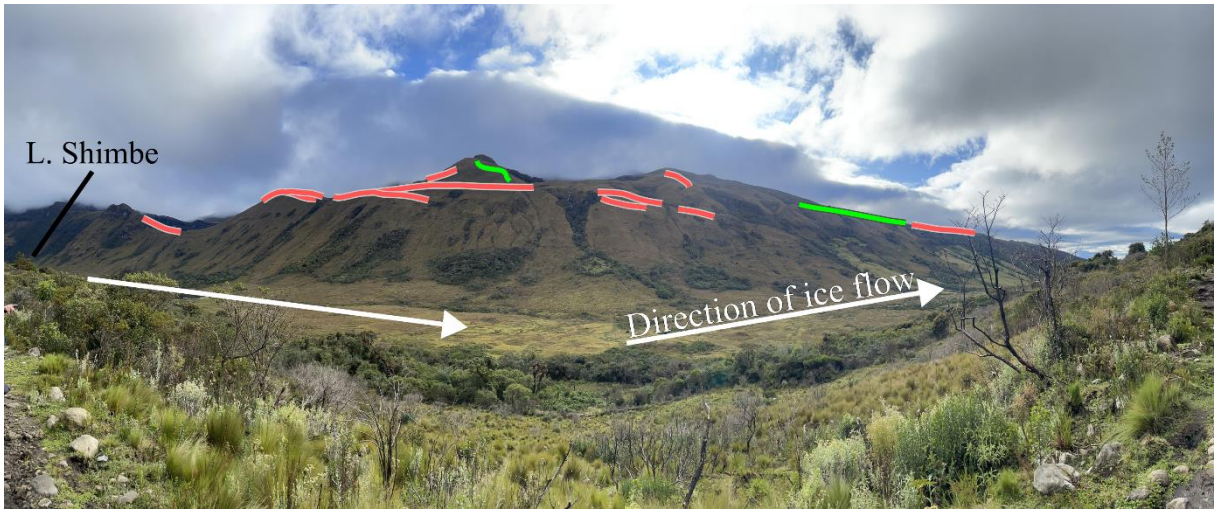

Figure 4.4: Panoramic image taken from the western valley wall of the Shimbe Valley, looking towards the eastern valley wall, just south of Laguna Shimbe (left of photo). Red lines denote remotely mapped geomorphic evidence while green lines denote new geomorphic features identified in the field. White arrows denote direction of ice flow.

Based on these field observations, additional inspection of the 30 m ALOS DEM hill shade (Figure 4.5a), and elevation profiles (Figure 4.5c & d), confirms a flatter surface (12°) ~100 m from the valley floor up the eastern wall before an increased slope (30°) thereafter. This lateral linear feature is also identifiable within the remotely sensed imagery, detected down valley by 2 km (Figure 4.5b). A connection to another lateral glacial feature further up-valley was not possible based on the remotely sensed pre-fieldwork geomorphic mapping. However, combining the field observations with the remote sensing mapping it is clear that the up-valley lateral linear features potentially connect to a further downvalley feature. This would extend its length to 4.4 km, however there is no geomorphic evidence that connects the features. It is plausible that this feature represents the regions LLGM extent of the glacier that filled the

Shimbe valley. However, further research (e.g., detailed field mapping, TCN dating etc.) would be required to test this hypothesis.

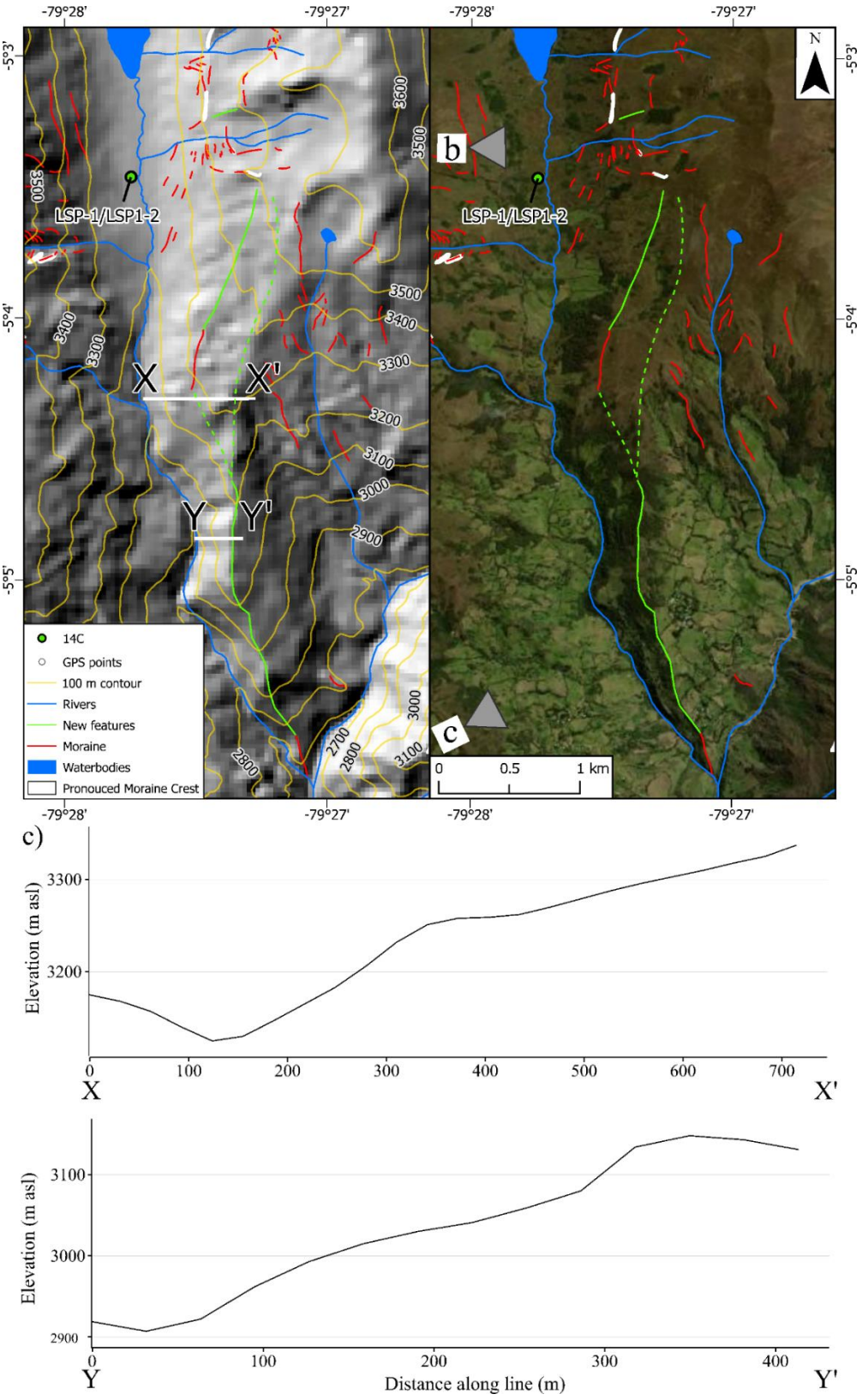

1870

Figure 4.5: Remotely sensed a) 30 m ALOS DEM hillshade (azimuth = 315º, altitude = 45) with contours of elevation in m asl, and b) Maxar imagery, of the downvalley section of the Shimbe valley showing the lateral linear feature on the east side of the valley, and a potential

connection to previously mapped up-valley geomorphology (connected by dotted green line for reference). c) Elevation profiles from the 30 m ALOS DEM of two locations detailing flatter surface indicating the features elevation. ‘b’ denotes direction and location Figure 4.4 was taken, and ‘c’ is off map, but shows relative location and direction for Figure 4.6.

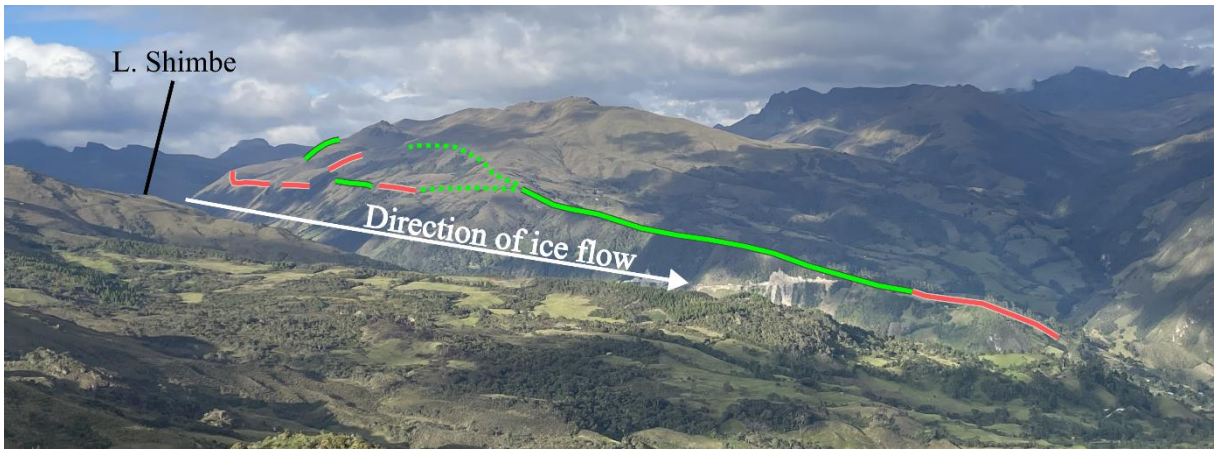

Figure 4.6: Photograph of the Shimbe valley taken further downvalley from Figure 4.4 facing northeast, L. Shimbe locations indicated to give indication of location. This shows how the identified lateral linear feature may extend and connect to geomorphic features further down valley. The dotted green lines indicate a gap in how the feature may connect to up-valley landforms. The white arrow indicates direction of ice flow.

The positions of the moraines located within the Laguna Shimbe valley, between the main lake of Laguna Shimbe, and the secondary lake to its north, Laguna Shimbe 2 were confirmed with GPS (Figure 4.3) In-field observations (Figure 4.7), led to the recognition of previously unidentified glacial moraines, along with a potential moraine drift limit (break in slope in the background), while an already mapped moraine was confirmed and its mapping refined (Figure 4.3). These morainic features are relatively subtle, between 1-2 m in height. This made them difficult to identify within the remote imagery, and from coarse-resolution DEMs.

Figure 4.7: A panoramic photo (view is approximately from the west side looking east) of the Shimbe valley, between Laguna Shimbe (downvalley to the left/south) and the Laguna Shimbe 2 (up-valley, off the image to the right/north). Red lines identify moraines that have already

been mapped via remote methods. Green lines identify new moraines mapped in the field and located using a handheld GPS. Moraines in this image are generally between the height of 1 to 2 m.

The updated map of the glacial geomorphology between Laguna Shimbe and Shimbe 2 (Figure 4.2), shows a number of small glacial moraines in close proximity to each other (i.e., 50-200 m apart). These moraines could be the result of: (i) multiple advances from subsequent cool periods after the most extensive LLGM glaciation, or (ii) multiple standstill events in response to a locally fluctuating ice margin. Either interpretation could be valid, and testing would require dating of the moraines. If dated as immediately after the regional LLGM, the moraines could be evidence of the deglaciation phase with a fluctuating ice margin. However, if dated to near the YD or ACR periods, the hypothesis that these moraines were due to readvance could be valid. This zone of multiple moraines, with very little evidence of moraines both up- and downvalley of them may be due to ice retreating out of the Laguna Shimbe overdeepening and being pinned between the two lakes (overdeepened terrain).

4.3.2. Lagune Shimbe – collected TCN and core samples

Two TCN samples were collected in the Shimbe valley (23-LS-1 and 23-LS-2; Figure 4.2a & b) (Figure 4.3). These were obtained from erratic boulders situated on moraines located in between the Laguna Shimbe (lower) and the Laguna Shimbe 2 (upper) lakes. These boulders, and the moraines they are situated on, were selected as they have the potential to provide an understanding of the timing of post-LLGM advances within the region. This is because they are located up valley of the proposed LLGM maximum limit (Chapter 3; Figure 3.3) (Lee *et al.*, 2022). These moraines could represent late glacial (e.g., YD, ACR), or early Holocene glacial advances. If these moraines were dated as being post-LLGM, they would provide confidence that during the LLGM glaciers advanced further down valley beyond the confines of the Laguna Shimbe over deepening.

Two peat cores (LSP-1 and LSP-2) were acquired 600 m south of Lagune Shimbe from the thickest measured peat depth (2.83 m) (Figure 4.8). This was collected following a peat depth survey (Figure 4.9). It is not clear if this represents the base of the peat, or the deepest locality, due to the limit constraints on the fieldwork however using the peat depth measuring sticks, we were unable to push any further past the measured depth. If this depth is the deepest section within the peat, collecting samples for ^{14}C dating of the base would provide a minimum limit

on the timing of deglaciation in the study area, providing an indication of the timing of maximum glaciation in the Shimbe valley were no terminal moraines exist.

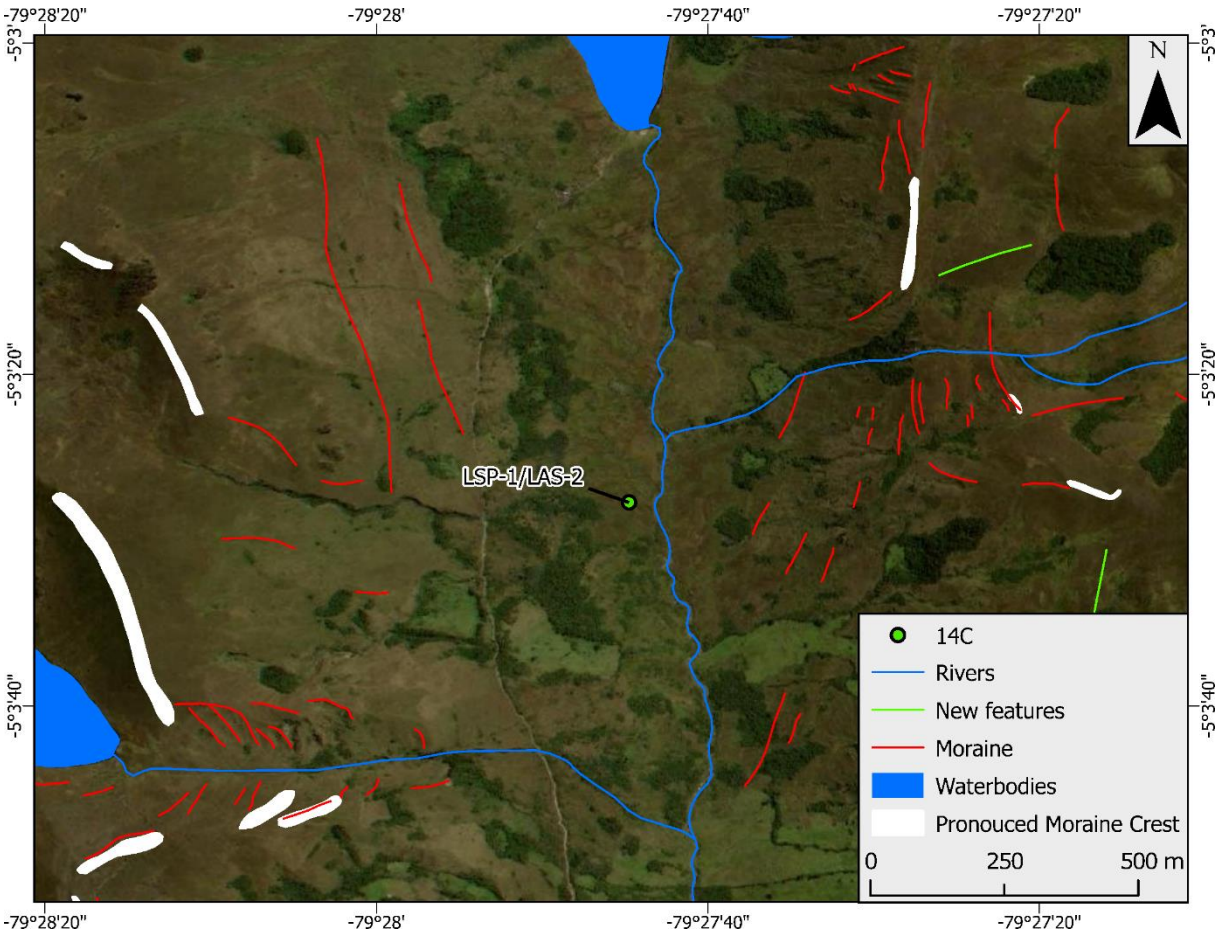

1930

Figure 4.8: Location of peat core LSP-1 and LSP-2, taken from the southern end of Laguna Shimbe at the deepest area within the peat (2.83 m). Figure location corresponds to Figure 4.1b). Green lines are newly mapped moraines identified in the field.

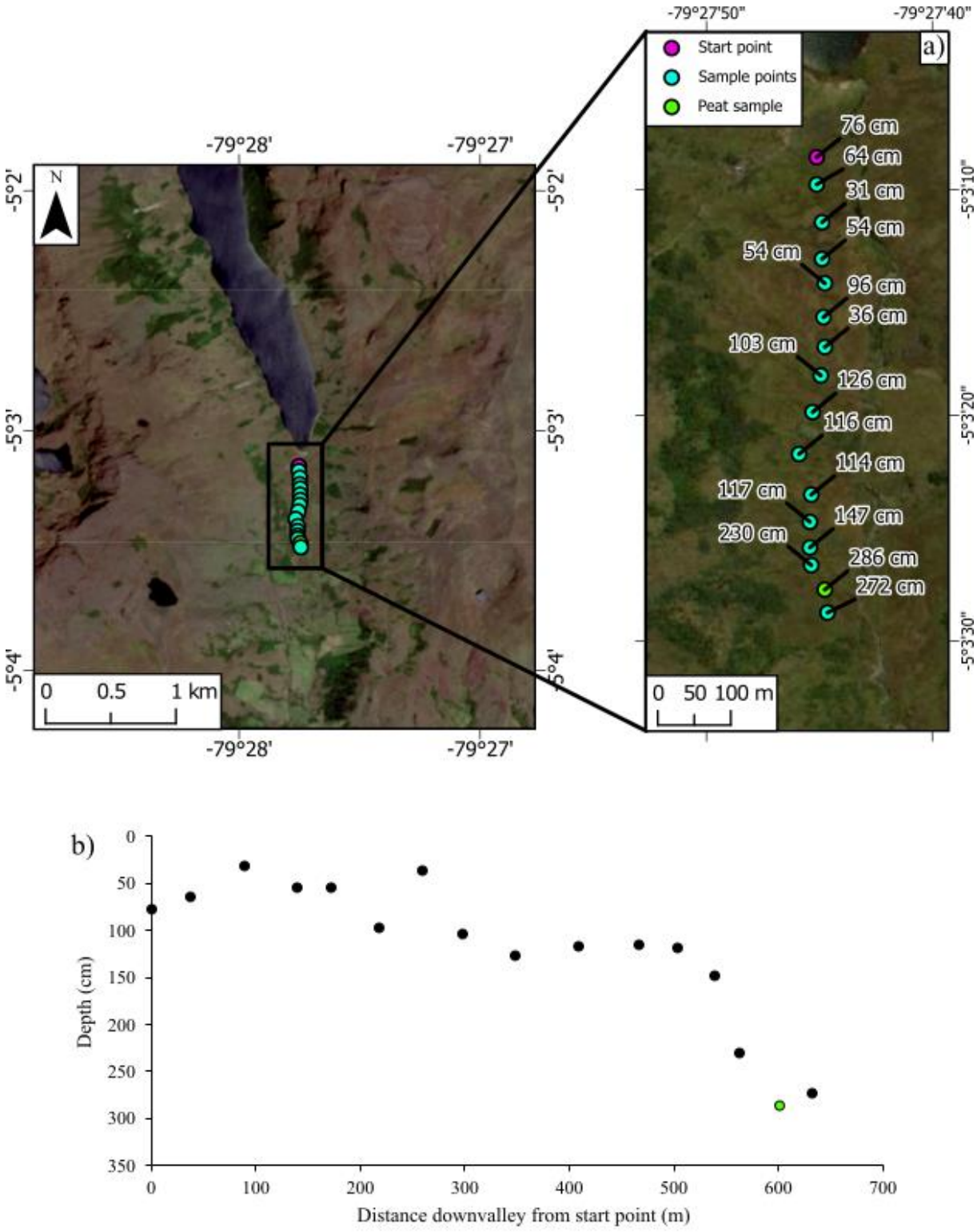

Figure 4.9: From the southern end of Laguna Shimbe, two peat cores were collected from the deepest point along the peat depth survey (286 cm), a) details the points along the valley floor and depth where the peat survey was conducted, and b) detailing the distance downvalley from the start point (pink circle in a) the collected depths..

The deepest section of the core collected was 286 cm when recovered. However, during transportation and storage, prior to any analysis, the final core length 'expanded' from 26 cm to 50 cm due to either gas expansion or relaxation of the peat, thus description and analysis is

reported here as between 0-300 cm (length of samples at analysis) rather than 0-286 cm (length of samples at time of recovery). The results described here are not impacted by this expansion, however future dating using ^{14}C will need to take this into account when incorporating an age depth model from the dates. The sediment sequence from the two overlapping cores comprises the following (Figure 4.10): (i) the base of the core between 300-220 cm is peat; (ii) Between 220-167 cm, are clays within fine peat ; up core there a gradual transition from more clay-dominated sediment to more light peat-dominant sediment; (iii) 167-98 cm depth is characterised by a dark brown peat with plant macrofossils interspersed within it, and fibrous material throughout; (iv) From 98-40 cm, the colour of the peat becomes lighter brown than deeper in the core, the texture of the peat is coarser, and included macro plant fossils become more abundant; (v) From 40-3 cm, the colour of the peat is more lighter brown and there is much more coarser peat with the continuation of plant macro fossils and roots from the above vegetation and occasional geological material (grains of rock).

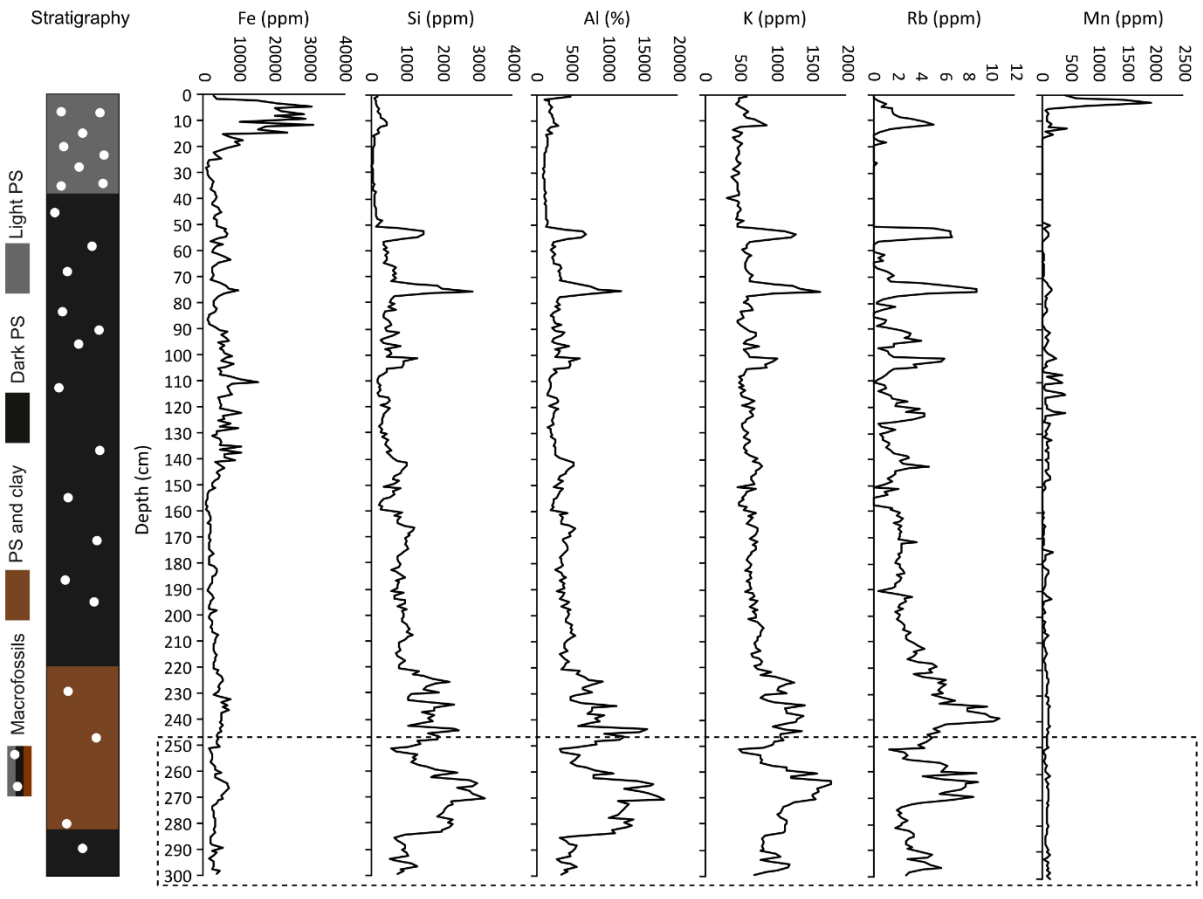

Figure 4.10: Shimbe valley peat core (LSP-1). Location of extraction shown in Figure 4.8 (green dot), with its stratigraphy (PS = Peat Sediment) and select XRF element concentrations throughout the core at 1 cm analysis increments. Depths are 0-300 cm due to the bottom core (LSP-1-DrF-2-2.8 m), shown by the dashed area, expanding post removal by 20 cm.

4.3.3. Laguna Millionaria and Laguna El Amor – field observations and geomorphological mapping

The Laguna Millionaria study site (Figure 4.11) comprises a lake enclosed by a series of large (up to 75 m in height) prominent moraines (Figure 4.12). The most prominent moraine extends up-valley from the lake front of Millionaria (right side of Figure 4.13), to just before the valley headwall. The moraine ranges in elevations between 3,577 m asl (left side of Figure 4.12), to 3845 m at the steep headwall to the east of Laguna Millionaria. The prominent moraines on the south (Figure 4.12) and north (Figure 4.13) sides of the valley are assumed to delimit the regions LLGM advance, due to their size and extent within the valley, but are currently undated.

Smaller moraines (1 m height) within the confines of the prominent Lagune Millionaria moraines are found at elevations between 3,360 – 3,410 m asl and could be recessional or readvance moraines post-dating LLGM glaciation. Beyond the prominent moraines identified, there are few clearly identifiable geomorphological features that can be attributed to glaciation. While the Lagune Millionaria moraines may be LLGM, they could also represent older glacial advances (e.g., MIS 3). Given the large overdeepening, now occupied by Laguna Millionaria (Figure 4.9), it is likely that this valley has seen multiple glaciations prior to the LLGM.

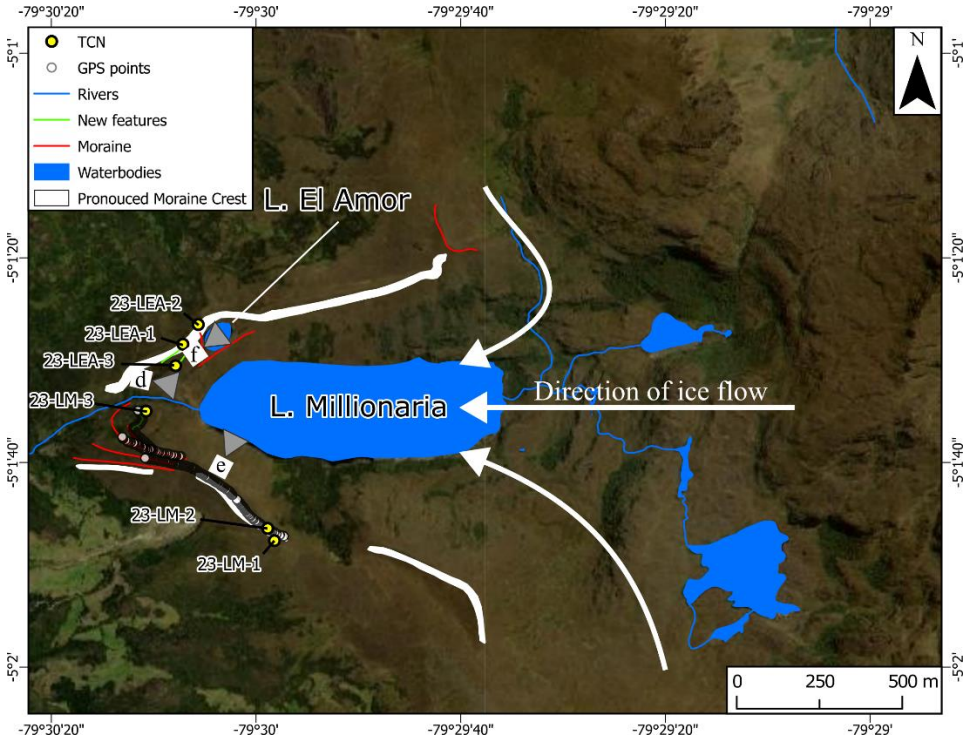

Figure 4.11: Remotely mapped palaeoglacial geomorphology to the terminal end of Laguna Millionaria, along with Laguna El Amor, with superimposed GPS points from infield confirmation. Figure location corresponds to Figure 4.1c. White arrow indicates the direction of ice flow reconstructed from the geomorphological record. 'd', 'e' and 'f' represent location and relative direction of images taken in Figure 4.12, Figure 4.13, and Figure 4.14 respectively.

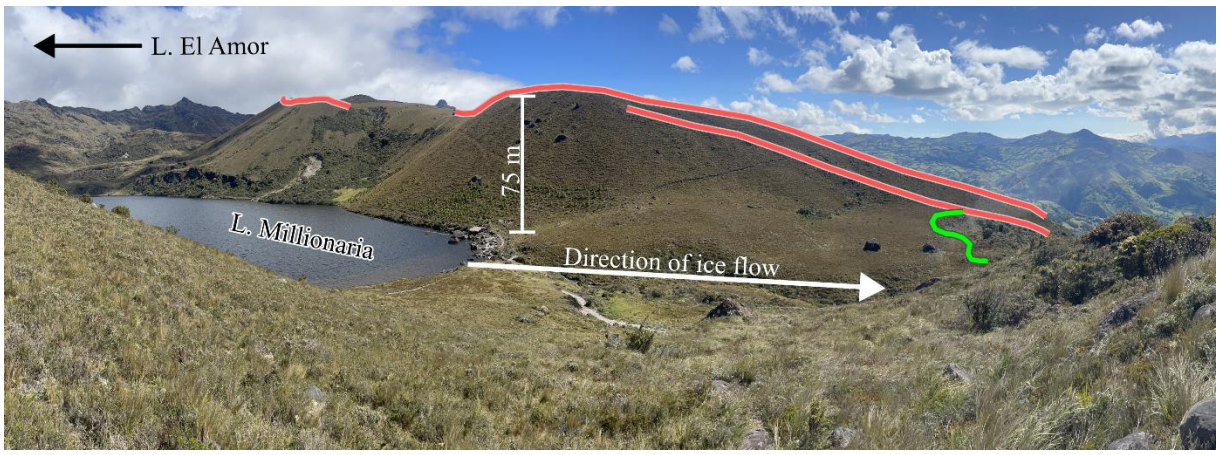

Figure 4.12: Infield panoramic image showing the southern prominent moraine that encloses Laguna Millionaria (lake in left of image). Red lines indicate features mapped using remote sensing datasets. Green line indicates a moraine mapped in-field using a handheld GPS. Direction of ice flow indicated. White verticakl line denotes the vertical relief (75 m) of the moraine.

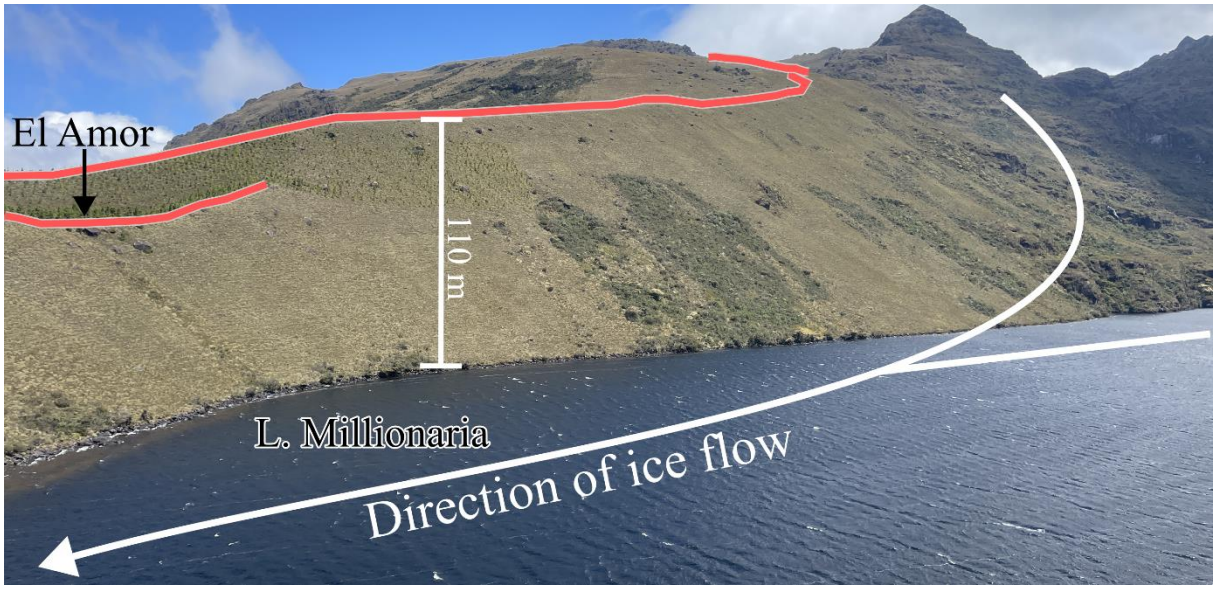

Figure 4.13: Infield photo showing the northern prominent moraine enclosing Laguna Millionaria. This moraine contains a smaller perched lake, Laguna El Amor (marked with black arrow). Red lines indicate features mapped using remote sensing methods. For accessibility reasons, we were unable to access this moraine further up-valley, so no mapping could be conducted in-field. Direction of ice flow indicated. White line denotes the vertical relief (110 m) of the moraine.

Field observations within the confines of the prominent Laguna Millionaria moraines indicated that, at least for the area surveyed in the field, the remote mapping was accurate and followed closely to the 'real world' geomorphology. The field observations revealed two additional low relief (i.e., 1-3 metres in height) moraines that were mapped on the southern edge of the north prominent moraine, between it and Laguna El Amor (two most northern green lines within Figure 4.11). One remotely mapped moraine was found to extend further than mapped pre-field,

and this moraine also connects to a small terminal moraine (see green line on right hand side of Figure 4.12).

The field-identified smaller moraines in front of Laguna Millionaria are logically younger than those of the largest prominent moraines due to their relative position within the confines of the moraines. Like the other newly identified smaller moraines elsewhere in the study region in this thesis, these moraines are hypothesised to be the result of late-glacial or early Holocene ice margin advances or standstills of less extensive, and probably thinner, ice masses due to their smaller size. Although many of the Laguna Millionaria moraines or subdued and of low relief, many could be mapped via remote methods (see Figure 3.15) (Lee *et al.*, 2022). However, if moraines were below a certain size threshold or were well blended into the landscape they could only be identified and mapped in-field, and so new moraines were mapped when infield.

Within the same complex as Laguna Millionaria, Laguna El Amor (Figure 4.14) (4,113 m asl) occupies a depression within the northern prominent moraine (seen in Figure 4.11) and is ~100 m at its widest dimension. This lake lies at an elevation of 3,420 m, with remotely mapped features that surround the lake. Although unable to identify its formation remotely, from infield observations the formation of this lake and the features around it are likely the result of post-glacial melt out of an ice-cored moraine due to its position on top of the large prominent moraine. This melt out of ice within the moraine would have created a cavity that then collapsed, thereafter becoming infilled with run off and melt water.

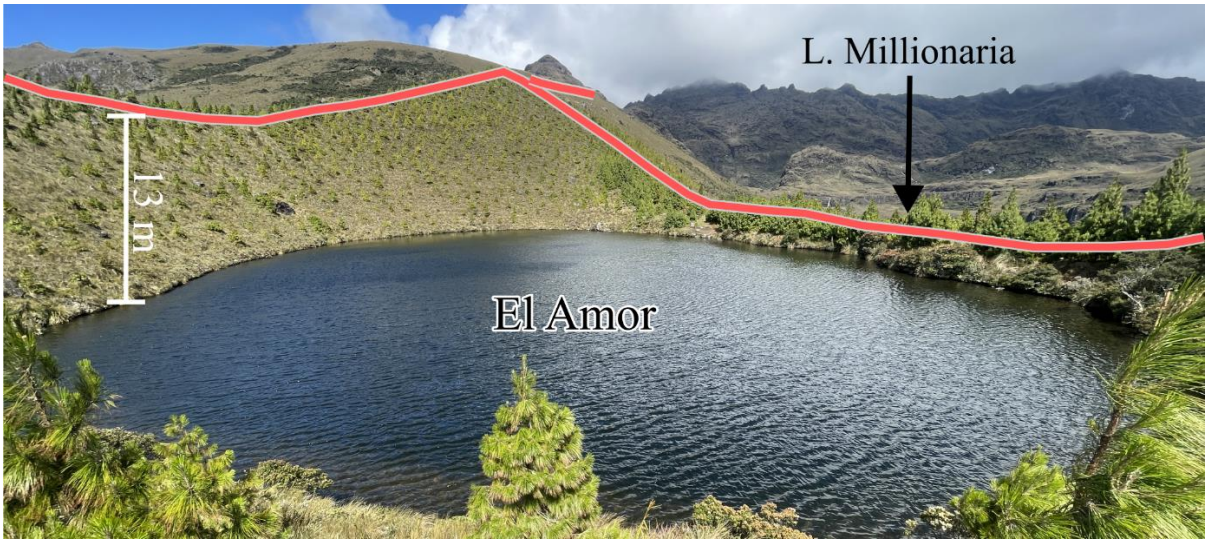

Figure 4.14: Infield image of Laguna El Amor (location of lake in Figure 4.11/4.13) showing the lake in context, within the confines of two potential moraines and the height difference (13 m left, 1 m right) in the two-sided 'moraines'. The red lines denote the remotely mapped geomorphology, splitting in the centre and going around the lake. Image taken on the southside

of the Laguna El Amor, with Laguna Millionaria indicated to the lakes right (south) beyond the feature. White line denotes the vertical relief (13 m) of the left moraine.

4.3.4. Laguna Millionaria and Laguna El Amor – collected TCN samples

Several glacial erratics from a range of Laguna Millionaria and Laguna El Amor moraines were sampled for TCN dating (shown in Figure 4.11). Samples 23-LM-1 and 23-LM-2 (Figure 4.2c&d) were collected from an erratic from the southern prominent lateral moraine, while 23-LEA-1 and 23-LEA-2 (Figure 4.2f&g) were collected from the northern prominent lateral moraine. These were collected in order to determine the timing of the maximum glacial advance within the valley.

23-LM-3 and 23-LEA-3 (Figure 4.2e&h; Figure 4.11) were acquired from erratics within the confines of the prominent moraines, from smaller moraine ridges. 23-LM-3 was within the terminal moraine position, and 23-LEA-3 proximal to Laguna El Amor. These moraines were selected due to them having the potential to constrain the last time that the overdeepening was glacier-filled rather than lake-filled. This moraine was selected as it would: (i) test hypotheses for the timing of post-LLGM glacial events (i.e., glacier readvances and/or standstills); and (ii) aid in constraining when glaciers were at this point primarily within numerical models when dated by TCN.

4.3.5. Laguna Negra – field observations and geomorphological mapping

The Laguna Negra site (Figure 4.15) includes a lake within a glacial overdeepening with an area of ~0.1 km^2 and is 400 m across. The lake is flanked by a prominent glacial moraine (111 m height) to the west, a smaller moraine to its south (5 m height), and high bedrock slopes to its north and east (356 m valley floor to valley top height) (overview seen in Figure 4.16). The lake is perched in an elevated position, ~50 m above the main valley floor (elevation difference can be noted in Figure 4.17). Fieldwork was conducted in and immediately around Laguna Negra and thus, any remotely sensed landforms mapped downvalley were not able to be thoroughly checked. However, the path up to Laguna Negra did take us past much of the remotely mapped geomorphology and this reconnaissance suggested there was little to change or add to the prior mapping.

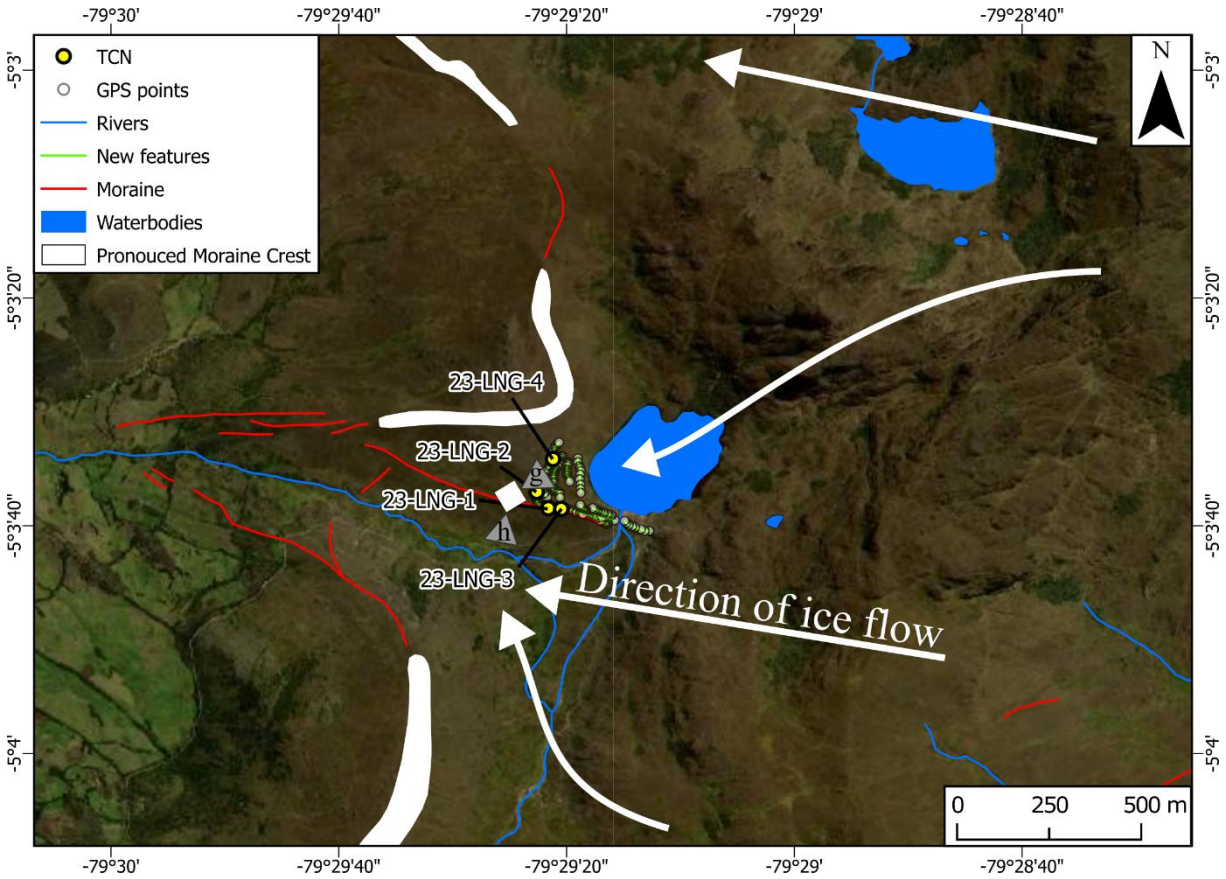

Figure 4.15: Remotely mapped palaeoglacial geomorphology from Laguna Negra (originally shown in Figure 3.16) with superimposed GPS survey points and newly mapped features. Figure location corresponds to Figure 4.1 d). White arrows indicate the direction of ice flow. White box denotes location images were taken from, and 'g' and 'h' denotes the approximate direction image was taken, shown in Figure 4.16 and Figure 4.17 respectively. Green line with transparent white dots are newly mapped moraines in front of Laguna Negra.

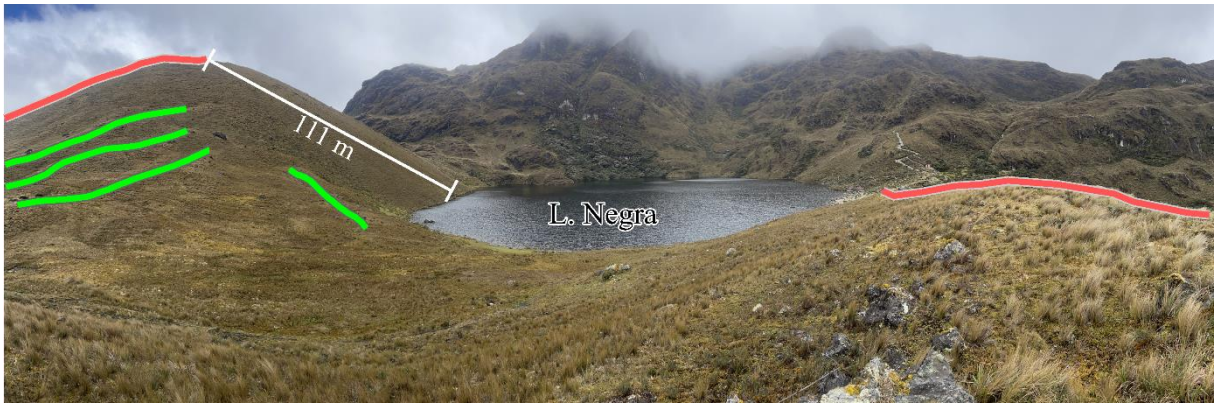

Figure 4.16: Infield panoramic image of Laguna Negra denoting the mapped moraines to its west (left), and south (right), with bedrock slopes to its north and east (background). Red lines denote remotely mapped moraines. Green lines denote moraines identified within the GPS survey. White line denotes the vertical relief (111 m) of the moraine. Location and direction of image taken from indicated in Figure 4.15 g.

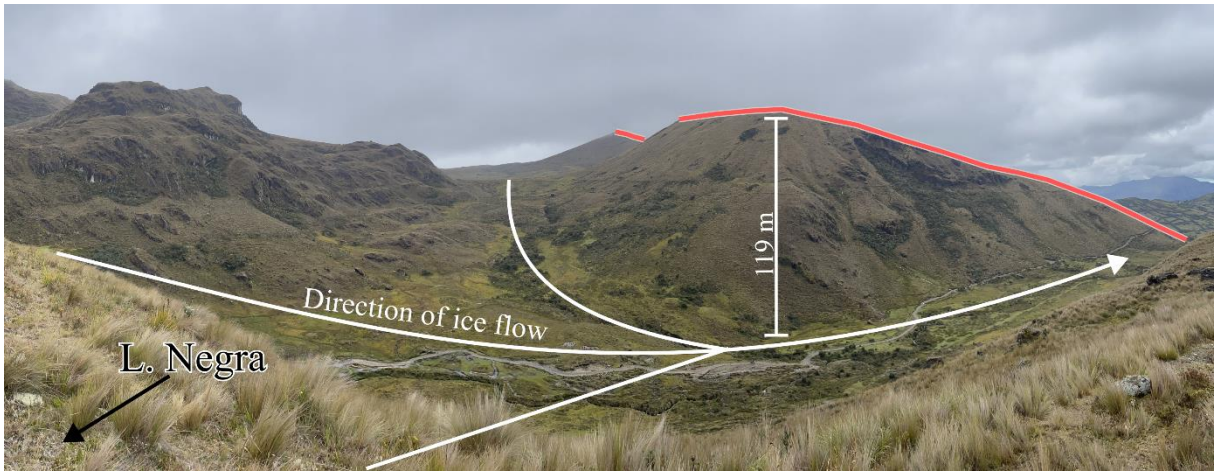

Figure 4.17: An infield panoramic image taken along the southern moraine of Laguna Negra looking downvalley (180 degree of Figure 4.16). The white vertical line notes the vertical relief between the valley bottom and prominent moraine across valley (119 m). Location and direction of image taken from indicated in Figure 4.15 h. White arrows indicate direction of glacial flow.

In-field mapping and a GPS survey was conducted around Laguna Negra. This identified a number of previously unidentified moraines (seen in the field image of Figure 4.16, and in Figure 4.17). These moraines were typically between 1 – 2 meters in height and were found immediately in front of Laguna Negra, with spacings of 20 – 40 m between the moraines. These smaller moraines were all found within the confines of the prominent moraine to the west, and the single remotely mapped moraine to its south. Their close proximity to each other, could reflect a fluctuating ice margin were cooler conditions caused ice retreat to stagnate during deglaciation of the valley. The recognition of this additional geomorphology has added further complexity to the region in terms of potential glacial evidence and glacial dynamics.

4.3.6. Lagune Negra – collected TCN samples

Within Laguna Negra, all samples for TCN dating were acquired from an erratic on lateral-terminal moraines up-valley of the prominent moraines (Figure 4.16). 23-LNG-2 and 23-LNG-4 (Figure 4.2j&l) were from the same moraine on the north side of the valley, from the lowest and most up-valley section respectively. Due to their location up-valley, potentially far away from the further down valley mapped moraines that are assumed to be LLGM in age, these samples are likely to result in ages younger than the regions LLGM.

The other samples from Lagune Negra (23-LNG-1 and 23-LNG-3; Figure 4.2i&k) were acquired from the lateral moraine to the south of 23-LNG-2 and 23-LNG-4. These are also likely to aid in the timing of glaciations after the assumed LLGM due to their positioning behind the most extensive moraines mapped and identified within the region.

4.4. Discussion

4.4.1. Accuracy assessment of remotely sensed mapping of the Las Huaringas

The January 2023 field season allowed an assessment of the accuracy and quality of the previously remotely mapped geomorphology. In general, the remotely sensed geomorphic mapping permitted identification of the majority of the palaeoglacial features, particularly the large prominent moraines, denoting the most extensive advance. However, the remotely sensed mapping clearly overlooked a number of less prominent low relief (i.e. 1-3 m) features in the locations visited in the field (Chandler *et al.*, 2018). The identification of these newly recognised moraines is likely to provide additional insight into the glacial dynamics of the region, albeit in the small regions of the wider study region visited during fieldwork; smaller scale features elsewhere in the study area not mapped here likely exist but have not been mapped. However, as the majority of features were mapped during the remote mapping phase, these new additions of moraines do not greatly change the overall picture.

In all valleys, small-scale geomorphic features that were not mapped in the highest resolution remotely sensed imagery available (i.e., PlanetScope) were mapped in field. The field mapping of these features suggests that within many locations across Laguna de la Huaringas (e.g., Lagune Shimbe and Laguna Negra) had a fluctuating ice margin post-LLGM, likely during a deglaciation phase due to their position behind prominent moraines. All the field-identified moraines are all located up-valley from the maximum mapped extents (e.g., Laguna Shimbe), or are behind prominent moraines that are hypothesised to be regions LLGM ice limits (e.g., Laguna Negra). It is highly likely that these smaller moraines date from younger glaciations – they are potentially late-glacial or early Holocene landforms. The presence of younger moraines, those that potentially denote standstills during deglacial phase, are useful for modelling to see if the model can capture deglaciation of a region accurately. However, moraines that denote a continuous retreat phase are unlikely to be in the geomorphological record.

4.4.2. Assessment of samples taken and next steps

The majority of TCN samples collected from around the study region are likely to represent post-LLGM dates, due to their position behind large prominent moraines (e.g., Laguna Negra) or being up-valley closer to valley head walls in regions where no prominent moraines are located (e.g., Laguna Shimbe). Some samples, such as those taken in Laguna Millionaria from

the prominent moraines, are likely to record the maximum advance (possibly LLGM) of the glacier that occupied that valley, however there is a possibility the dates from the sampled boulder will suggest glaciation older than the LLGM.

Other than the TCN samples, the peat core from the southern end of Laguna Shimbe can be used to provide a minimum-limiting age on the timing of deglaciation. Glacial ice has been reconstructed as extending downvalley beyond Laguna Shimbe, and evidence for more extensive glaciation is provided by the geomorphology of the valley (i.e., overdeepened basins). When the Shimbe Valley glacier deglaciated up-valley, and assuming a favourable climate, peat could develop. The base of the peat core therefore represents the interface between the deglaciated ground and the initiation of peat accumulation which can be dated. Very little work has been conducted on the core except basic XRF analysis (section 4.3.2.), and a preliminary description of the core stratigraphy. The core contains several macrofossil samples and is likely to provide adequate dates when sampled and dated using radiocarbon. Again, this analysis was beyond the scope of this PhD project due to the timelines involved.

Although the analysis of samples collected to understand and generate a geochronology of glacial advances within the region is not presented in this chapter or thesis, the acquisition of these samples is important. There has been no previous study constraining glaciation within this region, and any post-PhD analysis of these samples can provide novel results. Although attributing ages for advance or deglaciation on the sampled moraines is currently impossible, it is still possible to evaluate the likelihood of the ages these moraines may represent, by observing at their location in the context of the surrounding geomorphology.

4.4.3. Implications for future modelling work

Both the remote and in-field mapping (Chapter 3 and this chapter), along with the samples collected for dating purposes, will aid in constraining and understanding the numerical modelling outputs (Chapters 5 & Chapter 6). Future chapters will perform numerical modelling to determine the climate required for the most extensive (assumed to be the regions LLGM) glaciation, and to understand glacial dynamics pre, during, and post, the most extensive period of glaciation. It is unlikely that the most extensive moraines will have advanced at the same time but are likely to be during the same advance period. The mapping and confirmation of palaeoglacial geomorphological evidence at the furthest downvalley extent, assumed to be the regions LLGM, can aid in constraining the generated ice. Palaeoglacial geomorphic evidence (from both remote sensing and field observations) situated behind such prominent moraines,

and assumed to represent post-LLGM advances or standstills during retreat phases, can aid in constraining or confirming the accuracy of the model when using a time varying climate.

The dating of the most extensive palaeoglacial evidence can provide the timing upon which glaciers in the region were at their most extensive and can be integrated with numerical modelling to obtain potential climate. As models can use a number of differing glaciological parameters to generate glacial ice, knowing the timing and evidence of glacial extents can then aid in conducting sensitivity tests with varying parameterisation and climate inputs to generate a climatic envelope upon which glaciers could have been generated under. Knowing the timing of advances and retreat phases, and potential climate, can then allow a comparison with other regions, and integration of this regions determined climate to that during the time of advance (e.g., LGM; Garreaud *et al.*, 2003; Sugden *et al.*, 2005; Quesada-Román *et al.*, 2020).

4.5. Chapter summary

This chapter has demonstrated the collection of samples for cosmogenic dating has been conducted, and that they shall be analysed in the future to determine timing of glacial advances. This chapter has thus enabled:

- The improvement and assessment of the remotely sensed geomorphological mapping (Chapter 3), along with the collection of TCN and core samples, provides more information and increased confidence in the mapping previously conducted in Chapter 3. Providing more detailed knowledge and evidence on the ice frontal position, at least in locations behind the most extensive mapped moraines. These can be used to understand the past glaciologically of the study are and the wider tropical region.
- The features mapped from remote sensing and field observations, can be used in the modelling of the region to help constrain and understand modelled ice extents, thicknesses, and ice dynamics. These can potentially provide an understanding of the relative timing and climate needed for glacier margins to be found at or near those positions. However, from this point forward in the thesis, the collected samples shall not be mentioned further, due to at the time of the completion of this thesis, they have not been analysis for their exposure age.
- In future research, when the samples acquired during fieldwork are dated, they can be used to better understand the glacial dynamics in the region, providing a new data point within the Andean glaciers, and tropical glaciation, literature.

Chapter 5. Numerical modelling of the past glaciation of the Lagunas de Las Huaringas region – sensitivity analysis

5.1. Introduction

Across the tropical Andes few studies have conducted numerical modelling experiments of palaeo ice masses (e.g., Leger *et al.*, 2022). Studies that do conduct numerical modelling within South America, have been primarily focused on the Patagonian Ice Sheet (Hulton *et al.*, 2002; Sugden *et al.*, 2002; Hubbard *et al.*, 2005; Castillo *et al.*, 2022; Retamal-Ramírez *et al.*, 2022). Tropical Andean glaciers sit in a completely different climatic setting to extra tropical systems, and are generally topographically constrained (Clapperton, 1987b; Garreaud, 2009; Kiefer and Karamperidou, 2019). The primary limitation to modelling studies within the tropical Andes had been the ability to address the impact of substantial topographic variations associated with valley glaciers, and ice plateau, or ice cap, fed glaciers. In such settings, models need to take into account the glacier-topographical interactions that can affect glacier extents, thicknesses, and velocities (Candaş *et al.*, 2020).

Within this chapter, the Parallel Ice Sheet Model (PISM) (Winkelmann *et al.*, 2011; The PISM authors, 2018) is used to conduct modelling experiments. PISM can model local and regional ice at high (10s-100's of meters) resolutions, enabling valley-ice interactions to be solved. PISM has been extensively used to understand ice response to recent climate warming (e.g. Goelzer *et al.*, 2020; Noble *et al.*, 2020; Wunderling *et al.*, 2020), and in palaeoglacial local and regional studies in alpine landscapes that are not dissimilar to Las Huaringas (Seguinot *et al.*, 2018; Candaş *et al.*, 2020; Köse *et al.*, 2022; Martin *et al.*, 2022). This proven success in using PISM for palaeo-valley glaciation is the core justification for using it in this thesis. Due to these recent applications of PISM in palaeo mountain glaciation settings, and with its ability to model at high resolutions, the model can now be used to understand the former glaciation of the Las Huaringas whose valleys are steep sided (up to 50° slope) and narrow (200 m to 1 km across).

This chapter will explore and evaluate two important preliminary steps necessary for the glacial modelling of the study region: i) the sensitivity analysis of generated ice masses to a variety of different glaciological parameterisations within PISM, and ii) investigation of a range of steady state climatic conditions that generate glacial ice in the study area. This work is to aid in establishing the best-fit model input parameters for time varying modelling (Chapter 6). As Chapter 3 only determined temperature cooling (section 3.3.7.) without precipitation variation, this chapter will be the basis for providing appropriate climatic forcing and glaciological

parameterisation for modelling how any ice masses at Las Huaringas may have evolved (Chapter 6). The observed palaeoglacial geomorphology derived from remote sensing (Figure 3.2; Chapter 3) and field observations (Chapter 4), will be used to test the validity of the 'best-fit' models produced in this chapter, and can be used to determine the potential climatic envelope glaciers could have existed under during the last glacial period. A description of the best-fit model determined for the regions LLGM will be discussed in Chapter 6 during the period of maximum glacial extent (section 6.4.2.).

5.2. Aim and objectives

This chapter aims to investigate the sensitivity of maximum ice extent in Las Huaringas to climatic and glaciological parameters. Objectives to achieve this aim are:

- Evaluate which model parameters have the most influence on ice extent within the region.
- Determine which parameters produces a 'best fit' (i.e., ice mass area) match against observed maximum extents, assumed to be the regions LLGM.
- Determine a climatic envelope, of both temperature cooling and precipitation fraction, under which these glaciers could advance to their maximum extents.

5.3. Methods and data

5.3.1. The Parallel Ice Sheet Model

PISM (v1.2) is an open source, three-dimensional, numerical, finite-difference, hybrid shallow-ice shallow-shelf model (Winkelmann *et al.*, 2011; The PISM authors, 2018), created for modelling past and present-day ice sheets (Seguinot *et al.*, 2016; Albrecht *et al.*, 2020; Roberts *et al.*, 2020; Luo and Lin, 2022). More recently PISM has been used to model at much smaller scales, at higher resolutions. Such applications have been to model mountain glaciers under past and future climate estimates and scenarios (e.g. Seguinot *et al.*, 2018; Yan *et al.*, 2018; Candaş *et al.*, 2020; Roberts *et al.*, 2020; Žebre *et al.*, 2021; Köse *et al.*, 2022). PISM calculates ice extent and thickness, and can be used to assess how these, along with ice velocity, temperature, and mass balance, change over time. This section details the model choices made for glacial physics, and the input data used for the boundary conditions, to force a suite of sensitivity tests. Table 5.1 details the model parameters used.

Table 5.1: These are parameter values used within the ice sheet model sensitivity analysis for PISM. Values shown within parentheses are values that the parameter was varied by in the sensitivity analysis.

Parameters	Name	Value	Unit	Reference
Ice and Earth Dynamics				
ρ	Ice density	910	kg m^{-3}	Aschwanden *et al.* (2012)
g	Gravitational acceleration	9.81	m s^{-2}	Aschwanden *et al.* (2012)
n	Glen exponent	3	-	Cuffey and Paterson (2010)
ρ_b	Bedrock density	3300	kg m^{-3}	-
q_G	Geothermal heat flux	88	W m^{-2}	Vieira and Hamza (2019)
E_{SIA}	SIA enhancement factor	1 (1-5)	-	-
E_{SSA}	SSA enhancement factor	1 (0-1)	-	-
Basal sliding and subglacial hydrology				
q	Pseudo-plastic sliding exponent	0 (0-1)	-	Aschwanden *et al.* (2012)
$u_{threshold}$	Pseudo-plastic threshold velocity	100	m a^{-1}	Aschwanden *et al.* (2012)
c_0	Till cohesion	0	Pa	Tulaczyk *et al.* (2000)
e_0	Till reference void ratio	1	-	Tulaczyk *et al.* (2000)
C_c	Till compressibility coefficient	0.12	-	Tulaczyk *et al.* (2000)
N_0	Till reference effective pressure	1000	Pa	(Tulaczyk *et al.*, 2000)
δ	Minimum effective pressure ratio	0.02	-	Bueler and van Pelt (2015)
ϕ	Till friction angle	30	^{o}	Cuffey and Paterson (2010)
W_{max}	Maximum till water thickness	2	m	Bueler and van Pelt (2015)
Climate forcings				
T_{snow}	Temp for snow precipitation	273.15	K	Seguinot *et al.* (2018)
T_{rain}	Temp for rain precipitation	275.15	K	Seguinot *et al.* (2018)
DDF_{snow}	Degree-day factor for snow	3 (2-6)	mm d^{-1} °C	-
DDF_{ice}	Degree-day factor for ice	9 (3-11)	mm d^{-1} °C	-
$\theta_{refreeze}$	Refreezing fraction	0.6(0-0.7)	-	Ritz (1997)
σ	PDD temperature std. dev.	3.66	K	-

5.3.2. Glacial physics

PISM includes an enthalpy-based energy conservation scheme (Aschwanden *et al.*, 2012) combining a 'hybrid' shallow ice approximation (SIA; Figure 5.1a) (Hutter, 1983), and shallow shelf approximation (SSA; Figure 5.1b) (Weis *et al.*, 1999). This hybrid approach (SIA+SSA; Figure 5.1c) allows the consideration of both vertical deformation and longitudinal stretching, while allowing basal sliding to occur. Both SIA and SSA include an enhancement factor (E) and a Glen's flow law exponent (n); E accounts for unresolved effects of ice grain size, ice fabric, and ice impurities (Cuffey and Paterson, 2010). In model runs, E was set to 1 for both SIA and SSA, but was tested within the singular parameter sensitivity (section 5.4.4.), Glen's exponent for both SIA and SSA was set to 3 (Weertman, 1973; Weertman, 1983; Cuffey and Paterson, 2010).

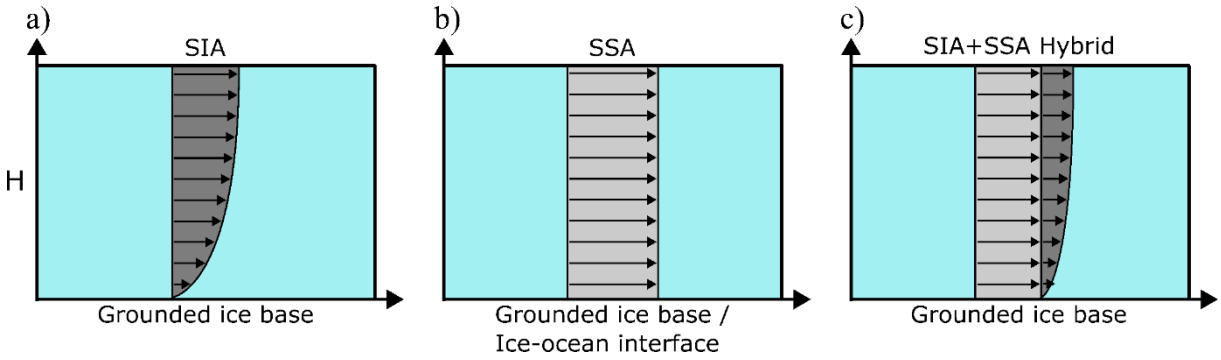

Figure 5.1: Visual representations of how PISM implements, a) SIA with internal deformation and b) SSA with sliding, into the modelling of ice movement, and how the c) SIA+SSA Hybrid model combines them (modified from Kirchner *et al.*, 2011).

Basal sliding in PISM occurs through the implementation of a 'pseudo-plastic' sliding law once the basal shear stress exceeds the yield stress. The yield stress is determined by the till friction, here determined by applying a constant till shear stress of 30 ($\phi = 30$) (Seguinot *et al.*, 2018). The sliding law is modified by the implementation of the Pseudo-plastic exponent q (Greve and Blatter, 2009) where, $q = 0$ denotes 'purely plastic' (or Coulomb) sliding, while $q = 1$ produces linear sliding. Within this model q is set to 0 for purely plastic sliding but is also tested with values between 0 and 1 within the sensitivity testing of singular parameters (section 5.4.5.).

5.3.3. Boundary conditions

PISM computes glacier flow across a model domain, which here covers ~1,260 km^2 (30 x 42 km) on a regular horizontal grid that is fixed in size (resolution) throughout. This chosen resolution affects inputted boundary condition data (topography, climate, and basal heat flux), and the resulting ice that accumulates. Model resolution is chosen as a balance between computation time and the ability to represent ice at the appropriate scale. The horizontal resolution of the inputted topographical data is 30 m, and thus any downscaling from this would lose detail but speed up computation time (due to fewer grid cells being computed). Downscaling will generate areas that have erroneously steep topographic gradients that could result in the modelled glaciers becoming poorly resolved, overestimating glacier dynamics (particularly velocity) at a local scale (Golledge *et al.*, 2012). With these potential issues in mind, resolution was initially tested in the sensitivity experiments (see section 5.4.1.). Simulations thereafter were run at the chosen resolution of 120 m; yielding a horizontal and vertical grid of 250 by 350 pixels, chosen due to its computational efficiency and ability to accurately represent the ice.

Inputted topography was derived from the ALOS 30 m resolution DEM (Tadono *et al.*, 2014). To produce a more realistic land surface topography, lakes within the model domain were removed. To do this, lake depths were estimated using a width/depth relationship from Muñoz *et al.* (2020), that was tested against lake depth estimates from previous infield experience of lake coring in the region (e.g., at Laguna Shimbe which is known to be at least 30 m deep). Estimated lake depths were differenced with the ALOS DEM, generating an ice-free DEM that was inputted into the model domain (Figure 5.2).

Geothermal heat flux (GHF) provides the lower boundary condition of the model domain, able to warm the bed of the ice (Seguinot *et al.*, 2016). Geothermal heat flux data from Vieira and Hamza (2019) includes 6,526 observations across South America, smoothed using a 2^{o} x 2^{o} grid system, and interpolated across locations with no observations using a heat flow relationship. Due to the size of the study region here, the remote nature, and no direct observation of GHF recorded in Las Huaringas, a value of 88 Wm^{-2} was used across the entire domain, determined by Vieira and Hamza (2019), due to the high likelihood of incurring the same lithology.

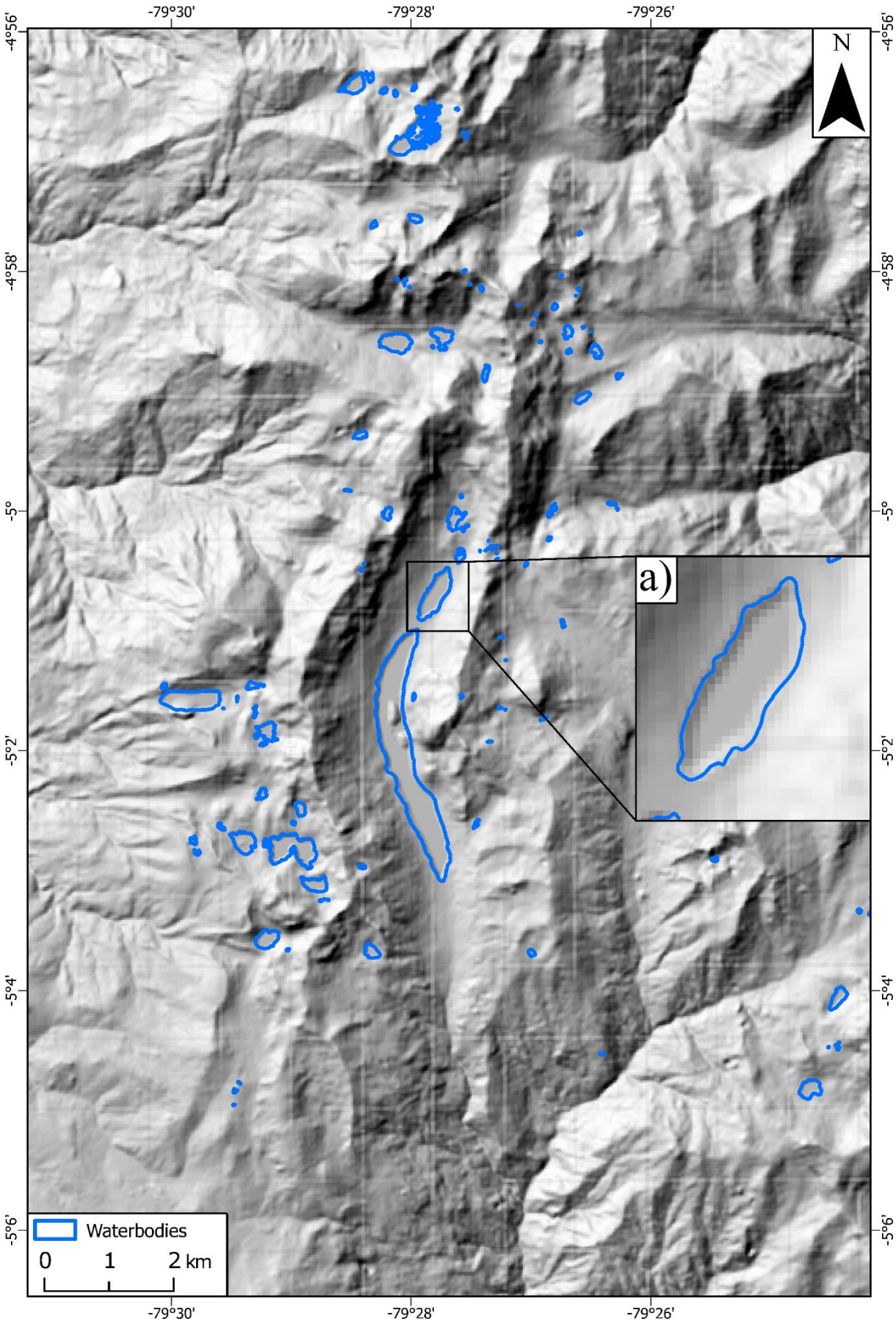

Figure 5.2: Study area preglacial topography hillshaded with the estimated lake depths difference with the 30 m ALSO DEM hillshade (Tadono et al., 2014). a) shows a zoom-in with Laguna Shimbe 2 with the lake boundary (blue polygon) with lake removed.

The upper boundary of the model, the interface between the ice and the climate, is determined by an expected positive degree day (EPDD) model (Braithwaite, 1995), that requires the input of climate information. We used the present day yearly average temperature (in K; Figure 5.3a&b) and total yearly precipitation (in mm; Figure 5.3c&d) from WorldClim data version 2.1 (Hijmans *et al.*, 2005; Fick and Hijmans, 2017) (http://www.worldclim.org/). These factors control the amount of accumulation and ablation over the model domain. All accumulation is determined to be snow, with accumulation linearly decreasing for air temperatures between 0 and 2°C (273.15 to 275.15 K) (Becker *et al.*, 2016). The amount of snow and ice melted per degree per positive degree day (PDD) is controlled by degree day factors for both snow (DDF_{snow}) and ice (DDF_{ice}). Any melt water from snow and ice may become refrozen, which is prescribed by a refreezing factor ($\theta_{refreeze}$**)** (The PISM authors, 2018). Lastly, a PDD temperature standard deviation is required to vary temperature across each model day. This was determined by the monthly variation of temperature in the study region from the WorldClim 2.1 data, determined to be 3.66°C. Due to the diurnal temperature variations in the tropics outweighing the seasonal or monthly temperature variations, it is important to parameterise. Within this chapter DDF and refreezing are unconstrained within the study area and required sensitivity testing to determine their parametrisation.

All model runs were set up with a vertical grid of 1000 m with 101 distributed layers with a corresponding vertical resolution, with equally spaced layers, of 10 m. All model simulations were initiated with an ice-free model domain, using the model parameters outlined in Table 5.1. This is used to understand the sensitivity of the model for generating ice in the region. Example model scripts, with both the 'set-physics.sh' and 'spin.sh' scrips, are found within Appendix C.

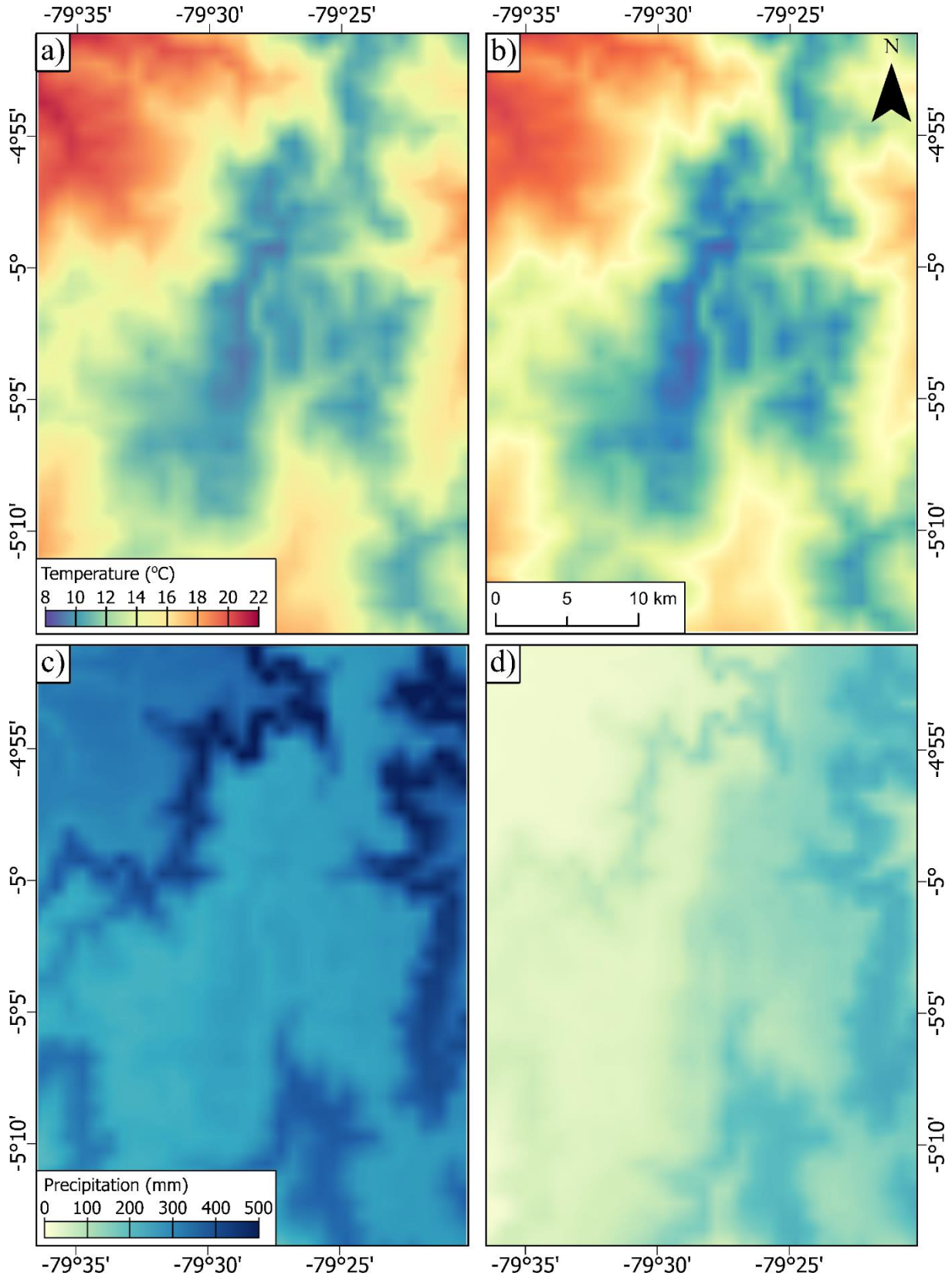

Figure 5.3: Inputted present-day southern hemispheric a) summer and b) winter mean near-surface air temperatures and present-day c) summer and d) winter mean total precipitation. Climate data is taken from WorldClim 2.1 (1960-1990; Fick and Hijmans, 2017). Subfigure extents match the extent of the model domain shown in subsequent figures in this chapter and thesis.

5.3.4. Climate forcing

While the EPDD model within PISM is based on the inputted modern climate data, this itself needs to be forced to enable sufficient cooling of the model domain to generate glacial ice. The temperature is modified (by a value of ΔT) and precipitation is scaled (by xP) as a proportion of present-day values inputted previously. These can be applied as either a steady climate (singular value), that allows the model domain and any generated ice to reach equilibrium with the surrounding climate, or a time varying climate, that can be inputting from real world data such as ice cores.

This chapter is concerned with conducting a sensitivity analysis to understand the influence of the model's parameterisations on generated ice masses. Thus, within all experiment runs conducted here, a constant climate was used. Within the single parameter sensitivity testing (detailed in sections 5.4.1. to 5.4.5) a ΔT of -10.5℃ of modern temperature, and a xP of 1 (0% increase) of modern precipitation were used to understand how ice flow physics choices may alter the growth and extent for a generated ice mass. These values were chosen to produce a big enough ice mass to understand model sensitivity. The multi-parameter sensitivity testing (detailed in sections 5.4.6. to 5.4.9.) used a range of ΔT and xP values; ΔT was varied -9 to -11℃, increasing in 0.5℃ increments, and xP was varied between -10% to +50% of present-day precipitation, increasing in 10% increments.

5.3.5. Varying parameterisation of glaciological physics in previous studies

There are varied parameterisations of the enhancement factor of SIA and the SSA solvers within modelling studies. For E_{SIA}, 1 denotes 'hard' ice, and increased values imply 'softer' ice that can deform more easily (Greve, 1997; Cuffey and Paterson, 2010). For E_{SSA}, values vary between 0 to 1, with values closer to 1 implying the propensity for faster streaming of ice. Previous observations of E_{SIA} from laboratory settings range between 1-10, and 4-120 on real-world glaciers. Observations of E_{SSA} have only been determined by anisotropic modelling studies, which determined ranges between 0.5 to 1 (Ma *et al.*, 2010) (Table 5.2). Modelling studies across different numerical ice models, particularly PISM, have generally used values of E_{SIA} of between 0.5 – 30. E_{SSA} values are typically 0.5-1. Considering the variability of observed and modelling studies values, for the singular parameter sensitivity tests we varied E_{SIA} across 1, 2, 3, 4, 5, and E_{SSA} across 0.2, 0.4, 0.6, 0.8, 1.

Table 5.2: E_{SIA} and E_{SSA} value ranges determined by past in-field studies or used within past modelling studies.

Glacier/Icesheet	Location	E	Reference	O/M*
Urumqi Glacier No. 1	China	E_{SIA} = 120	Echelmeyer and Zhongxiang (1987)	O
Dry 3	Greenland	E_{SIA} = 4	Dahl-Jensen and Gunderstrup (1987)	O
-	Lab experiments	E_{SIA} = 1.3-10.2	Treverrow *et al.* (2012)	O
Siple Dome	West Antarctica	E_{SIA} = ~9	Pettit *et al.* (2007)	O
Antarctic Icesheet	Antarctica	E_{SIA} = 1.2-1.5 E_{SSA} = 0.5-0.6	Golledge *et al.* (2015)	M
Mount Dedegöl	Turkey	E_{SIA} = 1 E_{SSA} = 1	Candaş *et al.* (2020)	M
European Alps	Europe	E_{SIA} = 2 E_{SSA} = 1	Seguinot *et al.* (2018)	M
Cordilleran Icesheet	North America	E_{SIA} = 1 E_{SSA} = 1	Seguinot *et al.* (2016)	M
-	Ice shelves Ice streams	E_{SSA} = 0.5-0.7 E_{SSA} = 0.6-1.0	Ma *et al.* (2010)	M
High Mountain Asia	-	E_{SIA} = 3 E_{SSA} = 0.5	Yan *et al.* (2018)	M
Rhine Glacier	European Alps	E_{SIA} = 1	Imhof *et al.* (2019)	M
Monte San Lorenzo	Patagonia	E_{SIA} = 3 E_{SSA} = 0.6	Martin *et al.* (2022)	M
Patagonia Icesheet	South America	E_{SIA} = 1-6	Yan *et al.* (2022)	M
Renland Ice Cap	East Greenland	E_{SIA} = 1-3 E_{SSA} = 1-3	Koldtoft *et al.* (2021)	M
West Antarctic Icesheet	Antarctic Icesheet	E_{SIA} = 2 E_{SSA} = 0.6	Kingslake *et al.* (2018)	M
Juneau Icefield	Alaska	E_{SIA} = 1 E_{SSA} = 1	Ziemen *et al.* (2016)	M
Southern Alps	New Zealand	E_{SIA} = 3	Golledge *et al.* (2012)	M

*O = Observations, M = Modelling

Studies that use PISM choose different *q* values between 0 and 1. There is little agreement on which value to use, either generally or for certain types of glacial ice that are being modelled (i.e., ice sheets or valley glaciers). Some similarities are present within the literature (Table 5.3). Studies that are concerned with smaller ice bodies, such as valley glaciers (Candaş *et al.*, 2020) or small ice sheets (Seguinot *et al.*, 2018), tend to use 0, while larger ice sheet studies (e.g. Kingslake *et al.*, 2018) use values closer to 1. Previous studies have found that smaller *q* values for ice sheets reduces glacier velocities, generating larger glacier volumes, while *q* would have negligible impact on valley type glaciers (Albrecht *et al.*, 2020; Candaş *et al.*, 2020). Given the variability of q values used in modelling studies, for the singular parameter sensitivity tests we varied *q* across 0, 0.25, 0.5, 0.75, 1.

Table 5.3: Differing *q* value ranges used within past modelling studies.

Glacier/Icesheet	Location	q	Reference
Mount Dedegöl	Turkey	0	Candaş *et al.* (2020)
European Alps	Europe	0.25	Seguinot *et al.* (2018)
Cordilleran Icesheet	North America	0.25	Seguinot *et al.* (2016)
West Antarctic Icesheet	Antarctic Icesheet	0.75	Kingslake *et al.* (2018)
Patagonia Icesheet	South America	0-1	Yan *et al.* (2022)
Laurentide Icesheet	North America	0-1	Moreno *et al.* (2022)

Observed DDF variations vary dramatically in space. DDF_{ice} observations range between 22 to 5 mm w.e. °C, while DDF_{snow} observation range between and 11.6 to 2.5 mm w.e. (Braithwaite, 1995; Hock, 2003). Across the Andes, and the tropics specifically, there is substantive variation in observed DDFs (Table 5.4), with DDF_{ice} between 3.6 and 9.99 mm w.e. °C and DDF_{snow} between 3.5 and 4.96 mm w.e. °C. These values are however from a limited number of studies that have conducted observations in the tropical Andes. Modelling studies (Table 5.5) have tested variations in DDFs values, either using DDFs informed by regional observations (e.g. Golledge *et al.*, 2012; Yan *et al.*, 2023), or those that allow the model to match the current glacial ice, or observed palaeo-ice positions (e.g. Ziemen *et al.*, 2016; Candaş *et al.*, 2020). A number of studies have performed DDF sensitivity tests due to poorly constrained parameterisation (Bravo *et al.*, 2015; Ziemen *et al.*, 2016; Martin *et al.*, 2022; Yan *et al.*, 2022) and show that DDFs can widely affect model outputs for glacial ice modelling (Ziemen *et al.*, 2016; Martin *et al.*, 2022). Within the singular parameter sensitivity testing, DDF_{ice} was varied across 3, 5, 7, 9, 11, and DDF_{snow} was varied across 2, 3, 4, 5, 6.

Table 5.4: Observed DDFs across the literature within the Andes and tropical glaciers (measured in mm w.e. d^{-1} °C), and a compilation of data from Hock (2003), Anderson *et al.* (2014), Fernández and Mark (2016) and Martin *et al.* (2022). NPI/SPI = Northern/Southern Patagonia Icesheet, NZ = New Zealand.

Glacier	Location	DDF_{snow}	DDF_{ice}	Reference
Antizana volcano	Ecuador	4.96	9.99	Maisincho *et al.* (2016)
Zongo Glacier	Bolivia	3.7	7.4	Blard *et al.* (2011)
Nef Glacier	NPI	-	9.99	Matsuoka and Naruse (1999)
San Rafael Glacier	NPI	3.9	6.6	Koppes *et al.* (2011)
SPI	SPI	3.5	6.5	De Angelis (2014)
Perito Moreno Glacier	SPI	-	7.1	Takeuchi *et al.* (1996)
Perito Moreno Glacier	SPI	-	2.7-4.3	Stuefer *et al.* (2007)
Chinco Glacier	SPI	4	6.5	Rivera (2004)
Gran Campo Nevado Ice Cap	SPI	-	7.6	Schneider *et al.* (2007)
Glacier Upsala	SPI	-	7.1	Brugger (2010)
Martial Este Glacier	SPI	4.7	9.4	Buttstädt *et al.* (2009)

Upsala Glacier	SPI	-	7.1	Naruse *et al.* (1997)
Franz Josef Glacier	NZ	3	6	Woo and Fitzharris (1992)
Franz Josef Glacier	NZ	4.6	7.1	Anderson (2004)
Franz Josef Glacier	NZ	4.55	7.17	Anderson *et al.* (2006)
Franz Josef Glacier	NZ	-	8.1	Brook *et al.* (2013)
Tasman Glacier	NZ	-	3.6-5	Kirkbride (1995)

Table 5.5: Modelled DDFs across the literature globally (measured in mm w.e. d^{-1} °C). NA = North America, NPI/SPI = Northern/Southern Patagonia Icesheet, NZ = New Zealand, HMA = High Mountain Asia.

Glacier	Location	DDF_{snow}	DDF_{ice}	Reference
Mount Dedegöl	Turkey	3	8	Candaş *et al.* (2020)
-	Alps	3.297	8.791	Seguinot *et al.* (2018)
Southeastern Tibet	HMA	5	10	Yan *et al.* (2023)
Juneau Icefield	Alaska	2	14	Ziemen *et al.* (2016)
Cordilleran Ice Sheet	NA	3.04	4.59	Seguinot *et al.* (2016)
Lorenzo Ice Cap	NPI	3	8	Martin *et al.* (2022)
-	PI	2	4	Yan *et al.* (2022)
Southern Alps	NZ	4.55	7.17	Golledge *et al.* (2012)

To what extent melted snow and ice becomes refrozen and retained by the glacier is uncertain and poorly constrained (Marshall, 2021) with limited direct observations available, and no observations within the tropical Andes. These observations are limited to locations of extensive ice sheets or glaciers (i.e., Greenland or the High Mountain Asia) (Table 5.6). Across limited observations and modelling studies, refreezing fractions vary between 0 (turned off in models) (e.g. Golledge *et al.*, 2012; Seguinot *et al.*, 2018; Martin *et al.*, 2022) and 0.65, while modelling studies use 0.6 generally (e.g. Candaş *et al.*, 2020; Žebre *et al.*, 2021; Köse *et al.*, 2022). Within the singular parameter sensitivity testing we varied the refreezing fraction across 0, 0.1, 0.2, 0.3, 0.4, 0.5, 0.6, 0.7. PISM is unable to 'turn off' refreezing, thus 0 equates to 0% of melt water being refrozen.

Table 5.6: Refreezing factors that have been reported in the literature either by being used within mass balance models (not glacier models), or via field observations.

Glacier	Location	$\theta_{refreeze}$	Reference	O/M*
Sätujökull	Central Iceland			
Nigardsbreen	Southern Norway	0.07	Jóhannesson *et al.* (1995)	O
Qamanärssûp sermia	West Greenland			
Qiyi Glacier	NW China	0.2	Jiang *et al.* (2010)	O
West Greenland	Greenland Ice Sheet	0.6	Braithwaite *et al.* (1994)	O
-	Greenland Ice Sheet	0.6	Ritz (1997)	M
Rikha Samba Glacier	High Mountain Asia	0.15	Gilbert *et al.* (2020)	M
Storglaciären	Sweden	0.58	Braithwaite and Zhang (1999)	M

Barnes Ice Cap	Canada	0.2	Gilbert *et al.* (2016)	M
Tanggula Mountains	Tibetan Plateau	0.2	Fujita *et al.* (2007)	M
Ötztal Alps	Austria	0.65	Hanzer *et al.* (2016)	M
Midre Lovénbreen	Svalbard	0.37	Wright *et al.* (2007)	M

*O = Observations, M = Modelling, mass balance

5.3.6. Model sensitivity analysis

The sensitivity analysis, conducted in a two-stage processes, is detailed below. The initial suite of model sensitivity tests was designed to understand the influence of individual model parameters that control ice flow behaviour and the generation of steady-state glaciers in the region. After understanding how these parameters influence ice, we selected a set of parameters that were then held stable, and which produced little variation in generated ice. This was so we could conduct the second set of sensitivity experiments to understand how climatic variables altered the extent and pattern of ice growth, while also varying the parameters with the most influence for ice generation. The outputted ice from these runs was compared to the most extensively mapped geomorphological evidence, assumed to denote the LLGM maximum extent, to determine the model with the best-fit to these observations. All sensitivity analysis runs were conducted so that the modelled ice reached equilibrium (as defined by a stable ice volume being reached) with the modelled climate. This took place after 3,500 yrs, when the model run was stopped. The diagnostic variables used is the ice thickness variable ('thk') to understand the spatial extent, and from the ice area ('ice_area_glacierized) and ice volume ('ice_volume') variables.

The individual parameter sensitivity experiments are not to evaluate how the ice looks or behaves in comparison to the hypothesised regional LLGM extent. They are to understand the influence of the model parameters and boundary lay inputs on ice generation within the model domain, primarily its area and volume of ice. No attempt shall be made for these single parameter tests to compare the extent of the glacial ice to the previously mapped glacial geomorphological evidence. Instead, this analysis will be made within the 'best-fit' runs within the second experiment of the sensitivity analysis (sections 5.4.7. and 5.4.9.). However, reference to the ice parameters (Table 5.7) and where ice can be grown within the model domain shall be made for the single parameter tests.

Within the initial sensitivity analysis, the parameters selected are those that have not been widely parameterised by observations, either locally (within the tropical Andes) or globally or are unconstrained within glacial modelling literature (discussed in section 5.3.2.). A suite of

model runs was conducted which tested the effect of a single parameter value on modelled glacial ice output, and therefore conducted 68 simulations to cover the parameter ranges indicated in Table 5.7. These parameters were varied for each model run across a range of likely values (as outlined in the previous sections). PISM also requires a large number of other parameter choices to be made (Table 5.1), but in the context of this work it was not possible to test them all. Therefore, for the majority of parameters we applied extensively used values from previous work (Seguinot *et al.*, 2018; Candaş *et al.*, 2020; Žebre *et al.*, 2021; Martin *et al.*, 2022).

Table 5.7: Initial sensitivity experiments conducted, detailing the parameter chosen, the range of values tested, along with the aim of the experiment.

Parameter	Range		Aim
1) Resolution (m)	80, 120, 150, 300, 600	m	The initial test, to understand the sensitivity of the modelled ice output to the model resolution to determine best resolution for ice detail and computation time
2) Degree day factors (DDFs)	Ice: 3, 5, 7, 9, 11 Snow: 2, 3, 4, 5,6	mm w.e. ℃	Test the sensitivity of the modelled ice output to changes in the degree day factors of snow and ice in combination.
3) Refreezing factor ($\theta_{refreeze}$)	0, 0.1, 0.2, 0.3, 0.4, 0.5, 0.6, 0.7	-	Test the sensitivity of the modelled ice output to the amount of refreezing in the ice and fern layer.
4) Ice rheology enhancement €	E_{SIA}: 1, 2, 3, 4, 5 E_{SSA}: 0.2, 0.4, 0.6, 0.8, 1	-	Test the sensitivity of the modelled ice output to the enhancement flow factors for both SIA (E_{SIA}) and SSA (E_{SSA}).
5) Sliding power law (q)	0, 0.25, 0.5, 0.75, 1	-	Test the sensitivity of the modelled basal ice velocities to the selection of the power law (q) value and how those effects glacial ice output.

The climate used in the sensitivity testing was steady state and was applied as a way to test the sensitivity of ice extent to the chosen model parameters. Although it therefore does not reflect the 'real' climate that would have been present during the regions LLGM, the chosen climate was chosen because it was able to generate substantial glacial ice within the model domain. The climate applied was a ΔT = -10.5℃ and xP = 100% relative to modern conditions and the model ran for 3,500 yrs until ice volume reached equilibrium with the climate.

After the initial sensitivity tests described above, two of the most influential parameters on the amount of glacial ice accumulation were assessed – DDFs and the refreezing factor. These were then varied individually, along with varying climatic forcing using ΔT and xP offsets. The

chosen values for DDF and refreezing were informed from the singular parameter sensitivity testing, using value combinations that were deemed realistic for ice generation in the model, and values observed in the real world (from Tables 5.3, 5.4 and 5.5). This allowed a further understanding into how variations in climate influence the parameters required to achieve an ice extent that is consistent with constraints from the glacial geomorphological evidence (Chapters 3 & 4 ; Lee *et al.*, 2022). This enables the determination of a potential climatic envelope required to build an ice mass to an extent approximating the mapped ice limits.

During DDF tests refreezing was held at 0.6, reflecting other studies modelling palaeo-glacial valley systems (e.g. Candaş *et al.*, 2020). During refreezing tests, the DDFs were held at a DDF_{ice} of 9 mm w.e. d^{-1} °C, and a DDF_{snow} of 3 mm w.e. d^{-1} °C. Climate forcing parameters were also varied. The ΔT ranged from -9°C to -11°C, increasing in increments of 0.5°C. xP was varied from -10 % to +50% of modern-day rainfall, increasing in increments of 10%. This is justified by literature for Perú and Bolivia that indicated that the LLGM period was potentially wetter than present (Clapperton *et al.*, 1997a; Fritz *et al.*, 2004; Chepstow-Lusty *et al.*, 2005), while regions within the northern tropical Andes had a mix of wetter, and drier LLGM climate (Vélez *et al.*, 2003; Novello *et al.*, 2019; Nunnery *et al.*, 2019). If no ice developed, the run was not included in the analysis. Thus values of ELA-derived temperature cooling of 6.5°C to 8.8°C, determined in Chapter 3 (Lee *et al.*, 2022), are not shown here (i.e., no ice was generated).

To understand which simulated modelled output was the 'best-fit' for each parameter-climate scenario, the horizontal mismatch between the observed potential maximum glacier extent (regional LLGM), and the modelled ice terminus limit was measured. This was measured along manually generated valley centre lines within 5 valleys (Figure 5.4). These were chosen due to these exhibiting the best, and well defined, evidence for the most extensive glaciation (i.e., terminal moraines). However, this is limited to the western valley region that may bias the best-fit model. Any more extensive (positive measurement) or less extensive (negative measurement) of ice to the glacial geomorphological evidence was changed to their absolute value, and each measurement summed together. The simulation with the lowest overall mismatch was determined to be the best fit within that suit of sensitivity testing. This enabled the determination of an envelope of climate (ΔT and xP) under which modelled ice extents could exhibit an LLGM ice extent within the Las Huaringas.

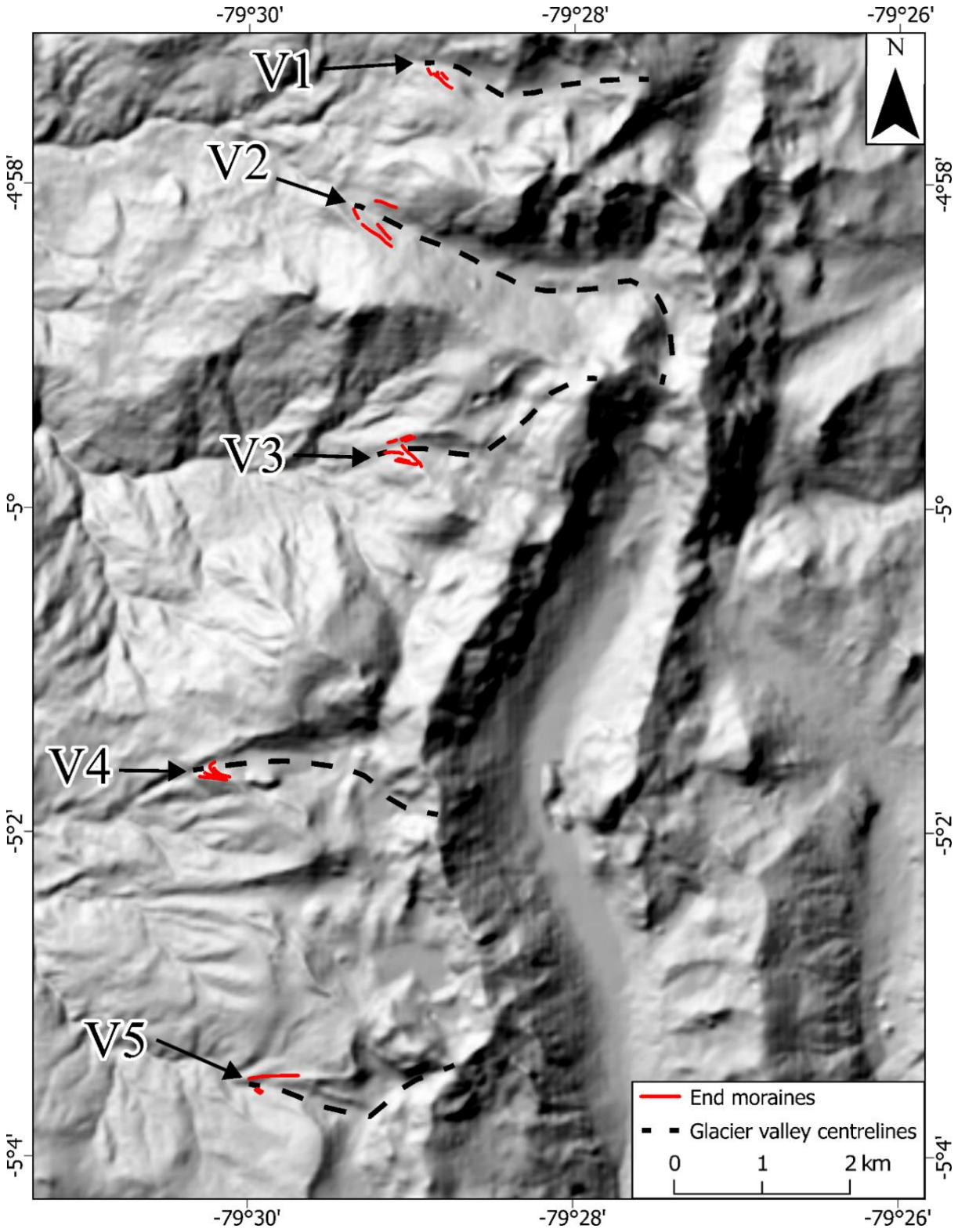

Figure 5.4: Centre line locations with end moraines tested against in order to determine the best fit model for model outputs during sections 5.4.6 and 5.4.8. V1 = Palo Blanco 2, V2 = Palo Blanco 1, V3 = El Ray Inca, V4 = Millionaria, V5 = Negra; names correspond to the columns shown in Appendix D Tables D.1 and D.2.

5.4. Results

5.4.1. Experiment 1 - Model resolution (m)

To conduct this sensitivity analysis, 5 runs were conducted. The model was run at horizontal resolutions of 600 m, 300 m, 150 m, 120 m, and 80 m until the model reached glacier-climate equilibrium (i.e., to changes in area and volume). Resolutions lower than 80 m were not undertaken due to the model runs becoming too computationally expensive and constraints on computational time.

The implementation of differing model resolutions resulted in spatially variable ice mass extent, thickness, and volume in the study region (Figure 5.5). It is important to note just how insufficient the use of coarser resolutions is for the modelling of mountain glaciers. A resolution of 600 m is unable to provide a glaciologically realistic ice extent, with a single pixel able to cover an entire valley width (Figure 5.5). 300 m provides a more extensive glaciation , yet still results in unrealistic ice extents, similar to 600 m with either a singular pixel, or too few pixels to accurately represent valley glacier extent. With a resolution of 150 m or higher, the model can better accommodate variations in mountainous topography, this is clearly shown in the western cirque area where glacial ice extents are constrained within the valley walls (Figure 5.5a). At resolutions of 120 m to 80 m, glacial ice extents do not change that much with the extents overlapping, generally being in close proximity to each other (and to the 150 m resolution output). The only locations where 120 m and 80 m extents do not overlap are in confined valleys where the topography has an important influence on glacial ice extents. Ice thicknesses are variable across model resolutions (Figure 5.6) but appear to decrease as resolution get finer.

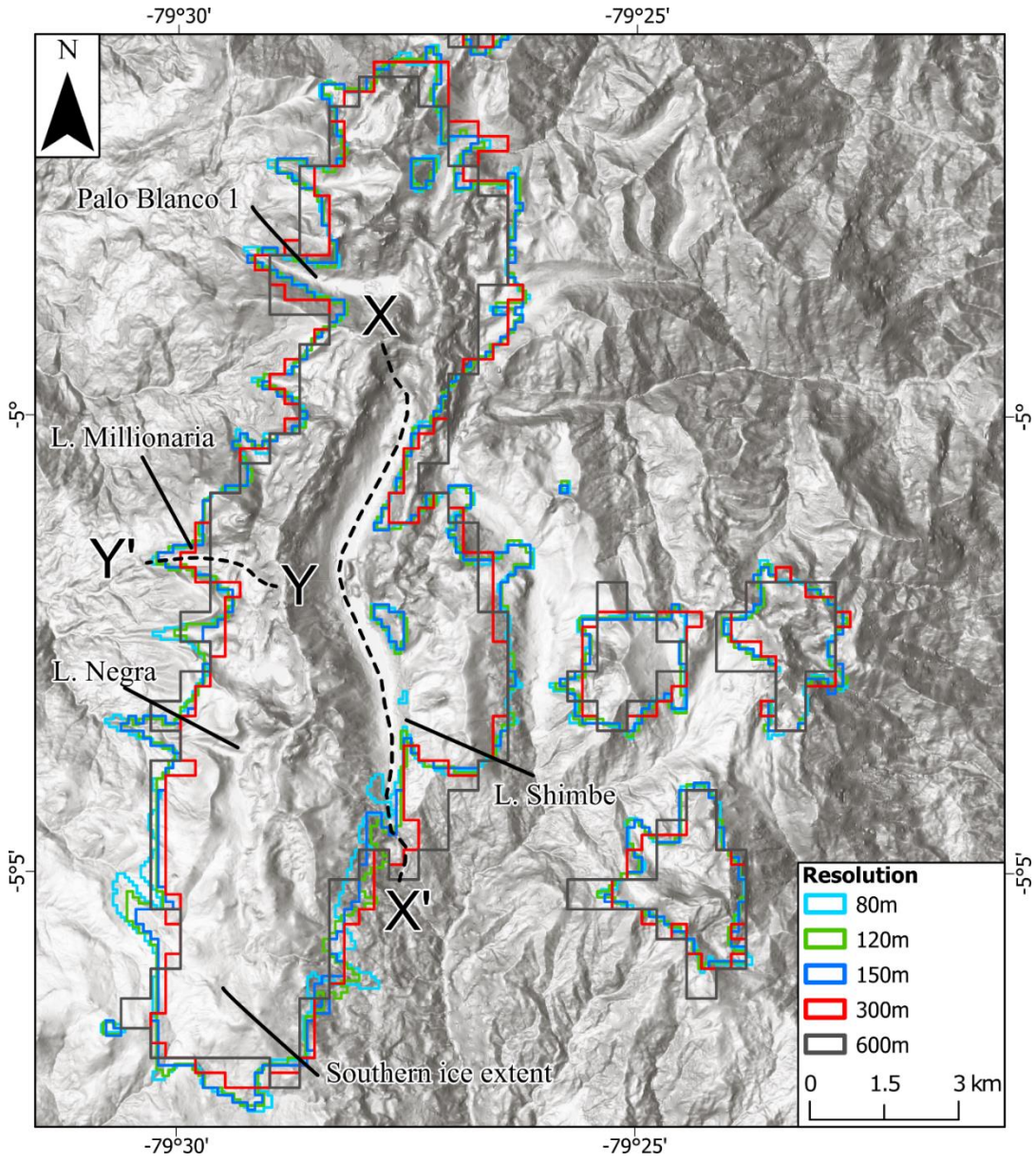

Figure 5.5: Model run output (ice extent) for differing horizontal resolutions for the Las Huaringas region and a) within the western glacial cirques, using the same model parameters and climate (ΔT = -10.5°C and xP = 100%). X – X' and Y-Y' corresponds to the location of the centre line ice thickness profiles in the Shimbe valley in Figure 5.10 and Laguna Millionaria in Figure 5.6.

Within the valley hosting Laguna Millionaria (Figure 5.6) ice thicknesses along flowlines for resolutions of 600 m and 300 m are not glaciological realistic. 600 m is too thin and the extent too limited, while a resolution of 300 m leads to large step changes in ice thickness. These coarser resolutions cannot therefore accurately represent the ice extent, nor the valley-ice interactions, that is the topography is too coarse leading to large step changes in elevation. Model runs at 300 m and higher resolution show that further down valley ice thicknesses increase, corresponding to the overdeepening of Laguna Millionaire. Resolutions at 150 m and higher are more glaciologically realistic with less variation in ice thicknesses between each pixel, resulting in a smooth ice surface. Very similar ice thickness estimates are also produced.

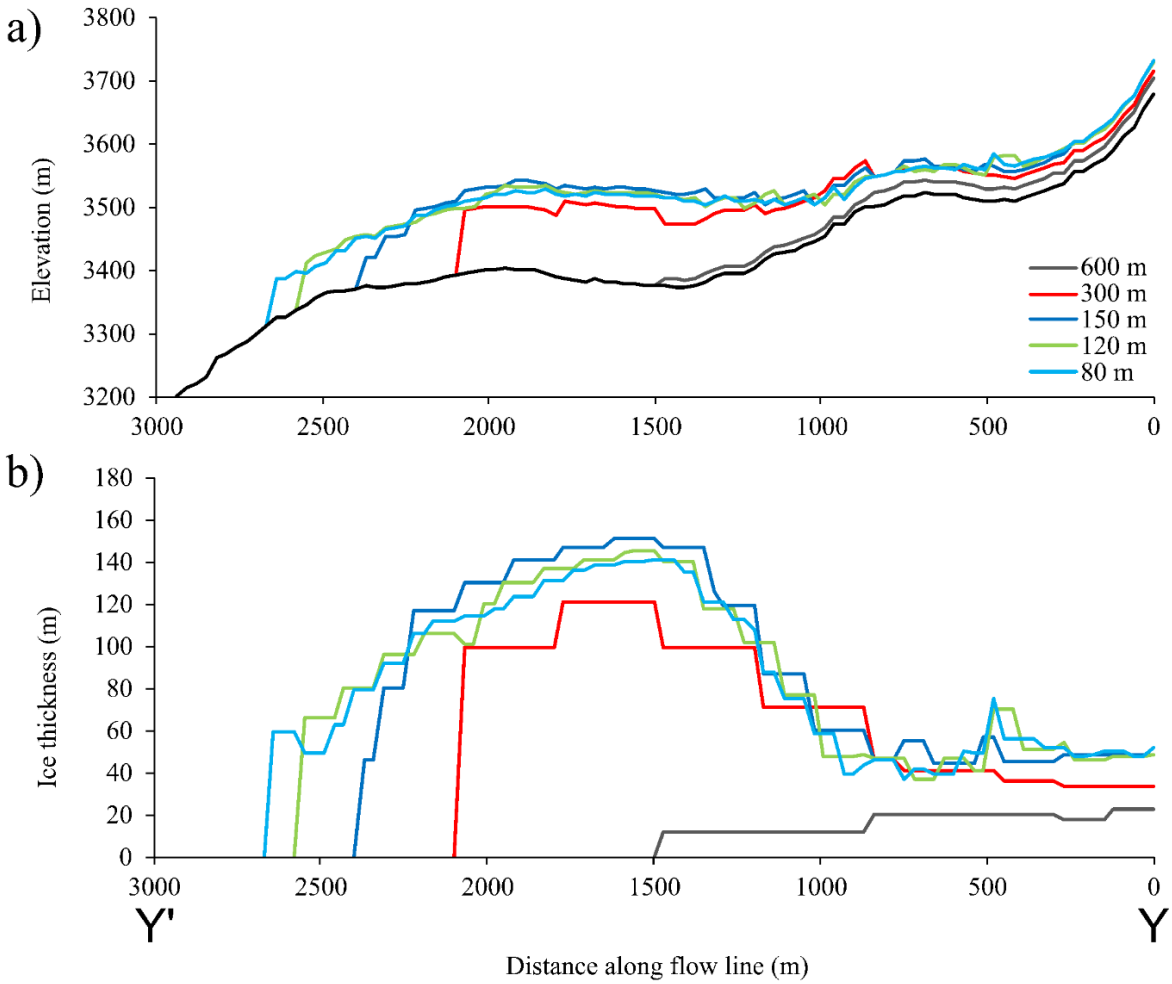

Figure 5.6: Data taken along the flowline (Y-Y') of the glacier situated within Laguna Millionaria along the western cirques (seen in Figure 5.5 a), showing a) ice surface elevation, and b) the ice thickness.

At higher resolutions (i.e., below 150 m), ice is constrained by valley walls, however glacial ice is able to extend further down valley (Figure 5.6), changes become smaller at finer resolutions. While it is outside the scope of this thesis, this may reflect the need for high-resolution 'nested grid' modelling in valleys to reconcile valley-ice interactions. Further, the presence of nunataks, one of which is apparent within the model in the Shimbe valley, only occurred using resolutions of 150 m or less. This further shows that coarse resolutions are unable to accurately consider valley geometry, generating ice extents that are not representative of realistic glaciology.

From the modelled ice mass statistics (Table 5.8 and Figure 5.6), the glacier area (Figure 5.7a) increases, but fluctuates less, as the model resolution becomes finer. As the grid becomes finer and the topography becomes smoother, ice is allowed to extend further down valley, increasing the area. Ice volume (Figure 5.7b) in the 600 m resolution run (5.1 km^3) is larger than model runs at higher resolutions. As the model resolution increases the ice volume decreases, dropping

to 4.7 km^3 at 300 m and remaining at a constant ice volume even at higher resolutions. This is potentially due to less spatially variable ice thicknesses (Figure 5.7c), as the maximum ice thickness drops from 222.4 m and 215.1 m at 600 m and 300 m resolution respectively, to 176.3 m for 150 m, with small decreases in maximum ice thickness thereafter (171.3 m and 165.2 m for resolutions of 120 m and 80 m respectively). Predictably, as the model resolution increases the ice perimeter increases almost linearly (Figure 5.7d) as the increased number of pixels increases the perimeter distance.

Table 5.8: Summary of resolution tests using the model parameters and climate (ΔT = -10.5°C and xP = 100%), also graphically represented in Figure 5.7. Bold indicates the chosen model resolution for subsequent model runs.

Resolution (m) *(Grids)*	Area (km^2)	Volume (km^3)	Maximum ice thickness (m)	Ice perimeter (km)	Compute Time (hh:mm:ss)
600 *(50 x 70)*	94.3	5.1	222.4	121.2	00:04:34
300 *(100 x 140)*	98.7	4.7	215.1	135.0	00:03:28
150 *(200 x 280)*	100.8	4.7	176.3	170.4	00:14:37
120 *(250 x 350)*	**101.8**	**4.7**	**171.3**	**176.9**	**00:29:46**
80 *(375 x 525)*	102.6	4.7	165.2	196.6	13:36:07

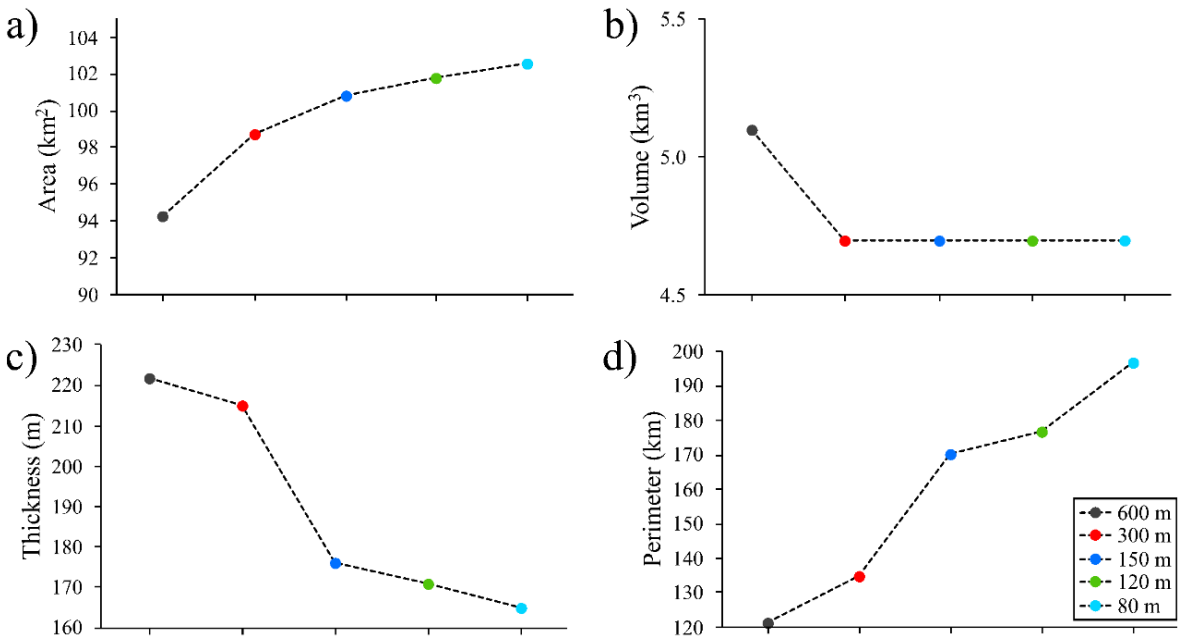

Figure 5.7: PISM ice model resolution tests detailing the difference between a) ice area, b) ice volume, c) maximum ice thickness, and d) ice perimeter.

The modelled glacial ice extents shown in Figure 5.5, the 80 m resolution extends the most downvalley within glacial valleys, thus showing how finer resolutions models provides the most detail to allow more accurate modelling of the glacial-topographical interaction. However, the need for a sufficient model run time is needed, as finer resolutions cause increasingly long model run times (Table 5.8). Thus, the resolution of 120 m was used for subsequent model simulations, including both sensitivity analysis (this chapter) and post-LLGM deglaciation

model runs (Chapter 6). This was due to the variation in modelled ice extent (Figure 5.5), area and volume having negligible differences at resolutions of 300 m and finer (Table 5.8). Within this, for a resolution of 120 m, the computation time was acceptable; a number of model simulations could be computed in a timely manner at this resolution.

5.4.2. Experiment 2 - Degree Day Factors (DDFs)

A range of values were used to evaluate the impact of varying DDF parametrization, generating 30 different model runs. The range covers observed values across the Andes and other tropical regions (Table 5.3), while also allowing values to reflect potential differences in energy flux across millennial timescales. The variation in values, shown in Table 5.9, is greater for DDF_{ice} due to observed values varying more in range due primarily to ice melt occurring within the ablation zone. DDF_{snow} varies les due to snow melt occurring in the accumulation zone which incurs less melt. While it is unrealistic to see values of DDF_{snow} higher than DDF_{ice}, they are still tested here to understand their effects on ice mass generation in the model domain.

Table 5.9: Summary of DDF sensitivity tests using the same model parameters and climate (ΔT = -10.5°C and xP = 100%) at 120 m grid resolution.

km²/km³		DDF_{snow}				
		2	**3**	**4**	**5**	**6**
DDF_{ice}	**3**	362.4 / 18.9	308.4 / 15.4	279.4 / 13.8	258.3 / 12.5	242.2 / 11.5
	5	292.8 / 15.5	221.3 / 11.4	172.9 / 8.4	129.7 / 5.8	94.3 / 3.7
	7	254.0 / 13.9	170.4 / 8.8	91.8 / 3.8	48.7 / 2.0	24.9 / 1.1
	9	233.4 / 13.0	130.4 / 6.6	51.4 / 2.2	18.6 / 0.9	7.1 / 0.3
	11	218.1 / 12.3	98.1 / 4.7	28.2 / 1.3	8.4 / 0.4	2.0 / 0.1

In all simulations, using increasingly higher values of both DDFs, leads to a reduction in the both glacial ice area and volume in the model domain (Figure 5.8). Using increasingly lower DDF values for both (DDF_{ice}; < 7, DDF_{snow}; < 4), leads to increased ice area and volume in the domain. This leads to the occupation of more cirques within the study region, creation of an extensive zone of ice in the southwestern region of the domain, and allows ice to flow down to lower elevations. Interestingly, ice only fills the Shimbe valley at these lower DDF values, and with each stepped decrease in DDF_{ice} and DDF_{snow} leads to increasingly more ice filling and advancing down valley, even to beyond the limits of the model domain. The lowest extremes of DDF values (3, 5 for DDF_{ice}; 2, 3 for DDF_{snow}) result in more ice across the domain, along with a substantial increase in computation time due to more ice needing to be computed within the model domain.

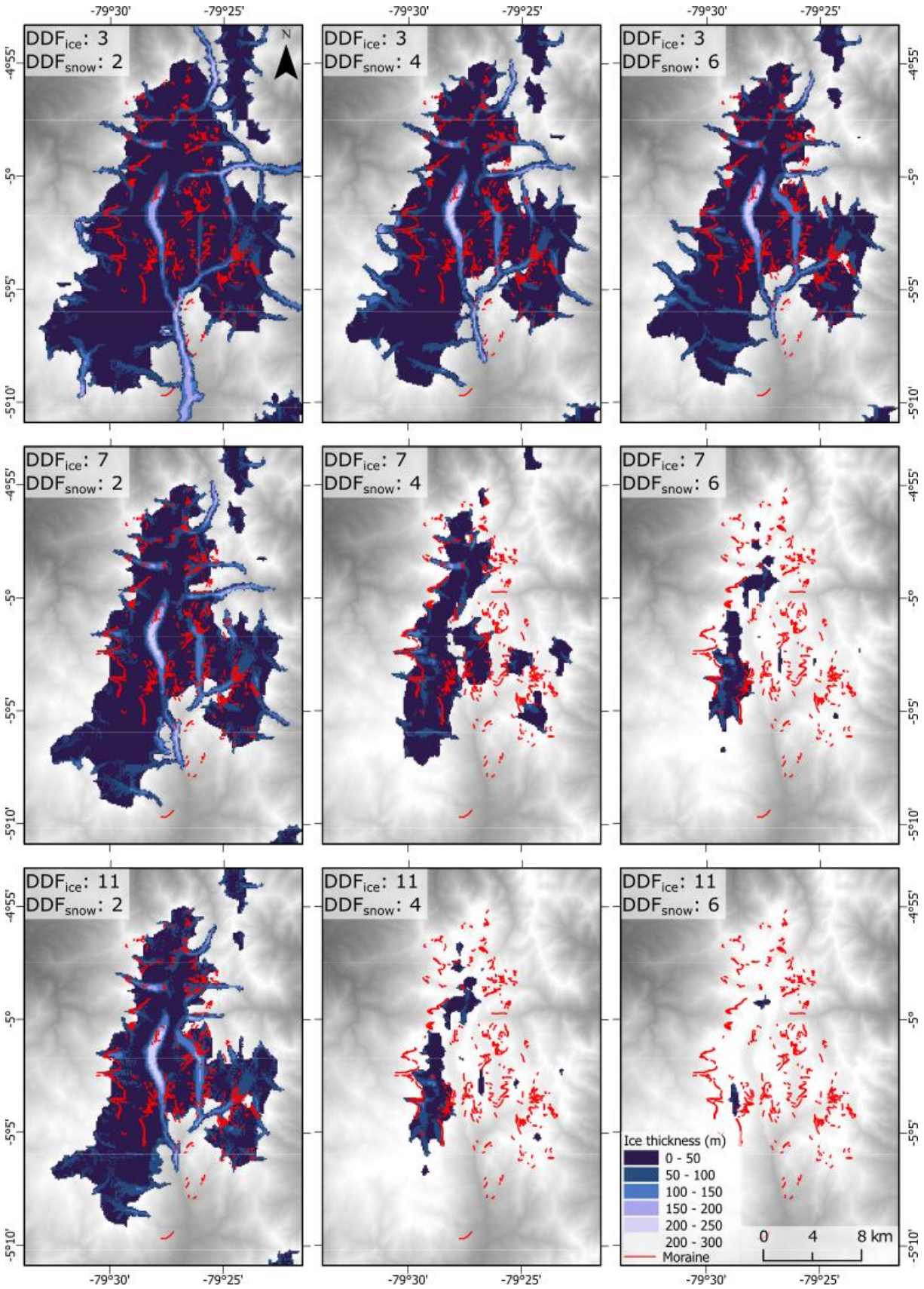

Figure 5.8: Modelled ice thickness using varying DDFs within the PDD model in PISM. Not all DDFs that were used are shown here, a selection is shown to provide an overview on how the model is affected. Across (left to right) increasing in DDF_{snow}, down (top to bottom) increase in DDF_{ice}. Black lines indicate mapped moraines (Chapter 3).

Using the highest DDF values tested, ice primarily comes from two source areas: the headwall area north of the Shimbe Valley, and the high topography above the western cirques (DDF_{ice} = 11 and DDF_{snow} = 6 in Figure 5.8). As DDF values begin to decrease, the ice in these source areas begin to coalesce along the valley tops creating an ice cap with outlet glaciers. Secondary ice caps in the eastern region of the model domain only form at certain DDF combinations (e.g., DDF_{ice} = 7; DDF_{snow} = 4) but are either non-existent at higher DDF values or become fully combined with glacial ice at lower DDF values. At the lowest tested DDF values (DDF_{ice} = 3 in Figure 5.8), these could be representative of periods of extreme glaciation (e.g., pre-LLGM), with interception of valley ice (e.g., Shimbe and eastern valley ice connecting to the south) advancing down valleys over substantive distances. Overall, DDF values hold a large influence over the generation of ice within the model domain.

5.4.3. Experiment 3 - Refreezing ($\theta_{refreeze}$)

During the sensitivity analysis, in order to capture the range of refreezing factors that have been used within the literature, the model was run 8 times using refreezing factors of 0, 0.1, 0.2, 0.3, 0.4, 0.5, 0.6 and 0.7. Values above 0.7 were not conducted due to it being unrealistic for there to be a large amount of refreezing close to 1, or closer to 100% of ice being refrozen after initial melt. Through the model runs, it can be seen that refreezing has an important control on ice mass growth within the model domain (Figure 5.9 and Table 5.10). As the refreezing factor is increased incrementally (+0.1 / +10%), both modelled glacier area and ice volume increase by double the previous model value. Similarly, the maximum ice thickness seen through the model domain increases in-step with the increase in refreezing value, thus increasing the volume.

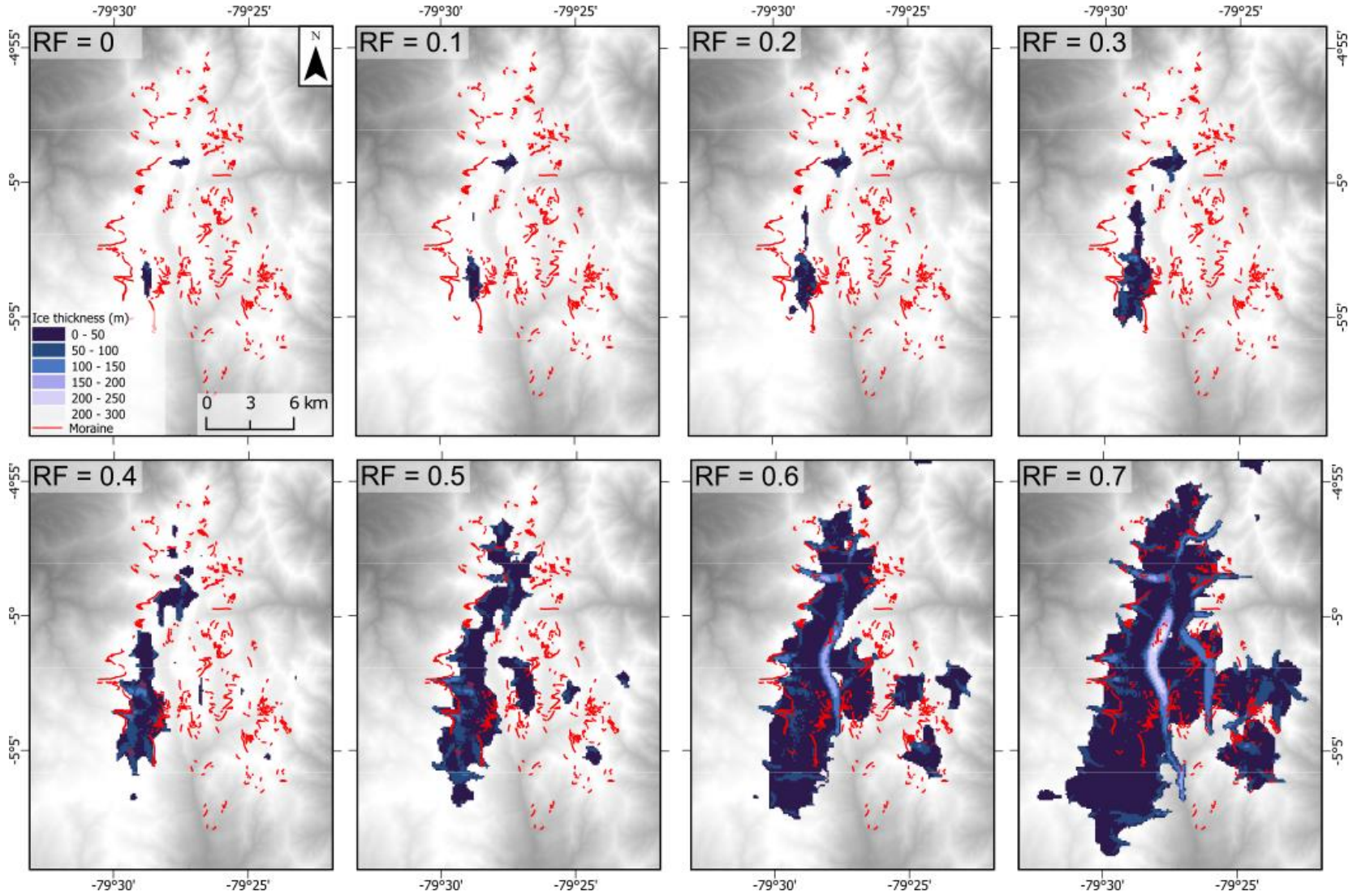

2645 **Figure 5.9**: Modelled ice thickness using varying within the Las Huaringas region due to different refreezing factors, using the same model parameters and climate (ΔT = -10.5°C and xP = 100%) at 120 m resolution. Black lines indicate mapped moraines (Chapter 3).

Table 5.10: Summary of refreezing factor tests using the model parameters and climate (ΔT = -10.5°C and xP = 100%) at 120 m grid resolution.

Refreezing Factor	Area (km^2)	Volume (km^3)	Maximum ice thickness (m)
0	1.7	0.1	80.9
0.1	3.2	0.1	98.4
0.2	6.6	0.3	102.8
0.3	13.3	0.6	116.6
0.4	24.1	1.2	130.0
0.5	51.7	2.3	132.0
0.6	102.6	4.8	172.4
0.7	184.9	9.6	256.9

Between refreezing values of 0-0.4, ice is limited to two localities, the western cirques, and within the most northern confines of the Shimbe valley. This is similar to that shown by the highest DDFs – the two primary locations where ice initially develops or persists within the region (Figure 5.9; RF = 0 – 0.4). This limited glaciation is reflected in the low area and glacier volume values of 1.7 to 24.1 km^2, and 0.1 to 1.2 km^3, while ice thicknesses increase slightly, from 80.9 m to 130.0 m (Table 5.10). At refreezing factors of 0.5 and above, ice begins to expand to other cirques within the model domain with the western valley cirque ice. Ice above the headwall of Shimbe connects with ice in the northern valley and along the valley top to the western glacial cirques, while ice from the valley walls extend down from their cirques, and ice in the eastern valley begins to accumulate (Figure 5.9; RF = 0.5). The increase in refreezing factor from 0.5 (50%) to 0.7 (70%), leads to substantial increases in area and volume of ice (51.7 to184.9 km^2, and 2.3 to 9.6 km^3 respectively) with maximum ice thickness increasing slightly to 132 m (Table 5.10). This increase initiates wider scale expansion of glacial ice (Figure 5.9; RF = 0.6 – 0.7). Ice completely fills the Shimbe valley at a refreezing value of 0.6, and the eastern valley area glaciates when the refreezing factor is 0.7. Maximum ice thickness also shows a stepped increase of 172.4 m for 0.6, and 256.9 m for 0.7 (Figure 5.9 and Table 5.10). This reveals an interesting dynamic of the Shimbe valley, being either almost total devoid of ice in its middle valley section or being completely filled by ice, showing how sensitive ice is within valley settings in the tropical Andes.

Similar to the DDF sensitivity tests, as the refreezing value increases the computation time also increases substantively as more ice is generated within the model domain. This is due to more ice within the model domain needing to be computed for. Overall, refreezing factors hold a large influence over the generation of ice within the model domain and is a value that needs to be taken into consideration for the appropriate computation of glacial ice.

5.4.4. Experiment 4 - Ice rheology enhancement (E)

For E_{SIA} 1 – 5 was used, increasing in increments of 1. for E_{SSA} values of 0.2-1 were used, increasing in increments of 0.2, generating 25 model runs. While this does not account for the higher end of observed values of E, the values used capture the majority of values determined within the literature (Table 5.1), primarily that of former modelling studies.

The steady state results from the E sensitivity tests (Table 5.11) show that using different E_{SSA} and E_{SIA} in varying combinations makes no difference to the modelled ice metrics. Both the area and volume of the reconstructed ice masses are similar throughout the tested ranges of E_{SIA} and E_{SSA}. An increased E_{SIA} leads to slightly lower ice thicknesses (Figure 5.10a). This is due to the increased E_{SIA} leading to softer modelled ice, allowing it to flow more easily, however the overall difference is negligible. This slight variation in ice thickness, however, does not lead to a corresponding difference in ice frontal positions bar internal variations in ice frontal positions in relation to seasonal temperature variations (set by the temperature standard deviation).

Varying E_{SSA} does not cause any difference in ice thickness (Figure 5.9b). While there are minor variations in ice frontal extent of around ~1 km, this can be explained by variations in the mass balance calculations creating fluctuations in the ice margin position between models. There is greater fluctuation in the terminus positions within the largest ice masses (i.e., Shimbe valley), when compared to locations where smaller ice masses develop within the model domain (e.g., western glacial cirques). Overall, the enhancement factors appear to have a negligible impact on the modelled ice extent.

Table 5.11: Summary of E_{SIA} and E_{SSA} used within the sensitivity tests using the same model parameters and climate (ΔT = -10.5°C and xP = 100%) at 120 m grid resolution.

km^2/km^3		**E_{SIA}**				
		1	**2**	**3**	**4**	**5**
E_{SSA}	**0.2**	103.1 / 5.0	103.7 / 4.9	103.5 / 4.9	104.0 / 4.8	104.0 / 4.8
	0.4	103.3 / 4.9	103.4 / 4.9	103.3 / 4.8	103.6 / 4.8	103.4 / 4.8
	0.6	102.9 / 4.9	102.8 / 4.8	102.9 / 4.8	103.3 / 4.7	103.1 / 4.7
	0.8	102.4 / 4.8	102.6 / 4.7	103.0 / 4.7	103.1 / 4.7	103.1 / 4.7
	1	102.6 / 4.8	102.7 / 4.8	102.5 / 4.7	102.7 / 4.7	102.9 / 4.7

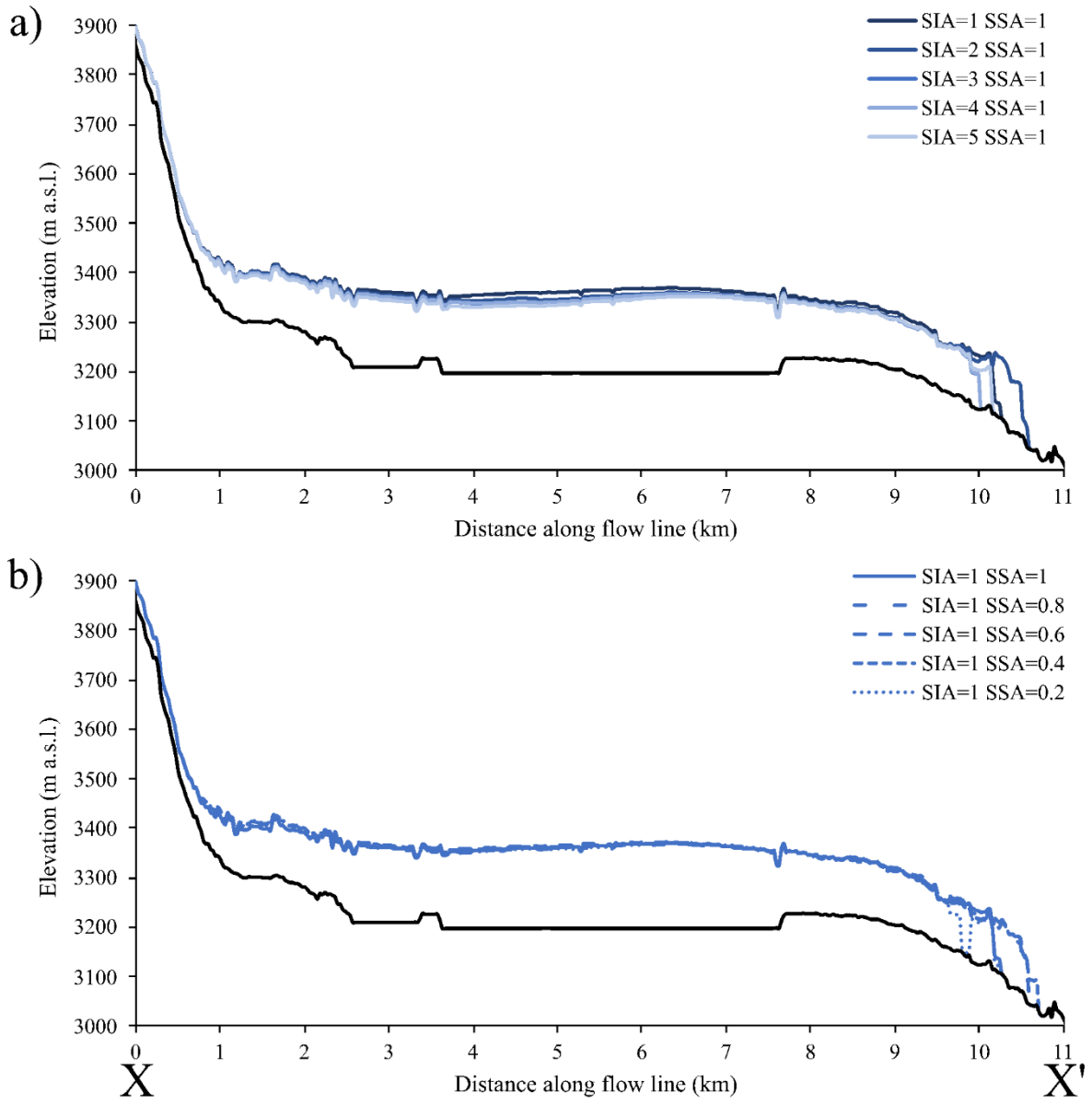

Figure 5.10: PISM ice model ice surface profile and ice thickness under ΔT = -10.5°C and xP = 100% using differing a) E_{SIA}, and b) E_{SSA}, along the centre line (X – X') in the Shimbe valley (Figure 5.4), basal topography (black line).

5.4.5. Experiment 5 – Sliding power law (*q*)

For the sensitivity tests here, values between 0 and 1 were used and increased in 0.25 increments resulting in 5 different model runs with all other parameters unchanged. These values reflect the range of values that have been used in other modelling studies (Table 5.2) that have used PISM.

The steady state results of the sensitivity tests for *q* (Table 5.12) show that as *q* increases, the modelled ice area and volume decreases slightly with each run, while maximum ice thickness gradually increases. The slight decrease in area and volume can potentially be explained by the

increased basal ice speed, and therefore mass flux, that causes ice to advance further downvalley. This extends the ice margin to lower elevations so that it then becomes more susceptible to the surrounding climate, and ablation occurs. The increase in maximum thickness for each model run, while area and volume decreases, is the opposite to that identified by Candaş *et al.* (2020). However, when looking at the thickest ice on some of the most prominent glaciers in the model domain (i.e. those shown in Figure 5.11), the thicknesses either decrease very slightly for the smallest glaciers, or remain the same or similar for the largest glaciers (i.e., Shimbe glacier). Albrecht *et al.* (2020) shows higher *q* led to thinner ice thicknesses. However, this was for ice sheets, which are more controlled by their basal sliding and ice streaming than valley glaciers.

Table 5.12: Summary of *q* values used within the sensitivity tests, using the same model parameters and climate (ΔT = -10.5°C and xP = 100%) at 120 m grid resolution.

q	**Area (km^2)**	**Volume (km^3)**	**Maximum ice thickness (m)**
0	102.7	4.8	170.8
0.25	101.9	4.7	173.0
0.50	101.2	4.6	176.9
0.75	100.0	4.6	176.7
1	99.3	4.5	177.0

Across the model domain, as values of *q* increase, there is a mixture of increases or no change in the basal ice velocities that are modelled (Figure 5.11). Within valley glaciers that extend extensively downvalley, as *q* increases the ice velocity increases either dramatically, as seen at the end of the Shimbe glacier (Figure 5.11d), or increases gradually seen at the end of the Palo Blanco 2 (Figure 5.11b) (Albrecht *et al.*, 2020). However, for smaller glaciers that do not extend as extensively downvalley (e.g., smaller cirque glaciers in the eastern valley), there is no increase, or a negligible increase, in the basal ice velocity magnitude identified (Figure 5.11a&c). This could be a result of the small scale of the glaciers, and basal sliding not being a major influence on smaller ice bodies. As these glaciers are relatively thin, they are more likely to be frozen to the bed.

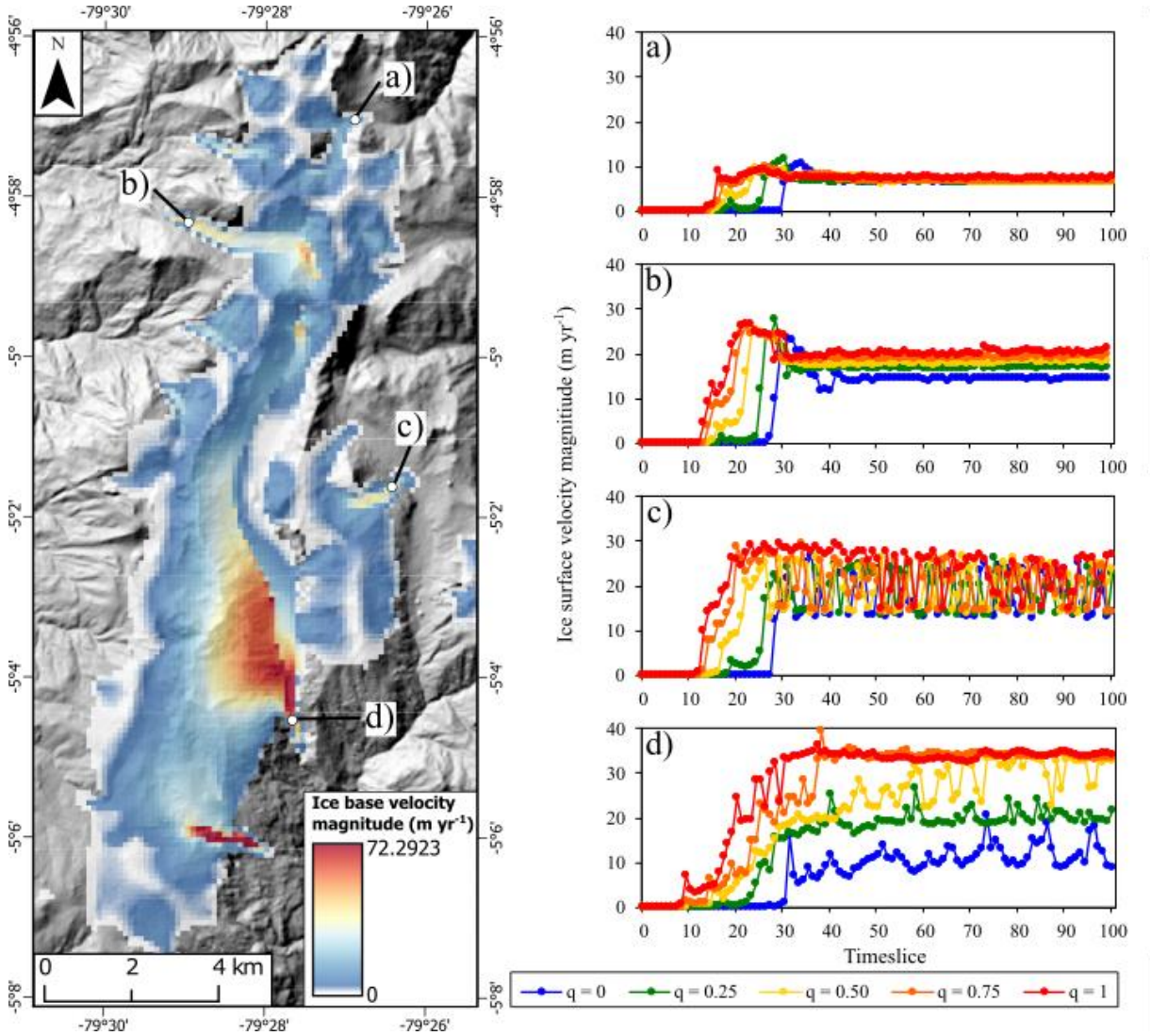

2735 **Figure 5.11**: PISM ice model basal ice speeds under constant climate (ΔT = -10.5°C and xP = 100%) with graphs detailing temporally variable ice surface velocity magnitude at four-point locations shown as a), b), c), and d), over the model run with their sampling locations identified within the map.

In all sampled regions, as *q* increases basal sliding activates earlier and ice flow speed increases 2740 rapidly. Across the model domain, there are negligible differences in ice extent, using different *q* values, similar to the findings of Candaş *et al.* (2020). Differences in area are of more importance for the criteria of the best-fit model, while volume, ice thickness, and basal ice velocities are of least importance. Overall, the sliding power law *q* values are not enough to impact ice generation or persistence in the model domain.

2745

5.4.6. Experiment 6 - Degree Day Factors (DDFs)

When running the multi-parameter DDF sensitivity analysis, too little, or no ice is generated within the model domain across almost all model runs at temperatures higher than ΔT -9.5°C, irrespective of the DDF value. Thus, no model that was run 'warmer' than this ΔT was able to

reach the mapped maximum glacial extents. It is therefore unlikely that modelled ice will extend to maximum mapped ice limits using the ELA-derived temperature cooling calculated in Chapter 3 (Lee *et al.*, 2022) (i.e., -6.5 to -8.8°C). The only way this could be achieved would be if unrealistic DDF values were used (i.e., beyond those in Table 5.5). Temperatures lower than -9.5°C offset from present resulted in the accumulation of glacial ice in the model domain.

When the temperature within the model domain is decreased by a further 0.5°C (i.e., from -9.5 to 10°C), the ice area increases by between 57% to 146% (average 96%) across all DDF runs. This is greater than the increase in area generated by a 10% increase in precipitation, which leads to an increase of glacial area of between 9% to 102% (average 32%) across all DDF runs (seen in Figure 5.12). As the precipitation fraction is increased further, the difference seen in the modelled ice area compared to the previous model run (e.g., xP 1.0 vs. xP 1.1), decreases (seen in Figure 5.12). The same trend is apparent with a decrease in temperature; the colder the climate is with each model run, there is a decrease in the relative amount of change compared to the previous temperature change (e.g., ΔT -9.5 vs -10) (seen in Figure 5.12). This is expected as smaller glaciers are more sensitive to climate and thus small temperature fluctuations can cause larger changes in small glaciers, while larger glaciers are more resistant to temperature changes. For example, doubling the area of a small glacier is relatively easy, requiring little additional cooling, while doubling the size of a much larger glacier requires much more cooling.

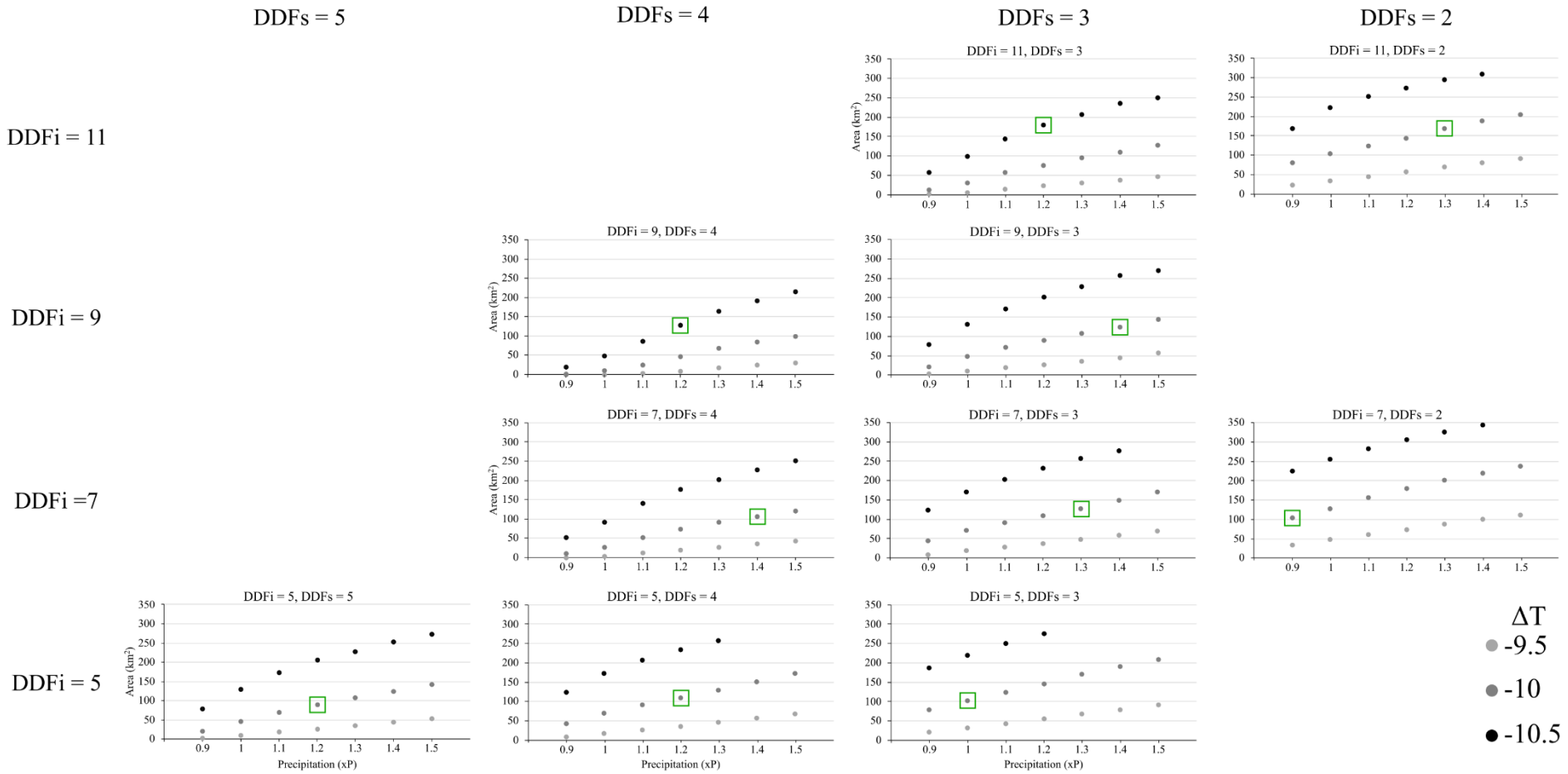

Figure 5.12: Multi-parameter sensitivity analysis for DDFi and DDFs, with the modelled ice area against precipitation fraction (xP) and temperature offset (ΔT). No dot represents modelled ice was too much and calculations diverged. Green boxes represent best-fit in valleys shown in Figure 5.4, and selected best fit model runs are shown in Appendix Figure D.1.

As the DDF_{snow} and DDF_{ice} are decreased, the percentage difference in area changes decreases, similar to that seen when temperature is decreased, or precipitation is increased. In absolute terms, by decreasing the DDF_{ice}, the modelled ice area increases with the same climate input. The same is noted for a reduction of the value of DDF_{snow}. With individual value increases in DDF values, the largest influence on glacial ice growth is from DDF_{snow}. On average, an increase in the DDF_{snow}, while keeping DDF_{ice} constant, results in an increase in ice area of between 5-50%. If DDF_{ice} is increased and DDF_{snow} is kept constant, an increase of ice area between 12-32% results. Lastly, as the DDF_{ice} and DDF_{snow} values area decreased, the difference seen in the increase in glacial ice area between each previous model run becomes smaller.

An important finding within this sensitivity analyses is the sensitivity of ice mass expansion to differing climate offsets. For example, within the Shimbe valley, glacial ice is rarely within the middle sections of the valley for an extended period of time; the Shimbe valley floor is either almost entirely devoid of glacial ice, bar along the western valley walls and near the headwall, or the valley becomes fully glaciated with an ice margin near the end of the valley. This leads to potentially large 'step changes' in the area and volume of glacial ice generated between model parameters which cause the ice mass to 'tip' from one steady state to another (i.e., very limited or very extensive ice within the Shimbe valley). This is not seen in smaller valley constrained glaciers, such as those within the western glacial cirques where more gradual glacier expansion occurs in response to temperature and precipitation increases, and to decreasing DDF values.

5.4.7. Experiment 6 - Best-fit models

When DDF values were varied in combinations with differing steady state climate scenarios, across all model runs a ΔT of -10°C generated the majority of the best-fit extent (green boxes in Figure 5.12), that reached the observed maximum ice extents most frequently. Of these, the majority of the determined best-fit models had a xP (precipitation above modern day) of between +10% and +40%. This demonstrates that a much cooler temperature alone is insufficient to generate a modelled ice mass of an appropriate size to reach the maximum mapped extents; a wetter climate is also required (Clapperton *et al.*, 1997a; Fritz *et al.*, 2004; Chepstow-Lusty *et al.*, 2005). All model runs using a range of DDF values, along with their area, volume and their measured horizontal offset to the mapped moraines are available in Appendix D Tables D.1.

Model runs with the lowest offset of evidence (Figure 5.4) to generated ice extent, were selected as 'best-fit'. Within the four valleys used for this assessment, the model with the determined best fit (lowest absolute offset) does not always result in all four measurements returning the lowest measured offset. This asynchronous nature of glacial advance reaching their maximum extent is commonly attributed to variations in valley topography (Pratt-Sitaula *et al.*, 2011).

Due to the paucity of long-term mass balance datasets on tropical glaciers, it is almost impossible to determine what realistic DDF_{ice} and DDF_{snow} values would be for tropical glaciers. Loomis *et al.* (2017) in the tropical Africa, and Kageyama *et al.* (2022) across the American Cordillera, both detailed how lapse rates on land were steeper during their regions LLGM than they are at present. Varying the lapse rate within the model domain is beyond the scope of this thesis, due to a) it is unknown what the lapse rate would have been during the LLGM in this area, and b) varying the lapse rate would add additional complexity to the model sensitivity experimentation. It is realistic to assume that a lower lapse rate would lead to lower then modern DDFs. This suggests that it is unrealistic to implement DDFs that reflect the modern regional climate, such as those obtained by Maisincho *et al.* (2016) and Blard *et al.* (2011).

5.4.8. Experiment 7 – Refreezing factor ($\theta_{refreeze}$)

Across all model runs with varying refreezing factors (Figure 5.13), when using a ΔT below -9°C, no or very little ice was generated within the model domain, even while using the highest chosen realistic value of 0.7 (70%) refreezing. Using any ΔT higher than this, with refreezing values within realistic values, would not generate glacial ice extending to the maximum ice mass limits. It is unlikely that the ELA-derived temperature cooling estimates from Chapter 3 would enable the maximum mapped ice limits to be reached by the modelled ice.

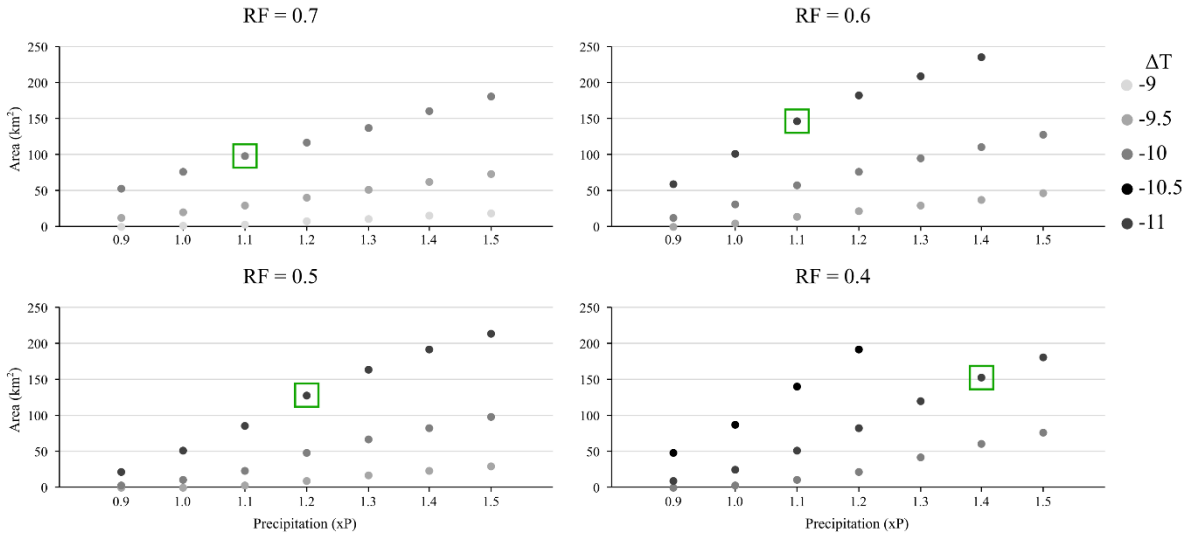

Figure 5.13: Multi-parameter sensitivity analysis for refreezing, with the modelled ice area against precipitation fraction (xP) and temperature offset (ΔT). No dot represents modelled ice was too much and calculations diverged (model errored out). Green boxes represent best fit and best fit model runs are shown in Appendix Figure D.2.

For the refreezing fraction test, using temperatures that result in ice accumulating within the model domain, decreasing ΔT by 0.5°C has a greater effect on the modelled glacial ice extents than a 10% increase in precipitation, leading to an average increase of 62.4 km^2. An increase in temperature by 0.5°C (i.e., from -9.5 to -10), when precipitation is kept constant, leads to between a 144% and 91% (average of 117%) increase in glacial area across all refreezing fraction runs (seen in Figure 5.13). When precipitation is increased by 10% (i.e., xP 1 to 1.1), and temperature is kept constant, there is a 20-97% (average of 44%) increase in glacial area.

As the refreezing factor decreases/increases by 0.1 (10%), whilst ΔT is kept constant, the amount of glacial ice decreases an average of 19.9 km^2, as already determined in the initial sensitivity tests (section 5.4.3.). However, the amount of change decreases as the refreezing faction is reduced, from a decrease of -47% in glacial area between refreezing values of 0.7 and 0.6, to -43% of change between 0.6-0.5, and a -43% difference between 0.5 and 0.4 (seen in Figure 5.13). This is all for a ΔT of -10°C, which is the only temperature that could grow ice realistically across all refreezing factors. This decrease in area change percentage between refreezing factors is the same across ΔT, which is expected as ice area decreases; there is less ice to be melted, and the ice masses are restricted to higher elevations, so they retain mass much more easily (i.e., ablation is reduced).

5.4.9. Experiment 7 - Best-fit models

While refreezing fractions were varied with differing steady state climates (Figure 5.13), across all model runs a ΔT -10.5°C resulted in the best-fit model with modelled ice extending to the observed maximum mapped limit most of the time. The majority of the best-fit models also used a xP of +10%, although this varied between +10% and +40% of modern precipitation. Therefore, for all model runs, for glacial ice to extend to the maximum observed ice extents, climate would need to be wetter than present. All model runs for varied refreezing fraction values, along with their modelled ice area and volume, and their measured horizontal offset from the mapped limits, are available in Appendix D Table D.2.

Like DDFs, there are very few studies globally, and more so none over tropical mountain glaciers, that detail the amount of refreezing that occurs on and within glaciers (Marshall, 2021). This makes it impossible to determine a 'correct' parameterisation of refreezing within numerical models of glaciers. Many models parameterise refreezing differently, with some using no refreezing at all (e.g. Seguinot *et al.*, 2018; Martin *et al.*, 2022), or using differing values for refreezing (shown in Table 5.4) (e.g. Candaş *et al.*, 2020; Yan *et al.*, 2023). It would be unrealistic to assume that refreezing should be negated from glacial models, due to refreezing being an important factor in the mass balance of glaciers (Cuffey and Paterson, 2010; Østby *et al.*, 2013), in-particular glaciers within the tropics.

5.5. Discussion

5.5.1. Model parameterisation influence on glacial ice growth

This chapter detailed the sensitivity testing of the PISM model within a tropical Andean setting. While PISM has been used within South American before, it has only been used within Patagonia (Martin *et al.*, 2022; Yan *et al.*, 2022), never in the tropical Andes. This leaves very little understanding on how PISM, and its variables, can affect the growth of ice within a tropical setting. Using the 5 variables that are used within the literature, sensitivity testing determined that the model resolution (m), DDFs, and the refreezing factor ($\theta_{refreeze}$) greatly impacted ice generation, excluding inputted climate offsets.

The resolution of the model plays a critical role in determining the complexity of the topography, which in turn influences the movement of glacial ice through the valley system. Of importance is the computational cost of model runs, and how this external factor can dictate the model resolution. Previous studies have shown that coarser grid sizes are inadequate in accurately capturing valley-ice interactions, primarily due to the sudden changes in elevation between adjacent grid cells (Golledge *et al.*, 2012). Therefore, a model resolution that can

efficiently and effectively capture the necessary level of detail in modelling the movement of glacial ice through the valley system is required. Accordingly, a resolution of 120 m was deemed suitable, as it allowed for greater detail in topography and resulted in more accurate modelling of glacial ice movement through the valley system. Variations in the modelled ice area and volume were negligible at resolutions of 300 m or finer, while still being computationally efficient and within acceptable limits. While finer resolutions would lead to a more accurate representation of ice-topographical interactions, it would lead to much longer computational time. Therefore, using 120 m resolutions makes this study one of the finest resolution ice mass modelling studies conducted within the tropical Andes when compared to other modern modelling studies in across the Andes (e.g., Leger et al., 2021; Yan et al., 2022).

DDFs and the refreezing factor greatly impact the modelled ice area extensively (Braithwaite, 1995; Hock, 2003) and need to be considered carefully, otherwise the model may not be representative of the regional dynamics. The DDFs dictate the amount of ice and snow melt for each PDD within the model. Using larger DDFs create less ice as there is increased melt, while smaller DDFs leads to decreased melt increasing overall accumulation. This is similar to that found by Martin *et al.* (2022) within the Monte San Lorenzo ice cap in the Patagonian Andes (high latitudes), DDF_{ice} impacts the growth of modelled ice less than an increase in DDF_{snow}, due to snow primarily occupying the ablation zone and being less susceptible to melting, while ice within the accumulation zone has an increased susceptibility to the surrounding warmer climate, and ice is important for the sustainment of the glaciers. Within the literature there is little consensus of the values used due to DDFs being determined by the local climate, and any observations of DDFs at the local level (glacial or valley) being limited. Modelling studies use either observed values where available (e.g. Golledge *et al.*, 2012) or determine their DDFs from best fit models (e.g. Ziemen *et al.*, 2016). Further, detailed in Mount Dedegöl in south-west Turkey, with a change in ±10% of DDFs reflecting a -11% and +13% changes in glacial area (Candaş *et al.*, 2020). There are no DDFs determined for this study area, nor in locations surrounding the study region, and thus the DDFs were fitted to our model using the mapped geomorphology as a control on ice mass size.

The refreezing factor ($\theta_{refreeze}$) determines how much ice, after melting has occurred, is refrozen to the surface of the glacier (Wright *et al.*, 2007; Cuffey and Paterson, 2010). It is suggested in this thesis that refreezing may be an important factor in controlling the mass of tropical glaciers. Due to the tropic's high diurnal temperature variance throughout the year, refreezing of melted ice can frequently occur when temperatures are lower in the evenings, thus influencing the glacier mass balance. Higher refreezing values result in more melted ice becoming refrozen,

and increasing glacial ice area and volume, while *vice versa* with lower values. In south-west Turkey, deviation of the refreezing factor ±0.1 from the default of 0.6 led to a 500 m difference in ice margin extent (Candaş *et al.*, 2020). Similar to DDFs, there is little consensus on what values are used, either they are from observations (Braithwaite *et al.*, 1994), mass balance models (Ritz, 1997), or determined via fitting the model to the refreezing factor. Many modelling studies use values of 0.6 (Candaş *et al.*, 2020; Žebre *et al.*, 2021; Köse *et al.*, 2022) or 0 (off) (Seguinot *et al.*, 2018; Martin *et al.*, 2022) with few using values in between. Similar to DDFs, there is no observation data of refreezing factors within the tropics. Due to this, the refreezing value used by other palaeo-modelling studies within valley system settings will be used. Due to it being unreasonable that freezing would not occur (0), a value of 0.6 will be used, in accordance with Candaş *et al.* (2020).

Other than the refreezing factor and DDFs that were determined via the sensitivity tests, the chosen climate will have the greatest impact on modelled glacial ice within the study area. With this better understanding of how these selected parameters impact the growth of glacial ice within the study region, the final model 'set-up' can now be designed. The last two variables to be tested are the use of stepped cooling and precipitation changes that will aid in understanding the potential climate needed to build ice to the maximum mapped extents (Chapter 3). The majority of the variables that have not been tested will reflect already noted constants within the glaciological literature, and those that have been used with the majority of other PISM modelling studies (Seguinot *et al.*, 2018; Candaş *et al.*, 2020; Köse *et al.*, 2022; Martin *et al.*, 2022).

5.5.2. The best-fit model to the hypothesised regional LLGM extent?

The understanding of the most influential model parameters allows an appreciation of how accurate the model is in representing the modelled glacial ice, when measured against the observed evidence of ice extent (terminal moraines in Figure 5.4). This can now provide a further understanding of the parameters that require additional study for determining the best-fit parameters for subsequent time transient model in the next Chapter. What also needs to be considered is the difference in the climate that would have been present during the regions LLGM, and how this would impact the chosen parameters, as these will not be the same as those seen today (Loomis *et al.*, 2017; Kageyama *et al.*, 2022).

The selected DDFs utilised for further sensitivity analysis represent values that are within the confines of those identified within current day glaciological literature (e.g., Anderson *et al.*,

2006; Blard *et al.*, 2011; Maisincho *et al.*, 2016). These are potentially realistic for what may have occurred during the regions LLGM in the tropics but there is no evidence for DDF values that accurately represent climate during the regions LLGM. The parameters of DDF_{ice} (5 mm w.e. d^{-1} °C to 11 mm w.e. d^{-1} °C) and DDF_{snow} (5 mm w.e. d^{-1} °C to 3 mm w.e. d^{-1} °C) were varied across all models runs, similar to the previous tests, but with the addition of differing steady state climates. This range was informed also by DDF values used in other modelling studies, however these come from extra-tropical locations such as Turkey (DDFice: 8, DDFsnow: 3; Candaş *et al.*, 2020), Croatia (DDFice: 8.8, DDFsnow: 3.3; Žebre *et al.*, 2021), and the Juneau Ice Field (DDFice: 10.5, DDFsnow: 4.0; Ziemen *et al.*, 2016). Throughout all model runs, the temperature cooling that incurred the best-fit was a ΔT of -10°C, while -10.5°C incurred some best-fit models using higher DDF values. This is much cooler than the temperature cooling estimated by Chapter 3 in section 3.3.7. using ELA depression and ATLR alone, which no other study as attempted to compare to before. This may be due to only being able to take into account temperature cooling, rather than precipitation as well.

Similar to the DDFs which were selected further sensitivity analysis, the refreezing factor values were selected to be in line with potential realistic values identified within the literature (Braithwaite *et al.*, 1994; Ritz, 1997; Jiang *et al.*, 2010). Values between 0.4 (40%) and 0.7 (70%) of refreezing were used with a varying climate. Identified by analysing model runs to determine the best-fit models within each used refreezing factor, a temperature cooling of -10.5°C resulted in the best-fit model. While a wetter climate was needed in all scenarios to generate a glacial extent in line with the observed geomorphology (Chapter 3) (Lee *et al.*, 2022). Although lower refreezing factors required a xP of 140%, this still provides confidence that a wetter climate is required.

5.5.3. Climate envelope for regional LLGM glacial extent

A climate envelope can be determined from the best fit models. The required xP, or modern precipitation modification, needed for the best-fit model within the sensitivity analysis varied between +10% and +40% of present-day precipitation (DDF: +10-40%, refreezing: +20-40%). This is while requiring a temperature offset of between -10°C and -10.5°C. This provides confidence that, within the model, to obtain glacial ice to the regions LLGM extents, along with all varied DDFs and refreezing parameters, a wetter climate is needed along with a cooler climate. This finding is in line with studies from surrounding regions in Perú and Bolivia, indicating that the climate was wetter than present in the topical Andes during the LGM (Rodbell, 1993b; Baker *et al.*, 2001b; Fritz *et al.*, 2004). Some studies across the northern Andes

have indicated a drier period in parts of the northern Andes (Heusser and Shackleton, 1994; Vélez *et al.,* 2003), which could be a possibility depending on the glaciological variables chosen, as there is at least one model run that reached its best-fit extent with 90% of present day precipitation.

The indicated increase in precipitation may have been facilitated by the zonal low-level flow of moisture being able to more impinge on the Andean mountains (Vizy and Cook, 2007). This would then generate the potential increase in precipitation seen during the regions LLGM even though there was potentially a drier Andean Amazon that provides a large amount of evapotranspiration for modern day precipitation. This cannot be confirmed from the model however, it can only indicate a wetter climate. Evidence for this, extra to the model, is that there has been a number of studies to determine a similar amount of precipitation in the northern Andes (Novello *et al.*, 2017), or wetter climate in the Peruvian Andes (Baker *et al.*, 2001b). This get this increase in precipitation, while the source of moisture (the Amazon) is mostly represented as being dryer in the ecological record (Novello *et al.*, 2019), is this enhanced zonal low-level flow to more easily allow precipitation to occur over the Andean mountains (Vizy and Cook, 2007).

5.5.4. Parameters for the growth to, and deglaciation from, regional LLGM model run

For modelling advance to, and deglaciation from, the maximum mapped extents, the above best-fit parameters have been used to inform the model parameterisation. The DDFs that will be used are a DDF_{ice} of 7 mm w.e. d^{-1} °C, and a DDF_{snow} of 3 mm w.e. d^{-1} °C, with a refreezing factor of 0.6 (60%). These values are similar to other palaeo modelling studies, however they are primarily extratropical (Candaş *et al.,* 2020; Köse *et al.,* 2022). Using these parameters in combination with both default parameters, and those that have been informed by the literature. This yielded a climate needed to reach the maximum mapped ice extent would be a ΔT of -10°C, and a xP of 1.3 (+30%).

Within that ΔT of -10°C and xP of +30%, there is inherent variability in what the actual climate was like. The climate offsets determined are only indicative of a steady state scenario, as in-reality climate will never be steady at -10°C for prolonged periods of time, but rather reach such temperatures at multiple points during the last glacial period, going above and below that temperature. Thus, this climate is used, not to be inputted into the proceeding model runs, but to inform our choice of the broad climate forcing input going forward. Chosen climate forcing inputs for time varying modelling are discussed in section 6.3.2.

5.5.5. Limitations and further considerations

While the chapter here has presented the justifications for, and testing of, differing parameterisation of PISM, there are still aspects that limit the use and understanding of the glacial dynamics that can be provided from the model. The climate forcing parameters demonstrate how sensitive glacial ice may be to change, primarily in temperature and precipitation. Within this chapter, broad approximations are used with the change in temperature cooling, using 0.5℃ intervals, and 10% intervals with precipitation. There is the potential to fine tune the best fit models by using smaller increments in temperature and precipitation to allow ice to align exactly with the mapped maximum ice limits. Further, the modifying of precipitation patterns that best reflect the regional level precipitation distribution may also aid in fine tuning the model outputs. This, however, will incur further computation time to change the climate input, and run the models to steady state, while having limited understanding of the regional precipitation pattern due to limited palaeo data. This type of parameterisation is outside the scope of this chapter, and the broad strokes used here provide the potential climate envelope conditions to enable realistic glaciation.

To best represent the glacial ice and its interaction with the topography, it may be advantageous to use the highest model resolution possible. Resolution use is limited by two factors; the first being the datasets used (e.g., the ALOS DEM) has a horizontal resolution of 30 meters, and second, the computation time. While a resolution 120 m will inevitability still have unresolved topographical issues that will limit a true representation of the subglacial topography, and thus ice-topographical interactions, it presents the best representation with the least-costly computation time. In the future, as computation technology improves, it may be possible to use increasingly lower resolutions to best resolve ice-topographical interactions and stressors.

Lastly, it should be noted that the valleys used to determine the best fit models, may introduce some bias in the chosen models. These valleys being on the western side (known as the western glacial cirques), were chosen due to this region incurring the best terminal evidence of the most extensive glacial advances. The location may incur slight differences in climate, with differing precipitation patterns, and due to being primarily valley based, may have differing topo-glacial interactions compared to the rest of the region. They may cause the required temperature and precipitation offsets to be slightly different, compared to if further valleys outside of the western glacial cirques' region were considered. However, it is likely these would only cause minor differences, and thus are unlikely to change the required model parameterisation and chosen climate.

5.6. Chapter summary

This chapter presents the outcomes of five experimental runs of PISM model to understand the impact of model parameter inputs and values on glacial ice growth. The selection of chosen parameters was based on their significance in both the construction and maintenance of glacial ice within the model, as well as their prevalence and variability within the existing literature. These resulted in a total of 468 model runs; 68 model runs for the first sensitivity test experiments that were used to determine the most impactful model parameters. A further two experimental runs were conducted using the most influence parameters (DDF and refreezing factor) along with variation in the climate forcing, generating a further 350 model runs. The summary of outcomes of this chapter are:

- Experiments 1 to 5 show that model resolution (m), degree-day factors (DDFs), and refreezing factor ($\theta_{refreeze}$) exert a large influence on the model's output of simulated ice.
- From preliminary model runs, it has been determined that glacial ice within the model domain is very sensitive to temperature. Of particular interest is the Shimbe valley, where glacial ice within the valley either covers the entire valley or is very limited to up valley parts only.
- From the best-fit model analysis conducted above, varying the most impactful parameters with climate, it is determined that realistic DDFs to use in the model would be DDF_{ice} of 7 mm w.e. d^{-1} ℃, and a DDF_{snow} of 3 mm w.e. d^{-1} ℃, with a refreezing factor of 0.6 (60%). This would detail steady state climate forcing a ΔT of -10℃, and a xP of +30% for the modelled ice to reach the mapped glacial limits.
- The subsequent experiments of 6 and 7 yielded a range of ΔT between -10℃ and -10.5℃, while a xP of between +10% and +40% when the chosen glaciological parameters are varied. These indicate that a colder but wetter climate is required with all varied parameters to ‘best-fit’ the geomorphic observations Appendix D.
- There is inherent variability in the determined steady state temperature for time varying model runs, as naturally temperature would never be steady at -10℃ to allow glaciers to reach equilibrium. This variability is exemplified in the climatic envelope the LLGM extent could have been generated under. This is used in the next chapter to understand what climate forcing is needed to aid in a time varying ice simulation to facilitate growth to, and deglaciation from, the LLGM.

Chapter 6. Modelling of the regional LLGM glaciation of the Lagunas de Las Huaringas region 38-0 ka

6.1. Introduction

Geomorphological mapping of palaeoglacial evidence has provided a first-order reconstruction of an assumed LLGM-age ice mass in the Las Huaringas region (Chapters 3 & 4) (Lee *et al.*, 2022). Though this work provided estimates of the area glaciated, ELAs, and the potential temperature cooling required for glaciation. The palaeo geomorphic-driven reconstructions suggested that glaciers were in a cirque to valley configuration. However, the potential for an ice plateau scenario, has been noted in Chapter 5. There is potential that there are limitations in the use of palaeoglacial geomorphology, that it can only provide temporal 'snapshots' of what the ice was doing, either a maximum extent or at periods of moraine generation, which may not all have occurred synchronously across the study region. There is limited ability to reconstruct the ice masses at periods which may have been erased from the geomorphic record, or times when no geomorphology was generated.

In this chapter, numerical modelling will be used to overcome the limitations of the geomorphic-based reconstructions, enabling an estimated timing of the most extensive glaciation, along with the factors driving glaciation and deglaciation in the Las Huaringas to be evaluated. The numerical model allows evaluation of: (i) the maximum extent compared to the most downvalley geomorphic evidence; (ii) the glaciological dynamics (i.e., modelled mass balances, velocity, ice thicknesses through time etc.) of the LLGM ice mass and how the ice evolved before and after the LLGM.

No other study has used numerical ice flow models within the northern tropical Andes, either to reconstruct glaciers during the LLGM, or any other time period during the late-Pleistocene. The work in this chapter will be the first application of a numerical glacier model such as PISM to ice mass reconstruction in the northern tropical Andes and will be used to explore regions LLGM ice extent and deglaciation dynamics.

6.2. Aim and objectives

The research aim of this chapter is to simulate the growth and retreat of ice within the Las Huaringas region during the period 38-0 ka. The objectives are:

- Reconstruct the growth, retreat, and geometry of modelled ice using a time-varying climate forcing.
- Evaluate how the modelled output compares to the geomorphic-derived reconstruction.

- Quantify ice dynamical changes associated with the advance, maximum extent, and retreat.

Table 6.1: Parameter values and constants used in ice sheet models within the PISM model. This is not an exhaustive list, however these are the values that were specifically parameterised within PISM, if otherwise stated, all other parameters were set to default.

Parameters	Name	Value	Unit	Reference
Ice and Earth Dynamics				
ρ	Ice density	910	kg m^{-3}	(Aschwanden *et al.*, 2012)
g	Gravitational acceleration	9.81	m s^{-2}	(Aschwanden *et al.*, 2012)
n	Glen exponent	3	-	(Cuffey and Paterson, 2010)
ρ_b	Bedrock density	3300	kg m^{-3}	-
q_G	Geothermal heat flux	88	W m^{-2}	(Vieira and Hamza, 2019)
E_{SIA}	SIA enhancement factor	1	-	-
E_{SSA}	SSA enhancement factor	1	-	-
Basal sliding and subglacial hydrology				
q	Pseudo-plastic sliding exponent	0	-	(Aschwanden *et al.*, 2012)
$u_{threshold}$	Pseudo-plastic threshold velocity	100	m a^{-1}	(Aschwanden *et al.*, 2012)
c_0	Till cohesion	0	Pa	(Tulaczyk *et al.*, 2000)
e_0	Till reference void ratio	1	-	(Tulaczyk *et al.*, 2000)
C_c	Till compressibility coefficient	0.12	-	(Tulaczyk *et al.*, 2000)
N_0	Till reference effective pressure	1000	Pa	(Tulaczyk *et al.*, 2000)
δ	Minimum effective pressure ratio	0.02	-	(Bueler and van Pelt, 2015)
ϕ	Till friction angle	30	^{o}	(Cuffey and Paterson, 2010)
W_{max}	Maximum till water thickness	2	m	(Bueler and van Pelt, 2015)
Climate forcings				
T_{snow}	Temperature for snow precipitation	273.15	K	(Seguinot *et al.*, 2018)
T_{rain}	Temperature for rain precipitation	275.15	K	(Seguinot *et al.*, 2018)
DDF_{snow}	Degree-day factor for snow	3	mm K^{-1} day^{-1}	This study – Chapter 5
DDF_{ice}	Degree-day factor for ice	7	mm K^{-1} day^{-1}	This study – Chapter 5
$\theta_{refreeze}$	Refreezing fraction	0.6	-	This study – Chapter 5
σ	PDD Temperature Standard Deviation	3.66	K	This study – Chapter 5

6.3. Methods and data

6.3.1. Model set-up

PISM (v1.2) was used to conduct time transient model runs from 38 ka to the present day. Chapter 5 outlines the physics used in PISM and tested the model parameters necessary to grow steady-state ice masses over the region. We tested the ice mass sensitivity to a variety of parameters, including: (i) constants derived from laboratory experiments (e.g., Glen's exponent); (ii) constants used frequently within other modelling studies (e.g., till reference void ratio); and (iii) parameters that required determination appropriate for this study area (i.e., DDFs and refreezing fraction). Based on this, we selected parameter values that enabled the closest fits with the geomorphologically mapped extents (Table 6.1) and now apply these to the time-dependent simulations of the LLGM ice masses here.

The model domain covers an area of ~1,260 km^2 (30 x 42 km). To set up the model, the previously determined (section 5.4.1) model resolution of 120 m was used, the computational

box was 250 x 350 cells, and the vertical grid was 1000 m. 101 distributed layers and a vertical resolution with equally spaced layers of 10 m were applied. The model was initiated with an ice-free model domain. Detailed information on PISM is available in section 5.3. of Chapter 5.

6.3.2. Climate forcing

The base modern climate input is described in Chapter 5 (section 5.3.3.). However, to force the growth and subsequent decay of the LLGM ice in this area, we perturbed the modern climate using a time-transient temperature record to represent temperature evolution through the late-Pleistocene (38 ka to present). The model was started a 38 ka due to this timing being at the start of cooling towards the global LGM's coldest period identified within the EPICA temperature record. This also allowed the model to start in a 'real-world' ice free scenario, allowing the generation of ice in the model domain that inherits the glaciological history to allow the accurate modelling of glacial ice as it advances and deglaciated.

The EPICA temperature record is described below and is applied within the same PDD model framework used in Chapter 5. Within the PDD model, as determined from the sensitivity analysis (Chapter 5), a DDF_{ice} of 7 mm w.e. ℃, a DDF_{snow} of 3 mm w.e. ℃, and a refreezing fraction of 0.6 (60%) were used. The sensitivity testing (Chapter 5) determined an LLGM maximum of an appropriate extent was achieved using a steady-state temperature offset (ΔT) of -10℃ compared to modern, and a wetter climate with +30% of modern precipitation. Within the EPICA temperature record, there are multiple periods where temperature reaches to, or is below, -10^{o}C, the most likely period will be between 20 ka and 27 ka. This provides the approximate regional LLGM conditions we wish to apply within our time-dependent climate framework, and we therefore adjust an existing climate record such that the temperature reduced by this amount at the regions LLGM. We assume that throughout the glaciation of this region, precipitation is distributed in the same pattern as modern, but at a 30% increased rate as the PISM model is unable to replicate complex climatic variations. Due to the lack of local palaeoprecipitation studies, it would be impossible to accurately determine the correct precipitation pattern, and change in precipitation rate, across the model time span.

Following a similar approach to (Seguinot *et al.*, 2018), the air temperature used in the PDD model was forced using the EPICA temperature curve (Lüthi *et al.*, 2008; Schilt *et al.*, 2010) between 38 ka to present. The lowest temperature within the raw EPICA temperature curve between this period is -10.58℃ at 24.0 ka and given that this temperature offset is similar to the offset required to produce an appropriate steady-state maximum (Chapter 5) we apply the

record without adjusting the magnitudes of its fluctuations. Due to the temporal spacing of the individual temperature estimates within the EPICA temperature time series (i.e., a 8 to 55 year resolution), the signal was smoothed using a 100-year moving average, similar to the smoothing approach of Imhof (2021). This smoothing of the temperature curve adjusted the minimum temperature in the record to -10.35°C (at ~25.3 ka), a 2.8% change in the maximum temperature offset. This lightly modified EPICA temperature curve (Figure 6.1) was primarily used to conduct time varying modelling of the Las Huaringas region. It should be noted that EPICA is from Antarctica, so cannot be entirely analogous to the climate of the study region, however EPICA is corelated with Southern Ocean Sea surface temperatures (Anderson *et al.*, 2021).

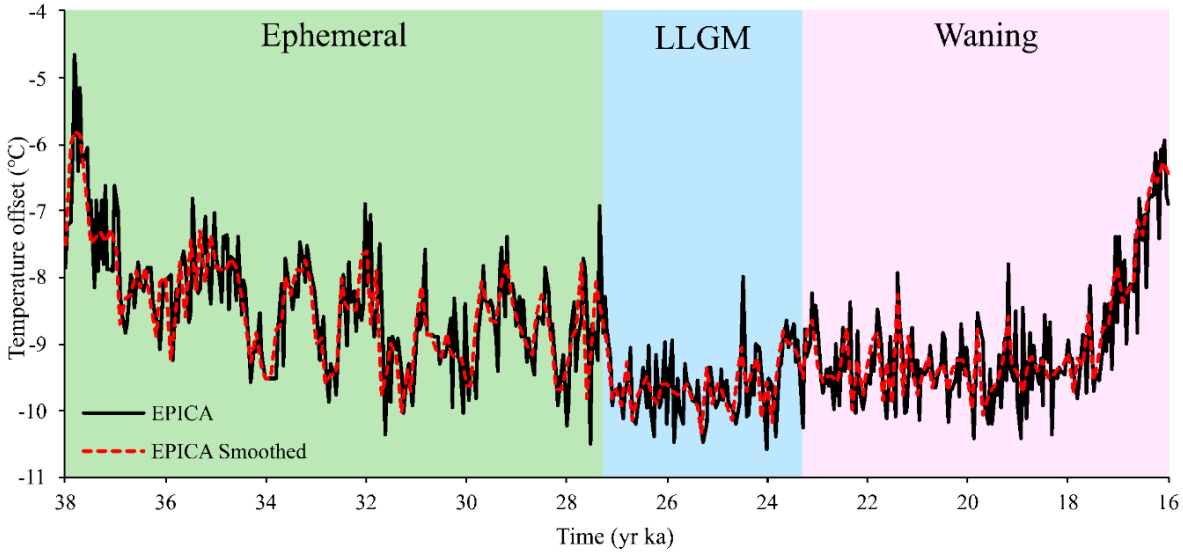

Figure 6.1: EPICA temperature time series (black), and smoothed time series (red dashed) using a 100-year moving average, between 38 ka to 16 ka. After 16 ka temperature offsets were too warm for modelled ice within the study region. Three ice periods are shown (i.e., ephemeral, LLGM, and waning), to reflect the structure used in this chapter.

Two more climatic scenarios were also applied in the modelling. These involved taking the smoothed EPICA temperature curve and increasing and decreasing temperatures by 0.5°C (shown in Figure 6.2). Performing these two models runs with increased and decreased temperatures allowed an assessment on the sensitivity of the region to temperature variations, while also allowing an assessment on the uncertainty of the model while using the time varying temperature curve.

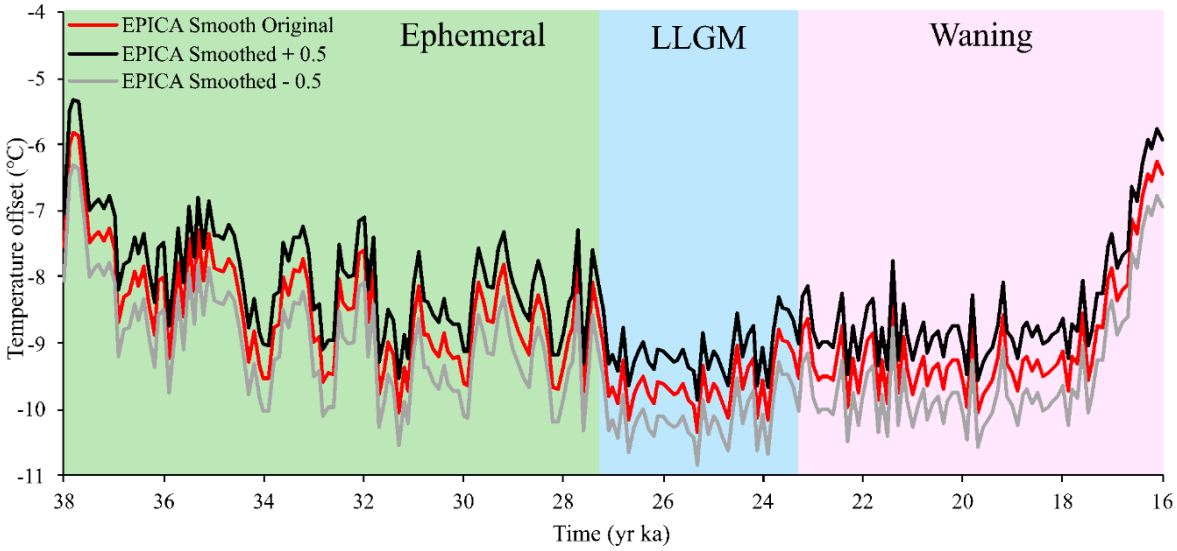

Figure 6.2: The EPICA smoothed temperature curve by 100 yrs intervals, with the original data with +0.5°C and -0.5°C.

6.3.3. Model outputs

To conduct an in-depth analysis of the model output, a number of diagnostic variables can be outputted from the model, using a user defined time interval, defined here as every 100 yrs. These outputs were used to assess the spatial and temporal dynamics of the glacial ice across the model domain. The model diagnostic variables used within this chapter are shown in Table 6.2. The only variable that needed post-processing to extract required information was 'surface mass balance' in order to define the evolution of the ELA which is defined as the boundary between annual accumulation and ablation.

Table 6.2: Extracted model diagnostic variables used to analyses the time varying model within this Chapter.

Variable name	Model variable name	Diagnostic variable description
Ice thickness	thk	The ice thickness in meters (m)
Ice surface elevation	usurf	The ice surface elevation in meters (m)
Ice surface velocity	velsurf_mag	Magnitude of horizontal velocity of ice at the ice surface (m yr^{-1})
Ice basal velocity	velbase_mag	Magnitude of horizontal velocity of ice at the ice base (m yr^{-1})
Surface mass balance	climatic_mass_balance	Ice surface mass balance (accumulation - ablation)

6.4. Results

Between 38-0 ka, a number of peaks of ice area and volume, indicating multiple periods of advances in relation to temperature cooling from the inputted EPICA ice core are apparent (Figures 6.1). These distinct periods show: (i) a period of ice generation but multiple phases of

disappearances (ephemeral ice; 38-27.5 ka); (ii) a period of sustained glacial ice within the Las Huaringas region (LLGM; 27.5-23.5 ka); and (iii) a period of fluctuating ice mass until entire deglaciation (waning ice; 23.5-16 ka).

The first period, between 38-27.5 ka, was characterised by 'ephemeral' glaciation when temperature was fluctuating above and below the threshold of -8.6 ℃ below present. Ice was generated below -8.6℃, and full deglaciation occurred above -8.6℃. This period was characterised by eight periods of glacial advances (Figure 6.3), 1,000-2,000 yrs apart, that generated ice no greater than 60 km^2 in area, with a maximum volume of 4 km^3. The most extensive ice in this period was at 31.3 ka, when maximum area and volume were 91 km^2 and 5.1 km^3 respectively.

The second period, between 27.5 ka and 23.5 ka, was a period where ice grew extensively when temperature cooling was on average below -9.5℃. This generated five closely spaced advances of the ice ~1,000 yrs apart. A particularly large advance occurred at 25.4 ka and is assumed to represent the study area's LLGM advance. Temperatures at this time cooled to -10.4℃, the lowest during the model run. The ice during this period was almost constantly greater than 70 km^2 in area with a volume greater than 4 km^3. This was the only period in the model run where ice area and volume exceeded 100 km^2 and 6 km^3 respectively (Figure 6.3). The largest advance reached a maximum area of 171 km^2 and a volume of 10.6 km^3. This period is here referred to as the 'LLGM period' as it is associated with some of the largest glacial advances in the model run.

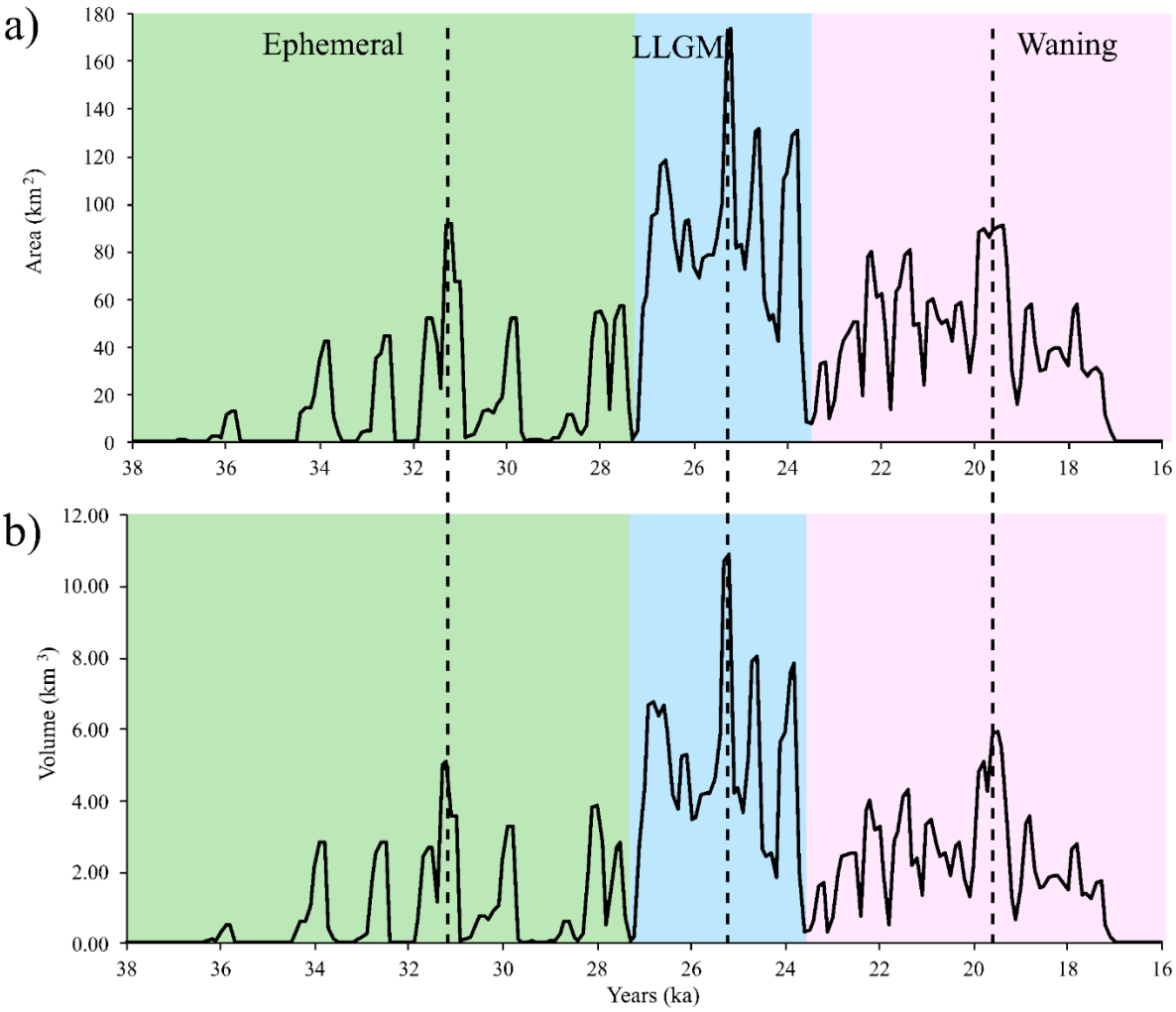

Figure 6.3: Modelled ice a) area, and b) volume, throughout the period of glacial ice presence between 38 ka and 16 ka. The three periods determined in this chapter are highlighted in the figure with green ('ephemeral' glaciation), blue (potential LLGM glaciation), pink ('waning' glaciation). Three dashed lines indicate the timing of each period's 'most extensive' advance.

The third and last period of glaciation in the model run, between 23.5-16 ka, was characterised by 'waning' ice, with a generally decreasing ice mass associated with ten ice advances (Figure 6.3; waning period). Temperatures below -8.5°C were capable of sustaining ice constantly within the model domain, but ice area and volume never exceeded 100 km^2 or 6 km^3 in this period and ice margins always sit inside the maximum extents denoted by the geomorphological record (Figure 3.2). The modelled ice advances were similar to, or slightly more extensive than, those in the ephemeral ice period. Ice in this period was constantly present until full deglaciation when temperature cooling increased to above -8°C at ~17.2 ka.

6.4.1. Ephemeral glaciations (38-27.5 ka)

The temperature between 38 ka to 27.5 ka fluctuated extensively (~1.5°C) while steadily decreasing towards the LLGM (Figure 6.1). The 'troughs' of the fluctuating temperature curve

were associated with short-lived glacial ice, while temperature 'peaks' were associated with full deglaciation. Prior to 34.5 ka, very small, short lived (<700 yrs), ice masses (max of 12.5 km^2) occupied topographic highs in the study area. Between 34.5 ka to 33.0 ka, the temperature offset dropped to below -8.5°C. Limited ice formed at elevations >3,400 m asl and was mainly limited to the main massif ridge to the west of the Shimbe valley (ice-oriented north to south in Figure 6.4; 34.0 ka). This limited ice cover had an ice thickness of 0-202 m, and ice surface velocity magnitudes of 0-68 m yr^{-1} (Figure 6.5). Intermittent periods of deglaciation occurred when temperatures increased above -8.5°C (e.g., between 33.0-32 ka, and 29.5-29.0 ka (Figure 6.4). Between 31.5 ka to 30.0 ka, in response to temporally limited cooling of -0.6°C, modelled ice extended partly down from their topographic highs into the larger glacial valleys, primarily along the western glacial cirques, and within the northern glacial region. Ice thicknesses between the period 31.5 ka to 30.0 ka, was between 22-174 m, with the maximum thickness found within the western cirque region. Average ice surface velocities during this period also increased, to 23-59 m yr^{-1} (average maximum was 36.9 m yr^{-1}). When ice was present, it was limited in extent with an overall area < 91 km^2 (average of 19.6 km^2) and an ice volume of < 5 km^3 (average of 1.1 km^3).

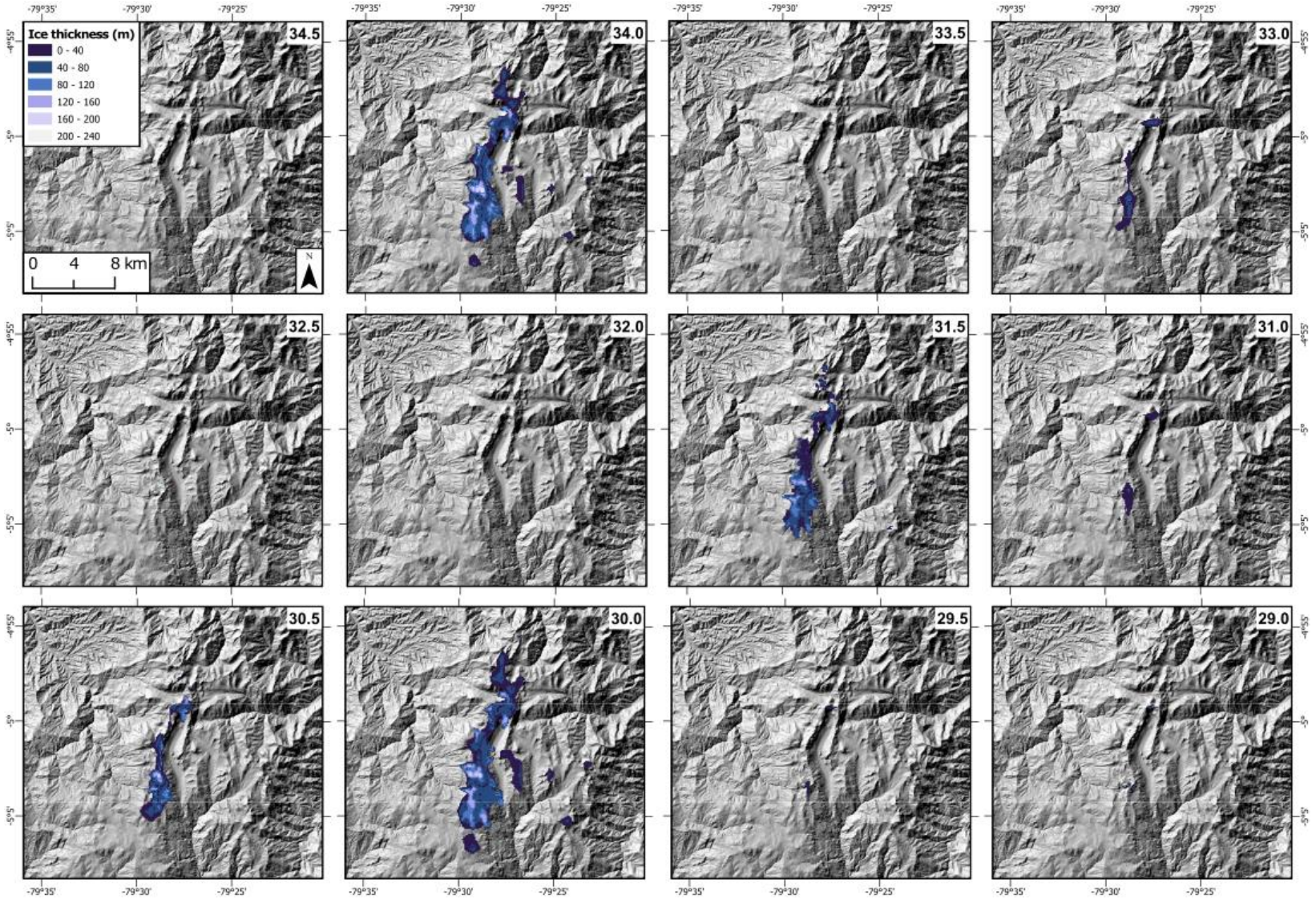

Figure 6.4: Varying ice thickness, between 34.5 ka and 29.0 ka. 31.3 ka (not shown above) was the most extensive ice during the period (seen in Figure 6.6). Legend scale is from the LLGM period in Figure 6.11 to allow comparison. 29.0 ka to 28.0 ka not shown due to no ice being present.

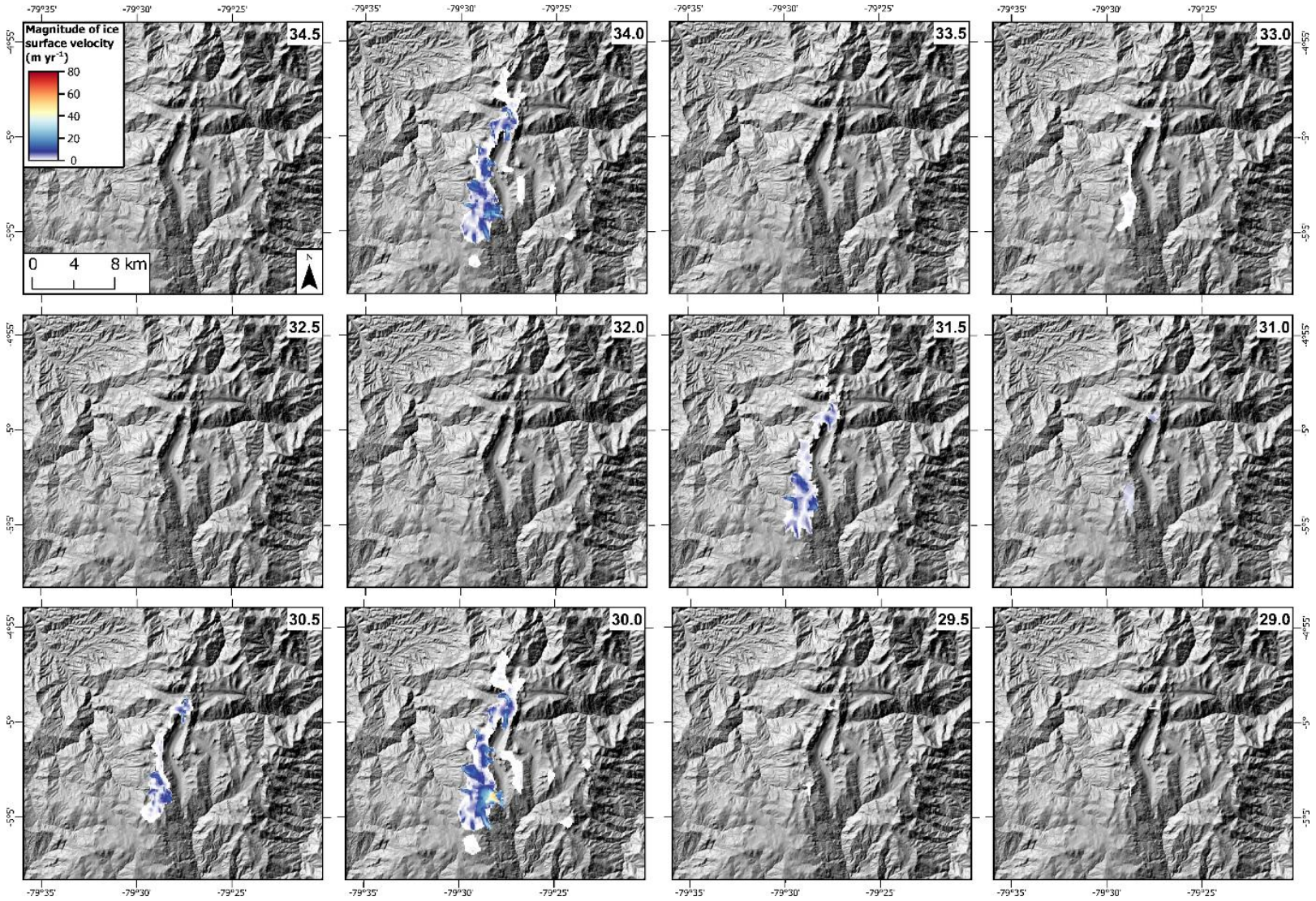

Figure 6.5: Varying extents of ice, detailing ice velocity magnitude, across the pre-LLGM between 34.5 ka and 29.0 ka. 31.3 ka (not shown above) was
3270 the most extensive ice during this period (seen in Figure 6.6). Legend values scaled to LLGM ice surface velocity magnitudes in Figure 6.11.

At 31.3 ka, when ice was at its most extensive extent during the ephemeral, pre-LLGM (38-27.5 ka) window (Figure 6.6) - it had an area of 91.4 km^2. The lowest elevation ice extended to at 31.3 ka was ~2,900 m asl. However, this expansion of ice did not extend to the most maximum extent moraines mapped in Chapter 3, making it not as extensive as the regional LLGM extent. Ice within the central region (Shimbe Valley) of the Las Huaringas was situated on the highest peaks, with outlet glaciers flowing down into lower elevation valleys. Examples of ice extending down to valley floors and downvalley are the ice extending off the western glacial cirques near Laguna Millionaire and Laguna Negra, and in the northern regions within Palo Blanco 1 valley north of the central Shimbe valley (Figure 6.6a). Other topographic highs, for example in the southeast of the region of Redondo de Zapalache 1, have ice at very high elevations only (> 3,400 m asl), with ice limited to their cirque valleys or ice capped peaks – the maximum elevation of this region being ~3,900 m asl. An extension of thin (< 70 m), slow flowing (< 10 m yr^{-1}) glacier ice to the southwest of Laguna Shimbe corresponds to an area where little glacial geomorphology was identified (Figure 3.4). Interesting locations identified are ice with the Shimbe valley (Figure 6.7), with ice clearly flowing from the headwall of the valley, while ice also flows from the western valley wall partly filling the valley floor. A region of faster moving ice extends down from the Laguna Negra region past the initially hypothesised LLGM (maximum extent) moraines (Figure 6.8).

The ELA of the maximum modelled ice mass at 31.3 ka has an average elevation of 3,459 m asl (Figure 6.6a). Much of the glacial ice area is above the ELA (~90% of ice) with some locations where ice does not extend past the modelled ELA. Only a small area of some minor outlet glaciers are below the ELA (~10%), these being limited to the ice within the Shimbe valley, the western cirque glaciers, and Palo Blanco 1 in the northern regions. These small, but thick, outlet glaciers descend to low elevations (< 3,200 m asl) and drain much of the ice along the ice capped terrain. This limited ice below the ELA may be due to the modelled ice not being in equilibrium with climate, thus the ice and ELA is constantly changing due to the time varying climate. If the ELA in reality was indeed this low on the glaciers, this would have important implications on the AABR of Tropical Glaciers, requiring a higher BR, that could influence the reconstructed LLGM ELAs, however small differences in BR show little change in reconstructed ELAs (as shown in Chapter 3).

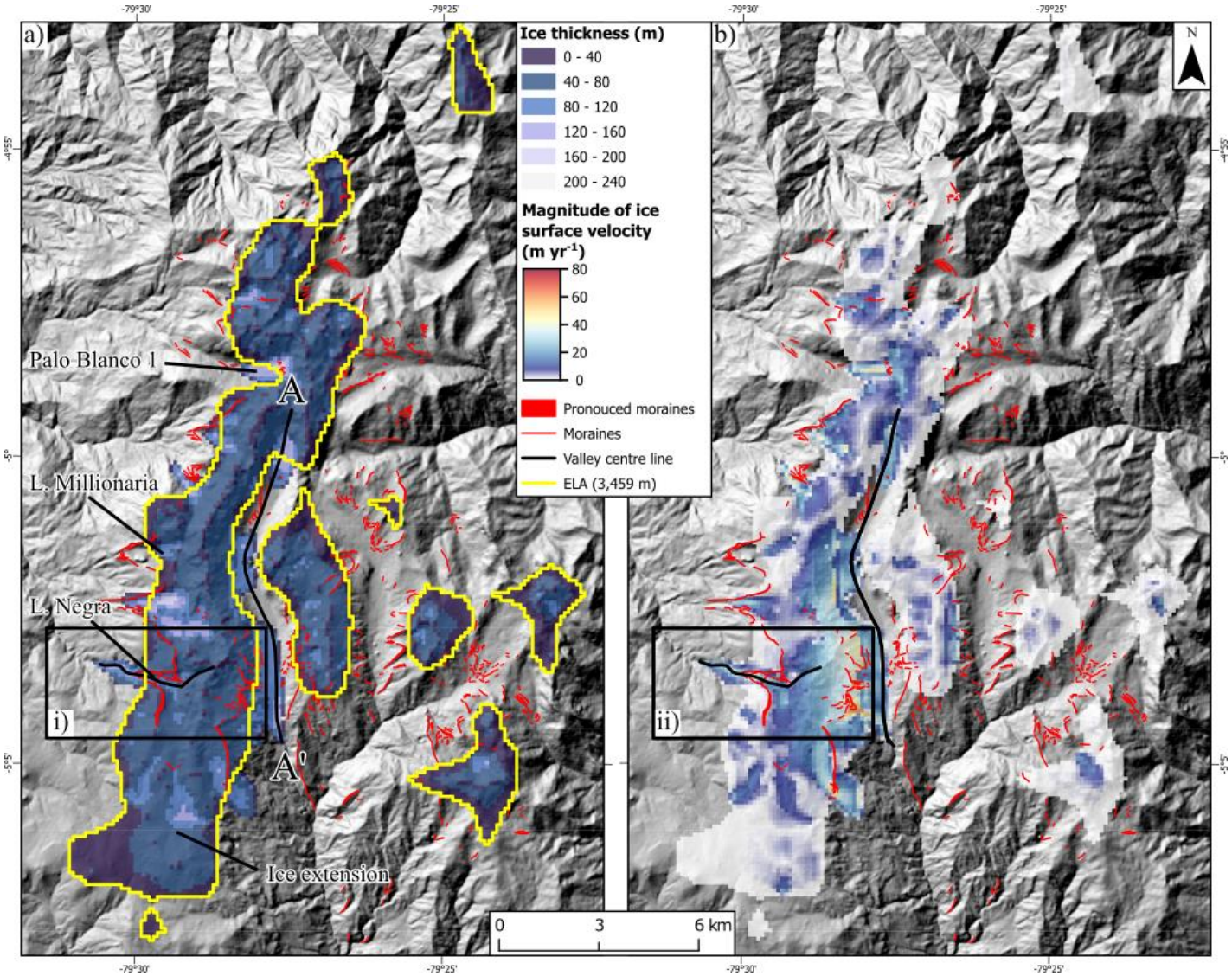

Figure 6.6: The most extensive ice area during the 'ephemeral glaciation' period, at 31.3 ka with a) ice thickness and ELA, and b) ice surface velocity magnitude. Valley centre line A – A' shown in Figure 6.7, insets i) and ii) correspond to Figure 6.8a&b. Legend scale the LLGM period in Figure 6.11.

This model snapshot (31.3 ka; Figure 6.6) shows ice flowing down from constrained glacial cirques into glacial valleys (e.g., Shimbe valley; Figure 6.7), and ice flowing from unconstrained valley wall locations into lower valleys (e.g., Negra valley; Figure 6.8). At the head of the Shimbe valley, ice flowed from the northern valley headwall and extended a relatively short distance (~2 km) downvalley with an ice thickness up to 160 m (Figure 6.7a). This ice flowed from the high elevation (3,900 m asl) source area to the north (connected with the Paleo Blanco 1 glacier) and was contiguous with ice that flowed westward (i.e., from the western glacial cirque's region into glaciers such as Millionaria and Negra). At this time, two extensive, and relatively thick (i.e., up to 120 m) extensions of ice flowed from the western valley wall into the Shimbe valley, partly filling the valley. These left gaps of ice-free terrain, an area between the northern ice and the first (most northern) ice extension ~4 km down valley, and the second area in between the first and second (most southern ~6.5 km downvalley) ice extensions (Figure 6.7). Ice surface velocity magnitudes (Figure 6.7b) near the northern headwall are slow (< 10 m yr^{-1}) but increase as the ice transitions onto the valley floor (~0.7 km downvalley – high of 37 m yr^{-1}), before decreasing again as the ice continues downvalley to the valley floor (from 37 to ~20 m yr^{-1}) (Figure 6.7c). The two small ice extensions that flow laterally onto the valley floor from the east-facing valley walls have similar ice velocities to the ice of the upper Shimbe ice (between 10 to 53 m yr^{-1}). The fast-moving ice in the area at the time is found within the most southern ice extension, that flows into the most southern end of the Shimbe valley ice from the western valley wall; this has an ice surface velocity magnitude of 61 m yr^{-1}.

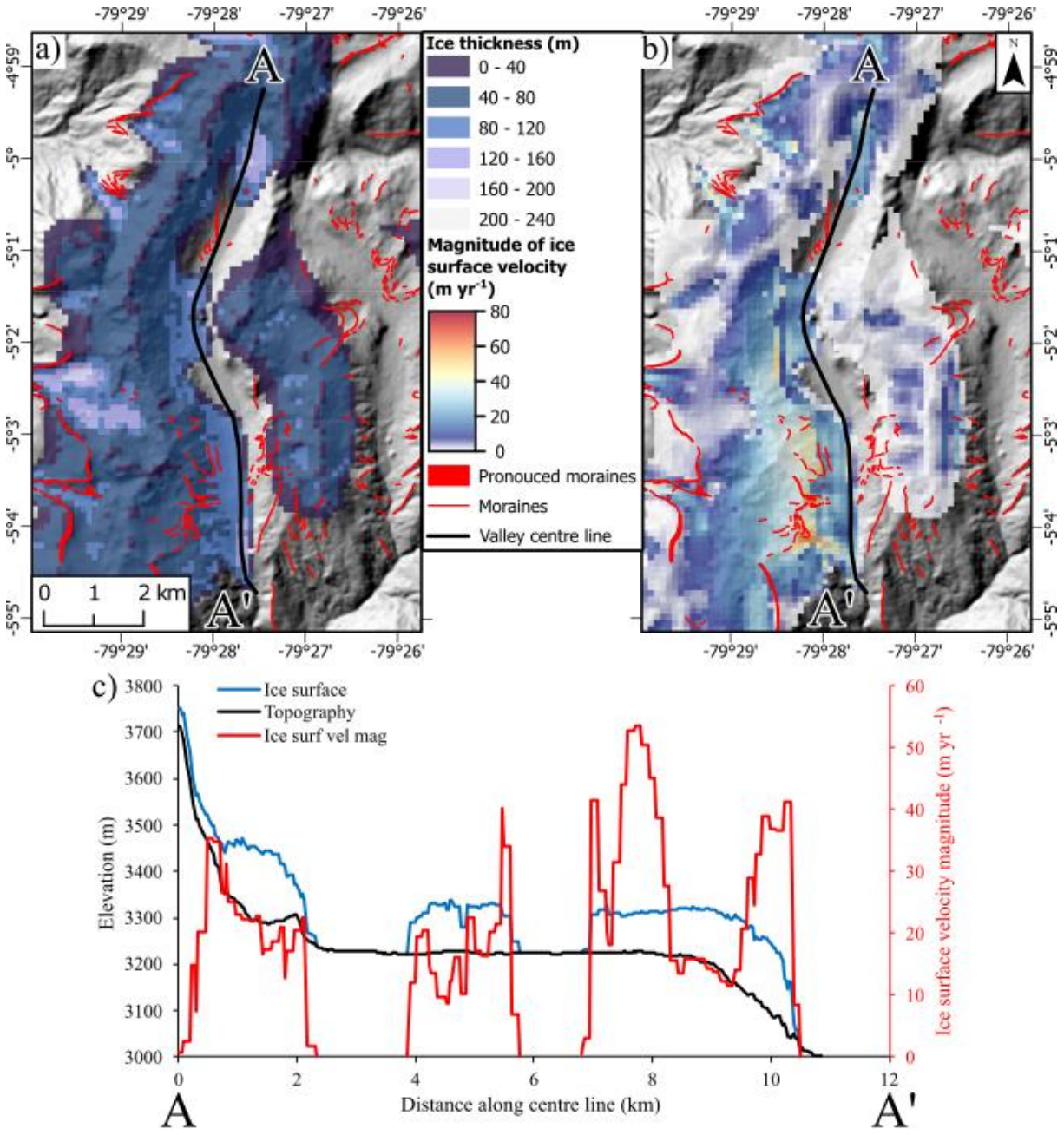

Figure 6.7: Interesting ice dynamics in the Shimbe valley during the pre-LLGM most extensive advance (31.3 ka), a) detailing ice, and b) ice surface velocity magnitude for ice in the Shimbe valley, and c) values taken along the valley centre line A-A'. Legend scale is from the LLGM period in Figure 6.11.

Within the Negra valley area (Figure 6.8), ice flows downvalley from the source area along the western face of the massif, from the ice field that extends northwards past the headwall of the Shimbe valley. The ice that fills the Negra valley converges from three source areas to the north, south and east. At 31.3 ka, the ice extends down valley to an elevation of ~3,150 m asl and contains some relatively fast-moving ice within the model domain compared to the other valley glacier ice within the western region. Along the ice flowline (B – B'; shown in Figure 6.8), ice is thin near the headwall (~50 m; Figure 6.8a) but increases downvalley; at ~2.5 km downvalley the ice is ~140 m thick. As the ice flows further downvalley (2-4 km along profile) the valley

floor drops in elevation and slopes downwards. Here the modelled ice thickness is relatively constant (~100 m) until it reaches the terminus. Ice surface velocity magnitudes (Figure 6.8b) along the flowline increase steadily as the ice flows downvalley, from < 27 m yr^{-1} (0-2 km along B-B' profile), to a maximum of ~40 m yr^{-1} at 2.5 km downvalley. Flow speed then reduces substantially down valley at lower elevations, from ~40 m yr^{-1} to ~5 m yr^{-1} near the glacier terminus (Figure 6.8c).

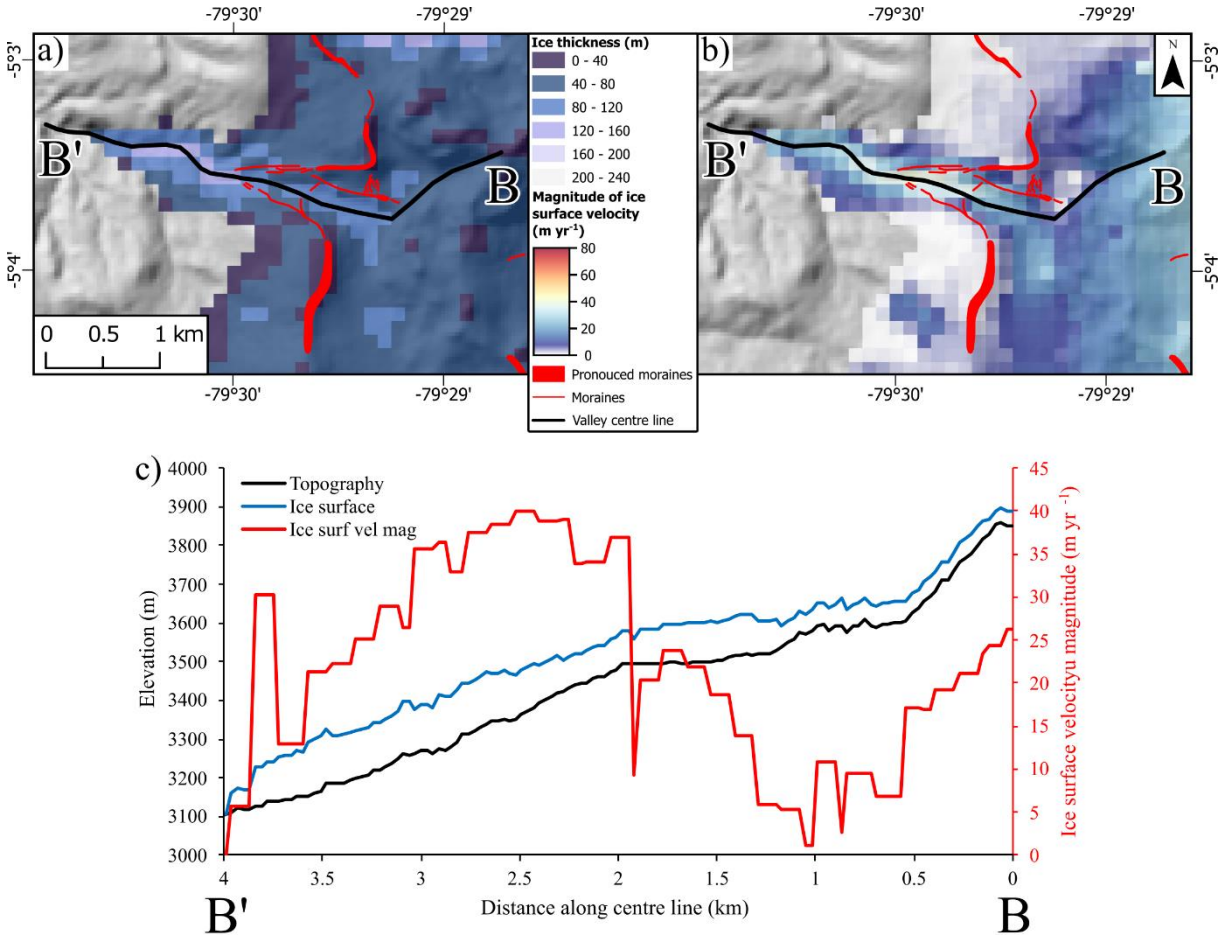

Figure 6.8: Interesting ice dynamics within the Negra valley during the pre-LLGM most extensive advance (31.3 ka), a) detailing ice thickness, and b) ice surface velocity magnitude for ice in the Negra valley, and c) with values along centre line B-B' from thickness and velocity. Legend scale is taken from the maximum scale from the LLGM period in Figure 6.11 to allow comparison.

After the period 31.3 ka where the temperature offset from present was -10°C, the temperature warmed by 1.3 °C over 400 yrs in response, by 31.0 ka the ice area reduced to 1.7 km^2 and ice volume reduced to 0.04 km^3 (Figure 6.3). Between 31.0 ka and 29.0 ka glacial ice remain restricted in the region, with ice limited to elevations comparable to those before 34.0 ka (i.e., >3,400 m asl). A minor increase in ice area (to 52 km^2) and volume (to 3.3 km^3) occurred between 30.0 ka and 29.8 ka in response to a short-lived decrease in temperature (to an offset of -9.6°C). Between 29.7 ka to 29.0 ka (Figure 6.3), ice retreated and became entirely deglaciated between 29.3 ka and 29.2 ka in response to temperatures cooling above -8°C, (>

3,500 m asl). After 29 to 27.5 ka (not shown in Figure 6.3) temperature cooling began to decrease (from -8.5°C to -9.6°C) with ice areas varying between 1.6-56.6 km^2, and ice volumes between 0.1-3.9 km^3.

6.4.2. Local last glacial maximum (27.5-23.5ka)

The period 27.5-23.5 ka was characterised by sustained temperature cooling with an average of -9.5°C over the period, and a maximum cooling of -10.5°C. Between 27.5 ka to 26.5 ka ice expanded and fluctuated in response to temperatures between -7.8°C to -10.2°C (Figure 6.1). During this period, ice across the model domain was limited in extent for example, ice does not extensively fill the Shimbe valley. However, ice in the northern regions (e.g., Palo Blanco 1 and 2) and western cirques (Negra and Arrebiatadas) began extending from their cirques downvalley. Ice within the southeast area was limited to high elevation (>3,400 m asl) terrain forming individual ice caps with little ice flowing down from source areas. Maximum ice thicknesses were 214 m in the Arrebiatadas (Figure 6.9), and the maximum ice surface velocity magnitude was 55.4 m yr^{-1} in the Negra glacier (Figure 6.10).

From ~26.0 ka to 24.0 ka, ice flowed into the Shimbe valley from its headwall source area and coalesced with ice flowing from its west and east-facing valley walls forming an extensive glacier. This coalescence was in response to substantial cooling (temperature offsets below -9.3°C). Ice started to fill the Shimbe valley and extended further down valley from glacial cirques (e.g., in the northern glacial region to the north of the Shimbe valley, and the western glacial cirques). The ice area through this period fluctuated between an average area of 68 km^2 and average volume of 4 km^3 in the early stages (27.5 ka to 26.5 ka), to a maximum area of 173 km^2, and a corresponding ice volume of 10.9 km^3. Outside the central ice plateau, ice was primarily limited to the topographic highs of the individual ranges (e.g.., high peaks to the southeast of the Shimbe valley). For example, at 27.0 ka BP an area of thin (65 m) slow-flowing (18 m yr^{-1}) ice develops in the southern parts of the model domain. This feature of the ice mass is persistent in the model run between 27.0-24.0 ka and is associated with relatively thin (< 107 m), slow flowing ice (< 34 m yr^{-1}).

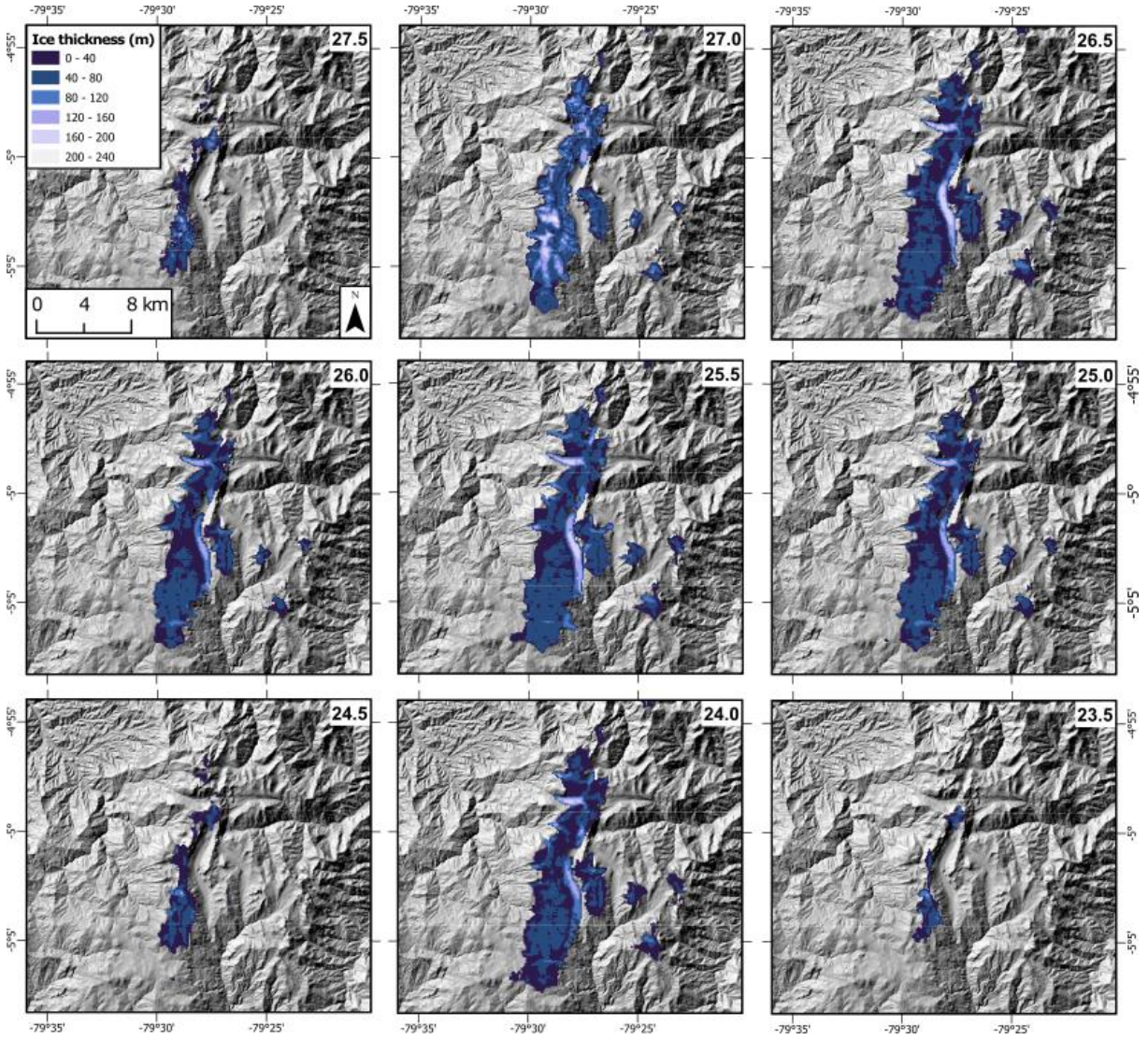

Figure 6.9: Varying extents of ice, detailing ice thickness, across the LLGM period between 27.5 ka and 23.5 ka. 25.4 ka (not shown) was the most extensive ice during this period (seen in Figure 6.11). Appendix E Figure E.1 details a more detailed view of the period between 26.0 ka and 25.0 ka.

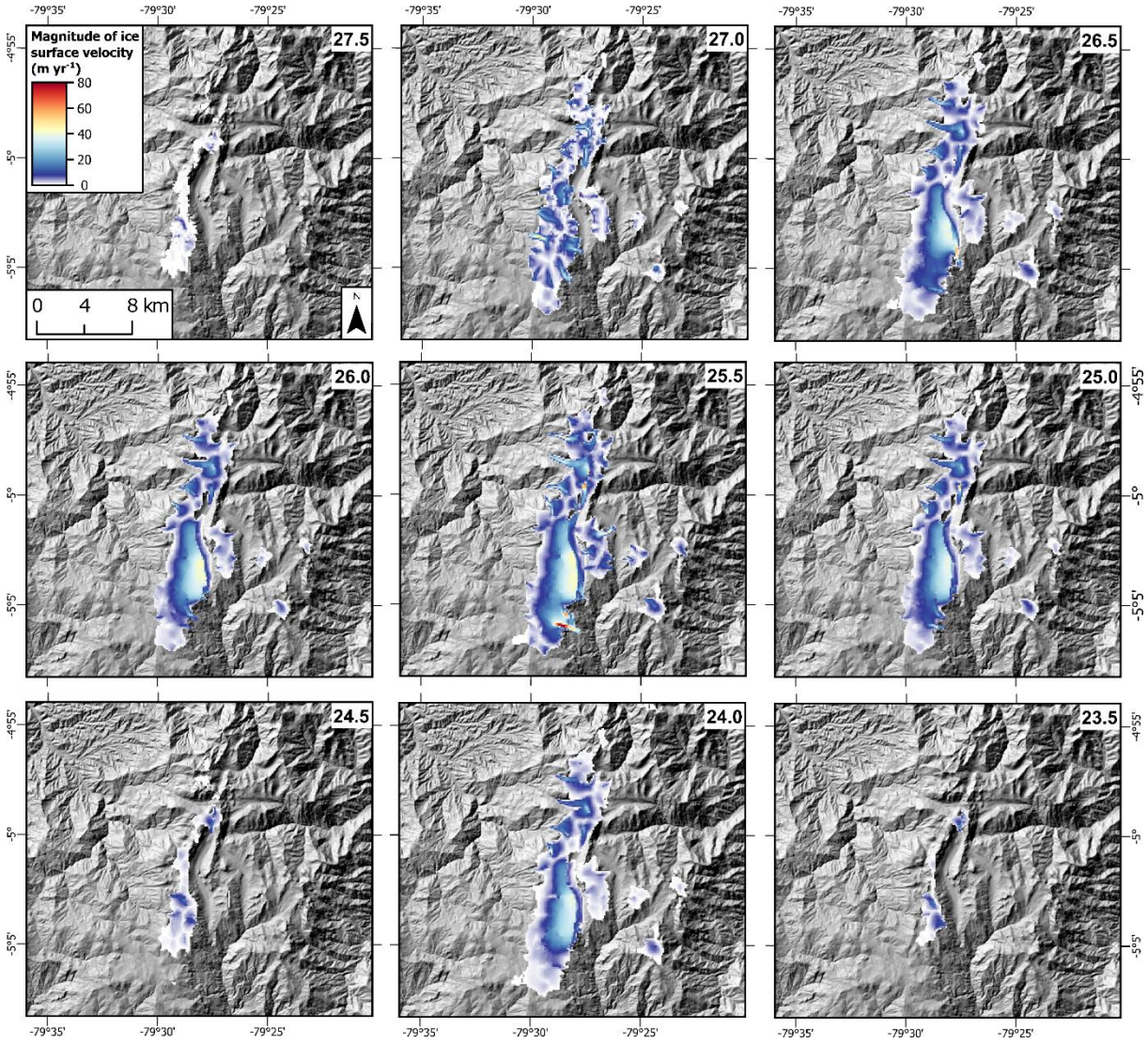

Figure 6.10: Varying extents of ice, detailing ice velocity magnitude, across the LLGM period between 27.5 ka and 23.5 ka. 25.4 ka (not shown) was the most extensive and fastest moving ice during this period (seen in Figure 6.11).

The modelled ice mass at the most extensive period (at 25.4 ka) is a large, interconnected ice plateau that extends from the top of the northern glacial valleys (~-4°55) to the south of the Shimbe valley (~-5°47). This ice mass includes outlet valley glaciers in the northern valley, the western glacial cirques (noted in Figure 6.11), and the Shimbe valley. The zone of thin and slow flowing ice in the southwest part of the model domain, observed in earlier model output, is present. Smaller distinct ice plateaus, not connected to the primary ice plateau, occupy high individual mountain tops (> 3,200 m asl) in the south-eastern glacial region (e.g., Redondo de Zapalache 1 glaciers), and northern glacial valleys (e.g., Aranza 1 glaciers). This results in a total ice area of 171 km^2, and a total ice volume of 10.6 km^3 (Figure 6.2, 6.11). The ELA was, on average, situated across the domain at 3,500 m asl, with ice within the Shimbe valley almost entirely below the ELA. Downvalley from the zone of thickest ice, the fastest modelled ice was located, with a maximum ice surface velocity magnitude of 67.5 m yr^{-1} (Figure 6.11).

Through the model output, and due to abrupt changes in climate, some model outputs are clearly unrealistic so are excluded from our analysis, and thus are not displayed here. During the model run here, two periods with very similar ice metrics (area and volume) occurred only 100 yrs apart (25.4 ka shown here, and 25.3; shown in Appendix E Figure E.1) equating to one recorded model interval. 25.4 ka is used here due to its more realistic appearance of its ice configuration, with the thickest ice within the central location of the Shimbe valley, within the up-glacier end, with ice thinning as it gets towards to terminus. The 25.3 ka snapshot (Appendix E Figure E.1), shows ice that extends further downvalley in all locations however, results in the thickest ice in the terminal end of the Shimbe valley glacier up to 281 m – the thickest anywhere within the model domain. This is potentially in relation to the substantial drop in temperature from 25.4 ka (-9.9℃) to 25.3 ka (-10.4℃). This would add a substantial input of accumulation in the model, that would then cause a large through put of glacial mass before the modelled ice could reconfigure itself. During other periods where temperatures reached below -10℃ (i.e., 31.3 ka, 26.7 ka, 24.7 ka, 24.1 ka) the ice does not reach as far as modelled for 25.3 ka, nor is the ice as thick. Further, while surge events may cause such a large amount of ice to be drawn down, the PISM model is unlikely to reconstruct such events due to their unique nature, and hard to replicate physics. Thus 25.4 ka is shown here, as it provides a ‘more realistic’ ice configuration, and it is only 100 yrs away from 25.3 ka.

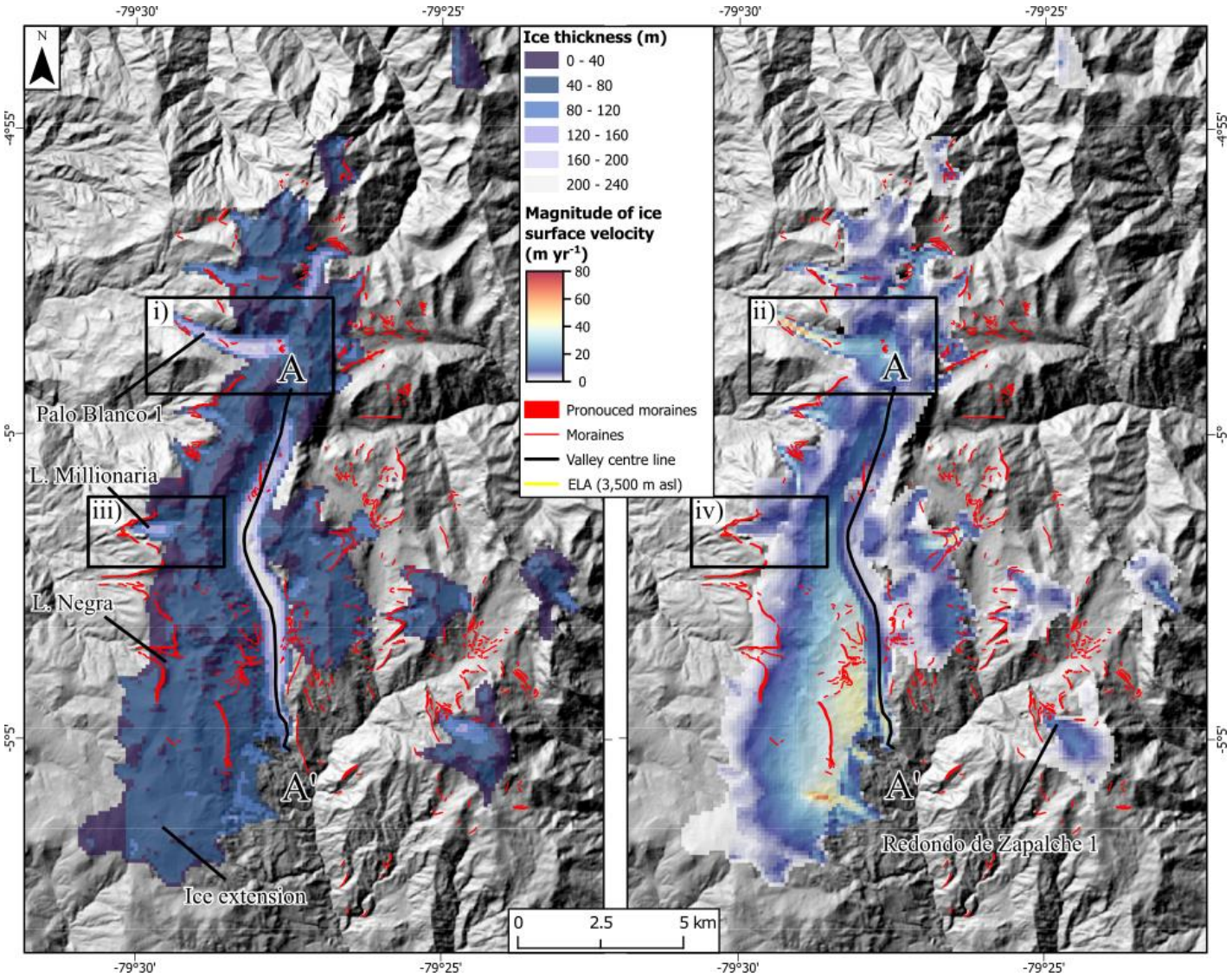

3425

Figure 6.11: The most extensive ice during the LLGM at 25.4 ka, a) ice thickness with reconstructed ELA, and b) magnitude of ice surface velocity. Flowline A to A' corresponds to Figure 6.12. Insets i) and ii) corresponds to Figure 6.13a&b, and iii) and iv) corresponds to Figure 6.13c&d.

The Shimbe glacier is the largest body of ice within the model domain, with a length of ~11.5 km. The maximum ice thickness within the Shimbe valley and across the entire model domain, is 222 m (Figure 6.12a) ~6 km downvalley of the headwall (Figure 6.12c). This coincides with the Laguna Shimbe overdeepening. The location of the thickest ice is coincident with some of the slowest ice surface velocity magnitudes within the Shimbe valley (< 10 m yr^{-1}) (Figure 6.12b). The fastest flowing ice within the Shimbe valley (60.5 m yr^{-1}) is ~10 km downvalley at the modelled glacier terminus. The fastest flowing ice coincides with the valley floor dropping in elevation (Figure 6.12c) from 3,200 m asl to 2,600 m asl over 4 km, before velocity decreases at the glacier margin. Ice flowing off the western and eastern valley wall coalesces with the Shimbe glacier and adds influx of ice into the glacier. The ice flowing from the western valley wall has the largest area of faster moving ice (< 44 m yr^{-1}), driving the ice into the Shimbe valley.

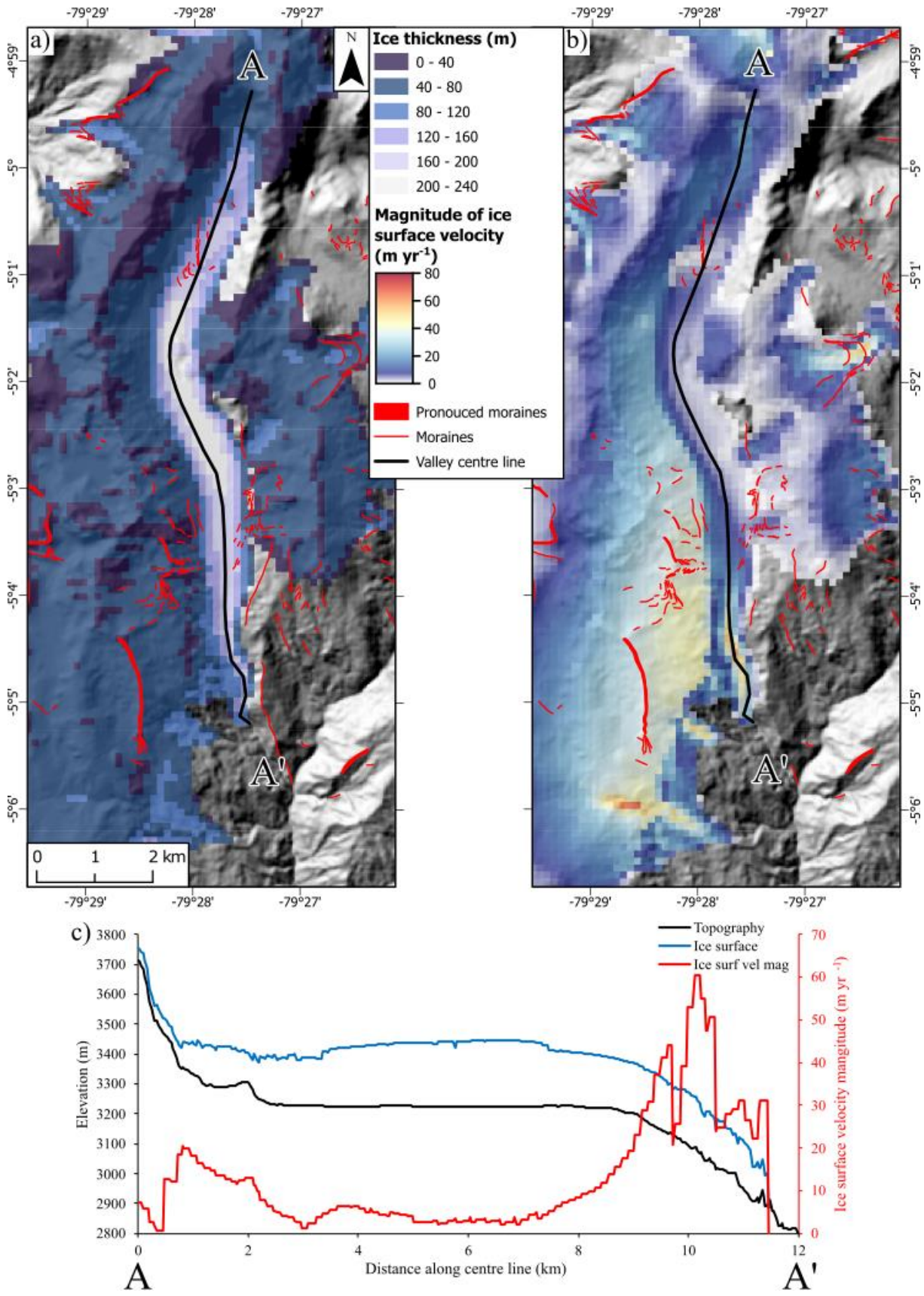

Figure 6.12: Model output of the Shimbe valley during the assumed LLGM extent with a) showing ice thickness, and b) showing ice surface velocity magnitude, and c) The flowline A – A' runs along the centre of the Shimbe valley glacier.

Two locations were used to evaluate the maximum ice area in the 27.5-22 ka period, the Laguna Millionaria valley (Figure 6.13a&b), and the Palo Blanco 1 valley (Figure 6.13c&d). Both valleys were filled with glacier ice that flowed from ice plateau source areas above the western wall of the Las Huaringas massif. Ice within the Laguna Millionaria complex extended down to 3,384 m asl, while ice within the Palo Blanco 1 valley extended down to 2,850 m asl. These two regions both underextend (by 420 m) and overextend (by 526 m) from the mapped maximum extent moraines respectively. The pattern of ice thickness is similar for both regions, with the thinnest ice seen at the headwalls the ice is flowing from (~ 45 m), thickening as it enters the valley floors. The thickest ice occurs after substantial dips is topographical elevation, e.g., in Millionaria ~1.75 km downvalley (145 m; Figure 13e), and Palo Blanco 1 ~2 km downvalley (200 m; Figure 13f). Within Laguna Millionaria the ice surface velocity magnitudes are very slow and did not exceed 12 m yr^{-1} across the entire ice mass. In the Palo Blanco 1 valley, the highest ice surface velocity magnitudes are identified within the middle of the valley 4 km downvalley of the source area, reaching a maximum of 61 m yr^{-1}.

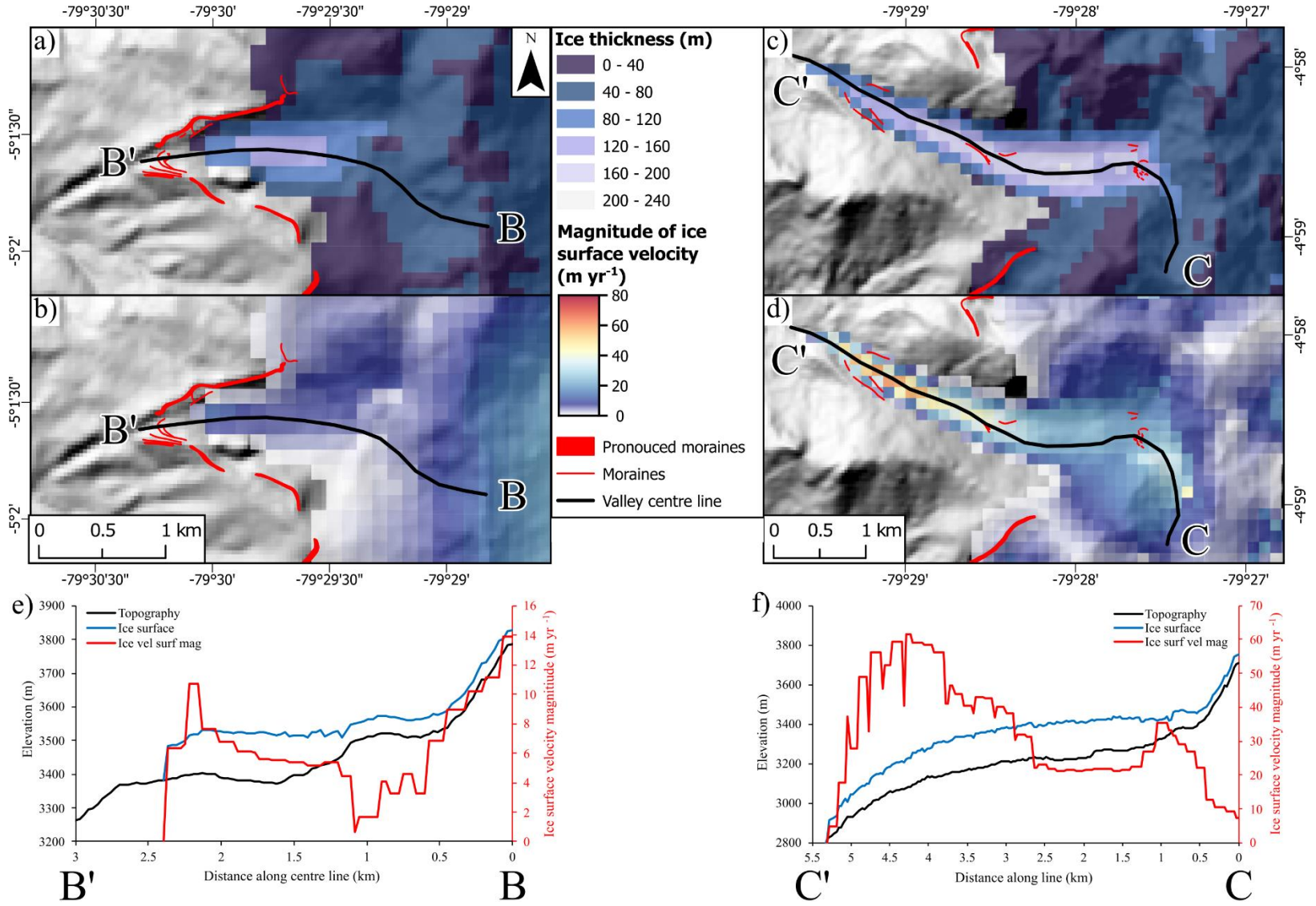

3460 **Figure 6.13**: a) and b) ice thickness and velocity magnitude for the Laguna Millionaria area, c) and d) detailing ice thickness and velocity magnitude for the Palo Blanco 1 valley, e) and f) show values along the valley centre line for Millionaria (B-B') and Palo Blanco 1 (C-C') respectively.

After 25.0 ka to 23.5 ka, glaciers receded back from their maximum LLGM extents in response to slight warming, from -10.35℃ to short periods of temperatures above -10℃. This promoted some readvances of the ice, but temperatures after 22 ka were typically -9.5℃ or above causing glaciers to retreat from the Shimbe valley. When temperatures are offset by -9.3℃ or more, the ice in the central region is contiguous along the high elevation ridge of the massif (i.e., between 24.5 and 24.0 ka, and at 23.5 ka) (Figure 6.9).

6.4.3. Waning ice (23.5-16 ka)

During the 'waning' ice period (Figures 6.14 and 6.15) between 23.5 ka and 16.0 ka temperatures fluctuated between -8.3℃ and -10℃, with an average of -9.4℃ (Figure 6.1). These temperatures generated regionally limited ice, that never entirely deglaciated until after 17.2 ka where temperature cooling increased to above, and never again dropped below, -8.5℃. These temperatures generated ice that was characterised by a generally limited but fluctuating ice area and volume (Figure 6.2). The ice mass across this post-LLGM period fluctuated between 4-90 km^2 (average of 37 km^2). Ice volume varied between 5.9 km^3 and 0.1 km^3 (average of 2.5 km^3).

Similar to the pre-LLGM period (38-27.5 ka), glacier ice was primarily limited to topographical highs (> 3,400 m asl) with short lived ice growth between 23.5 ka to 22.0 ka (area between 11 km^2 and 80 km^2) with a small period of advance at 21.5 ka (up to an area of 80 km^2) before ice retreated up to high elevation cirques between 21.0 ka and 20.0 ka (area between 42 km^2 and 59 km^2).

Between 21.5 ka and 20.0 ka, the ice mass within the model domain was limited and highly variable, ranging from limited ice caped mountain tops (average area of 51 km^2) to almost entire deglaciation with ice at only the highest peaks (area down to 24 km^2). This latter very limited ice occurred when the climate warmed to a temperature offset of above -8.9℃ offset from present (e.g., at 21.2 ka), while ice that was limited to the mountain tops occurred at temperature off sets of between -9.2℃ and -9.8℃ (e.g., 21.0 ka). This latter scenario (21.0 ka) generated ice thicknesses of 134-166 m within the overdeepening of Arrebiatadas glacier. Maximum ice surface velocity magnitudes between 45-80 m yr^{-1} were modelled within the Shimbe valley and were associated with ice flowing from the western valley wall, and from ice flowing from the valley head.

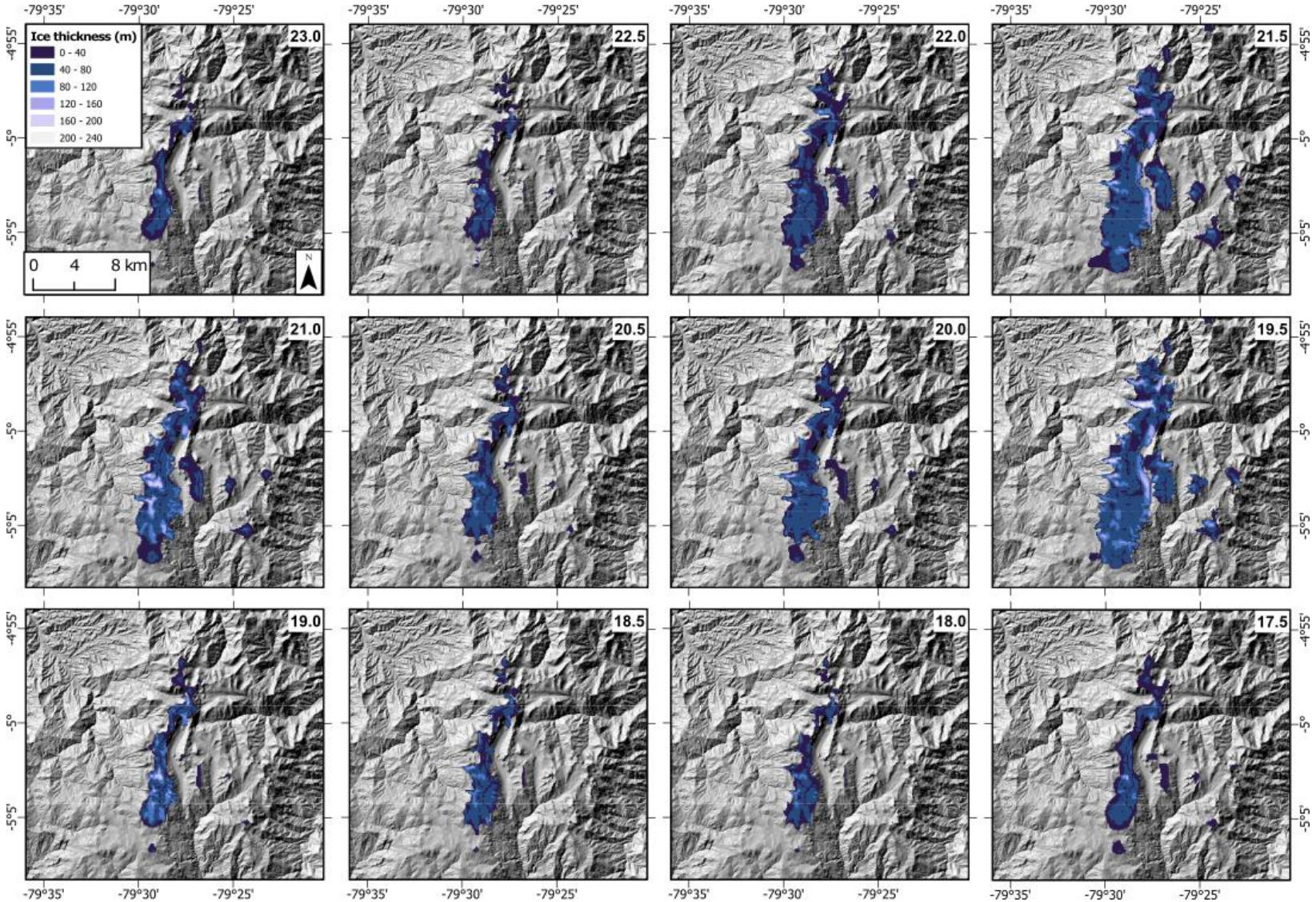

Figure 6.14: Varying extents of ice, detailing ice thickness across the post-LLGM between 23.5 ka and 17.5 ka. 19.5 ka was the most extensive ice during this period (seen in Figure 6.14). Legend values are scaled to LLGM ice thickness in Figure 6.11 to allow comparison. Deglaciated after 17.5 ka.

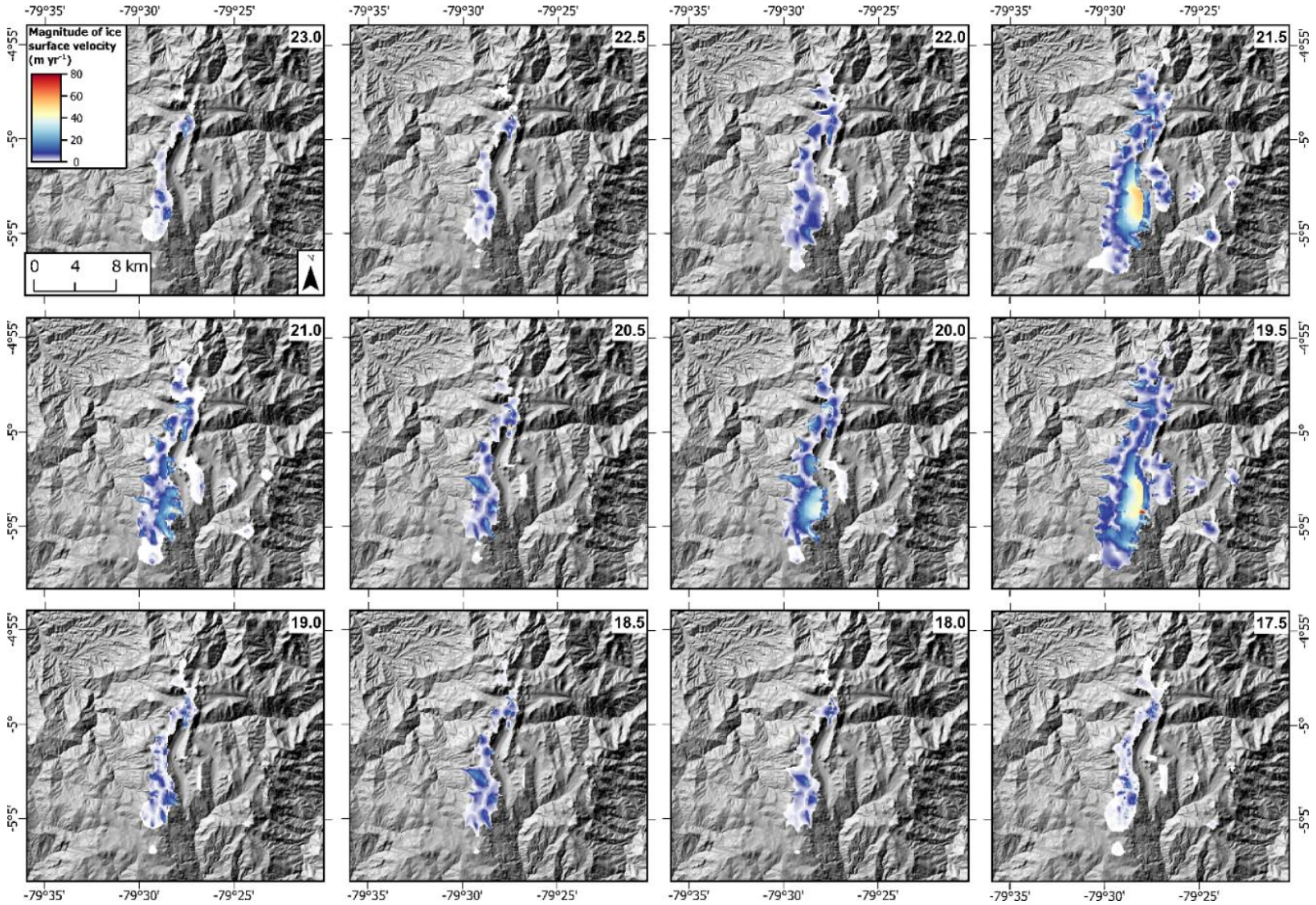

Figure 6.15: Varying extents of ice, detailing ice surface velocity magnitudes, across the post-LGM period 23.5 ka and 17.5 ka. 19.5 ka was the most extensive ice during this period (seen in Figure 6.14). Legend values are scaled to LLGM ice surface velocity magnitudes in Figure 6.11.

A period of ice mass advance occurred between 20-19 ka. The last maximum advance of ice between 20 ka to 19.5 ka associated with a temperature cooling between -9.6℃ and -10.1℃, resulted in a maximum ice area of 90.5 km^2 and an ice volume of 5.4 km^3. After this maximum ice advance at 19.5 ka, ice began to retreat in response to warmer temperatures (<-9.5℃ cooling). After 19.5 ka, glaciers receded back to their source areas (>3,400 m asl at their lowest in Shimbe valley) and fluctuated around their minimal extents, with ice areas between 4.5-57.4 km^2, and ice volumes between 0.2-1.3.5 km^3. From 17.2 ka onwards the region was completely deglaciated and no further ice developed in the model domain.

The greatest post-LLGM extent of ice occurred at 19.5 ka (Figure 6.16). Ice extent at this time was very similar to the former extent of the determined LLGM extent at 25.4 ka. Glacial ice within the model domain coalesced along the valley tops connecting to the northern regions, the Shimbe valley, and the western glacial cirques. However, unlike during the LLGM (25.4 ka), the Shimbe valley was not entirely glaciated. A small section of unglaciated terrain occurs between ice originating from the Shimbe headwall, and ice extending off the western valley wall. Further, the ice extension to the southwest of the Shimbe valley was at a similar extent to its LLGM position, while still incurring relatively thin ice (< 50 m). Ice area for this extent was 90 km^2 and the ice volume was 5.4 km^3, with ice extending slightly behind the former LLGM extent at 25.4 ka. This advance was in response to a cooling of -10.1℃ offset from present and resulted in an average ELA of 3,573 m (Figure 6.16). All the Shimbe valley ice was below the ELA at this time. Maximum ice thickness during this most extensive period was 221 m, found within the centre of the Palo Blanco 1 glacial valley. The maximum ice surface velocity magnitude occurred near the terminus of the Shimbe valley glacier, from ice flowing off the western valley wall at high velocities (80 m yr^{-1}) (Figure 6.17). This fast-moving ice is identified where the valley walls slope increases (40°) 2 km along the profile line (Figure 6.17).

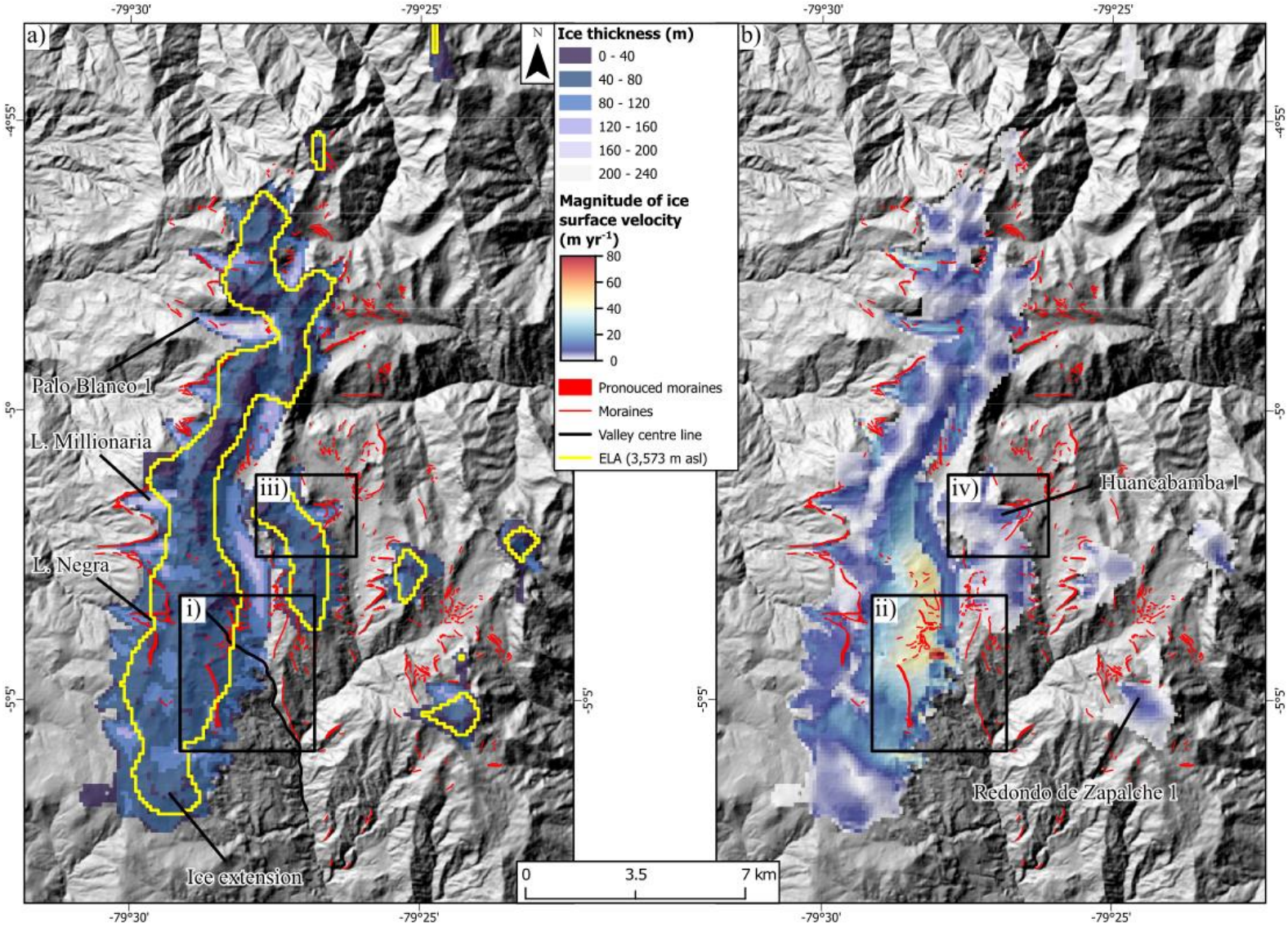

Figure 6.16: The most extensive area of ice during his waning ice period, at 19.5 ka, with a) ice thickness and ELA, and b) magnitude of ice surface velocity. Insets i) and ii) corresponds to Figure 6.17a&b, and iii) and iv) corresponds to Figure 6.18a&b. Named areas are referenced in the text.

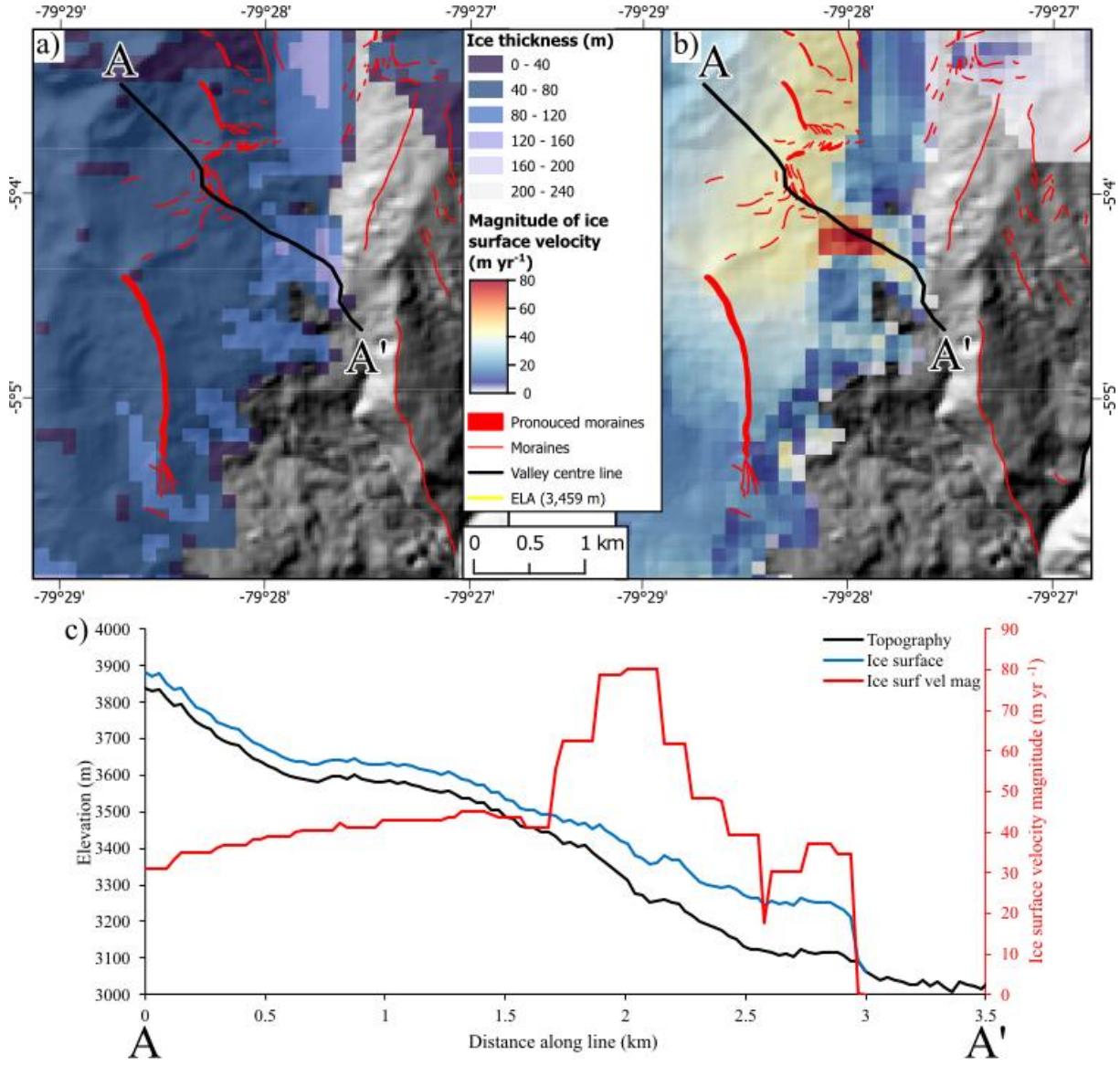

Figure 6.17: The terminus zone of the Shimbe valley glacier at 19.5 ka, a) detailing the glacial ice thickness and c) detailing ice surface velocity magnitude. Graph below follows the A – A' valley centre line and extracts the ice surface elevation, and ice surface velocity magnitude.

During the LLGM snapshot (25.4 ka), the Huancabamba valley western glaciers, east of the Shimbe valley, contained glacier ice that extended beyond the mapped moraine extents. At 19.5 ka, the modelled glacier extends to, and its terminus end sits at, the mapped 'maximum' moraines, and the alignment between the two is qualitatively near perfect (Figure 6.18). The ice flows down from an area of glacial ice that bifurcates into two ice lobes, one going east and another northward. The ice thickness within both lobes is relatively thin near the headwall (26 m), and becomes thicker as it moves down valley, with the thickest ice located ~1.5 km from its headwall at 122 m at the centre of the glacial cirque. The ice surface velocity magnitude also gradually increases moving downvalley, reaching a maximum of 19 m yr^{-1} ~2 km along the profile (Figure 6.18b&c).

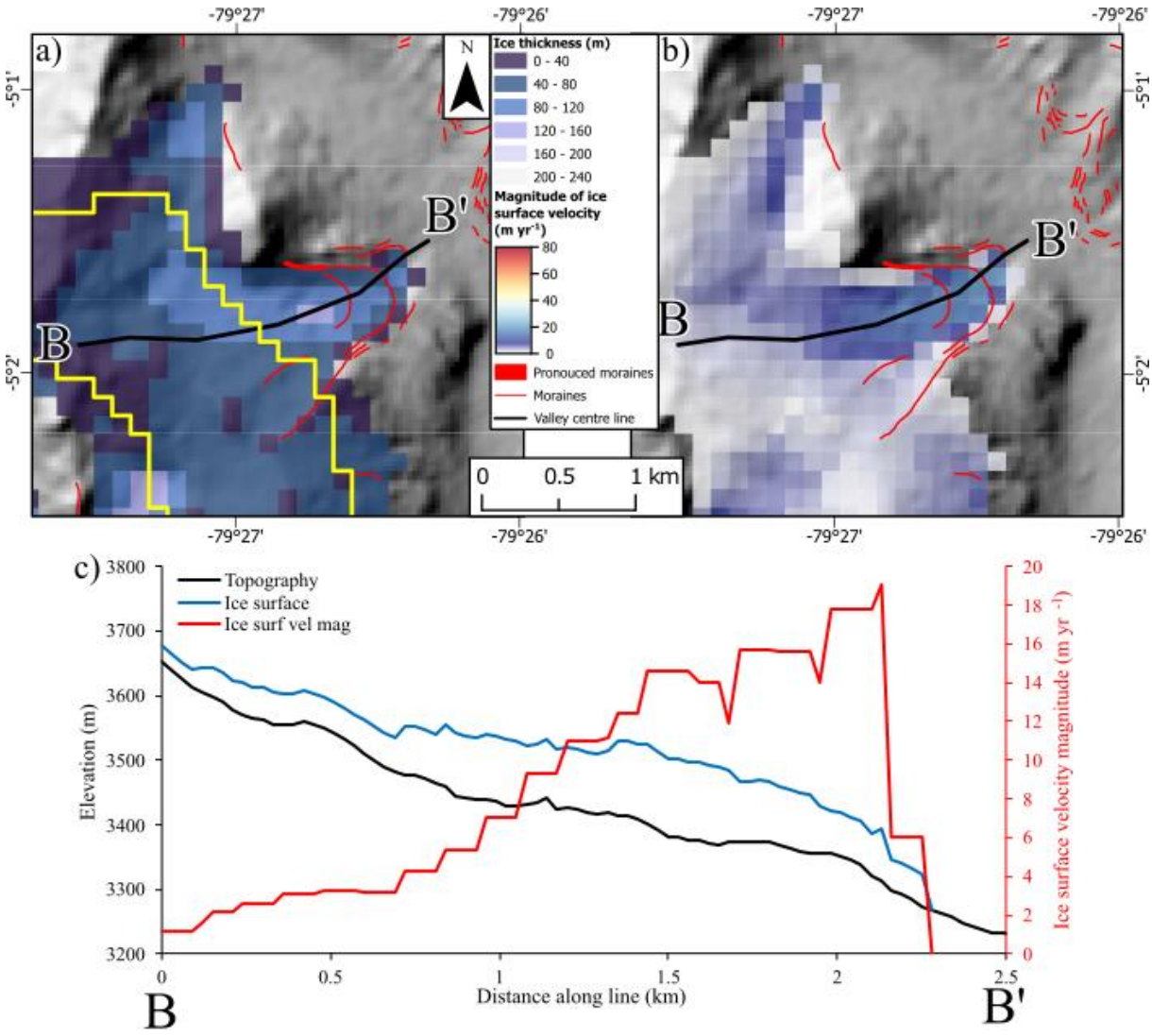

Figure 6.18: The Huancabamba 1 valley at 19.5 ka from ice spilling from its glacial cirque to its west, a) detailing ice thickness, b) ice surface velocity magnitude and c) details the values extracted along B – B' line.

Between 19.5 ka to 17.5 ka the remaining ice is limited to the high ridge west of the Shimbe valley. Temperatures in this period are offset from present by between -9.7°C to -8.6°C. The maximum area of ice varied between 15.4 km^2 to 89 km^2, with a maximum volume of between 0.6-5.9 km^3. The maximum ice thickness within the region in this period (181 m) was modelled at 19.5 ka, within the Arrebiatadas glacier accumulation area. Nearing, and at, 17.5 ka, ice retreated to higher elevations onto the mountain tops, with ice limited to elevations >3,400 m asl. The only locations where ice was present were: (i) the head of the Shimbe and Palo Blanco 1 glaciers, both fed by the same accumulation area; and (ii) the western glacial cirques. These locations are the only areas within the model domain that allow glacial ice to persist at this time. All remaining ice source locations are now devoid of glacial ice.

After 17.5 ka no glacial ice was present within the model domain. From the maximum ice extent in the LLGM period, during temperature offset of -10.1°C, they fall to above -8.2°C (Figure

6.1), completely deglaciating the region. At no point during the rest of the model run does ice build back within the model domain. This is also the case when temperatures decrease again for the ACR/YD period, however temperature offsets only reach a maximum cooling offset from present of -5.5℃ at 12.8 ka.

6.4.4. +/- 0.5℃ model runs

Running the model, with the same model parameters (e.g., precipitation at 130 % of present), but with temperatures +0.5℃ and -0.5℃ offset from the primary model run results in substantial differences in the area and volume of ice within the model domain. While the timing, and number of advances during the model run, remained the same or very similar, ice area and ice volume were half (+0.5℃) or double (-0.5℃) (Figure 6.19) that of the initial model run shown throughout this chapter. As can be seen, the -0.5℃ run outputs stop around 25 ka, this is due to the PISM model erroring out due to the amount of ice that is being generated, this causing KSP (Linear Solvers and Krylov Methods) errors that the stress balance could not be solved. However, due to the modelling erroring out, and seeing the amount of ice produced, in relation to the geomorphological record, these were not restarted (Figure 6.20). Precipitation variations similar, to temperature, were not conducted due to time limitations of the thesis.

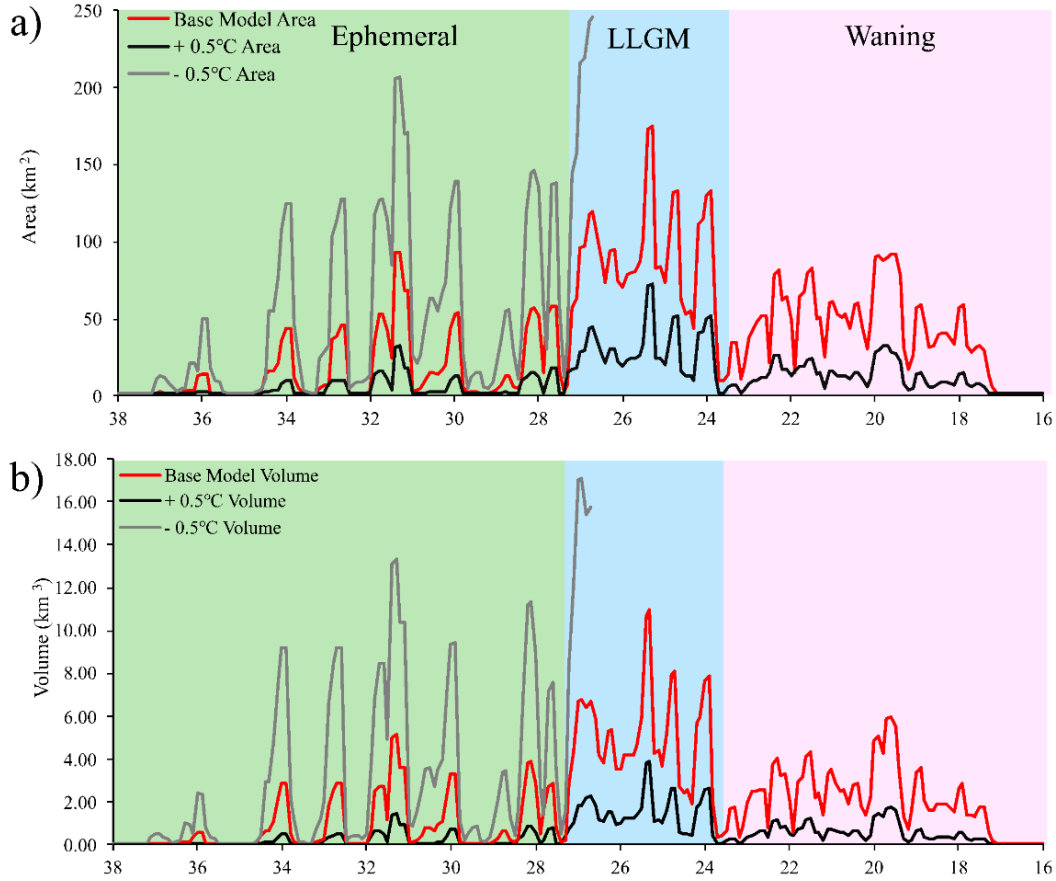

Figure 6.19: Area and volume of both + and – 0.5°C with the base model for reference.

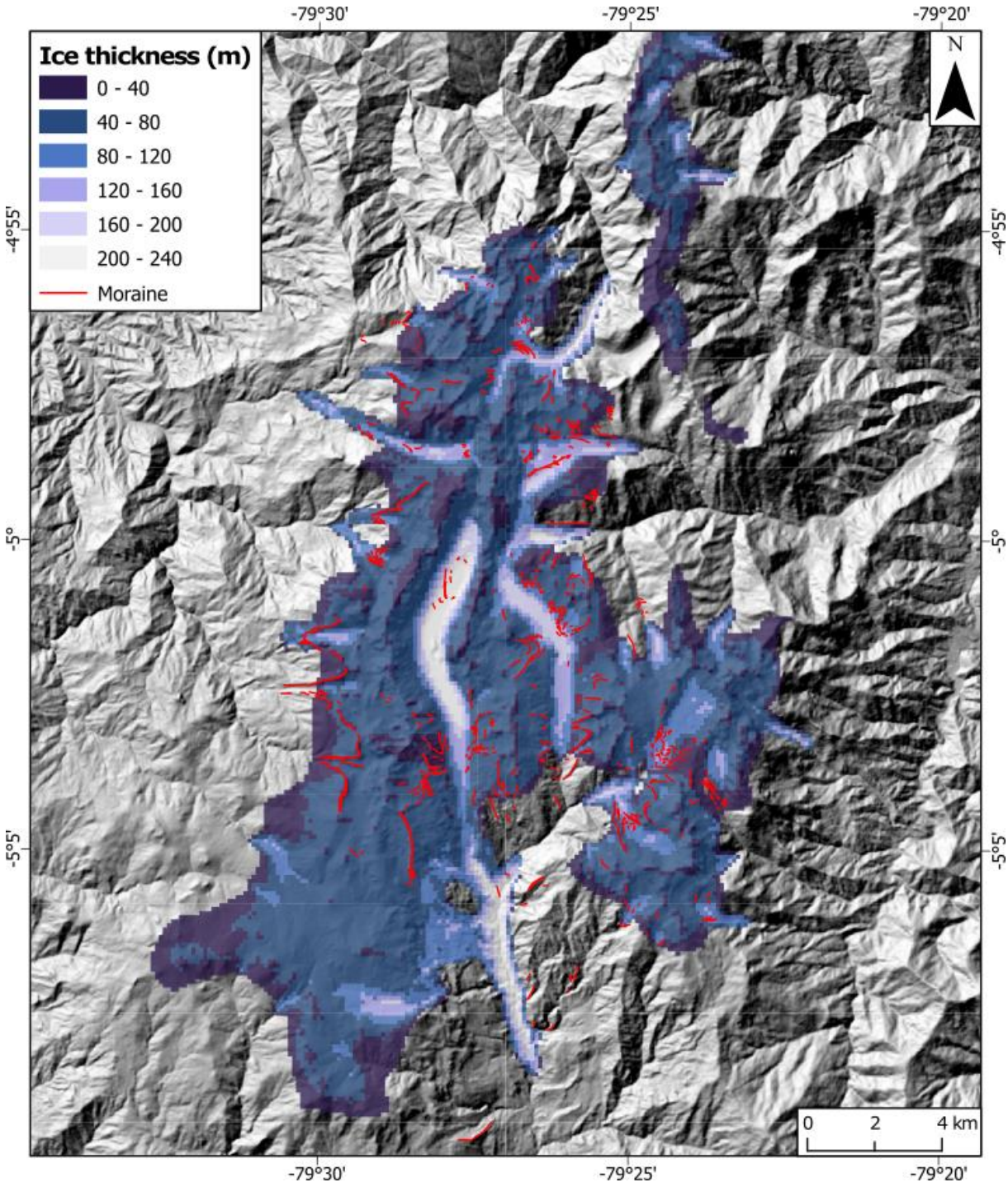

Figure 6.20: The final time slice (26.7 ka) before the -0.5°C model run crashed due to ice physics computation errors, detailing the ice thickness and ice extent overlayed the 30 m ALOS DEM hillshade, and the moraine geomorphology.

Generally, the final time slice of the -0.5°C model run (26.7 ka), at one of the lowest cooling in the EPICA time series, and the non-modified EPICA run assumed to be the LLGM, are characterised by ice that advanced further downvalley when compared to the LLGM period (25.4 ka) in Figure 6.8. The Shimbe valley ice extends further downvalley by ~7 km and has the thickest ice (~310 m) within the downvalley portion of the Shimbe glacier. Within the northern region, ice has advance past the most downvalley moraine evidence, overextending

between 700 m and 3.3 km. Ice in the western glacial region, due to being constrained topographically, and the ice divide drawing ice away from the west towards the Shimbe glacier, is only within 1 km of the assumed regional LLGM moraine. Ice is now able to overextend into the eastern glacial valley, causing the valley to fill with ice. That scenario never occurs throughout the entire non-scaled EPICA model runs. Lastly, ice now being generated within other high topographical areas, for example to the east of the northern glacial region, where ice caps are being generated where none were previously. Decreasing temperature by 0.5℃ can cause new locations to become ice covered, detailing the regions sensitivity to temperature changes. These new locations are primarily beyond the mapped geomorphology in Chapter 3, however, no evidence is mapped due to there being no evidence clearly identifiable within the remote sensing due to vegetation cover, or future postglacial reworking of the geomorphology. While it is not definitive that there was no glacial ice down to these extents shown in Figure 6.20, there is no geomorphological evidence to corroborate this extent. However, ice that advances over the topographical dip (shown in Chapter 3, Figure 3.5) now has ice advancing over it that does have some evidence in the geomorphology, if the temperature was this cool to allow ice to be this extensive.

An increase and increase of precipitation were not conducted due to time constraints within this thesis. However, as doing the +/- runs for the temperature, a +/- run for precipitation would aid in understanding with a time varying temperature, if there would be differences in ice extent. This would be future work after the completion of this thesis.

6.5. Further results from the model

6.5.1. Ice persistence

Within this section, persistency is determined between the period from initial glaciation (34.6 ka) to the final deglaciation (17.2 ka), and the amount of time an area is glaciated (not continuously but if ice is present) is denoted by a percentage (%) of time. There are regions where ice persists and provides the source area for glacial ice (Figure 6.21). The most persistent ice is seen at the head of the Shimbe valley (80%; 3,827 m asl), and the highest peaks on the western cirques (80%; 3,882 m asl). These locations, whilst not continually glaciated (e.g., they were ice-free between 32.5 ka to 32.0 ka) are locations of extensive ice accumulation that during periods of extensive temperature cooling, below -10℃, (e.g., 26.0 ka to 25.0 ka) coalesced and permitted ice to extend across the model domain. Other locations, that are characterised by the presence of ice for extended periods of time (~50% of the time) are generally along topographic

highs at elevations > 3,500 m asl, such as the eastern ice cap regions, and the region north of the Shimbe valley.

Ice presidency of >50% of the time (Figure 6.21), has the largest concentration over the western glacial cirques than any other region in the model domain. The head of the Shimbe valley has a smaller area that has also been glaciated for >50% of the time. These regions are at a high elevation (>3,800 m asl)while the surrounding areas that incur less time glaciated, are lower elevation glacial source areas (~3,600 m asl) and have substantial differences in source area to valley floor elevation change, with around 550 m in glacial valley relief to the north of the Shimbe valley. This drains the accumulation zone and makes the ice more susceptible to high temperatures in this area, while the lower elevation source area means that when temperatures warm, the areas are more susceptible to deglaciation. The glacial valleys within the western glacial region, have a similar elevation drop to their valley floors (~600 m), but due to having higher source areas, ice can be sustained across an extensive area above the western cirques.

Within the zones where ice was present > 50% of the time between 34.6-17.2 ka, there are ice margins near prominent (large) moraines. These locations are at the southern end of the study site at the Huancabamba 3 glacier (Figure 6.21a), and at the northern end of the el Ray Inca glacier (Figure 6.21b). These could explain the formation of such large moraines within the region, with glaciers being at, or near, these mapped moraine limits for long periods of time. Contrary to this, the down-valley end of Laguna Millionaria (Figure 6.21c) is surrounded by large prominent moraines, but the ice persistency output suggests that ice was present here < 25% of the time, and was at, or near, the terminal moraines only < 3% of the time.

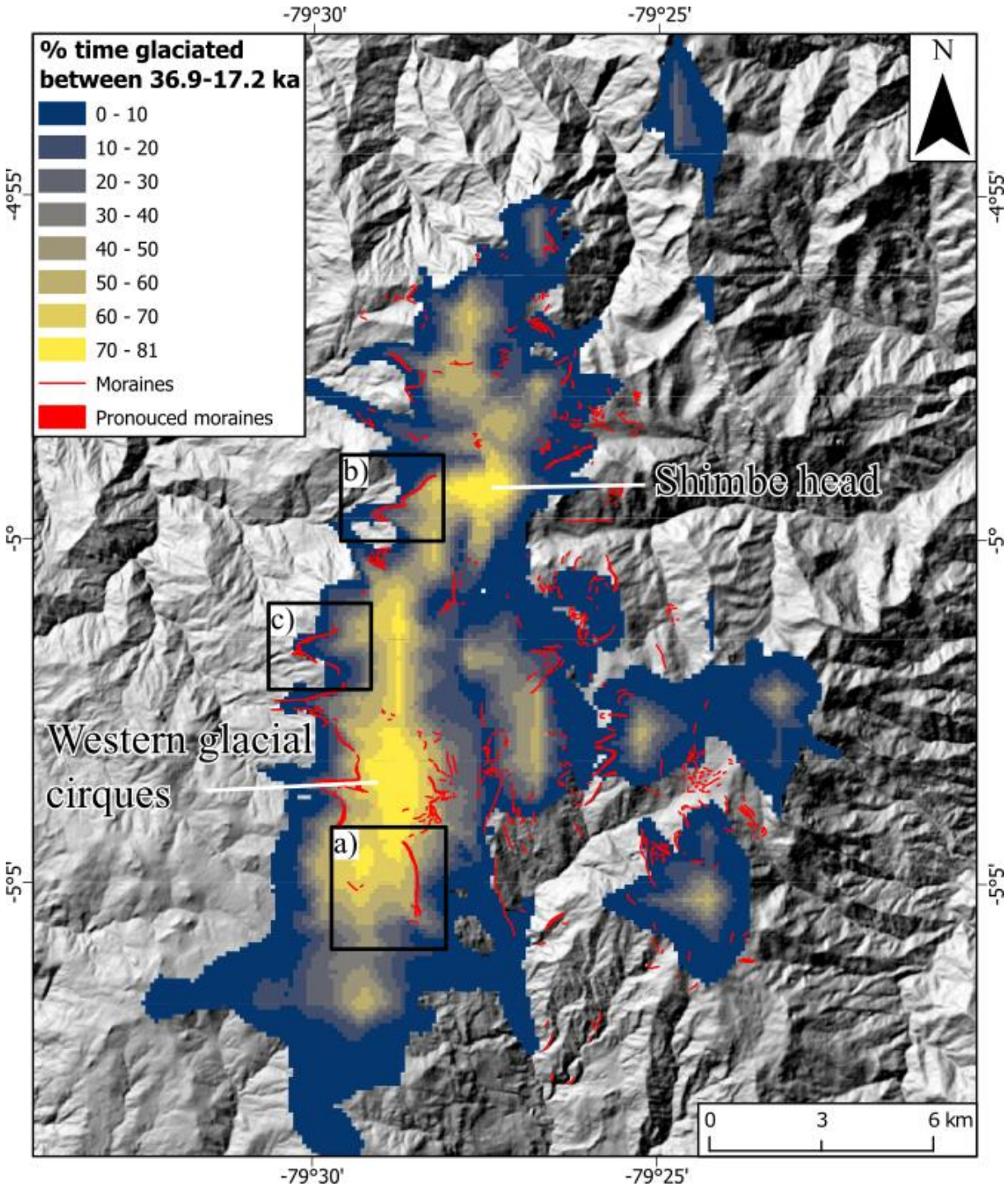

Figure 6.21: Percentage of time glaciated during the periods where glacial ice is present within the model domain, when first ice first grew in the domain in (36.9 ka) to the final time ice was present (17.2 ka). The darkest grey areas denote the main accumulation zones. The highest extent, seen in the blue area, is discussed in section 6.4.2.

6.5.2. Mass Balance

Throughout the period of glaciation, when temperatures were above -9.5°C (such as in the Ephemeral and Waning ice period) ice may only fill the Shimbe valley to a limited extent (limited to near the headwall), or not at all. When temperatures decrease to near -10°C (LLGM

period) from present, ice entirely fills the Shimbe valley. At no point in the model run does ice half-fill the Shimbe valley. The mass balance of the ice at this most extensive period (25.4 ka; LLGM) (Figure 6.22) at outlet glaciers below the elevations of 3,100 m asl, are characterised by high rates of mass loss of > 2,000 kg m^2 yr^{-1}. This considerably outweighs the mass accumulation maximum of 863.7 kg m^2 yr^{-1}, with most of the ice area above 3,500 m asl, incurring between 400 to 863.7 kg m^2 yr^{-1} of accumulation.

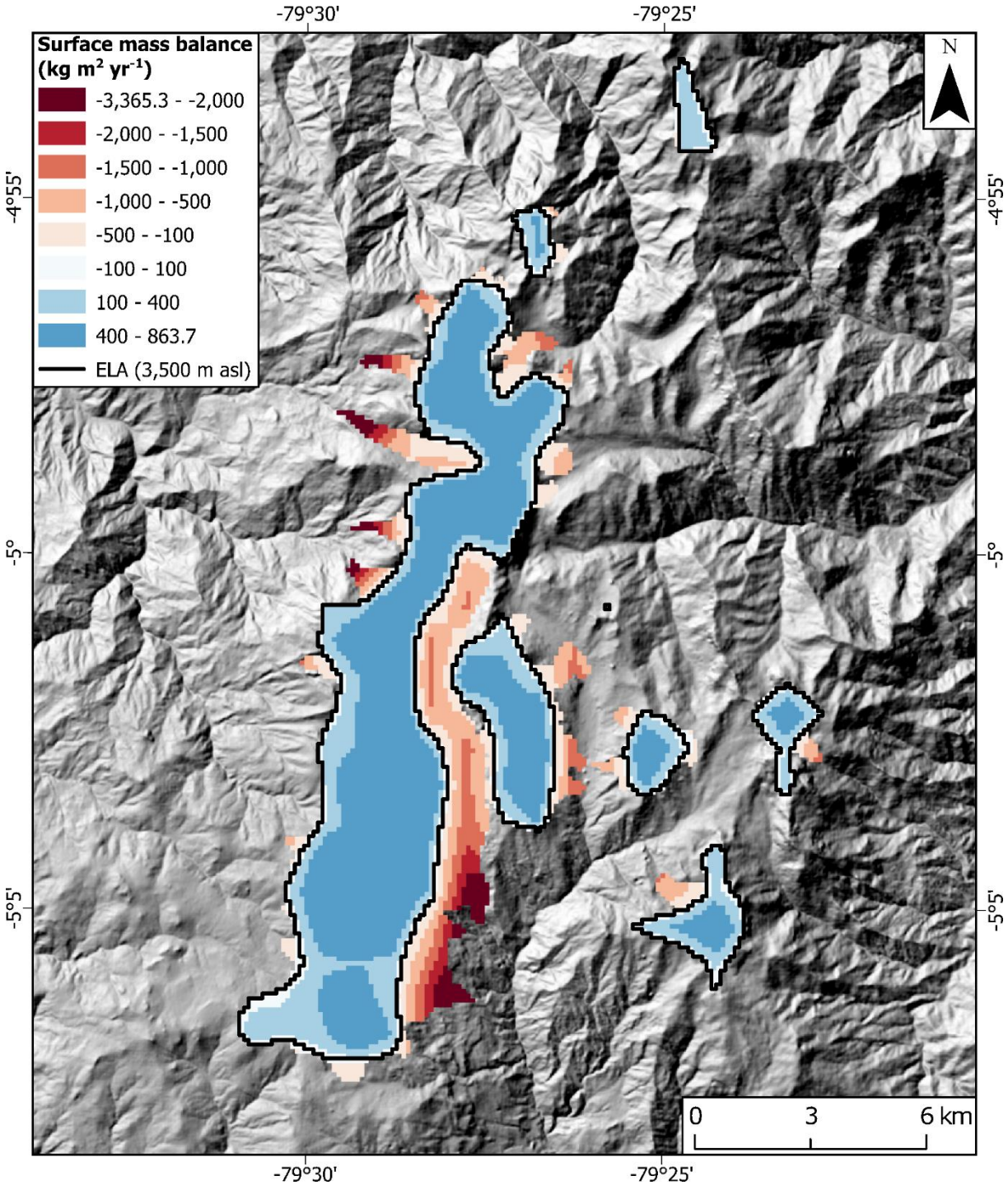

Figure 6.22: Modelled annual mass balance for the Las Huaringas LLGM extent with ELA at an average elevation of 3,500 m. Extreme mass loss (>2,000 kg m^2 yr^{-1}) is seen at low elevations (< 3,100 m) drawing ice down via gravitational transport.

The most negative surface mass balance is seen at the glacial terminus locations where ice extends down to the lowest elevations, such as at the end of the Shimbe valley, Palao Blanco 1 and 2, and El Ray Inca glaciers, in the northwestern section of the model domain. As these ice masses extend from their glacial cirques and headwall source areas, they have steep surface mass balance gradients. Glacial ice within the eastern glacial ice caps, have their lowest mass balance of ~-1,000 kg m^2 yr^{-1}, however due to their much lower maximum elevations, they also incur a lower accumulation of up to 600 kg m^2 yr^{-1} that limits their glacial extent potential.

6.5.3. Ice flow

During all periods where glacial ice has been extensive enough to fill the Shimbe valley (e.g., LLGM; 25.4 ka), the fastest flowing ice has been located either at the terminating end of the Shimbe valley glacier, or within ice on western valley wall flowing into the Shimbe valley. These have led to ice velocities in this location of up to 60.5 m yr^{-1} during the LLGM (25.4 ka) and up to 80 m yr^{-1} during the final most extensive ice extent in the waning ice period (19.8 ka), where ice flows from the western valley wall (Figure 6.23). The presence of ice within the Shimbe valley appears to 'drawdown' ice from the western valley cirques, and into the Shimbe, causing the ice divide to migrate from the top of the western valley wall, to within the western glacial region. This can be seen in the velocity flow patterns (Figure 6.23; 25.4 ka), with little to no ice in the southern portions of the western glacial cirques flowing into extensive glacial ice tongues, extending down from the main ice mass during the LLGM period. This sort of ice flow configuration is not seen during any other time during the model run, and only occurs during the LLGM period, where there is a large expansion of glacial ice, increasing the catchment area of where ice flows from.

Valley-constrained ice in surrounding regions is associated with slightly slower ice surface velocities compared to those found in the Shimbe valley. For example, ice in the Negra valley reaches a maximum of 13 m yr^{-1}, but the Palo Blanco 1 glacier in the northern regions reached velocities up to 60.5 m yr^{-1}, during periods of extensive glacial ice (LLGM; 25.4 ka). At no point during other time snapshots in the model did glacial ice within valleys reach ice velocities that high. Where the fastest velocities do exist within valley-constrained glacial ice, these are all located near the terminal end of the glaciers where the valley reaches lower elevations in response to convergent ice flow and ablation (Benn and Evans, 2014).

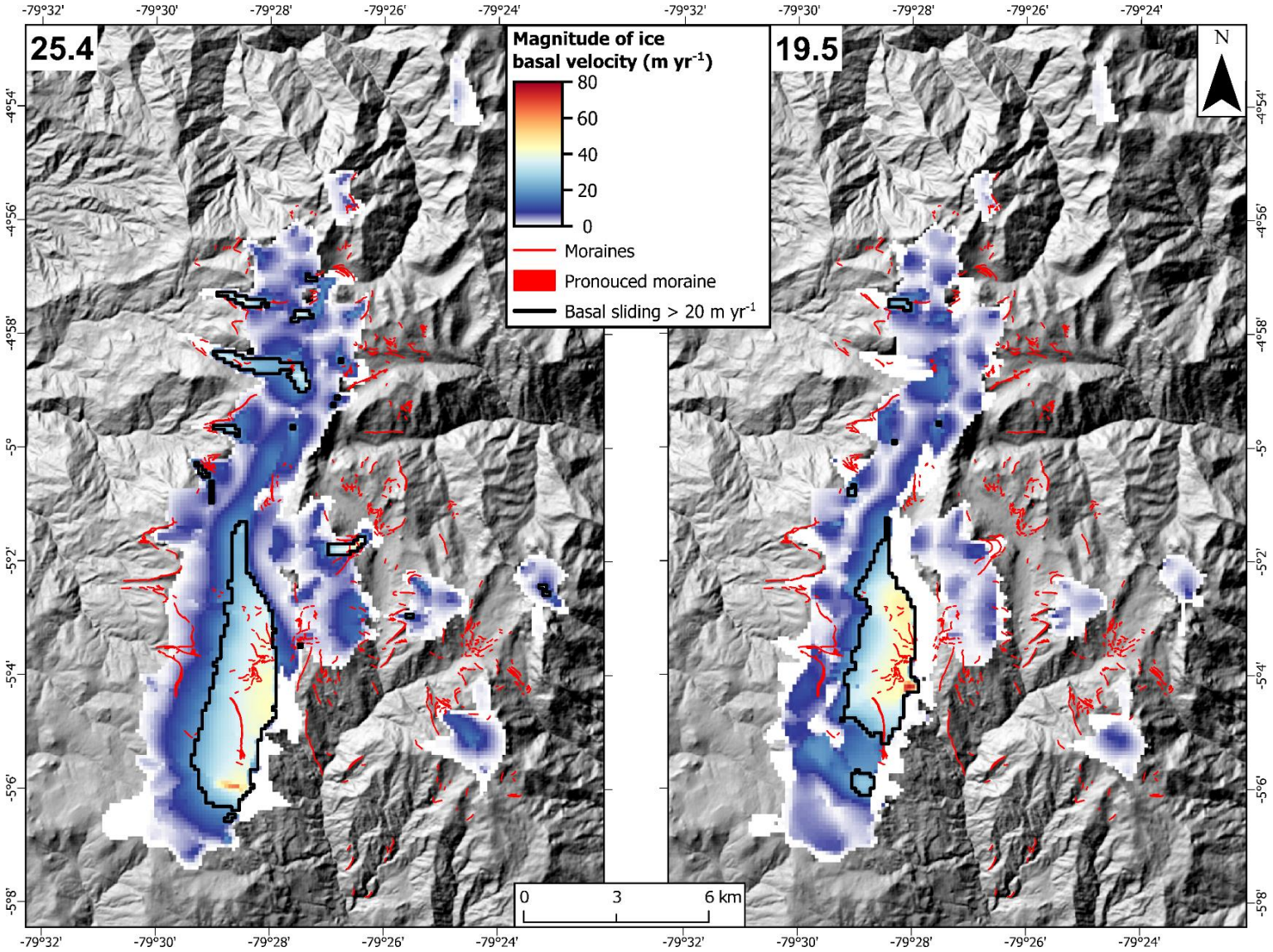

Figure 6.23: Basal ice velocity magnitudes from the LLGM period (25.4 ka), and the most extensive glacial ice during the waning ice period (19.5 ka).

The model can also provide 'basal velocity' outputs useful for inferring whether the ice mass is moving primarily due to internal deformation, or if sliding is occurring. Here, it is assumed that ice is flowing primarily by internal deformation where the basal velocities are < 20 m yr^{-1}. Internal deformation accounts for most of the velocities seen across the model region (Figure 6.23), primarily for ice within valleys (e.g., within the Shimbe valley at 25.4 ka and 19.5 ka). However, basal sliding does occur at locations where ice is situated on down-sloped terrain with gradients greater than 25°. A prime example is along the western valley wall where basal sliding occurs most of the time throughout the model run when ice flows from the valley wall (Figure 6.23). More sliding also occurs at times of increased glacial accumulation in the model (e.g., following a sudden temperature cooling, for example towards the LLGM; 25.4 ka). The glacier margins and termini are characterised by no basal sliding (Figure 6.23; 25.4 ka).

6.5.4. Basal ice temperature

While the presence of some basal sliding within the model may indicate some warm based glaciation. The model, across all time slices and thus all time periods, however, indicates that ice temperatures at the base of all the ice within the model domain was at 0°C (Figure 6.24). This is at the intersection of ice melting at the bed, allowing sliding, and ice being frozen at the bed, reducing sliding. There is no point within the model run, at any time slice, where basal ice temperatures were over 0°C.

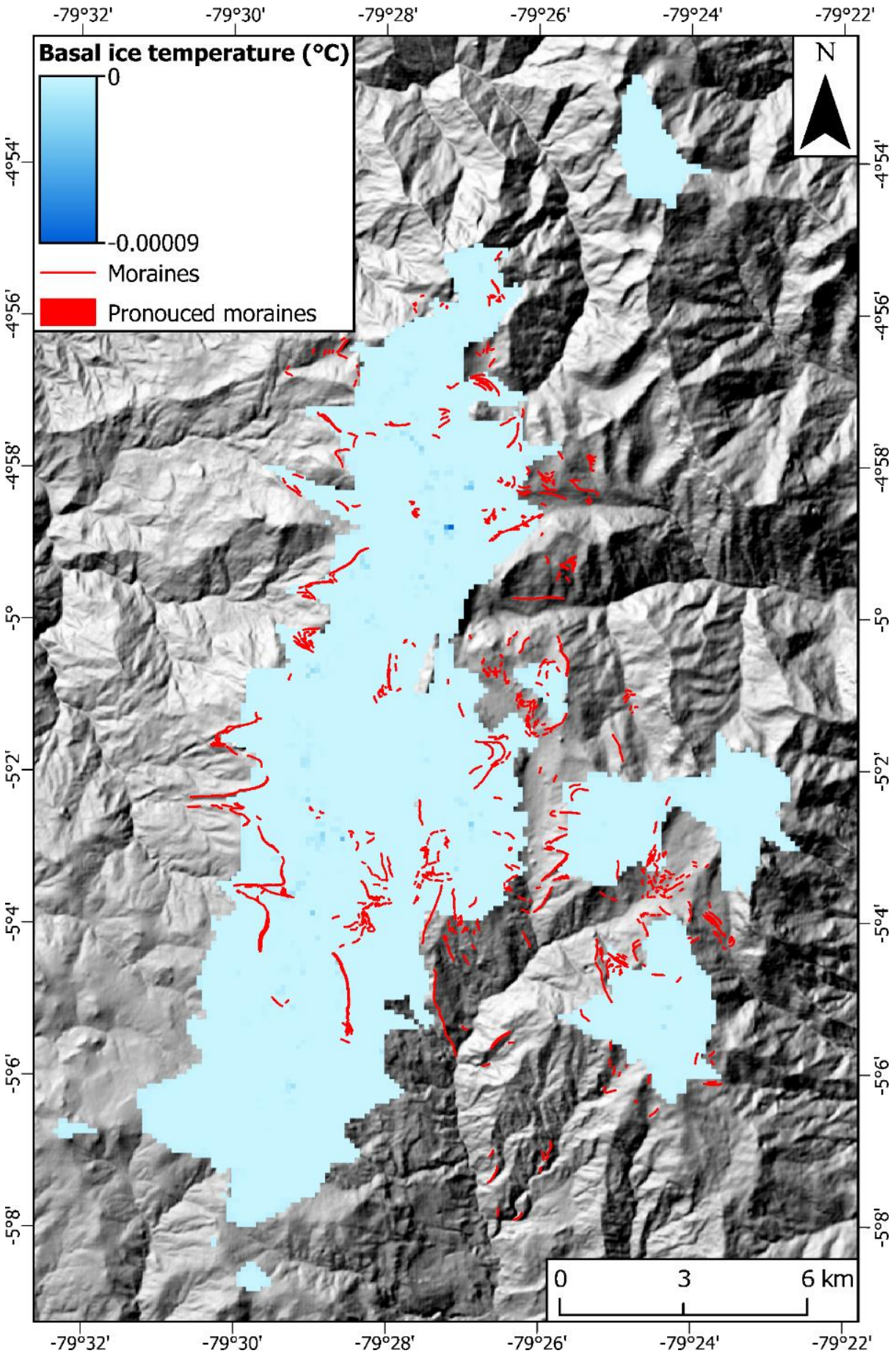

Figure 6.24: The basal ice temperature of the most extensive ice during the model run at the LLGM (25.4 ka), however this is indicative of basal ice temperatures at all time slices.

6.6. Discussion

This chapter, along with the parameterisation of the model from the previous Chapter 5, has enabled a numerical modelling framework for the glacial history of the Laguna de Las Huaringas area, permitting us to reconstruct the glacial dynamics of the area, throughout the period 38-0 ka. While it is clear that certain valleys and regions within the Las Huaringas have been characterised by extensive glaciation (Chapter 3: Lee *et al.*, 2022), it is unknown for how long, how many times, and how extensively. Using the modelling here it is possible to; i) assess the timing and persistency of ice within the region, ii) understand how the ice was configured i.e., if it was cirque-to-valley, or an ice plateau, and iii) see how sensitive to climate glaciers in this region may have been, and to assess the mass balance regime of the ice masses. Lastly, in lieu of geochronological dated moraine features, models can provide potential estimates on the timing of glacial advances of interest (e.g., the LLGM), but can be also tested against the dated moraines when dates become available.

6.6.1. Model evaluation - ephemeral glaciation (38-27.5 ka)

Within this section, by model evaluation, it is compared against the mapped geomorphology from both Chapter 3 and Chapter 4. It is likely that due to more extensive advances of glaciers after 38-27.5 ka, both at the LLGM (29-23.5 ka), and during the later waning ice period (23.5-16 ka), that any geomorphological evidence that was deposited between 38-27.5 ka would not have survived. Geomorphic evidence may exist from this period, but it would likely be difficult to confirm without extensive infield investigations (e.g., sedimentological analysis of glacial deposits) due to it being either covered by post deposition processes, or eroded away by subsequent glaciations, but overall are unlike to have survived in an unmodified state. This section will only discuss agreement and disagreement with geomorphological evidence of modelled ice dating to the maximum extent of the determined LLGM, and modelled ice extents during the waning ice period. However, it is noted that between 38-29 ka the model output often has ice extents that align well with the mapped moraines (Chapter 3) (Lee *et al.*, 2022).

6.6.2. Model evaluation - local last glacial maximum (27.5-23.5 ka)

It is reasonable to expect that across the study area the assumed LLGM extent of individual valley glaciers would be asynchronous due to topographical and microclimatic controls on ice mass formation and evolution (Thackray, 2008). However, at ~25.4 ka nearly all modelled valley glaciers were within a few hundred metres of their mapped maximum extent moraine.

There is a difference of 97.4 km^2 between the regions LLGM reconstruction from the geomorphological evidence in Chapter 3 (Figure 3.2) (Lee *et al.*, 2022) (75.6 km^2), and the modelled LLGM area (173.2 km^2). This difference in area can be explained by the glacial ice coalescing together over the topographical highs to form a large primary ice plateau, and multiple secondary ice caps. While unable to be compared with the geomorphic record, the modelled ice volume at 25.4 ka (assumed LLGM) was 10.9 km^3.

The model is unable to reconcile the potential spilling over of ice from the Shimbe valley into the eastern valley, as interpreted in the geomorphological record (Chapter 3; Figure 3.4a). The model did confirm that the estimated thickest ice (200 m) from Chapter 3, during the LLGM, was centred over the overdeepening of Laguna Shimbe, with a maximum thickness of 222 m. However, the ice thickness near the identified topographical dip, was not thick enough to allow ice to spill over and flow into the eastern valley (Figure 6.25a). The model therefore disagrees with the suggestion in Chapter 3 that ice spilled over from Shimbe into the eastern valley. However, the model does suggest that glaciers within the eastern valley cannot expand to fill the entire valley without input either from ice within the Shimbe valley, or additional mass accumulation (cooler temperatures, or more precipitation). This is further supported by the -0.5℃ model run, where the final time slice shows ice almost entirely filling the eastern glacial valley, due to ice being able to advance over the valley walls from within the Shimbe valley. At only more cooler temperatures, does the eastern region incur an ice configuration that closely resembles that was inferred within Chapter 3 (Figure 3.4b). It is likely that the model parameters as is, does not capture the dynamics correctly, but due to the lack of observation data for climate, it is hard to parameterise the model correctly.

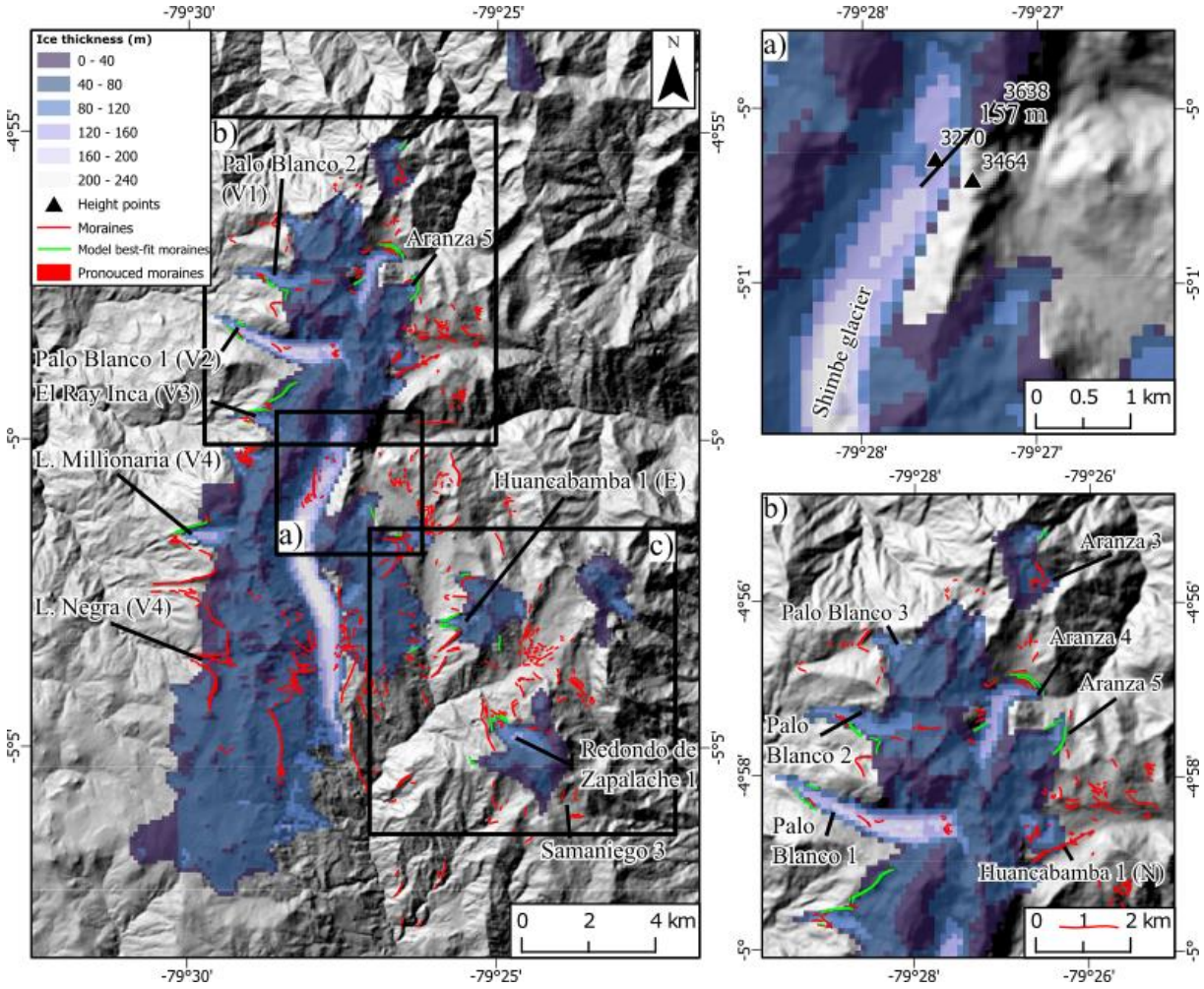

Figure 6.25: Ice extent and thickness during the LLGM (25.4 ka), with moraines that are determined in the model as from the LLGM (green moraines). a) Ice thickness located near, and at the topographical dip, detailing the ice is not thick enough (157 m) to spill over into the eastern valley leaving a nunatak, and b) the northern region detailing ice that both over- and under-shoots assumed LLGM moraine positions. c) The eastern ice capped region that primarily undershoots there assumed LLGM moraine positions (shown in Figure 6.26).

There are regions of good agreement between the model output and the mapped geomorphology for many of outlet glaciers within the Las Huaringas study area. The EPICA temperature offsets result in similar ice extents to the best fit model within the five glacial valleys of the western cirque glaciers (Figure 5.4). Redondo de Zapalache 1, Palo Blanco 1 and 2, El Ray Inca, Millionaire, Huancabamba 1 (E = eastern ice capped section), and Aranza 5 (see Figure 6.25 for names) show good agreement with their assumed LLGM terminal moraines, being within 200 m of the maximum mapped moraines. The extent of ice in the Negra valley falls short of the mapped moraines by 450 m, though the ice does not appear to match the topography. This could provide some evidence of the model requiring a resolution higher than 150 m to reconcile all glacial-topographical interactions.

There are some regions where mapped maximum-extent LLGM moraines are both in front of, or within the confines of, the modelled terminal ice. Modelled glaciers within the northern

region of the study region (Figure 6.25b), attached to the interconnected ice field during the LLGM, both over- and under-shoot the maximum extent moraines. Outlet glaciers situated on the eastern side of this northern location, Aranza 3, and Palo Blanco 2, are more extensive than their most extensive mapped moraines by between 300 m and 650 km. The Palo Blanco 3 glacier and Huancabamba 1 (N = northern section) glaciers are less extensive than their mapped maximum ice limits by up to 1.6-2 km. Such over and under extents may indicate incorrect assumptions made in Chapter 3 of their LLGM positions (Figure 3.11), and that evidence behind their assumed LLGM moraines may be LLGM in origin, while those in front are older. There may also be the potential that the model cannot resolve such detail due to glacial-topographical effects in the model.

The modelled ice extent of the ice caps in the east of the model domain (Figure 6.26) shows that almost all glaciers do not extend to their assumed LLGM moraines. While some glaciers extend close to other inset moraines (e.g., Huancabamba 5), these do not match what was interpreted within Chapter 3 (Figure 3.6) The Redondo de Zapalache 2, and Samaniego 1 glaciers, situated on the most eastern ice cap, are 3 km shorter than the furthest extent moraines. Similarly, the southern ice cap, which includes the Huancabamba 5 glacier, under-shoots its assumed LLGM moraines by 1.5 km. Such a substantial ‘under-shooting’ may be due to topographic effects, due to the model not being able to resolve small-scale topographic variations. Further, potentially the model is unable to replicate precipitation gradients. The spatially homogenous +30% precipitation used here does not consider the E-W precipitation gradients that were hypothesised within Chapter 3 (section 3.3.7.)

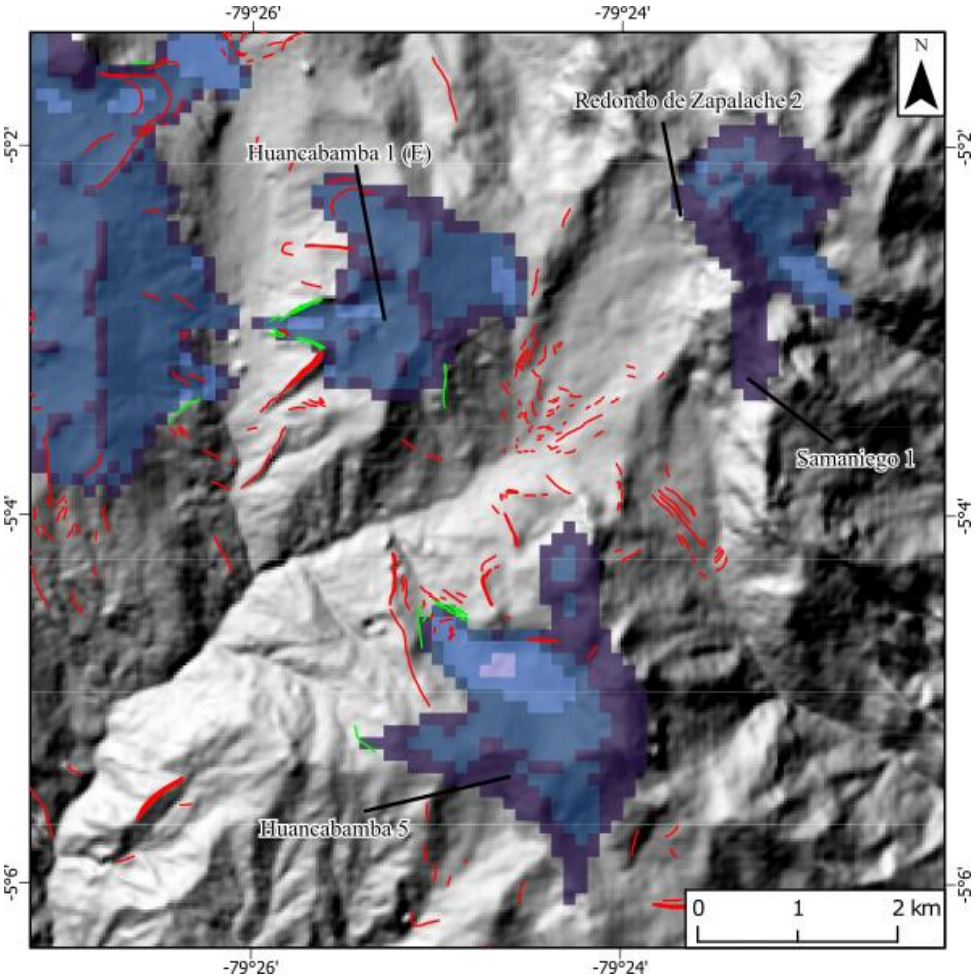

Figure 6.26: Location shown in Figure 6.25c, details the eastern ice caps in the model region, with moraines that are close to LLGM position (green lines), and identified glaciers that largely under-shoot their assumed LLGM moraines. Legend same as in Figure 6.25.

These differences between the reconstructed ice extents in Chapter 3 (Lee *et al.*, 2022) and the modelled ice within the northern and eastern regions (Figures 3.6 & 18) may reflect locations where the mapped maximum extent is incorrect. Without geochronological control on these mapped moraines (e.g., cosmogenic nuclide dating), the actual LLGM extent evidence may be at or near the modelled terminus location and may not have been mapped due to the limitations of the remote-sensing based mapping. Alternatively, any landforms may have been removed by post-glacial processes (i.e., fluvial, or periglacial). These differences could also result from the precipitation offset used (+30%), or different precipitation patterns not considered in the model. For example, the potential east-west precipitation gradient within the study area may be steeper than inputted into the model. This has also been identified across other localities within the tropical Andes (cf. Porter, 2001; Martini *et al.*, 2017). A final potential reasoning for any discrepancies seen, may also be the asynchronous nature of glacial advance, with outlet glaciers reaching their individual assumed LLGM (or most extensive) positions at different times because of valley specific topographic controls that can influence glacial extent and thickness within valleys.

6.6.3. Model evaluation - waning ice (23.5-16 ka)

Between 23.5 ka to 16.0 ka, there is little understanding of ice dynamics and history within Las Huaringas. The geomorphological evidence (Chapters 3 & Chapter 4) evidence detailed moraine formation behind the most extensive moraines, that must postdate the maximum ice limits. In Chapters 3 & Chapter 4 (Lee *et al.*, 2022) it has been suggested that these moraines could date to the Late Glacial or even Holocene periods. However, in the absence of chronological control, the numerical modelling output can be used to test whether glaciation was viable post-LLGM, and potentially when such glaciation might have occurred.

The most extensive period of glaciation in the model between 23.5-16 ka was at 19.5 ka. The modelled ice masses then were slightly less extensive than that of the LLGM, but the Shimbe valley was partially filled. The only moraines identified in the Shimbe valley are found between Laguna Shimbe and Shimbe 2, or along the valley wall. In the 19.5 ka snapshot this area was ice free (Figure 6.27a), but the modelled ice front was proximal (~200 m) to the mapped moraines. This provides the potential for these moraines to have been generated during this time period, before retreating for the reminder of the waning ice period. At 19.5 ka, other outlet glaciers were connected to the ice plateau and reached, or were near too, their previous most extensive ice positions, near to the maximum moraines (within ~200 m).

The eastern ice caps are at similar extents to those identified during the LLGM (Figure 6.25) if less extensive, being further behind discernible moraines at 19.5 ka, and their margins are located either just behind (i.e., Redondo de Zapalache 1 by 100 m), or are at the limits of their accumulation area (i.e., Redondo de Zapalache 2; Figure 6.27b). This may suggest that the ice caps glaciers were more responsive to warmer temperatures and began to deglaciate first, due to less ice mass. They are thus unable to re-expand during rapid drops in temperature (e.g. lasting 100 yrs) due to much of their ice mass already having been lost (Gardner *et al.*, 2011; Marshall, 2021).

At 19.5 ka, glaciers connected to the primary modelled ice plateau (i.e., Laguna Millionaria, Palo Blanco 1) are at, or near, their former maximum extents, similar to their LLGM extents. Laguna Negra ice, however, extends 900 m downvalley from the mapped maximum moraines (Figure 6.27c), this is in comparison to the 200 m under-extent seen within the LLGM (Figure 6.26). This reinforces the assumption of a migrating ice divide as ice grows and expands into the Shimbe valley, as ice is reduced, it can flow again into and down their respective western valleys. The larger volume of ice in the primary ice plateau acts as a buffer to warming temperatures allowing it to maintain ice volume for a period of time after warming occurs, the opposite of that seen in the eastern glacial valley ice (Huss and Fischer, 2016). During later

short temperatures drops it is then able to advance back to, or near, its prior extensive positions. Some glaciers, however, are close to other moraines behind and deposited later than the LLGM extents. For example, the inner moraines (green lines) of the outlet glacier Huancabamba 1 (W = western) are reached by the modelled ice extent at 19.5 ka (Figure 6.27d). In the geomorphological mapping reconstruction (Chapters 3 & Chapter 4; Figure 3.2) these inner moraines were proposed to represent glacial advances or standstill locations post-LLGM. As many of the mapped extents in the western glacial cirques were reached in the model at both the LLGM and 19.5 ka, the large moraines in this part of the model domain could be the cumulative result of multiple phases of glaciation, with ice retreating and then readvancing due to cold snaps, entraining dropped debris, or further eroding the valley.

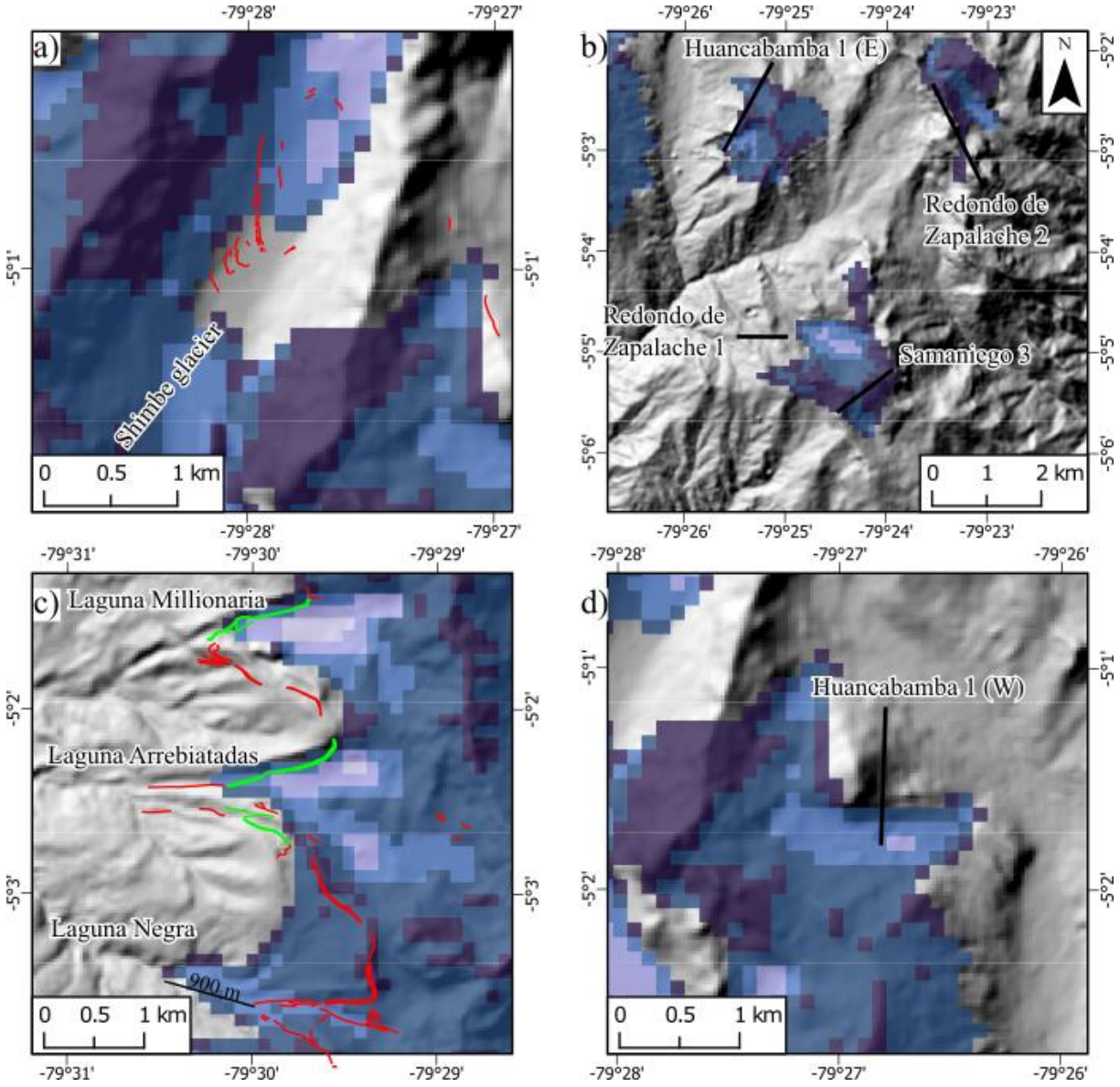

Figure 6.27: Glacier extent in relation to mapped moraines during the most extensive period of the waning glacial period (19.5 ka) in a) the eastern ice cap region, b) outlet glacier from the Huancabamba 1 (W) glacier, c) the western glacial cirques, and d) the Shimbe valley. Legend is same as Figure 6.25.

While the evidence presented here is for 19.5 ka, for most of the waning ice period, the ice was limited. The model snapshot at 20.5 ka, provides a more representative extent for the full waning ice period, with ice close to moraines located further up-valley of the maximum mapped moraines (Figure 6.28). At 20.5 ka, the Shimbe glacier is restricted to its headwall, 1.2 km away from the closest mapped moraines (Figure 6.28a). At no point within the model domain during the waning ice period (21-16 ka) is ice at the moraines just up valley of Laguna Shimbe. The differences between the geomorphic reconstruction and the modelled ice extents, could be because the model inputs are not able to accurately model glacial dynamics in the Shimbe valley, or perhaps evidence (e.g., moraines) has been removed by post-glacial processes.

Modelled glacial ice in the western cirque area at 20.5 ka was able to persist at elevations comparable to the most extensive positions (3,200-3,400 m asl) but were set 600 m to 1 km behind the maximum positions. Some of these valleys have no discernible evidence that detail ice at this extent (e.g., Laguna Millionaria) (Figure 6.28b), which may be due to evidence being precluded by the lake, while in the Arrebiatadas glacier has some lateral moraines close to the modelled ice position.

At 20.5 ka, ice associated with the thin slow-flowing ice in the southwest parts of the model domain had largely receded. The limits of the modelled Huancabamba 3 glacier are within the large prominent moraine that flanks the valley to the east, with ice extending beyond smaller mapped moraines (Figure 6.28c). This matches very well with the palaeoglacial geomorphology, initially determined to be its LLGM extent (Figure 3.3), providing further need for the geochronological evidence to enable an understanding and confirmation of assertions made in Chapter 3 and in this chapter. Modelled glaciers within the northern region are substantively retreated from their previous maximum extensive positions. However, similar to those in the western cirque area, the modelled ice is not associated with any mapped geomorphology. Instead, the mapped landforms are either in front of, or within, the ice margins. This lack of moraines may be due to lakes that preclude the mapping of moraines within them, or the moraines have been washed away by drainage of more extensive lakes. Alternatively, the size of moraines associated with these short-lived ice positions may be small enough to prevent them from being mapped from remotely sensed observations.

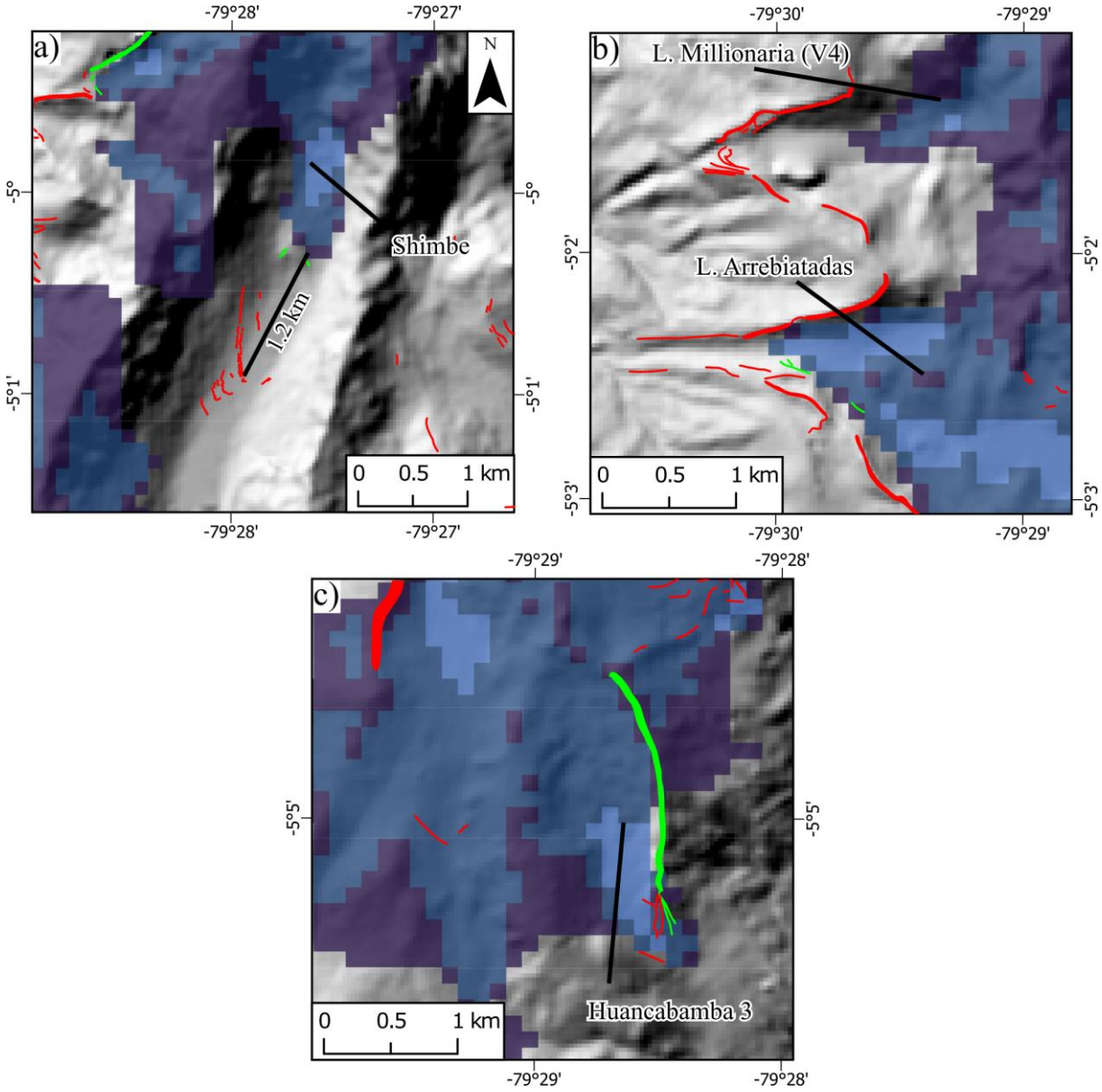

Figure 6.28: Glacier extent in relation to mapped moraines during 20.5 ka in the model time, which provides a representative extent of the extent most glaciers were at during the waning ice period. a) showing the head of the Shimbe valley, b) showing Lagunas Millionaria and Laguna Arrebiatadas, and c) the Huancabamba 3 ice extents. Legend is same as Figure 6.25.

Throughout the waning ice period, there are few moraines that correspond closely to the modelled ice margins. Many moraines are either located within the modelled ice extent (e.g., during the periods maximum extent at 19.5 ka) or are down valley when ice was at its minimal extents (i.e., 20.5 ka). Such disagreement could be due to: (i) the years captured within the model may not represent the ice positions which moraines were deposited under (Kirchner *et al.*, 2011), (ii) smaller moraines may denote ice positions modelled, but are unable to be mapped via remote methods (Chandler *et al.*, 2018), (iii) due to the early deglaciation of the region moraines may have been modified or eroded entirely by post-glacial processes preventing their mapping (Kirkbride and Winkler, 2012), or (iv) model inputs may not entirely reflect the

glaciological parameters of the region and is not able to entirely capture the high-resolution detail of deglaciation of this region (Silwal *et al.*, 2023).

6.6.4. Model evaluation - areas with limited geomorphological evidence identified

An apparent absence of geomorphic evidence meant that maximum ice limits in some parts of the study area were poorly constrained by mapping (Chapter 3; Lee *et al.*, 2022). The Shimbe valley glacier (Figure 3.4), Huancabamba 1 (Figure 3.6), and the southern end of the Negra glacier (Figure 3.10) had too little, or no, evidence to reconstruct glacier extents confidently for these outlets. This, when compared to the model output, resulted in large underestimation; 4.3 km for the southern end of the Negra glacier (ice extension), and 1.3 km for the Shimbe valley. The Huancabamba 1 glacier was over estimated, with the entire valley never filling with ice in the model, and much of the Huancabamba ice being split to either end of the valley, and the LLGM ice extent corresponding to the hypothesised post-LLGM moraines. Potential reasons for the differences between modelled and mapped could be that: (i) the southern ice extent, to the south of the Negra glacier, was primarily cold based and may have generated no or short-lived moraine evidence (Waller, 2001); whilst (ii) the Shimbe valley is a fluvially active valley and the morainic evidence for glaciation downvalley could either be buried by alluvial sediment, or has been fluvially eroded (Barr and Lovell, 2014).

There are three locations within the model domain where ice is modelled but the geomorphic mapping did not identify any evidence, and thus was not reconstructed with ice during the LLGM (Lee *et al.*, 2022). The first is in the northern parts of the model domain, where a topographically limited ice cap was modelled (Figure 6.29a), the second is at the northern most end of the model domain (Figure 6.29a), and the third is to the east of the Huancabamba 1 glacier region (Figure 6.29b). The first and third ice masses are locations with high elevation topography, up to 3,600 m asl, high enough in the model for glacial ice to accumulate at the LLGM. The latter, while having mapped glacial geomorphology to its south, has no evidence that could be identified to its north and east. Due to these regions not having any mapped geomorphological evidence, yet the model suggesting ice accumulation, they would be good targets for future detailed geomorphological mapping. They may indicate locations where, whilst there may be little or no obvious geomorphological evidence, either due to the censoring of evidence via post-glacial processes or are an indication of cold based glaciers in the region, glaciers may have still occupied that region, but were unable to generate geomorphic evidence. The second region, at the northernmost end of the model domain, is likely to be due to errors within the model attempting to reconcile edge cases of glaciers that are generated at the edge of the model domain. Whilst it is likely that this region is at a high enough elevation (> 3,400

m) for ice accumulation, their location at the edge of the model domain means that the modelled ice there is potentially unreliable and as a result is not further discussed in this chapter.

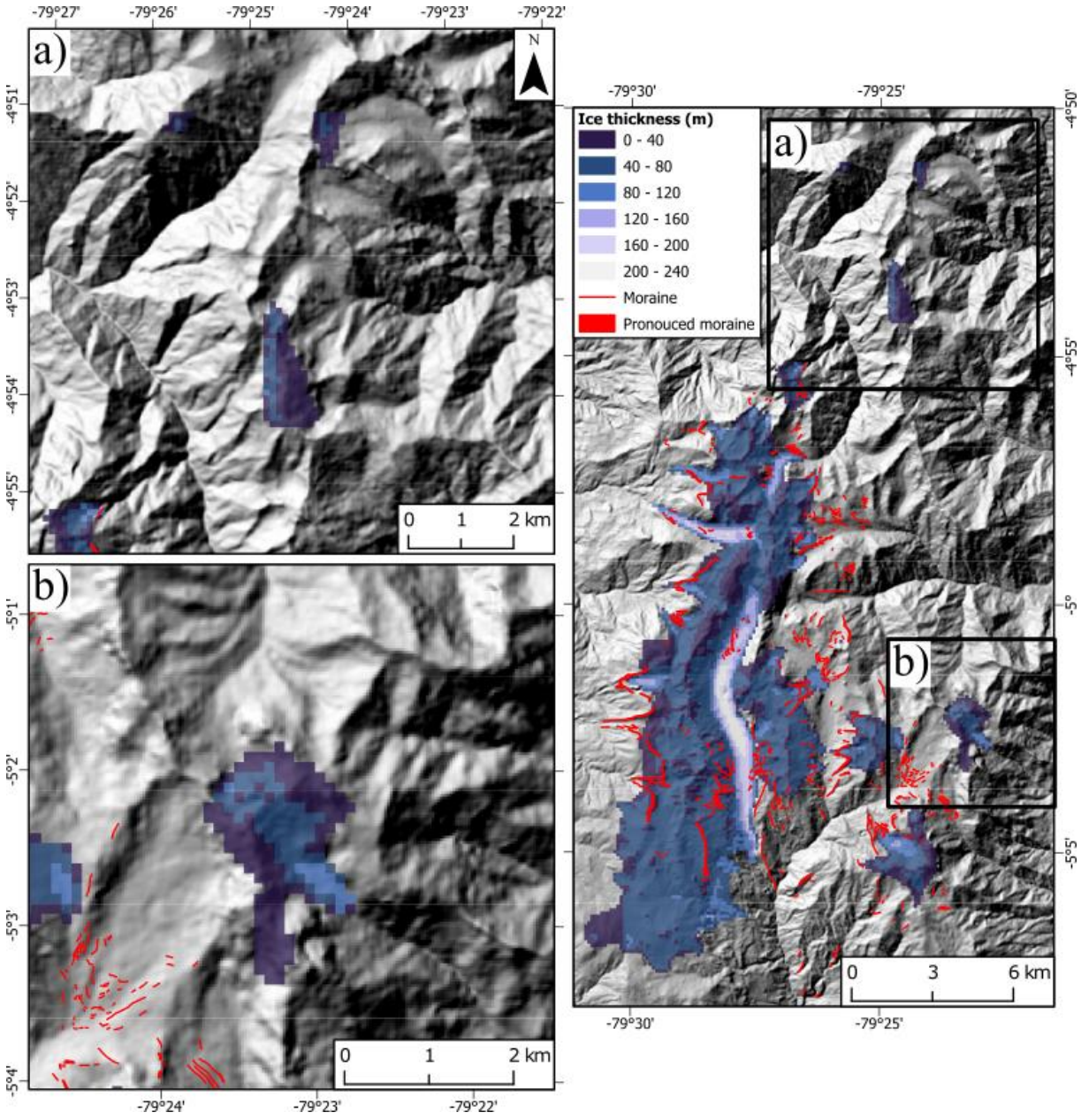

Figure 6.29: Unconstrained locations where no geomorphological evidence was identified, and no glacial ice was reconstructed for the LLGM period (25.4 ka in model); such locations are a) two ice caps to north of the main ice plateau, the north most ice on the model domain edge, and b) an ice cap to the east.

6.6.5. Ice configuration

The model results show that there are three ice configurations in the study area, which occur at different, and recurring, times in the model run. The first and largest configuration 'full glaciation', occurs primarily at periods of maximum glaciation, e.g., 25.4 ka (Figure 6.30) with the largest ice extent. The palaeoglacial geomorphological evidence (Chapter 3; Figure 3.2)

suggested a valley based glacial system with no, or limited, interconnected glaciers during the most extensive ice (assumed to be the regions LLGM) was likely (Figure 3.3). However, the model output suggests that an ice plateau style configuration is glaciologically more likely, as seen by the interconnected nature of the ice within the central glacial region. In the model (e.g., Figure 6.4), ice initially accumulates on high topography and develops a contiguous primary ice plateau with ice outlets (e.g., flowing into the Shimbe valley and from the glacial western cirques into Negra and Millionaria). In addition to the primary ice plateau, secondary smaller independent ice caps form on topographic highs within the model domain. While there are no ice plateaus within tropical Andes, similar ice caps are seen in contemporary glaciated regions within the tropical Andes, such as the Cordillera Vilcanota (Mark *et al.*, 2002), while in the paleo-record, ice caps have been inferred within southern Ecuador (Clapperton *et al.*, 1997b), primarily due to their topographical locations, on volcanoes tops. An ice plateau configuration is possible within the tropical Andes, should temperature offsets (< -10 °C) allow a large ice mass to be sustained. It is highly likely that the most extensive glacial geomorphological evidence mapped (Figure 3.2), and which was hypothesised to be LLGM, was generated at a time when ice was at such a 'full glaciation' configuration. This is due to previous, and later, modelled ice extents in the model run never reaching similar extents again.

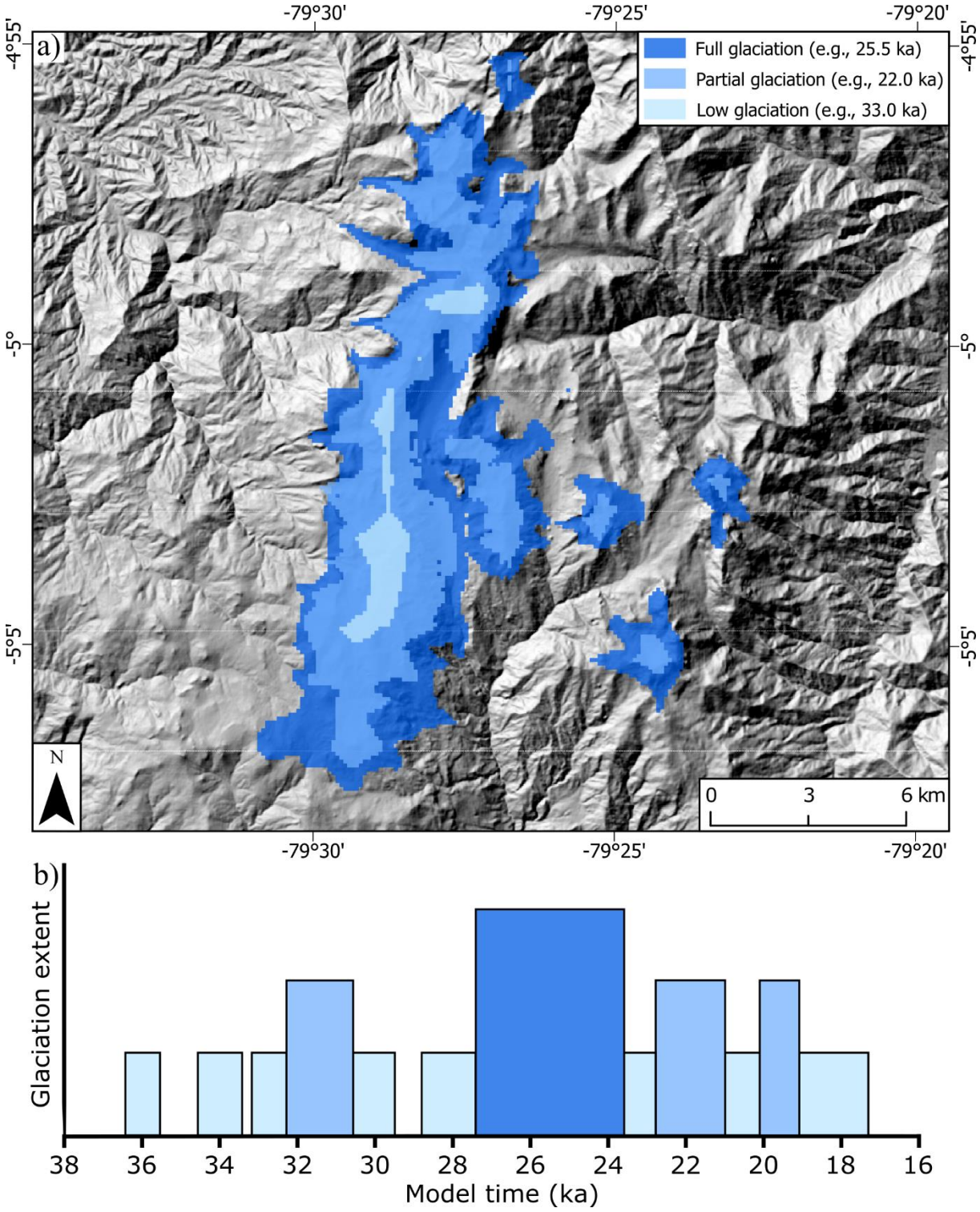

Figure 6.30: a) representative ice extents detailing three differing ice configurations that occur within the model domain at differing periods in response to varying temperatures, while b) presents a graphical view of the timing of when these extents were present with the colour matching that in the image. Gaps represent no ice.

The second configuration 'partial glaciation' is less extensive than the ice during 'full glaciation' (Figure 6.30). Examples of this occurring in the model are 34.0 ka, 27.0 ka, and 22.0 ka to 21.0 ka. The main feature of this configuration is a more limited ice area, with ice not entirely filling the Shimbe valley, and the primary ice plateau splitting in two, along the centre

of the Shimbe valley. An extensive primary ice plateau still exists, with ice flowing out from the western glacial cirques, and from the northern glacial region (north of the Shimbe valley). All glaciers that flow from the primary ice field from the western valley cirques, extend almost to positions within the maximum glacial ice limits of the 'full glaciation' configuration but are generally 700 m from former maximal ice positions. This is similar to ice that used to fill Laguna Paron within the Cordillera Blanca, where ice is no limited to the topographical hights, and still interconnected, but does not fill the overdeepened valleys. Ice in the northern regions is much smaller than 'full glaciation', with ice in the Palo Blanco 1 valley deglaciating almost by 2.3 km, while other glacial valleys (Palo Blanco 2, 3, and Aranza 4, 4) are between 600 m to 1.5 km from the maximal ice positions. Ice on the eastern side of the Shimbe valley becomes disconnected from the primary ice field to its west. Peripheral independent ice caps still exist on high terrain but are now limited to the high elevation areas >3,600 m asl (i.e., Redondo de Zapalache 1). In periods of partial glaciation, one, or multiple, these individual ice caps completely deglaciate. These ice caps are present during the most extensive periods of glaciation (< -9.5℃), while at warmer temperatures become very limited ice caps, and are the first areas in the model domain to entirely deglaciate.

The third configuration is of 'low glaciation', which is characterised by very restricted ice within the model domain (Figure 6.30). 'Low glaciation' is characteristic of the waning glaciation post-LLGM, or periods where temperatures can only sustain ice at high elevations (e.g., > -9.5 ℃, example between 23.5 ka to 22.0 ka; Figure 6.11). In this configuration, the primary ice plateau has further disconnected (compared to 'partial ice') and has separated into two ice caps – north of the head of the Shimbe valley, and an ice caps on the massif that hosts the western cirques. Ice no longer flows extensively to lower elevations and is limited to the higher topography. The independent smaller ice caps, once found outside of the primary ice plateau, have now fully deglaciated. The northern regions have no ice present on the valley tops. This is similar to glacial ice in the southern Cordillera Real, being limited to high elevations with ice that has become disconnected and becoming more analogous to singular valley glaciers.

6.6.6. Ice flow patterns

The model shows that there are regions were ice is flowing at substantially faster velocities then other locations within the model domain. Increased basal ice velocities within the Shimbe valley ice (up to 60.5 m yr^{-1}) clearly show fast moving ice that can erode, while slower velocities (up

to 10 m yr^{-1}) are modelled at the ice extension in the southern east section of the study region. However, there is a mixture of locations where the geomorphological evidence indicates high levels of erosion (i.e., overdeepenings), that does align with where basal ice velocities are indicative of sliding, while other areas do not. An example of where they do not align is that within the Shimbe valley where Laguna Shimbe, a now lake filled overdeepening indicative of substantial erosion, incurs very limited basal velocities (up to 4 m yr^{-1}; Figure 6.22) while the fastest surface velocities (60.5 m yr^{-1}) are seen at the end of the Shimbe valley, where no discernible palaeoglacial evidence could be delineated in Chapter 3. This is clearly indicative of substantial glacial erosion due to the largest overdeepening in the study region, and the general geometry of the valley clearly exemplifying a glacial valley.

However, some locations do align with the modelled ice flow condition, and the presence (or absence) of palaeoglacial geomorphology. A location where little to no geomorphological evidence was identified, the region covered by the southwestern ice extent, does incur slow surface (19 m yr^{-1}) and basal (4 m yr^{-1}) velocities at the LLGM (Figure 6.11). The northern glacial regions (at least during the LLGM at 25.4 ka) show substantive erosional and depositional geomorphological features (Figure 3.19). This region has higher basal velocities (20 - 40 m yr^{-1} within the valleys), with surface velocities up to 60 m yr^{-1}, that are in line with the extensively eroded valleys, lake filled overdeepenings, eroded bedrock, and the presence of moraines at the termination end of the model ice, with inset moraines within their confines. This mixture of well aligned geomorphological evidence to model output, and not very well aligned evidence, may be a factor of the model not entirely capturing the glaciological physics or ice-valley interactions. This may present that the parameterisation of the model may need to be improved or adjusted to match the glacial physics, and the geomorphic evidence.

Throughout the model time span, there is limited basal sliding seen within the valleys, bar that shown in the LLGM when increased basal velocity occurs where ice is thick or flowing down substantial relief (e.g., Figure 6.12). The model determined that all the ice in the model domain is at 0°C (Figure 6.23). This would result in very little sliding occurring. Cold-based ice would generate very little palaeoglacial geomorphology (Hubbard and Sharp, 1989; Waller, 2001), but as shown in Chapter 3 (Figure 3.2) there is a plethora of geomorphological evidence with glacially smoothed bedrock. There is high confidence that, at least within the area of thin (<100 m) slow-flowing ice to the southwest of the model domain, where few geomorphological features were mapped, could have been cold-based, as thinner ice is most susceptible to the surrounding air temperature (Carrivick *et al.*, 2023). However, cold based ice across the entire study region would be unlikely.

This combination of mismatched evidence to model output, and potential erroneous cold based glacial ice brings into question the validity of the model, with the cold based glacier potentially being explained by just how cold the model needs to be cooled by to allow such extensive glaciation at the LLGM (-10.4°C). While cold based glaciation has been identified within the tropical Andes before, with the evidence of 'bouldery moraines' in the Nevado Sajama, Bolivia, (Smith *et al.*, 2009) it is not common. Many other palaeo reconstruction studies across the tropical Andes clearly indicating that ice during the LLGM was primarily warm-based or poly-thermal (Rodbell *et al.*, 2008; Stansell *et al.*, 2013; Stansell *et al.*, 2015; Angel, 2016). The remote sensing (Chapter 3) and field observations (Chapter 4) provide clear evidence for large, pronounced moraines throughout the study area, and smaller moraines inset within these moraines. This is inconsistent with the model, as provides evidence that much of the ice was warm based, or at least polythermal. Further, the geomorphological evidence suggests there are some regions of glacially smoothed bedrock, that would require sliding and warmed based ice to produce. Due to limited time availability for fieldwork, we were unable to go to locations of identified glacially smoothed bedrock and cannot confirm the identified evidence.

6.6.7. Marginal glaciation within the Las Huaringas region

Within the Las Huaringas region, the model suggests that glacial ice only exists at very low temperatures, with the initial ice growth initiating at ~-8.5°C offset from the present-day. While very cold, this allows glacial ice to exist at the highest elevations (> 3,500 m asl). A decrease of 0.5°C to -9.5°C allows ice to expand from the higher ice caps down into valleys, and downvalley walls, and results in a contiguous ice plateau forming. A further 0.5°C cooling can bring the onset of 'Full Glaciation' ice conditions with an extensive ice plateau with outlet glaciers to low elevations. This 1°C to 1.5°C range between no, or very limited, ice to 'Full Glaciation' conditions, leaves very marginal climatic conditions for glacial existence and expansion. This marginal glaciation, within a small range of temperature cooling (i.e., 1.5 °C) has not previously been proposed for tropical Andean ice masses, where regions during their LLGM experienced extreme mass wasting due to climatic warming after colder conditions. This may be due to the steep mass balance gradients seen, even during the LLGM, with such extensive mass loss at low elevations, combined with warmer temperatures (-9°C), exacerbated by increased velocities due to gravitational transport due to deep elevation relief (Doughty *et al.*, 2023). This is that, the elevation of the region is at a cross over where as soon as ice advances to lower elevations, it melts abruptly, which is only enhanced when climatic warming occurs after the LLGM cool period.

While marginal changes in temperatures can cause extreme changes in ice configuration in such high relief tropical settings, the temperatures required for glaciation in the current model are much cooler than previous studies have predicted within the tropical Andes. Geomorphological-based estimations suggest the regional LLGM temperature lowering estimates of -2°C to -8.8°C (Porter, 2001; Mark *et al.*, 2005; Stansell *et al.*, 2007; Bromley *et al.*, 2011a) and -6.5°C to -8.8°C (see Chapter 3; section 3.3.7.) (Lee et al., 2022). Using palaeoglacial geomorphological evidence alone as a palaeoclimate indicator (Barr and Spagnolo, 2015; Pearce *et al.*, 2017; Oien *et al.*, 2022a) cannot provide an entirely accurate cooling prediction, but can provide a first-order estimate on how extensive cooling might need to be to incur glaciations at certain times (e.g. LLGM). Further, there is the potential that the model framework used here is not entirely representative of the climate conditions at the time, or ice physics.

6.6.8. Timing of the Local Last Glacial Maximum

Within the model simulations, the maximum area covered by glacial ice is reached at 25.4 ka (Figure 6.2 & 6.11), but the period between 25.5 ka ta 24.7 ka was associated with persistent and large glacial ice extents, close or near the maximum mapped palaeoglacial geomorphological evidence. The existing geochronological studies (Chapter 2), provide a range of dates collected between 40.5 ± 1.0 ka and 16.8 ± 0.4 ka overall, which this model dates falls in between, and close to the average of 25.3 ± 5.8 ka, but is earlier than the median age of 23.8 ka. The timing shown is similar to the early-LLGM advances seen in the Cordillera Carabaya, 25.8 ± 0.9 ka (Bromley *et al.*, 2016), the Cordillera Huayhuash, 25.7 ± 1.1 ka (Hall *et al.*, 2009), the Rurec valley in the Cordillera Blanca, 24.7 ± 4.5 ka (Farber *et al.*, 2005), and within the Junín Plain, between 24.9 ± 1.2 ka and 35.5 ± 1.5 ka (Smith *et al.*, 2005b). The broad agreement between the modelled LLGM and existing evidence is reassuring, despite the model being driven by the EPICA temperature curve which may not be locally realistic. It is, however, realistic to assume an early-LLGM within this region (i.e., ~ 25.4 ka), though dating of the Las Huaringas moraines is needed to test this model derived estimate of maximum glaciation.

6.6.9. Model limitations

Within the sensitivity analysis (Chapter 5), it was determined that 120 m was an adequate horizontal resolution to resolve ice-valley interactions. Despite this, the model resolution may still be an issue in smaller narrower valleys or other parts of the model domain. Some valleys

may have topographical variations that are not accurately represented in the model, and they may lead to either inaccurate ice margin positions or incorrect glaciology. A clear example is the ice flowing off the western Shimbe valley wall that contributes a considerable proportion of ice to the Shimbe valley. Where multiple moraines are within 120 m of each other, the model resolution makes it challenging to compare modelled ice extents with the mapped geomorphology. While overall (i.e., at the full model domain) the modelled ice looks and changes in a realistic manner, accurate modelling at an individual glacier level will require either valley specific models, or a finer model resolution. A nested grid approach (e.g. Prakash *et al.*, 2022) would allow locations where the 120 m grid cell is not enough to capture topographic detail, though PISM is currently unable to consider nested grids within the computational domain.

The model itself does not use the full Stokes laws that are the most comprehensive calculations of glacier ice physics. However, their inclusion would be too computationally intensive for the chosen resolution, and their absence is not a fundamental limitation. In a comparison of PISM's hybrid SIA+SSA to Elma/Ice full Stokes model, Imhof *et al.* (2019) showed that PISM can overestimate thickness in an ice-field by 500 m, however, its extent agrees well with full Stokes model. Further, the use of the hybrid SIA+SSA approach has been adopted by a number of studies undertaking palaeoglacial modelling (Seguinot *et al.*, 2016; Seguinot *et al.*, 2018; Imhof *et al.*, 2019) and shows good agreement with at least the glacier extents, which are most important for palaeoglacial reconstructions (e.g. the comparison with geomorphic-derived reconstructions here).

The use of Antarctic ice core record EPICA as the climatic forcing record for temperature does not entirely represent the climate variation that would have been present within the region at that time. It does not consider microclimatic variations that occur in specific climatic zones. It is known that during the last glacial period climatic weather patterns were different and could have implications for localised precipitation and wind patterns (Vizy and Cook, 2007; Fogwill *et al.*, 2015). In addition, the temperature cooling, along with the temperature variation within the EPICA ice core, will not be entirely realistic for this tropical region. The study region is a large distance (~11,000 km south) from the location of the EPICA ice core. Tropical glaciers in northern South America may be more influenced by northern hemisphere, so EPICA may not be entirely appropriate (Sugden *et al.*, 2005; Licciardi *et al.*, 2009; Bromley *et al.*, 2016). Therefore, driving the modelling with a northern hemisphere temperature record such as NGRIP or GISP2 may result in different spatial and temporal patterns of glaciation. Geochronological dating may provide further evidence on the relative influence of the northern

and southern hemisphere on tropical glaciers; – however, this such information is lacking for this study site at present.

While a time varying palaeo temperature record is used, a similarly varying palaeo precipitation record is not. Instead, precipitation was held throughout at 130% of present-day. It would be unrealistic to assume that as temperature changes, that precipitation would stay constant. Further, spatial patterns in precipitation would also vary with changes in the glacial surface, along with regional and global changes in circulatory patterns. While there are indicators of the amount of precipitation through time, it is relatively difficult to quantify this into a percentage difference, many studies simply determine that it was 'wetter' or 'drier' then present (Baker *et al.*, 2001a; Berman *et al.*, 2016).

Lastly, the model is unable to, or harder to parameterise to, account for all the intricacies of glaciations and their physics. However, there may be issues with model set up that, due to user experience of the PISM model, may not have been entirely correctly set up. The use of PISM has never been done in the tropics before, leading to this being very exploratory, that may lead to incorrect assumptions from the model. Tropical glaciers are different when compared to their extra-tropical cousins, which as mentioned before, may require extensive model parameterisation, and set up. Tropical glaciers have differing mass balance regimes, with ablation occurring all year round due to the climate homogeneity of the tropics (Rodbell *et al.*, 2009; Winkler *et al.*, 2009). Further, tropical glaciers can lose a large proportion of their mass by sublimation when above the 0℃ isotherm which is also not integrated into the model used here. Other than how they lose mass, how they gain mass is not entirely represented, as accumulation can occur either for a singular season or have multiples of accumulation each year. Mass input can also be received through windblown snow, and avalanching processes. Taking these limitations into account, the model run shown here performs effectively at the scale it is applied. The model does not attempt to construct an accurate reconstruction of the regional ice extent, due to limited empirical data that can be used for comparison. This is compounded by the limited palaeoclimate records that can be used to accurately force the climate within the model, with accurate regional climate pattern and dynamics. This chapter presents an insight into the dynamics of the local ice mass, at its extent at the LLGM, and provides a first order look at the glaciology of the Las Huaringas ice masses.

6.7. Chapter summary

This chapter has demonstrated the dynamics of glacial ice within the study region from the initial inception of ice masses from 38 ka, through the LLGM maximum (25.4 ka), to final

deglaciation around 17 ka. This model was parameterised using the sensitivity testing conducted in Chapter 5, and its performance evaluated against the geomorphic evidence mapped in Chapter 3 (Lee *et al.*, 2022) and Chapter 4. It has discovered that:

- The ice masses between 38 ka to 29 ka were ephemeral in nature. The ice masses were topographically limited (i.e., to elevations > 3,400 m asl), and existed for short periods (< 700 yrs). Modelled ice masses at this time were ice caps at high elevations, with limited ice advancing down from their cirque and source locations. There is no geomorphological evidence that could be determined as being representative of this time period, and thus these modelled extents are remain unconstrained.
- The modelled maximum extent is 25.4 ka, suggesting an early LLGM. This is similar to other regions within the Perúvian tropical Andes, where the LLGM has been determined between 35.5ka and 24.7 ka (Farber *et al.*, 2005; Smith *et al.*, 2005b; Hall *et al.*, 2009; Bromley *et al.*, 2016). It is likely this modelled date is broadly close to, or representative, of the timing of the LLGM, though confirmation of this awaits analysis of acquired cosmogenic isotope samples from Las Huaringas (Chapter 5).
- At the LLGM, the model clearly models an ice plateau. This is developed between the western cirques and the head of the Shimbe valley, with ice flowing into surrounding valleys. A series of smaller secondary peripheral ice caps formed on higher elevation areas in the east and north of the model domain. This ice plateau configuration is similar to ice masses in both the palaeo-evidence (cf. Clapperton *et al.*, 1997b), and current glacial areas (cf. Thompson *et al.*, 1985) of the tropical Andes.
- The LLGM ice extent is consistent with some of the maximum mapped ice extents from geomorphologic evidence. Many locations show ice extending beyond, or not extending to, the mapped maximum ice limits. This may reflect where evidence: (i) does not represent the LLGM; (ii) could not be identified from remote sensing; or (iii) reflects asynchronicity in outlet advances to maximum mapped extents that cannot be entirely captured within the model (Seguinot *et al.*, 2018).
- After the LLGM, ice 'waned' with contraction and advances due to variable climatic conditions. Ice was either limited to topographical highs (e.g., at 20.5 ka), or extended almost as far as the LLGM extents due to a short-lived cooling (e.g., 19.5 ka). As temperature rose above the -9°C offset, the region deglaciated (~17 ka). At no point after this time does glacier ice reoccupy the Las Huaringas uplands.
- The ice within the study region is very sensitive to temperature changes, with marginal conditions for low to full-scale glaciation. Small differences in temperature offsets (i.e.,

between -9.5°C and -10°C) can cause large changes to the modelled ice configuration; from being limited to topographic highs (> 3,500 m asl) and limited ice in the Shimbe valley, to extensive glaciation (terminal positions down to 2,900 m asl) and ice over 200 m thick filling the Shimbe valley.

- The model performs well within the tropical region focused on in this thesis. The model grows glacial ice in a realistic manner, which is glaciologically sound and appears to demonstrate spatial coincidence with the glacial geomorphic evidence. However, the model cannot model the intricacies of tropical glaciers. Sublimation, ablation throughout the year, input from avalanching and windblown snow, and the general climatic dynamics of the tropics are not able to be represented.
- The broader implications of the modelling are: (i) just how marginal climates conditions are for glacial ice to occupy a tropical area such as the Las Huaringas region; (ii) how much cooling is needed to initiate and sustain glaciation within the region, with the most extensive glaciation being at -10.3°C offset from the present-day; (iii) the generation of an ice plateau here contradicts that of a cirque-to-valley configuration if Chapter 3, that may point to an inaccurate reconstruction using the geomorphological mapping alone.

Chapter 7. Discussion

7.1. Introduction

The aim of this thesis was to reconstruct the glacial history of the Las Huaringas. This is a region below the traditional LLGM snowline that can enable an understanding of LLGM ice advances and climate that may be uncomplicated by later advances during Holocene climate fluctuations. Holocene readvances in higher elevation regions can become complicated by advances near to, or at extensive as, their regions LLGM advance that can make determining past climate more difficult. The research questions (Chapter 1) to achieve this aim were:

RQ1: Has the Lagunas de Las Huaringas glaciated in the past, and what was the maximum extent of glaciation? (Chapter 3, Chapter 4, and Chapter 6)

RQ2: When did the glaciation within the study region occur? (Chapter 4 and Chapter 6)

RQ3: What were the climate conditions at the time of glaciation? (Chapter 3 and Chapter 5)

RQ4: What was the glaciology of the ice masses during advance to, during, and retreat from, the maximum glacial extent? (Chapter 6)

This chapter will: (i) provide a high-level synthesis of this thesis, addressing each of the four research questions; (ii) detail additional interesting findings outside the research questions, and (iii) discuss future research opportunities for glacier reconstruction in the currently unglaciated parts of the tropics.

7.2. RQ1: Has the Lagunas de Las Huaringas been glaciated in the past, and what was the maximum extent of glaciation?

The evidence from remote (Chapter 3) and infield (Chapter 4) geomorphological mapping (Chapter 3, Figure 3.2), demonstrates that the Las Huaringas have been extensively glaciated at some point during its history. All evidence and results generated within the thesis confirms the initial hypothesis from Clapperton (1993), that the high topographic areas of the northern Perúvian Andes (at least in the Las Huaringas) were glaciated, at least during the regions LLGM (Figure 2.2). While the Las Huaringas is a low latitude (~5°S), and a relatively low elevation (i.e., max elevation < 4,000 m asl), locations below the elevations of the South American LLGM snowline reconstruction (Figure 2.14) for this latitude. This suggests that it would likely be

worthwhile to investigate other locations within similar latitudinal and elevational regions in South America for evidence of past glaciation (see section 7.9.1).

Most of the evidence for glaciation is found within the valleys as opposed to on the valley tops and the moraines representing the most extensive glaciation at Las Huaringas are some of the lowest elevation (3,200 m asl) moraines identified within Perú and Ecuador that are potentially linked to the last glacial cycle. The average elevation of the assumed to be the regional LLGM terminal moraines in Perú and Ecuador is 4,140 m asl. The lowest previously recorded moraine evidence in Perú was from the Cajamarca Valley, where LLGM-age moraines are found at 3827-3,932 m asl (Shakun *et al.*, 2015b). The particularly low elevations of the glacial evidence at Las Huaringas could be due to high mass turnover, incurring accumulation up to ~863.7 km m^2 yr^{-1} in the highest regions (>3,800 m asl) (Figure 6.22), while multiple glaciers from hanging valleys feed into the Shimbe valley – this is also inferred in the geomorphological reconstruction (Figure 3.3). Alternatively, the low elevation moraines could be due to the Las Huaringas being at lower latitudes (~5°S), compared to the majority of other studied former ice masses (> 6.8°S/> 6.5°N). This latitudinal difference may have resulted in different atmospheric circulation patterns (Espinoza *et al.*, 2020) during the LLGM period, where moist air more readily precipitated over the Andes due to the SALLJ impinging on the eastern Andes (Figure 2.8). This would have resulted in increased precipitation and changes in precipitation patterns (Figure 2.4), cooler temperatures (Porter, 2001; Vizy and Cook, 2007; Hastenrath, 2009), along with differing topographical controls (Rabatel *et al.*, 2013b), and may have allowed glaciers at Las Huaringas to extend to low elevations than glaciers at slightly higher latitudes.

Reconstruction of the ice extents from the geomorphic record suggested a cirque-to-valley glaciation (87.5 km^2) (Chapter 3), while the numerical model output, constrained by the geomorphic record, suggested an ice plateau glaciation (171 km^2) (Chapter 5 and 6). The ice in the model was comparable to the sizes of the Cordillera Real in Bolivia, and the Monte San Lorenzo ice cap in Chile (both ~200 km^2) (Seehaus *et al.*, 2020; Martin *et al.*, 2022). The ice plateau, covering the top of the headwalls, suggested by the numerical model, is similar to ice caps identified within the palaeorecord record of the tropical Andes (Clapperton, 1979; Clapperton *et al.*, 1997b; Dirszowsky *et al.*, 2005; Mahaney *et al.*, 2010) with ice covering the highest elevation valley tops, then advancing down into constrained valleys. However, the Las Huaringas ice plateau would be one of the smallest (at 171 km^2), and lowest elevation (max elevation of 3,900 m asl), ice plateaus within the tropical Andes during the LLGM. Reconstructed ice caps during the LLGM were considerably bigger, for example an ice cap in Ecuador, reconstructed to being ~800 km^2 (Clapperton *et al.*, 1997b), while contemporary ice

caps, such as the Nevado Coropuna (~46 km^2) (Úbeda *et al.*, 2018), are much smaller than the ice plateau generated here, but were much bigger during the LLGM at 365 km^2 (Bromley *et al.*, 2011a). Many studies that investigate the LLGM timing of glaciation do not always reconstruct the ice masses, so are unable to report their area size (Leger *et al.*, 2022). This makes comparisons, and the amount of change seen, hard to determine and limits regional comparisons. Future studies that reconstruct glaciers at a regional level should reconstruct glacial extents, their estimated area cover and ice volume, and potential ice thicknesses if evidence exists.

From the reconstructed maximum extent from the geomorphological mapping (Figure 3.3), the mean ELA was 3,422 m asl (using a Balance Ratio of 1.75), with mean ELA lowing of 1,178 ± 10 m (Table 3.3). When this is compared to that estimated at the LLGM extent within the model (Figure 6.11), the ELA is at 3,500 m asl, generating an ELA lowering of 1,100 m, a minimal difference of 78 m. Both estimated ELA change are compatible to the largest changes of reconstructed ELAs across the tropical Andes (Klein *et al.*, 1999; Porter, 2001; Mark *et al.*, 2005). They are comparable to those in northern Perú (Cordillera Blanca; ELA lowering of ~1,000 m) (Rodbell, 1992; Mark *et al.*, 2005) but are more than double those calculated from southern Perú (ELA lowering of 200-770 m) (Ramage *et al.*, 2005; Smith *et al.*, 2005b; Bromley *et al.*, 2011a). The ELA change at Las Huaringas is similar to identified LLGM ELA shifts in the Venezuelan (lowering of 850-1,420 m) (Stansell *et al.*, 2007) and Colombian (lowering of 1,217 m) (Mark and Helmens, 2005) Andes. There is a lack of Ecuadorian glacial ELA reconstructions for the its LLGM, however present-day ELA estimates from (Clapperton, 1987a) indicate that Ecuadorian glaciers exhibit an east (lower) to west (higher) gradient, similar to the Las Huaringas. While at the Chimborazo and Carihuairazo ice cap in Ecuador, one of the only locations with ELA estimates, indicate a ELA lowing of ~500 m during the LLGM (Clapperton, 1990). Within northern Perú, the maximum elevation difference between Las Huaringas (4,000 m) and the Cordillera Blanca (6,000 m; Figure 2.14) (Bromley *et al.*, 2016) suggests that regional or local climatic conditions over Las Huaringas allowed glaciers to form and to advance as far downvalley, as glaciers do in high elevation locations elsewhere in northern Perú. This may have been due a steepening of the temperature lapse rates during the LLGM with greater cooling at higher elevations (Loomis *et al.*, 2017), while a corresponding increase in precipitation would provide increased mass input (Vizy and Cook, 2007).

7.3. RQ2: When did the glaciations within the study region occur, and when was the most extensive glaciation?

As there are currently no absolute dates for glacial landforms within the Las Huaringas accurately constraining the timing of glaciation is not possible at this point in time. Dates should become available soon as samples for cosmogenic dating were collected in January 2023 (Chapter 4) and are currently at the Scottish Universities Environmental Research Centre (SUERC) for analysis (at the time of thesis completion). However, using the timing of maximum glaciation in the numerical model runs (25.4 ka) (Chapter 6; Figure 6.11), and the database of dated LLGM moraines within the surrounding regions (Table 2.2), it is possible to make inferences about the likely timing of the most extensive glaciation of Las Huaringas. Many moraine ages from the surrounding regions (in Perú and Ecuador) (Figure 2.14) are associated with a large spread of ages, ranging between 40.5 ± 1.0 ka and 16.8 ± 0.4 ka, with a mean age from the dataset being 25.3 ± 5.8 ka (Figure 7.1) and a median age of 23.9 ka, these were generated in Excel using the respective mean and standard deviation formulas. This wide spread of LLGM assigned ages encapsulate all three period maximums (Ephemeral, LLGM, and Wanning), providing a first-order indication that the model is accurately generating the maximum extents of ice within the correct periods. The mean age from the dates collected are provide a most likely value that can be used to understand if the timing of maximum ice extent in the numerical model of the Las Huaringas area is realistic, which it is with the model providing a model age of 25.4 ka (Figure 6.11). However, this is a modelled age using the EPICA time series and can only give an indication of a potential time period to which the LLGM occurred in for the study area, not placing a definitive date, also further, the variability in ages across the database, with very little latitudinal pattern, it would be impossible to accurately assigned an LLGM date at this time. This variability, may reflect precipitation variability across regions (Baker *et al.*, 2001b), topographical influences over glaciers (Pratt-Sitaula *et al.*, 2011), and unforced natural glacier variability driven by internal glacial dynamics (Roe and O'Neal, 2009), or the potential influence of post-depositional processes, along with inheritance, resulting in younger or older cosmogenic nuclide ages respectively (Applegate *et al.*, 2010).

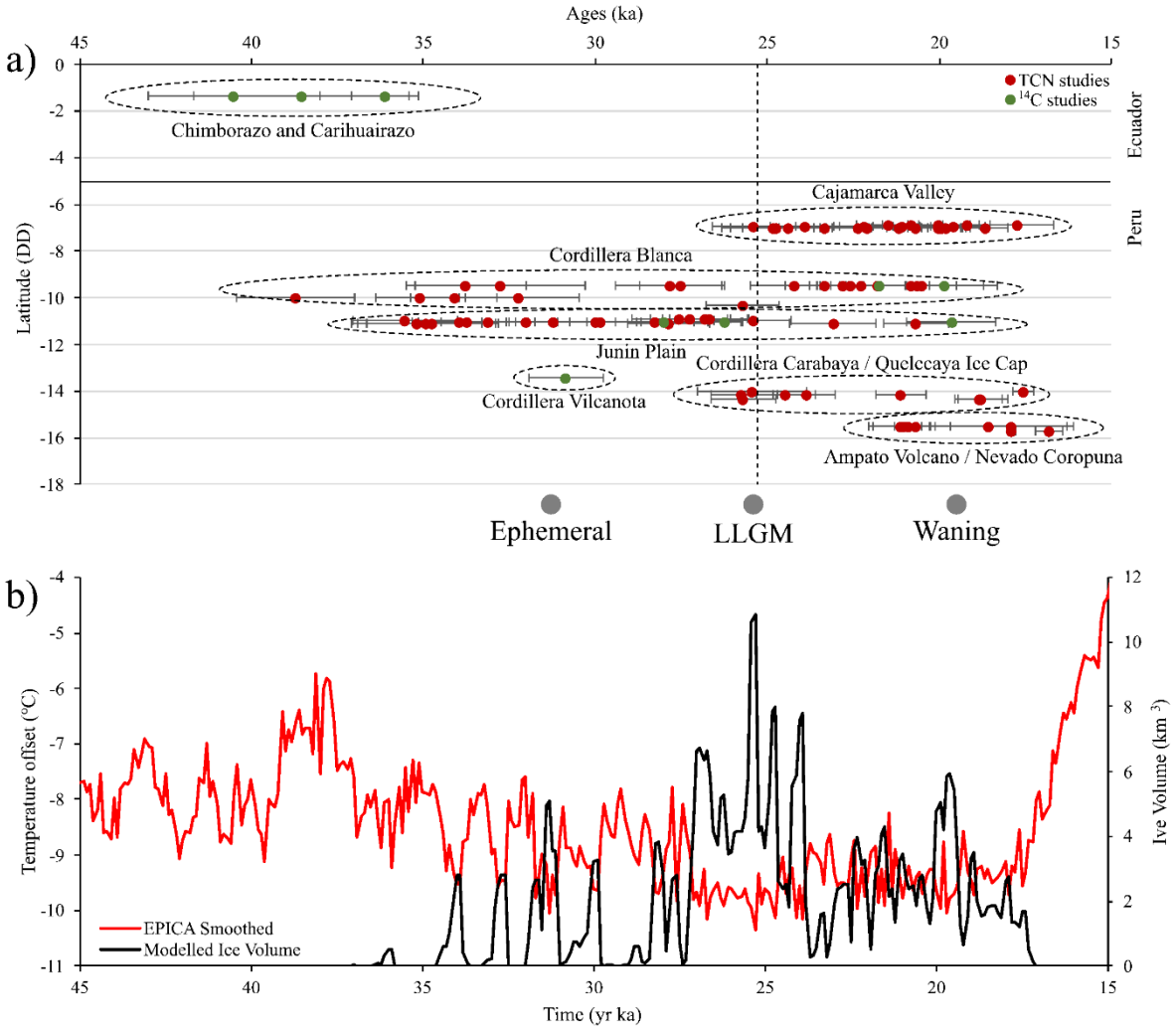

Figure 7.1: A summary of chronologies for the last glacial maximum from TCN (red) and ^{14}C (green) dates in Perú and Ecuador, compared against the model timing of maximum ice extents (grey) in the context of temperature changes between 45 and 15 ka. a) individual moraine ages represent determined LLGM timings: Chimborazo and Carihuairazo, Ecuador (Clapperton, 1987b; Clapperton, 1998), Cajamarca Valley, Perú (Shakun *et al.*, 2015b), Cordillera Blanca, Perú (Rodbell, 1993a; Farber *et al.*, 2005; Hall *et al.*, 2009; Smith and Rodbell, 2010), the Junin Plain, Perú (Wright, 1983; Seltzer *et al.*, 2000; Smith *et al.*, 2005a), Cordillera Vilcanota, Perú (Mercer and Palacios, 1977), Cordillera Carabaya and the Quelccaya Ice Cap (Goodman, 1999; Bromley *et al.*, 2016), and the Ampato Volcano and Nevado Coropuna (Bromley *et al.*, 2009; Alcalá *et al.*, 2011; Úbeda *et al.*, 2018) with the dataset average (vertical dashed line). Model inferred 'LLGM' age (from Chapter 6) for the study area (grey), and b) the EPICA timeseries (Jouzel *et al.*, 2007) showing temperature cooling with the modelled ice volume through the model.

The age for the maximum modelled ice extent at Las Huaringas (25.4 ka; LLGM grey dot Figure 7.1) is consistent with the mean age (25.3 ± 5.8 ka) identified from the dated moraines within Perú and Ecuador. However, due to the variability in ages, this oldest age is at least consistent with the range of identified ages for glaciation at multiple locations between 9-11°S (e.g., Cordillera Blanca, and the Junín Plain) (Farber *et al.*, 2005; Smith *et al.*, 2005b; Smith and Rodbell, 2010) that are assigned to their LLGM. The LLGM for these regions has been

dated at between 32.2 ± 1.7 ka and 24.7 ± 4.5 ka, an overall early-LLGM. However, there is a difference between the modelled maximum and the LLGM timing in the Cajamarca Valley in Perú at 7°S (Shakun *et al.*, 2015b) – the closest previously studied area to the Las Huaringas. The age of the LLGM there is between 23.7 ± 1.3 ka and 19.9 ± 1.0 ka, later than the maximum extent suggested by the Las Huaringas model, in line with traditional global LGM timing. Although the age of maximum glaciation (25.4 ka) and the mean age of the LLGM in Perú and Ecuador (25.3 ka) coincides well, it is impossible to address RQ2 accurately without absolute dating of the Las Huaringas moraines. What can be stated with confidence is that, from the modelled ice extent and volume (Figure 7.1b), ice was almost constantly within Las Huaringas during the timing of its regional LLGM, spreading almost the full range of identified ages, from first inception of glacial ice (~34 ka) to the final entire deglaciation (~17 ka). If the modelled timing of an early-LLGM is indeed correct, this would have important implication on the role of tropical Andean insolation and CO_2 that are traditionally thought to drive glacial periods (Clement and Cane, 1999; Bromley *et al.*, 2016).

Moraines just behind the maximum terminal moraines at Las Huaringas (Chapter 4) must post-date the maximum extent of the Las Huaringas ice masses (i.e., they are younger than 25.4 ka if the model age is assumed to be correct). In the numerical model output, during the waning ice period, two periods of great advance occurred at 21.5 ka and 19.5 ka (Figure 6.14), with glacial ice near the former LLGM assigned moraines. After 19.5 ka there are only smaller scale advances, up to 17.0 ka (Figure 6.14) that are limited to high elevations (< 3,400 m asl). In the model there was no glacial ice after 17.0 ka. It is therefore likely that the moraine evidence just inside the bounds of the maximum moraines date to be between 19.5-17 ka, while moraines that are set further back from the maximum extent moraines, up valley near the headwalls, are likely to between 19.5 ka and 17.0 ka. Sampling for dating of some of these moraines has been undertaken (Chapter 4), but it will likely be difficult to assign an age or period for all, or most, of the identified moraines, as their advances may not have been time synchronous. It is well documented that glacial ice within the wider region advanced asynchronously due to individual differences in microclimate and topography (Gillespie and Molnar, 1995; Smith *et al.*, 2005b; Kull *et al.*, 2008; Pratt-Sitaula *et al.*, 2011).

The potential ages of further 'inner' moraines may be consistent with evidence from Perú and Ecuador (Chapter 2), but it is impossible to postulate to their timing. After the traditional conclusion of the global LGM advances (~20 ka), there is evidence for glacial advances at 18.8 ± 0.7 ka in the Cordillera Carabaya (14°S) (Bromley *et al.*, 2016), between 17.9 ± 0.1 ka and 16.8 ± 0.4 ka in the Ampato Volcanic Complex (15.5°S) (Alcalá *et al.*, 2011) and 17.5 ± 0.3 ka

at the Quelccaya Ice Cap (14°S) (Goodman, 1999). Similar ages are from a location at a similar latitude to Las Huaringas are those from the Cajamarca Valley (between 20.0 ± 0.7 ka and 17.7 ± 1.1 ka) (6.9°S) (Shakun *et al.*, 2015b). Thus, the presence of ice at similar time periods to that estimated in the model, within the tropical Andes, provides some confidence to the models output, and the period of which ice could have been presented to generate such evidence. These advances occurred earlier than Heinrich-1 Stadial (~17 ka) (Palacios *et al.*, 2020) and deglaciation thereafter. If the EPICA temperature time series used to drive the ice mass modelling is representative of broader scale shifts in regional temperature, then it is unlikely that any landforms or geomorphic evidence from Las Huaringas would date to the ACR (14.7-13.0 ka) or YD (12.9-11.7 ka) cold periods. This would place such identified readvance or standstill, evidence immediately after the regions LLGM. This is due to the marginal conditions for glaciation, requiring low temperatures (< -8.8℃), of which temperatures during the ACR and YD were above this (~-4℃).

7.4. RQ3: What were the climate conditions at the time of when glaciers were present?

The temperature cooling estimates from the reconstructed average ELA change (max -8.8℃; Chapter 3) (Lee *et al.*, 2022), and the numerical model (max -10.4℃; Chapter 5 and 6), provide evidence of a substantially cooler LLGM, when compared to present day temperatures, in Las Huaringas, and therefore the wider region. Estimates here are similar to the higher estimates for LLGM cooling estimated for Perú (-9℃) and Venezuela (-8.8 ± 2℃) (Klein *et al.*, 1999; Stansell *et al.*, 2007), but are much more than the majority of cooling estimates from the tropical Andes (range between -2.5℃ to -7.9℃) that primarily come from higher elevation regions, above 5,000 m (e.g., Rodbell, 1992; Porter, 2001; Mark *et al.*, 2005; Bromley *et al.*, 2011a). This is due to higher elevation location requiring less cooling, being either at or above the snowline, while lower elevations require mor cooling to push the snowline to lower elevations. The highest temperature cooling here is almost an order of magnitude higher than SST estimates (depression of 1.7℃ – 3.5℃; see Figure 2.5) (Lea *et al.*, 2003; MARGO Project Members, 2009; Tierney *et al.*, 2020b), this is due to cooling occurring more readily over land, while oceans are much slower to react to temperature changes (Byrne and O'Gorman, 2013). Comparing the Las Huaringas cooling to the trend of the SST records from the eastern equatorial Pacific, shows periods of a cooling between 30 ka to 25 ka (Lea *et al.*, 2000) that correspond with advances of glaciers to their LLGM extent. The equatorial Atlantic shows cooling between ~35 ka and ~17 ka, also coinciding with the LLGM inferred from the model (25.4 ka). Following this cooling there is a sharp rise in SSTs after 17 ka in the equatorial

Atlantic, and a similar pattern in the southwestern tropical Atlantic SST (Hou *et al.*, 2020). This rise in SST temperatures after 17 ka (Figure 2.5) coincides with the complete deglaciation of modelled glaciers at Las Huaringas (after 17.5 ka),and the Heinrich 1 event. Thus, the onset of higher SST and Heinrich 1 event from the northern hemisphere led to exacerbated deglacial conditions within the Las Huaringas.

An increase in precipitation (+30% of modern precipitation) was needed in the time varying modelling to facilitate ice to reach the maximum mapped extent of glaciation (Chapter 3 and Chapter 6). An increase in precipitation during the last glacial cycle is supported by palaeolake studies. Lake Titicaca and Salar de Coipasa in Bolivia indicate a wet period between 25 ka to 15 ka (Baker *et al.*, 2001b; Nunnery *et al.*, 2019) while an ice core from Sajama, Bolivia, suggests the onset of a drier climate after 21 ka (Thompson *et al.*, 1998) (Figure 2.6) – all coinciding with the timing of greatest ice extent within the Las Huaringas. This is in contrast to palaeoecological evidence from within the northern Andes (Heusser and Shackleton, 1994; Behling and Hooghiemstra, 1999; Vélez *et al.*, 2003) and Amazon basin (Mourguiart and Ledru, 2003; Novello *et al.*, 2019) that indicate no change in precipitation, or a drier climate respectively. However, changes in SALLJ (Figure 2.8) over the Amazon and Andean mountains during the LLGM could have supported a wetter LLGM in northern Perú by allowing the SALLJ to more closely impinge on the eastern Andes. This would allow the available moisture to precipitate more readily, even if the moisture sources were associated with a drier environment (Vizy and Cook, 2007). Further lake studies from northern Perú, and southern Ecuador, would be needed to further validate this hypothesised increase precipitation.

Although Chapter 6 presented one potential climate configuration (max ΔT of -10.4°C, xP of +30%) that enabled glaciation to reach mapped geomorphic extents, alternative configurations are also possible. Chapter 5 demonstrated that a number of temperature and precipitation offsets can result in the same, or similar, maximum glacier extents. The equifinality demonstrated in this sensitivity analysis determined a climatic envelope within which the Las Huaringas ice masses could extend to their maximum mapped positions during the assumed LLGM period. This required a temperature offsets between -10°C and -10.5°C, and precipitation offsets +10% to +40%, depending on how the DDF and refreezing values were also varied. Similar modelling studies in the extra-tropics have seen differing combinations of climate (temperature cooling and precipitation) generating similar glacial extents (Becker *et al.*, 2017; Candaş *et al.*, 2020; Köse *et al.*, 2022), but varying model parameters has not been as widely conducted in the literature previously (Leger *et al.*, 2022), bar simple sensitivity analysis. This not only demonstrates how a range of different model input combinations can generate similar ice

extents, but how when unconstrained parameters (DDF and refreezing within this study) need to be parameterised, their selection can potentially drastically change the climate needed, impacting the inferred climate and the implications that may have on palaeoclimate for a region.

7.5. RQ4: What was the glacial dynamics of the ice masses during advance to, during, and retreat from, the maximum glacial extent?

Using numerical glacier models like PISM can give us glaciological insights that geomorphology alone cannot provide due to lost evidence, or where evidence did not form (Oreskes *et al.*, 1994). Throughout both the ephemeral (38 – 27.5 ka) and waning (23.5 – 16 ka) periods in the model, ice was generally limited to topographic highs (> 3,400 m asl) with relatively limited periods of glacial ice growth (up to a maximum of ~100 km^2). The ephemeral period was associated with ice that fluctuated between no ice, and ice present within the model domain, with eight individual advance phases on average up to 57 km^2 (Figure 6.4). The waning glacial period was characterised by the presence of ice almost constantly until full deglaciation, but the extent and thickness of this ice fluctuated considerably with climate (Figure 6.14), with ten noticeable ice advances with an average area up to 67 km^2. The model indicated periods of complete deglaciation prior to the LLGM, while the temperature was still < -8°C. This demonstrates that although a large amount of cooling is required to initiate glaciation, ice masses in this locality are highly sensitive to subsequent temperature changes. This is in line with modern tropical glacial behaviour (Kaser, 2001; Kaser and Osmaston, 2002; Seehaus *et al.*, 2020), which can react abruptly to small changes in air temperature. However, there could be potential issues with glacial ice nucleation, how the ease of generating initial glacial ice upon which all grown ice stems from. This could require further parameterisation of them model. There are similar sensitivities to small temperature changes have been identified or modelled in extratropical high-elevation regions (Braithwaite and Zhang, 2000; Kinnard *et al.*, 2022) in response to recent climatic warming.

The output from the PISM experiments also suggested that most of the ice mass flowed primarily by internal deformation (Figure 6.23). This may be a function of how much cooling of the air temperature was required in the model for glaciers to form within the region (up to -10.4°C), resulting in a frozen bed to be modelled (Figure 6.24). Such influence of temperatures on the occurrence of basal sliding has been inferred within glacial modelling of the Quelccaya Ice Cap, Perú, during the YD (Malone *et al.*, 2015), indicating that basal freezing could have been present due to past cooler climates (i.e., the global LGM) (Thompson *et al.*, 2013). Any modelled basal sliding at Las Huaringas was primarily limited to periods of increased ice extent,

such as the LLGM, or to basal sliding within the mid-sections of glacial valleys where the thickest glacial ice was located (e.g., over the present-day Laguna Shimbe). At periods of restricted ice (e.g., 22.0 ka) (Figure 6.15), there was little to no basal sliding due to the limited thickness of the ice, and ice being restricted to high elevations. Basal sliding has been identified and inferred across the tropical Andes (e.g., Malone *et al.*, 2015; Kos *et al.*, 2021) and may be more prevalent across other glaciers within the tropics. The minimal model evidence for basal sliding at Las Huaringas could be because the model is not realistically representing the true thermal regime of the glaciers and could require improvements to the model setup and parameterisation. If basal sliding occurred more readily within the Las Huaringas region, glacial ice would have flowed downvalley to the mapped maximum extents at warmer temperatures then those used in the model and would also have permitted considerable erosion. There is some geomorphological evidence of sliding within the region from Chapter 3, for example glacially smoothed bedrock, while extensive erosion of overdeepenings would require sliding to incur substantial erosion. Due to time limitations for fieldwork, I was unable to confirm evidence of sliding, but it would be justifiable to expect some sliding to occur due to the amount of erosion generating overweening's and extensive moraines systems.

No other study within the tropical Andes has looked at providing a reconstruction of the ice dynamics before, during, and after the potential LLGM. Studies generally focus on snapshots in time (e.g., their study regions LLGM period only), generally dictated by the evidence that is present or of most interest. Such studies provide a snapshot into the past glaciation of a region, similar to what was conducted within Chapter 3 (Lee *et al.*, 2022), but they do not provide a wider context for how glaciers existed and evolved. Numerical modelling, now demonstrated to work effectively for reconstructing the extent and glaciology of former ice masses in the tropics, can be used to test palaeoclimate in specific regions, to understand if the temperatures and precipitation offsets inferred from the palaeorecord, or glacial ELA reconstruction studies, are able to produce glacial ice at their respective maximums.

7.6. Style of glaciation – ice plateau or valley glaciation?

Differences were seen in the style of glaciation initially interpreted in the geomorphic record (Chapter 3; Figure 7.2a) (i.e., a cirque-to-valley glacier system), when compared to the modelled glacial system (Chapter 5 and 6; Figure 7.2b) (i.e., ice plateau system). The initial interpretation shown in Figure 3.3 (Lee *et al.*, 2022) was conducted using examples of surrounding present day glaciation. Taking the output of the numerical model and comparing to the geomorphological mapping, an ice plateau is more plausible, with the land system

following the majority of the criteria set out by Bickerdike *et al.* (2018b). The main evidence for an ice plateau configuration is that of the model indicating slow flow in the upper reaches. This provides the potential for polythermal glaciers to incur cold based ice in the upper reaches of the valleys that would preclude evidence generation, this is noted in the geomorphological mapping (Chapter 3) with little to no evidence identified very close to the headwalls which could be analogous to Himalayan glaciers, but data is sparse on such subglacial dynamics (Miles *et al.*, 2018). Further, ice reconstructed within the region incurs topographical concordant flow, with ice flowing off the ice plateau into valleys and becomes more topographically constrained.

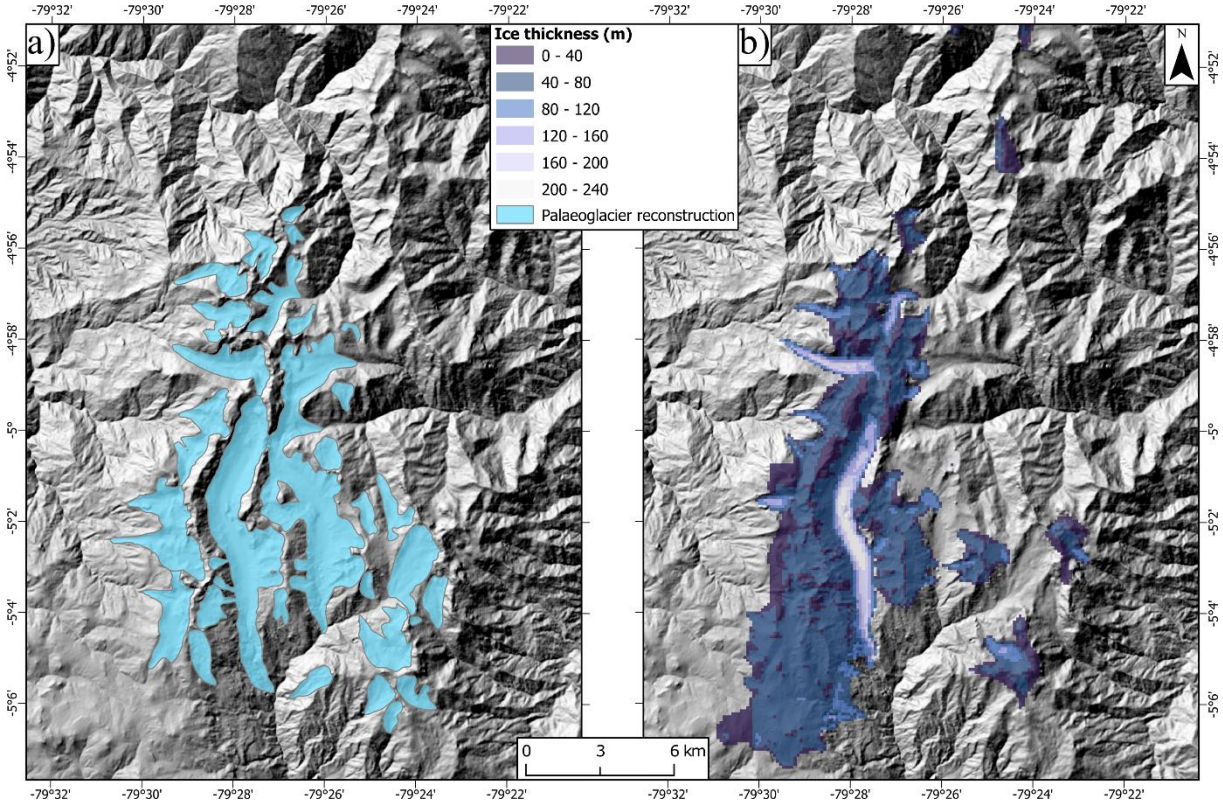

Figure 7.2: Comparison of the two differing styles of glaciation reconstructed within the study region, a) the geomorphologically informed reconstruction (Chapter 3); and b) PISM model LLGM time slice (25.4 ka) output using the EPICA time varying temperature record (Chapter 6).

Such changes in hypothesised ice configurations have been seen across the literature within locations of extensive study (e.g., the Lake District; McDougall, 2013). This difference may be due to an inherent bias in existing literature that tends to reconstruct, or infer, valley-based glaciers (Smith *et al.*, 2005b; Shakun *et al.*, 2015b; Bromley *et al.*, 2016), which may be due to the selection of modern day analogues that are used to inform how glaciers are reconstructed. Ice capped terrain within the tropical Andes however, is not uncommon (Thompson *et al.*, 1995; Edwards *et al.*, 2018; Yarleque *et al.*, 2018; Taylor *et al.*, 2022), and former ice caps have been reconstructed from palaeogeomorphology (e.g., Clapperton *et al.*, 1997b). However, there has

been very little, to no, inference for ice plateaus within the tropical Andes, making this location unique or unusual, while also direct comparisons with similar glaciated regions surround the Las Huaringas impossible. This may be due to the glacial buzzsaw hypothesis (Egholm *et al.*, 2009) within region across the Andes that incur fast uplift rates (Muller *et al.*, 2024), allowing glacial ice to erode into the headwall and eroding deeply into the landscape that may limit or preclude the preservation of plateaus. However, much of the uplift rate in the central and northern Andes is around 0.2 and 0.3 mm yr^{-1} (Gregory-Wodzicki, 2000), while maximum uplift rates are seen around Patagonia with around 41 mm yr^{-1} (Muller *et al.*, 2024). Ice here may have preserved a plateau ice field within the region due to potential slower uplift, this region is in a region that is overall lower in elevation compared to the rest of the Andes and may have occurred less aggressive glacial erosion, evidence by the potential for slow flowing and cold based ice in the upper reaches.

This change in inference, from a valley based ice, to an ice plateau can have important implications for the ELA reconstructions, and thus regional palaeoclimate interpretations (Barr and Spagnolo, 2015; Bickerdike *et al.*, 2018a). That is, an ice plateau, or ice cap ELA, with the same downvalley extent, has a higher ELA (Úbeda *et al.*, 2018). This would generate a reduced ELA depression, which would therefore require less temperature cooling to develop and sustain glaciation, but perhaps more temperature warming to deglaciate. This is produced in line with just temperature cooling, and no inference of changes in precipitation. Within the model (Figure 6.11), reconstructing an ice plateau, the ELA was indeed at a slightly higher elevation (+70 m) when compared to the geomorphological reconstruction (Figure 3.2 & Table 3.2), but required more temperature cooling, with higher precipitation, to force an extent of glacial ice to the identified geomorphic evidence. Although the ELA difference is small, the inferred climate is largely different. This may indicate that temperature cooling extracted from ELA reconstructions (e.g., Mark *et al.*, 2005; Martin *et al.*, 2020) alone may underestimate the temperature cooling during the LLGM, or that the lapse rate during the LLGM in tropical regions had been steeper then what it is today (Loomis *et al.*, 2017). The latter, would have important implications on modelling studies that have generally used the global average of 6.5°C (Seguinot *et al.*, 2018; Candaş *et al.*, 2020; Martin *et al.*, 2022) that may infer the incorrect climate.

7.7. Why are the most extensive Las Huaringas moraines so large?

Las Huaringas is characterised by a number of large ‘pronounced’ moraines (example seen in Figure 4.17) (>75 m relief) situated within the western glacial region. The presence of such

large moraines suggests a large supply of sediment was required for their formation. Many of these large moraines are found near areas where the model experiments suggest that glacier ice was present for ~50% of the model time (~17.3 ka yrs) (e.g., Figure 6.21a&b). This suggests that ice was persistently proximal to these moraines for extended periods of times (e.g., during the LLGM period), potentially enabling the erosion and transport of sufficient sediment to build the large Las Huaringas moraines.

To generate the supply of large volumes of sediment to generate such moraines, there are a number of processes that could have been operating (Figure 7.3). These include: 1) the glacier slowly eroding due to being partially frozen to the bed, and transporting material and then depositing moraines over a long time period (Hallet *et al.*, 1996), which would require the terminus to be in a particular position for that entire length of time (Figure 7.3a); 2) a rapidly eroding glacier transporting debris to its terminus over a shorter time period (Cook *et al.*, 2020) (Figure 7.3b); 3) the addition of an extra supply of debris not being directly eroded from under the glacier and that this is transported to the terminus (e.g., debris from landslides onto the glacier surface; Tovar *et al.*, 2008) (Figure 7.3c); or 4) the fluctuation of glacial ice at the ice margin which retreats and dumps its sediment generating hummocky moraines, and in subsequent readvances remobilises the sediment and deposits it at the glacier terminus (Bennett, 2001) (Figure 7.3d). The geomorphic evidence behind the most prominent moraines (e.g., Laguna Negra; Figure 4.17), as well as glacial ice in the time varying model fluctuating between periods of high ice extents (Figure 6.9; 25.5 ka), and then smaller limited glaciers (Figure 6.9: 24.5 ka), could provide the precondition of deposited glacial debris as it retreats due to climate warming, before readvancing due to cooling temperatures and re-entrains the glacial debris.

For large moraines to form, through either of the processes (Figure 7.3), an adequate supply of sediment is required (Antoniazza and Lane, 2021). Other than sediment readily available from processes operating before glaciation, e.g. from alluvium, lacustrine, weathering of the bedrock, and mass movement deposits within a fluvially active system (Antoniazza and Lane, 2021), subglacial erosion will occur (Bernard, 1979; Iverson, 2012) generating overdeepenings (Cook and Swift, 2012), such as those seen within the Shimbe valley (Figure 3.4). Availability of preglacial material, and glacial erosion could provide sufficient sediment to form the moraines. Throughout the study region however, such erosion to the bedrock at headwalls and valley tops is not pronounced. There is substantial erosion of the valley floor, producing overdeepenings, near the valley headwall, especially across the western glacial cirques (Laguna Arrebiatadas region; Figure 3.15), that are potentially a primary source of sediment for the pronounced moraines located downvalley in the western region. Variations in the spatial pattern of basal

thermal regime within the ice are likely, with a cold-based ice cap, and ice cap outlet glaciers having a warm-base (Fu *et al.*, 2019). This will result in erosion being focused on valleys and near valley headwalls rather than on higher elevation ridges and plateaus. Testing the potential source sediment, and the potential moraine generation theory, would require sedimentological evidence and an understanding of the provenance of sediment sources (cf. Cook *et al.*, 2017). However, the presence of the large moraines at Las Huaringas, as well as the modelling evidence for ice extending down to, or slightly beyond, these moraines, provides some confidence in the assumption of the landforms being generated when glaciers reach their most extensive glacial positions. However, a clear determination of the process of moraine formation would require structural and sedimentological analysis of the moraines (e.g., clast analysis) to understand the processes involved.

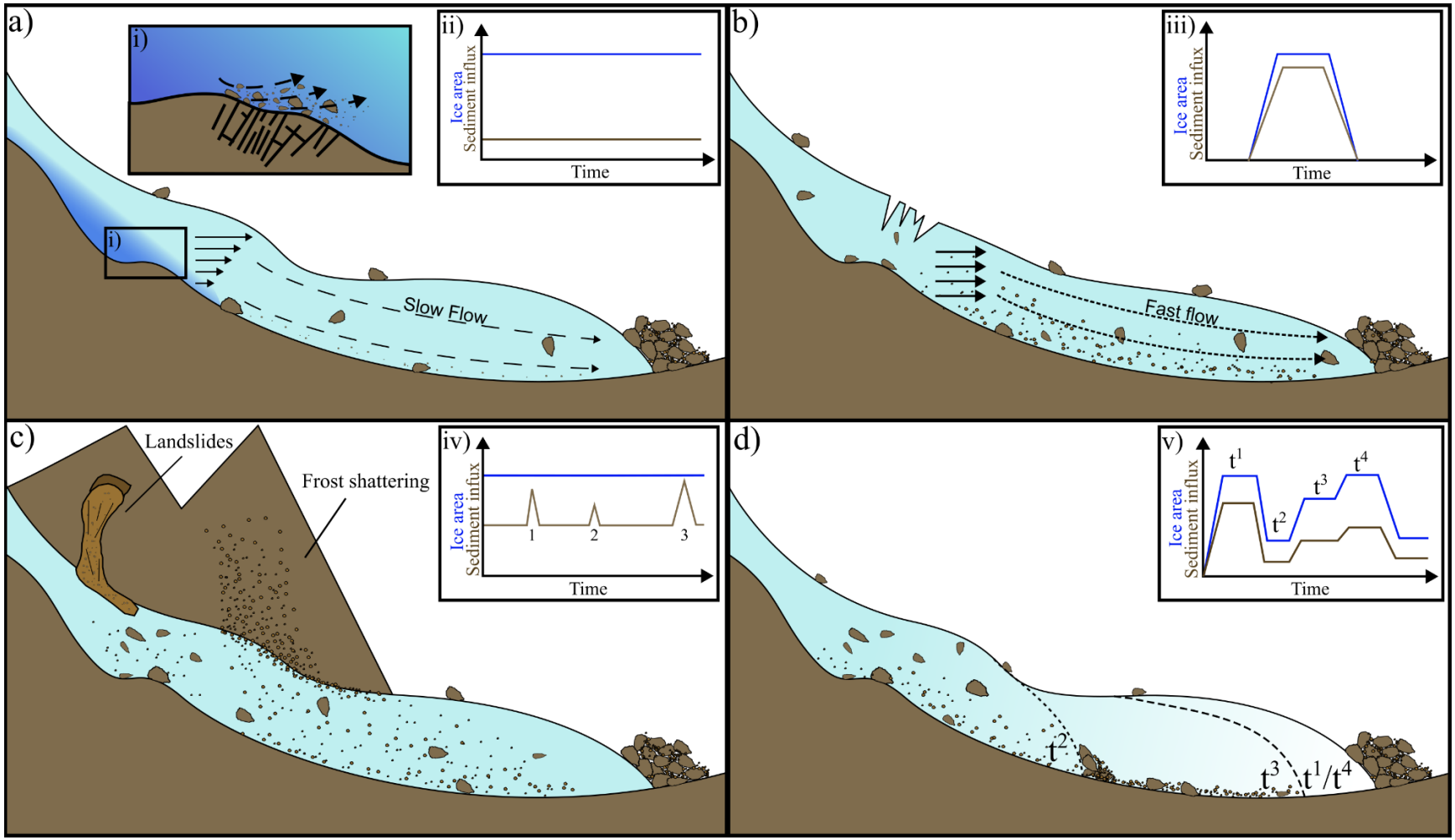

Figure 7.3: Differing examples of moraine generation theories for that may be at play within the study area. a) of a long lasted, slow moving (internal
4665 deformation) but persistent ice mass with a cold base (i) up valley (dark blue) while sediment influx is low (ii), b) a short lived but fast flowing (with sliding) glacier with high erosion and high sediment influx (iii), c) ice that persists for a period of time can have an influx of sediment from the surrounding topography extra to subglacial erosion causing periods of increase sediment influx (iv), and d) a fluctuating ice margin with multiple periods of advances (v) that can lead to varying max influx, but also cause the sediment load of the glaciers to be deposited on retreat, and then restrained by the glacier.

The majority, or all, or the major moraines within the Las Huaringas region would require some form of warm based glaciation to allow such erosion of material needed for their generation (Benn and Evans, 2014). However, the PISM model experiments indicating minimal sliding within the accumulation's zones, while at the largest extents (during the LLGM), sliding can occur more readily downvalley (e.g., Figure 6.24). Accounting for the geomorphic evidence (e.g. moraines, eroded bedrock, valley morphology), the formation of large moraines would not occur if much of the ice mass was entirely frozen to the bed, therefore it is hypothesized that the up-valley portions were cold based, while warm based in the valleys, similar to present day glaciers (Hambrey and Glasser, 2012; Kos *et al.*, 2021) and those from previous tropical glacial reconstructions (Rodbell *et al.*, 2008; Stansell *et al.*, 2013; Stansell *et al.*, 2015; Angel, 2016). Cold based glaciers cannot generate extensive erosion (Boulton, 1972; Bernard, 1979; Waller, 2001). It is not impossible for cold based portions within glaciers to be present within the tropical Andes during the LLGM (e.g., Smith *et al.*, 2009). The model attributing 0°C across the entire glacier may be due to the cooling required to generate ice in the region (~ -10°C), or erroneous climatological or glaciological parameters used within the model (i.e., DDFs, refreezing factor etc.). While this thesis is not using the model to understand glacial erosion, caution should be taken in PISM to ensure it is actually modelling the glaciological parameters accurately (i.e., ensuring parameterisation is as realistic as possible), and thus able to generate an accurate basal thermal regime, and routing pathways for subglacial hydrological systems (Kazmierczak *et al.*, 2024).

7.8. Modelling tropical glaciers: limitations

Using PISM has shown that the Las Huaringas region is associated with interesting glaciology that may be indicative of the differing climatic and glacial regimes of tropical glaciers but may point to potential issues and challenges that need to be refined within the numerical model to accurately represent tropical glaciers. One of the most striking is the very cold temperature conditions required in the model to enable ice to extend to the low elevations of the Shimbe valley (ΔT~-10°C) and for ice to be present across the topographic highs only (ΔT ~-9.5°C) (Figure 7.4) (Chapter 6, section 6.5.1.4.). This is likely due to very steep mass balance gradients (Figure 6.22) (Kaser and Osmaston, 2002; Vuille *et al.*, 2008).

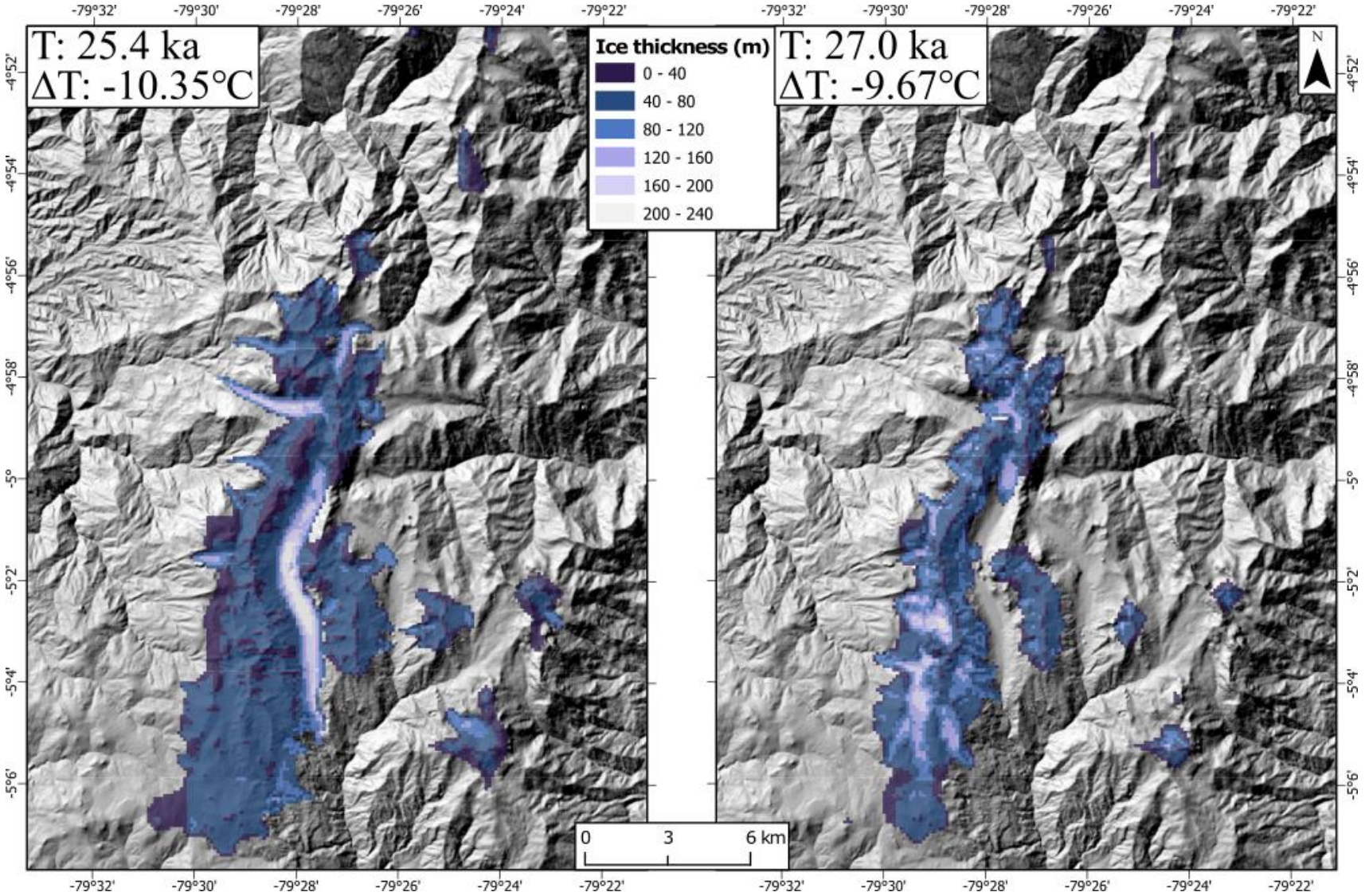

4700 **Figure 7.4**: Two periods of glaciation during the 'LLGM' phase, detailing ~1°C difference in temperature cooling causing a drastic change in ice configuration with ice filling the Shimbe valley in 25.4 ka to the valley being almost entire ice free and ice across the reason being reduced.

While PISM itself is able to accurately model glaciers in a glaciological sound manner, it is unable to resolve to mass balance differences of tropical glaciers, when compared to extra-tropical glaciers. To enable accurate modelling, the PDD model used here would need to be tuned for tropical glaciers, however knowledge on past rainfall and temperatures a poorly constrained within the local region. Further, processes such as sublimation can cause major mass loss on tropical glaciers, causing up to a maximum potential of 81% of ablation, but usually around 2-4% (Winkler *et al.*, 2009; Fyffe *et al.*, 2021), while avalanching (Kaser and Georges, 1999; Rabatel *et al.*, 2013a) and windblown snow (Veettil and Kamp, 2019) can also be a large proportion of mass input that are not modelled within PISM. Such processes can add mass to glaciers, independent of temperature cooling (Laha *et al.*, 2017), that would provide less cooling needed to grow, and allow the persistence of glaciers at lower elevations. From this, while the PISM model can capture most of the ice-climate processes, there are still some processes that are not represented within the model used here, such as sublimination that are important over tropical glaciers (Fyffe *et al.*, 2021).

Further for the numerical modelling with PISM, there is the potential for the model itself to produce incorrect model output. While here, in Section 7.6 it is suggested that the model output could indicate that we reconstruct glaciers at their most extensive advances as an ice field could be incorrect, at least for the up-valley sections. This is because the highest elevation peaks could be ice free while the model produces ice on the highest areas of the topography. This is seen in other regions that have used PISM (Candaş *et al.*, 2020; Köse *et al.*, 2022) which may present support for the model building ice on all high topography, interconnecting valley ice. This could mean we need to take model output from PISM with some scepticism, only using the downvalley frontal modelled ice and disregarding the up-valley ice. Further investigation would be needed to see if this is really the case.

Lastly, and worth reiterating here, the biggest challenge in modelling tropical glaciers are the available studies that aid in the parameterisation of glaciological and climatological parameters. Model parameters are uncertain, meaning that there may be multiple parameters sets which can lead to a glacier extent that matches, or are close to, the geomorphology. Many of the of the parameters used however are generated over extra-tropical locations (Candaş *et al.*, 2020; Köse *et al.*, 2022; Martin *et al.*, 2022). Using the wrong parameters that are inappropriate for the region these glaciers exist in can propagate down to the model output, producing either incorrect ice behaviour, or leading to inferences of the wrong climate (Silwal *et al.*, 2023) – this is why in this thesis extensive sensitivity testing was conducted. What would help to understand if the model used here, and those generated in the future, are correctly inferring climate, is more local

climate records from sources (e.g., lakes) that are proximal, but in front of the limit of LLGM glaciation. This would enable to constraint of temperature and precipitation fluctuations through time prior to, and after, the LLGM.

7.9. Recommendations for future research

This thesis has presented new results into the glaciation of the Las Huaringas, northern Perúvian Andes. Although we address a specific set of questions, in doing so this work allows further research questions to be posed. These are outlined below.

7.9.1. Investigate other potential sites in southern Ecuador and northern Perú for evidence of past glaciation

The evidence from Las Huaringas suggests that there are potentially still regions across the tropical Andes where past glaciation has occurred but that no, or very little, research has been conducted. These include regions that may have been glaciated during the Andes LLGM (Clapperton, 1993), and which deglaciated immediately following the LLGM termination, or during the late-glacial or early-Holocene, and regions that are below the estimated LLGM snowline (Broecker and Denton, 1990a; Egholm *et al.*, 2009). Due to this, these locations have not been investigated, due to there being no direct link to current and future climate changes. There are several locations (generally in locations with elevations < 4,000 m asl), within the latitudinal data gap that Las Huaringas is located, that also appear to be characterised by landforms evidencing past glaciation (Figure 7.5, Table 7.1). Many of these regions appear to have been deglaciated for an extended period due to heavy vegetation in locations where glaciers could have been present. While on the figures there are some very preliminary mapped evidence, to provide credence for glaciers to have been there, much evidence may be precluded due to this vegetation. However, glacial overdeepenings being lake filled in the upper reaches of the valleys, provides further evidence of palaeoglaciation due to glacial erosion being require for their existence. Some locations also appear to have poor remote sensing imagery that may limit remote mapping. Future studies of these sites should include: (i) high-resolution geomorphological mapping, to reconstruct the extent, volume, and glaciology of these former ice masses; (ii) generation of a geochronological identified palaeoglacial evidence using TCN dating to determine the timing of the maximum glaciation, while the coring of lakes outside, and within, the confines of identified evidence to constrain the timing of deglaciation; and (iii)

numerical modelling to provide further context under what climate these glaciers would have advanced under, and the physical properties (e.g. basal thermal regime) of these ice masses.

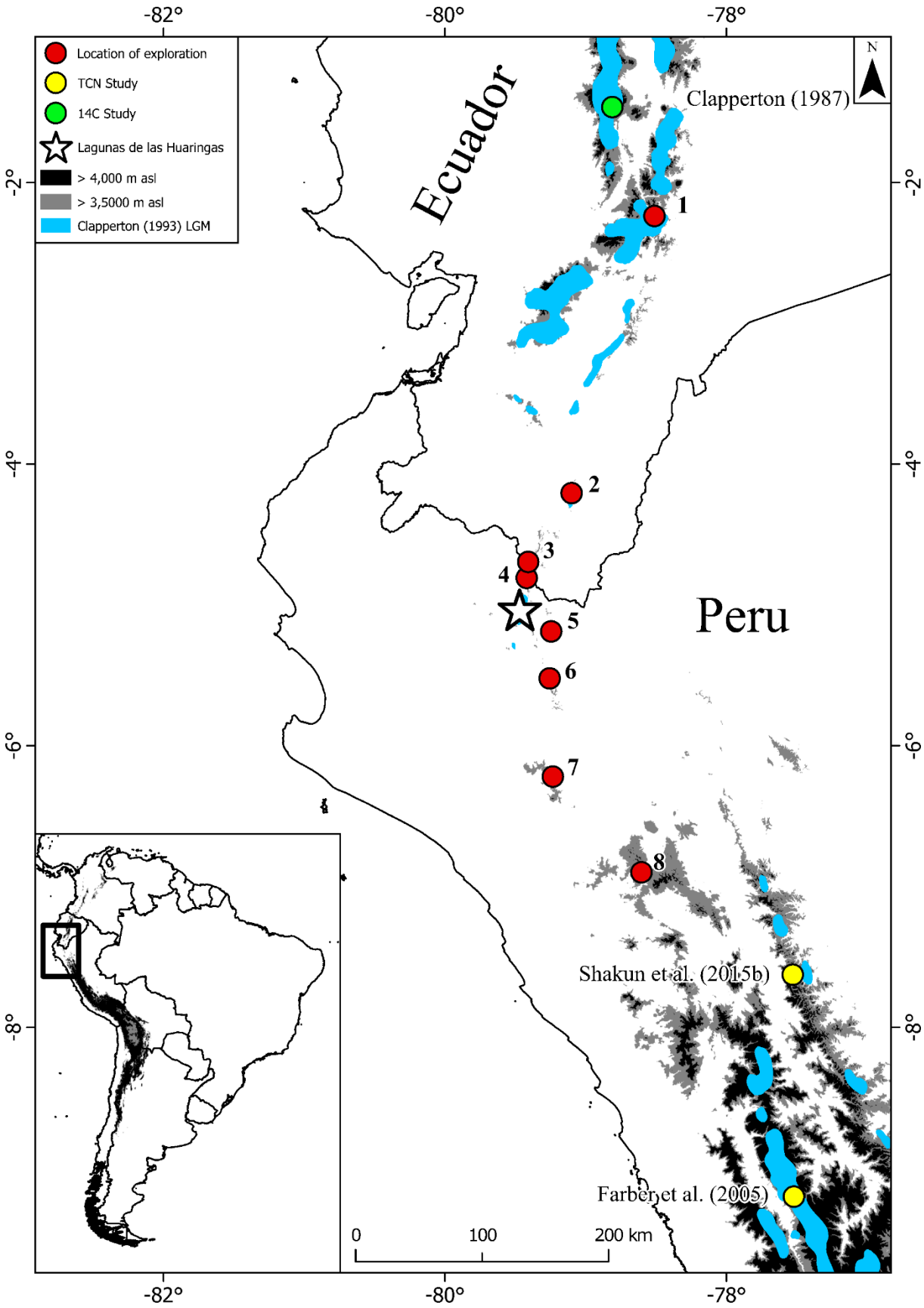

Figure 7.5: The study region (Las Huaringas) in relation to published palaeoglacial studies in the tropical Andes (focused on Perú and Ecuador). The South American LLGM ice limit

estimated by Clapperton (1993) is shown, as are locations of unstudied, potential areas of former glaciation that may be future locations for exploration (generally in regions > 3,500 m asl). Details for these locations are provided in Table 7.1.

Table 7.1: Preliminary evidence of the former glacial activity within the areas for further explanation. Numbers correspond to numbered location within in Figure 7.6.

#	Locality	Coordinates	Max elv.	Description
1	Partque Nacional Sangay, Ecuador	S 2° 14.4 W 78° 30.6	4,579 m	Clear evidence of palaeoglaciation with clearly eroded glacial valleys. Some lakes occupy relict cirque floors, while many overdeepenings are lake filled with stepped lakes in the landscape. There are visible moraines extending down from cirques, reaching down to 3,484 m.
2	Cerro Toronche, Ecuador	S 4° 12.6 W 79° 6.0	3,610 m	Clear glacial erosion with lakes occupying bases cirque floors. Glacial depositional evidence (i.e., moraines) is hard to discern from remote imagery (Google Earth), but the morphology of valleys clearly shows glacial influence with u-shaved valleys and stepped glacial lakes within overdeepenings.
3	Lagunas de Jimbura, Perú	S 4° 41.4 W 79° 24.6	3,860 m	Lake-filled cirques and overdeepenings with clearly discernible lateral moraines located down to a minimum elevation of 2,850 m. Inset moraines potentially indicate later periods of advance and retreat.
4	Cascada El Sombrero, Perú	S 4° 48.6 W 79° 25.2	3,859 m	Limited lake-filled overdeepenings, however large (~60 m) high lateral moraines are clearly identified within the region, with moraines extending down to 3,050 m. Some moraines are closely spaced (30-60 m) indicating a fluctuating ice margin.
5	Tabaconas-Namballe, Perú	S 5° 11.4 W 79° 15	3,661 m	Heavily vegetated region with lakes occupying relict cirques. Lateral moraines are identified within the region with moraines extending down to 3,160 m.
6	Cerro Bravo, Perú	S 5° 31.2 W 79° 15.6	3,960 m	Small region along a massif with lakes filling cirque floors and overdeepenings. Lateral moraines line the exit of cirques and connect with other moraines going into small glacial valleys. These moraines extend down to a minimum elevation of 3,090 m. Inset moraines are identified within the confines of the lowest moraines.
7	Lagunas Inahuanga, Perú	S 6° 13.2 W 79° 13.8	4,040 m	Heavily eroded valleys, with lateral moraines extend down from relict cirques. Smaller medial moraines present, and moraines terminate at a minimum elevation of 3,112 m. Inset moraines within these lateral moraines, with some closely spaced (30-100 m).
8	Cerro San Cirilo, Perú	S 6° 54 W 78° 36	4,133 m	Numerous lakes across a pot-holed landscape. Such evidence that may be indicative of a small, localised ice cap. There is also evidence of lakes filling the bottom of cirques (or glacial source areas). Moraines are hard to discern in this region.

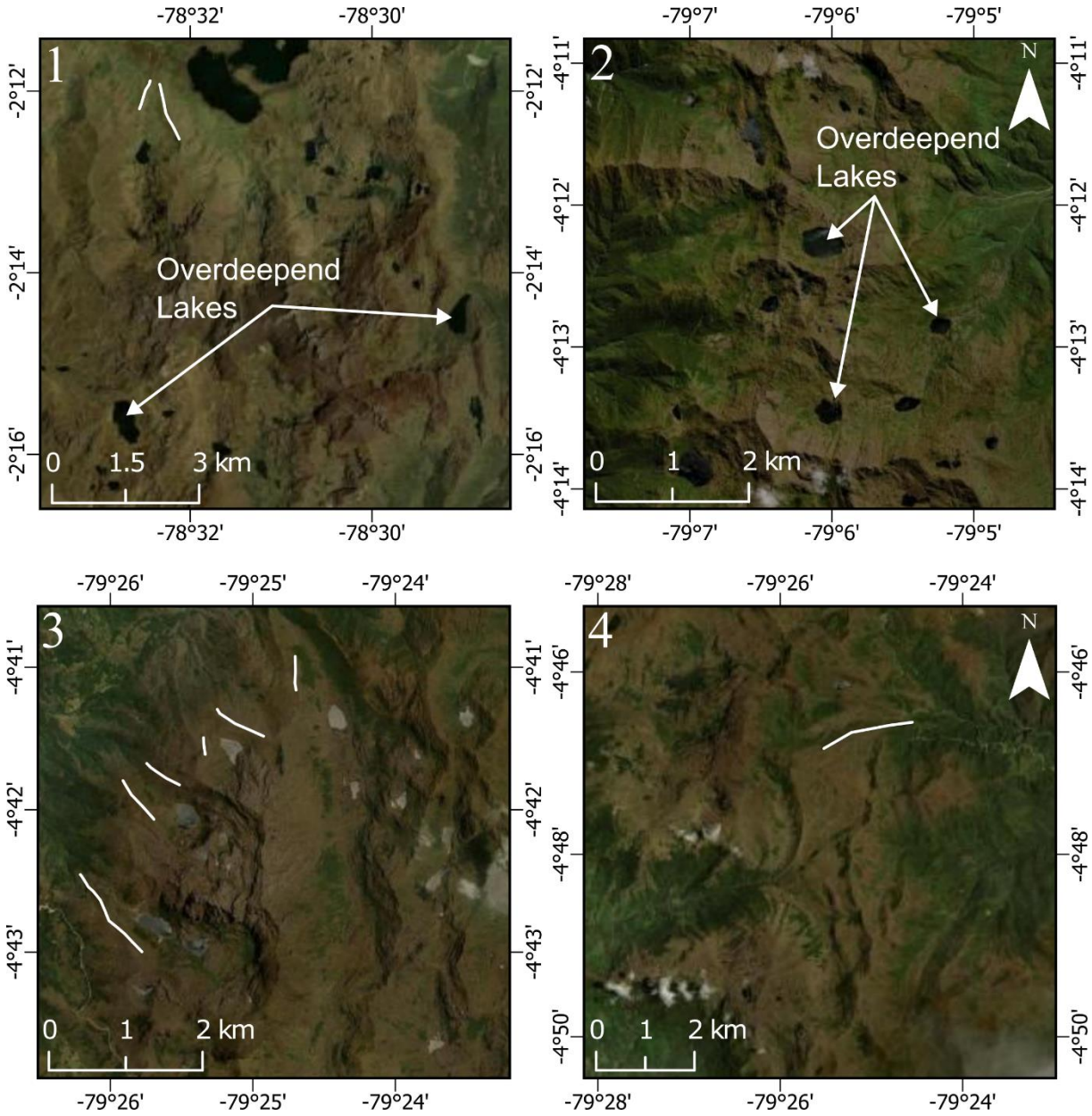

Figure 7.6: Indicated locations in Table 7.1 showing satellite imagery from Esri Imagery of the regions that show and indicates potential palaeoglacial activity. White lines indicate moraines, the white arrows point towards overdeepened lakes that signify glacial activity Numbers correspond to the numbered regions in Table 7.1, with their location within Ecuador or Perú shown in Figure 7.5.

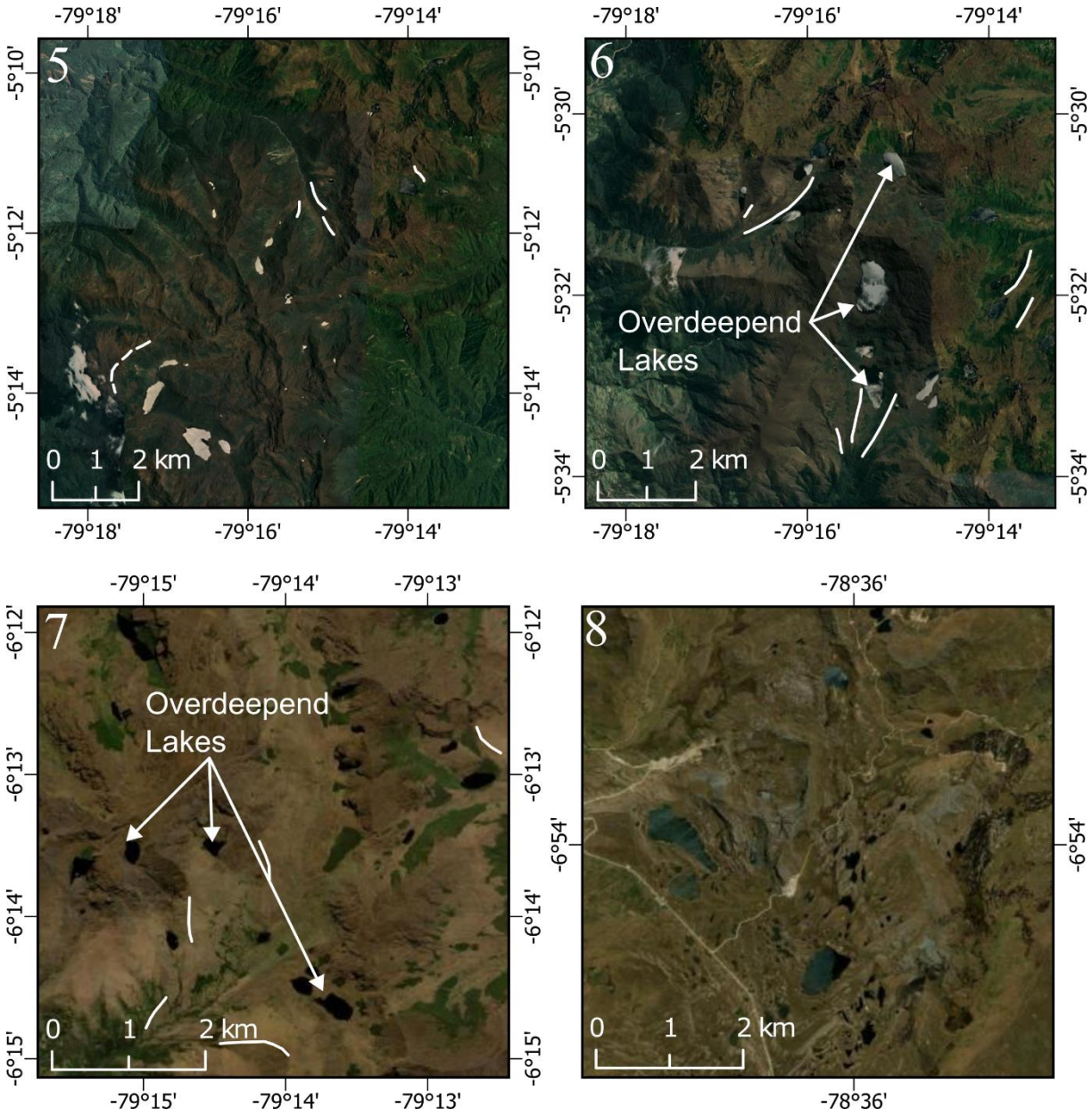

Figure 7.6: *Continued.* 5 is a location with a lot of vegetation potentially indicating older glaciation that has retreated earlier. 8 has a lot of lakes that could represent a former ice cap, however moraine evidence is hard to map remotely.

7.9.2. Expand conducting cosmogenic nuclide dating within the tropical Andes, and revisit previous study sites with new dating techniques

While there is an increase in the number of studies that conduct cosmogenic nuclide dating of glacial landforms within the tropical Andes (e.g., Palacios *et al.*, 2020; the ICD-D database), there is still a lack of age constraints in many regions. Much of Perú and Bolivia have received extensive investigations that constrain glaciation ages from the LLGM through to the late-Holocene (Mark *et al.*, 2017), and there is also evidence of recent Neoglacial advances (e.g., during the Little Ice Age) (Solomina *et al.*, 2007; Jomelli *et al.*, 2008; Rabatel *et al.*, 2008).

Elsewhere across the northern tropical Andes, the glaciation of Ecuador, Venezuela, and Columbia have received the least attention, despite strong evidence for glaciations since the LLGM. One important location that has not been investigated extensively with cosmogenic dating is the Cordillera Vilcanota, in Perú, which has no, or very little, cosmogenic age constraints on the most extensive advance identified within that region but is an important region for understand current climate change and its effects on tropical glaciers. In addition to recommending the investigation of new sites, it would be worthwhile revisiting previously investigated study sites with modern dating techniques (e.g., Schubert, 1974; Wright, 1984; Helmens, 1988). Many formerly glaciated regions in Ecuador have not been investigated or revisited for ~20 years (Mahaney *et al.*, 2010), and pre-2004 studies that included cosmogenic ages used old scaling techniques that mean they cannot be easily compared to more recent studies (e.g., Goodman, 1999), along with the inability to accurately determine ages from volcanic rock (which many Ecuadorian glaciers were on), requiring differing cosmogenic analysis (Cl-36) that were not available at the time. Many older studies only used radiocarbon dating, using lake sediments, basal peat layers, or peat within moraines (Clapperton and McEwan, 1985; Schubert and Clapperton, 1990; Clapperton, 1993). This dating technique does not enable a direct date of the glacial feature, instead providing a relative minimum-limiting or maximum-limiting age, which can only be deemed as useful if both are obtained (Rodbell *et al.*, 2009). Revisiting such sites, using modern-day cosmogenic techniques can test existing ages, increasing the confidence of the timing of past glaciation within the tropics.

7.9.3. Expand the use of numerical models to improve knowledge of the glaciology and dynamics of former ice masses within the tropical Andes.

As this thesis has shown, the use of numerical models such as PISM, within the tropical Andes (or tropical setting) can generate ice masses with a glaciologically sound configuration, and time varying models can provide insights into ice mass response to climate warming and cooling over time (Chapter 6). At present however, no other study conducting such modelling on a semi-regional scale exists, other examples using PISM have been limited to individual glacial valleys. While the palaeo-geomorphology, and the timing of the LLGM and other glacial advances (YD or ACR), are relatively well constrained within many parts of the tropical Andes (Schubert and Clapperton, 1990; Zech *et al.*, 2007; Bromley *et al.*, 2016; Angel *et al.*, 2017; Martin *et al.*, 2020), these often represent snapshots in time. They do not give a detailed understanding of the possible dynamics of the ice mass unless moraines up valley from the maximum regional LLGM extent are well preserved. Time-varying numerical modelling can

provide an improved understanding of how glaciers responded to a fluctuating climate in the past and future (Zekollari *et al.*, 2022), suggesting subsequent advances and retreats that may not be represented in the geomorphological record and providing insights as to whether ice margin advances were synchronous or asynchronous (Batbaatar *et al.*, 2018). Steady state modelling can also provide a reconstruction of ice within valleys at time periods of interest (e.g., Candaş *et al.*, 2020), and can reconstruct ice across a large region that may not have had extensive geomorphological mapping (infield and remote sensing), providing locations for targeting infield geomorphological mapping, and increasing fieldwork efficiency. Steady state modelling can also enable preliminarily understanding of the potential climate ice was built under, allowing easily modifiable climate inputs (e.g., temperature cooling, precipitation fractions, precipitation patterns etc.). Numerical modelling, as shown above, has a plethora of benefits that can provide researchers with further information and data in which to fully understand the glacial history of a region, and thus should be used more in reconstructions of former ice masses.

7.9.4. Improve knowledge of (palaeo) ice surface mass balances in the tropics

Glacial models use glacial physics and surface mass balance parameters in order to solve equations that enable the building of glacial ice and force glacial flow. The accuracy of these models is entirely reliant on the determination of representative values of not only glacier physical properties (e.g., ice fabric, water content etc.) but also the acquisition of surface mass balance measurements used to constrain ice model parameterisation (i.e., degree day factors, refreezing factors etc.). What limits models, and what is a primary limitation of the analysis undertaken in Chapter 5, is how few modern-day observations of such parameters are, especially for the tropical Andes limited to individual glaciers (Molina, 2020), let alone those of palaeo observations to help constrain numerical models. Without these accurate real-world constraints, the numerical models cannot replicate reality, and may therefore lead to inaccurate model output. Using model input parameters derived from different regions of the world with very different glaciology and climate (primarily those related to mass balance), introduces substantive uncertainties in numerical models of tropical glaciers. For example, using degree day factors parameterised across the Greenland Ice Sheet (Ritz, 1997), for a high mountain environment or even within tropical regions, will result in inaccurate climate and glacier dynamics. Though recent thought has been given to the use of present day values for parameterisation of palaeo modelling studies, and whether these are entirely realistic (e.g. Kageyama *et al.*, 2022) (i.e., lapse rates), there is little critical assessment of this issue, and too

few studies that provide parameterisations for much of the worlds glacial regions. There is a need for: a) an increase in the number of regional studies that obtain surface mass balance data across the globe, particularly in the tropical Andes; and b) studies that explore the potential for reconstructing surface mass balance values that will enable a more realistic parameterisation of palaeo modelling studies.

Chapter 8. Conclusions

This thesis aimed to investigate the glacial history of the Las Huaringas, northern Perú, reconstructing the glacial dynamics that may have occurred within this region, and an estimation of the potential palaeoclimate under which the maximum glaciation could have occurred. Such a region has never been detailed within the literature before. Other parts of the tropical Andes (e.g., Perú and Ecuador) have been previously investigated for evidence of past glaciation, but Las Huaringas has not. This location provides a unique opportunity to understand the potential LLGM timing in a region that has not undergone modification by later Holocene advances due to increased climate variations. This thesis used a multi-method approach, combining geomorphological mapping (remote and infield) with numerical modelling techniques to characterise the glaciology of past ice masses at Las Huaringas and to determine the climatic envelope glaciers could have existed under.

Results show that Las Huaringas, a relatively low elevation and low latitude location, has been extensively glaciated in the past, likely during the last glacial cycle. A number of large prominent moraines, smaller inset moraines, glacial smoothed bedrock, lake filled overdeepenings, and glacial lineations, all evidence past glaciation. This evidence is within a region that is substantially below the estimated South American LLGM snowline (Broecker and Denton, 1990a). Evidence observed both remotely via satellite imagery and in the field, enabled the reconstruction of glaciers within the study area. The initial, remotely sensed reconstruction suggested valley type glaciation (Chapter 3), with a maximum glaciated area of 75.6 km^2, while the model-based reconstruction (Chapter 6) suggested an ice plateau type glaciation with larger an area of 173.2 km^2. The ELA derived from this reconstruction was 3,422 ± 30 m asl, an ELA lowering of 1,178 ± 10 m, while the modelled ELA for the most extensive glaciation (25.4 ka) was 3,500 m asl. The potential for the presence of an ice plateau within the region is unique, and ice plateaus have not been reported within any other palaeoglaciation studies in the tropical Andes. The results presented here provided the first ever results of glaciation within northern Perú, providing evidence of glaciation at low elevations below the traditional South American LLGM snowline. Evidence of glaciation at such low elevation provides further credence for other studies to investigate low elevation glaciations, as they can provide a unique opportunity to evidence LLGM advances without modification from Holocene climatic fluctuations.

Although at this time, the collected samples have not undergone analysis for understanding the timing of exposure, thus it is impossible to assign definitive timing of glaciation within this region. However, using first ever numerical modelling of ice masses within the tropical Andes, with the EPICA temperature series (Chapter 6), the timing of the potential LLGM is 25.4 ka. This date falls within the variability of previously dated LLGM moraines within the tropical Andes, between 40.5 ± 1.0 ka and 16.8 ± 0.4 ka. If the numerical modelling is indeed correct, in the absence of absolute dating, an early-LLGM advance is consistent with other study regions across Perú (e.g., Cordillera Blanca, and the Junín Plain) (Farber *et al.*, 2005; Smith *et al.*, 2005b; Smith and Rodbell, 2010). This would have important constraints on the roles of insolation and CO_2 within the tropical Andes and its effect on glacial advance timings in relation to the global temperature cooling. Further, the expansion of dating of low latitude glacial regions, along with locations within similar elevational ranges (< 4,000 m asl) as this region (see section 7.9.1. in Chapter 7), shall aid in filling the longitudinal gap between more southerly Perú studies, and those in northern Ecuador (Figure 2.12), to fully realize and constrain latitudinal patterns of glacial advances, and palaeoclimate variations, during the LLGM. While reanalysis of formerly dated locations that used older, or indirect dating methods, should be a focus of future research to ensure accurate advance timings of glaciations – especially within the Ecuadorian Andes.

Observations of moraines behind the most extensive moraines, assumed to be LLGM, provide evidence of younger glacial advances, postdating the LLGM. The numerical modelling experiments support post-LLGM advances due to climate variability. Cooler periods (e.g., at 19.5 ka) resulted in the modelled ice mass having glaciers readvancing downvalley near to, but not as extensive as, the former maximum ice extent. The model was, however, unable to reconcile the potential timing of these inset moraines, however it is highly likely that these moraines are dating to between 19.5 and 17 ka due to after 19.5 ka glaciers were limited to topographical highs. After 17 ka the model domain was entirely deglaciated, that is linked to a rise in SST across the tropical Pacific and Atlantic oceans, this is also just prior to the Heinrich-1 event, that would have exacerbated deglacial conditions preventing the reoccupation of ice within the region. Thus, it is likely there was no ice in the region during the YD/ACR cool periods. Geomorphic evidence of pre-LLGM advances is unlikely to have survived unmodified. Further sedimentological-oriented work could uncover evidence for older glaciations in the Las Huaringas region. Such evidence is not uncommon across the tropical Andes (Clapperton, 1993).

Temperature cooling across the geomorphological derived estimates, and that from the numerical model, all support a substantially cooler LLGM; maximum of -8.8℃ from the geomorphology (Chapter 3), and -10.4℃ from the numerical model (Chapter 4). This is in line with cooling estimates from Perú and Venezuela (Klein *et al.*, 1999; Stansell *et al.*, 2007) while being one of the coldest estimates within the tropical Andes. Model experiments demonstrate that glaciation required increased precipitation (+30% relative to the present-day) alongside the enhanced cooling, for glaciation to occur and reach their most expansive positions. These results demonstrate that care must be taken when using geomorphological mapping alone to reconstruct past glaciation. The use of this method alone may lead to unrealistic palaeoclimatic inferences, with implications for reconstruction of past ELAs and palaeotemperatures. Numerical models can help us to test geomorphologically derived reconstructions and can provide us with further information on the dynamics of the reconstructed ice mass that we cannot gain from the geomorphological record alone.

While numerical modelling can aid in fitting geomorphological evidence to glacial extents, that aid in inferring palaeoclimate, these advances can exist under differing conditions, or a climatic envelope. This is only exacerbated by glacial numerical models requiring parameterisation of glaciological and climatological parameters that generally use values that are generated over non-tropical glaciers. The sensitivity analysis of the model to inputted climate parameters (DDF and refreezing factor), to allow ice to expand to observed palaeoglacial evidence at its maximum extent, required a temperature cooling of -10℃ and -10.5℃, with precipitation offsets of between +10% and +40%. Further palaeoclimate reconstructions are required at low elevation glacial regions to fully realize and understand the latitudinal variations in palaeoclimate during the tropical Andean LLGM.

The numerical model enabled insights into the potential glacial dynamics of the Las Huaringas ice masses, not just at certain timesteps, but across the model run duration of 38 ka yrs This contrasts with the geomorphological reconstruction that can only provide snapshots of glacial activity, primarily of maximum extents and readvances or stillstands. The numerical model suggested that between 38 ka to 27.5 ka (Ephemeral ice period) ice was limited to the highest elevations (~3,500 m asl), or the study area was completely deglaciated. Between 27.5 ka to 23.5 ka (LLGM period), was associated with the largest ice extent (173.2 km^2) at 25.4 ka. The LLGM period had extensive ice across the entire region, reconstructed as an ice plateau with outlet glaciers that extended to the maximum moraine extents, while ice fluctuated at the maximum extent due to climatic temperature variations. The last period of, between 27.5 ka and 16 ka (waning ice period), was characterised by the presence of ice consistently across the

period, retreating to topographical highs, with small periods of expansion, until complete deglaciation after 17.5 ka. After this period, at no time during the rest of the model run, even during recognised cooling periods such as the YD and ACR, no ice reformed within the model domain. The model indicated substantive sensitivities to surrounding climate, with glacial ice switching limited to topographical hights, to advancing down to their most extensive positions, within a 1°C range. Ice is then completely deglaciated from the region within a 2°C range. While tropical glaciers are extremely sensitive to their surrounding climate, it has never been reported in the literature how marginal conditions can be for ice to exist at the lowest elevations, before retreating up valley due to minor temperature variations. While palaeoglacial studies can determine timing of the LLGM advances, understanding how fast glacial deglaciated can enable an understanding of the driving mechanism for deglaciation of the tropical Andes, these primarily being tropical SST of the Pacific and Atlantic. The use of numerical models, as demonstrated here, can provide further insights into glaciations within the tropical Andes, however the prerequisites of increased mass balance records, along with model parametrisation studies are needed to enable accurate representation of tropical glacial systems.

To conclude, the results of this thesis present for the first time the presence of palaeoglacial evidence in a low elevation, and low latitude location of the tropical Andes. The findings provide evidence for glaciation previously unrecognised in the literature, and below the traditionally through South American LLGM snowline. The thesis demonstrates the role that numerical models (e.g., PISM) can have in tropical glacier reconstructions, providing validation of geomorphic evidence, as well as new understandings of glacial dynamics when parameterized accurately. Further work is needed, however, to allow numerical models to be parameterised to the unique climate and glacier behaviours within the tropics (e.g., differing mass balance regimes, insolation etc.). The priority parameters to better constrain via observations are degree day factors over more tropical glaciers and refreezing factors, as these control the accumulation of ice the most. Finally, there are a number of further sites located near to Las Huaringas, within the northern Perúvian and southern Ecuadorian Andes that can provide further insights into low elevation glaciation within the tropical Andes. These sites, also below <4000 m asl, warrant further investigation. This thesis contributes to our knowledge of past glacial dynamics and palaeoclimate within the tropical Andes. It fills an important latitudinal data gap between studies conducted in more southern Perú and northern Ecuador and provides a proof of concept for numerical modelling in the tropics, raising awareness of past glaciations in this region below < 4,000 m asl, and indicates areas that require further research and development.

Appendix A. Data used to map the geomorphology of the Lagunas de Las Huaringas

Table A.1: Summary of remotely sensed data used for geomorphological mapping of the Las Huaringas region.

Satellite	Image ID	Date Acquired	Cloud Cover
Landsat 8	LC08_L1TP_010063_20161120_20200905_02_T1	20/11/16	5.4%
Sentinel-2	L1C_T17MPQ_A003669_20171118T153646	18/11/17	2.5%
RapidEye	20200106_151210_1736721_RapidEye-3	06/01/20	3%
RapidEye	20200106_151209_1736722_RapidEye-3	06/01/20	0%
RapidEye	20200106_151206_1736821_RapidEye-3	06/01/20	0%
RapidEye	20200106_151206_1736822_RapidEye-3	06/01/20	0%
PlanetScope	20200528_145133_93_2304	28/05/20	0%
PlanetScope	20200528_145136_32_2304	28/05/20	0%
PlanetScope	20200528_145138_72_2304	28/05/20	1%
Pléiades	DS_PHR1B_201512041554053_PS1_PX_W080S06_0624_02618	04/12/15	4.5%
Pléiades	DS_PHR1B_201801031552304_FR1_PX_W080S06_0618_03920	03/01/18	0.6%
Pléiades	DS_PHR1B_201911171547555_FR1_PX_W080S05_0802_01804	17/11/19	7.5%
Bing Maps[a]	NA	NA	~0%
Google Earth™[a]	NA	NA	~0%
ALOS DEM[b]	ALPSMLC30 v3.1	06/20	NA
SPOT 7[c]	DS_SPOT7_202005111517362_FR1_FR1_SV1_SV1_W079S05_01140	11/05/20	20.9%

[a] Bing Maps and Google Earth™ imagery are from multiple sources, cloud cover estimated upon manual inspection.
[b] The ALOS DEM is generated from images from the JAXA ALOS collected between 2006 – 2011.
[c] Captured in tri-stereo producing three images, but the image ID represents the entire collection.

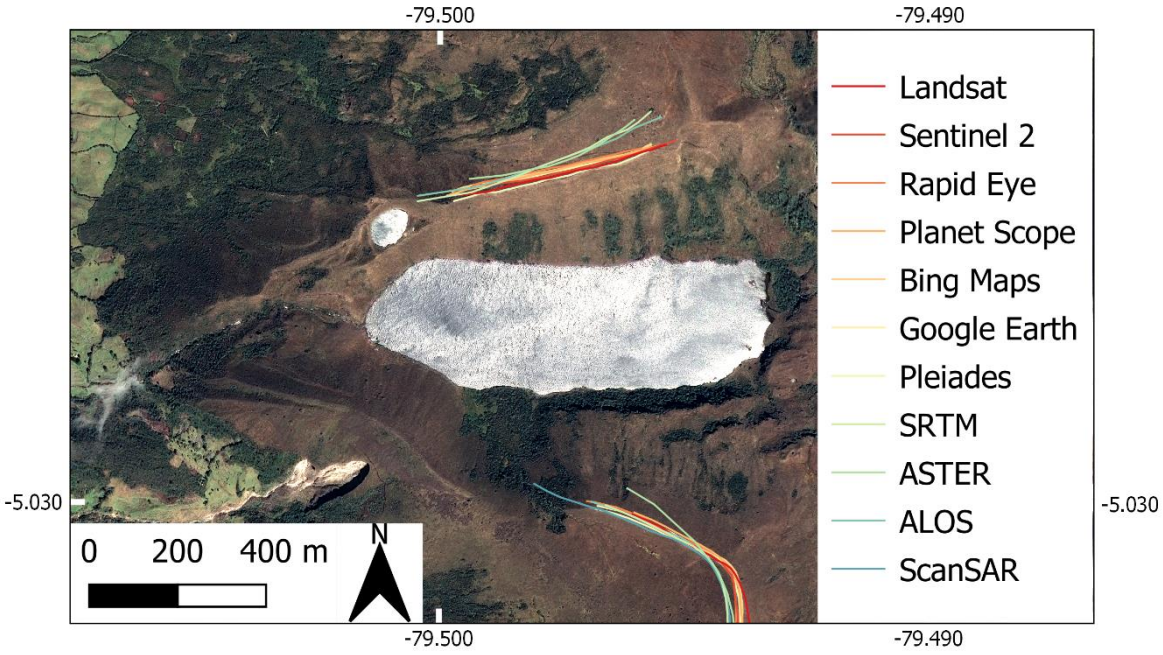

Figure A.1: Two mapped moraines around the Laguna Millionaria, within the western glacial region, using different remotely sensed sources. The very crest of the moraine is mapped from each remotely sensed image or dataset. These remotely sensed sources are ordered in the legend with remotely sensed imagery sources from coarsest to finest resolution: Landsat = 30 m, Sentinel 2 = 10 m, Rapid Eye = 5 m, PlanetScope = 3 m, and Bing Maps and GoogleEarth™ are viable. DEM sources are also used from coarsest to finest resolution; SRTM = 30 m, ASTER = 30 m, ALOS – 30 m, and ScanSAR 18 m). Maximum off set between the two mapped moraines was ± 30 m. Base image is the highest resolution Pléiades imagery.

Appendix B. Visualisation of palaeoglacial aspects.

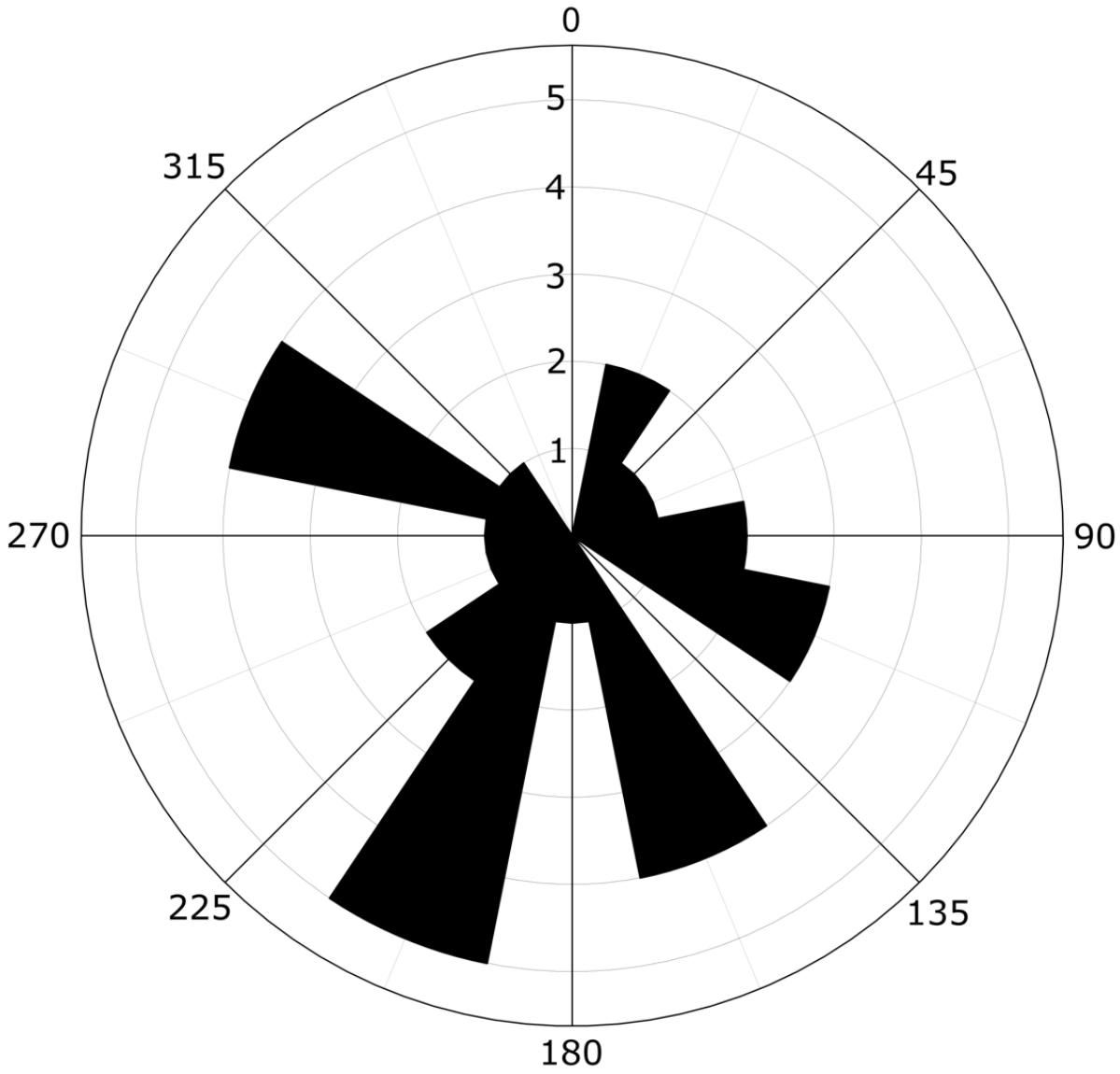

Figure B.1: Reconstructed palaeoglacier aspects. These were manually delineated by digitizing a straight line from the head of the glacier towards the terminus. The majority of the reconstructed glaciers point southwards (SE and SW).

Appendix C. The scripts used to run the PISM model on the Newcastle University ROCKET HPC, detailing the "set-physics_Perú_100.sh" script, and the "spin_Perú.sh" scripts

"set-physics_Perú_100.sh" script, used to parameterise the model, and called to in the "spin_Perú.sh" script.

```
# Copyright (C) 2009-2021 PISM authors
##############################################################################
# This is the physics file for Ethan Lee's Lagunas de las Huaringas glacial
# modelling. This is for his PhD project at the Newcastle University under
# the supervision of Dr. Neil Ross. The modelling was supervised by Dr.
# Stewart Jamieson from Durham University. This is taken from the basic
# set-physics.sh file template from the PISM Authors 'antartic-spin'
# example.
##############################################################################

# grids
export ONETWENTYMGRID="-Mx 250 -My 350 -Lz 1000 -Lbz 0 -Mz 101 -Mbz 1 -
z_spacing equal -bed_smoother_range 50"

# skips
export SKIPONETWNETYM=40

#notes:
export LASHASPHYS="stress_balance ssa+sia -sia_e 1 -ssa_e 1 -sia_n 3"

#Read climate from delta T and delta precip files
export LASHAS_COUPLING2="-atmosphere given,delta_T,frac_P -
atmosphere_given_file $PISM_INDATANAME -surface pdd
surface.pdd.std_dev_use_param yes -surface.pdd.std_dev 3.66 -
surface.pdd.factor_ice 0.009 -surface.pdd.factor_snow 0.003 -
surface.pdd.balance_year_start_day 125 -surface.pdd.refreeze 0.6 -
atmosphere_delta_T_file DeltaT_10_stepped.nc -atmosphere_frac_P_file
FracP_100.nc"

# dynamics related options
export PARAMS="-pseudo_plastic -pseudo_plastic_q 0 -
pseudo_plastic_uthreshold 100 -till_effective_fraction_overburden 0.02 -
till_reference_effective_pressure 1000 -till_compressibility_coefficient
0.12 -till_reference_void_ratio 1 -till_cohesion 0 -hydrology_tillwat_max 2
-yield_stress mohr_coulomb"

export TILLPHI="-plastic_phi 30"

export FULLPHYS="-stress_balance ssa+sia -
stress_balance.sia.max_diffusivity 3000 -hydrology null $PARAMS $TILLPHI"

export LASHASPHYS="-stress_balance ssa+sia -sia_e 1.0 -ssa_e 1.0 -sia_n 3.0
-ssa_n 3.0 -stress_balance.sia.max_diffusivity 5000 -hydrology null $PARAMS
$TILLPHI"

# use if KSP "diverged" errors occur
export STRONGKSP="-ssafd_ksp_type gmres -ssafd_ksp_norm_type
unpreconditioned -ssafd_ksp_pc_side right -ssafd_pc_type asm -
ssafd_sub_pc_type lu"
```

“spin _Perú_100.sh” script used to run the PISM model on the HPC.

```
# Copyright (C) 2009-2021 PISM authors
##############################################################################
# This is the spin up file for Ethan Lee's Lagunas de las Huaringas glacial
# modelling. This is for his PhD project at the Newcastle University under
# the supervision of Dr. Neil Ross. The modelling was supervised by Dr.
# Stewart Jamieson from Durham University. This is taken from the basic
# spin.sh file template from the PISM Authors 'antartic-spin' example.
##############################################################################

SCRIPTNAME="#(E_lee_Perú-spin.sh)"

echo "$SCRIPTNAME"

set -e # exit on error

# naming files, directories, executables
RESDIR=
BOOTDIR=
PISM_EXEC=${PISM_EXEC:=pismr}
PISM_MPIDO="mpiexec"

# input data:
export PISM_INDATANAME=${BOOTDIR}PerúPISMinput_new.nc

###source set-physics.sh
source set-physics_Perú_100.sh

echo "$SCRIPTNAME MPI tasks = $SLURM_NTASKS"
set -e # exit on error

if [ -n "${PISM_DO:+1}" ] ; then
  echo "$SCRIPTNAME          PISM_DO = $PISM_DO"
else
  PISM_DO=""
fi
DO=$PISM_DO

# These change the resolution of the model
# higher resolution, slow the computation
GRID=$ONETWENTYMGRID
SKIP=$SKIPONETWNETYM
GRIDNAME=120m

echo "$SCRIPTNAME              PISM = $PISM_EXEC"
echo "$SCRIPTNAME       LASHASPHYS = $LASHASPHYS"
echo "$SCRIPTNAME LASHAS_COUPLING2 = $LASHAS_COUPLING2"
echo "$SCRIPTNAME PIKPHYS_COUPLING = $PIKPHYS_COUPLING"



# ##############################################################################
# run into steady state with constant climate forcing
# ##############################################################################
stage=LH_Spin_rf_0_4_T_11_xP_100
INNAME=$PISM_INDATANAME
RESNAME=${RESDIR}${stage}_${GRIDNAME}.nc
TSNAME=${RESDIR}ts_${stage}_${GRIDNAME}.nc
RUNTIME=3500
EXTRANAME=${RESDIR}extra_${stage}_${GRIDNAME}.nc
exvars="pdd_fluxes,pdd_rates,thk,usurf,velbase_mag,velsurf_mag,mask,bmelt,t
illwat,temppabase,amount_fluxes,climatic_mass_balance,ice_surface_temp,topg
```

```
,effective_precipitation,ice_mass,effective_air_temp,effective_precipitatio
n,velbar,tempicethk"
expackage="-extra_times 0:50:$RUNTIME -extra_vars $exvars"

echo "$SCRIPTNAME run into steady state with constant climate forcing for
$RUNTIME a"
cmd="$PISM_MPIDO $PISM_EXEC -skip -skip_max $SKIP -i $PISM_INDATANAME -
bootstrap $GRID \
    $SIA_ENHANCEMENT $LASHAS_COUPLING2 $LASHASPHYS $STRONGKSP \
    -ys 0 -y $RUNTIME \
    -ts_file $TSNAME -ts_times 0:1:$RUNTIME \
    -extra_file $EXTRANAME $expackage \
    -o $RESNAME -o_size big"
$DO $cmd

echo
echo "$SCRIPTNAME $GRIDNAME simulation complete"
```

Appendix D. Summary of best-fit runs when compared to the geomorphological record

Table D.1: The absolute horizontal mismatch between model runs of different DDF combinations along with climate. '-' denotes a model run that built too much ice and errored out. 0 denotes no ice was built in the valley to facilitate an offset measurement. Green fill denotes the 'best-fit' model run for the DDF combination.

DDF	ΔT (K)	xP (%)	Ice area (km^2)	Ice volume (km^3)	Horizontal mismatch along valley centrelines (m)					
					V1	V2	V3	V4	V5	Average
Ice:	-9.5	90	0.3	0.0	0	0	0	0	0	0
11	-9.5	100	4.2	0.2	0	4386.85	2349.86	0	1715.03	8451.74
Snow:	-9.5	110	13.3	0.6	0	3740.45	1922.85	2935.16	1051.91	9650.37
3	-9.5	120	21.7	1.2	0	3628.08	1690.86	2648.05	175.56	8142.55
	-9.5	130	29.5	1.6	1276.18	3065.65	1542.88	2510.85	168.2	8563.76
	-9.5	140	37.4	1.9	790.53	2891.13	997.49	1413.76	293.89	6386.80
	-9.5	150	45.8	2.3	477.43	2435.71	403.07	1191.62	681	5188.83
	-10	90	12.5	0.5	0	4160.88	2642.79	4221.95	1465.75	12491.37
	-10	100	29.2	1.3	1646.67	3229.96	1915.01	3526.97	71.78	10390.39
	-10	110	56.0	2.5	585.05	2571.13	732.99	1113.52	64.68	5067.37
	-10	120	75.4	3.6	245	801.67	275	980.64	718.35	3020.66
	-10	130	94.2	5.1	146.63	369.03	166.03	689.54	610.03	1981.26
	-10	140	108.7	6.3	213.8	49.42	79.25	326.7	418.13	1087.30
	-10	150	127.6	7.7	89.63	342.24	93.34	205.53	554.91	1285.65
	-10.5	90	56.2	2.6	585.27	1796.9	636.4	813.83	840.44	4672.84
	-10.5	100	98.1	4.7	26.16	504.53	204.58	565.87	1093.74	2394.88
	-10.5	110	143.6	7.6	217.46	243.59	92.11	83.86	421.14	1058.16
	-10.5	120	179.0	9.9	26.48	409.29	211.08	157.05	171.43	975.33
	-10.5	130	206.8	11.7	263.31	879.9	211.95	405.87	49.25	1810.28
	-10.5	140	235.4	15.2	386.86	776.56	212.18	280.69	70.71	1727.00
	-10.5	150	250.0	14.2	506.34	1045.01	92.01	48.1	72.05	1763.51
Ice:	-9.5	90	23.0	1.3	0	3449.48	1565.7	2601.19	46.86	7663.23
11	-9.5	100	33.7	1.8	1040.53	3071.01	1241.32	3169.54	48.18	8570.58
Snow:	-9.5	110	44.5	2.2	588.68	2434.46	522.68	1053.95	1401.39	6001.16
2	-9.5	120	56.5	2.9	216.14	1792.81	1891.03	153.09	926.53	4979.60
	-9.5	130	68.7	3.7	25.57	1077.81	32.93	857.74	905.65	2899.70
	-9.5	140	79.7	4.4	143.76	515.9	396.91	750.45	687.62	2494.64
	-9.5	150	91.0	5.2	145.48	326.24	274.07	724.81	546.3	2016.90
	-10	90	80.3	4.2	93.64	861.38	274.33	741.26	423.52	2394.13
	-10	100	103.8	5.9	146.5	315.7	155.13	446.3	421.15	1484.78
	-10	110	124.3	7.4	215	78.44	91.8	206.12	295.41	886.77
	-10	120	144.0	8.6	25.81	509.53	91.8	46.27	169.37	842.78
	-10	130	167.9	10.2	25.8	328.7	212.2	46.26	171.06	784.02
	-10	140	188.9	11.7	146.23	714.46	91.35	44.91	171.45	1168.40
	-10	150	204.5	12.7	266.34	879.59	91.03	36.5	48.04	1321.50
	-10.5	90	167.9	11.4	25.54	612.22	212.69	294.74	842.69	1987.88
	-10.5	100	222.2	14.1	263.71	775.76	332.06	572.3	620.54	2564.37
	-10.5	110	251.0	15.9	503.95	942.17	330.4	36.53	461.56	2274.61
	-10.5	120	272.6	16.3	626.55	1143.25	566.94	575.24	522.52	3434.50
	-10.5	130	295.3	18.4	749.32	1204.57	455.62	461.99	627.54	3499.04
	-10.5	140	309.8	18.6	754.78	1416.33	987	1342.63	623.07	5123.81
	-10.5	150	KSP	KSP	-	-	-	-	-	-
Ice:	-9.5	90	0.0	0.0	0	0	0	0	0	0
9	-9.5	100	0.1	0.0	0	0	0	0	0	0
Snow:	-9.5	110	2.8	0.1	0	4612.17	2486.69	0	1892.16	8991.02
4	-9.5	120	9.5	0.4	0	4268.14	2100.83	3372.68	1358.2	11099.85
	-9.5	130	17.7	0.9	0	4053.86	1688.27	2651.8	679.24	9073.17
	-9.5	140	24.6	1.3	1652.36	3158.13	1543.34	2752.54	72.41	9178.78
	-9.5	150	30.8	1.5	1153.41	3512.38	1394.94	2916.38	173.08	9150.19
	-10	90	2.0	0.1	0	4637.99	2484.4	0	2052.71	9175.10

	-10	100	9.9	0.5	0	3829.72	2090.45	3013.95	1057.73	9991.85
	-10	110	24.2	1.2	0	3401.15	1545.69	2584.1	310.98	7841.92
	-10	120	46.5	2.2	763.95	2432.27	1250.94	1170.01	192.23	5809.40
	-10	130	68.2	3.3	310.72	1117.29	399.07	807.76	347.78	2982.62
	-10	140	85.0	4.5	27.73	508.98	154.52	815.12	547.12	2053.47
	-10	150	99.2	5.4	266.86	180.67	28.23	571.39	545.78	1592.93
	-10.5	90	20.0	1.1	2220.29	2514.33	1707.73	2513.63	347.22	9303.20
	-10.5	100	47.9	2.4	1034.98	1921.67	647.72	1159.67	943.55	5707.59
	-10.5	110	87.1	4.3	90.61	447.73	166.03	448.38	848.25	2001.00
	-10.5	120	128.7	6.7	28.35	79.17	94.26	82.69	313.15	597.62
	-10.5	130	164.3	9.2	26.98	508.75	332.22	46.82	295.02	1209.79
	-10.5	140	192.4	10.5	146.87	619.53	331.71	159.56	172.82	1430.49
	-10.5	150	215.1	12.0	271.99	785.54	212.42	49.81	59.89	1379.65
Ice:	-9.5	90	2.4	0.1	0	4691.18	2901.47	0	2025.86	9618.51
9	-9.5	100	9.7	0.4	0	5004.77	2090.48	2887.71	1568.01	11550.97
Snow:	-9.5	110	18.9	0.9	0	3631.39	1695.63	2653.23	353.77	8334.02
3	-9.5	120	26.6	1.3	1393.54	3154.76	1576.98	2508.39	59.89	8693.56
	-9.5	130	35.2	1.8	904.04	2798.8	1000.8	1287.9	169.48	6161.02
	-9.5	140	44.5	2.2	468.52	2407.77	414.1	1170.51	678.33	5139.23
	-9.5	150	55.8	2.7	306.31	1651.65	30.8	1054.06	935.21	3978.03
	-10	90	20.6	0.9	0	3168.01	1702.72	2654.72	48.51	7573.96
	-10	100	47.4	2.1	763.95	2434.28	1273.29	1053.92	75.45	5600.89
	-10	110	70.6	3.2	296.71	992.23	398.63	797.68	428.7	2913.95
	-10	120	89.6	4.6	146.62	458.26	277.18	708.71	546.56	2137.33
	-10	130	106.6	6.0	264.73	75.98	91.25	447.38	424.29	1303.63
	-10	140	122.6	7.2	27.45	340.36	210.77	82.8	352.1	1013.48
	-10	150	142.2	8.4	29.48	616.29	332.84	92.17	295.39	1366.17
	-10.5	90	78.8	3.4	28.44	580.5	283.1	694.61	847.62	2434.27
	-10.5	100	129.9	6.5	28.44	76.06	91.25	96.42	844.83	1137.00
	-10.5	110	170.0	9.0	27.94	614.89	450.09	161.2	166.65	1420.77
	-10.5	120	201.3	11.2	266.74	880.81	330.69	160.7	59.89	1698.83
	-10.5	130	228.0	12.7	395.3	943.56	209.46	584.36	59.89	2192.57
	-10.5	140	255.9	17.1	644.48	1043.95	101.58	844.88	73.56	2708.45
	-10.5	150	268.4	15.2	653.36	1313.58	704.22	554.07	528.96	3754.19
Ice:	-9.5	90	0.3	0.0	0	0	0	0	0	0
7	-9.5	100	3.5	0.1	0	4624.64	2626.53	0	1910.91	9162.08
Snow:	-9.5	110	11.9	0.5	0	4540.74	1935.35	2931.46	1184.79	10592.34
4	-9.5	120	19.7	0.9	0	3606.36	1699.47	2640.83	294.61	8241.27
	-9.5	130	26.7	1.3	1396.83	3224.85	1544.45	3317.63	74.79	9558.55
	-9.5	140	35.2	1.7	903.63	3160.08	1005.76	1288.48	72.55	6430.50
	-9.5	150	43.9	2.1	588.92	2308.37	522.82	1054.05	352.21	4826.37
	-10	90	10.7	0.4	0	3759.45	2213.45	3062.5	1433.22	10468.62
	-10	100	26.6	1.1	2253.39	3170.86	1541.96	2507.63	309.04	9782.88
	-10	110	52.9	2.2	477.13	2164.54	757.92	1060.32	468.22	4928.13
	-10	120	73.9	3.3	307.37	486.61	277.22	684.23	59.89	1815.32
	-10	130	91.3	4.5	146.62	314.54	275.54	693.22	386.5	1816.42
	-10	140	106.7	5.8	268.47	346.54	92.26	325.01	412.92	1445.20
	-10	150	121.9	6.9	28.85	617.14	329.26	85.76	417.32	1478.33
	-10.5	90	51.9	2.3	1156.89	2056.34	763.4	1168.76	1114.24	6259.63
	-10.5	100	91.6	3.8	27.65	180.81	166.03	329.99	1333.85	2038.33
	-10.5	110	140.5	6.9	25.49	245.06	210.88	46.4	1340.85	1868.68
	-10.5	120	177.9	9.3	146.62	776.34	333.26	278.19	59.89	1594.30
	-10.5	130	202.8	10.9	266.33	1045.51	333.35	426.32	59.89	2131.40
	-10.5	140	227.8	12.4	383.61	1154.7	209.52	45.3	59.89	1853.02
	-10.5	150	250.9	13.6	625.15	1041.69	572.08	44.58	70.69	2354.19
Ice:	-9.5	90	8.0	0.3	0	4286.92	2206.79	2891.27	1549.28	10934.26
7	-9.5	100	18.3	0.8	0	3457.25	1696.02	2648.43	419.08	8220.78
Snow:	-9.5	110	26.5	1.3	1677.04	3167.5	1548.66	2524.27	69.31	8986.78
3	-9.5	120	36.6	1.7	789.88	2687.45	1007.97	1292.77	70.04	5848.11
	-9.5	130	46.8	2.3	473.97	2068	392.63	1054.2	422.16	4410.96
	-9.5	140	57.5	2.8	212.53	1080.26	166.03	1328.52	546.17	3333.51
	-9.5	150	68.0	3.5	143.97	1388.51	91.82	932.94	801.21	3358.45
	-10	90	42.8	1.8	1031.1	2547.99	1005.4	1175.66	202.14	5962.29

	-10	100	69.8	3.0	303.01	987.86	399.36	815.3	433.61	2939.14
	-10	110	90.6	4.5	145.81	332.96	277.82	752.2	546.35	2055.14
	-10	120	109.3	6.0	387.21	346.31	90.28	330.22	421.53	1575.55
	-10	130	127.3	7.3	27.76	513.24	332.25	88.18	290.63	1252.06
	-10	140	149.0	8.6	150.65	777.82	444.65	153.89	289.87	1816.88
	-10	150	170.5	10.0	266.14	613.7	449.05	156.2	171.73	1656.82
	-10.5	90	122.4	5.8	141.66	46.14	94.85	160.15	1332.17	1774.97
	-10.5	100	170.5	8.8	150.92	509.56	454.61	151.65	957.26	2224.00
	-10.5	110	202.1	10.8	272.37	1045.71	331.37	43.12	59.89	1752.46
	-10.5	120	231.4	12.7	506.58	1046.74	30.77	74.38	92.74	1751.21
	-10.5	130	255.4	13.9	641.95	1314.5	1077.56	267.34	71.2	3372.55
	-10.5	140	277.0	15.5	761.12	1460.38	1079.26	158.2	193.96	3652.92
	-10.5	150	KSP	KSP	-	-	-	-	-	-
Ice:	-9.5	90	33.7	1.6	904.24	2793.66	1365.23	1292.85	59.89	6415.87
7	-9.5	100	47.2	2.3	473.06	2316.61	400.73	1054.02	548.27	4792.69
Snow:	-9.5	110	60.6	2.9	92.2	1117.29	29.83	812.26	810.66	2862.24
2	-9.5	120	73.2	3.8	266.64	509.96	213.47	742.35	681.56	2413.98
	-9.5	130	86.7	4.9	392.25	49.63	93.58	571.21	542.92	1649.59
	-9.5	140	99.0	5.7	506.05	245.7	94.94	451.47	552.76	1850.92
	-9.5	150	110.4	6.6	96.9	410.83	213.82	329.77	420.32	1471.64
	-10	90	104.1	5.5	265.71	50.33	92.01	323.24	420.27	1151.56
	-10	100	127.4	7.2	146.48	509.65	336.1	36.5	292.84	1321.57
	-10	110	154.6	8.8	265.89	881.33	210.09	160.36	296.49	1814.16
	-10	120	179.6	10.3	265.66	772.16	334.99	282.79	173.96	1829.56
	-10	130	199.7	11.7	384.05	1210.6	331.93	275.65	49.63	2251.86
	-10	140	218.1	12.9	507.57	1047.85	210.95	476.85	48.84	2292.06
	-10	150	236.6	14.0	504.67	1212.79	88.14	797.9	71.29	2674.79
	-10.5	90	224.1	12.2	386.57	1211.69	329.35	630.31	624.49	3182.41
	-10.5	100	255.5	13.8	757.27	1275.18	613.14	152.94	526.9	3325.43
	-10.5	110	282.3	15.5	263.53	886.92	207.52	155	294.46	1807.43
	-10.5	120	305.2	16.7	745.38	1475.71	683.77	951.24	842.09	4698.19
	-10.5	130	324.2	17.8	875.76	1686.56	1664.32	781.63	840.61	5848.88
	-10.5	140	343.5	21.4	1175.45	2091.47	1761.49	846	427.08	6301.49
	-10.5	150	KSP	KSP	-	-	-	-	-	-
Ice:	-9.5	90	2.2	0.1	0	0	0	0	0	0
5	-9.5	100	9.3	0.3	0	4549.99	2210.21	2853.83	1534.62	11148.65
Snow:	-9.5	110	18.4	0.8	0	3528.61	1694.72	2634.37	684.3	8542.00
5	-9.5	120	25.9	1.2	1532.17	3111.16	1727.1	2812.5	319.72	9502.65
	-9.5	130	34.4	1.6	763.81	3243.14	1347.15	1300.7	312.64	6967.44
	-9.5	140	44.6	2.0	585.88	2469.52	395.93	1054.05	90.9	4596.28
	-9.5	150	54.0	2.4	298.32	1517.21	144.1	923.52	754.83	3637.98
	-10	90	20.6	0.9	0	3256.15	1532.66	2636.5	679.23	8104.54
	-10	100	46.8	1.8	967.54	2493.44	945.69	1055.3	734.45	6196.42
	-10	110	70.2	2.9	215	1070.75	393.87	732.85	756.53	3169.00
	-10	120	89.3	4.0	27.31	324.67	155.56	505.28	49.31	1062.13
	-10	130	108.0	5.5	388.36	87.67	209.11	208.62	419.14	1312.90
	-10	140	123.8	6.6	28.4	509.3	331.5	47.34	281.1	1197.64
	-10	150	141.4	7.6	148.99	1041.9	217.81	47.82	298.04	1754.56
	-10.5	90	78.0	3.2	470.67	1069.81	92.67	797.68	1446.2	3877.03
	-10.5	100	128.9	5.7	272.61	78.95	93.2	159.18	1572.97	2176.91
	-10.5	110	172.4	8.4	267.17	723.85	456.83	573.34	2406.73	4427.92
	-10.5	120	205.8	10.6	387.18	1209.85	447.81	580.18	1450.29	4075.31
	-10.5	130	228.0	11.9	507.76	1321.27	585.07	680.03	1451.32	4545.45
	-10.5	140	252.5	13.0	751.82	1588.19	1239.24	1013.96	71.02	4664.23
	-10.5	150	272.3	14.5	783.9	1693.51	1544.77	410.05	189.61	4621.84
Ice:	-9.5	90	8.2	0.3	0	4615.44	2199.04	3085.65	1524.92	11425.05
5	-9.5	100	18.4	0.8	0	3943.88	1705.19	2610.66	677.74	8937.47
Snow:	-9.5	110	26.6	1.2	1472.16	3603.71	1447.73	2525.05	355.98	9404.63
4	-9.5	120	36.4	1.7	787.56	2672.17	1288.21	1167.03	201.07	6116.04
	-9.5	130	47.3	2.2	471.17	1924.08	395.95	931.98	161.88	3885.06
	-9.5	140	57.7	2.7	216.79	1381.56	27.47	931.36	937.09	3494.27
	-9.5	150	68.0	3.3	143.95	448.13	94.14	763.32	810.89	2260.43
	-10	90	43.7	1.7	975.77	2576.07	1000.7	1171.43	840.94	6564.91

	-10	100	70.1	2.9	216.97	215.43	1819.23	396.53	690.43	3338.59
	-10	110	91.2	4.2	146.83	316.39	154.23	700.25	48.17	1365.87
5170	-10	120	110.4	5.7	26.4	244.25	211.33	86.77	419.97	1348.78
	-10	130	129.3	7.0	26.4	781.81	209.39	46.94	293.67	1358.21
	-10	140	150.2	8.2	268.96	1048.1	331.16	279	320.39	2247.61
	-10	150	172.0	9.6	268.12	1044.41	449.18	36.04	167.9	1965.65
	-10.5	90	123.5	5.3	147.84	47.43	92.27	311.33	1449.33	2048.20
	-10.5	100	172.1	8.4	264.84	534.99	448	577.42	2407.63	4232.88
	-10.5	110	206.8	10.5	386.4	1211.37	210.14	746.14	1337.01	3891.06
	-10.5	120	234.5	12.1	504.47	1568.9	565.05	756.35	71.47	3466.24
	-10.5	130	257.8	13.4	755.58	1572.97	1077.07	836.64	72.02	4314.28
	-10.5	140	KSP	KSP	-	-	-	-	-	-
	-10.5	150	KSP	KSP	-	-	-	-	-	-
Ice:	-9.5	90	21.3	0.9	0	3296.53	1538.25	2518.01	70.86	7423.65
5	-9.5	100	31.5	1.4	1033.27	3014.89	1366.11	2294.46	472.85	8181.58
Snow:	-9.5	110	43.8	2.0	1053.63	2166.47	522.17	1053.74	213.93	5009.94
3	-9.5	120	56.4	2.5	300.74	1389.55	28.81	808.51	553.84	3081.45
	-9.5	130	67.9	3.3	146.85	503.4	92.78	752.99	810.48	2306.50
	-9.5	140	79.8	4.2	387.32	182.37	91.92	695.05	681.33	2037.99
	-9.5	150	91.4	5.1	506.22	509.17	333.01	569.89	386.91	2305.20
	-10	90	78.2	3.3	216.93	506.85	166.03	574.38	956.43	2420.62
	-10	100	102.0	5.0	267.04	79.45	30.26	324.05	415.24	1116.04
	-10	110	123.3	6.6	26.75	510.06	448.99	36.34	350.36	1372.50
	-10	120	146.1	7.9	266.79	945.01	450.27	160.21	234.39	2056.67
	-10	130	171.2	9.6	266.87	944.66	572.49	37.96	166.71	1988.69
	-10	140	191.0	10.9	387.39	1317.87	470.69	516.77	170.28	2863.00
	-10	150	209.6	12.1	630.1	1210.8	358.74	641.13	59.89	2900.66
	-10.5	90	187.6	9.3	268.8	944.96	330.02	573.44	2293.63	4410.85
	-10.5	100	220.0	11.3	503.7	1475.64	452.19	909.73	310.61	3651.87
	-10.5	110	250.7	12.9	746.01	1580.63	685.82	1011.89	73.35	4097.70
	-10.5	120	276.2	14.8	777.68	1676.67	1424.47	417.16	190.71	4486.69
	-10.5	130	KSP	KSP	-	-	-	-	-	-
	-10.5	140	KSP	KSP	-	-	-	-	-	-
	-10.5	150	KSP	KSP	-	-	-	-	-	-

Table D.2: The absolute horizontal mismatch between model runs of different refreezing values varied with climate. '-' denotes a model run that built too much ice and errored out. 0 denotes no ice was built in the valley to facilitate an offset measurement. Green fill denotes the 'best-fit' model run for the refreezing value.

RF	ΔT (K)	xP (%)	Ice area (km^2)	Ice volume (km^3)	Horizontal mismatch along valley centrelines					
					V1	V2	V3	V4	V5	Average
0.7	-9.0	90	0.7	0.0	0	0	0	0	0	0
	-9.0	100	2.2	0.1	0	4608.81	2865.02	0	1911.18	9385.01
	-9.0	110	4.1	0.2	0	4385.89	2347.22	0	1736.79	8469.90
	-9.0	120	7.4	0.3	0	4944.05	2237.82	3007.45	1538.85	11728.17
	-9.0	130	11.8	0.6	0	4448.24	2104.33	3204.54	1112.84	10869.95
	-9.0	140	15.8	0.8	0	3467.38	1864.57	2663.95	538.05	8533.95
	-9.0	150	19.6	1.0	0	3288.84	1684.47	2645.81	72.26	7691.38
	-9.5	90	12.08	0.5	0	3784.42	2019.51	2831.19	1062.70	9697.82
	-9.5	100	21.3	1.0	0	3288.78	1576.98	2698.64	74.34	7638.74
	-9.5	110	30.4	1.5	1154.42	3044.06	1399.16	2353.37	202.70	8153.71
	-9.5	120	41.3	2.0	615.97	2408.87	640.22	1159.88	173.99	4998.93
	-9.5	130	52.5	2.5	298.93	1660.55	166.03	1402.93	48.39	3576.83
	-9.5	140	62.7	3.1	96.73	744.52	91.68	1083.30	940.72	2956.95
	-9.5	150	73.4	3.9	267.04	63.82	211.43	739.30	682.25	1963.84
	-10	90	53.4	2.2	470.64	2057.21	762.20	1054.01	1519.5	5863.56
	-10	100	77.4	3.4	214.83	731.51	277.28	726.94	295.94	2246.50
	-10	110	99.3	5.1	265.67	47.05	31.63	445.44	420.76	1210.55
	-10	120	117.5	6.5	26.85	511.30	212.56	85.46	420.71	1256.88
	-10	130	138.4	7.8	149.95	780.47	331.89	47.63	294.53	1604.47
	-10	140	161.9	9.4	267.26	1315.38	449.91	160.78	293.14	2486.47
	-10	150	182.0	10.6	271.28	1041.29	456.87	37.07	167.24	1973.75
0.6	-9.5	90	0.6	0.0	0	4899.79	2818.75	0	2298.15	10016.69
	-9.5	100	4.6	0.2	0	4391.67	2542.65	3450.51	1726.49	12111.32
	-9.5	110	14.0	0.6	0	3772.07	1854.83	2877.07	935.97	9439.94
	-9.5	120	21.5	1.1	0	3295.4	1576.81	2507.76	49.6	7429.57
	-9.5	130	29.3	1.5	1115.67	3047.61	1397.58	2459.44	171.21	8191.51
	-9.5	140	37.8	1.9	781	2673.11	759.84	1168.5	50.66	5433.11
	-9.5	150	46.4	2.3	406.26	2323.91	345.68	1048.82	800.85	4925.52
	-10	90	13.4	0.6	0	3774.39	2038.28	2938.48	801.1	9552.25
	-10	100	31.5	1.3	1641.83	2912.95	1393.47	1056.57	194.8	7199.62
	-10	110	58.3	2.5	471.93	1790.86	516.54	1054.06	71.98	3905.37
	-10	120	77.3	3.6	214.46	767.44	274.63	809.93	675.42	2741.88
	-10	130	96.2	5.1	142.98	245.91	154.56	691.35	542.49	1777.29
	-10	140	111.1	6.3	94.22	241.07	90.27	329.39	417.6	1172.55
	-10	150	128.3	7.5	26.84	310.67	212.19	83.99	292.85	926.54
	-10.5	90	58.9	2.6	586.38	1628.69	396.81	799.5	956.51	4367.89
	-10.5	100	102.0	4.8	27.53	316.92	470.34	328.83	844.41	1988.03
	-10.5	110	147.4	7.6	93.29	347.55	212.62	37.24	46.82	737.52
	-10.5	120	182.6	9.9	148.7	616.76	332.51	157.22	167.65	1422.84
	-10.5	130	209.9	11.6	266.43	614.77	331.19	276.45	48.7	1537.54
	-10.5	140	236.3	13.3	386.53	1043.09	211.98	35.74	72.36	1749.70
	-10.5	150	KSP	KSP	-	-	-	-	-	-
0.5	-9.5	90	0.0	0.0	0	0	0	0	0	0
	-9.5	100	0.3	0.0	0	0	0	0	0	0
	-9.5	110	3.0	0.1	0	5541.9	3602.83	0	1911.26	11055.99
	-9.5	120	9.9	0.4	0	5578.27	2483.56	3435.27	1431.98	12929.08
	-9.5	130	17.8	0.9	0	3529.55	1760.09	2770.48	674.35	8734.47
	-9.5	140	24.1	1.2	1647.96	3426.02	1536.17	2622.9	361.02	9594.07
	-9.5	150	30.7	1.6	1153.86	3127.9	1350.23	2509.43	295.08	8436.50
	-10	90	2.6	0.1	0	5373.85	2572.75	0	2503.79	10450.39
	-10	100	10.7	0.5	0	3691.67	2325.65	3959.21	1088.98	11065.51
	-10	110	24.4	1.1	0	3221.17	1566.12	2506.62	191.96	7485.87
	-10	120	47.9	2.1	616.71	2445.71	883.40	1169.10	349.45	5464.37

5175		-10	130	67.3	3.2	306.67	1116.47	397.13	933.65	553.41	3307.33
		-10	140	83.2	4.1	90.52	590.00	151.44	811.93	545.77	2189.66
		-10	150	99.0	5.5	265.81	240.91	153.48	572.08	545.98	1778.26
		-10.5	90	22.5	1.1	0	4095.97	1964.71	3043.09	422.44	9526.21
		-10.5	100	51.9	2.4	1030.95	2058.57	639.26	1168.13	960.04	5856.95
		-10.5	110	86.6	3.9	27.02	449.77	152.68	685.02	313.05	1627.54
		-10.5	120	129.1	6.7	26.98	49.04	91.42	84.40	49.09	300.93
		-10.5	130	164.2	9.1	27.42	333.70	210.57	35.61	288.65	895.95
		-10.5	140	192.1	10.8	144.12	508.95	331.78	36.10	49.00	1069.95
		-10.5	150	214.1	12.2	268.84	504.91	212.31	403.03	59.89	1448.98
	0.4	-10	90	0.1	0.0	0	0	0	0	0	0
5180		-10	100	2.8	0.1	0	4589.18	2968.10	0	1911.16	9468.44
		-10	110	10.7	0.5	0	3742.25	2087.23	2882.96	1036.57	9749.01
		-10	120	22.7	1.1	0	3154.25	1576.52	2583.32	192.29	7506.38
		-10	130	42.8	1.9	782.71	2707.77	1245.37	1286.60	352.55	6375.00
		-10	140	61.5	2.9	468.69	1652.60	522.56	1054.02	673.92	4371.79
		-10	150	76.85	3.8	215.45	861.11	401.60	750.81	661.54	2890.51
		-10.5	90	9.9	0.5	0	4078.29	2204.41	3015.54	1365.45	10663.69
		-10.5	100	24.5	1.2	0	3775.08	1664.59	2681.20	71.93	8192.80
		-10.5	110	51.8	2.4	907.01	2059.43	637.74	1170.84	731.70	5506.72
		-10.5	120	82.6	3.8	89.18	506.28	276.13	687.62	312.57	1871.78
		-10.5	130	120.8	6.3	146.41	243.87	30.52	210.54	71.91	703.25
5185		-10.5	140	153.9	8.5	94.82	169.47	89.78	86.55	166.53	607.15
		-10.5	150	181.4	10.2	93.12	412.83	92.28	36.01	170.30	804.54
		-11	90	48.7	2.4	1158.15	2314.09	883.40	1169.22	1217.87	6742.73
		-11	100	87.0	4.2	388.61	277.35	166.03	323.75	1566.95	2722.69
		-11	110	140.6	7.5	386.96	72.93	91.66	155.71	1685.74	2393.00
		-11	120	192.0	10.5	386.58	610.97	330.76	684.41	2084.82	4097.54
		-11	130	KSP	KSP	-	-	-	-	-	-
		-11	140	KSP	KSP	-	-	-	-	-	-
		-11	150	KSP	KSP	-	-	-	-	-	-

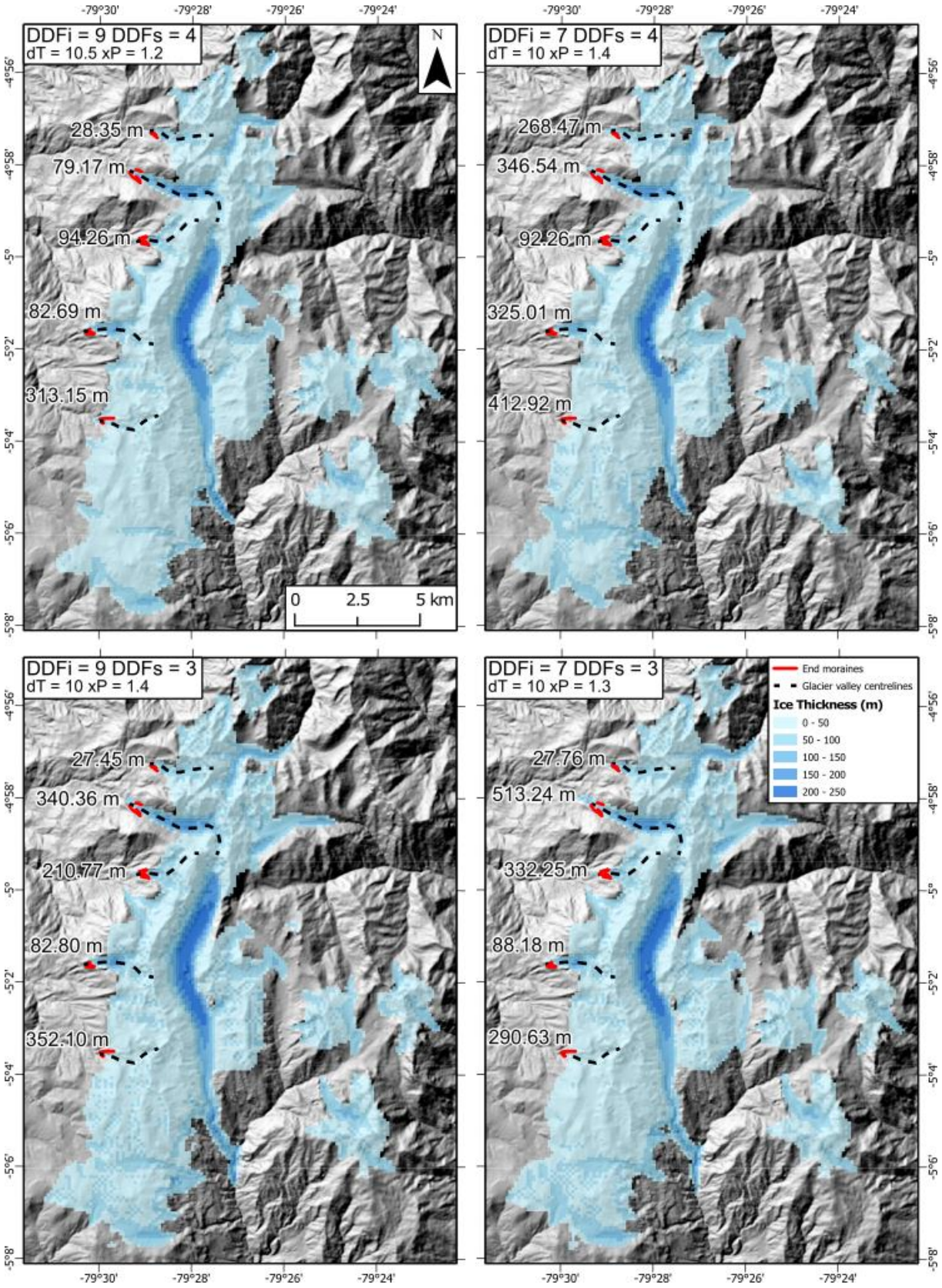

Figure D.1: Selected DDF best fit model output detailing the DDF combination, and the temperature offset, and precipitation offset required. The valleys used to determine the best fit are shown with the centre line and end moraines, along with the calculated absolute horizontal offset for the valley.

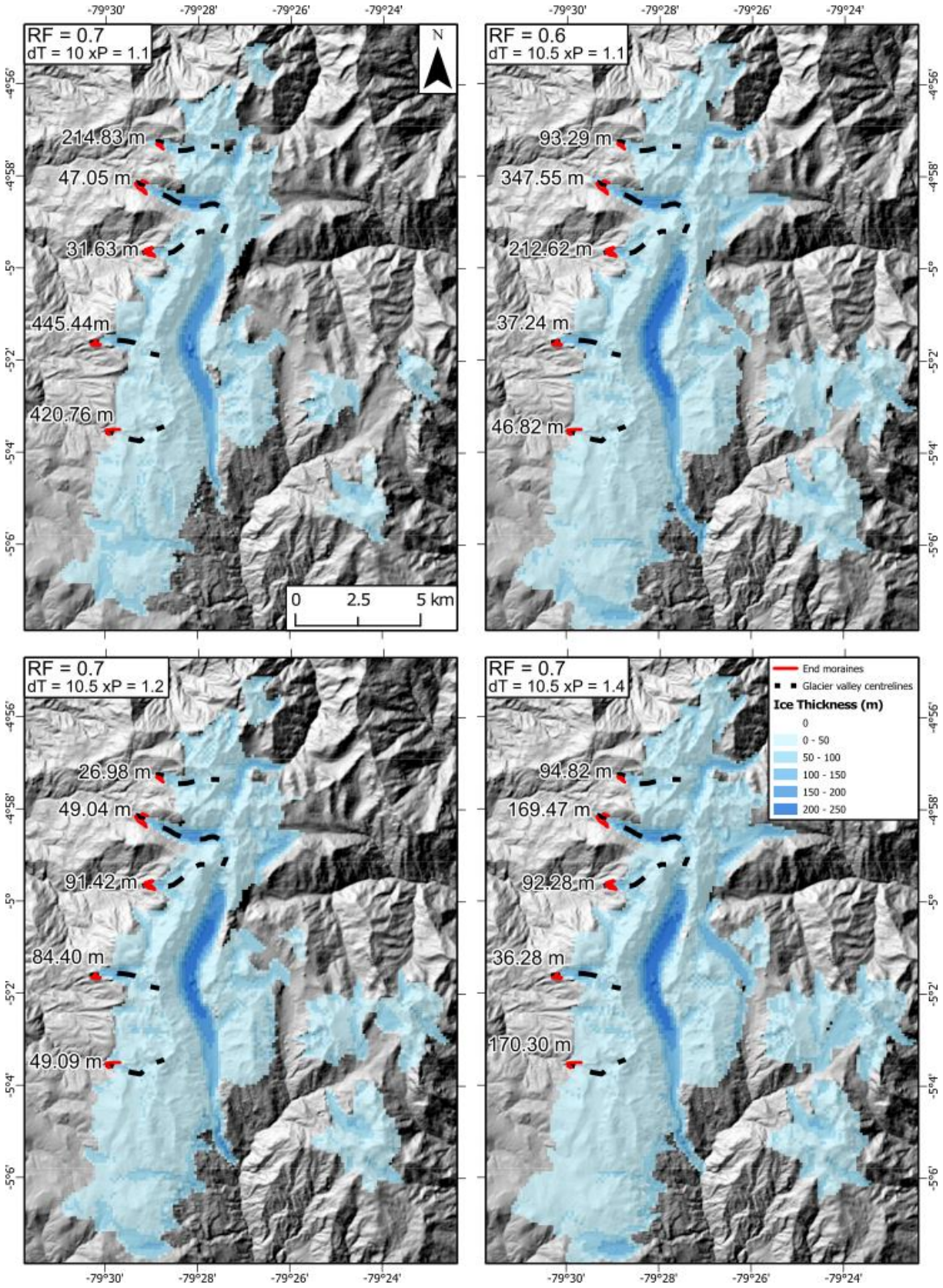

Figure D.2: Refreezing factor best fit model output detailing the temperature offset, and precipitation offset required. The valleys used to determine the best fit are shown with the centre line and end moraines, along with the calculated absolute horizontal offset for the valley.

Appendix E. Further detail on the ice extent, every 100 yrs during the period of great ice extent within the model run.

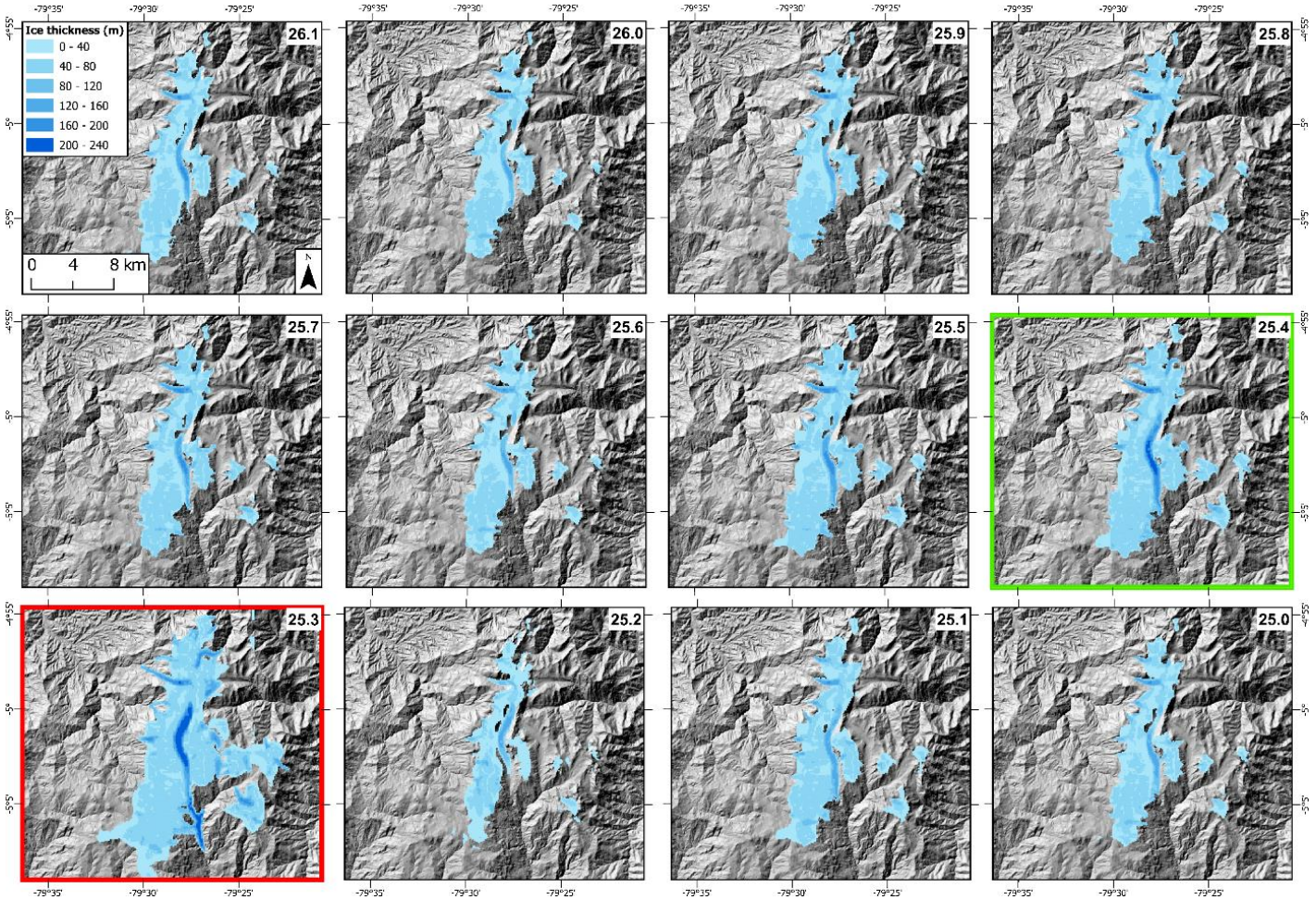

Figure E.1: The period of greatest ice extent between 26.1 ka and 25.0 ka. 25.4 ka (green outline) the determined LLGM extent of glaciers due to their close proximity to the assumed LLGM moraines within the 5 valleys used to test the ice extent. 25.3 ka (red outline) exhibited potential artifacts of the model with very thick ice in the down valley section of the Shimbe valley glacier. This was deemed erroneous and not chosen as the LLGM. This period shows the Shimbe valley incurring continue ice occupation of the Shimbe valley for at least 1,000 yrs

References

Abbott, M.B., Wolfe, B.B., Wolfe, A.P., Seltzer, G.O., Aravena, R., Mark, B.G., Polissar, P.J., Rodbell, D.T., Rowe, H.D. and Vuille, M. (2003) 'Holocene paleohydrology and glacial history of the central Andes using multiproxy lake sediment studies', *Palaeogeography, Palaeoclimatology, Palaeoecology*, 194(1-3), pp. 123-138.

Albrecht, T., Winkelmann, R. and Levermann, A. (2020) 'Glacial-cycle simulations of the Antarctic Ice Sheet with the Parallel Ice Sheet Model (PISM) – Part 1: Boundary conditions and climatic forcing', *The Cryosphere*, 14(2), pp. 599-632.

Alcalá, J., Palacios, D., Zamorano, J.J. and Vázquez-Selem, L. (2011) 'Last Glacial Maximum and deglaciation of Ampato volcanic complex, southern Peru.', *Cuaternario y Geomorfología*, 25, pp. 121-136.

Álvarez-Villa, O.D., Vélez, J.I. and Poveda, G. (2011) 'Improved long-term mean annual rainfall fields for Colombia', *International Journal of Climatology*, 31(14), pp. 2194-2212.

Anderson, B., Lawson, W., Owens, I. and Goodsell, B. (2006) 'Past and future mass balance of 'Ka Roimata o Hine Hukatere' Franz Josef Glacier, New Zealand', *Journal of Glaciology*, 52(179), pp. 597-607.

Anderson, B.M. (2004) *The response of "Ka Roimata o Hine Hukatere" Franz Josef Glacier to climate change*. University of Canterbury.

Anderson, H.J., Pedro, J.B., Bostock, H.C., Chase, Z. and Noble, T.L. (2021) 'Compiled Southern Ocean sea surface temperatures correlate with Antarctic Isotope Maxima', *Quaternary Science Reviews*, 255, p. 106821.

Anderson, L.S., Roe, G.H. and Anderson, R.S. (2014) 'The effects of interannual climate variability on the moraine record', *Geology*, 42(1), pp. 55-58.

Angel, I. (2016) *Late Pleistocene deglaciation histories in the central Mérida Andes (Venezuela)*. Université de Grenoble Alpes-Universidad Central de Venezuela.

Angel, I., Guzman, O. and Carcaillet, J. (2017) 'Pleistocene Glaciations in the Northern Tropical Andes, South America (Venezuela, Colombia and Ecuador)', *Cuadernos de Investigación Geográfica*, 43(2), p. 20.

Antoniazza, G. and Lane, S.N. (2021) 'Sediment yield over glacial cycles: A conceptual model', *Progress in Physical Geography: Earth and Environment*, 45(6), pp. 842-865.

Applegate, P.J., Urban, N.M., Laabs, B.J.C., Keller, K. and Alley, R.B. (2010) 'Modeling the statistical distributions of cosmogenic exposure dates from moraines', *Geosci. Model Dev.*, 3(1), pp. 293-307.

Aschwanden, A., Bueler, E., Khroulev, C. and Blatter, H. (2012) 'An enthalpy formulation for glaciers and ice sheets', *Journal of Glaciology*, 58(209), pp. 441-457.

Baker, P.A., Rigsby, C.A., Seltzer, G.O., Fritz, S.C., Lowenstein, T.K., Bacher, N.P. and Veliz, C. (2001a) 'Tropical climate changes at millennial and orbital timescales on the Bolivian Altiplano', *Nature*, 409(6821), pp. 698-701.

Baker, P.A., Seltzer, G.O., Fritz, S.C., Dunbar, R.B., Grove, M.J., Tapia, P.M., Cross, S.L., Rowe, H.D. and Broda, J.P. (2001b) 'The History of South American Tropical Precipitation for the Past 25,000 Years', *Science*, 291(5504), pp. 640-643.

Balco, G. (2019) 'Why are there no exposure-age data from glaciated Mexican volcanoes?', *The bleeding edge of cosmogenic-nuclide geochemistry*. Available at: https://cosmognosis.wordpress.com/2019/11/08/why-are-there-no-exposure-age-data-from-glaciated-mexican-volcanoes/.

Balco, G., Stone, J.O., Lifton, N.A. and Dunai, T.J. (2008) 'A complete and easily accessible means of calculating surface exposure ages or erosion rates from ^{10}Be and ^{26}Al measurements', *Quaternary Geochronology*, 3(3), pp. 174-195.

Ballantyne, A.P., Lavine, M., Crowley, T.J., Liu, J. and Baker, P.B. (2005) 'Meta-analysis of tropical surface temperatures during the Last Glacial Maximum', *Geophysical Research Letters*, 32(5).

Ballantyne, C.K. (1989) 'The Loch Lomond Readvance on the Isle of Skye, Scotland: Glacier reconstruction and palaeoclimatic implications', *Journal of Quaternary Science*, 4(2), pp. 95-108.

Ballantyne, C.K. and Stone, J.O. (2012) 'Did large ice caps persist on low ground in north-west Scotland during the Lateglacial Interstade?', *Journal of Quaternary Science*, 27(3), pp. 297-306.

Barr, I.D. and Lovell, H. (2014) 'A review of topographic controls on moraine distribution', *Geomorphology*, 226, pp. 44-64.

Barr, I.D. and Spagnolo, M. (2014) 'Testing the efficacy of the glacial buzzsaw: insights from the Sredinny Mountains, Kamchatka', *Geomorphology*, 206, pp. 230-238.

Barr, I.D. and Spagnolo, M. (2015) 'Glacial cirques as palaeoenvironmental indicators: Their potential and limitations', *Earth-Science Reviews*, 151, pp. 48-78.

Batbaatar, J., Gillespie, A.R., Fink, D., Matmon, A. and Fujioka, T. (2018) 'Asynchronous glaciations in arid continental climate', *Quaternary Science Reviews*, 182, pp. 1-19.

Becker, P., Funk, M., Schlüchter, C. and Hutter, K. (2017) 'A study of the Würm glaciation focused on the Valais region (Alps)', *Geogr. Helv.*, 72(4), pp. 421-442.

Becker, P., Seguinot, J., Jouvet, G. and Funk, M. (2016) 'Last Glacial Maximum precipitation pattern in the Alps inferred from glacier modelling', *Geographica Helvetica*, 71(3), pp. 173-187.

Behling, H. and Hooghiemstra, H. (1999) 'Environmental history of the Colombian savannas of the Llanos Orientales since the Last Glacial Maximum from lake records El Pinal and Carimagua', *Journal of Paleolimnology*, 21(4), pp. 461-476.

Bendix, J., Rollenbeck, R. and Reudenbach, C. (2006) 'Diurnal patterns of rainfall in a tropical Andean valley of southern Ecuador as seen by a vertically pointing K-band Doppler radar', *International Journal of Climatology*, 26(6), pp. 829-846.

Bendle, J.M. and Glasser, N.F. (2012) 'Palaeoclimatic reconstruction from Lateglacial (Younger Dryas Chronozone) cirque glaciers in Snowdonia, North Wales', *Proceedings of the Geologists' Association*, 123(1), pp. 130-145.

Benn, D. and Evans, D.J. (2014) *Glaciers and Glaciation*. Routledge.

Benn, D.I., Owen, L.A., Osmaston, H.A., Seltzer, G.O., Porter, S.C. and Mark, B. (2005) 'Reconstruction of equilibrium-line altitudes for tropical and sub-tropical glaciers', *Quaternary International*, 138-139, pp. 8-21.

Bennett, M.M. and Glasser, N.F. (2009) *Glacial geology ice sheets and landforms*. 2nd edn. Oxford: John Wiley & Sons.

Bennett, M.R. (2001) 'The morphology, structural evolution and significance of push moraines', *Earth-Science Reviews*, 53(3), pp. 197-236.

Berman, A.L., Silvestri, G.E. and Tonello, M.S. (2016) 'Differences between Last Glacial Maximum and present-day temperature and precipitation in southern South America', *Quaternary Science Reviews*, 150, pp. 221-233.

Bernard, H. (1979) 'A Theoretical Model of Glacial Abrasion', *Journal of Glaciology*, 23(89), pp. 39-50.

Bickerdike, H.L., Evans, D.J.A., Stokes, C.R. and Ó Cofaigh, C. (2018a) 'The glacial geomorphology of the Loch Lomond (Younger Dryas) Stadial in Britain: a review', *Journal of Quaternary Science*, 33(1), pp. 1-54.

Bickerdike, H.L., Ó Cofaigh, C., Evans, D.J.A. and Stokes, C.R. (2018b) 'Glacial landsystems, retreat dynamics and controls on Loch Lomond Stadial (Younger Dryas) glaciation in Britain', *Boreas*, 47(1), pp. 202-224.

Birkeland, P.W., Rodbell, D.T. and Short, S.K. (1989) 'Radiocarbon dates on deglaciation, Cordillera Central, Northern Peruvian Andes', *Quaternary Research*, 32(1), pp. 111-113.

Blard, P.-H., Lave, J., Farley, K.A., Ramirez, V., Jimenez, N., Martin, L.C.P., Charreau, J., Tibari, B. and Fornari, M. (2014) 'Progressive glacial retreat in the Southern Altiplano (Uturuncu volcano, 22°S) between 65 and 14ka constrained by cosmogenic ^{3}He dating', *Quaternary Research*, 82(1), pp. 209-221.

Blard, P.H., Wagnon, P., Lavé, J., Soruco, A., Sicart, J.E. and Francou, B. (2011) 'Degree-day melt models for paleoclimate reconstruction from tropical glaciers: calibration from mass balance and meteorological data of the Zongo glacier (Bolivia, 16° S)', *Clim. Past Discuss.*, 2011, pp. 2119-2158.

Boulton, G. (1972) 'The role of thermal regime in glacial sedimentation', *Polar geomorphology*, 4(Special Publication), pp. 1-19.

Braithwaite, R.J. (1995) 'Positive degree-day factors for ablation on the Greenland ice sheet studied by energy-balance modelling', *Journal of Glaciology*, 41(137), pp. 153-160.

Braithwaite, R.J., Laternser, M. and Pfeffer, W.T. (1994) 'Variations of near-surface firn density in the lower accumulation area of the Greenland ice sheet, Pâkitsoq, West Greenland', *Journal of Glaciology*, 40(136), pp. 477-485.

Braithwaite, R.J. and Zhang, Y. (1999) 'Modelling changes in glacier mass balance that may occur as a result of climate changes', *Geografiska Annaler: Series A, Physical Geography*, 81(4), pp. 489-496.

Braithwaite, R.J. and Zhang, Y. (2000) 'Sensitivity of mass balance of five Swiss glaciers to temperature changes assessed by tuning a degree-day model', *Journal of Glaciology*, 46(152), pp. 7-14.

Bravo, C., Rojas, M., Anderson, B.M., Mackintosh, A.N., Sagredo, E. and Moreno, P.I. (2015) 'Modelled glacier equilibrium line altitudes during the mid-Holocene in the southern mid-latitudes', *Clim. Past*, 11(11), pp. 1575-1586.

Briner, J.P. and Swanson, T.W. (1998) 'Using inherited cosmogenic 36Cl to constrain glacial erosion rates of the Cordilleran ice sheet', *Geology*, 26(1), pp. 3-6.

Brocklehurst, S.H. and Whipple, K.X. (2004) 'Hypsometry of glaciated landscapes', *Earth Surface Processes and Landforms*, 29(7), pp. 907-926.

Broecker, W.S. and Denton, G.H. (1990a) 'The role of ocean-atmosphere reorganizations in glacial cycles', *Quaternary Science Reviews*, 9(4), pp. 305-341.

Broecker, W.S. and Denton, G.H. (1990b) 'What Drives Glacial Cycles?', *Scientific American*, 262(1), pp. 48-43.

Bromley, G.R.M., Hall, B.L., Rademaker, K.M., Todd, C.E. and Racovteanu, A.E. (2011a) 'Late Pleistocene snowline fluctuations at Nevado Coropuna (15°S), southern Peruvian Andes', *Journal of Quaternary Science*, 26(3), pp. 305-317.

Bromley, G.R.M., Hall, B.L., Schaefer, J.M., Winckler, G., Todd, C.E. and Rademaker, K.M. (2011b) 'Glacier fluctuations in the southern Peruvian Andes during the late-glacial period, constrained with cosmogenic ^{3}He', *Journal of Quaternary Science*, 26(1), pp. 37-43.

Bromley, G.R.M., Schaefer, J.M., Hall, B.L., Rademaker, K.M., Putnam, A.E., Todd, C.E., Hegland, M., Winckler, G., Jackson, M.S. and Strand, P.D. (2016) 'A cosmogenic ^{10}Be chronology for the local last glacial maximum and termination in the Cordillera Oriental, southern Peruvian Andes: Implications for the tropical role in global climate', *Quaternary Science Reviews*, 148, pp. 54-67.

Bromley, G.R.M., Schaefer, J.M., Winckler, G., Hall, B.L., Todd, C.E. and Rademaker, K.M. (2009) 'Relative timing of last glacial maximum and late-glacial events in the central tropical Andes', *Quaternary Science Reviews*, 28(23), pp. 2514-2526.

Brook, M.S., Hagg, W. and Winkler, S. (2013) 'Debris cover and surface melt at a temperate maritime alpine glacier: Franz Josef Glacier, New Zealand', *New Zealand Journal of Geology and Geophysics*, 56(1), pp. 27-38.

Brown, V.H., Evans, D.J.A., Vieli, A. and Evans, I.S. (2013) 'The Younger Dryas in the English Lake District: reconciling geomorphological evidence with numerical model outputs', *Boreas*, 42(4), pp. 1022-1042.

Brugger, K.A. (2010) 'Climate in the Southern Sawatch Range and Elk Mountains, Colorado, U.S.A., during the Last Glacial Maximum: Inferences Using a Simple Degree-Day Model', *Arctic, Antarctic, and Alpine Research*, 42(2), pp. 164-178.

Bueler, E. and van Pelt, W. (2015) 'Mass-conserving subglacial hydrology in the Parallel Ice Sheet Model version 0.6', *Geosci. Model Dev.*, 8(6), pp. 1613-1635.

Builes-Jaramillo, A. and Poveda, G. (2018) 'Conjoint Analysis of Surface and Atmospheric Water Balances in the Andes-Amazon System', *Water Resources Research*, 54(5), pp. 3472-3489.

Buttstädt, M., Möller, M., Iturraspe, R. and Schneider, C. (2009) 'Mass balance evolution of Martial Este Glacier, Tierra del Fuego (Argentina) for the period 1960–2099', *Adv. Geosci.*, 22, pp. 117-124.

Byrne, M.P. and O'Gorman, P.A. (2013) 'Land–Ocean Warming Contrast over a Wide Range of Climates

Convective Quasi-Equilibrium Theory and Idealized Simulations', *Journal of Climate*, 26(12), pp. 4000-4016.

Candaş, A., Sarikaya, M.A., Köse, O., Şen, Ö.L. and Çiner, A. (2020) 'Modelling Last Glacial Maximum ice cap with the Parallel Ice Sheet Model to infer palaeoclimate in south-west Turkey', *Journal of Quaternary Science*, 35(7), pp. 935-950.

Carcaillet, J., Angel, I., Carrillo, E., Audemard, F.A. and Beck, C. (2013) 'Timing of the last deglaciation in the Sierra Nevada of the Mérida Andes, Venezuela', *Quaternary Research*, 80(3), pp. 482-494.

Carrivick, J.L., Smith, M.W., Sutherland, J.L. and Grimes, M. (2023) 'Cooling glaciers in a warming climate since the Little Ice Age at Qaanaaq, northwest Kalaallit Nunaat (Greenland)', *Earth Surface Processes and Landforms*, 48(13), pp. 2446-2462.

Castillo, A., Prange, M., Bernales, J., Retamal-Ramírez, F., Schulz, M. and Rogozhina, I. (2022) 'Numerical reconstructions of the Patagonian Ice Sheet: Growth and demise through the Late Quaternary', *EGU General Assembly 2022*. Vienna, Austria, 23–27 May 2022.

Chandler, B.M.P., Lovell, H., Boston, C.M., Lukas, S., Barr, I.D., Benediktsson, Í.Ö., Benn, D.I., Clark, C.D., Darvill, C.M., Evans, D.J.A., Ewertowski, M.W., Loibl, D., Margold, M., Otto, J.-C., Roberts, D.H., Stokes, C.R., Storrar, R.D. and Stroeven, A.P. (2018) 'Glacial geomorphological mapping: A review of approaches and frameworks for best practice', *Earth-Science Reviews*, 185, pp. 806-846.

Chepstow-Lusty, A., Bush, M.B., Frogley, M.R., Baker, P.A., Fritz, S.C. and Aronson, J. (2005) 'Vegetation and climate change on the Bolivian Altiplano between 108,000 and 18,000 yr ago', *Quaternary Research*, 63(1), pp. 90-98.

Chueca, J. and Julián, A. (2004) 'Relationship between solar radiation and the development and morphology of small cirque glaciers (Maladeta Mountain massif, Central Pyrenees, Spain)', *Geografiska Annaler: Series A, Physical Geography*, 86(1), pp. 81-89.

Çiner, A., Sarıkaya, M.A. and Yıldırım, C. (2017) 'Misleading old age on a young landform? The dilemma of cosmogenic inheritance in surface exposure dating: Moraines vs. rock glaciers', *Quaternary Geochronology*, 42, pp. 76-88.

Clapperton, C.M. (1979) 'Glaciation in Bolivia before 3.27 Myr', *Nature*, 277(5695), pp. 375-377.

Clapperton, C.M. (1987a) 'Glacial geomorphology, Quaternary glacial sequences and palaeoclimatic inferences in the Ecuadorian Andes', *International Geomorphology 1986*, pp. 843-870.

Clapperton, C.M. (1987b) 'Maximal extent of late Wisconsin glaciation in the Ecuadorian Andes', *Quaternary of South America and Antarctic Peninsula*, 5, pp. 165-179.

Clapperton, C.M. (1990) 'Glacial and volcanic geomorphology of the Chimborazo-Carihuairazo Massif, Ecuadorian Andes', *Transactions of the Royal Society of Edinburgh: Earth Sciences*, 81(2), pp. 91-116.

Clapperton, C.M. (1993) 'Late Cenozic Glacial History of the Andes Part III: The Last Glacial Maximum (Isotope Stage 2)', in *Quaternary Geology and Geomorphology of South America*. Oxford, UK: Elsevier, pp. 395–424.

Clapperton, C.M. (1998) 'Late Quaternary glacier fluctuations in the Andes: Testing the synchrony of global change', *Quaternary Proceedings*, 6, pp. 65-73.

Clapperton, C.M., Clayton, J.D., Benn, D.I., Marden, C.J. and Argollo, J.B. (1997a) 'Late Quaternary glacier advances and palaeolake highstands in the Bolivian Altiplano', *Quaternary International*, 38-39, pp. 49-59.

Clapperton, C.M., Hall, M., Mothes, P., Hole, M.J., Still, J.W., Helmens, K.F., Kuhry, P. and Gemmell, A.M.D. (1997b) 'A Younger Dryas Icecap in the Equatorial Andes', *Quaternary Research*, 47(1), pp. 13-28.

Clapperton, C.M. and McEwan, C. (1985) 'Late Quaternary moraines in the Chimborazo area, Ecuador.', *Arctic and Alpine Research*, 17(2), pp. 135-142.

Clement, A.C. and Cane, M. (1999) 'A role for the tropical Pacific coupled ocean-atmosphere system on Milankovitch and millennial timescales. Part I: A modeling study of tropical Pacific variability', *Geophysical monograph series*, 112, pp. 363-371.

CLIMAP project (1976) 'The Surface of the Ice-Age Earth', *Science*, 191(4232), pp. 1131-1137.

Cockburn, H.A.P. and Summerfield, M.A. (2004) 'Geomorphological applications of cosmogenic isotope analysis', *Progress in Physical Geography: Earth and Environment*, 28(1), pp. 1-42.

Cook, C.P., Hemming, S.R., van de Flierdt, T., Pierce Davis, E.L., Williams, T., Galindo, A.L., Jiménez-Espejo, F.J. and Escutia, C. (2017) 'Glacial erosion of East Antarctica in the Pliocene: A comparative study of multiple marine sediment provenance tracers', *Chemical Geology*, 466, pp. 199-218.

Cook, S.J. and Swift, D.A. (2012) 'Subglacial basins: Their origin and importance in glacial systems and landscapes', *Earth-Science Reviews*, 115(4), pp. 332-372.

Cook, S.J., Swift, D.A., Kirkbride, M.P., Knight, P.G. and Waller, R.I. (2020) 'The empirical basis for modelling glacial erosion rates', *Nature Communications*, 11(1), p. 759.

Crowley, T.J. (2000) 'CLIMAP SSTs re-revisited', *Climate Dynamics*, 16(4), pp. 241-255.

Cuffey, K.M., Conway, H., Gades, A.M., Hallet, B., Lorrain, R., Severinghaus, J.P., Steig, E.J., Vaughn, B. and White, J.W.C. (2000) 'Entrainment at cold glacier beds', *Geology*, 28(4), pp. 351-354.

Cuffey, K.M. and Paterson, W.S.B. (2010) *The Physics of Glaciers*. Fourth edn. Amsterdam: Academic Press.

Dahl-Jensen, D. and Gunderstrup, N. (1987) 'Constitutive properties of ice at Dye 3, Greenland', *International Association of Hydrological Sciences Publication*. Vancouver, 1987. pp. 31–43.

Davies, B. (2020) *Cosmogenic nuclide dating*. Available at: http://www.antarcticglaciers.org/glacial-geology/dating-glacial-sediments-2/cosmogenic_nuclide_datin/ (Accessed: 10/12/2020).

De Angelis, H. (2014) 'Hypsometry and sensitivity of the mass balance to changes in equilibrium-line altitude: the case of the Southern Patagonia Icefield', *Journal of Glaciology*, 60(219), pp. 14-28.

Deplazes, G., Lückge, A., Peterson, L.C., Timmermann, A., Hamann, Y., Hughen, K.A., Röhl, U., Laj, C., Cane, M.A., Sigman, D.M. and Haug, G.H. (2013) 'Links between tropical rainfall and North Atlantic climate during the last glacial period', *Nature Geoscience*, 6(3), pp. 213-217.

Desilets, D. and Zreda, M. (2003) 'Spatial and temporal distribution of secondary cosmic-ray nucleon intensities and applications to in situ cosmogenic dating', *Earth and Planetary Science Letters*, 206(1), pp. 21-42.

Dirszowsky, R.W., Mahaney, W.C., Hodder, K.R., Milner, M.W., Kalm, V., Bezada, M. and Beukens, R.P. (2005) 'Lithostratigraphy of the Mérida (Wisconsinan) glaciation and Pedregal interstade, Mérida Andes, northwestern Venezuela', *Journal of South American Earth Sciences*, 19(4), pp. 525-536.

Doughty, A.M., Kelly, M.A., Russell, J.M., Jackson, M.S., Anderson, B.M., Chipman, J. and Nakileza, B.R. (2023) 'Last Glacial Maximum Reconstructions of Rwenzori Mountain Glaciers', *Paleoceanography and Paleoclimatology*, 38(1), p. e2022PA004527.

Dunai, T.J. (2010) *Cosmogenic Nuclides: Principles, Concepts and Applications in the Earth Surface Sciences*. Cambridge: Cambridge University Press.

Echelmeyer, K. and Zhongxiang, W. (1987) 'Direct Observation of Basal Sliding and Deformation of Basal Drift at Sub-Freezing Temperatures', *Journal of Glaciology*, 33(113), pp. 83-98.

Edwards, B.R., Enderlin, E.M., Kochtitzky, W.H., Marino, J. and Marinque, N. (2018) 'Improved estimates of glacier change rates at Nevado Coropuna Ice Cap, Peru', *Journal of Glaciology*, 64(244), pp. 175-184.

Egholm, D.L., Nielsen, S.B., Pedersen, V.K. and Lesemann, J.E. (2009) 'Glacial effects limiting mountain height', *Nature*, 460(7257), pp. 884-887.

Ely, J.C., Clark, C.D., Hindmarsh, R.C.A., Hughes, A.L.C., Greenwood, S.L., Bradley, S.L., Gasson, E., Gregoire, L., Gandy, N., Stokes, C.R. and Small, D. (2019) 'Recent progress on combining geomorphological and geochronological data with ice sheet modelling,

demonstrated using the last British–Irish Ice Sheet', *Journal of Quaternary Science*, n/a(n/a).

Emmer, A., Le Roy, M., Sattar, A., Veettil, B.K., Alcalá-Reygosa, J., Campos, N., Malecki, J. and Cochachin, A. (2021) 'Glacier retreat and associated processes since the Last Glacial Maximum in the Lejiamayu valley, Peruvian Andes', *Journal of South American Earth Sciences*, 109, p. 103254.

Esper Angillieri, M.Y. (2013) 'Geomorphological of a portion of the Andes and Pre-Andes of San Juan, Argentina', *Journal of Maps*, 9(3), pp. 353-360.

Espinoza, J.C., Garreaud, R., Poveda, G., Arias, P.A., Molina-Carpio, J., Masiokas, M., Viale, M. and Scaff, L. (2020) 'Hydroclimate of the Andes Part I: Main Climatic Features', *Frontiers in Earth Science*, 8(64).

Evans, I.S. (1977) 'World-Wide Variations in the Direction and Concentration of Cirque and Glacier Aspects', *Geografiska Annaler: Series A, Physical Geography*, 59(3-4), pp. 151-175.

Evans, I.S. (2021) 'Glaciers, rock avalanches and the 'buzzsaw' in cirque development: Why mountain cirques are of mainly glacial origin', *Earth Surface Processes and Landforms*, 46(1), pp. 24-46.

Evans, I.S. and Cox, N. (1974) 'Geomorphometry and the Operational Definition of Cirques', *Area*, 6(2), pp. 150-153.

Evans, I.S. and Cox, N.J. (2005) 'Global variations of local asymmetry in glacier altitude: separation of north–south and east–west components', *Journal of Glaciology*, 51(174), pp. 469-482.

Evans, I.S. and Cox, N.J. (2010) 'Climatogenic north–south asymmetry of local glaciers in Spitsbergen and other parts of the Arctic', *Annals of Glaciology*, 51(55), pp. 16-22.

Farber, D.L., Hancock, G.S., Finkel, R.C. and Rodbell, D.T. (2005) 'The age and extent of tropical alpine glaciation in the Cordillera Blanca, Peru', *Journal of Quaternary Science*, 20(7-8), pp. 759-776.

Favier, V., Wagnon, P. and Ribstein, P. (2004) 'Glaciers of the outer and inner tropics: A different behaviour but a common response to climatic forcing', *Geophysical Research Letters*, 31(16).

Fernández, A. and Mark, B.G. (2016) 'Modeling modern glacier response to climate changes along the Andes Cordillera: A multiscale review', *Journal of Advances in Modeling Earth Systems*, 8(1), pp. 467-495.

Fick, S.E. and Hijmans, R.J. (2017) 'WorldClim 2: new 1-km spatial resolution climate surfaces for global land areas', *International Journal of Climatology*, 37(12), pp. 4302-4315.

Fogwill, C.J., Turney, C.S.M., Hutchinson, D.K., Taschetto, A.S. and England, M.H. (2015) 'Obliquity Control On Southern Hemisphere Climate During The Last Glacial', *Scientific Reports*, 5(1), p. 11673.

Francou, B. (2004) 'Andes del Ecuador: los glaciares en la epoca de los viajeros (siglos XVIII a XX)', in Deler, J.P. and Mesclier, E. (eds.) *Los Andes el reto del espacio mundo andino homenaje a Olivier Dollfus*. Lima: IFEA-IEP, pp. 137-152.

Francou, B. and Pizarro, L. (1985) 'El Niño y la sequia en los altos andes centrales:(Peru y Bolivia)', *Bulletin de l'Institut francais d'études Andins*, XIV.

Francou, B., Vuille, M., Favier, V. and Cáceres, B. (2004) 'New evidence for an ENSO impact on low-latitude glaciers: Antizana 15, Andes of Ecuador, 0°28′S', *Journal of Geophysical Research: Atmospheres*, 109(D18).

Fritz, S.C., Baker, P.A., Lowenstein, T.K., Seltzer, G.O., Rigsby, C.A., Dwyer, G.S., Tapia, P.M., Arnold, K.K., Ku, T.-L. and Luo, S. (2004) 'Hydrologic variation during the last 170,000 years in the southern hemisphere tropics of South America', *Quaternary Research*, 61(1), pp. 95-104.

Fu, P., Stroeven, A.P., Harbor, J.M., Heyman, J., Hättestrand, C. and Caffee, M.W. (2019) 'Ice cap erosion patterns from bedrock 10Be and 26Al, southeastern Tibetan Plateau', *Earth Surface Processes and Landforms*, 44(4), pp. 918-932.

Fujita, K., Ohta, T. and Ageta, Y. (2007) 'Characteristics and climatic sensitivities of runoff from a cold-type glacier on the Tibetan Plateau', *Hydrological Processes*, 21(21), pp. 2882-2891.

Fyffe, C.L., Potter, E., Fugger, S., Orr, A., Fatichi, S., Loarte, E., Medina, K., Hellström, R.Å., Bernat, M., Aubry-Wake, C., Gurgiser, W., Perry, L.B., Suarez, W., Quincey, D.J. and Pellicciotti, F. (2021) 'The Energy and Mass Balance of Peruvian Glaciers', *Journal of Geophysical Research: Atmospheres*, 126(23), p. e2021JD034911.

Gagliardini, O., Zwinger, T., Gillet-Chaulet, F., Durand, G., Favier, L., de Fleurian, B., Greve, R., Malinen, M., Martín, C., Råback, P., Ruokolainen, J., Sacchettini, M., Schäfer, M., Seddik, H. and Thies, J. (2013) 'Capabilities and performance of Elmer/Ice, a new-generation ice sheet model', *Geosci. Model Dev.*, 6(4), pp. 1299-1318.

Gantayat, P. and Ramsankaran, R. (2023) 'Modelling evolution of a large, glacier-fed lake in the Western Indian Himalaya', *Scientific Reports*, 13(1), p. 1840.

Gardner, A.S., Moholdt, G., Wouters, B., Wolken, G.J., Burgess, D.O., Sharp, M.J., Cogley, J.G., Braun, C. and Labine, C. (2011) 'Sharply increased mass loss from glaciers and ice caps in the Canadian Arctic Archipelago', *Nature*, 473(7347), pp. 357-360.

Garreaud, R.D. (2009) 'The Andes climate and weather', *Advances in Geosciences*, 22, pp. 3-11.

Garreaud, R.D. and Aceituno, P. (2001) 'Interannual rainfall variability over the South American Altiplano', *Journal of Climate*, 14(12), pp. 2779-2789.

Garreaud, R.D., Molina, A. and Farias, M. (2010) 'Andean uplift, ocean cooling and Atacama hyperaridity: A climate modeling perspective', *Earth and Planetary Science Letters*, 292(1), pp. 39-50.

Garreaud, R.D., Vuille, M. and Clement, A.C. (2003) 'The climate of the Altiplano: Observed current conditions and mechanisms of past changes', *Palaeogeography, Palaeoclimatology, Palaeoecology*, 194(1-3), pp. 5-22.

Gilbert, A., Flowers, G.E., Miller, G.H., Rabus, B.T., Van Wychen, W., Gardner, A.S. and Copland, L. (2016) 'Sensitivity of Barnes Ice Cap, Baffin Island, Canada, to climate state and internal dynamics', *Journal of Geophysical Research: Earth Surface*, 121(8), pp. 1516-1539.

Gilbert, A., Gagliardini, O., Vincent, C. and Wagnon, P. (2014) 'A 3-D thermal regime model suitable for cold accumulation zones of polythermal mountain glaciers', *Journal of Geophysical Research: Earth Surface*, 119(9), pp. 1876-1893.

Gilbert, A., Sinisalo, A., Gurung, T.R., Fujita, K., Maharjan, S.B., Sherpa, T.C. and Fukuda, T. (2020) 'The influence of water percolation through crevasses on the thermal regime of a Himalayan mountain glacier', *The Cryosphere*, 14(4), pp. 1273-1288.

Gillespie, A. and Molnar, P. (1995) 'Asynchronous maximum advances of mountain and continental glaciers', *Reviews of Geophysics*, 33(3), pp. 311-364.

Glasser, N.F., Clemmens, S., Schnabel, C., Fenton, C.R. and McHargue, L. (2009) 'Tropical glacier fluctuations in the Cordillera Blanca, Peru between 12.5 and 7.6ka from cosmogenic ^{10}Be dating', *Quaternary Science Reviews*, 28(27), pp. 3448-3458.

Glasser, N.F., Jansson, K.N., Harrison, S. and Kleman, J. (2008) 'The glacial geomorphology and Pleistocene history of South America between 38°S and 56°S', *Quaternary Science Reviews*, 27(3-4), pp. 365-390.

Goelzer, H., Nowicki, S., Payne, A., Larour, E., Seroussi, H., Lipscomb, W.H., Gregory, J., Abe-Ouchi, A., Shepherd, A., Simon, E., Agosta, C., Alexander, P., Aschwanden, A., Barthel, A., Calov, R., Chambers, C., Choi, Y., Cuzzone, J., Dumas, C., Edwards, T., Felikson, D., Fettweis, X., Golledge, N.R., Greve, R., Humbert, A., Huybrechts, P., Le clec'h, S., Lee, V., Leguy, G., Little, C., Lowry, D.P., Morlighem, M., Nias, I., Quiquet, A., Rückamp, M., Schlegel, N.J., Slater, D.A., Smith, R.S., Straneo, F., Tarasov, L., van de Wal, R. and van den Broeke, M. (2020) 'The future sea-level contribution of the Greenland ice sheet: a multi-model ensemble study of ISMIP6', *The Cryosphere*, 14(9), pp. 3071-3096.

Golledge, N.R., Kowalewski, D.E., Naish, T.R., Levy, R.H., Fogwill, C.J. and Gasson, E.G.W. (2015) 'The multi-millennial Antarctic commitment to future sea-level rise', *Nature*, 526(7573), pp. 421-425.

Golledge, N.R., Mackintosh, A.N., Anderson, B.M., Buckley, K.M., Doughty, A.M., Barrell, D.J.A., Denton, G.H., Vandergoes, M.J., Andersen, B.G. and Schaefer, J.M. (2012) 'Last Glacial Maximum climate in New Zealand inferred from a modelled Southern Alps icefield', *Quaternary Science Reviews*, 46, pp. 30-45.

Gómez, J., Schobbenhaus, C. and Montes, N.E. (2019) *Geological Map of South America 2019*, Scale 1:5 000 000. Paris: (Commission for the Geological Map of the World (CGMW), Colombian Geological Survey, and Geological Survey of Brazil).

Goodman, A.Y. (1999) *Subdivision of Glacial Deposits in Southeastern Perú Based on Pedogenic Development and Radiometric Ages*. Syracuse University.

Goodman, A.Y., Rodbell, D.T., Seltzer, G.O. and Mark, B.G. (2001) 'Subdivision of Glacial Deposits in Southeastern Peru Based on Pedogenic Development and Radiometric Ages', *Quaternary Research*, 56(1), pp. 31-50.

Gosse, J.C. and Phillips, F.M. (2001) 'Terrestrial in situ cosmogenic nuclides: Theory and application', *Quaternary Science Reviews*, 20(14), pp. 1475-1560.

Gregory-Wodzicki, K.M. (2000) 'Uplift history of the Central and Northern Andes: A review', *GSA Bulletin*, 112(7), pp. 1091-1105.

Greve, R. (1997) 'A Continuum-Mechanical Formulation for Shallow Polythermal Ice Sheets', *Philosophical Transactions: Mathematical, Physical and Engineering Sciences*, 355(1726), pp. 921-974.

Greve, R. and Blatter, H. (2009) *Dynamics of Ice Sheets and Glaciers*. 1 edn. Springer-Verlag Berlin Heidelberg.

Guo, Q., Li, W., Yu, H. and Alvarez, O. (2010) 'Effects of Topographic Variability and Lidar Sampling Density on Several DEM Interpolation Methods', *Photogrammetric Engineering and Remote Sensing*, 76.

Häggi, C., Chiessi, C.M., Merkel, U., Mulitza, S., Prange, M., Schulz, M. and Schefuß, E. (2017) 'Response of the Amazon rainforest to late Pleistocene climate variability', *Earth and Planetary Science Letters*, 479, pp. 50-59.

Hall, S.R., Farber, D.L., Ramage, J.M., Rodbell, D.T., Finkel, R.C., Smith, J.A., Mark, B.G. and Kassel, C. (2009) 'Geochronology of Quaternary glaciations from the tropical Cordillera Huayhuash, Peru', *Quaternary Science Reviews*, 28(25), pp. 2991-3009.

Hallet, B., Hunter, L. and Bogen, J. (1996) 'Rates of erosion and sediment evacuation by glaciers: A review of field data and their implications', *Global and Planetary Change*, 12(1), pp. 213-235.

Hambrey, M.J. and Glasser, N.F. (2012) 'Discriminating glacier thermal and dynamic regimes in the sedimentary record', *Sedimentary Geology*, 251-252, pp. 1-33.

Hammond, J.C., Saavedra, F.A. and Kampf, S.K. (2018) 'Global snow zone maps and trends in snow persistence 2001–2016', *International Journal of Climatology*, 38(12), pp. 4369-4383.

Hanzer, F., Helfricht, K., Marke, T. and Strasser, U. (2016) 'Multilevel spatiotemporal validation of snow/ice mass balance and runoff modeling in glacierized catchments', *The Cryosphere*, 10(4), pp. 1859-1881.

Harris, I., Osborn, T.J., Jones, P. and Lister, D. (2020) 'Version 4 of the CRU TS monthly high-resolution gridded multivariate climate dataset', *Scientific Data*, 7(1), p. 109.

Hastenrath, S. (2002) 'The intertropical convergence zone of the eastern Pacific revisited', *International Journal of Climatology*, 22(3), pp. 347-356.

Hastenrath, S. (2009) 'Past glaciations in the tropics', *Quaternary Science Reviews*, 28, pp. 790-798.

Helmens, K.F. (1988) 'Late pleistocene glacial sequence in the area of the high plain of Bogotá (Eastern Cordillera, Colombia)', *Palaeogeography, Palaeoclimatology, Palaeoecology*, 67(3-4), pp. 263-283.

Helmens, K.F. (2011) 'Chapter 58 - Quaternary Glaciations of Colombia', in Ehlers, J., Gibbard, P.L. and Hughes, P.D. (eds.) *Developments in Quaternary Sciences*. Elsevier, pp. 815-834.

Helmens, K.F., Barendregt, R.W., Enkin, R.J., Baker, J. and Andriessen, P.A.M. (1997a) 'Magnetic Polarity and Fission-Track Chronology of a Late Pliocene–Pleistocene Paleoclimatic Proxy Record in the Tropical Andes', *Quaternary Research*, 48(1), pp. 15-28.

Helmens, K.F., Rutter, N.W. and Kuhry, P. (1997b) 'Glacier fluctuations in the Eastern Andes of Colombia (South America) during the last 45,000 radiocarbon years', *Quaternary International*, 38-39, pp. 39-48.

Herd, D.G. (1975) *Glacial and volcanic geology of the Ruiz-Tolima volcanic complex Cordillera Central, Colombia*. University of Washington.

Heusser, L.E. and Shackleton, N.J. (1994) 'Tropical Climatic Variation on the Pacific Slopes of the Ecuadorian Andes Based on a 25,000-Year Pollen Record from Deep-Sea Sediment Core Tri 163-31B', *Quaternary Research*, 42(2), pp. 222-225.

Hijmans, R.J., Cameron, S.E., Parra, J.L., Jones, P.G. and Jarvis, A. (2005) 'Very high resolution interpolated climate surfaces for global land areas', *International Journal of Climatology*, 25(15), pp. 1965-1978.

Hock, R. (2003) 'Temperature index melt modelling in mountain areas', *Journal of Hydrology*, 282(1), pp. 104-115.

Hou, A., Bahr, A., Schmidt, S., Strebl, C., Albuquerque, A.L., Chiessi, C.M. and Friedrich, O. (2020) 'Forcing of western tropical South Atlantic sea surface temperature across three glacial-interglacial cycles', *Global and Planetary Change*, 188, p. 103150.

Hubbard, A., Hein, A.S., Kaplan, M.R., Hulton, N.R.J. and Glasser, N. (2005) 'A modelling reconstruction of the Last Glacial Maximum ice sheet and its deglaciation in the vicinity of the Northern Patagonian Icefield, South America', *Geografiska Annaler: Series A, Physical Geography*, 87(2), pp. 375-391.

Hubbard, B. and Sharp, M. (1989) 'Basal ice formation and deformation: a review', *Progress in Physical Geography: Earth and Environment*, 13(4), pp. 529-558.

Hulton, N.R.J., Purves, R.S., McCulloch, R.D., Sugden, D.E. and Bentley, M.J. (2002) 'The Last Glacial Maximum and deglaciation in southern South America', *Quaternary Science Reviews*, 21(1), pp. 233-241.

Huss, M. and Fischer, M. (2016) 'Sensitivity of Very Small Glaciers in the Swiss Alps to Future Climate Change', *Frontiers in Earth Science*, 4.

Hutter, K. (1983) 'The Application of the Shallow-Ice Approximation', in *Theoretical Glaciology: Material Science of Ice and the Mechanics of Glaciers and Ice Sheets*. Dordrecht: Springer Netherlands, pp. 256-332.

Imhof, M.A. (2021) *Combined climate-ice flow modelling of the Alpine Ice Field during the Last Glacial Maximum*. ETH Zurich [Online]. Available at: https://www.research-collection.ethz.ch/bitstream/handle/20.500.11850/471073/doktor_thesis_imhof.pdf?sequence=2.

Imhof, M.A., Cohen, D., Seguinot, J., Aschwanden, A., Funk, M. and Jouvet, G. (2019) 'Modelling a paleo valley glacier network using a hybrid model: an assessment with a Stokes ice flow model', *Journal of Glaciology*, 65(254), pp. 1000-1010.

Iverson, N.R. (2012) 'A theory of glacial quarrying for landscape evolution models', *Geology*, 40(8), pp. 679-682.

Ivy-Ochs, S. and Briner, J.P. (2014) 'Dating disappearing ice with cosmogenic nuclides', *Elements*, 10(5), pp. 351-356.

Ivy-Ochs, S. and Schaller, M. (2009) 'Chapter 6 Examining Processes and Rates of Landscape Change with Cosmogenic Radionuclides', in Froehlich, K. (ed.) *Radioactivity in the Environment*. Elsevier, pp. 231-294.

Jiang, X., Wang, N., He, J., Wu, X. and Song, G. (2010) 'A distributed surface energy and mass balance model and its application to a mountain glacier in China', *Chinese Science Bulletin*, 55(20), pp. 2079-2087.

Jóhannesson, T., Sigurdsson, O., Laumann, T. and Kennett, M. (1995) 'Degree-day glacier mass-balance modelling with applications to glaciers in Iceland, Norway and Greenland', *Journal of Glaciology*, 41(138), pp. 345-358.

Jomelli, V., Grancher, D., Brunstein, D. and Solomina, O. (2008) 'Recalibration of the yellow Rhizocarpon growth curve in the Cordillera Blanca (Peru) and implications for LIA chronology', *Geomorphology*, 93(3-4), pp. 201-212.

Jouvet, G., Cohen, D., Russo, E., Buzan, J., Raible, C.C., Haeberli, W., Kamleitner, S., Ivy-Ochs, S., Imhof, M.A., Becker, J.K., Landgraf, A. and Fischer, U.H. (2023) 'Coupled climate-glacier modelling of the last glaciation in the Alps', *Journal of Glaciology*, pp. 1-15.

Jouzel, J., Masson-Delmotte, V., Cattani, O., Dreyfus, G., Falourd, S., Hoffmann, G., Minster, B., Nouet, J., Barnola, J.M., Chappellaz, J., Fischer, H., Gallet, J.C., Johnsen, S., Leuenberger, M., Loulergue, L., Luethi, D., Oerter, H., Parrenin, F., Raisbeck, G., Raynaud, D., Schilt, A., Schwander, J., Selmo, E., Souchez, R., Spahni, R., Stauffer, B., Steffensen, J.P., Stenni, B., Stocker, T.F., Tison, J.L., Werner, M. and Wolff, E.W. (2007) 'Orbital and Millennial Antarctic Climate Variability over the Past 800,000 Years', *Science*, 317(5839), pp. 793-796.

Jull, A.J.T. (2013) 'Dating Techniques', in *Encyclopedia of Quaternary Science: Second Edition*. pp. 447-452.

Jull, A.J.T. (2018) 'Chapter 19 - Geochronology Applied to Glacial Environments', in Menzies, J. and van der Meer, J.J.M. (eds.) *Past Glacial Environments (Second Edition)*. Elsevier, pp. 665-687.

Kageyama, M., Blard, P.-H., Bourdin, S., Charreau, J., Kluft, L., Leduc, G. and Legrain, E. (2022) 'Last Glacial Maximum atmospheric lapse rates: a model-data study on the American Cordillera case', May 01, 2022. pp. EGU22-11955. Available at: https://ui.adsabs.harvard.edu/abs/2022EGUGA..2411955K.

Kaser, G. (1999) 'A review of the modern fluctuations of tropical glaciers', *Global and Planetary Change*, 22(1-4), pp. 93-103.

Kaser, G. (2001) 'Glacier-climate interaction at low latitudes', *Journal of Glaciology*, 47(157), pp. 195-204.

Kaser, G. and Georges, C. (1999) 'On the Mass Balance of Low Latitude Glaciers with Particular Consideration of the Peruvian Cordillera Blanca', *Geografiska Annaler. Series A, Physical Geography*, 81(4), pp. 643-651.

Kaser, G. and Osmaston, H. (2002) *Tropical glaciers*. New York: Cambridge University Press.

Kazmierczak, E., Gregov, T., Coulon, V. and Pattyn, F. (2024) 'A fast and unified subglacial hydrological model applied to Thwaites Glacier, Antarctica', *EGUsphere*, 2024, pp. 1-36.

Kelly, M.A., Lowell, T.V., Applegate, P.J., Phillips, F.M., Schaefer, J.M., Smith, C.A., Kim, H., Leonard, K.C. and Hudson, A.M. (2015) 'A locally calibrated, late glacial ^{10}Be production rate from a low-latitude, high-altitude site in the Peruvian Andes', *Quaternary Geochronology*, 26, pp. 70-85.

Kiefer, J. and Karamperidou, C. (2019) 'High-Resolution Modeling of ENSO-Induced Precipitation in the Tropical Andes: Implications for Proxy Interpretation', *Paleoceanography and Paleoclimatology*, 34(2), pp. 217-236.

Kingslake, J., Scherer, R.P., Albrecht, T., Coenen, J., Powell, R.D., Reese, R., Stansell, N.D., Tulaczyk, S., Wearing, M.G. and Whitehouse, P.L. (2018) 'Extensive retreat and re-advance of the West Antarctic Ice Sheet during the Holocene', *Nature*, 558(7710), pp. 430-434.

Kinnard, C., Larouche, O., Demuth, M.N. and Menounos, B. (2022) 'Modelling glacier mass balance and climate sensitivity in the context of sparse observations: application to Saskatchewan Glacier, western Canada', *The Cryosphere*, 16(8), pp. 3071-3099.

Kirchner, N., Hutter, K., Jakobsson, M. and Gyllencreutz, R. (2011) 'Capabilities and limitations of numerical ice sheet models: a discussion for Earth-scientists and modelers', *Quaternary Science Reviews*, 30(25), pp. 3691-3704.

Kirkbride, M.P. (1995) 'Relationships between temperature and ablation on the Tasman Glacier, Mount Cook National Park, New Zealand', *New Zealand Journal of Geology and Geophysics*, 38(1), pp. 17-27.

Kirkbride, M.P. and Winkler, S. (2012) 'Correlation of Late Quaternary moraines: impact of climate variability, glacier response, and chronological resolution', *Quaternary Science Reviews*, 46, pp. 1-29.

Klein, A.G., Seltzer, G.O. and Isacks, B.L. (1999) 'Modern and last local glacial maximum snowlines in the Central Andes of Peru, Bolivia, and Northern Chile', *Quaternary Science Reviews*, 18(1), pp. 63-84.

Koldtoft, I., Grinsted, A., Vinther, B.M. and Hvidberg, C.S. (2021) 'Ice thickness and volume of the Renland Ice Cap, East Greenland', *Journal of Glaciology*, 67(264), pp. 714-726.

Koppes, M., Conway, H., Rasmussen, L.A. and Chernos, M. (2011) 'Deriving mass balance and calving variations from reanalysis data and sparse observations, Glaciar San Rafael, northern Patagonia, 1950–2005', *The Cryosphere*, 5(3), pp. 791-808.

Kos, A., Amann, F., Strozzi, T., Osten, J., Wellmann, F., Jalali, M. and Dufresne, A. (2021) 'The Surface Velocity Response of a Tropical Glacier to Intra and Inter Annual Forcing, Cordillera Blanca, Peru', *Remote Sensing*, 13(14), p. 2694.

Köse, O., Sarıkaya, M.A., Çiner, A., Candaş, A., Yıldırım, C. and Wilcken, K.M. (2022) 'Reconstruction of Last Glacial Maximum glaciers and palaeoclimate in the central Taurus Range, Mt. Karanfil, of the Eastern Mediterranean', *Quaternary Science Reviews*, 291, p. 107656.

Kull, C., Imhof, S., Grosjean, M., Zech, R. and Veit, H. (2008) 'Late Pleistocene glaciation in the Central Andes: Temperature versus humidity control - A case study from the eastern Bolivian Andes (17°S) and regional synthesis', *Global and Planetary Change*, 60(1-2), pp. 148-164.

Kumar, S., Vidal, Y.-S., Moya-Álvarez, A.S. and Martínez-Castro, D. (2019) 'Effect of the surface wind flow and topography on precipitating cloud systems over the Andes and associated Amazon basin: GPM observations', *Atmospheric Research*, 225, pp. 193-208.

Laha, S., Kumari, R., Singh, S., Mishra, A., Sharma, T., Banerjee, A., Nainwal, H.C. and Shankar, R. (2017) 'Evaluating the contribution of avalanching to the mass balance of Himalayan glaciers', *Annals of Glaciology*, 58(75pt2), pp. 110-118.

Lai, J. and Anders, A.M. (2021) 'Climatic controls on mountain glacier basal thermal regimes dictate spatial patterns of glacial erosion', *Earth Surf. Dynam.*, 9(4), pp. 845-859.

Lal, D. (1991) 'Cosmic ray labeling of erosion surfaces: in situ nuclide production rates and erosion models', *Earth and Planetary Science Letters*, 104(2-4), pp. 424-439.

Lea, D.W., Pak, D.K., Peterson, L.C. and Hughen, K.A. (2003) 'Synchroneity of Tropical and High-Latitude Atlantic Temperatures over the Last Glacial Termination', *Science*, 301(5638), pp. 1361-1364.

Lea, D.W., Pak, D.K. and Spero, H.J. (2000) 'Climate Impact of Late Quaternary Equatorial Pacific Sea Surface Temperature Variations', *Science*, 289(5485), pp. 1719-1724.

Lee, E., Carrivick, J.L., Quincey, D.J., Cook, S.J., James, W.H.M. and Brown, L.E. (2021a) 'Accelerated mass loss of Himalayan glaciers since the Little Ice Age', *Scientific Reports*, 11(1), p. 24284.

Lee, E., Ross, N., Henderson, A.C.G., Russell, A.J., Jamieson, S.S.R. and Fabel, D. (2022) 'Palaeoglaciation in the Low Latitude, Low Elevation Tropical Andes, Northern Peru', *Frontiers in Earth Science*, 10.

Lee, K.E., Clemens, S.C., Kubota, Y., Timmermann, A., Holbourn, A., Yeh, S.-W., Bae, S.W. and Ko, T.W. (2021b) 'Roles of insolation forcing and CO2 forcing on Late Pleistocene seasonal sea surface temperatures', *Nature Communications*, 12(1), p. 5742.

Leger, T., Hein, A., Goldberg, D. and Fabel, D. (2022) 'Late-glacial to Neoglacial evolution of glacier extent and surface mass balance in the Cordillera Blanca, Peruvian Andes', *EGU General Assembly 2022*. Vienna, Austria, 23–27 May 2022.

Licciardi, J.M., Schaefer, J.M., Taggart, J.R. and Lund, D.C. (2009) 'Holocene Glacier Fluctuations in the Peruvian Andes Indicate Northern Climate Linkages', *Science*, 325(5948), pp. 1677-1679.

Lila, F.D.H.P., Joshua, T.M.G.V., Solorzano, A.C.C. and Mott, G.M.G.C. (2016) *Paisaje Cultural "Complejo de Lagunas las Huaringas"*. Magraf E.I.R.L., Peru: Ministro de Cultura.

Loomis, S.E., Russell, J.M., Verschuren, D., Morrill, C., De Cort, G., Sinninghe Damsté, J.S., Olago, D., Eggermont, H., Street-Perrott, F.A. and Kelly, M.A. (2017) 'The tropical lapse rate steepened during the Last Glacial Maximum', *Science Advances*, 3(1), p. e1600815.

Lovell, A.M., Carr, J.R. and Stokes, C.R. (2019) 'Spatially Variable Glacier Changes in the Annapurna Conservation Area, Nepal, 2000 to 2016', *Remote Sensing*, 11(12), p. 1452.

Lozano Gacha, M.F. and Koch, M. (2021) 'Distributed Energy Balance Flux Modelling of Mass Balances in the Artesonraju Glacier and Discharge in the Basin of Artesoncocha, Cordillera Blanca, Peru', *Climate*, 9(9), p. 143.

Lukas, S. and Bradwell, T. (2010) 'Reconstruction of a Lateglacial (Younger Dryas) mountain ice field in Sutherland, northwestern Scotland, and its palaeoclimatic implications', *Journal of Quaternary Science*, 25(4), pp. 567-580.

Luo, X. and Lin, T. (2022) 'A Semi-Empirical Framework for ice sheet response analysis under Oceanic forcing in Antarctica and Greenland', *Climate Dynamics*.

Lüthi, D., Le Floch, M., Bereiter, B., Blunier, T., Barnola, J.-M., Siegenthaler, U., Raynaud, D., Jouzel, J., Fischer, H., Kawamura, K. and Stocker, T.F. (2008) 'High-resolution carbon dioxide concentration record 650,000–800,000 years before present', *Nature*, 453(7193), pp. 379-382.

Ma, Y., Gagliardini, O., Ritz, C., Gillet-Chaulet, F., Durand, G. and Montagnat, M. (2010) 'Enhancement factors for grounded ice and ice shelves inferred from an anisotropic ice-flow model', *Journal of Glaciology*, 56(199), pp. 805-812.

MacGregor, K.R., Anderson, R.S., Anderson, S.P. and Waddington, E.D. (2000) 'Numerical simulations of glacial-valley longitudinal profile evolution', *Geology*, 28(11), pp. 1031-1034.

Mahaney, W.C., Kalm, V., Menzies, J., Hancock, R.G.V. and Milner, M.W. (2010) 'Reconstruction of the pre-Merida glaciation, northwestern Venezuelan Andes', *Sedimentary Geology*, 230(1), pp. 10-20.

Maisincho, L., Favier, V., Wagnon, P., Jomelli, V., Basantes Serrano, R., Francou, B., Villacis, M., Rabatel, A., Ménégoz, M., Mourre, L. and Cáceres, B. (2016) 'Glacier surface mass balance modeling in the inner tropics using a positive degree-day approach', *The Cryosphere Discuss.*, 2016, pp. 1-52.

Małecki, J., Lovell, H., Ewertowski, W., Górski, Ł., Kurczaba, T., Latos, B., Miara, M., Piniarska, D., Płocieniczak, J., Sowada, T., Spiralski, M., Warczachowska, A. and Rabatel, A. (2018) 'The glacial landsystem of a tropical glacier: Charquini Sur, Bolivian Andes', *Earth Surface Processes and Landforms*, 43(12), pp. 2584-2602.

Malone, A.G.O., Pierrehumbert, R.T., Lowell, T.V., Kelly, M.A. and Stroup, J.S. (2015) 'Constraints on southern hemisphere tropical climate change during the Little Ice Age and Younger Dryas based on glacier modeling of the Quelccaya Ice Cap, Peru', *Quaternary Science Reviews*, 125, pp. 106-116.

Manley, G. (1961) 'The late-glacial climate of North-West England', *Geological Journal*, 2(2), pp. 188-215.

MARGO Project Members (2009) 'Constraints on the magnitude and patterns of ocean cooling at the Last Glacial Maximum', *Nature Geoscience*, 2(2), pp. 127-132.

Mark, B., Stansell, N. and Zeballos, G. (2017) 'The last deglaciation of Peru and Bolivia', *Cuadernos de Investigación Geográfica*, 43(2), pp. 591-628.

Mark, B.G., Harrison, S.P., Spessa, A., New, M., Evans, D.J.A. and Helmens, K.F. (2005) 'Tropical snowline changes at the last glacial maximum: A global assessment', *Quaternary International*, 138-139, pp. 168-201.

Mark, B.G. and Helmens, K.F. (2005) 'Reconstruction of glacier equilibrium-line altitudes for the Last Glacial Maximum on the High Plain of Bogotá, Eastern Cordillera, Colombia: climatic and topographic implications', *Journal of Quaternary Science*, 20(7-8), pp. 789-800.

Mark, B.G., Seltzer, G.O., Rodbell, D.T. and Goodman, A.Y. (2002) 'Rates of Deglaciation during the Last Glaciation and Holocene in the Cordillera Vilcanota-Quelccaya Ice Cap Region, southeastern Perú', *Quaternary Research*, 57(3), pp. 287-298.

Marshall, S.J. (2021) 'Regime shifts in glacier and ice sheet response to climate change: examples from the Northern Hemisphere', *Frontiers in Climate*, 3.

Martin, J., Davies, B.J., Jones, R. and Thorndycraft, V. (2022) 'Modelled sensitivity of Monte San Lorenzo ice cap, Patagonian Andes, to past and present climate', *Frontiers in Earth Science*, 10.

Martin, L.C.P., Blard, P.H., Lavé, J., Jomelli, V., Charreau, J., Condom, T., Lupker, M., Arnold, M., Aumaître, G., Bourlès, D.L. and Keddadouche, K. (2020) 'Antarctic-like temperature variations in the Tropical Andes recorded by glaciers and lakes during the last deglaciation', *Quaternary Science Reviews*, 247, p. 106542.

Martini, M.A., Kaplan, M.R., Strelin, J.A., Astini, R.A., Schaefer, J.M., Caffee, M.W. and Schwartz, R. (2017) 'Late Pleistocene glacial fluctuations in Cordillera Oriental, subtropical Andes', *Quaternary Science Reviews*, 171, pp. 245-259.

Matsuoka, K. and Naruse, R. (1999) 'Mass Balance Features Derived from a Firn Core at Hielo Patagónico Norte, South America', *Arctic, Antarctic, and Alpine Research*, 31(4), pp. 333-340.

Maussion, F., Butenko, A., Champollion, N., Dusch, M., Eis, J., Fourteau, K., Gregor, P., Jarosch, A.H., Landmann, J., Oesterle, F., Recinos, B., Rothenpieler, T., Vlug, A., Wild, C.T. and Marzeion, B. (2019) 'The Open Global Glacier Model (OGGM) v1.1', *Geosci. Model Dev.*, 12(3), pp. 909-931.

McDougall, D. (2013) 'Glaciation style and the geomorphological record: evidence for Younger Dryas glaciers in the eastern Lake District, northwest England', *Quaternary Science Reviews*, 73, pp. 48-58.

McDougall, D.A. (2001) 'The geomorphological impact of Loch Lomond (Younger Dryas) Stadial plateau icefields in the central Lake District, northwest England', *Journal of Quaternary Science*, 16(6), pp. 531-543.

Mercer, J.H. and Palacios, O., M. (1977) 'Radiocarbon dating of the last glaciation in Peru', *Geology*, 5(10), pp. 600-604.

Miles, K.E., Hubbard, B., Quincey, D.J., Miles, E.S., Sherpa, T.C., Rowan, A.V. and Doyle, S.H. (2018) 'Polythermal structure of a Himalayan debris-covered glacier revealed by borehole thermometry', *Scientific Reports*, 8(1), p. 16825.

Mitchell, S.G. and Humphries, E.E. (2015) 'Glacial cirques and the relationship between equilibrium line altitudes and mountain range height', *Geology*, 43(1), pp. 35-38.

Molina, E.P. (2020) 'Iniciación de un monitoreo del balance de masa en el glaciar Suyuparina, Cordillera Vilcanota, Perú', *Cambio Climático en los Andes Tropicales*, 2(2).

Moreno, D., Alvarez-Solas, J., Blasco, J., Montoya, M. and Robinson, A. (2022) 'Simulating the Laurentide ice sheet of the Last Glacial Maximum', *The Cryosphere Discuss.*, 2022, pp. 1-23.

Mourguiart, P. and Ledru, M.-P. (2003) 'Last Glacial Maximum in an Andean cloud forest environment (Eastern Cordillera, Bolivia)', *Geology*, 31(3), pp. 195-198.

Müller, P.J., Kirst, G., Ruhland, G., von Storch, I. and Rosell-Melé, A. (1998) 'Calibration of the alkenone paleotemperature index U37K′ based on core-tops from the eastern South Atlantic and the global ocean (60°N-60°S)', *Geochimica et Cosmochimica Acta*, 62(10), pp. 1757-1772.

Muller, V.A.P., Sternai, P. and Sue, C. (2024) 'Fast uplift in the southern Patagonian Andes due to long- and short-term deglaciation and the asthenospheric window underneath', *Solid Earth*, 15(4), pp. 387-404.

Muñoz, R., Huggel, C., Frey, H., Cochachin, A. and Haeberli, W. (2020) 'Glacial lake depth and volume estimation based on a large bathymetric dataset from the Cordillera Blanca, Peru', *Earth Surface Processes and Landforms*, 45(7), pp. 1510-1527.

Naruse, R., Skvarca, P. and Takeuchi, Y. (1997) 'Thinning and retreat of Glaciar Upsala, and an estimate of annual ablation changes in southern Patagonia', *Annals of Glaciology*, 24, pp. 38-42.

NASA JPL (2013) 'NASA Shuttle Radar Topography Mission Global 1 arc second [Dataset]' *NASA EOSDIS Land Processes DAAC*. Available at: https://doi.org/10.5067/MEaSUREs/SRTM/SRTMGL1.003 (Accessed: 2019-11-27).

Ng, F.S.L., Barr, I.D. and Clark, C.D. (2010) 'Using the surface profiles of modern ice masses to inform palaeo-glacier reconstructions', *Quaternary Science Reviews*, 29(23), pp. 3240-3255.

Noble, T.L., Rohling, E.J., Aitken, A.R.A., Bostock, H.C., Chase, Z., Gomez, N., Jong, L.M., King, M.A., Mackintosh, A.N., McCormack, F.S., McKay, R.M., Menviel, L., Phipps, S.J., Weber, M.E., Fogwill, C.J., Gayen, B., Golledge, N.R., Gwyther, D.E., Hogg, A.M., Martos, Y.M., Pena-Molino, B., Roberts, J., van de Flierdt, T. and Williams, T. (2020) 'The Sensitivity of the Antarctic Ice Sheet to a Changing Climate: Past, Present, and Future', *Reviews of Geophysics*, 58(4), p. e2019RG000663.

Novello, V.F., Cruz, F.W., McGlue, M.M., Wong, C.I., Ward, B.M., Vuille, M., Santos, R.A., Jaqueto, P., Pessenda, L.C.R., Atorre, T., Ribeiro, L.M.A.L., Karmann, I., Barreto, E.S.,

Cheng, H., Edwards, R.L., Paula, M.S. and Scholz, D. (2019) 'Vegetation and environmental changes in tropical South America from the last glacial to the Holocene documented by multiple cave sediment proxies', *Earth and Planetary Science Letters*, 524, p. 115717.

Novello, V.F., Cruz, F.W., Vuille, M., Stríkis, N.M., Edwards, R.L., Cheng, H., Emerick, S., de Paula, M.S., Li, X., Barreto, E.d.S., Karmann, I. and Santos, R.V. (2017) 'A high-resolution history of the South American Monsoon from Last Glacial Maximum to the Holocene', *Scientific Reports*, 7(1), p. 44267.

Nunnery, J.A., Fritz, S.C., Baker, P.A. and Salenbien, W. (2019) 'Lake-level variability in Salar de Coipasa, Bolivia during the past ~40,000 yr', *Quaternary Research*, 91(2), pp. 881-891.

Oien, R.P., Barr, I.D., Spagnolo, M., Bingham, R.G., Rea, B.R. and Jansen, J. (2022a) 'Controls on the altitude of Scandinavian cirques: What do they tell us about palaeoclimate?', *Palaeogeography, Palaeoclimatology, Palaeoecology*, 600, p. 111062.

Oien, R.P., Rea, B.R., Spagnolo, M., Barr, I.D. and Bingham, R.G. (2022b) 'Testing the area–altitude balance ratio (AABR) and accumulation–area ratio (AAR) methods of calculating glacier equilibrium-line altitudes', *Journal of Glaciology*, 68(268), pp. 357-368.

Oreskes, N., Shrader-Frechette, K. and Belitz, K. (1994) 'Verification, Validation, and Confirmation of Numerical Models in the Earth Sciences', *Science*, 263(5147), pp. 641-646.

Osman, M.B., Tierney, J.E., Zhu, J., Tardif, R., Hakim, G.J., King, J. and Poulsen, C.J. (2021) 'Globally resolved surface temperatures since the Last Glacial Maximum', *Nature*, 599(7884), pp. 239-244.

Østby, T.I., Schuler, T.V., Hagen, J.O., Hock, R. and Reijmer, C.H. (2013) 'Parameter uncertainty, refreezing and surface energy balance modelling at Austfonna ice cap, Svalbard, 2004-08', *Annals of Glaciology*, 54(63), pp. 229-240.

Otto, J.-C. and Smith, M.J. (2013) '2.6. Geomorphological mapping', in Cook, S.J., Clarke, L.E. and Nield, J.M. (eds.) *Geomorphological Techniques (Online Edition)*. London, UK: British Society for Geomorphology.

Palacios, D., Stokes, C.R., Phillips, F.M., Clague, J.J., Alcalá-Reygosa, J., Andrés, N., Angel, I., Blard, P.-H., Briner, J.P., Hall, B.L., Dahms, D., Hein, A.S., Jomelli, V., Mark, B.G., Martini, M.A., Moreno, P., Riedel, J., Sagredo, E., Stansell, N.D., Vázquez-Selem, L., Vuille, M. and Ward, D.J. (2020) 'The deglaciation of the Americas during the Last Glacial Termination', *Earth-Science Reviews*, 203, p. 103113.

Pearce, D., Rea, B.R., Bradwell, T. and McDougall, D. (2014) 'Glacial geomorphology of the Tweedsmuir Hills, Central Southern Uplands, Scotland', *Journal of Maps*, 10(3), pp. 457-465.

Pearce, D.M., Ely, J.C., Barr, I.D. and Boston, C.M. (2017) '3.2.9 Glacier Reconstruction', in Cook, S.J., Clarke, L.E. and Nield, J.M. (eds.) *Geomorphological Techniques*. London, UK: British Society for Geomorphology.

Pellitero, R., Rea, B.R., Spagnolo, M., Bakke, J., Hughes, P., Ivy-Ochs, S., Lukas, S. and Ribolini, A. (2015) 'A GIS tool for automatic calculation of glacier equilibrium-line altitudes', *Computers & Geosciences*, 82, pp. 55-62.

Peterson, L.C. and Haug, G.H. (2006) 'Variability in the mean latitude of the Atlantic Intertropical Convergence Zone as recorded by riverine input of sediments to the Cariaco Basin (Venezuela)', *Palaeogeography, Palaeoclimatology, Palaeoecology*, 234(1), pp. 97-113.

Pettit, E.C., Thorsteinsson, T., Jacobson, H.P. and Waddington, E.D. (2007) 'The role of crystal fabric in flow near an ice divide', *Journal of Glaciology*, 53(181), pp. 277-288.

Pierrehumbert, R.T. (1995) 'Thermostats, Radiator Fins, and the Local Runaway Greenhouse', *Journal of the Atmospheric Sciences*, 52, pp. 1784-1806.

Placzek, C.J., Quade, J. and Patchett, P.J. (2013) 'A 130ka reconstruction of rainfall on the Bolivian Altiplano', *Earth and Planetary Science Letters*, 363, pp. 97-108.

Porter, S. (1977) 'The glacial ages: Late Cenozoic climatic variability on several time scales', *Man and nature-makers of climatic variation*, pp. 1-27.

Porter, S.C. (1981) 'Pleistocene glaciation in the southern Lake District of Chile', *Quaternary Research*, 16(3), pp. 263-292.

Porter, S.C. (1988) 'Landscapes of the last ice age in North America', *American Before Columbus: Ice-Age Origins, Ethnology Monographs. University of Pittsburgh, Pittsburgh*, p. 1.

Porter, S.C. (2001) 'Snowline depression in the tropics during the Last Glaciation', *Quaternary Science Reviews*, 20(10), pp. 1067-1091.

Prakash, A., Zhou, Q., Hattermann, T., Bao, W., Graversen, R. and Kirchner, N. (2022) 'A nested high-resolution unstructured grid 3-D ocean-sea ice-ice shelf setup for numerical investigations of the Petermann ice shelf and fjord', *MethodsX*, 9, p. 101668.

Pratt-Sitaula, B., Burbank, D.W., Heimsath, A.M., Humphrey, N.F., Oskin, M. and Putkonen, J. (2011) 'Topographic control of asynchronous glacial advances: A case study from Annapurna, Nepal', *Geophysical Research Letters*, 38(24).

Principato, S.M. and Lee, J.F. (2014) 'GIS analysis of cirques on Vestfirðir, northwest Iceland: implications for palaeoclimate', *Boreas*, 43(4), pp. 807-817.

Quesada-Román, A., Campos, N., Alcalá-Reygosa, J. and Granados-Bolaños, S. (2020) 'Equilibrium-line altitude and temperature reconstructions during the Last Glacial Maximum in Chirripó National Park, Costa Rica', *Journal of South American Earth Sciences*, 100, p. 102576.

Raasveldt, C.H. (1957) 'Las glaciaciones de la Sierra Nevada de Santa Marta', *Revista de la Academia Colombiana de Ciencias Exactas, Físicas y Naturales*, 41(Suplemento), p. 450.

Rabatel, A., Ceballos, J.L., Micheletti, N., Jordan, E., Braitmeier, M., González, J., Mölg, N., Ménégoz, M., Huggel, C. and Zemp, M. (2018) 'Toward an imminent extinction of Colombian glaciers?', *Geografiska Annaler: Series A, Physical Geography*, 100(1), pp. 75-95.

Rabatel, A., Francou, B., Jomelli, V., Naveau, P. and Grancher, D. (2008) 'A chronology of the Little Ice Age in the tropical Andes of Bolivia (16°S) and its implications for climate reconstruction', *Quaternary Research*, 70(2), pp. 198-212.

Rabatel, A., Francou, B., Soruco, A., Gomez, J., Cáceres, B., Ceballos, J.L., Basantes, R., Vuille, M., Sicart, J.-E., Huggel, C., Scheel, M., Lejeune, Y., Arnaud, Y., Collet, M., Condom, T., Consoli, G., Favier, V., Jomelli, V., Galarraga, R., Ginot, P., Maisincho, L., Mendoza, J., Ménégoz, M., Ramirez, E., Ribstein, P., Suarez, W., Villacis, M. and Wagnon, P. (2013a) 'Current state of glaciers in the tropical Andes: a multi-century perspective on glacier evolution and climate change', *The Cryosphere*, 7(1), pp. 81-102.

Rabatel, A., Letréguilly, A., Dedieu, J.P. and Eckert, N. (2013b) 'Changes in glacier equilibrium-line altitude in the western Alps from 1984 to 2010: evaluation by remote sensing and modeling of the morpho-topographic and climate controls', *The Cryosphere*, 7(5), pp. 1455-1471.

Ramage, J.M., Smith, J.A., Rodbell, D.T. and Seltzer, G.O. (2005) 'Comparing reconstructed Pleistocene equilibrium-line altitudes in the tropical Andes of central Peru', *Journal of Quaternary Science*, 20(7-8), pp. 777-788.

Ramírez, I.J. and Briones, F. (2017) 'Understanding the El Niño Costero of 2017: The Definition Problem and Challenges of Climate Forecasting and Disaster Responses', *International Journal of Disaster Risk Science*, 8(4), pp. 489-492.

Ramírez, N., Melfo, A., Resler, L.M. and Llambí, L.D. (2020) 'The end of the eternal snows: Integrative mapping of 100 years of glacier retreat in the Venezuelan Andes', *Arctic, Antarctic, and Alpine Research*, 52(1), pp. 563-581.

Ramirez, V.M., Cruz, F.W., Vuille, M., Novello, V.F., Stríkis, N.M., Cheng, H., Zhang, H.W., Bernal, J.P., Du, W.J., Ampuero, A., Deininger, M., Chiessi, C.M., Tejedor, E., Campos, J.L., Ait Brahim, Y. and Edwards, R.L. (2023) 'Summer insolation controlled movements of Intertropical Convergence Zone during last glacial cycle in northern South America', *Communications Earth & Environment*, 4(1), p. 495.

Rea, B., Whalley, W., Evens, D., Gordon, J. and McDougall, D. (1998) 'Plateau icefields: Geomorphology and dynamics', *Journal of Quaternary Science*, 13(6), pp. 35-54.

Rea, B.R. (2009) 'Defining modern day Area-Altitude Balance Ratios (AABRs) and their use in glacier-climate reconstructions', *Quaternary Science Reviews*, 28(3), pp. 237-248.

Reinardy, B.T.I., Booth, A.D., Hughes, A.L.C., Boston, C.M., Åkesson, H., Bakke, J., Nesje, A., Giesen, R.H. and Pearce, D.M. (2019) 'Pervasive cold ice within a temperate glacier – implications for glacier thermal regimes, sediment transport and foreland geomorphology', *The Cryosphere*, 13(3), pp. 827-843.

Retamal-Ramírez, F., Castillo, A., Bernales, J. and Rogozhina, I. (2022) 'Reconstruction of the Patagonian Ice Sheet during the Last Glacial Maximum using numerical modelling and geological constraints', *EGU General Assembly 2022*. Vienna, Austria, 23–27 May 2022.

Richardson, A., Carr, R. and Cook, S. (2024a) 'Investigating the past, present and future responses of Shallap and Zongo Glaciers, Tropical Andes, to the El Niño Southern Oscillation', *Journal of Glaciology*, pp. 1-21.

Richardson, A., Carr, R. and Cook, S. (2024b) 'Investigating the Past, Present and Future Responses of Shallap and Zongo Glaciers, Tropical Andes, to the El Niño Southern Oscillation', *Journal of Glaciology*, pp. 1-50.

Ritz, C. (1997) 'EISMINT Intercomparison Experiment: comparison of existing Greenland models.'. Available at: homepages.vub.ac.be/~phuybrec/ eismint/greenland.html.

Rivera, A. (2004) *Mass balance investigations at Glaciar Chico, Southern Patagonia Icefield, Chile*. University of Bristol.

Roberts, D.H., Ó Cofaigh, C., Ballantyne, C.K., Burke, M., Chiverrell, R.C., Evans, D.J.A., Clark, C.D., Duller, G.A.T., Ely, J., Fabel, D., Small, D., Smedley, R.K. and Callard, S.L. (2020) 'The deglaciation of the western sector of the Irish Ice Sheet from the inner continental shelf to its terrestrial margin', *Boreas*, 49(3), pp. 438-460.

Rodbell, D. (1992) 'Late Pleistocene equilibrium-line reconstructions in the northern Peruvian Andes', *Boreas*, 21(1), pp. 43-52.

Rodbell, D.T. (1993a) 'Subdivision of Late Pleistocene Moraines in the Cordillera Blanca, Peru, Based on Rock-Weathering Features, Soils, and Radiocarbon Dates', *Quaternary Research*, 39(2), pp. 133-143.

Rodbell, D.T. (1993b) 'The timing of the last deglaciation in Cordillera Oriental, northern Peru, based on glacial geology and lake sedimentology', *Geological Society of America Bulletin*, 105(7), pp. 923-934.

Rodbell, D.T., Bagnato, S., Nebolini, J.C., Seltzer, G.O. and Abbott, M.B. (2002) 'A Late Glacial–Holocene Tephrochronology for Glacial Lakes in Southern Ecuador', *Quaternary Research*, 57(3), pp. 343-354.

Rodbell, D.T., Hatfield, R.G., Abbott, M.B., Chen, C.Y., Woods, A., Stoner, J.S., McGee, D., Tapia, P.M., Bush, M., Valero-Garcés, B.L., Lehmann, S.B., Mark, S.Z., Weidhaas, N.C., Hillman, A.L., Larsen, D.J., Delgado, G., Katz, S.A., Solada, K.E., Morey, A.E., Finkenbinder, M., Valencia, B., Rozas-Davila, A., Wattrus, N., Colman, S.M., Bustamante, M.G., Kück, J. and Pierdominici, S. (2022) '700,000 years of tropical Andean glaciation', *Nature*, 607(7918), pp. 301-306.

Rodbell, D.T., Seltzer, G.O., Mark, B.G., Smith, J.A. and Abbott, M.B. (2008) 'Clastic sediment flux to tropical Andean lakes: records of glaciation and soil erosion', *Quaternary Science Reviews*, 27(15-16), pp. 1612-1626.

Rodbell, D.T., Smith, J.A. and Mark, B.G. (2009) 'Glaciation in the Andes during the Lateglacial and Holocene', *Quaternary Science Reviews*, 28(21-22), pp. 2165-2212.

Rodríguez-Zorro, P.A., Ledru, M.-P., Bard, E., Aquino-Alfonso, O., Camejo, A., Daniau, A.-L., Favier, C., Garcia, M., Mineli, T.D., Rostek, F., Ricardi-Branco, F., Sawakuchi, A.O., Simon, Q., Tachikawa, K. and Thouveny, N. (2020) 'Shut down of the South American summer monsoon during the penultimate glacial', *Scientific Reports*, 10(1), p. 6275.

Roe, G.H. and O'Neal, M.A. (2009) 'The response of glaciers to intrinsic climate variability: observations and models of late-Holocene variations in the Pacific Northwest', *Journal of Glaciology*, 55(193), pp. 839-854.

Santos-González, J., Redondo-Vega, J.M., González-Gutiérrez, R.B. and Gómez-Villar, A. (2013) 'Applying the AABR method to reconstruct equilibrium-line altitudes from the last glacial maximum in the Cantabrian Mountains (SW Europe)', *Palaeogeography, Palaeoclimatology, Palaeoecology*, 387, pp. 185-199.

Schilt, A., Baumgartner, M., Blunier, T., Schwander, J., Spahni, R., Fischer, H. and Stocker, T.F. (2010) 'Glacial–interglacial and millennial-scale variations in the atmospheric nitrous oxide concentration during the last 800,000 years', *Quaternary Science Reviews*, 29(1), pp. 182-192.

Schneider, C., Kilian, R. and Glaser, M. (2007) 'Energy balance in the ablation zone during the summer season at the Gran Campo Nevado Ice Cap in the Southern Andes', *Global and Planetary Change*, 59(1), pp. 175-188.

Schubert, C. (1974) 'Late Pleistocene Mérida Glaciation, Venezuelan Andes', *Boreas*, 3(4), pp. 147-151.

Schubert, C. and Clapperton, C.M. (1990) 'Quaternary Glaciations in the northern Andes (Venezuela, Colombia and Ecuador)', *Quaternary Science Reviews*, 9(2-3), pp. 123-135.

Seehaus, T., Malz, P., Sommer, C., Lippl, S., Cochachin, A. and Braun, M. (2019) 'Changes of the tropical glaciers throughout Peru between 2000 and 2016 – mass balance and area fluctuations', *The Cryosphere*, 13(10), pp. 2537-2556.

Seehaus, T., Malz, P., Sommer, C., Soruco, A., Rabatel, A. and Braun, M. (2020) 'Mass balance and area changes of glaciers in the Cordillera Real and Tres Cruces, Bolivia, between 2000 and 2016', *Journal of Glaciology*, 66(255), pp. 124-136.

Seguinot, J., Ivy-Ochs, S., Jouvet, G., Huss, M., Funk, M. and Preusser, F. (2018) 'Modelling last glacial cycle ice dynamics in the Alps', *The Cryosphere*, 12(10), pp. 3265-3285.

Seguinot, J., Rogozhina, I., Stroeven, A.P., Margold, M. and Kleman, J. (2016) 'Numerical simulations of the Cordilleran ice sheet through the last glacial cycle', *The Cryosphere*, 10(2), pp. 639-664.

Segura, H., Junquas, C., Espinoza, J.C., Vuille, M., Jauregui, Y.R., Rabatel, A., Condom, T. and Lebel, T. (2019) 'New insights into the rainfall variability in the tropical Andes on seasonal and interannual time scales', *Climate Dynamics*, 53(1-2), pp. 405-426.

Seltzer, A.M., Ng, J., Aeschbach, W., Kipfer, R., Kulongoski, J.T., Severinghaus, J.P. and Stute, M. (2021) 'Widespread six degrees Celsius cooling on land during the Last Glacial Maximum', *Nature*, 593(7858), pp. 228-232.

Seltzer, G.O. (1992) 'Late Quaternary glaciation of the Cordillera Real, Bolivia', *Journal of Quaternary Science*, 7(2), pp. 87-98.

Seltzer, G.O., Rodbell, D. and Burns, S. (2000) 'Isotopic evidence for late Quaternary climatic change in tropical South America', *Geology*, 28(1), pp. 35-38.

Shakun, J.D. and Carlson, A.E. (2010) 'A global perspective on Last Glacial Maximum to Holocene climate change', *Quaternary Science Reviews*, 29(15), pp. 1801-1816.

Shakun, J.D., Clark, P.U., He, F., Lifton, N.A., Liu, Z. and Otto-Bliesner, B.L. (2015a) 'Regional and global forcing of glacier retreat during the last deglaciation', *Nature Communications*, 6(1), p. 8059.

Shakun, J.D., Clark, P.U., Marcott, S.A., Brook, E.J., Lifton, N.A., Caffee, M. and Shakun, W.R. (2015b) 'Cosmogenic dating of Late Pleistocene glaciation, southern tropical Andes, Peru', *Journal of Quaternary Science*, 30(8), pp. 841-847.

Sicart, J.E., Hock, R., Ribstein, P. and Chazarin, J.P. (2010) 'Sky longwave radiation on tropical Andean glaciers: parameterization and sensitivity to atmospheric variables', *Journal of Glaciology*, 56(199), pp. 854-860.

Sifeddine, A., Spadano Albuquerque, A.L., Ledru, M.-P., Turcq, B., Knoppers, B., Martin, L., Zamboni de Mello, W., Passenau, H., Landim Dominguez, J.M., Campello Cordeiro, R., Abrão, J.J. and da Silva Pinto Bittencourt, A.l.C. (2003) 'A 21 000 cal years paleoclimatic record from Caçó Lake, northern Brazil: evidence from sedimentary and pollen analyses', *Palaeogeography, Palaeoclimatology, Palaeoecology*, 189(1), pp. 25-34.

Silwal, G., Ammar, M.E., Thapa, A., Bonsal, B. and Faramarzi, M. (2023) 'Response of glacier modelling parameters to time, space, and model complexity: Examples from eastern slopes of Canadian Rocky Mountains', *Science of The Total Environment*, 872, p. 162156.

Sissons, J.B. (1974) 'A Late-Glacial Ice Cap in the Central Grampians, Scotland', *Transactions of the Institute of British Geographers*, (62), pp. 95-114.

Sissons, J.B. (1980) 'The Loch Lomond Advance in the Lake District, northern England', *Transactions of the Royal Society of Edinburgh: Earth Sciences*, 71(1), pp. 13-27.

Skinner, B.J. and Porter, S.C. (1987) *Physical Geology*. Wiley.

Smith, C.A., Lowell, T.V. and Caffee, M.W. (2009) 'Lateglacial and Holocene cosmogenic surface exposure age glacial chronology and geomorphological evidence for the presence of cold-based glaciers at Nevado Sajama, Bolivia', *Journal of Quaternary Science*, 24(4), pp. 360-372.

Smith, C.A., Lowell, T.V., Owen, L.A. and Caffee, M.W. (2011) 'Late Quaternary glacial chronology on Nevado Illimani, Bolivia, and the implications for paleoclimatic reconstructions across the Andes', *Quaternary Research*, 75(1), pp. 1-10.

Smith, J.A., Finkel, R.C., Farber, D.L., Rodbell, D.T. and Seltzer, G.O. (2005a) 'Moraine preservation and boulder erosion in the tropical Andes: interpreting old surface exposure ages in glaciated valleys', *Journal of Quaternary Science*, 20(7-8), pp. 735-758.

Smith, J.A., Mark, B.G. and Rodbell, D.T. (2008) 'The timing and magnitude of mountain glaciation in the tropical Andes', *Journal of Quaternary Science*, 23(6-7), pp. 609-634.

Smith, J.A. and Rodbell, D.T. (2010) 'Cross-cutting moraines reveal evidence for North Atlantic influence on glaciers in the tropical Andes', *Journal of Quaternary Science*, 25(3), pp. 243-248.

Smith, J.A., Seltzer, G.O., Farber, D.L., Rodbell, D.T. and Finkel, R.C. (2005b) 'Early Local Last Glacial Maximum in the Tropical Andes', *Science*, 308(5722), pp. 678 - 681.

Smith, R.J., Mayle, F.E., Maezumi, S.Y. and Power, M.J. (2020) 'Relating pollen representation to an evolving Amazonian landscape between the last glacial maximum and Late Holocene', *Quaternary Research*, pp. 1-17.

Solomina, O., Jomelli, V., Kaser, G., Ames, A., Berger, B. and Pouyaud, B. (2007) 'Lichenometry in the Cordillera Blanca, Peru: "Little Ice Age" moraine chronology', *Global and Planetary Change*, 59(1), pp. 225-235.

Staal, A., Tuinenburg, O.A., Bosmans, J.H.C., Holmgren, M., van Nes, E.H., Scheffer, M., Zemp, D.C. and Dekker, S.C. (2018) 'Forest-rainfall cascades buffer against drought across the Amazon', *Nature Climate Change*, 8(6), pp. 539-543.

Staiger, J.K.W., Gosse, J.C., Johnson, J.V., Fastook, J., Gray, J.T., Stockli, D.F., Stockli, L. and Finkel, R. (2005) 'Quaternary relief generation by polythermal glacier ice', *Earth Surface Processes and Landforms*, 30(9), pp. 1145-1159.

Stansell, N.D., Abbott, M.B., Rull, V., Rodbell, D.T., Bezada, M. and Montoya, E. (2010) 'Abrupt Younger Dryas cooling in the northern tropics recorded in lake sediments from the Venezuelan Andes', *Earth and Planetary Science Letters*, 293(1), pp. 154-163.

Stansell, N.D., Licciardi, J.M., Rodbell, D.T. and Mark, B.G. (2017) 'Tropical ocean-atmospheric forcing of Late Glacial and Holocene glacier fluctuations in the Cordillera Blanca, Peru', *Geophysical Research Letters*, 44(9), pp. 4176-4185.

Stansell, N.D., Mark, B.G., Licciardi, J.M., Rodbell, D.T., Fairman, J.G., Schoessow, F.S., Shutkin, T.Y. and Sorensen, M. (2022) 'Energy mass balance and flow modeling of early Holocene glaciers in the Queshque valley, Cordillera Blanca, Peru', *Quaternary Science Reviews*, 281, p. 107414.

Stansell, N.D., Polissar, P.J. and Abbott, M.B. (2007) 'Last glacial maximum equilibrium-line altitude and paleo-temperature reconstructions for the Cordillera de Mérida, Venezuelan Andes', *Quaternary Research*, 67(1), pp. 115-127.

Stansell, N.D., Polissar, P.J., Abbott, M.B., Bezada, M., Steinman, B.A. and Braun, C. (2014) 'Proglacial lake sediment records reveal Holocene climate changes in the Venezuelan Andes', *Quaternary Science Reviews*, 89, pp. 44-55.

Stansell, N.D., Rodbell, D.T., Abbott, M.B. and Mark, B.G. (2013) 'Proglacial lake sediment records of Holocene climate change in the western Cordillera of Peru', *Quaternary Science Reviews*, 70, pp. 1-14.

Stansell, N.D., Rodbell, D.T., Licciardi, J.M., Sedlak, C.M., Schweinsberg, A.D., Huss, E.G., Delgado, G.M., Zimmerman, S.H. and Finkel, R.C. (2015) 'Late Glacial and Holocene glacier fluctuations at Nevado Huaguruncho in the Eastern Cordillera of the Peruvian Andes', *Geology*, 43(8), pp. 747-750.

Steer, P., Huismans, R.S., Valla, P.G., Gac, S. and Herman, F. (2012) 'Bimodal Plio–Quaternary glacial erosion of fjords and low-relief surfaces in Scandinavia', *Nature Geoscience*, 5(9), pp. 635-639.

Stone, J.O. (2000) 'Air pressure and cosmogenic isotope production', *Journal of Geophysical Research: Solid Earth*, 105(B10), pp. 23753-23759.

Stríkis, N.M., Chiessi, C.M., Cruz, F.W., Vuille, M., Cheng, H., de Souza Barreto, E.A., Mollenhauer, G., Kasten, S., Karmann, I., Edwards, R.L., Bernal, J.P. and Sales, H.d.R. (2015) 'Timing and structure of Mega-SACZ events during Heinrich Stadial 1', *Geophysical Research Letters*, 42(13), pp. 5477-5484A.

Stuefer, M., Rott, H. and Skvarca, P. (2007) 'Glaciar Perito Moreno, Patagonia: climate sensitivities and glacier characteristics preceding the 2003/04 and 2005/06 damming events', *Journal of Glaciology*, 53(180), pp. 3-16.

Sugden, D.E., Bentley, M.J., Fogwill, C.J., Hulton, N.R.J., McCulloch, R.D. and Purves, R.S. (2005) 'Late-Glacial Glacier Events in Southernmost South America: A Blend of 'Northern' and 'Southern' Hemispheric Climatic Signals?', *Geografiska Annaler. Series A, Physical Geography*, 87(2), pp. 273-288.

Sugden, D.E., Hulton, N.R.J. and Purves, R.S. (2002) 'Modelling the inception of the Patagonian icesheet', *Quaternary International*, 95-96, pp. 55-64.

Sutherland, J.L., Carrivick, J.L., Evans, D.J.A., Shulmeister, J. and Quincey, D.J. (2019) 'The Tekapo Glacier, New Zealand, during the Last Glacial Maximum: An active temperate glacier influenced by intermittent surge activity', *Geomorphology*, 343, pp. 183-210.

Sylvestre, F. (2002) 'A high-resolution diatom reconstruction between 21,000 and 17,4000 14C yr BP from the southern Bolivian Altiplano (18–23°S)', *Journal of Paleolimnology*, 27(1), pp. 45-57.

Tadono, T., Ishida, H., Oda, F., Naito, S., Minakawa, K. and Iwamoto, H. (2014) 'Precise Global DEM Generation by ALOS PRISM', *ISPRS Annals of the Photogrammetry, Remote Sensing and Spatial Information Sciences*, II-4, pp. 71-76.

Takeuchi, Y., Naruse, R. and Skvarca, P. (1996) 'Annual air-temperature measurement and ablation estimate at Moreno Glacier, Patagonia', *Bulletin of glacier research*, (14), pp. 23-28.

Tardif, R., Hakim, G.J., Perkins, W.A., Horlick, K.A., Erb, M.P., Emile-Geay, J., Anderson, D.M., Steig, E.J. and Noone, D. (2019) 'Last Millennium Reanalysis with an expanded proxy database and seasonal proxy modeling', *Clim. Past*, 15(4), pp. 1251-1273.

Taylor, L.S., Quincey, D.J., Smith, M.W., Potter, E.R., Castro, J. and Fyffe, C.L. (2022) 'Multi-decadal glacier area and mass balance change in the southern Peruvian Andes', *Frontiers in Earth Science*, 10.

Temovski, M., Madarász, B., Kern, Z., Milevski, I. and Ruszkiczay-Rüdiger, Z. (2018) 'Glacial Geomorphology and Preliminary Glacier Reconstruction in the Jablanica Mountain, Macedonia, Central Balkan Peninsula', *Geosciences*, 8(7), p. 270.

Thackray, G.D. (2008) 'Varied climatic and topographic influences on Late Pleistocene mountain glaciation in the western United States', *Journal of Quaternary Science*, 23(6-7), pp. 671-681.

The PISM authors (2018) 'PISM, a Parallel Ice Sheet Model (Technical Report).'.

Thompson, L.G., Davis, M.E., Mosley-Thompson, E., Sowers, T.A., Henderson, K.A., Zagorodnov, V.S., Lin, P.-N., Mikhalenko, V.N., Campen, R.K., Bolzan, J.F., Cole-Dai,

J. and Francou, B. (1998) 'A 25,000-Year Tropical Climate History from Bolivian Ice Cores', *Science*, 282(5395), pp. 1858-1864.

Thompson, L.G., Mosley-Thompson, E., Bolzan, J.F. and Koci, B.R. (1985) 'A 1500-Year Record of Tropical Precipitation in Ice Cores from the Quelccaya Ice Cap, Peru', *Science*, 229(4717), pp. 971-973.

Thompson, L.G., Mosley-Thompson, E., Brecher, H., Davis, M., León, B., Les, D., Lin, P.-N., Mashiotta, T. and Mountain, K. (2006) 'Abrupt tropical climate change: Past and present', *Proceedings of the National Academy of Sciences*, 103(28), pp. 10536-10543.

Thompson, L.G., Mosley-Thompson, E., Davis, M.E. and Brecher, H.H. (2011) 'Tropical glaciers, recorders and indicators of climate change, are disappearing globally', *Annals of Glaciology*, 52(59), pp. 23-34.

Thompson, L.G., Mosley-Thompson, E., Davis, M.E., Lin, P.N., Henderson, K.A., Cole-Dai, J., Bolzan, J.F. and Liu, K.B. (1995) 'Late glacial stage and holocene tropical ice core records from Huascarán, Peru', *Science*, 269(5220), pp. 46-50.

Thompson, L.G., Mosley-Thompson, E., Davis, M.E., Zagorodnov, V.S., Howat, I.M., Mikhalenko, V.N. and Lin, P.-N. (2013) 'Annually Resolved Ice Core Records of Tropical Climate Variability over the Past ~1800 Years', *Science*, 340(6135), pp. 945-950.

Tierney, J.E., Poulsen, C.J., Montañez, I.P., Bhattacharya, T., Feng, R., Ford, H.L., Hönisch, B., Inglis, G.N., Petersen, S.V., Sagoo, N., Tabor, C.R., Thirumalai, K., Zhu, J., Burls, N.J., Foster, G.L., Goddéris, Y., Huber, B.T., Ivany, L.C., Kirtland Turner, S., Lunt, D.J., McElwain, J.C., Mills, B.J.W., Otto-Bliesner, B.L., Ridgwell, A. and Zhang, Y.G. (2020a) 'Past climates inform our future', *Science*, 370(6517), p. eaay3701.

Tierney, J.E., Zhu, J., King, J., Malevich, S.B., Hakim, G.J. and Poulsen, C.J. (2020b) 'Glacial cooling and climate sensitivity revisited', *Nature*, 584(7822), pp. 569-573.

Tovar, D.S., Shulmeister, J. and Davies, T.R. (2008) 'Evidence for a landslide origin of New Zealand's Waiho Loop moraine', *Nature Geoscience*, 1(8), pp. 524-526.

Trachte, K. (2018) 'Atmospheric Moisture Pathways to the Highlands of the Tropical Andes: Analyzing the Effects of Spectral Nudging on Different Driving Fields for Regional Climate Modeling', *Atmosphere*, 9(11), p. 456.

Treverrow, A., Budd, W.F., Jacka, T.H. and Warner, R.C. (2012) 'The tertiary creep of polycrystalline ice: experimental evidence for stress-dependent levels of strain-rate enhancement', *Journal of Glaciology*, 58(208), pp. 301-314.

Tripati, A.K., Sahany, S., Pittman, D., Eagle, R.A., Neelin, J.D., Mitchell, J.L. and Beaufort, L. (2014) 'Modern and glacial tropical snowlines controlled by sea surface temperature and atmospheric mixing', *Nature Geoscience*, 7(3), pp. 205-209.

Troll, C. (1941) *Studien zur vergleichenden Geographie der Hochgebirge der Erde*. Bonner Universität [Bonn].

Tulaczyk, S., Kamb, W.B. and Engelhardt, H.F. (2000) 'Basal mechanics of Ice Stream B, west Antarctica: 1. Till mechanics', *Journal of Geophysical Research: Solid Earth*, 105(B1), pp. 463-481.

Úbeda, J., Bonshoms, M., Iparraguirre, J., Sáez, L., De la Fuente, R., Janssen, L., Concha, R., Vásquez, P. and Masías, P. (2018) 'Prospecting Glacial Ages and Paleoclimatic Reconstructions Northeastward of Nevado Coropuna (16° S, 73° W, 6377 m), Arid Tropical Andes', *Geosciences*, 8(8), p. 307.

Úbeda, J., Palacios, D. and Vázquez-Selem, L. (2009) 'Reconstruction of Equillbrium Line Altitudes of Nevado Coropuna Glaciers (Southern Peru) from the late Pleistocene to present.', *EGU General Assembly 2009*. Viena.

van der Hammen, T., Werner, J.H. and van Dommelen, H. (1973) 'Palynological record of the upheaval of the Northern Andes: A study of the pliocene and lower quaternary of the Colombian Eastern Cordillera and the early evolution of its high-Andean biota', *Review of Palaeobotany and Palynology*, 16(1), pp. 1-122.

Veettil, B.K. (2012) 'Three decadal monitoring of mountain glaciers in Ecuador - A case study on ENSO impact on Andean glaciers: A Remote sensing perspective', *International Journal of Geomatics and Geosciences*, 3(1), pp. 269-284.

Veettil, B.K. and Kamp, U. (2019) 'Global Disappearance of Tropical Mountain Glaciers: Observations, Causes, and Challenges', *Geosciences*, 9(5).

Veettil, B.K., Wang, S., Florêncio de Souza, S., Bremer, U.F. and Simões, J.C. (2017) 'Glacier monitoring and glacier-climate interactions in the tropical Andes: A review', *Journal of South American Earth Sciences*, 77, pp. 218-246.

Vélez, M.I., Hooghiemstra, H., Metcalfe, S., Martínez, I. and Mommersteeg, H. (2003) 'Pollen- and diatom based environmental history since the Last Glacial Maximum from the Andean core Fúquene-7, Colombia', *Journal of Quaternary Science*, 18(1), pp. 17-30.

Vieira, F. and Hamza, V. (2019) 'Assessment of Geothermal Resources of South America - A New Look', *International Journal of Terrestrial Heat Flow and Applied Geothermics*, 2(1), pp. 46-57.

Vilímek, V., Klimeš, J. and Červená, L. (2016) 'Glacier-related landforms and glacial lakes in Huascarán National Park, Peru', *Journal of Maps*, 12(1), pp. 193-202.

Vizy, E.K. and Cook, K.H. (2007) 'Relationship between Amazon and high Andes rainfall', *Journal of Geophysical Research*, 112(D7), p. D07107.

Vuille, M., Francou, B., Wagnon, P., Juen, I., Kaser, G., Mark, B.G. and Bradley, R.S. (2008) 'Climate change and tropical Andean glaciers: Past, present and future', *Earth-Science Reviews*, 89(3-4), pp. 79-96.

Waller, R.I. (2001) 'The influence of basal processes on the dynamic behaviour of cold-based glaciers', *Quaternary International*, 86(1), pp. 117-128.

Wang, X., Edwards, R.L., Auler, A.S., Cheng, H., Kong, X., Wang, Y., Cruz, F.W., Dorale, J.A. and Chiang, H.-W. (2017) 'Hydroclimate changes across the Amazon lowlands over the past 45,000 years', *Nature*, 541(7636), pp. 204-207.

Weertman, J. (1973) 'Position of Ice Divides and Ice Centers on Ice Sheets', *Journal of Glaciology*, 12(66), pp. 353-360.

Weertman, J. (1983) 'Creep deformation of ice', *Annual Review of Earth and Planetary Sciences*, 11(1), pp. 215-240.

Weis, M., Greve, R. and Hutter, K. (1999) 'Theory of shallow ice shelves', *Continuum Mechanics and Thermodynamics*, 11(1), pp. 15-50.

Wilson, P. and Clark, R. (1998) 'Characteristics and implications of some Loch Lomond Stadial moraine ridges and later landforms, eastern Lake District, northern England', *Geological Journal*, 33(2), pp. 73-87.

Winkelmann, R., Martin, M.A., Haseloff, M., Albrecht, T., Bueler, E., Khroulev, C. and Levermann, A. (2011) 'The Potsdam Parallel Ice Sheet Model (PISM-PIK) – Part 1: Model description', *The Cryosphere*, 5(3), pp. 715-726.

Winkler, M., Juen, I., Mölg, T., Wagnon, P., Gómez, J. and Kaser, G. (2009) 'Measured and modelled sublimation on the tropical Glaciar Artesonraju, Perú', *The Cryosphere*, 3(1), pp. 21-30.

Wolff, I.W., Glasser, N.F., Harrison, S., Wood, J.L. and Hubbard, A. (2023) 'A steady-state model reconstruction of the patagonian ice sheet during the last glacial maximum', *Quaternary Science Advances*, 12, p. 100103.

Woo, M.-K. and Fitzharris, B.B. (1992) 'Reconstruction of Mass Balance Variations for Franz Josef Glacier, New Zealand, 1913 to 1989', *Arctic and Alpine Research*, 24(4), pp. 281-290.

Wright, A.P., Wadham, J.L., Siegert, M.J., Luckman, A., Kohler, J. and Nuttall, A.M. (2007) 'Modeling the refreezing of meltwater as superimposed ice on a high Arctic glacier: A comparison of approaches', *Journal of Geophysical Research: Earth Surface*, 112(F4).

Wright, H.E. (1983) 'Late-Pleistocene Glaciation and Climate around the Junín Plain, Central Peruvian Highlands', *Geografiska Annaler. Series A, Physical Geography*, 65(1/2), p. 35.

Wright, H.E. (1984) 'Late glacial and late Holocene moraines in the Cerros Cuchpanga, central Peru', *Quaternary Research*, 21(3), pp. 275-285.

Wunderling, N., Willeit, M., Donges, J.F. and Winkelmann, R. (2020) 'Global warming due to loss of large ice masses and Arctic summer sea ice', *Nature Communications*, 11(1), p. 5177.

Yan, Q., Owen, L.A., Wang, H. and Zhang, Z. (2018) 'Climate Constraints on Glaciation Over High-Mountain Asia During the Last Glacial Maximum', *Geophysical Research Letters*, 45(17), pp. 9024-9033.

Yan, Q., Wei, T. and Zhang, Z. (2022) 'Modeling the climate sensitivity of Patagonian glaciers and their responses to climatic change during the global last glacial maximum', *Quaternary Science Reviews*, 288, p. 107582.

Yan, Q., Wei, T. and Zhang, Z. (2023) 'Modeling the timing and extent of glaciations over southeastern Tibet during the last glacial stage', *Palaeogeography, Palaeoclimatology, Palaeoecology*, 610, p. 111336.

Yarleque, C., Vuille, M., Hardy, D.R., Timm, O.E., De la Cruz, J., Ramos, H. and Rabatel, A. (2018) 'Projections of the future disappearance of the Quelccaya Ice Cap in the Central Andes', *Scientific Reports*, 8(1), p. 15564.

Žebre, M., Sarıkaya, M.A., Stepišnik, U., Colucci, R.R., Yıldırım, C., Çiner, A., Candaş, A., Vlahović, I., Tomljenović, B., Matoš, B. and Wilcken, K.M. (2021) 'An early glacial maximum during the last glacial cycle on the northern Velebit Mt. (Croatia)', *Geomorphology*, 392, p. 107918.

Zech, R., Kull, C., Kubik, P.W. and Veit, H. (2007) 'LGM and late glacial glacier advances in the Cordillera Real and Cochabamba (Bolivia) deduced from ^{10}Be surface exposure dating', *Climate of the Past*, 3(4), pp. 623-635.

Zekollari, H., Huss, M., Farinotti, D. and Lhermitte, S. (2022) 'Ice-Dynamical Glacier Evolution Modeling—A Review', *Reviews of Geophysics*, 60(2), p. e2021RG000754.

Zemp, M., Huss, M., Thibert, E., Eckert, N., McNabb, R., Huber, J., Barandun, M., Machguth, H., Nussbaumer, S.U., Gärtner-Roer, I., Thomson, L., Paul, F., Maussion, F., Kutuzov, S. and Cogley, J.G. (2019) 'Global glacier mass changes and their contributions to sea-level rise from 1961 to 2016', *Nature*, 568(7752), p. 382.

Ziemen, F.A., Hock, R., Aschwanden, A., Khroulev, C., Kienholz, C., Melkonian, A. and Zhang, J. (2016) 'Modeling the evolution of the Juneau Icefield between 1971 and 2100 using the Parallel Ice Sheet Model (PISM)', *Journal of Glaciology*, 62(231), pp. 199-214.